

UNIVERSITÀ DEGLI STUDI DELL'INSUBRIA
FACOLTÀ DI SCIENZE FISICHE
DIPARTIMENTO DI SCIENZA E ALTA TECNOLOGIA

DOTTORATO DI RICERCA IN FISICA ED ASTROFISICA – XXIX CICLO

Observing neutron stars at the magnetic extremes

Francesco Coti Zelati

Supervisors:	Prof. A. Treves Dr. S. Campana Dr. N. Rea	Università degli Studi dell'Insubria INAF – Osservatorio astronomico di Brera University of Amsterdam
Reviewers:	Dr. N. Bucciantini Dr. J. W. T. Hessels	INAF – Osservatorio Astrofisico di Arcetri University of Amsterdam
Committee:	Prof. T. Di Salvo Prof. F. Haardt Dr. J. W. T. Hessels Prof. R. Turolla	Università degli Studi di Palermo Università degli Studi dell'Insubria University of Amsterdam Università degli Studi di Padova



The research reported in this thesis was carried out in part at the Osservatorio Astronomico di Brera of the Italian National Institute for Astrophysics (INAF – OAB) and at the Astronomical Institute ‘Anton Pannekoek’ of the University of Amsterdam. This thesis was supported by an Italian PhD fellowship of the University of Insubria, a Vidi award of the Netherlands Organization for Scientific Research and the European Cooperation in Science and Technology Action MP1304 ‘Exploring fundamental physics with compact stars’ (NewCompStar).

Cover image:

The core of the Milky Way over Grigna Meridionale.

© E. Borghese / NASA / Chandra X-ray Center Press Office

To Enrica, Enrico, Michele

Summary

This thesis comprises new results on the emission phenomena associated with neutron stars. Neutron stars represent one of the possible final evolutionary stages of the gravitational collapse of massive stars, and are the densest objects directly observable in our Universe. They hence constitute prime astrophysical laboratories to study the properties of matter under the most extreme physical conditions: immense gravitational fields, ultra-strong magnetic fields, vigorous radiation fields, and supra-nuclear densities. Moreover, a magnetized neutron star orbiting a companion star in a binary system constitutes an unmatched opportunity to investigate the nature of the interaction between plasma accreting onto astrophysical objects and magnetic fields, undoubtedly an issue of paramount concern in current astrophysical research. The specific targets of this thesis are magnetars and transitional millisecond pulsars.

- Magnetars represent a subclass of isolated neutron stars whose X-ray emission is thought to be ultimately powered by the instability and dissipation of their exceptionally large magnetic field (up to $10^{14} - 10^{15}$ Gauss at the surface). About half of the 23 known magnetars have been observed over many years at a relatively steady X-ray luminosity of $\sim 10^{35} - 10^{36}$ erg s $^{-1}$. Other sources spend most of their time at a much lower luminosity, and unpredictably undergo large and rapid enhancements of the persistent X-ray flux (typically by a factor of $\sim 10 - 1000$ above that in quiescence and up to values comparable to those of the persistently bright magnetars), which then decline and attain the pre-outburst level ($\sim 10^{32} - 10^{33}$ erg s $^{-1}$) on a timescale ranging from a few weeks up to several years. Although it is widely accepted that these outbursts are attributable to some form of heat deposition in a spatially confined region of the star surface which then cools, the mechanism responsible for their activation and the energy reservoir responsible for sustaining their long-term emission still remain somewhat elusive. This thesis aims at gathering new insights on the physics of magnetars through the study of their X-ray outbursts, from the very first active phases throughout the decay.

Chapter 2 is devoted to the study of magnetar SGR 1745–2900. Discovered in 2013 April via its bursting activity in the hard X-/soft gamma-ray energy range at an angular distance of only 2.4 arcsec from the 4-million-solar mass black hole at the centre of the Milky Way, SGR 1745–2900 holds the record as the closest neutron star to a black hole observed to date. The bursting activity coincided with an abrupt enhancement of the persistent X-ray luminosity, up to a few 10^{35} erg s $^{-1}$, marking the onset of a major outburst. Since then, SGR 1745–2900 has been regularly observed in the X-rays by the *Chandra* (26 times) and *XMM-Newton* (8 times) satellites. A detailed analysis of the magnetar X-ray properties during the first 500 days of its outburst (up to 2014 September) unveiled a unique behavior: the decay of its X-ray flux is indeed extremely slow if compared to other magnetar outbursts, and it is challenging the neutron star crustal cooling models successfully applied to other outburst decays. This study provides the compelling observational evidence that, at least in this magnetar, a substantial contribution to the prolonged high luminosity comes from physical processes operating outside the neutron star, presumably from the

bombardment onto its surface of currents of charged particles in a twisted magnetosphere.

Chapter 3 discusses the study of the source 1E 161348–5055, a member of the small and heterogeneous family of central compact objects. These are X-ray emitting neutron stars located close to the geometrical centre of shell-like supernova remnants, with no associated nebulae and counterparts at other wavelengths. On 2016 June 22, a short burst of hard X-rays was detected by the *Swift* satellite from the direction of 1E 161348–5055 at the centre of the supernova remnant RCW103, which corresponded to a major enhancement of its persistent X-ray flux. Observations of this outburst were carried out soon after with the X-ray instruments aboard the *Chandra*, *NuSTAR* and *Swift* satellites. The duration and spectral decomposition of the burst, the discovery of a hard X-ray tail in the spectrum, and the long-term outburst history (from 1999 to 2016 July) point towards a magnetar classification for this source. In this context, the well-known modulation of the X-ray emission at a period of 6.67 hr can only be interpreted as the rotation period of a strongly magnetized neutron star: 1E 161348–5055 represents the slowest pulsar ever detected, with a spin period orders of magnitude longer than those of ordinary pulsars. With an estimated age of about 2000 years, 1E 161348–5055 cannot have slowed down to its current period via rotational energy loss alone. A scenario invoking the fall back onto the neutron star magnetosphere of debris of material ejected soon after the supernova explosion may justify the considerable spin-down measured for this object in our recent observations.

Chapter 4 deals with SGR J1935+2154, a recently discovered member of the magnetar class, and the extensive monitoring campaign carried out between 2014 July and 2015 March with *Chandra* and *XMM–Newton*. We discovered the spin period of SGR J1935+2154 through the detection of coherent pulsations at a period of about 3.24 s, and inferred the main parameters of this source via detailed timing analysis. This magnetar is characterized by a dipolar magnetic field of $\sim 2.2 \times 10^{14}$ Gauss at the surface, an age of about 3600 years and releases rotational energy at a rate of about 1.7×10^{34} erg s⁻¹. The source showed moderate long-term variability, with a decay in the X-ray flux of ~ 25 per cent during the first 4 months since its discovery, and a re-brightening of the same amount during the ensuing 4 months. We also unveiled diffuse emission around the source, constant in flux and extending from about 1 arcsec up to at least 1 arcmin. Although a scattering halo seems to be a likely explanation for the diffuse emission, the possibility that part, if not all, of this component is due to a pulsar wind nebula cannot be ruled out.

Chapter 5 is focused on the magnetar XTE J1810–197, the first to have shown a major X-ray outburst as well as radio emission pulsed at its spin period. We analyzed *XMM–Newton* and *Chandra* observations of this source covering more than 11 years from the initial phases of the outburst in 2003 to the current quiescent level. The spin down rate of this pulsar was highly variable during the outburst decay and more stable during quiescence, a result in agreement with the behavior expected if the outburst of XTE J1810–197 was due to a magnetospheric twist.

Chapter 6 reports the discovery of a narrow and strongly phase-variable absorption feature in the spectrum of an X-ray dim isolated neutron star (XDINS). The XDINSs form a group of seven nearby ($\lesssim 500$ parsec) X-ray pulsars characterized by spin periods in the

3–12 s range, very soft quasi-thermal spectra, X-ray luminosity of 10^{30} – 10^{33} erg s⁻¹, faint optical counterparts, and absence of radio emission. This discovery represents the result of a systematic and careful search for absorption features in all archival observations of XDINSs performed with *XMM-Newton* (for a total of about 100 observations). The absorption line was detected by means of a detailed phase-resolved spectroscopy of the data collected during 20 *XMM-Newton* observations between 2000 May and 2012 September, and appears to be stable over this timespan. This feature, if interpreted as the result of proton resonant cyclotron absorption and/or scattering in a confined magnetic structure close to the stellar surface, provides the first clear demonstration for the existence of non-purely-dipolar magnetic field configurations near the surface of these neutron stars. These are not totally unexpected in the XDINSs, since the estimated magnetic fields of these sources, $\sim 10^{13}$ – 10^{14} Gauss at the surface, and recent evolutionary models, strongly suggest that they are likely the descendants of magnetars.

Chapter 7 concerns an overall systematic analysis of the spectral properties of magnetars outbursts, from the very first active phases throughout the decay. In particular, we report the results of the spectral modelling for 18 magnetar outbursts through a reduction and reanalysis of data of more than 800 X-ray observations, we track the temporal evolution of the flux and luminosity for all these events, and investigate the anti-correlation between the maximum flux increase reached during these episodes and the source quiescent X-ray flux. We model empirically the decays of the bolometric luminosities, and estimate the characteristics decay time scales and the total energetics involved.

- Transitional millisecond pulsars in binary systems are neutron stars rotating at a period of a few milliseconds which undergo rapid transitions between three states: a bright (X-ray luminosity $> 10^{36}$ erg s⁻¹) X-ray pulsar regime powered by the accretion onto the neutron star surface of matter transferred by the companion star through an accretion disk; a radio (and possibly gamma-ray) pulsar regime powered by the energy loss due to the fast rotation of the neutron star magnetic field (about 10^8 – 10^9 Gauss at the surface) and characterized by a lower X-ray luminosity ($\sim 10^{32}$ erg s⁻¹); an intermediate ($\sim 10^{34}$ erg s⁻¹) accretion regime in which an accretion disk is present around the neutron star, and matter accretes only intermittently onto the neutron star surface owing to the onset of a magnetospheric centrifugal barrier. The transitions between the three regimes take place on short time-scales of less than a few weeks, and are interpreted within some simplified scenarios in terms of variations of the inward pressure exerted by the in-flowing matter onto the rotating magnetosphere of the neutron star, causing the boundary between the disk and the magnetosphere to expand and contract. However, the driver of the variations of the mass in-flow rates has not been identified yet. Transitional pulsars offer a unique and ideal observational test bed of theory and modelling of the coupling between accretion disks and magnetic fields, and can be used to probe how the accretion/ejection cycles observed in a variety of astrophysical contexts operate in systems with well established physical parameters (e.g., the neutron star spin period and magnetic field).

Chapter 8 is dedicated to the transitional millisecond pulsar PSR J1023+0038, and is structured in two parts. We first present a comprehensive multi-wavelength study of the system following the formation of an accretion disk around the neutron star, in 2013 June. We show how the emission properties of the system could be interpreted in terms of an engulfed radio pulsar: the neutron star could be active as a radio pulsar, but was undetected in the radio band due to a large amount of ionized material surrounding the compact object. However, more recently, several deep *XMM-Newton* observations disclosed a puzzling trimodal behavior in the soft X-rays: PSR J1023+0038 spends about 70–80 per cent of the time in a stable ‘high’ mode (with 0.3–10 keV luminosity of $\sim 3 \times 10^{33}$ erg s⁻¹), which unpredictably alternates to a ‘low’ mode (for about 20 per cent of the time), where the 0.3–10 keV luminosity drops to $\sim 5 \times 10^{32}$ erg s⁻¹. Sporadic, brighter flaring episodes are also observed reaching luminosities of the order of $\sim 10^{34}$ erg s⁻¹. The switches between these modes occur on a timescale of tens of seconds. Prompted by this discovery, we developed and put forward a plausible physical scenario for the observed transitions. In particular, we interpreted the repeated switches between the high and low X-ray modes in terms of fast swings between the propeller and radio pulsar regimes, and showed how this model could satisfactorily reproduce the X-ray spectral properties of the different modes.

- Observational studies were also conducted on two additional X-ray sources. Appendix A concerns the multiwavelength study of the source RX J2015.6+3711. This was tentatively classified as a cataclysmic variable, namely a binary system where a white dwarf accretes from a low-mass companion. However, its spatial coincidence with a gamma-ray source had opened the possibility that it may belong to the class of transitional millisecond pulsars in the intermediate accretion phase. We clinched the case via a detailed timing and spectral analysis of data acquired during a deep *XMM-Newton* observation of the field, as well as of archival X-ray and UV/optical pointings. All the observed X-ray and UV properties nailed down the source as a magnetic cataclysmic variable. In particular, we detected a coherent X-ray modulation at a period of 2 hr, which we interpreted as the spin period of the white dwarf. On the other hand, the GeV emission is most likely related to the other X-ray source spatially compatible with the gamma-ray source, which has already been identified as a blazar in the literature.

Appendix B is a report on the identification of the newly discovered transient source Swift J174540.7–290015. This turned on in the X-rays on 2016 February 6, at only 16 arcsec from the supermassive black hole at the centre of the Milky Way. We observed the field around the source once with *XMM-Newton* and repeatedly with *Swift* and *INTEGRAL*. On February 26 the source was detected in a soft state characterised by a low level of variability and a soft X-ray thermal spectrum with a high column density of neutral absorbing material and a high energy tail, up to ~ 50 keV. We found no evidence for X-ray periodicities nor radio counterparts to Swift J174540.7–290015. The location of the transient was observed also in the near infrared before and after the onset of the outburst: numerous objects are positionally coincident with the transient, but none of them show marked variations of their brightness. We identified this source either as an accreting neutron star or black hole in a low-mass X-ray binary system.

Riassunto

Questa tesi include nuovi risultati sui fenomeni di emissione associati alle stelle di neutroni. Le stelle di neutroni rappresentano uno dei possibili stadi evolutivi finali del collasso gravitazionale di stelle massive e sono gli oggetti più densi direttamente osservabili nel nostro Universo. Costituiscono pertanto eccellenti laboratori astrofisici per studiare le proprietà della materia nelle condizioni fisiche più estreme: immensi campi gravitazionali, potentissimi campi magnetici, forti campi radiativi e densità sovra-nucleari. Inoltre una stella di neutroni magnetica in orbita attorno ad una stella compagna in un sistema binario costituisce un'opportunità unica per studiare la natura dell'interazione tra il plasma in accrescimento su oggetti astrofisici e i campi magnetici, senza dubbio un argomento di primaria importanza nell'attuale ricerca astrofisica. Nello specifico, questa tesi si occupa delle magnetar e delle cosiddette 'pulsar al millisecondo in fase di transizione'.

- Le magnetar rappresentano una sottoclasse di stelle di neutroni isolate la cui emissione in X è fondamentalmente alimentata dall'instabilità e dalla dissipazione del loro campo magnetico eccezionalmente alto (fino a $10^{14} - 10^{15}$ Gauss alla superficie). Circa metà delle 23 magnetar ad oggi note sono state osservate nel corso di parecchi anni ad una luminosità X relativamente stabile, circa $\sim 10^{35} - 10^{36}$ erg s⁻¹. Altre sorgenti trascorrono la maggior parte del loro tempo ad un livello di luminosità molto più basso e in modo imprevedibile aumentano notevolmente e rapidamente in flusso (tipicamente di un fattore $\sim 10 - 1000$ al di sopra del livello quiescente e fino a valori comparabili a quelli delle sorgenti persistentemente luminose) per poi diminuire e raggiungere il livello antecedente all'outburst ($\sim 10^{32} - 10^{33}$ erg s⁻¹) su tempi scala che vanno da alcune settimane a parecchi anni. Sebbene sia ampiamente accettato che questi outburst siano attribuibili ad una forma di deposizione di calore in una regione ristretta della superficie della stella che successivamente si raffredda, il meccanismo responsabile per la loro attivazione e la riserva di energia responsabile per sostenere la loro emissione a lungo termine rimangono ancora per certi versi elusivi. Questa tesi ha lo scopo di comprendere in maggior dettaglio la fisica delle magnetar attraverso lo studio dei loro outburst in X, dalle prime fasi attive e nel corso del decadimento.

Il Capitolo 2 è dedicato allo studio della magnetar SGR 1745–2900. Scoperta in aprile 2013 attraverso la sua attività di burst nei raggi X duri ad una distanza angolare di soli 2.4 arcsec dal buco nero supermassivo al centro della Via Lattea, SGR 1745–2900 detiene il record della stella di neutroni più vicina ad un buco nero ad oggi nota. I burst si sono accompagnati ad un aumento repentino della luminosità X persistente, fino a 10^{35} erg s⁻¹, segnalando l'inizio di un outburst. Da quel momento in poi, SGR 1745–2900 è stata regolarmente osservata nei raggi X dai satelliti *Chandra* (26 volte) e *XMM-Newton* (8 volte). Un'analisi dettagliata delle proprietà nella banda X della magnetar nel corso dei primi 500 giorni dell'outburst (fino a settembre 2014) ha svelato un comportamento unico: il decadimento del flusso X è infatti estremamente lento se paragonato ad altri outburst di magnetar e sta mettendo alla prova i modelli di raffreddamento della crosta di stelle di neutroni applicati con successo ad altri decadimenti di outburst. Questo studio fornisce

un'efficace evidenza osservativa che, almeno per questa magnetar, un contributo sostanziale alla prolungata alta luminosità sia dovuto a processi fisici che operano al di fuori della stella di neutroni, presumibilmente dal bombardamento sulla sua superficie di correnti di particelle cariche in moto lungo le linee di campo attorcigliate nella magnetosfera.

Il Capitolo 3 riguarda lo studio della sorgente 1E 161348–5055, un membro della classe degli oggetti compatti centrali. Si tratta di stelle di neutroni che emettono in banda X, sono collocate vicino al centro geometrico di resti di supernova e non sono associate a nebulose o a controparti ad altre lunghezze d'onda. Il 22 giugno 2016, un breve burst nei raggi X duri è stato rivelato dal satellite *Swift* dalla direzione di 1E 161348–5055 al centro del resto di supernova RCW103 ed è stato accompagnato da un aumento del flusso persistente in X della sorgente. Osservazioni di questo outburst sono state effettuate subito dopo con gli strumenti per raggi X a bordo dei satelliti *Chandra*, *NuSTAR* e *Swift*. La durata e la decomposizione spettrale del burst, la scoperta di una coda nei raggi X duri nello spettro e la curva di luce a lungo termine (dal 1999 al mese di luglio 2016) suggeriscono fortemente che la sorgente sia una magnetar. In questo contesto, la ben nota modulazione dell'emissione X ad un periodo di 6.67 ore può essere interpretata unicamente come il periodo di rotazione di una stella di neutroni estremamente magnetica: 1E 161348–5055 rappresenta la pulsar più lenta mai osservata, con un periodo di rotazione ordini di grandezza più alto di quello delle pulsar ordinarie. Con un'età stimata intorno ai 2000 anni, 1E 161348–5055 non può aver rallentato e aver raggiunto il suo periodo di rotazione attuale esclusivamente attraverso la perdita di energia rotazionale. Uno scenario in base al quale detriti di materiale espulsi nel corso dell'esplosione di supernova si sono successivamente accumulati sulla magnetosfera della stella di neutroni, letteralmente 'arrestandola', potrebbe giustificare il rallentamento considerevole della rotazione misurato per questo oggetto nel corso delle nostre recenti osservazioni.

Il Capitolo 4 tratta di SGR J1935+2154, un membro recentemente scoperto della classe delle magnetar, e dell'estesa campagna osservativa effettuata tra luglio 2014 e marzo 2015 con *Chandra* e *XMM-Newton*. Abbiamo scoperto il periodo di rotazione di SGR J1935+2154 attraverso la rivelazione di pulsazioni coerenti ad un periodo di circa 3.24 s e abbiamo determinato i parametri principali di questa sorgente attraverso un'analisi dettagliata delle sue proprietà temporali. Questa magnetar è caratterizzata da un campo magnetico dipolare di circa 2.2×10^{14} Gauss alla superficie, un'età di circa 3600 anni, e realizza energia rotazionale ad un tasso di circa 1.7×10^{34} erg s⁻¹. La sorgente ha mostrato variabilità moderata a lungo termine, con un decadimento nel flusso X del 25 per cento circa nel corso dei primi 4 mesi a partire dalla sua scoperta, e un nuovo aumento in flusso dello stesso fattore nel corso dei 4 mesi seguenti. Abbiamo anche scoperto emissione diffusa attorno alla sorgente, costante in flusso ed estesa da circa 1 arcsec fino ad almeno 1 arcmin. Sebbene un alone di scattering sembri una spiegazione probabile per l'emissione diffusa, rimane aperta la possibilità che parte di questa componente (se non tutta) sia dovuta ad una nebulosa alimentata dal vento della pulsar.

Il Capitolo 5 è incentrato sulla magnetar XTE J1810–197, la prima ad aver mostrato un outburst nei raggi X e così pure emissione radio modulata al suo periodo di rotazione.

Abbiamo analizzato osservazioni con *XMM–Newton* e *Chandra* di questa sorgente effettuate a partire dalle fasi iniziali dell’outburst nel 2003 fino all’attuale livello quiescente. Il tasso di rallentamento del periodo di rotazione di questa pulsar è risultato altamente variabile durante il decadimento dell’outburst e più stabile nel corso della quiescenza, un risultato in accordo con il comportamento atteso se l’outburst di XTE J1810–197 si fosse verificato a causa di un attorcigliamento significativo delle linee di campo magnetico nella magnetosfera.

Il Capitolo 6 riporta la scoperta di una peculiare linea in assorbimento fortemente variabile con la fase rotazionale nello spettro di una stella di neutroni isolata e debole nei raggi X (XDINS). Le XDINS formano un gruppo di 7 pulsar X relativamente vicine ($\lesssim 500$ parsec) e sono caratterizzate da periodi di rotazione nell’intervallo 3–12 s, spettri quasi termici e molto soffici in banda X, luminosità X di 10^{30} – 10^{33} erg s $^{-1}$, deboli controparti ottiche e assenza di emissione nella banda radio. Questa scoperta rappresenta il risultato di una ricerca sistematica di linee in assorbimento in tutte le osservazioni in archivio delle XDINS effettuate con *XMM–Newton* (per un totale di circa 100 osservazioni). La linea in assorbimento è stata rivelata per mezzo di una dettagliata analisi spettrale risolta in fase dei dati acquisiti durante 20 osservazioni con *XMM–Newton* tra maggio 2000 e settembre 2012 e appare stabile nel corso di questo periodo. Questa linea, se interpretata come il risultato dell’assorbimento di ciclotrone risonante da protoni e/o come scattering in una ristretta struttura magnetica vicino alla superficie della stella, fornisce la prima evidenza dell’esistenza di configurazioni del campo magnetico non puramente dipolari vicino alla superficie di queste stelle di neutroni. Queste non sono tuttavia inaspettate nelle XDINS, dal momento che i campi magnetici stimati per queste sorgenti, circa 10^{13} – 10^{14} Gauss alla superficie, e recenti modelli evolutivi, suggeriscono fortemente che esse rappresentino probabilmente i discendenti delle magnetar.

Il Capitolo 7 contiene un’analisi sistematica delle proprietà spettrali degli outburst di magnetar, dalle prime fasi attive e nel corso del decadimento. Abbiamo riportato in particolare i risultati della modellizzazione degli spettri di 18 outburst dopo aver ridotto e rianalizzato dati di oltre 800 osservazioni in X. Abbiamo seguito l’evoluzione temporale del flusso e della luminosità per tutti questi eventi e studiato l’anticorrelazione esistente tra il massimo aumento in flusso raggiunto durante questi episodi e il flusso X quiescente della sorgente. Abbiamo modellizzato in maniera empirica i decadimenti delle luminosità bolometriche e stimato i tempi scala di decadimento caratteristici e l’energia totale coinvolta.

- Le pulsar al millisecondo in fase di transizione sono stelle di neutroni appartenenti a sistemi binari che ruotano a periodi dell’ordine dei millisecondi e che effettuano rapide transizioni tra tre stati: un regime di pulsar X (con luminosità X $> 10^{36}$ erg s $^{-1}$) alimentato dall’accrescimento sulla superficie della stella di neutroni di materia trasferita dalla stella compagna attraverso un disco di accrescimento; un regime di pulsar radio (e possibilmente gamma) alimentato dalla perdita di energia dovuta alla veloce rotazione del campo magnetico della stella di neutroni (circa 10^8 – 10^9 Gauss alla superficie), che espelle la materia trasferita dalla compagna (la luminosità X è circa 10^{32} erg s $^{-1}$); una fase

intermedia di accrescimento (con luminosità X di circa 10^{34} erg s⁻¹) in cui è presente il disco di accrescimento, ma parte della materia non accresce sulla superficie della stella di neutroni per via dell'attivazione di una barriera centrifuga nella magnetosfera (propeller). Le transizioni hanno luogo su tempi scala che vanno dalle decine dei secondi fino ad alcune settimane e sono interpretate (in alcuni scenari semplificati) in termini di variazioni della pressione esercitata dalla materia in accrescimento sulla magnetosfera rotante della stella di neutroni, con conseguente spostamento del confine tra il disco e la magnetosfera. Ad ogni modo, la causa delle variazioni del tasso di accrescimento di massa non è stata ancora identificata. Le pulsar in fase di transizione offrono un banco di prova osservativo unico ed ideale per la teoria e la modellizzazione dell'interazione tra i dischi di accrescimento e i campi magnetici, e possono essere utilizzate per esplorare come i processi di accrescimento ed espulsione di materia osservati in numerosi contesti astrofisici si alternano in sistemi con parametri fisici noti (come il periodo di rotazione della stella di neutroni, il suo campo magnetico ed il tasso di accrescimento di massa). Questa tesi si focalizza sulla caratterizzazione a più lunghezze d'onda e sulla modellizzazione di una pulsar in fase di transizione ad oggi tra le più studiate.

Il Capitolo 8 è dedicato alla pulsar al millisecondo in fase di transizione PSR J1023+0038 ed è strutturato in due parti. Abbiamo presentato dapprima uno studio esauriente del sistema su più lunghezze d'onda e successivamente alla formazione di un disco di accrescimento attorno alla stella di neutroni, nel giugno 2013. Abbiamo mostrato come le proprietà di emissione del sistema potessero essere interpretate in termini di una pulsar radio 'ingolfata': la stella di neutroni potrebbe essere attiva come una pulsar radio, ma non essere rivelata nel radio per via di una gran quantità di materiale ionizzato attorno all'oggetto compatto. Tuttavia, più recentemente, parecchie osservazioni lunghe con *XMM-Newton* hanno rivelato un comportamento bizzarro nei raggi X soffici: PSR J1023+0038 trascorre circa il 70–80 per cento del suo tempo in uno stato stabile 'alto' (con una luminosità nel range 0.3–10 keV di circa 3×10^{33} erg s⁻¹) che si alterna in maniera imprevedibile ad uno stato 'basso' (per circa il 20 per cento del tempo), dove la luminosità 0.3–10 keV scende ad un valore di circa 5×10^{32} erg s⁻¹. Si osservano anche episodi di aumenti repentini e sporadici in flusso, con luminosità dell'ordine di 10^{34} erg s⁻¹. Le transizioni tra questi stati si verificano su tempi scala delle decine dei secondi. In seguito a questa scoperta, abbiamo sviluppato e proposto uno scenario fisico plausibile per le transizioni osservate tra gli stati alto e basso in termini di cambiamenti rapidi tra i regimi di propeller e di pulsar radio. Abbiamo inoltre mostrato come questo modello può riprodurre in maniera soddisfacente le proprietà spettrali in X nei differenti stati.

- Sono stati condotti studi osservativi anche su due ulteriori sorgenti. L'Appendice A tratta dello studio su più lunghezze d'onda della sorgente RX J2015.6+3711. Questa è stata provvisoriamente classificata come una variabile cataclismica, ovvero un sistema binario in cui una nana bianca accresce materia da una stella compagna di bassa massa. Tuttavia, la sua posizione compatibile con una sorgente gamma ha aperto la possibilità che essa potesse invece appartenere alla classe delle pulsar al millisecondo in fase di transizione nella fase intermedia di accrescimento. Abbiamo chiuso il caso attraverso un'analisi

dettagliata delle proprietà temporali e spettrali di dati acquisiti durante un'osservazione profonda del campo con *XMM-Newton* e puntamenti in X, ultravioletto e ottico in archivio. Tutte le proprietà osservate puntano ad una classificazione della sorgente come una variabile cataclismica magnetica. In particolare, abbiamo misurato una modulazione coerente in X ad un periodo di 2 ore che abbiamo interpretato come il periodo di rotazione della nana bianca. Un valore così alto per il periodo di rotazione è insolito per questi sistemi e possibilmente getterà luce nella comprensione del cammino evolutivo delle variabili cataclismiche magnetiche.

L'Appendice B riporta l'identificazione della nuova sorgente transiente Swift J174540.7–290015. Essa si è accesa nei raggi X il 6 febbraio 2016 a soli 16 arcsec dal buco nero supermassivo al centro della Via Lattea. Abbiamo osservato il campo attorno alla sorgente una volta con *XMM-Newton* e ripetutamente con *Swift* e *INTEGRAL*. Il 26 febbraio la sorgente è stata osservata in uno stato soft caratterizzato da un basso livello di variabilità e uno spettro termico soft con un'alta densità colonnare di materiale neutro e una coda alle alte energie, fino a circa 50 keV. Non abbiamo trovato alcuna evidenza di periodicità in X e neppure controparti nella banda radio. Il campo della sorgente è stato osservato anche nel vicino infrarosso prima e dopo l'inizio dell'outburst: numerose sorgenti sono consistenti con la posizione del transiente, ma nessuna di loro mostra variazioni pronunciate in luminosità. Abbiamo identificato questa sorgente come una stella di neutroni o un buco nero in accrescimento da una stella compagna in un sistema binario X di piccola massa.

Contents

1	Introduction	1
1.1	Rotation-powered pulsars	6
1.1.1	Millisecond pulsars	8
1.2	Accretion-powered pulsars	11
1.2.1	Accretion regimes	12
1.3	Transitional millisecond pulsars	15
1.4	Magnetars	18
1.4.1	Historical excursion	18
1.4.2	Phenomenology	22
1.4.3	The magnetar model: an overview	24
1.5	Other classes of isolated neutron stars	26
1.5.1	Central Compact Objects	26
1.5.2	X-ray Dim Isolated Neutron Stars	29
2	The 1.5-year X-ray outburst of magnetar SGR J1745-2900	31
2.1	Introduction	32
2.2	Observations and data analysis	33
2.2.1	Timing analysis	35
2.2.2	Spectral analysis of <i>Chandra</i> observations	41
2.2.3	Spectral analysis of <i>XMM-Newton</i> observations	45
2.2.4	Pulse phase-resolved spectral analysis	48
2.2.5	X-ray brightness radial profiles	49
2.3	Discussion	49
2.3.1	Outburst evolution and comparison with other magnetars	49
2.3.2	Crustal cooling modelling	52
2.3.3	Bombardment by magnetospheric currents in a bundle	55
2.4	Conclusions	56

3	Magnetar-like activity from the CCO in the SNR RCW103	59
3.1	Introduction	60
3.2	X-ray observations and data analysis	61
3.2.1	<i>Swift</i>	61
3.2.2	<i>Chandra</i>	62
3.2.3	<i>NuSTAR</i>	62
3.3	Results	63
3.3.1	Burst properties	63
3.3.2	Timing analysis	63
3.3.3	Spectral analysis	64
3.3.4	Outburst history	66
3.4	Discussion	67
4	The discovery and monitoring of magnetar SGR J1935+2154	69
4.1	Introduction	70
4.2	X-ray observations	71
4.2.1	<i>Chandra</i>	71
4.2.2	<i>XMM-Newton</i>	71
4.2.3	<i>Swift</i>	72
4.3	Analysis and results	72
4.3.1	Position	72
4.3.2	Spatial analysis	74
4.3.3	Timing analysis	76
4.3.4	Spectral analysis	78
4.3.5	Pre-outburst observations	79
4.4	Radio observations	81
4.5	Discussion	82
5	The variable spin-down rate of magnetar XTE J1810-197	87
5.1	Introduction	88
5.2	Observations and data reduction	88
5.3	Timing analysis	90
5.4	Discussion	94
5.5	Conclusions	95
6	Discovery of a phase-variable spectral feature in an isolated neutron star	97
6.1	Introduction	98
6.2	Data analysis and results	98
6.3	Discussion	104

7	Systematic study of magnetar outbursts	107
7.1	Introduction	108
7.2	The magnetar sample	108
7.2.1	SGR 1627–41	108
7.2.2	1E 2259+586	109
7.2.3	XTE J1810–197	109
7.2.4	SGR 1806–20	109
7.2.5	CXOU J164710.2–455216	110
7.2.6	SGR 0501+4516	110
7.2.7	1E 1547–5408	110
7.2.8	SGR 0418+5729	111
7.2.9	SGR 1833–0832	111
7.2.10	Swift J1822.3–1606	111
7.2.11	Swift J1834.9–0846	112
7.2.12	1E 1048.1–5937	112
7.2.13	SGR 1745–2900	112
7.2.14	SGR 1935+2154	113
7.3	Data reduction and extraction	113
7.3.1	<i>Swift</i> data	113
7.3.2	<i>XMM–Newton</i> data	115
7.3.3	<i>Chandra</i> data	117
7.4	Spectral analysis	118
7.5	Cooling curves and empirical modelling	120
7.6	Quiescent flux vs. maximum flux increase	135
7.7	<i>Swift</i> XRT light curves	140
7.8	High-statistics quality X-ray spectra and fitted models	140
8	Multiwavelength study of PSR J1023+0038 and its transitions	147
8.1	Phenomenology of the system in its current state	148
8.2	Structure of the chapter	150
8.3	Swift observations	151
8.3.1	X-ray data	151
8.3.2	UV data, X-ray/UV correlations and power spectra	153
8.4	Optical and infrared photometry	155
8.4.1	REM observations	155
8.4.2	Liverpool telescope observations	155
8.4.3	Results	155
8.5	Optical spectroscopy	159
8.6	Spectral energy distribution	161
8.7	Enshrouding of a radio pulsar	163
8.8	Conclusions – Part I	164
8.9	The physical picture for the X-ray mode transitions	166

8.9.1	The spectral model	168
8.10	Data analysis	170
8.11	Spectral fitting	171
8.12	Timing analysis	175
8.13	Conclusions – Part II	175
A	RX J2015.6+3711: a magnetic CV with a 2-hr spin period	179
A.1	Introduction	180
A.2	X-ray observations and data analysis	181
A.2.1	<i>XMM–Newton</i>	181
A.2.2	<i>Chandra</i>	193
A.2.3	<i>Swift</i>	194
A.3	UV/optical observations and data analysis	195
A.4	Discussion	196
A.4.1	The X-ray periodicities and the accretion geometry	196
A.4.2	The X-ray spectral properties	198
A.4.3	The long-term X-ray variability and multiwavelength emission	198
A.4.4	The system parameters	199
A.5	Conclusions	199
B	Swift J174540.7–290015: a new accreting binary in the Galactic Centre	201
B.1	Introduction	202
B.2	X-ray observations and data reduction	203
B.2.1	<i>XMM–Newton</i>	203
B.2.2	<i>Swift</i>	204
B.2.3	<i>INTEGRAL</i>	206
B.2.4	<i>Karl G. Jansky Very Large Array</i>	207
B.3	Short term variability	208
B.3.1	The <i>XMM–Newton</i> light curve	208
B.3.2	Timing analysis: broad band noise	208
B.3.3	Timing analysis: search for periodic signals	209
B.4	Spectral analysis of the deep <i>XMM–Newton</i> observation	211
B.4.1	Characterisation of the mean spectrum	211
B.4.2	Ionised absorption	214
B.4.3	X-ray properties of the interstellar medium	214
B.5	Long term spectral variations	215
B.5.1	The <i>Swift</i> monitoring	215
B.5.2	The <i>INTEGRAL</i> monitoring	219
B.6	Possible near infra-red counterpart	223
B.7	Discussion	225
	Bibliography	229

List of publications	269
-----------------------------	------------

Acknowledgements	275
-------------------------	------------

Introduction

The discovery of the subatomic particles in the late 19th and early 20th centuries certainly represented a major milestone in physics. The existence of the neutron was heralded in 1932 (Chadwick 1932), and very shortly afterward the astronomers Baade and Zwicky surmised that extremely compact and stable stars made of neutrons could be produced in the collapse of a massive star, releasing enough gravitational energy to account for the anomalously large luminosities emitted by supenovae (Baade & Zwicky 1934). However, in the ensuing decades, *neutron stars* were considered just mere theoretical speculations, and little effort was devoted on theory or observation of these objects.

The smoking gun for the existence of neutron stars came in 1967, when the graduate student Jocelyn Bell Burnell, who was working on radio observations of quasars with the Interplanetary Scintillation Array of the Mullard Radio Astronomy Observatory under the supervision of Antony Hewish, serendipitously detected a 1.337-s coherent modulation of the radio emission from an unknown source in the sky at R.A. = 19^h19^m, Decl. = +21°. The signal was exceptionally regular, with variations of the period of 1 part in 10¹⁰ (Hewish et al. 1968). Under the assumption that the regular pulses reflect the rotational period P of a compact star and by equating the gravitational attraction at the surface of the object with the centrifugal action due to rotation, one can compute from first principles an upper limit on the radius, $R_{\text{break}} = [GMP^2/4\pi^2]^{1/3} = 1800 M^{1/3}$ km (M is the mass in Solar units). This simple calculation gives a rough idea about the compactness of the celestial object responsible for the observed pulsed emission. In the same years, Pacini (1968) and Gold (1968, 1969) put forward a scenario to explain the source properties in which the observed behavior was ascribed to the radiation emitted by relativistic electrons accelerated by the magnetic field of a rapidly spinning neutron star, termed *pulsar* (an acronym for ‘pulsating star’). A prediction of the model was the increase of the pulse period over time as rotational energy was progressively radiated away.

The discovery of the first pulsar, initially named CP 1919+21 and now known as PSR J1921+2153, initiated a prolific research activity within the community of radio astronomers, which has still not abated. A handful of new pulsars were discovered soon after,

including the pulsar in the supernova remnant Vela (Large et al. 1968) and that in the Crab nebula (Staelin & Reifenstein 1968), site of the famous supernova exploded in 1054 that was observed by human eye and documented by different civilizations in China, Arabia and North America (Stephenson & Green 2002). The identification between pulsars and rotating neutron stars became even more convincing following the measurement of the spin down of the Crab pulsar (Richards & Comella 1969), as predicted by Gold (1968).¹

In 1970, the first X-ray satellite *Uhuru*² was launched above the Earth's atmosphere, opening the opportunity to detect the emission from celestial objects at X-ray wavelengths (X-rays are absorbed at altitudes of 20 – 100 km), and providing a window to study high energy phenomena in the Universe (Giacconi 2003). It took less than a year to detect 4.84-s pulsations in the X-ray emission of the source Centaurus X-3 (aka 4U 1118–60) in the constellation Centaurus (Giacconi et al. 1971). The first pulsar in the X-rays had just been discovered. The pulse frequency was sinusoidally modulated on a 50-hr timescale, a behavior which was attributed to the Doppler effect caused by orbital motion of the source (Schreier et al. 1972), and provided the clear demonstration that the source belonged to a binary system. This discovery put almost beyond any doubt the existence of neutron stars emitting X-rays from the accretion of material transferred from a companion star.

The year 1972 marked the beginning of gamma-ray astronomy, with the launch of the pioneering mission *Small Astronomy Satellite 2 (SAS-2)*. Kniffen et al. (1974) and Thompson et al. (1975) soon revealed pulsed gamma-ray emission from the Crab and Vela pulsars (the two brightest sources in the gamma-ray sky) taking advantage of their well-known radio ephemerides, thereby demonstrating that pulsars are also gamma-ray emitters. Furthermore, another radio-quiet object, shining next to the Crab in the Galactic Anticentre, was observed by *SAS-2*, and was initially named γ 195+5 (Fichtel et al. 1975). The nature of this source remained controversial for about 20 years, a wait that led astronomers to dub the source as Geminga (a name inspired by its position within the Gemini constellation, but also a pun in the Lombard dialect of Milan meaning 'it is not there' or 'there is nothing'). The recognition that this object was indeed a pulsar came in 1992, when the *Roentgen X-ray satellite (ROSAT)* detected 237-ms X-ray pulsations from the object (Halpern & Holt 1992), and gamma-ray data collected almost simultaneously by the EGRET instrument on board the *Compton Gamma Ray Observatory* showed evidence for a modulation at the X-ray period (Bertsch et al. 1992). Geminga represented the first neutron star pulsating in X- and gamma-rays but not at radio wavelengths: pulsars can be radio-quiet³ (see e.g. Caraveo 2014 and Grenier & Harding 2015 for comprehensive reviews on gamma-ray pulsars).

The number of known pulsars has increased considerably over the last 50 years, and the

¹The possibility that the extremely regular pulses of CP 1919+21 could be due to some form of communication from an intelligent extraterrestrial civilization (the source was initially dubbed as LGM–1, an acronym for 'Little Green Man 1') was ruled out following the above-mentioned discoveries.

²The Swahili word for 'freedom' in recognition of the hospitality of Kenya. The satellite was indeed launched from the Italian San Marco platform near Malindi, Kenya.

³Note however that the non detection of radio emission from pulsars may be simply due to an unfavorable viewing geometry: the radio beam could be narrow enough that it does not intercept our line of sight.

current census includes more than 2500 members only in our Galaxy (see Kaspi & Kramer 2016 for a review), with rotational periods spanning from 1.4 ms (Hessels et al. 2006) to 6.67 h (De Luca et al. 2006; this thesis). This number is destined to constantly increase thanks to ongoing radio pulsar surveys using single dish radio antennas such as Parkes, Green Bank, Jodrell Bank, Arecibo (e.g., Lyne et al. 2016; Stovall et al. 2016), and the new gamma-ray data continuously collected by the currently flying Large Area Telescope aboard *Fermi*. As of 2016 February, 205 gamma-ray pulsars are securely known.⁴

A neutron star is a self-gravitating object formed during the gravitational collapse of a progenitor star with initial mass in the range 9–25 M_{\odot} (Heger et al. 2003; $M_{\odot} = 2 \times 10^{33}$ g is the Solar mass), in a process called core-collapse supernova explosion. The measured masses of neutron stars typically range from $\sim 1M_{\odot}$ to $\sim 2M_{\odot}$ ⁵ (see e.g. Lattimer 2012 for a review) and their radii are in the 8 – 15 km range. These values translate into densities of $10^{14} - 10^{15}$ g cm⁻³, which make the degeneracy pressure among neutrons strong enough to balance the gravitational tendency to collapse. The current consensus is that the interior of a neutron star is composed of three regions: the atmosphere, the crust and the core (in order of decreasing distance from the centre; see Figure 1.1).

- The atmosphere is a thin (0.1 – 10 cm) layer consisting of ionised nuclei and non-degenerate electrons, and constitutes a negligible fraction of the total stellar mass. It plays a crucial role in shaping the thermal photon spectrum emerging from the neutron star surface.
- The crust comprises about 1 per cent of the stellar mass, and can be subdivided into an outer and an inner part. The former extends a few hundred meters from the bottom of the atmosphere down to the region where the neutron drip density $\rho_{\text{drip}} \sim 4.3 \times 10^{11}$ g cm⁻³ is reached (the neutron drip point is defined as the region at the base of the outer crust where neutrons become so abundant that they are no longer bound and start to drip out of the nuclei, forming a free neutron gas). It is composed of ions and ultra-relativistic, degenerate free electrons. The latter has a thickness of about 1 – 2 km (Chamel & Haensel 2008), and covers the region from the neutron drip density to approximately the density of nuclear matter, $\sim 2.8 \times 10^{14}$ g cm⁻³. It is a very hot fluid composed mainly of electrons, free neutrons and neutron-rich nuclei.
- The core constitutes the largest portion of the neutron star, containing approximately 99 per cent of the total mass, and can also be subdivided into an outer and an inner part. The outer core extends for a few kilometers in the radial direction, and occupies the density range $\rho \sim 10^{14} - 10^{15}$ g cm⁻³. Matter consists mainly of degenerate neutrons, which provide the bulk of pressure sustaining the star against gravity. The

⁴See <https://confluence.slac.stanford.edu/display/GLAMCOG/Public+List+of+LAT+Detected+Gamma-Ray+Pulsars>.

⁵The system 4U 1538–52 and the pulsar PSR J0348+0432 respectively hold the record as the least and most massive neutron star known, with well-constrained masses of $(1.00 \pm 0.10) M_{\odot}$ (assuming circular orbit; Rawls et al. 2011) and $(2.01 \pm 0.04) M_{\odot}$ (Antoniadis et al. 2013).

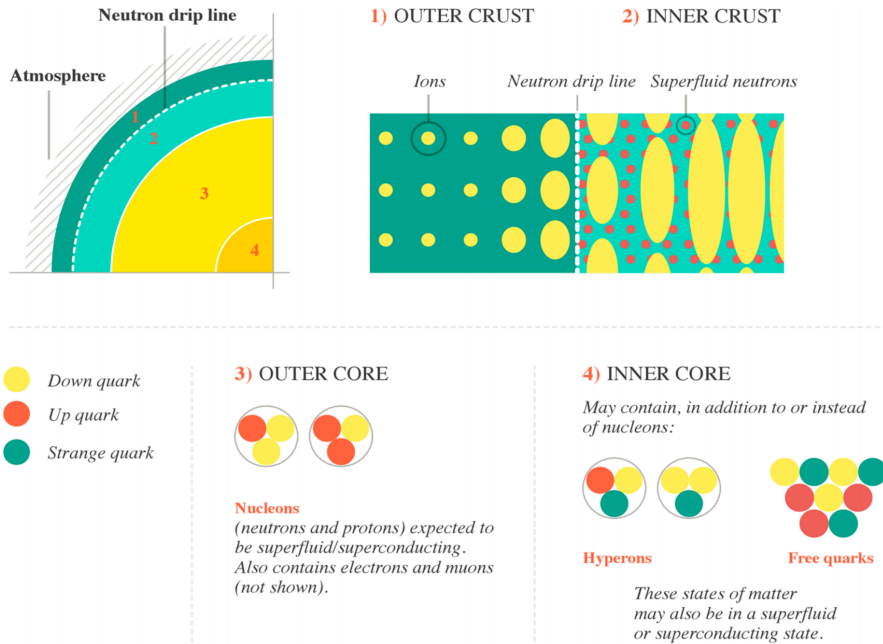


Figure 1.1: Schematic illustration of the structure and composition of a neutron star. Credit: LOFT Yellow Book (<http://sci.esa.int/loft/53447-loft-yellow-book/>).

composition of the inner core is largely unknown. At such large densities, more exotic particles besides the standard composition of protons, neutrons and electrons may appear, such as hyperons, pions/kaons or deconfined quarks.

Neutron stars possess the largest magnetic fields observed in the Universe (up to 10^{14} – 10^{15} G at the surface), which can exceed the quantum electrodynamic limit $B_{QED} = 4.414 \times 10^{13}$ G at which the energy of the first Landau level for electrons equals their rest mass energy. For $B > B_{QED}$ different quantum mechanical effects start to be dominant (e.g., Harding & Lai 2006): the vacuum becomes anisotropic and birefringent causing vacuum polarization. The light becomes decomposed in ordinary and extraordinary photons and is able to distort and magnify images (‘magnetic lensing’). Other effects include atom deformations to long spaghetti-like cylinders, photon splitting or merging and pair production, a process where photons are temporarily converted into electron-positron pairs. Neutron stars are also surrounded by the magnetosphere, a conducting region filled with magnetized plasma. In localized regions of the magnetosphere close enough to the neutron star, the dynamics of a charged particle is completely controlled by the magnetic stresses. Particles accelerated along the curved field lines emit beamed radiation throughout the whole electromagnetic spectrum, which can be detected as regular pulses every time the

radiation periodically crosses our line of sight, provided that the neutron star magnetic and rotational axes are misaligned (the so called lighthouse effect). The emitted radiation is ultimately shaped by the plasma in the magnetosphere.

Neutron stars manifest themselves in a number of ways, depending on the main channel powering their emission. These are:

- **rotation.** The emission of energy of rotation-powered neutron stars is due to the rotation of the electro-magnetic dipole and leads to a simultaneous deceleration of the object. They can be observed as pulsars, or via the nebular radiation arising from the interaction of a relativistic wind of particles emitted by the neutron star with a surrounding nebula. They can be either isolated or part of a binary system.
- **accretion** of mass. The emission of accretion-powered neutron stars is due to the release of gravitational binding energy as material transferred from the companion star hits the stellar surface. For this reason, all accretion-powered neutron stars belong to binary systems. A (X-ray) pulsar is observed in an accretion-powered system only if the magnetic field is large enough to form a magnetosphere around the neutron star.
- **magnetic energy.** Magnetic powered neutron stars generally have X-ray luminosities too large to be fed by the rotation power alone, and no sign of an accretion process is observed. According to the magnetar model, their emission is ultimately due to the instability and decay of their exceptionally large ($\gtrsim 10^{14}$ G) magnetic fields.
- **cooling.** Thermally-powered neutron stars emit their internal heat, which can either be the residual content stored since the neutron star formation (only observable for the first $\sim 10^5$ yr), or can be renewed by an external source such as accretion or returning currents from the magnetosphere.

The variety of emission mechanisms reflects into different categories of neutron stars. Rotation and accretion power represent still nowadays the two main channels that make these, otherwise small and faint objects, observable. Besides the ‘canonical’ rotation-powered pulsars and accreting X-ray pulsars, we are now aware of magnetars, X-ray dim isolated neutron stars and central compact objects. I now review the categories of neutron stars which are useful to understand the motivation of this thesis. First I will describe rotation-powered pulsars (Section 1.1) and accreting X-ray pulsars (Section 1.2), and illustrate how these two classes were recently shown to be tightly evolutionary linked following the discovery of the so-called transitional millisecond pulsars (Section 1.3). I will then focus on strongly magnetised isolated neutron stars and recap the main properties and predictions of the magnetar model (Section 1.4). An overview of central compact objects and X-ray dim isolated neutron stars follows in Sections 1.5.1 and 1.5.2, respectively.

1.1 Rotation-powered pulsars

Historically, rotation powered pulsars were initially referred to as ‘radio pulsars’, just because they were first discovered in the radio band. The more physically-motivated term ‘rotation powered’ was coined later on, when it was realized that the bulk of energy of pulsars is mainly emitted in the form of high-energy radiation (with the radio 100 MHz – 100 GHz emission typically representing about 10^{-6} of the overall energy reservoir), and pulsars not emitting in the radio band were discovered (e.g., Geminga).

Isolated rotation powered pulsars in the Galaxy are all observed to spin down, and after the discovery of the Crab pulsar it was soon recognized that the released rotational energy was large enough to power the emission of its surrounding nebula (Ostriker & Gunn 1969; Finzi & Wolf 1969). We now know that for young pulsars such as the Crab, a magnetised wind of relativistic particles accelerated by the pulsar can be confined by the circumstellar material (the ejected envelope of the progenitor), and that the result of this confinement is a (often spectacular) synchrotron nebula which is X-ray luminous due to the interaction of the relativistic electrons with the ambient magnetic field (see Gaensler & Slane 2006).

A decelerating rotating spherical object releases energy at a rate $\dot{E} = -I\omega\dot{\omega} = 4\pi^2 I \dot{P} P^{-3}$, where $I = 0.4MR^2$ is the moment of inertia (assuming uniform density), $\omega = 2\pi P^{-1}$ is the angular frequency, P is the spin period, and $\dot{P} = dP/dt$ is its time derivative. In the following we will consider the standard parameters adopted for neutron stars, i.e. mass $M = 1.4M_{\odot}$ and radius $R = 10$ km. Once P and \dot{P} are measured, the energy budget available to power the emission, the so-called spin down luminosity, can be evaluated as

$$\dot{E} = -I\omega\dot{\omega} = 4\pi^2 I \dot{P} P^{-3} \simeq 4 \times 10^{33} \dot{P}_{13} P^{-3} \quad \text{erg s}^{-1}, \quad (1.1)$$

where P is expressed in s and \dot{P}_{13} is the spin period derivative in units of $10^{-13} \text{ s s}^{-1}$.

The ‘magnetic-dipole braking model’ (Pacini 1967, 1968; Gunn & Ostriker 1969) assumes that the neutron star rotates in vacuum at angular frequency ω , and possesses a magnetic field with a dipolar configuration ($B(r) = \mu r^{-3}$, where $\mu = B_p R^3$ is the magnetic dipole moment, B_p is the magnetic field strength at the magnetic pole and R is the neutron star radius). The magnetic dipole moment μ and the rotation axis are misaligned by an angle α . The direction of the magnetic dipole moment varies with time because of rotation. The energy release rate can then be expressed using the Larmor formula as

$$\dot{E} = \frac{2}{3c^3} |\ddot{\mu}|^2 = \frac{2}{3c^3} \mu^2 (\sin\alpha)^2 \omega^4 = \frac{B_p^2 (\sin\alpha)^2 R^6 \omega^4}{6c^3}, \quad (1.2)$$

where $\ddot{\mu} = d^2\mu/dt^2$. By assuming that the spin down of the neutron star is caused by the torque of the magnetic field with its surroundings and that the emission process is dipole radiation, one can infer an estimate of the dipolar component of the magnetic field by equating Equation 1.1 with Equation 1.2:

$$B_p \sin \alpha = \left(\frac{3c^3}{8\pi^2} \frac{I}{R^6} \right)^{1/2} (P\dot{P})^{1/2} \simeq 3.2 \times 10^{19} (P\dot{P})^{1/2} \quad [\text{G}]. \quad (1.3)$$

Relativistic magnetohydrodynamic simulations of plasma-filled magnetospheres have shown that the above estimate is correct within a factor of 2 – 3 (Spitkovsky 2006; Contopoulos et al. 2014). Once P and \dot{P} are measured, it is then possible to extract information on the strength of the dipolar component of the neutron star magnetic field.

The above equation can be generalized by assuming a spin down formula of the form $\dot{\nu} \propto \nu^{-n}$, where $\nu = P^{-1}$ is the spin frequency and $n = -\nu\dot{\nu}^{-2}$ is the ‘braking index’. Integration of the spin down formula then leads to an estimate of the age of the pulsar:

$$\tau = \frac{P}{(n-1)\dot{P}} \left[1 - \left(\frac{P_0}{P} \right)^{n-1} \right], \quad (1.4)$$

where P_0 is the period of the pulsar at birth. Assuming a pulse period at birth much smaller than the current pulse period ($P_0 \ll P$) and spin down via magnetic dipole radiation ($n = 3$), the ‘characteristic spin down age’ (a first-order estimate of the pulsar’s true age) no longer depends on P_0 , and is given by $\tau_c = P/2\dot{P}$.

Although the magnetic-dipole braking model turns out to be very useful in providing important physical information, it is almost certainly wrong in the assumptions that pulsars rotate in vacuum and the magnetic field remains constant with time (i.e. $n = 3$). A rotating magnetic dipole surrounded by vacuum will induce a Lorentz force parallel to the magnetic field that, in the case of pulsars, exceeds the gravitational force by orders of magnitude, as first shown by Goldreich & Julian (1969). Charged particles will be lifted from the surface into the magnetosphere in the attempt of cancelling the total electromagnetic force acting on them. A charge density $\rho_G \simeq -\omega B/2\pi c$ forms in the magnetosphere, shorting out the global electric field and allowing the magnetosphere to corotate with the star in a stationary configuration within the light cylinder, namely the radius at which matter would corotate with the star at the speed of light. Gaps are thought to form in the sites where no charges are present and the surviving electric field is not cancelled out, so that charges can be there accelerated to relativistic speeds (Ruderman & Sutherland 1975).

The acceleration of charges is widely recognized as the primer for the pulsar emission, but the location of the gaps is still matter of debate. According to polar-cap models (e.g., Daugherty & Harding 1996), acceleration occurs near the magnetic poles on the neutron star surface; outer-gap models (e.g., Cheng, Ho & Ruderman 1986; Romani 1996) suggest instead that the acceleration takes place in vacuum gaps that form near the last closed field lines, near the light cylinder radius. The outer-gap models apply only to gamma-ray emission and disentangle the gamma-ray and the radio emitting regions. A comprehensive discussion of the proposed scenarios is beyond the scope of this thesis, and I refer to the works of Viganò et al. (2015a,b,c) for more details and recent progresses on the topic.

Therefore, a magnetized neutron star can be naively seen as an accelerator of particles (electrons) powered by the electro-magnetic field induced by rotation. The charge outflow follows the magnetic field lines, as the energy density of the electromagnetic field is still

much larger than the material energy density. While moving along the field lines, the charges emit curvature and inverse Compton radiation with energies up to the gamma-ray band. Those rays with energies above ~ 1 GeV are the seed for a copious creation of relativistic electron-positron pairs, which further interact with the magnetic field, emitting synchrotron radiation and producing a second generation of pairs. Such a cascade will continue until the synchrotron photons fail to meet the energetic requirements to pair produce and can escape to contribute to the high-energy pulsar emission. The process takes place at low altitudes above the stellar magnetic poles. This model accounts satisfactorily for the non thermal part of the emitted spectrum (from the infrared up to the X-rays and gamma-rays), where the largest part of the energy is emitted. The instabilities that develop among plasma flows of different densities are likely the origin of electromagnetic oscillation leading to the eventual radio coherent emission. It is worth noting that pulsations can be observed both in the soft and hard band of the broadband spectral energy distribution.

Figure 1.3 shows the spin period derivative as a function of the spin period ($P - \dot{P}$ diagram) for all pulsars discovered between 1967 and 2014. Three large groups are immediately visible: a large population of slow pulsars that spin down on a fast timescale ($\tau_c \sim 10^5 - 10^7$ yr) and possess magnetic fields of about $10^{11} - 10^{12}$ G (red dots); a more restricted group of rapidly rotating pulsars that spin down on very long timescales ($\tau_c \sim 10^8 - 10^{10}$ yr) and have $B \sim 10^8 - 10^9$ G (blue circles in the bottom-left corner); and about 30 pulsars spinning down at comparatively large rates (with characteristic age $\tau_c \sim 10^3 - 10^5$ yr). These represent in all respects the strongest magnets in the Universe, with $B \sim 10^{13} - 10^{15}$ G (green and pink triangles in the top-right corner).

Newly born pulsars appear in the top left corner of the $P - \dot{P}$ diagram. If B is conserved, they gradually move to the right and down, along lines of constant B and crossing lines of constant τ_c . It is thought that when radio pulsars cross the so-called ‘death line’ on the $P - \dot{P}$ diagram, the radio emission mechanism switches off and the pulsar enters the ‘pulsar graveyard’. In fact, pulsars with long periods and small period derivatives are not observed, which accounts for the relatively empty region in the bottom-right corner of the diagram. Once the neutron star has crossed the ‘death line’, it keeps evolving as an isolated neutron star by emitting thermal radiation from its cooling surface.

1.1.1 Millisecond pulsars

The first millisecond pulsar was discovered in 1982, following the detection of a coherent modulation in the radio emission of PSR B1937+21 at a period of 1.56 ms (Backer et al. 1982). Unexpectedly, no observational hints (such as the presence of a supernova remnant around the source) were found able to justify the extreme youth of PSR B1937+21 implied by the afore-mentioned model for rotation powered pulsars (assuming standard values for the period derivative; Section 1.1). The idea that this pulsar could belong to a completely different class of objects with respect to the canonical pulsars started to emerge.

Six years before this exciting discovery, Smarr & Blandford (1976) had already suggested that the 59-ms pulsar PSR 1913+16 could have achieved such a short spin period because of a prolonged ($\sim 10^7$ yr) phase of transfer of angular momentum through accre-

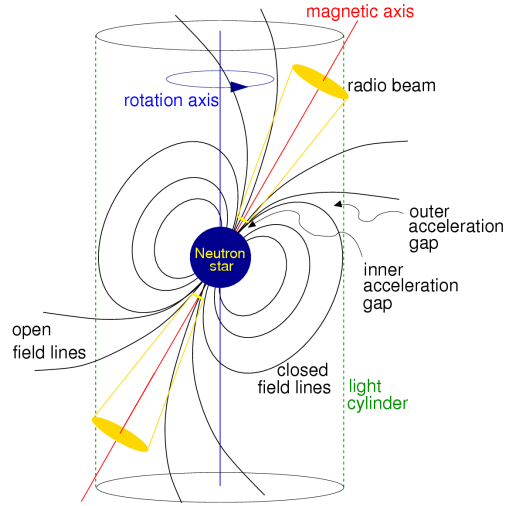


Figure 1.2: Schematic view of a pulsar as a spinning magnetised neutron star with misaligned rotation and magnetic axes. From Longair (2011).

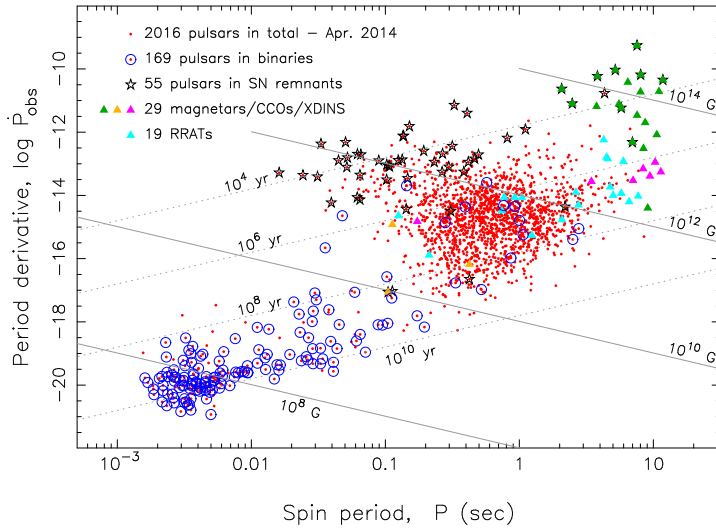


Figure 1.3: $P - \dot{P}$ diagram relative to all detected pulsars as of 2014 April. Red dots indicate known radio pulsars. Blue circles represent those that are found in binaries. Stars represent pulsars associated with supernova remnants. Green triangles represent magnetars. The X-ray dim isolated neutron stars and the central compact objects are pink and yellow triangles, respectively. Solid grey lines are of constant magnetic field (Equation 1.1) and dotted lines are of constant characteristic age (Equation 1.2). From Tauris et al. (2014).

tion of matter from a companion star in a binary system. The minimum spin period that can be attained from the accretion of mass via a disk (see Section 1.2), before the neutron star attains spin equilibrium, grows as $B^{6/7}$, a consideration that led Alpar et al. (1982) and Radhakrishnan & Srinivasan (1982) to suggest that the ms-period of PSR B1937+21 was reflecting a magnetic field in the range $10^8 - 10^9$ G. These independent works thus stated that the first millisecond pulsar discovered had to be characterized by a magnetic field lower by 3 – 4 orders of magnitude with respect to those of all pulsars already discovered. They proposed that the most plausible evolutionary history for such an object was that of a ‘*recycling*’ of an old pulsar. According to their scenario, the pulsar could shine again after having crossed the death line owing to the torques imparted by a Gyr-long phase of accretion of matter from a low-mass companion (see Srinivasan 2010 for a recent review). This process not only results in the spin-up of the star, but also in the screening or burial of its magnetic field (Bisnovatyi-Kogan & Komberg 1976). However, the exact mechanism responsible for the magnetic field decay by many orders of magnitude during the spin up phase is not yet fully understood.

The missing ingredient to corroborate the recycling scenario, the presence of a companion star, was successfully unearthed with the subsequent discoveries of more millisecond pulsars in binary systems. However, an outstanding mystery still had to be solved, namely the existence of seemingly isolated millisecond pulsars (as for the case of PSR B1937+21). This puzzle was initially circumvented by arguing that the companion star would have been lost in some way. This idea was strikingly confirmed with the discovery of the 1.6-ms pulsar PSR B1957+20 in a 9.1-hr orbit around a very low mass ($M_c \sim 0.02M_\odot$) companion (Fruchter, Stinebring & Taylor 1988). The most appealing explanation was proposed by Ruderman, Shaham & Tavani (1989) in terms of evaporation (ablation) of the companion by means of energetic particles and/or gamma-rays produced by the pulsar wind. The so-called black widow pulsars, defined as binary pulsars whose donor star is currently losing mass ($M_c \ll 0.1M_\odot$), are typically identified via the irregular extended eclipses of the radio pulsed emission caused by absorption and scattering by the intrabinary material. A related population of eclipsing millisecond pulsars with low mass companions is that of the redbacks ($M_c \sim 0.2 - 0.4M_\odot$; D’Amico et al. 2001). Black widows and redbacks collectively form the class of ‘spiders’ millisecond pulsars⁶ (see Roberts 2013 for a review).

The list of millisecond pulsars, if defined as pulsars with spin periods $\lesssim 30$ ms and magnetic fields $\lesssim 10^{11}$ G at the surface, comprises more than 350 members as of 2014 August⁷, the majority of which ($\gtrsim 80$ per cent) belong to binary systems. Among them, we are now aware of 18 black widows and 12 redbacks residing in globular clusters.⁸

⁶Black widows and redbacks are a highly venomous species of spider native to North America and Australia, respectively. The female is known to occasionally consume the male during the process of mating.

⁷See <https://apatruno.wordpress.com/about/millisecond-pulsar-catalogue/> for a catalogue.

⁸See <http://www.naic.edu/~pfreire/GCpsr.html> for a complete list.

1.2 Accretion-powered pulsars

Soon after the birth of X-ray astronomy (Giacconi et al. 1962) it was realized that the brightest sources in the X-ray sky were powered by accretion of matter onto a compact object in interacting binary systems (e.g., Shklovsky 1967; Pringle & Rees 1972).

Consider mass accretion onto a compact star with mass M_* and radius R_* . As a mass dm is accreted onto the star, it releases its gravitational binding energy, $dE = (GM_*/R_*)dm$. The time derivative of the above relation gives an expression for the accretion luminosity,

$$L_{\text{accr}} = \frac{dE}{dt} = \frac{GM_*\dot{M}}{R_*}, \quad (1.5)$$

where $\dot{M} = dm/dt$ is the mass accretion rate. This expression can be reformulated by introducing the efficiency term, $\eta_{\text{accr}} = L_{\text{accr}}/\dot{M}c^2 = GM_*/R_*c^2 = R_S/2R_*$, where $R_S = GM_*/2c^2 = R_g/2$ is the Schwarzschild radius of the star, and R_g is the gravitational radius. The extraction of a significant amount of energy through this process requires the accreting object to be compact. For a rotating neutron star, $\eta_{\text{accr}} \sim 0.2$ can be easily reached. Accretion appears therefore as one of the most effective ways by which a neutron star converts energy into radiation.

The temperature of the emitted radiation must lie between the temperatures of the least and the most thermally efficient ways of converting heat into radiation: that of a black body emitting the accretion energy, $T_b = (L_{\text{accr}}/4\pi R_*^2\sigma)^{1/4}$, and that reached if the accretion energy is entirely converted in thermal energy, $T_{th} = GM_*m_p/3kR_*$. For $M_* = 1M_\odot$, $R_* = 10$ km and standard accretion rates, the radiated emission is in the 1 keV – 50 MeV energy range: accreting neutron stars emit mainly in the X-ray/gamma-ray band of the electromagnetic spectrum, with $L_{\text{accr}} \simeq L_X$.

All accretion powered neutron stars belong to the class of X-ray binaries. These are typically classified in high mass X-ray binaries (HMXBs) and low mass X-ray binaries (LMXBs), depending on the mass of the companion star. This can be generally estimated at a first glance from the ratio between the optical and X-ray emission, which is usually > 1 for HMXBs and $\ll 1$ for LMXBs. In a simplified toy model, in HMXBs mass transfer occurs via the strong stellar wind of the massive ($M_c > 10M_\odot$) companion star, whereas in LMXBs it occurs through Roche lobe overflow: at a certain stage of its evolution, the companion star (with $M_c \lesssim 1M_\odot$) fills its own Roche lobe (i.e., its gravitational sphere of influence), either because of an increase in its size or a shrink in the orbital separation, and transfers gas into the gravitational well of the compact object via the inner Lagrangian point. Conservation of angular momentum prevents matter from directly falling onto the compact star, and the process generally involves the formation of an accretion disk (Frank, King & Raine 2002). Within the disk, magnetic or viscous forces operate to allow the gas to drift in slowly as it orbits, and eventually reach the compact object. Half of the liberated gravitational energy is converted into kinetic energy, whereas the other half is thermalized and radiated away in the form of X-rays. If the accreting body is a neutron star, the kinetic

energy is also radiated at X-ray wavelengths, once the matter hits the stellar surface.

The first LMXB showing accretion driven X-ray millisecond pulsations (at a period of 2.5 ms) was discovered by Wijnands & van der Klis (1998). The discovery of such a system, SAX J1808.4–3658, represented the first compelling proof that mass accretion is able of spinning up neutron stars to periods of the order of ms, and heralded the existence of a new class of accreting neutron stars: the *accreting millisecond X-ray pulsars* (AMXPs). Among the 23 currently known pulsating neutron stars in Galactic LMXBs, 17 AMXPs are known, with spin periods ranging from 1.67 ms to 5.49 ms (see Patruno & Watts 2012 for a review). All AMXPs are transient systems, namely they exhibit episodes of outbursts of accretion which are interleaved by periods of quiescence, during which little or no matter is accreted onto the neutron star. The former lasting weeks or months and with peak luminosities up to 10^{36} erg s⁻¹, the latter lasting years and with X-ray luminosities of the order of $10^{31} - 10^{33}$ erg s⁻¹. The currently accepted model to explain the transient behavior is the thermal-viscous disk instability model (Lasota 2001), according to which the disk oscillates between a cold neutral state (i.e. quiescence) and a hot ionized state (i.e. outburst). Matter builds up in the disk during quiescence and is then transferred to the neutron star during outburst. Pulsations have been observed only during outbursts in the majority of the cases, with two notable exceptions that will be mentioned in Section 1.3. The large accretion rate variations implied by this process enable the exploration of a variety of physical regimes and mechanisms which are unaccessible to persistent low-mass X-ray binaries. I will briefly review these regimes in the following section.

1.2.1 Accretion regimes

A first-order estimate of where and whether the magnetic field disrupts the flow of accreting gas, R_d , can be easily determined in the case of spherical accretion, by equating the magnetic pressure [$B(r)^2/8\pi$] to the sum of the ram and thermal pressure of the infalling matter [$\rho(r)v(r)^2 + p(r)$]. As accretion is highly supersonic next to the compact object, the thermal pressure can be safely neglected with respect to the ram pressure. In the simplest case of a purely dipolar configuration for the magnetic field ($B(r) = \mu/r^3$), and noting that the velocity of accreted matter is close to free fall ($v = [2GM/r]^{1/2}$), it is possible to put $|\rho v| = \dot{M}/4\pi r^2$ and obtain the radius for which the two pressures equate, the so-called Alfvén radius (Pringle & Rees 1972; Davidson & Ostriker 1973; Elsner & Lamb 1977):

$$R_A = \mu^{4/7} \dot{M}^{-2/7} (2GM)^{-1/7}. \quad (1.6)$$

This sets the scale where magnetic field begins to influence significantly the mass flow. It is clear from the above formula that an increase in the mass accretion rate leads to a ‘compression’ of the magnetosphere, whereas a decrease in the rate implies an expansion of the magnetosphere, as the pressure exerted by the plasma gets lower and lower. If $R_d \simeq R_A > R_*$, a substantial fraction of the completely ionized magnetospheric plasma will move along the magnetic field lines because of its high conductivity, thereby corotating

with the neutron star. Given the steep dependence of the magnetic pressure with radius ($\propto r^{-6}$), this process occurs in a thin layer, so that mass will be channeled towards a narrow region near the magnetic poles of the neutron star, where two hot spots will form. The X-ray radiation produced by the matter infall will be modulated at the neutron star spin period as the emitting spots rotate around the spin axis. If the line of sight is favorable, the radiation is then detected by the distant observer as a sequence of X-ray pulses, whose frequency may be modulated at the binary orbital period due to the Doppler effect.

This treatment is however too simplistic since, as shown above, the gas orbits in a disk rather than falling radially onto the neutron star from every direction. Therefore, a self-consistent scenario must account for the presence of an accretion disk around the neutron star and hence the coupling between the magnetic field and matter in the disk. The widely accepted ‘magnetically threaded disk model’, first developed in detail by Ghosh et al. (1977) and Ghosh & Lamb (1978, 1979) and later revised by Wang (1987, 1995), assumes that the magnetic field lines penetrate to some extent into the disk (resulting in a magnetic torque that exchanges angular momentum between the neutron star and the disk), and that the inner disk is truncated at the magnetospheric radius. The determination of an analytical relation for the magnetospheric radius as a function of the main physical quantities is one of the open problems of the current theoretical investigation in the field (see Lai 2014 for a recent review). It is usually expressed as $r_m = \eta R_A$, where the term η is a dimensionless parameter accounting for the non-spherical geometry of the accretion flow, and the uncertainties in the topology of the magnetic field and in the detailed physics of the coupling between the magnetic field and the accretion flow. Recent simulations have generally found $\eta \sim 0.5 - 0.7$ (e.g., Zanni & Ferreira 2013; Lii et al. 2014).

Another helpful definition to treat the interaction of the magnetic field with the disk is the corotation radius, r_c , namely the radius at which the angular frequency of matter moving in the disk along the Keplerian orbit [$\Omega_K = (GM/r^3)^{1/2}$] equals that of the neutron star – magnetosphere corotating system ($\Omega_* = 2\pi/P$). Imposing $\Omega_K(r_c) = \Omega_*$ and solving for r_c yields $r_c = (GM/\Omega_*^2)^{1/3} = (GMP^2/4\pi^2)^{1/3}$.

We can then identify two different regimes, depending on the value of the mass accretion rate and thus on the reciprocal positions of the magnetospheric and the corotation radii: if $r_m < r_c$, the centrifugal force exerted on the plasma by the rotating magnetosphere is lower than the gravitational force, the gas accretes onto the neutron star surface and applies a positive torque on the star: the star will spin up. On the other hand, if $r_m > r_c$, the rotating field lines spin at a super-Keplerian velocity, and the mass flow encounters a centrifugal barrier impossible to cross: matter is ejected from the system at the expense of the star rotational energy, and the star will spin down. As such a situation was initially thought to effectively halt accretion, it is known as the ‘propeller’ state (Illarionov & Sunyaev 1975). However, numerical simulations have shown that, even in the propeller regime, some matter can build up at the inner disk radius and still accrete at a reduced rate onto the neutron star (see Romanova et al. 2014 for a recent review). In the strong propeller regime ($r_m \gg r_c$), strong supersonic collimated outflows (jets) can be launched by the open field lines.

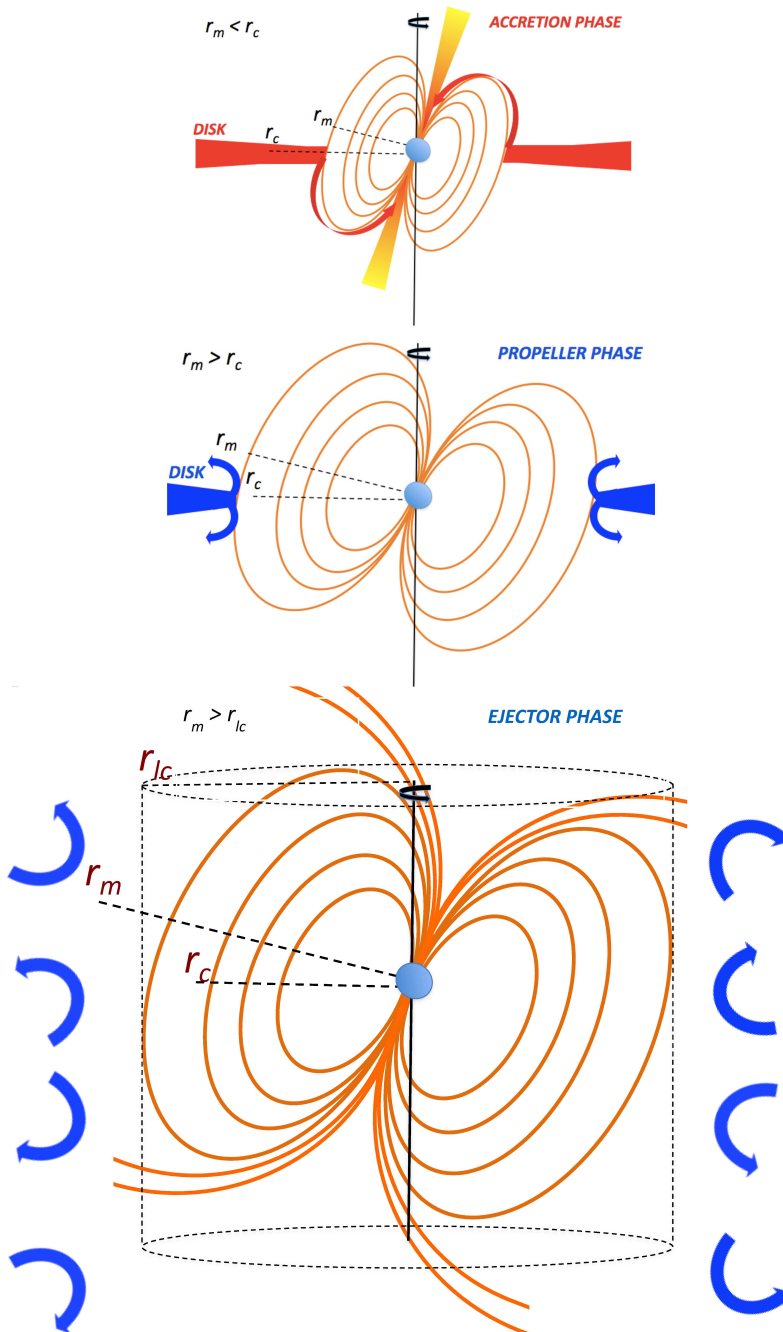


Figure 1.4: Cartoon view of the three different regimes of a neutron star in a binary system for decreasing mass accretion rates (from top to bottom). Credit: M. G. Bernardini, P. D'Avanzo.

Finally, the light cylinder radius can be introduced, namely the distance from the neutron star spin axis at which a particle corotating with the magnetosphere would move at the speed of light: $r_{lc} = c/\Omega_* = cP/2\pi$. This radius defines the surface (light cylinder) within which the magnetic field lines are closed. If the mass accretion rate is low enough, the magnetospheric radius will move outwards (see Equation 1.6), and become comparable to the light cylinder radius. When $r_m > r_{lc}$, the electromagnetic pressure of the neutron star overcomes that of the infalling plasma. The field lines open and no more stable equilibrium can be attained. The accreting plasma starts to be pushed outwards in the form of an energetic wind of relativistic particles: the neutron star shines as a rotation-powered pulsar (see Figure 1.4 for a schematic view).

The first relativistic simulations of the interaction between a pulsar magnetosphere and an accretion flow were recently presented by Parfrey, Spitkovsky & Beloborodov (2016a,b). They found that the rotational energy can be efficiently extracted in the form a powerful pulsar wind, even for stars with comparatively low magnetic dipole moments, if the large difference in angular velocity between the star and matter in the threaded accretion disk leads to the stretching and opening of the magnetic field lines which couple the star to the disk. The consequent spin down torque applied to the pulsar can be of the order of the estimated spin up torque from accreting material, thus substantially larger than that predicted by existing models of the disk-magnetosphere interaction.

1.3 Transitional millisecond pulsars

The discovery of the first AMXP definitively established how accretion onto a low magnetized ($B \sim 10^8 - 10^9$ G) neutron star can effectively spin it up to millisecond periods. The existence of this kind of source highlighted the tight evolutionary link existing between neutron stars in LMXBs and millisecond pulsars. During a Gyr-long phase of accretion of mass from a low-mass companion star through an accretion disk, neutron stars shine as X-ray sources. When mass transfer eventually declines, a pulsar powered by rotation of its magnetic field turns on, emitting from the radio to the gamma-ray band. The ~ 350 radio millisecond pulsars in our Galaxy are thus believed to be the recycled descendants of accreting neutron stars in LMXBs.

However, in the last decades, another unresolved issue concerned if the transition of neutron stars from an accretion-disk-dominated LMXB state to a rotation-powered millisecond pulsar state had to be considered only as an irreversible (i.e., once for all), long-lasting process or could also occur on the time scales compatible with those of the variations of the mass inflow rate onto the neutron star. In principle, as shown in the previous sections, an accreting neutron star in a LMXB can turn on as a rotation powered pulsar for very low mass accretion rate: the magnetosphere expands up to the light cylinder activating the radio pulsar, the disk disappears and the system is faint in X-rays ($L_X \lesssim 10^{32}$ erg s $^{-1}$). Conversely, at sufficiently high mass rates, the pressure of the matter transferred from the companion overcomes the pulsar pressure: radio pulsed activity is shut off, a disk forms around the neutron star, matter is channelled towards the magnetic poles of the neutron

star, and a bright X-ray outburst takes place ($L_X \gtrsim 10^{36}$ erg s⁻¹).

Up to 2010, systematic searches for millisecond radio pulsars in AMXPs were inconclusive (Iacolina et al. 2010). However, it was argued that matter may completely enshroud these systems, making radio pulsations undetectable and thus leaving open the possibility that the neutron stars in these systems could anyway turn on as rotation-powered pulsars for very low mass accretion rates. But the smoking gun had yet to be found. The turning point came very recently, with the discovery of repeated swings between the two states in IGR J18245–2452, a LMXB in the globular cluster M28. This system turned on as a bright ($L_X \sim 10^{36}$ erg s⁻¹) AMXP in 2013, and was observed as a rotationally-powered millisecond pulsar a few years before, and a few weeks after, the accretion episode (Papitto et al. 2013). At the moment of writing, the class of the *transitional millisecond pulsars* includes three confirmed members: IGR J18245–2452 (Papitto et al. 2013), PSR J1023+0038 (Archibald et al. 2009) and XSS J12270–4859 (Bassa et al. 2014).

The possibility that the number of transitional millisecond pulsars will increase in the future is not remote if we are confident that some of the known AMXPs may turn on as rotation powered pulsars in quiescence, and, viceversa, a few millisecond radio pulsars may activate as AMXPs for large enough mass accretion rates: most of the accreting and rotation-powered neutron stars in close binary systems could be indeed transitional systems observed so far in one of the two possible states. The time scale of the transitions is however largely unknown, and is currently only loosely constrained to less than a few months.

Strikingly, besides the X-ray accreting state and the radio pulsar state, the three transitional millisecond pulsars discovered so far have also been observed in an extremely peculiar and enigmatic intermediate regime, commonly referred to as the sub-luminous disk state in the literature. In this state, an accretion disk is present but the X-ray luminosity ($L_X \sim 10^{33} - 10^{34}$ erg s⁻¹) is much lower than during full-fledged accretion outbursts. The X-ray emission is highly variable on timescales of a few tens of seconds (e.g., Jaodand et al. 2016), and the detection of X-ray pulsations (Archibald et al. 2015; Papitto et al. 2015) indicates that matter in the disk accretes intermittently onto the neutron star surface. However, the relatively low mass accretion rate deduced from the observed X-ray luminosity, and the observation of enhanced gamma-ray flux and of a bright radio continuum emission characterized by a flat spectrum (typical of jets of accreting compact objects; Deller et al. 2015), suggest that large mass outflows could be launched by the fast rotating propelling magnetosphere of these pulsars (Papitto et al. 2014; Papitto & Torres 2015). It is worth remarking that, when in the sub-luminous disk state, transitional millisecond pulsars are the only LMXBs from which gamma-ray emission has been detected so far by *Fermi*. Their 0.1 – 10 GeV luminosity is $\sim 10^{34}$ erg s⁻¹, similar to that in the X-rays and up to ten times larger with respect to the levels attained during the rotation-powered state (de Martino et al. 2010; Hill et al. 2011; Papitto et al. 2014; Stappers et al. 2014). The gamma-ray emission is interpreted in terms of residual acceleration of leptons along magnetospheric field lines even in presence of a disk, or through a Fermi process taking place at the disk-magnetosphere boundary (e.g., Papitto et al. 2014).

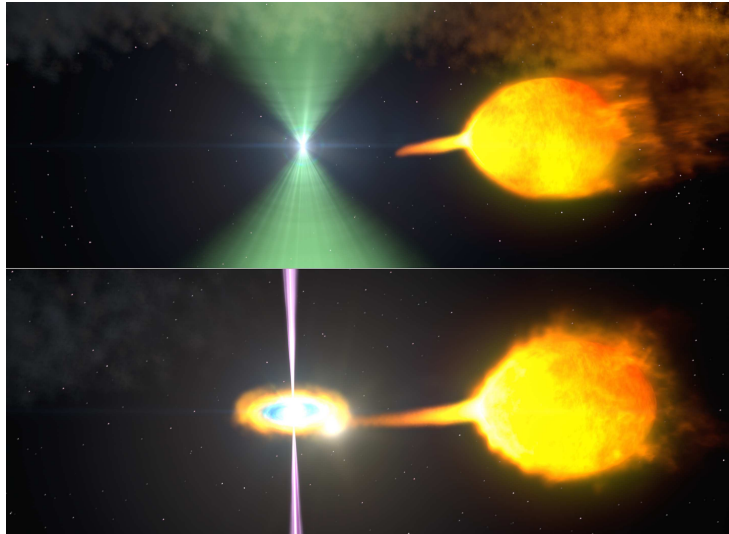


Figure 1.5: Artistic view of a transitional millisecond pulsar. The top panel shows the rotation-powered radio pulsar state: an outflow of high-energy particles from the pulsar (in green) staves off the gas stream from its companion. The bottom panel shows the accretion-powered X-ray pulsar state: when the stream surges, the stronger flow pushes through the pulsar wind and establishes an accretion disk. This fuels the development of relativistic particle outflows (in magenta) that obscure the radio beam. Credit: National Aeronautics and Space Administration’s Goddard Space Flight Center.

So far, only IGR J18245–2452 has been observed to go through all the three phases accessible to these systems (accretion powered X-ray pulsar regime, rotation powered radio pulsar regime and sub-luminous disk regime), while PSR J1023+0038 and XSS J12270–4859 were only observed to switch between the radio pulsar state and the sub-luminous disk state. The observation of systems lying in the sub-luminous disk state for a decade or more was unexpected (Papitto et al. 2014), and motivates the formulation of new models able to account for the coexistence of the accretion disk with a source which propels away the in-flowing matter over such long time-scales. Observing millisecond pulsars in the sub-luminous disk state is then of paramount importance to understand not only the evolution of neutron stars towards the maximum rotational velocities that they can achieve, but also how accretion and ejection of plasma are coupled, and what is the role of the magnetic fields in driving outflows and jets. Moreover, understanding the process underlying the gamma-ray emission in this state would assess whether a new class of accreting gamma-ray sources with a low mass companion star could be established. These are the reasons why Chapter 8 of this thesis is devoted to the multiwavelength characterization and modelling of one of the best studied transitional millisecond pulsars so far: PSR J1023+0038.

1.4 Magnetars

Although historically divided in two classes, the so-called *anomalous X-ray pulsars* (AXPs) and *soft gamma-ray repeaters* (SGRs) were gradually recognized to be the same kind of astrophysical objects based on several observed similarities. According to the magnetar model, both classes are the observational manifestations of the same underlying source: an isolated neutron star ultimately powered by the instability and (impulsive and/or steady) dissipation of its extremely high magnetic field (up to $10^{14} - 10^{15}$ G at the surface), hence the name *magnetar* (a portmanteau of ‘magnetic star’). Indeed, their X-ray luminosity (at the persistent level or when in outburst for transient sources) generally exceeds the rotational energy loss rate, and their temperatures are often higher than what non-magnetic cooling models predict. However, other scenarios have been proposed, including models based on isolated neutron stars accreting from a fossil disk formed by the fallback of material produced in the supernova explosion or during a common-envelope interaction, as well as models involving quark stars (see Turolla & Esposito 2013 for a review). In this thesis I will focus on the widely accepted magnetar scenario. After a brief excursion highlighting the historical milestones regarding these extremely peculiar and enigmatic objects, I will summarize the key ingredients of the magnetar model and its observational predictions, with a particular focus on the recent progresses in the field. Recent and comprehensive reviews on the topic are provided by Mereghetti, Pons & Melatos (2015), Turolla, Zane & Watts (2015) and Kaspi & Kramer (2016). Detailed studies of many different X-ray properties of magnetars across their outburst decays are reported in Chapters 2, 4 and 5.

1.4.1 Historical excursion

On 1979 March 5 at 15:51 UT, the Gamma-Ray Burst experiment Konus on the *Venera 11* and *Venera 12* spacecrafts was hit by a blast of gamma-ray radiation (Mazets et al. 1979). The count rate measured on both probes increased from about 10^2 counts s^{-1} to about 2×10^5 counts s^{-1} in only a fraction of a millisecond. The episode lasted about 0.2 s, and was recorded by nine different satellites throughout the Solar System. The relative timing among the detectors enabled the localization of the source of the gamma-ray radiation to an accuracy of about 2 arcseconds (Cline et al. 1982). The direction of the source, currently known as SGR 0526–66⁹, corresponded with the supernova remnant N49, which is located in the Large Magellanic Cloud at a distance of about 50 kpc (Pietrzyński et al. 2013). At this distance, the peak luminosity of the spike had to be extremely large, more than 10^{45} erg s^{-1} (assuming isotropic emission). After the initial spike, the gamma-ray emission was observed to decay quasi-exponentially over a time scale of about 200 s, with a clear modulation at a period of about 8.1 s (Terrell et al. 1980). The energy released during the burst, about 5×10^{44} erg, made this episode the highest intensity gamma-ray event of extra-solar origin ever detected up to that point (over 100 times more intense than any known previous extra-solar burst). Another burst, orders of magnitude less intense,

⁹SGR stands for soft gamma-ray repeater, to distinguish from the typical gamma ray bursts.

was detected from SGR 0526–66 within a day (Aptekar et al. 2001).

The ‘March 5 event’, as it is usually recollected, was however not the first soft-gamma ray burst ever observed. Indeed, another burst had been already detected on 1979 January 7. Initially catalogued as a gamma-ray burst (GRB 790107) based on observations by *Konus* (Mazets et al. 1981) and other all-sky monitors of the interplanetary network (Laros et al. 1986), the source was recognized to be a member of a distinct class of astrophysical transients after the detection of more than 100 bursts of soft gamma-rays between 1979 and 1986 from the same location (Laros et al. 1987), a property never observed in any of the cosmological gamma-ray bursts. The source was then termed as SGR 1806–20. Two observations were carried out by the *Advanced Satellite for Cosmology and Astrophysics* soon after an intense bursting activity in 1993 October (as unveiled by the Burst and Transient Source Experiment aboard the *Compton Gamma Ray Observatory*), leading to the identification of a previously uncatalogued, persistent, point-like X-ray counterpart (Murakami et al. 1994, Sonobe et al. 1994). A periodicity of ~ 7.47 s and a period derivative of $8 \times 10^{-11} \text{ s s}^{-1}$ were later detected in the persistent X-ray emission by means of 5 observations with the *Rossi X-ray Timing Explorer (RXTE)*, which were performed in 1996 November following another reactivation of the source (Kouveliotou et al. 1998).

Another recurrent burster (SGR 1900+14) was discovered in 1979, when three soft gamma-ray short bursts were detected from the same location on March 24, 25, and 27.

At the moment of writing, three SGRs have shown particularly powerful ‘*giant flares*’. The second giant flare was detected from SGR 1900+14 on 1998 August 27 at 10:22:16 UT (Feroci et al. 1999; Hurley et al. 1999), about 20 years after the ‘March 5 event’. The bright spike lasted about 0.35 s, and saturation of the detectors by the enormous photon flux prevented a reliable measurement of the peak luminosity (estimated to be $\gtrsim 8.3 \times 10^{44} \text{ erg s}^{-1}$ for a distance of 12.5 kpc; Davies et al. 2009) and reconstruction of the true shape of the light curve. The event also caused an ionospheric disturbance in the Earth’s upper atmosphere that was recorded around the globe¹⁰ (Inan et al. 1999). During the 400-s tail of the flare, the light curve maintained large-amplitude modulations at a period of 5.16 s, the same periodicity that had been previously detected in the persistent emission of the X-ray counterpart. Finally, on 2004 December 27 at 21:30:26 UT, more than 20 satellites caught the most energetic Galactic gamma-ray transient event ever: during the first 0.5 s of this extremely powerful event, SGR 1806–20 outshone by a factor of 1000 all the stars in our Galaxy, reaching a peak luminosity upwards of $2 \times 10^{47} \text{ erg s}^{-1}$ (for a distance of 8.7 kpc), and released a total energy of about $4 \times 10^{46} \text{ erg}$ (Hurley et al. 2005; Mereghetti et al. 2005; Palmer et al. 2005). A ‘ringing tail’ was again observed, this time lasting about 600 s, modulated at a period of 7.56 s over a time span of about 380 s. The light curves of the three giant flares detected so far are shown in Figure 1.6.

¹⁰The atoms in the ionosphere, which are usually ionized by the radiation from the Sun by day and recombine to neutral atoms by night, were ionized at night time at levels not much lower than the normal daytime level.

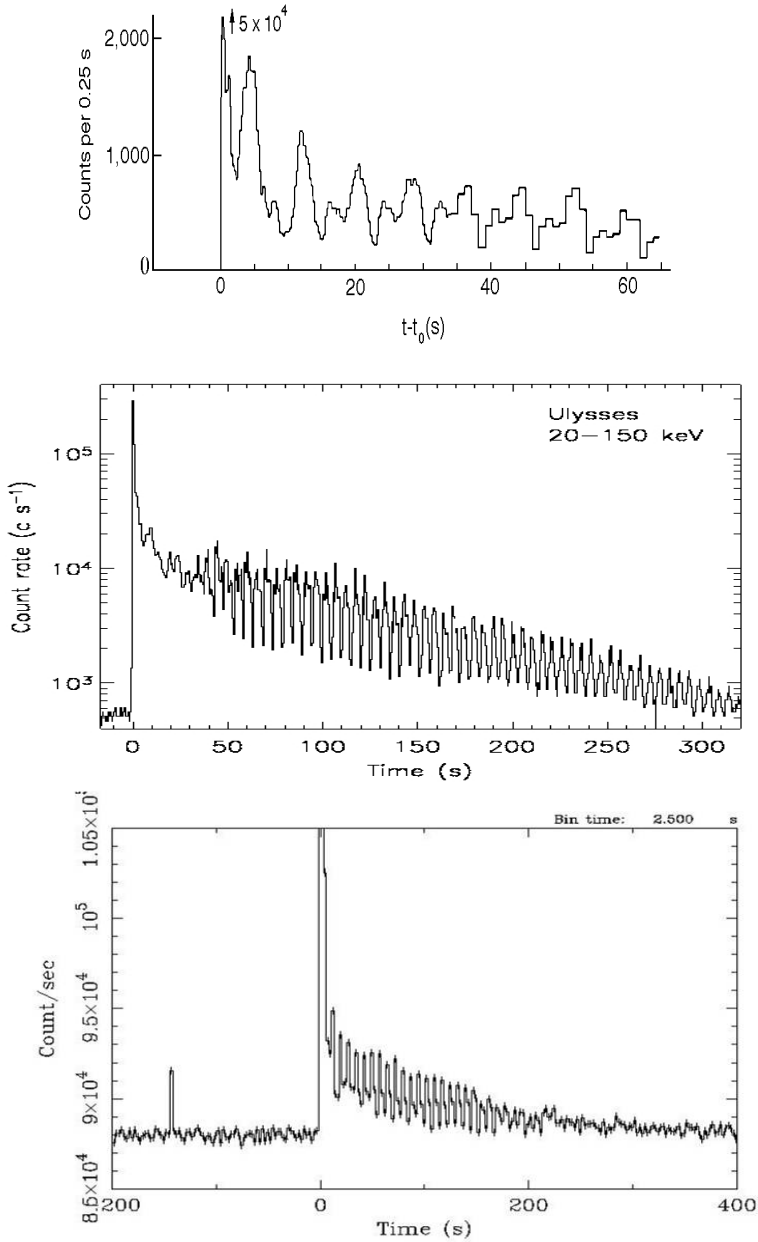


Figure 1.6: Light curves of the three giant flares from SGRs. Top panel: SGR 0526–66 (50–150 keV range; Mazets et al. 1979); middle panel: SGR 1900+14 (20–150 keV range, Hurley et al. 1999); bottom panel: SGR 1806–20 (>80 keV; Mereghetti et al. 2005).

Following the announcement of the discovery of SGRs as a peculiar class of bursting neutron stars, a variety of models were proposed. These include thermonuclear energy release on a neutron star (Woosley & Wallace 1982), cometary accretion onto quark stars (Alcock, Farhi & Olinto 1986), as well as accretion onto neutron stars (e.g. Livio & Taam 1987; Katz, Toole & Unruh 1994). The drawback of all these models was the lack of an adequate explanation for the giant flares.

The association of SGRs with relatively young supernova remnants, the value for the measured periodicities of their X-ray counterpart and the strength of the dipolar component of the magnetic field estimated for SGR 1806–20 in the pulsar scenario (8×10^{14} G under the assumption of pure magnetic dipole braking) led to hypothesize that an isolated neutron star endowed with an extremely strong magnetic field could be one possible origin for the bursting behavior of these sources. The suggestion that SGRs could be indeed neutron stars whose emission was ultimately powered by the decay and the instability of their ultra-strong magnetic field was first invoked in the '90s, to interpret the exceptional properties of the 'March 5 event' (Duncan & Thompson 1992; Paczynski 1992; Thompson & Duncan 1993, 1995). It was noticed that a magnetic field of about 10^{15} Gauss was required for the neutron star to spin down via magnetic braking from the expected spin period at birth (less than a second) to the current period (about 8 s) in about 5 kyr (the age estimated for the supernova remnant associated with SGR 1806–20; e.g., Shull 1983). The term magnetar was coined.

While SGRs were first identified through intense, repeated bursts in the hard X-/gamma-ray band, anomalous X-ray pulsars (AXPs) were revealed thanks to their persistent emission in the soft X-rays. The archetypical AXP, 1E 2259+586, was discovered as a bright persistent X-ray source at the centre of the supernova remnant G109.1–1.0 (aka CTB 109) in 1979 December (Fahlman & Gregory 1981). The spin period of 6.98 s and its derivative of $\sim 5 \times 10^{-13}$ s s⁻¹ (Koyama, Hoshi & Nagase 1987), made it immediately clear that the loss of rotational energy released via spin down was orders of magnitude too small to power the observed luminosity of a few 10^{35} erg s⁻¹: 1E 2259+586 could not be a rotation powered pulsar. Stringent limits on the mass of an unseen (possibly obscured by interstellar extinction) companion star were derived from repeated measurements of the pulsation period, which did not reveal any Doppler modulation produced by a possible binary orbit (Mereghetti, Israel & Stella 1998). Several additional sources were found with similar characteristics and with a narrow distribution of rotational periods, such as 1E 1048.1–5937 and 4U 0142+614 (with spin periods of 6.46 s and 8.69 s, respectively). They were all tentatively recognized as a subclass of X-ray pulsars accreting from a very low mass companion star¹¹ (Mereghetti & Stella 1995; van Paradijs, Taam & van den Heuvel 1995; Mereghetti et al. 2002) with very peculiar and unique characteristics (hence the adjective 'anomalous'): unlike most X-ray emitting neutron stars in accreting binary systems, they were characterized by a very soft energy spectrum and a relatively stable secular spin down rate (on timescales of $10^3 - 10^5$ yr); unlike radio pulsars, none of these

¹¹The possibility that AXPs might be neutron stars accreting from the interstellar medium (Israel et al. 1994) was ruled out owing to the very high densities required to produce their observed luminosity.

sources were originally observed at radio wavelengths. These characteristics naturally raised the issue of where the X-ray emission was originated, and what could power their persistent emission.

1E 2259+586 attracted attention on 2002 June 18, when a storm of more than 80 bursts were detected within 3 h of observing time by *RXTE*, and the persistent flux rose by a factor of ~ 10 (Kaspi et al. 2003). The previous year, a systematic search for bursts in the *RXTE* data of 1E 1048.1–5937 revealed that the source underwent two bursts in 2001 October – November (Gavriil, Kaspi & Woods 2002): the defining characteristic of a SGR, the rapid and short bursts of hard X-/soft gamma-rays, had been discovered from well-known AXPs. On the other hand, the number of SGRs with X-ray counterparts showing persistent pulsations was significantly increasing. These observations started pointing out many similarities between these two classes of objects.

The apparent lack of pronounced variability was thought to be among the defining properties that led to the initial identification of AXPs. This conjecture was later challenged following the discovery of a major enhancement of the X-ray flux of the source XTE J1810–197. Originally a soft and faint X-ray source serendipitously recorded by *ROSAT* during four observations between 1991 and 1993, the transient nature of XTE J1810–197 was revealed in 2003, when the *RXTE* detected it at an X-ray flux a factor about 100 larger with respect to the historical level (Ibrahim et al. 2004). Moreover, radio pulsations at the spin period inferred from X-ray observations (5.54 s) were detected about one year later, a property never observed before in any other AXP that proved that pulsed radio emission could definitely be produced in this class of sources (Camilo et al. 2006). Today we know that 4 sources among SGRs and AXPs (XTE J1810–197, 1E 1547–5408, PSR 1622–4950 and SGR 1745–2900) are occasionally shining as radio pulsars in the outburst phase (Camilo et al. 2006, 2007; Levin et al. 2010; Eatough et al. 2013).

1.4.2 Phenomenology

The magnetar model certainly represents the most convincing scenario to explain the variety of behaviors observed in AXPs and SGRs, and these sources are usually labelled as magnetar candidates. At the moment of writing (2016 October), the magnetar family comprises 23 confirmed members (see Olausen & Kaspi 2014 for a catalogue). It is worth remarking that the Burst Alert Telescope aboard *Swift* and the Gamma-ray Burst Monitor aboard *Fermi* represent still nowadays excellent ‘hunting machines’ for magnetars, and their continuous surveys of the hard X-/gamma-ray sky led (and lead still nowadays) to the discovery of several new SGRs thanks to their bursting activity. With the exception of SGR 0526–66 and CXOU J0100–7211, which are located in the Magellanic Clouds, all magnetars are Galactic sources distributed at low latitudes in the Galactic plane. Three sources (CXOU J1647–4552, SGR 1806–20 and SGR 1900+14) are likely located in clusters of massive stars, suggesting that magnetars are formed in the collapse of very massive stars (Olausen & Kaspi 2014). The associations with supernovae remnants and young star clusters, as well as their distribution in the Galactic plane, indicate that magnetars are relatively young neutron stars.

Magnetars rotate at comparatively long periods ($P \sim 2 - 12$ s) and are characterized by large secular spin down rates ($\dot{P} \sim 10^{-15} - 10^{-10}$ s s $^{-1}$). These values place magnetars in the upper right corner of the $P - \dot{P}$ diagram (see Figure 1.3) and, if interpreted in terms of electromagnetic losses from a rotating dipole in vacuo, yield field strengths in the range $10^{14} - 10^{15}$ G according to the standard magnetic braking formula.

Besides the rare giant flares, magnetars frequently emit unpredictable short bursts and intermediate flares of hard X-/soft gamma-rays.¹² The former have peak luminosities of $\sim 10^{36} - 10^{41}$ erg s $^{-1}$, with a typical duration of about 0.01–1 s. The morphology of the light curves is extremely heterogeneous and consists of single or multiple peaks with rise times usually shorter than the decay times. No simple phenomenological model has yet been found that satisfactorily fits the shape of the different burst light curves. The latter involve a lower energy compared to the giant flares, but they are definitely brighter ($\sim 10^{41} - 10^{43}$ erg s $^{-1}$) than the normal short bursts, hence the name ‘intermediate’. Their duration is within the 1 – 40 s interval. The structure of the light curves is varied: some display a clear decay and an abrupt end, others show instead an extended decaying tail lasting up to several thousands of seconds. The most powerful intermediate flare ever was observed on 2001 April 18 from SGR 1900+14 (Kouveliotou et al. 2001; Guidorzi et al. 2004). It lasted about 40 s, and showed pulsations at the neutron star rotation period, as in the tails of giant flares, but it lacked an initial spike.

In the last 15 years, following the advent of the new generation of imaging instruments on board *Swift*, *Chandra* and *XMM-Newton*, it has been possible to obtain very accurate flux measurements. About half of the magnetars have been observed over many years at a relatively steady X-ray luminosity of $\sim 10^{35} - 10^{36}$ erg s $^{-1}$. The other sources spend most of their time at a much lower luminosity, and their past bursting episodes have been accompanied by large and rapid enhancements of the persistent X-ray flux (typically by a factor of $\sim 10 - 1000$ above that in quiescence and up to values comparable to those of the persistently bright magnetars), which then declined and attained the pre-outburst level ($\sim 10^{32} - 10^{33}$ erg s $^{-1}$) on a timescale ranging from a few weeks up to several years. I will refer to these phases as outbursts, to distinguish from the short bursts. In the last decades, several magnetar outbursts have been monitored in the X-rays. In some cases, the monitoring campaigns covered the whole outburst evolution, and disclosed the source quiescent level. Although the cooling pattern significantly varies from outburst to outburst, the spectral softening throughout the decay seems an ubiquitous characteristic for these events (see Rea & Esposito 2011 for an observational review).

The soft X-ray ($\lesssim 10$ keV) emission of magnetars is typically described by a combination of a soft, thermal component (a black body with temperature $kT \sim 0.3 - 0.9$ keV) plus a power-law tail with photon index $\Gamma \sim 2 - 4$. In some cases a multiple-black body model provides an adequate description as well, and it is usually ascribed to thermal emission from regions of different temperature and size on the star surface (e.g. Tiengo, Esposito & Mereghetti 2008; Alford & Halpern 2016). In other cases a single power-law is enough,

¹²See the Amsterdam Magnetar Burst Library at <http://staff.fnwi.uva.nl/a.l.watts/magnetar/mb.html>.

even if an additional thermal component is often required in deeper observations of the same source. Several sources have been detected also in the hard X-ray range (> 20 keV), with the *International Gamma-Ray Astrophysics Laboratory (INTEGRAL)*, *Suzaku*, the *Nuclear Spectroscopic Telescope Array (NuSTAR)* and *RXTE* (e.g., Kuiper et al. 2004; An et al. 2013, 2014, 2015; Mori et al. 2013; Vogel et al. 2014). The power-law-like emission in the hard X-rays is generally modulated at the spin period, and is characterized by a luminosity comparable to, and in some cases higher than, that in the soft X-ray band. On the other hand, a search for gamma-ray emission from 20 magnetars using 6 years of data acquired with the Large Area Telescope aboard *Fermi* yielded only upper limits between 10^{-12} and 10^{-13} erg cm $^{-2}$ s $^{-1}$ (in the 0.1–10 GeV band; Li et al. 2016). Searches for TeV emission with ground based telescopes also resulted in no detections (Aleksić et al. 2013). The study of the optical and infrared counterparts of magnetars is instead hampered by their location in strongly absorbed regions of the Galactic plane and the typically large number of field sources located within their X-ray error circles. Faint counterparts have been found for about one third of the known magnetars, and optical pulsations have been detected in three cases: 4U 0142+614 (Dhillon et al. 2005), 1E 1048.1–5937 (Dhillon et al. 2009) and SGR 0501+4516 (Dhillon et al. 2011).

1.4.3 The magnetar model: an overview

According to the magnetar model, bursting and flaring activity is due to rapid magnetic field reconfiguration. Different locations have been proposed for the origin of the triggering mechanism: it may be due to the evolution of the magnetic field into an unstable configuration within the liquid core of the neutron star, leading to large-scale magnetohydrodynamical instabilities and to the injection of Alfvén waves into the magnetosphere that generate the observed burst emission (Flowers & Ruderman 1977); alternatively, bursts may arise from magnetic stresses in the solid crust imparted by the decay of the magnetic field in the core: the crust initially deforms elastically, but then ruptures catastrophically via rapid plastic deformation once its braking strain is exceeded (Thompson & Duncan 1995, 2001; Beloborodov & Levin 2014). The final option attributes bursts to magnetospheric stresses taking place via a plasma instability that involves spontaneous and explosive magnetic reconnection (Lyutikov 2006; Beloborodov 2009; Parfrey, Beloborodov & Hui 2012, 2013).

One essential feature of the magnetar model is the presence of significant twists in the magnetosphere, either on a global scale (Thompson, Lyutikov & Kulkarni 2002), or, more realistically, confined to localized regions (Beloborodov & Thompson 2007). These twists result in a structure quite at odds with that of the simple dipolar geometry assumed for canonical rotation-powered pulsars, and in large-scale magnetospheric currents with a charge density much larger than the classical Goldreich-Julian value. The copious flow of charged particles produces a significant optical depth for resonant cyclotron scattering in the magnetosphere, which is proportional to the twist angle. The twisted magnetic field leads to the formation of an electron/positron corona in the closed magnetosphere, consisting of closed flux tubes anchored on the neutron star surface and permeated by

currents of charged particles (Beloborodov & Thompson 2007).

The paradigm that the bursting activity of magnetar might be related mainly to the presence of a significant toroidal component of the internal field (responsible for the deformation of the crust and able to produce magnetospheric twists), rather than to a high dipolar field, was strengthened by the recent discovery of a few full-fledged sources showing magnetar-like activity, despite having a dipolar magnetic field $\lesssim 10^{13}$ G (i.e. comparable with that of standard radio pulsars; Esposito et al. 2010; Rea et al. 2010, 2012; van der Horst et al. 2010; Livingstone et al. 2011; Scholz et al. 2012).

The soft X-ray emission of magnetars is usually interpreted in terms of repeated resonant Compton up-scattering of thermal photons from the star surface onto the charges flowing in the twisted magnetosphere (Thompson et al. 2002; Nobili, Turolla & Zane 2008a,b; Rea et al. 2008; Zane et al. 2009), whereas two possibilities have been proposed to explain the persistent tails at high energy: thermal bremsstrahlung from a thin turbulent layer of the star surface heated up to $kT \sim 100$ keV by magnetospheric returning currents (Thompson & Beloborodov 2005); and synchrotron emission from mildly relativistic pairs produced at a height of about 100 km above the neutron star (Heyl & Hernquist 2005). Compton up-scattering of soft thermal photons on a population of highly relativistic electrons threaded in the magnetosphere has also been considered (Baring & Harding 2007). The origin of the infrared and optical emissions is still matter of debate, and the possibility that they may be generated due to plasma instabilities in the inner region of the magnetosphere seems promising (Beloborodov & Thompson 2007). However, detailed modeling and/or numerical simulations are still lacking.

Outbursts

Although it is widely accepted that magnetar outbursts are attributable to some form of heat deposition in a restricted region of the star surface which then cools, the mechanism responsible for their activation, as well as the energy supply responsible for sustaining their long-term emission, still remain somewhat elusive. They are probably triggered by local internal magnetic stresses strong enough to irreversibly deform part of the stellar crust, possibly in the form of a prolonged avalanche of plastic failures (Li, Levin & Beloborodov 2016). An additional contribution may be provided by magnetospheric Alfvén waves created during flaring activity (Parfrey et al. 2013). According to Li & Beloborodov (2015), these waves are impulsively transmitted inside the star, and induce a strong oscillating plastic flow in the crust that subsists for a few ms, after which the waves are damped. Independently from the triggering mechanism, the plastic flows induced in the crust lead to transient thermo-plastic waves that move the crust, mechanically convert its magnetic energy into heat, and relieve the stresses (Beloborodov & Levin 2014). A fraction of the deposited heat is then conducted up to the surface and radiated, producing a delayed thermal afterglow emission that can be sustained up to a few years (see also Beloborodov & Li 2016). The crustal cooling timescale chiefly depends on the thermal properties of the outer crust, the depth at which the energy is released, and the neutrino emission processes operating in the crust (Pons & Rea 2012; Li et al. 2016). Moreover, the crustal

displacements implant a strong external magnetic twist, presumably confined to a bundle of current-carrying closed field lines anchored in the crust. Additional heating of the surface layers is then produced as the currents flowing along the field lines of the twisted bundle impact upon the star (e.g. Thompson et al. 2002; Beloborodov & Thompson 2007; Beloborodov 2009). As the energy reservoir stored in the star interior is progressively depleted, the twist must decay to support its currents. Consequently, the spatial extent of the bundle gets gradually more and more limited, the area on the star's surface hit by the charges shrinks and the luminosity decreases. The timescale of the resistive untwisting can be of the order of a few years if the crustal motions take place at high latitudes and the footpoints of the bundle are positioned close to the magnetic poles (Beloborodov 2009). Both heating mechanisms – internal and external – are likely at work.

1.5 Other classes of isolated neutron stars

Besides magnetars and transitional millisecond pulsars, this thesis encompasses also X-ray studies of sources belonging to two additional classes of isolated neutron stars: the central compact objects in supernova remnants (Chapter 3) and the X-ray dim isolated neutron stars (Chapter 6).

1.5.1 Central Compact Objects

The Central Compact Objects (CCOs) form a small, heterogeneous family of X-ray emitting neutron stars located close to the geometrical centre of shell-like supernova remnants and with no associated nebulae and counterparts at other wavelengths (see De Luca 2008 for a review). Three CCOs have spin periods in the 0.1–0.4 s range and spin down rates $\dot{P} \lesssim 2.5 \times 10^{-16} \text{ s s}^{-1}$, yielding estimates for the magnetic field at the surface $\lesssim 10^{11} \text{ G}$ (Gotthelf, Halpern & Alford 2013). Their characteristic ages – at most of a few tens kyrs – exceed by orders of magnitude the ages of their associated supernova remnants, implying that these isolated neutron stars were probably born with spin periods very close to the current values. Two main scenarios have been put forward to explain the unusually low magnetic field estimated for these objects. First, these neutron stars may be born with a magnetic field much lower than that of their siblings, the rotation-powered pulsars. An alternative possibility, the ‘hidden magnetic field’ scenario, considers the accretion of the fallback of the supernova debris onto the neutron star (e.g., Geppert et al. 1999; Shabaltas & Lai 2012). Recent simulations have shown that an amount of mass in the range $10^{-3} - 10^{-2} M_{\odot}$ accreting onto the neutron star surface on a typical timescale of hours to days can bury a magnetic field of a few 10^{12} G into the inner crust (Viganò & Pons 2012; Torres-Forné et al. 2016). As a result, the strength of the external magnetic field is significantly lower than the internal ‘hidden’ magnetic field. Once the accretion process stops, the magnetic field might eventually re-emerge on a typical time-scale of 1–100 kyr, and after this stage the magnetic field at the surface is restored close to its value at birth.

The rotational energy loss of the three CCOs for which the spin period has been measured is certainly too small to give a detectable contribution to their observed X-ray luminosity, assuming a typical efficiency of 10^{-3} . Most CCOs have thermal-like X-ray emission, with black body temperatures in the range $\sim 0.2\text{--}0.5$ keV, and no evidence for additional non-thermal components. In some cases single-temperature black body spectra do not provide acceptable fits, and more satisfactory results are obtained with a double black body model with $kT_1 \sim 0.2 - 0.5$ keV and $kT_2 \sim 2 kT_1$. The two-black body model implies small X-ray emitting areas ($R_1 \sim 0.4\text{--}4$ km, $R_2 \sim 0.06\text{--}0.8$ km). The hotter black body is energetically significant, and the ratio of the bolometric luminosities of the two components is $L_2/L_1 \sim 0.2\text{--}0.7$. The emission of CCOs could be due both to residual thermal cooling following formation and weak accretion from a residual disk. The non-uniform distribution of the surface thermal emission, while difficult to reconcile with the former option (e.g., Halpern & Gotthelf 2010), is instead a natural prediction of the hidden magnetic field scenario (Viganò & Pons 2012), and thus favors the latter scenario.

The source near the centre of the ~ 330 yr old (Fesen et al. 2006) supernova remnant Cassiopea A, CXOU J232327.9+584843, is one of the best studied CCOs. It has a very soft spectrum and most spectral fits, with a variety of thermal models, indicate an emitting area smaller than the whole surface of the neutron star. Particularly puzzling is the lack of X-ray periodicity and of associated nebulosity (Pavlov et al. 2000; Mereghetti, Tiengo & Israel 2002; Pavlov & Luna 2009; Halpern & Gotthelf 2010). Ho & Heinke (2009) suggested that the CCO may be surrounded by a carbon atmosphere, showing that its X-ray spectrum is well fit by such a model, and implies a stellar radius consistent with expectations for a neutron star, in contrast to hydrogen or helium atmosphere models. With the entire surface radiating, the absence of pulsations would not be surprising. CXOU J185238.6+004020 is at the centre of the supernova remnant Kesteven 79 (Gotthelf, Halpern & Seward 2005; Halpern et al. 2007). It has a spin period of 105 ms and its characteristic age, $\tau_c = 192$ Myr (Halpern & Gotthelf 2010), is many orders of magnitude larger than the age of the associated supernova remnant (~ 7 kyr). The magnetic field strength, $B = 3.1 \times 10^{10}$ G, is the smallest yet seen in young neutron stars, prompting Halpern & Gotthelf to dub this source ‘anti-magnetar’. Interestingly, this source sits in a sparsely populated region of the $P\text{-}\dot{P}$ diagram (see Figure 1.3), among several recycled binary pulsars. A similar case is the CCO in the supernova remnant G296.5+10.0, 1E 1207.4–5209. This 0.424-s X-ray pulsar (Zavlin et al. 2000) has $B = 9.8 \times 10^{10}$ G and $\tau_c = 302$ Myr (Gotthelf et al. 2013), three orders of magnitude greater than the age of the supernova remnant (~ 7 kyr). Yet another low- B CCO is RX J0852–4622 in Puppis A, with $P = 112$ ms, $B = 2.9 \times 10^{10}$ G and $\tau_c = 254$ Myr (Gotthelf et al. 2013). Arguably the most bizarre CCO is 1E 161348–5055 at the centre of the 2000 yr old supernova remnant RCW 103 (see Figure 1.7). More details on this source and its recent outburst will be given in Chapter 3.



Figure 1.7: Image of the central compact object 1E 161348–5055 in the supernova remnant RCW 103. The composite RGB image was obtained by stacking the data from 22 observations carried out by *Chandra* between 2000 February and 2006 June (for a total exposure time of about 360 ks) and data from the Digitized Sky Survey (DSS). Credit: X-ray: NASA/CXC/University of Amsterdam/Rea et al. (2016)/this thesis; Optical: DSS.

1.5.2 X-ray Dim Isolated Neutron Stars

The X-ray Dim Isolated Neutron Stars (XDINSs) are a group of seven nearby ($\lesssim 500$ pc) X-ray pulsars discovered in the *ROSAT* satellite All Sky Survey (see van Kerkwijk & Kaplan 2007 and Turolla 2009 for reviews).¹³ They are characterized by relatively long spin periods (in the 3–12 s range), very soft quasi-thermal spectra with black body temperatures in the range 40–110 eV, X-ray luminosity of 10^{30} – 10^{33} erg s⁻¹, faint optical counterparts (with typical X-ray-to-optical flux ratios of the order of $F_x/F_{opt} \sim 10^4$ – 10^5), and absence of radio emission. The most recent upper limits of 0.14–5 μ Jy kpc², obtained at 1400 MHz (Kondratiev et al. 2009), correspond to pulsed luminosities well below those of the faintest observed rotation-powered pulsars. However, the possibility that the lack of radio emission could be simply due to unfavorable orientations cannot be ruled out. The complete absence of non-thermal emission and, in a few cases, the accurate measurement of parallax distances, make XDINSs ideal targets to infer the neutron star size and atmospheric composition through detailed modeling of their thermal emission. XDINSs may represent an interestingly large fraction of all Galactic neutron stars, but the detection of more distant sources of this type is hampered by the severe absorption of their soft X-ray emission by the interstellar medium.

Timing analyses of several XDINSs have revealed that they are spinning down regularly, with period derivatives of the order of 10^{-14} – 10^{-13} s s⁻¹ (Pires et al. 2014 and references therein). The derived dipolar surface magnetic fields, typically ~ 1 – 3×10^{13} G, suggest then a possible relation with the magnetars. Magnetic fields in the $\sim 10^{13}$ – 10^{14} G range are also inferred once the broad (and occasionally time-variable) absorption lines observed in the ~ 0.2 – 0.8 keV energy range of several X-ray spectra are interpreted either in terms of proton cyclotron lines or H (He) atomic transitions.¹⁴

The X-ray emission of XDINSs is thought to be powered mainly by the internal heat stored since the neutron star formation. Their luminosity is much lower than that of younger thermally cooling rotation-powered pulsars (because of their much larger ages: ~ 1 – 4 Myr), but still too large for conventional cooling. This is suggestive of an additional source of heating. Magnetic field decay could be easily reconciled with their surprisingly high magnetic fields (Viganò et al. 2013).

Chapter 6 reports the discovery of a narrow and strongly phase-variable absorption feature in the spectrum of the XDINS RX J0720.4–3125, a result which provides important implications on the magnetic structures at the exterior of these isolated neutron stars and on the tight evolutionary link between XDINSs and magnetars.

¹³They are also known as ‘The Magnificent Seven’, the title of a 1960 American Western film.

¹⁴Note that the lines measure the surface field, which can be higher than the dipolar component dominating at large radii and responsible for the spin down.

Chapter **2**

The X-ray outburst of the Galactic Centre magnetar SGR J1745-2900 during the first 1.5 year

Coti Zelati F., Rea N., Papitto A., Viganò D., Pons J. A., Turolla R., Esposito P., Haggard D., Baganoff F. K., Ponti G., Israel G. L., Campana S., Torres D. F., Tiengo A., Mereghetti S., Perna R., Zane S., Mignani R. P., Possenti A., Stella L. (2015),

**The X-ray outburst of the Galactic Centre magnetar
SGR J1745–2900 during the first 1.5 year,**

*Published in Monthly Notices of the Royal Astronomical Society,
Volume 449, Issue 3, pp. 2685–2699*

In 2013 April a new magnetar, SGR 1745–2900, was discovered as it entered an outburst, at only 2.4 arcsec angular distance from the supermassive black hole at the Centre of the Milky Way, Sagittarius A*. SGR 1745–2900 is the neutron star closest to a black hole ever observed, and was detected both in the radio and X-ray bands, with a peak X-ray luminosity $L_X \sim 5 \times 10^{35} \text{ erg s}^{-1}$. It has a dipolar magnetic field of $\sim 2 \times 10^{14} \text{ G}$ at the surface. Here we report on the long-term *Chandra* (25 observations) and *XMM-Newton* (8 observations) X-ray monitoring campaign of SGR 1745–2900 from the onset of the outburst in 2013 April until 2014 September. This unprecedented dataset allows us to refine the timing properties of the source, as well as to study the outburst spectral evolution as a function of time and rotational phase. Our timing analysis confirms the increase in the spin period derivative by a factor of ~ 2 around 2013 June, and reveals that a further increase occurred between 2013 October 30 and 2014 February 21. We find that the period derivative changed from $6.6 \times 10^{-12} \text{ s s}^{-1}$ to $3.3 \times 10^{-11} \text{ s s}^{-1}$ in 1.5 yr. On the other hand, this magnetar shows a slow flux decay compared to other magnetars and a rather inefficient surface cooling. In particular, starquake-induced crustal cooling models alone have difficulty in explaining the high luminosity of the source for the first ~ 200 days of its outburst, and additional heating of the star surface from currents flowing in a twisted magnetic bundle is probably playing an important role in the outburst evolution.

2.1 Introduction

The discovery of SGR 1745–2900 dates back to 2013 April 24, when the Burst Alert Telescope (BAT) on board the *Swift* satellite detected a short hard X-ray burst at a position consistent with that of the supermassive black hole at the centre of the Milky Way, Sagittarius A* (hereafter Sgr A*). Follow-up observations with the *Swift* X-ray Telescope (XRT) enabled to characterize the 0.3–10 keV spectrum with an absorbed black body (with $kT \sim 1 \text{ keV}$), and estimate a luminosity of $\sim 3.9 \times 10^{35} \text{ erg s}^{-1}$ (for an assumed distance of 8.3 kpc; Kennea et al. 2013a). The following day, a 94.5 ks observation performed with the *Nuclear Spectroscopic Telescope Array* (*NuSTAR*) revealed pulsations at a period of 3.76 s from the XRT source (Mori et al. 2013). This measurement was subsequently confirmed by a 9.8 ks pointing on April 29 with the High Resolution Camera (HRC) onboard the *Chandra* satellite, which was able to single out the magnetar counterpart at only 2.4 ± 0.3 arcsec from Sgr A*, confirming that the new source was actually responsible for the X-ray brightening observed in the Sgr A* region (Rea et al. 2013a). Follow-up observations in the 1.4–20 GHz radio band revealed the radio counterpart of the source and detected pulsations at the X-ray period (e.g. Eatough et al. 2013a; Shannon & Johnston 2013). The SGR-like bursts, the X-ray spectrum, and the surface dipolar magnetic field inferred from the measured spin period and spin-down rate, $B_p \sim 2 \times 10^{14} \text{ G}$, led to classify this source as a magnetar (Mori et al. 2013; Kennea et al. 2013; Rea et al. 2013a).

SGR 1745–2900 holds the record as the closest neutron star to a supermassive black hole detected to date. The dispersion measure $DM = 1778 \pm 3 \text{ cm}^{-3} \text{ pc}$ is also the highest ever measured for a radio pulsar and is consistent with a source located within 10 pc of the

Galactic Centre. The neutral hydrogen column density along the line of sight, $N_{\text{H}} \sim 10^{23} \text{ cm}^{-2}$, is characteristic of a location at the Galactic Centre (Baganoff et al. 2003). The angular separation of 2.4 ± 0.3 arcsec from Sgr A* corresponds to a minimum physical separation of 0.09 ± 0.02 pc (at a 95 per cent confidence level; Rea et al. 2013a) for an assumed distance of 8.3 kpc (see e.g. Genzel et al. 2010). Recent observations of the radio counterpart with the *Very Long Baseline Array* (VLBA) succeeded in measuring its transverse velocity of $236 \pm 11 \text{ km s}^{-1}$ at position angle of 22 ± 2 deg East of North (Bower et al. 2015). If born within 1 pc of Sgr A*, the magnetar has a ~ 90 per cent probability of being in a bound orbit around the black hole, according to the numerical simulations of Rea et al. (2013a).

SGR 1745–2900 has been monitored intensively in the X-ray and radio bands since its discovery. Three high-energy bursts were detected from a position consistent with that of the magnetar on 2013 June 7, August 5 by *Swift*/BAT, and on September 20 by the *INTErnational Gamma-Ray Astrophysics Laboratory* (*INTEGRAL*) (Barthelmy et al. 2013a,b; Kennea et al. 2013b,c; Mereghetti et al. 2013). Kaspi et al. (2014) reported timing and spectral analysis of *NuSTAR* and *Swift*/XRT data for the first ~ 4 months of the magnetar activity (2013 April–August). Interestingly, an increase in the source spin-down rate by a factor ~ 2.6 was observed, possibly corresponding to the 2013 June burst. The source has been observed daily with *Swift*/XRT until 2014 October, and its 2–10 keV flux has decayed steadily during this time interval (Lynch et al. 2015). Radio observations made possible a value of the rotational measure, $RM = 66960 \pm 50 \text{ rad m}^{-2}$, which implies a lower limit of ~ 8 mG for the strength of the magnetic field in the vicinity of Sgr A* (Eatough et al. 2013b). Observations with the *Green Bank Telescope* showed that the source experienced a period of relatively stable 8.7-GHz flux between 2013 August and 2014 January and then entered a state characterized by a higher and more variable flux, until 2014 July (Lynch et al. 2015).

In this chapter we report on the X-ray long-term monitoring campaign of SGR 1745–2900 covering the first 1.5 yr of the outburst decay. In Section 2.2 we describe the *Chandra* and *XMM-Newton* observations and the data analysis. In Section 2.3 we discuss our results; conclusions follow in Section 2.4.

2.2 Observations and data analysis

The *Chandra X-ray Observatory* observed SGR 1745–2900 26 times between 2013 April 29 and 2014 August 30. The first observation was performed with the HRC to achieve the best spatial accuracy to localize the source in the crowded region of the Galactic Centre (Rea et al. 2013a). The remaining observations were performed with the Advanced CCD Imaging Spectrometer (ACIS; Garmire et al. 2003) set in faint timed-exposure imaging mode with a 1/8 sub-array (time resolution of 0.4 s), and in three cases with the High Energy Transmission Grating (HETG; Canizares et al. 2005). The source was positioned on the back-illuminated S3 chip. Eight observations were carried out by the *XMM-Newton* satellite using the European Photon Imaging Camera (EPIC), with the pn (Strüder et al.

Table 2.1: Log of *Chandra*/ACIS-S and *XMM-Newton*/EPIC observations. Exposure times for the *XMM-Newton* observations are reported for the pn, MOS1 and MOS2 detectors respectively, and source net counts refer to the pn detector.

Obs. ID	MJD	Start time (TT) (yyyy/mm/dd hh:mm:ss)	End time (TT) (yyyy/mm/dd hh:mm:ss)	Exposure time (ks)	Source net counts ($\times 10^3$)
14702*	56 424.55	2013/05/12 10:38:50	2013/05/12 15:35:56	13.7	7.4
15040**	56 437.63	2013/05/25 11:38:37	2013/05/25 18:50:50	23.8	3.5
14703*	56 447.48	2013/06/04 08:45:16	2013/06/04 14:29:15	16.8	7.6
15651**	56 448.99	2013/06/05 21:32:38	2013/06/06 01:50:11	13.8	1.9
15654**	56 452.25	2013/06/09 04:26:16	2013/06/09 07:38:28	9.0	1.2
14946*	56 475.41	2013/07/02 06:57:56	2013/07/02 12:46:18	18.2	7.1
15041	56 500.36	2013/07/27 01:27:17	2013/07/27 15:53:25	45.4	15.7
15042	56 516.25	2013/08/11 22:57:58	2013/08/12 13:07:47	45.7	14.4
0724210201†	56 535.19	2013/08/30 20:30:39	2013/08/31 12:28:26	55.6/57.2/57.2	39.7
14945	56 535.55	2013/08/31 10:12:46	2013/08/31 16:28:32	18.2	5.3
0700980101†	56 545.37	2013/09/10 03:18:13	2013/09/10 14:15:07	35.7/37.3/37.3	24.9
15043	56 549.30	2013/09/14 00:04:52	2013/09/14 14:19:20	45.4	12.5
14944	56 555.42	2013/09/20 07:02:56	2013/09/20 13:18:10	18.2	5.0
0724210501†	56 558.15	2013/09/22 21:33:13	2013/09/23 09:26:52	41.0/42.6/42.5	26.5
15044	56 570.01	2013/10/04 17:24:48	2013/10/05 07:01:03	42.7	10.9
14943	56 582.78	2013/10/17 15:41:05	2013/10/17 21:43:58	18.2	4.5
14704	56 588.62	2013/10/23 08:54:30	2013/10/23 20:43:44	36.3	8.7
15045	56 593.91	2013/10/28 14:31:14	2013/10/29 05:01:24	45.4	10.6
16508	56 709.77	2014/02/21 11:37:48	2014/02/22 01:25:55	43.4	6.8
16211	56 730.71	2014/03/14 10:18:27	2014/03/14 23:45:34	41.8	6.2
0690441801†	56 750.72	2014/04/03 05:23:24	2014/04/04 05:07:01	83.5/85.2/85.1	34.3
16212	56 751.40	2014/04/04 02:26:27	2014/04/04 16:49:26	45.4	6.2
16213	56 775.41	2014/04/28 02:45:05	2014/04/28 17:13:57	45.0	5.8
16214	56 797.31	2014/05/20 00:19:11	2014/05/20 14:49:18	45.4	5.4
16210	56 811.24	2014/06/03 02:59:23	2014/06/03 08:40:34	17.0	1.9
16597	56 842.98	2014/07/04 20:48:12	2014/07/05 02:21:32	16.5	1.6
16215	56 855.22	2014/07/16 22:43:52	2014/07/17 11:49:38	41.5	3.8
16216	56 871.43	2014/08/02 03:31:41	2014/08/02 17:09:53	42.7	3.6
16217	56 899.43	2014/08/30 04:50:12	2014/08/30 15:45:44	34.5	2.8
0743630201†	56 900.02	2014/08/30 19:37:28	2014/08/31 05:02:43	32.0/33.6/33.6	9.2
0743630301†	56 901.02	2014/08/31 20:40:57	2014/09/01 04:09:34	25.0/26.6/26.6	7.8
0743630401†	56 927.94	2014/09/27 17:47:50	2014/09/28 03:05:37	25.7/32.8/32.8	7.7
0743630501†	56 929.12	2014/09/28 21:19:11	2014/09/29 08:21:11	37.8/39.4/39.4	11.7

* Observations already analysed by Rea et al. (2013a). An additional *Chandra*/HRC observation was carried out on 2013 April 29. ** *Chandra* grating observations. † *XMM-Newton* observations.

2001) and the two MOS (Turner et al. 2001) CCD cameras operated in full-frame window mode (time resolution of 73.4 ms and 2.6 s, respectively), with the medium optical blocking filter in front of them. A log of the X-ray observations is given in Table 2.1.

Chandra data were analysed following the standard analysis threads¹ with the *Chandra* Interactive Analysis of Observations software package (CIAO, version 4.6; Fruscione et al. 2006). *XMM–Newton* data were processed using the Science Analysis Software (SAS², version 13.5.0). For both *Chandra* and *XMM–Newton* data, we adopted the most recent calibration files available at the time the data reduction and analysis were performed.

2.2.1 Timing analysis

We extracted all *Chandra* and *XMM–Newton*/EPIC-pn source counts using 1.5 and 15-arcsec circles, respectively, centred on the source position. Background counts were extracted using a nearby circular region of the same size. We adopted the coordinates reported by Rea et al. (2013a), i.e. RA = 17^h45^m40^s.169, Dec = −29°00′29″.84 (J2000.0), to convert the photon arrival times to Solar System barycentre reference frame. The effects of the proper motion relative to Sgr A* on the source position are negligible on the timescales considered for our analysis (best-fit parameters are $1.6 < \mu_\alpha < 3.0$ mas yr^{−1} and $5.7 < \mu_\delta < 6.1$ mas yr^{−1} at a 95 per cent confidence level; Bower et al. 2015).

To determine a timing solution valid over the time interval covered by the *Chandra* and *XMM–Newton* observations (from 2013 April 29 to 2014 August 30), we first considered the timing solutions given by Rea et al. (2013a; using *Chandra* and *Swift*) and Kaspi et al. (2014; using *NuSTAR* and *Swift*). In the overlapping time interval, before 2013 June 14 (MJD 56457), both papers report a consistent timing solution (see first column in Table 2.2 and green solid line in the upper panel of Figure 2.1). Kaspi et al. (2014) then added more observations covering the interval between 2013 June 14 and August 15 (MJD 56457–56519), and observed a period derivative (\dot{P}) roughly two times larger than the previous value (see Table 2.2). The uncertainties on the Kaspi et al. (2014) solution formally ensure unambiguous phase connection until 2013 November 11 (MJD 56607), allowing us to extend that phase-coherent analysis with the data reported here, and follow the evolution of the pulse phases between 2013 July 27 and October 28 (MJD 56500–56594; after which we have a gap in our data coverage of about 115 days; see Table 2.2).

In this time interval, we measured the pulse phase at the fundamental frequency by dividing our observations in intervals of 10 ks and using the solution given by Kaspi et al. (2014) to determine univocally the number of cycles between the various observations. By fitting the measured pulse phases with a cubic function, we obtained the solution dubbed A in Table 2.2, which shows only slight deviations with respect to the solution published by Kaspi et al. (2014), but extends until 2013 October 28 (MJD 56594). The period evolution implied by solution A is plotted with a blue solid line in the upper panel of Figure 2.1. Our *Chandra* and *XMM–Newton* observations allow us to confirm the change in the \dot{P} , which

¹See <http://cxc.harvard.edu/ciao/threads/pointlike>.

²See <http://xmm.esac.esa.int/sas/>.

increased by a factor of ~ 2 around 2013 June (i.e. about two months after the onset of the outburst in 2013 April), and remained stable until at least 2013 October 28.

Formally, the accuracy of solution A should guarantee that phase coherence is not lost before 2014 March 3 (MJD 56721), comprising the first observation available after the 115 day gap between MJD 56594.1 and MJD 56709.5. However, fitting the phases derived for that observation with solution A shows large residuals. These clearly indicate that solution A is not valid after the gap. To investigate this change in the spin evolution of the source, we measured the spin frequency for all the observations performed after the gap by fitting with a linear function the phases determined over time intervals with lengths ranging from 2 to 10 ks, depending on the source flux. The values for the frequencies we measured in this way after 2014 February 21 (MJD 56709) are much smaller than those predicted by solution A (see blue dashed line in the upper panel of Figure 2.1).

To determine the spin evolution of the source after the 115 day gap in the observations (i.e. from MJD 56709), we then fitted the values of the spin frequency with a quadratic function, obtaining the non-coherent solution B (see Table 2.2), plotted in the upper panel of Figure 2.1 with a magenta solid line. Unfortunately, this solution is not accurate enough to determine univocally the number of rotations among the various observations. Still, the trend followed by the spin frequency after the gap clearly deviates from that shown before 2013 October 28 via solution A, indicating a further increase of the spin-down rate. In particular, the \dot{P} has further increased by a factor of ~ 2.5 , and the \ddot{P} is smaller than that measured by solution A, even if the large error prevents us from detecting a change in the sign of the \ddot{P} at high significance.

The large changes in the timing properties of the source since the onset of the outburst are also shown by the fact that a quadratic function gives a poor fit for the spin frequency evolution over the whole time interval covered by the observations ($\chi^2_\nu = 5.04$ for 26 d.o.f.; see black solid line in the upper panel of Figure 2.1).

Summarizing, we derive a phase coherent solution (solution A, see Table 2.2 and blue solid line in the upper panel of Figure 2.1) that can model the pulse phase evolution before the observations gap starting at MJD 56600, and which is compatible with the solution given by Kaspi et al. (2014) for the partly overlapping interval MJD 56457 – 56519. After the observation gap, solution A is no longer able to provide a good description of pulse phases, and we are only able to find a solution based on the analysis of the spin frequency evolution (solution B, see Table 2.2 and magenta solid line in the upper panel of Figure 2.1). We then use timing solution A (up to MJD 56594.1) and solution B (from MJD 56709.5 onwards) to fold all background-subtracted and exposure-corrected light curves at the neutron star spin period during the corresponding observation (see Figs 2.2 and 2.3). This allows us to extract the temporal evolution of the pulsed fraction, defined as $PF = [\text{Max} - \text{Min}] / [\text{Max} + \text{Min}]$ (Max and Min being the maximum and the minimum count rate of the pulse profile, respectively). To investigate possible dependences on energy, we calculate the pulsed fractions in the 0.3–3.5 and 3.5–10 keV intervals for the *Chandra* observations and in the 0.3–3.5, 3.5–5, 5–6.5, 6.5–10 keV ranges for the *XMM-Newton* observations (see Figure 2.4).

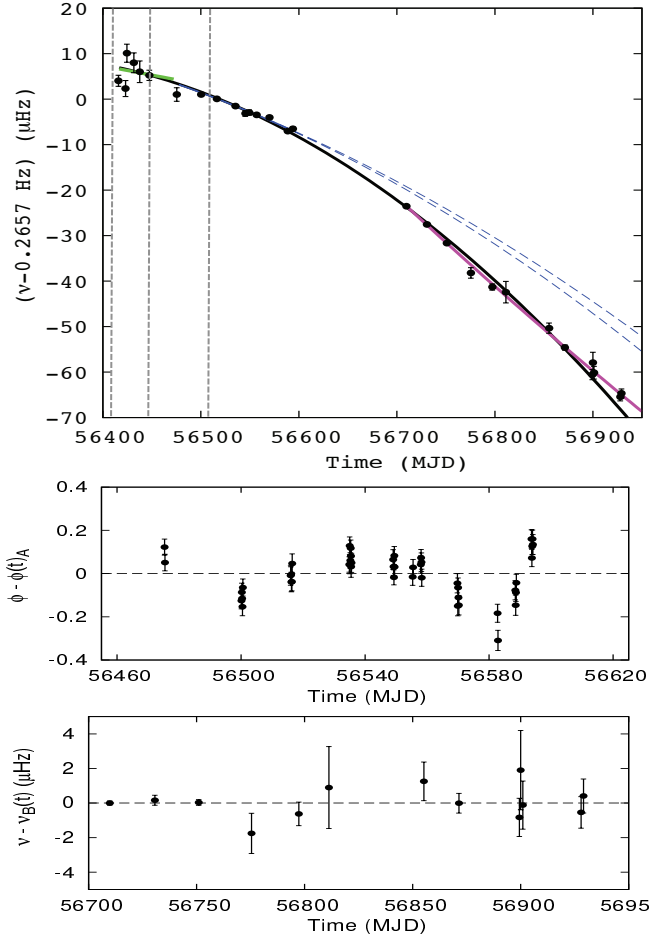


Figure 2.1: *Top panel*: temporal evolution of the spin frequency of SGR 1745–2900. The solution given by Rea et al. (2013a) is plotted as a green solid line. The blue and magenta solid lines show solutions A and B of this work, respectively. The blue dashed lines are the extrapolation of solution A over the time-span of solution B. The black line represents the fit over the whole time interval covered by observations (see text), while the vertical dashed lines refer to the times of the SGR-like short bursts detected by *Swift*/BAT (on 2013 April 25, June 7, and August 5). *Central panel*: phase residuals with respect to solution A (labelled as $\phi(t)_A$), evaluated over the time validity interval MJD 56500.1 – 56594.1. *Bottom panel*: phase residuals with respect to solution B (labelled as $\nu_B(t)$), evaluated over the time validity interval MJD 56709.5 – 56929.

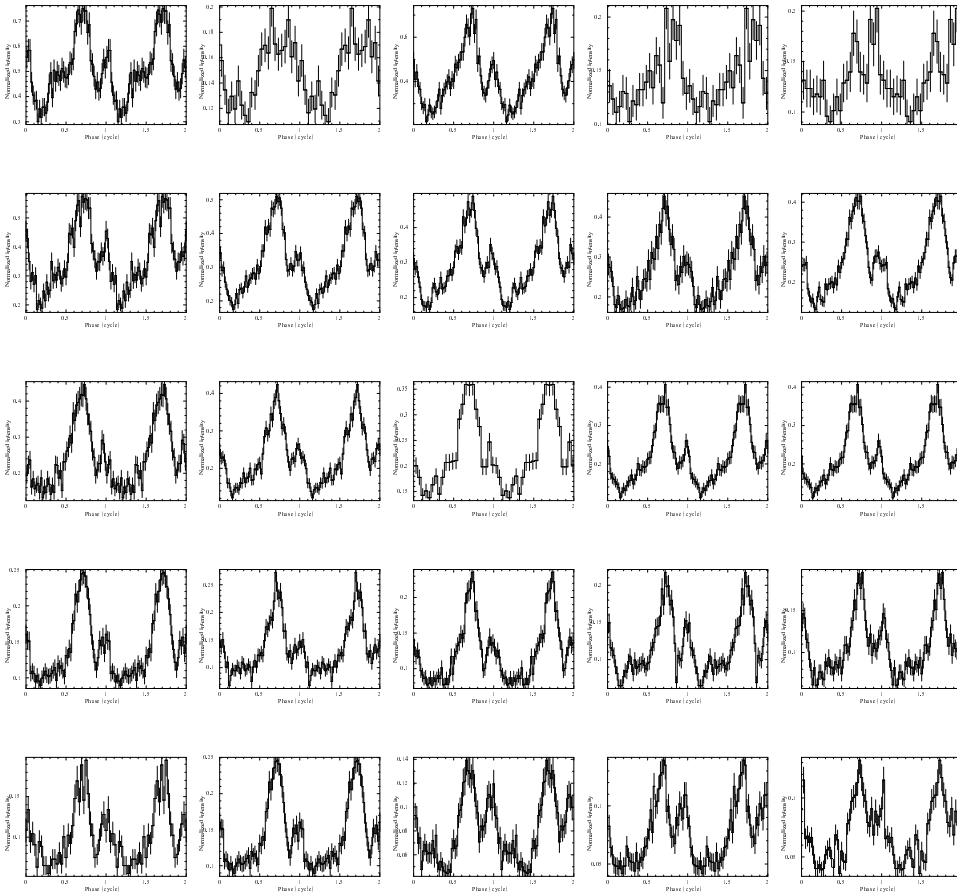


Figure 2.2: Pulse profiles of SGR 1745–2900 obtained from *Chandra* observations in the 0.3–10 keV energy range. Epoch increases from left to right, top to bottom. Two cycles are shown for clarity.

Table 2.2: Timing solutions for SGR 1745–2900. Errors were evaluated at the 1σ confidence level, scaling the uncertainties by the value of the rms ($\sqrt{\chi^2_{\nu}}$) of the respective fit to account for the presence of unfitted residuals.

Solution	Rea et al. (2013a)	Kaspi et al. (2014)	This work (Solution A)	This work (Solution B)
Epoch T_0 (MJD)	56424.5509871	56513.0	56513.0	56710.0
Validity range (MJD)	56411.6 – 56475.3	56457 – 56519	56500.1 – 56594.1	56709.5 – 56929
$P(T_0)$ (s)	3.7635537(2)	3.76363824(13)	3.76363799(7)	3.7639772(12)
$\dot{P}(T_0)$	$6.61(4) \times 10^{-12}$	$1.385(15) \times 10^{-11}$	$1.360(6) \times 10^{-11}$	$3.27(7) \times 10^{-11}$
\ddot{P} (s^{-1})	$4(3) \times 10^{-19}$	$3.9(6) \times 10^{-19}$	$3.7(2) \times 10^{-19}$	$(-1.8 \pm 0.8) \times 10^{-19}$
$\nu(T_0)$ (Hz)	0.265706368(14)	0.265700350(9)	0.26570037(5)	0.26567642(9)
$\dot{\nu}(T_0)$ (Hz s^{-1})	$-4.67(3) \times 10^{-13}$	$-9.77(10) \times 10^{-13}$	$-9.60(4) \times 10^{-13}$	$-2.31(5) \times 10^{-12}$
$\ddot{\nu}$ (Hz s^{-2})	$-3(2) \times 10^{-20}$	$-2.7(4) \times 10^{-20}$	$-2.6(1) \times 10^{-20}$	$(1.3 \pm 0.6) \times 10^{-20}$
rms residual	0.15 s	51 ms	0.396 s	1.0 μHz
χ^2_{ν} (d.o.f.)	0.85 (5)	1.27 (41)	6.14 (44)	0.66 (10)

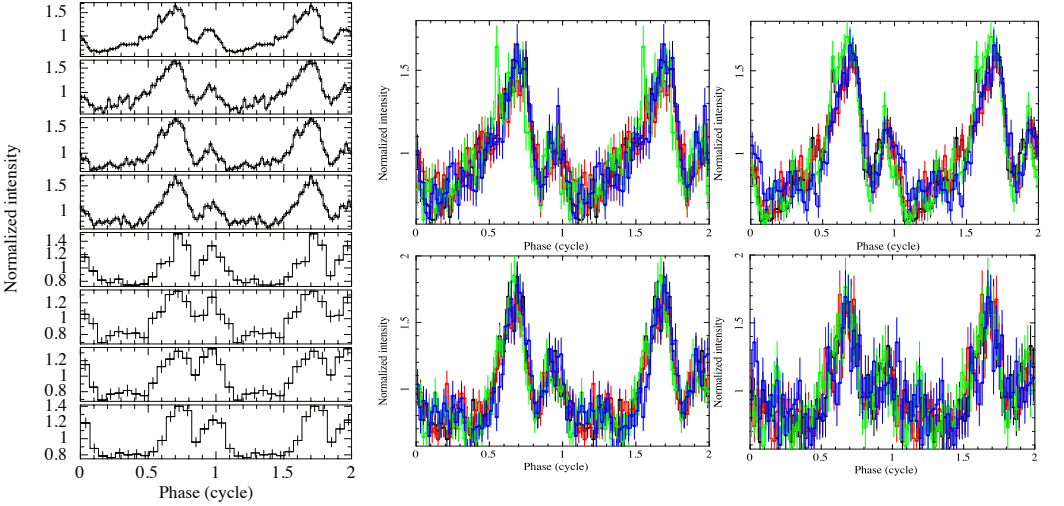


Figure 2.3: Pulse profiles of SGR 1745–2900 obtained from *XMM–Newton*/EPIC-pn observations. Two cycles are shown for clarity. *Left-hand panel*: pulse profiles in the 0.3–10 keV energy band. *Right-hand panel*: pulse profiles in the 0.3–3.5, 3.5–5, 5–6.5, 6.5–10 keV energy bands (from left to right, top to bottom) for the first four observations. Black, red, green and blue colors refer to the first, second, third and fourth observation, respectively.

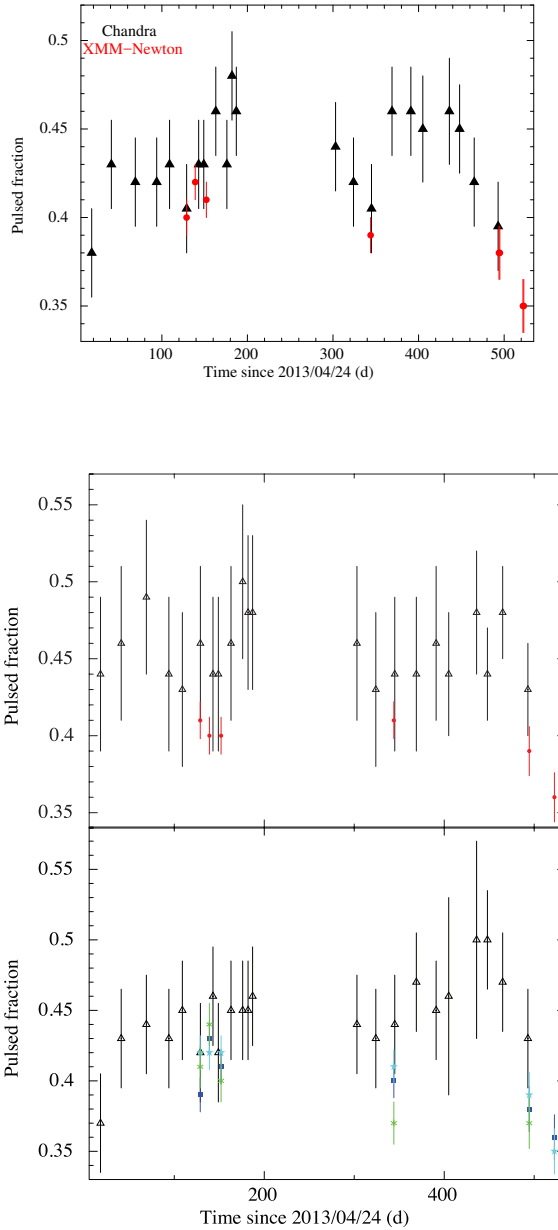


Figure 2.4: Temporal evolution of the pulsed fraction (see text for our definition). Uncertainties on the values were obtained by propagating the errors on the maximum and minimum count rates. *Top panel*: in the 0.3–10 keV band. *Central panel*: in the 0.3–3.5 keV band for the *Chandra* (black triangles) and *XMM-Newton* (red points) observations. *Bottom panel*: in the 3.5–10 keV band for the *Chandra* observations (black) and in the 3.5–5 (blue), 5–6.5 (light blue) and 6.5–10 keV (green) ranges for the *XMM-Newton* observations.

2.2.2 Spectral analysis of *Chandra* observations

For all the *Chandra* observations, we extracted the source counts from a 1.5-arcsec radius circular region centred on SGR 1745–2900. This corresponds to an encircled energy fraction of ~ 85 per cent of the *Chandra* point spread function (PSF) at 4.5 keV. A larger radius would have included too many counts from the Sgr A* PSF, overestimating the flux of SGR 1745–2900 with only a marginal increase of the encircled energy fraction (less than ~ 5 per cent). We extracted the background counts using three different regions: an annulus (inner and outer radius of 14 and 20 arcsec, respectively), four 2-arcsec radius circles arranged in a square centred on the source, and a 1.5-arcsec radius circle centred on the source position in an archival *Chandra*/ACIS-S observation (i.e. when the magnetar was still in quiescence). For grating observations we considered instead a circle of radius 10 arcsec as far as possible from the grating arms but including part of the diffuse emission present in the Galactic Centre.

For ‘non-grating’ observations, we created the source and background spectra, the associated redistribution matrix files and ancillary response files using the SPEXTRACT tool³. For the three grating observations, we analyzed only data obtained with the High Energy Grating (0.8–8 keV). In all cases SGR 1745–2900 was offset from the zeroth-order aim point, which was centered on the nominal Sgr A* coordinates (RA = 17^h45^m40^s.00, Dec = –29°00′28″.1 (J2000.0)). We extracted zeroth-order spectra with the TGEXTRACT tool and generated redistribution matrices and ancillary response files using MKGRMF and FULLGARF, respectively.

We grouped background-subtracted spectra to have at least 50 counts per energy bin, and fitted in the 0.3–8 keV energy band (0.8–8 keV for grating observations) with the XSPEC⁴ spectral fitting package (version 12.8.1g; Arnaud 1996), using the χ^2 statistics. The photoelectric absorption was described through the TBABS model with photoionization cross-sections from Verner et al. (1996) and chemical abundances from Wilms, Allen & McCray (2000). The small *Chandra* PSF ensures a negligible impact of the background at low energies and allows us to better constrain the value of the hydrogen column density towards the source.

We estimated the impact of photon pile-up in the non-grating observations by fitting all the spectra individually. Given the pile-up fraction (up to ~ 30 per cent for the first observation as determined with WebPIMMS, version 4.7), we decided to correct for this effect using the pile-up model of Davis (2001), as implemented in XSPEC. According to ‘*The Chandra ABC Guide to pile-up*’,⁵ the only parameters allowed to vary were the grade-migration parameter (α), and the fraction of events in the source extraction region within the central, piled up, portion of the PSF. Including this component in the spectral modelling, the fits quality and the shape of the residuals improve substantially especially for the spectra of the first 12 observations (from obs ID 14702 to 15045), when the flux is larger.

³Ancillary response files are automatically corrected to account for continuous degradation in the ACIS CCD quantum efficiency.

⁴See <http://heasarc.gsfc.nasa.gov/xanadu/xspec/>.

⁵See [http://cxc.harvard.edu/ciao/download/doc/pile-up\\$_-\\$abc](http://cxc.harvard.edu/ciao/download/doc/pile-up$_-$abc).

We then compared our results over the three different background extraction methods (see above) and found no significant differences in the parameters, implying that our reported results do not depend significantly on the exact location of the selected background region.

We fitted all non-grating spectra together, adopting four different models: a black body, a power-law, the sum of two blackbodies, and a black body plus a power-law. For all the models, we left all parameters free to vary. However, the hydrogen column density was found to be consistent with being constant within the errors⁶ among all observations and thus was tied to be the same. We then checked that the inclusion of the pile-up model in the joint fits did not alter the spectral parameters for the last 10 observations (from obs ID 16508 onwards), when the flux is lower, by fitting the corresponding spectra individually without the pile-up component. The values for the parameters are found to be consistent with being the same in all cases.

A fit with an absorbed black body model yields $\chi^2_\nu = 1.00$ for 2282 degrees of freedom (d.o.f.), with a hydrogen column density $N_{\text{H}} = 1.90(2) \times 10^{23} \text{ cm}^{-2}$, temperature in the 0.76–0.90 keV range, and emitting radius in the 1.2–2.5 km interval. When an absorbed power-law model is used ($\chi^2_\nu = 1.05$ for 2282 d.o.f.), the photon index is within the range 4.2–4.9, much larger than what is usually observed for this class of sources (see Mereghetti 2008; Rea & Esposito 2011 for reviews). Moreover, a larger absorption value is obtained ($N_{\text{H}} \sim 3 \times 10^{23} \text{ cm}^{-2}$). The large values for the photon index and the absorption are likely not intrinsic to the source, but rather an artifact of the fitting process which tends to increase the absorption to compensate for the large flux at low energies defined by the power-law. The addition of a second component to the black body, i.e. another black body or a power-law, is not statistically required ($\chi^2_\nu = 1.00$ for 2238 d.o.f. in both cases). We thus conclude that a single absorbed black body provides the best modelling of the source spectrum in the 0.3–8 keV energy range (see Table 2.3).

Taking the absorbed black body as a baseline, we tried to model all the spectra tying either the radius or the temperature to be the same for all spectra. We found $\chi^2_\nu = 1.38$ for 2303 d.o.f. when the radii are tied, with $N_{\text{H}} = 1.94(2) \times 10^{23} \text{ cm}^{-2}$, $R_{\text{BB}} = 1.99^{+0.06}_{-0.05}$ km and temperatures in the 0.66–0.97 keV range. We found instead $\chi^2_\nu = 1.04$ for 2303 d.o.f. when the temperatures are tied, with $N_{\text{H}} = 1.89(2) \times 10^{23} \text{ cm}^{-2}$, $kT_{\text{BB}} = 0.815(7)$ keV and radii spanning from ~ 1.1 to ~ 3.0 km. The goodness of fit of the latter model improves considerably if the temperatures are left free to vary as well (F -test probability of $\sim 2 \times 10^{-17}$). We conclude that both the temperature and the size of the black body emitting region are presumably varying. Zeroth-order spectral data of the three grating observations were fitted together and independently with this model, without including the pile-up component and fixing N_{H} to that obtained in non-grating fit: $1.9 \times 10^{23} \text{ cm}^{-2}$ (see Table 2.3 and Figure 2.5).

⁶Here, and in the following, uncertainties are quoted at the 90 per cent confidence level for a single parameter of interest ($\Delta\chi^2 = 2.706$), unless otherwise noted.

Table 2.3: *Chandra* spectral fitting results obtained with an absorbed black body model ($\chi^2_\nu = 1.00$ for 2282 d.o.f.). The hydrogen column density was tied to be the same in all the observations, resulting in $N_{\text{H}} = 1.90(2) \times 10^{23} \text{ cm}^{-2}$ (photoionization cross-sections from Verner et al. (1996) and chemical abundances from Wilms et al. (2000)). The α is a parameter of the XSPEC pile-up model (see Davis 2001 and “*The Chandra ABC Guide to pile-up*”). The pile-up model was not included when fitting the HETG/ACIS-S spectra (obs. ID: 15040, 15651, 15654). The black body radius and luminosity are calculated assuming a source distance of 8.3 kpc (see e.g. Genzel et al. 2010). Fluxes and luminosities were calculated after removing the pile-up model. All errors are quoted at a 90 per cent confidence level for a single parameter of interest ($\Delta\chi^2 = 2.706$).

Obs. ID	α	kT_{BB} (keV)	R_{BB} (km)	1–10 keV absorbed flux ($10^{-12} \text{ erg cm}^{-2} \text{ s}^{-1}$)	1–10 keV luminosity ($10^{35} \text{ erg s}^{-1}$)
14702	0.47(6)	0.87(2)	$2.6^{+0.2}_{-0.1}$	$16.5^{+1.0}_{-0.8}$	4.7 (3)
15040	-	0.90(2)	2.5(1)	$15.5^{+0.03}_{-1.3}$	4.7 (4)
14703	$0.47^{+0.07}_{-0.06}$	0.84(2)	2.6(1)	$12.7^{+0.5}_{-0.6}$	3.9 (3)
15651	-	0.87(3)	2.4(2)	$12.5^{+0.07}_{-0.9}$	3.8 (4)
15654	-	0.88(4)	2.4(2)	$12.4^{+0.05}_{-0.9}$	3.5 (4)
14946	0.43(8)	0.82(2)	2.5(1)	$10.5^{+0.4}_{-0.7}$	3.3(3)
15041	$0.42^{+0.06}_{-0.05}$	0.83(1)	$2.22^{+0.10}_{-0.09}$	$9.3^{+0.2}_{-0.3}$	$2.9^{+0.2}_{-0.4}$
15042	0.55(7)	0.83(1)	2.14(9)	8.3(3)	$2.6^{+0.2}_{-0.4}$
14945	0.4(1)	0.85(2)	1.9(1)	$7.6^{+0.3}_{-0.4}$	2.3(2)
15043	0.51(8)	0.82(1)	$2.09^{+0.10}_{-0.09}$	$7.2^{+0.2}_{-0.3}$	$2.4^{+0.2}_{-0.3}$
14944	0.6(1)	0.84(2)	1.9(1)	7.0(4)	$2.2^{+0.2}_{-0.3}$
15044	$0.48^{+0.09}_{-0.08}$	0.81(1)	$2.03^{+0.10}_{-0.09}$	6.4(2)	$2.1^{+0.2}_{-0.3}$
14943	0.4(1)	0.80(2)	$2.0^{+0.2}_{-0.1}$	$6.1^{+0.2}_{-0.4}$	2.0(3)
14704	0.5(1)	$0.80^{+0.02}_{-0.01}$	2.0(1)	$6.0^{+0.2}_{-0.3}$	2.0 (2)
15045	0.42(9)	$0.82^{+0.02}_{-0.01}$	1.88(9)	$5.9^{+0.1}_{-0.2}$	$1.9^{+0.1}_{-0.2}$
16508	0.6(2)	$0.80^{+0.02}_{-0.01}$	$1.65^{+0.09}_{-0.10}$	$3.8^{+0.1}_{-0.2}$	$1.3^{+0.1}_{-0.2}$
16211	0.3(2)	0.79(2)	$1.64^{+0.10}_{-0.09}$	$3.6^{+0.1}_{-0.2}$	1.2 (2)
16212	0.4(2)	0.80(2)	$1.51^{+0.10}_{-0.09}$	3.2(1)	1.1(1)
16213	0.3(2)	0.79(2)	$1.49^{+0.08}_{-0.07}$	3.1(1)	1.1 (1)
16214	0.4(2)	0.79(2)	$1.45^{+0.10}_{-0.09}$	2.8(1)	1.0 (1)
16210	0.4(2)	0.82(3)	1.3(1)	2.70(7)	0.9(1)
16597	0.5(2)	0.76(3)	$1.4^{+0.2}_{-0.1}$	$2.20^{+0.04}_{-0.05}$	0.8 (1)
16215	0.4(2)	0.80(2)	$1.22^{+0.09}_{-0.08}$	2.11(4)	0.7 (1)
16216	0.3(2)	0.76(2)	$1.34^{+0.10}_{-0.09}$	1.91(4)	0.7(1)
16217	0.3(2)	0.76(2)	1.3(1)	1.80(3)	0.67(9)

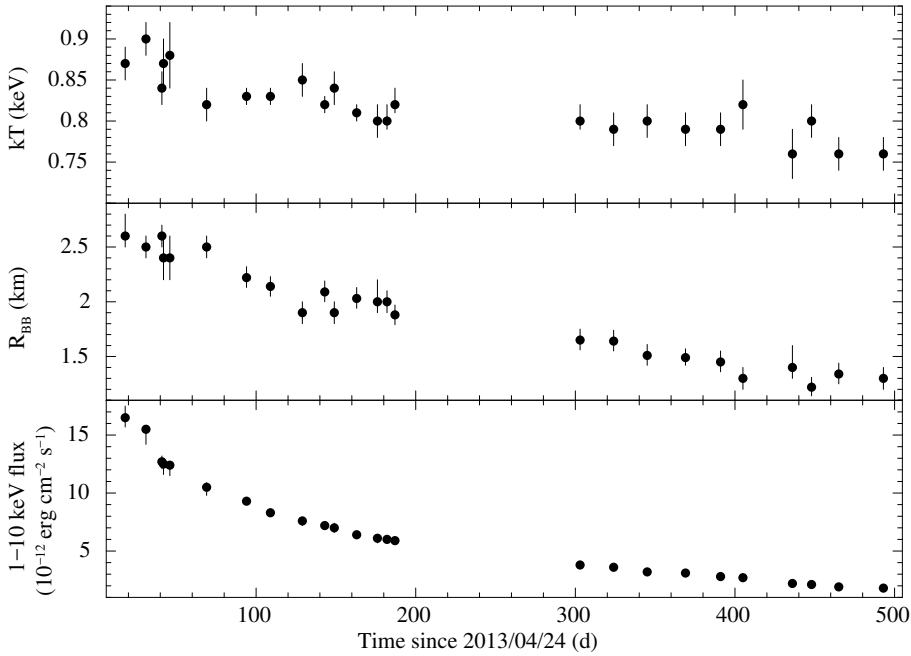


Figure 2.5: Temporal evolution of the spectral parameters for the black body model and of the 1–10 keV absorbed flux of SGR 1745–2900 from *Chandra* observations.

2.2.3 Spectral analysis of *XMM-Newton* observations

For all the *XMM-Newton* observations, we extracted the source counts from a circular region of radius 15 arcsec centred on the source PSF, and the background counts through the same circle at the same position in an archival (2011) *XMM-Newton* observation of the Galactic Centre (obs. ID 0694640301), when the magnetar was not detected and no transient events were identified within the source PSF. We built the light curves for the source and background event files to visually inspect and filter for high particle background flaring in the selected regions. We checked for the potential impact of pile-up using the EPATPLOT task of SAS: the observed pattern distributions for both single and double events are consistent with the expected ones (at a 1σ confidence level) for all the three cameras, proving that the *XMM-Newton* data are unaffected by pile-up.

We restricted our spectral analysis to photons having FLAG = 0 and PATTERN ≤ 4 (12) for the pn (MOSs) data and created spectral redistribution matrices and ancillary response files. We co-added the spectral files of consecutive observations (obs. ID 0743630201-301 and 0743630401-501; see Table 6.1) to increase the signal-to-noise ratio and improve the fit statistics. We then grouped the source spectral channels to have at least 200 counts per bin and fitted the spectra in the 2–12 keV range, given the high background contamination within the source PSF at lower energies. The spectral data extracted from the two MOS cameras gave values for the parameters and fluxes consistent with those obtained from the pn camera. To minimize the systematic errors introduced when using different instruments, we considered only the pn data, which provide the spectra with the highest statistics.

Due to the large PSF of *XMM-Newton* it is not possible to completely remove the contamination of both the Galactic Centre soft X-ray diffuse emission and the emission lines from the supernova remnant Sgr A East, including in particular the iron line (Fe XXV; rest energy of 6.7 keV) and the sulfur line (S XV; rest energy of 2.46 keV) (see e.g. Maeda et al. 2002; Sakano et al. 2004; Ponti et al. 2010, 2013; Heard & Warwick 2013). These features were clearly visible especially in the spectra of the last observations, when the flux is lower, and prevented us from obtaining a good spectral modelling in XSPEC. We thus decided to discard the energy interval comprising the Fe XXV line (6.4–7.1 keV) for all the spectra, as well as that associated with the S XV line (2.3–2.7 keV) for the spectrum of the last observations (obs. ID 0690441801, 0743630201-301, 0743630401-501), involving a loss of ~ 9 per cent in the total number of spectral bins.

Based on the results of the *Chandra* spectral analysis, we fitted the data first with an absorbed black body model. The hydrogen column density was consistent with being constant at a 90 per cent confidence level among all observations and was tied to be the same in the spectral fitting. We obtained $\chi^2_\nu = 2.2$ for 636 d.o.f., with large residuals at high energies. The latter disappear if an absorbed power-law component is added and the fit improves considerably ($\chi^2_\nu = 1.13$ for 624 d.o.f.; see left panel of Figure 2.6). A fit with a two-black body model is statistical acceptable as well ($\chi^2_\nu = 1.13$ for 624 d.o.f.) and yields temperatures of $\sim 2 - 4$ keV and emitting radii of $\sim 0.04 - 0.12$ km for the second black body. However, this model would be physically hard to justify, since it is unlikely that these large temperatures can be maintained on a neutron star surface for such

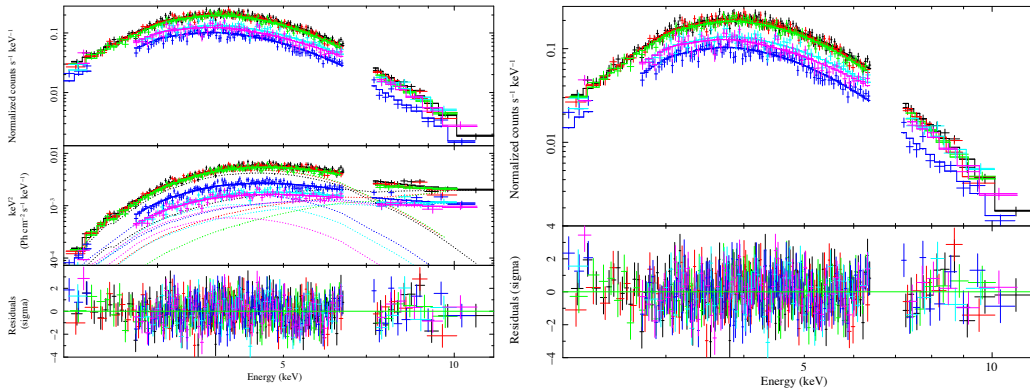


Figure 2.6: Results of the phase-averaged spectral analysis for the *XMM-Newton*/EPIC-pn observations of SGR 1745–2900. *Left-hand panel*: source spectra fitted together with an absorbed black body plus power-law model in the 2–12 keV range and after removal of the Fe XXV and S XV lines (see text). $E^2 \times f(E)$ unfolded spectra together with the contributions of the two additive components and residuals (in units of standard deviations) are also shown. *Right-hand panel*: source spectra fitted together with an absorbed 3-D resonant cyclotron scattering model in the 2–12 keV range and after removal of the Fe XXV and S XV lines (see text). Residuals (in units of standard deviations) are also shown.

a long time. As an alternative to these fits, we applied a 3D resonant cyclotron scattering model (NTZ: Nobili et al. 2008a,b; Zane et al. 2009), obtaining $\chi^2_{\nu} = 1.14$ for 624 d.o.f. (see right panel of Figure 2.6). The hydrogen column densities and fluxes inferred both from the BB+PL and the NTZ models are consistent with each other within the errors (see Table 2.4). To test the robustness of our results, we compared the inferred parameters with those derived by fitting the spectra without filtering for the spectral channels and applying the VARABS model for the absorption, which allows the chemical abundances of different elements to vary (only the sulfur and iron abundances were allowed to vary for the present purpose). We found consistent values over the two methods.

We conclude that both models successfully reproduce the soft X-ray part of the SGR 1745–2900 spectra up to ~ 12 keV, implying that, similar to other magnetars, the reprocessing of the thermal emission by a dense, twisted magnetosphere produces a non-thermal component. The power-law detected by *XMM-Newton* is consistent with that observed by *NuSTAR* (Kaspi et al. 2014), and its very low contribution below 8 keV is consistent with its non-detection in our *Chandra* data.

Table 2.4: *XMM-Newton*/EPIC-pn spectral fitting results obtained with an absorbed black body plus power-law model ($\chi^2_{\nu} = 1.13$ for 624 d.o.f.) and an absorbed 3D resonant cyclotron scattering model ($\chi^2_{\nu} = 1.14$ for 624 d.o.f.). β_{bulk} denotes the bulk motion velocity of the charges in the magnetosphere and $\Delta\phi$ is the twist angle. For both models the hydrogen column density was tied to be the same in all the observations, yielding $N_{\text{H}} = 1.86^{+0.10}_{-0.08} \times 10^{23} \text{ cm}^{-2}$ for the former and $N_{\text{H}} = 1.86^{+0.05}_{-0.03} \times 10^{23} \text{ cm}^{-2}$ for the latter (photoionization cross-sections from Verner et al. (1996) and chemical abundances from Wilms et al. (2000)). The black body emitting radius and luminosity are calculated assuming a source distance of 8.3 kpc (see e.g. Genzel et al. 2010). Fluxes were determined with the CFLUX model in XSPEC. All errors are quoted at a 90 per cent confidence level for a single parameter of interest ($\Delta\chi^2 = 2.706$).

BB+PL						
Obs. ID	kT_{BB} (keV)	R_{BB} (km)	Γ	PL norm (10^{-3})	1–10 keV BB/PL abs flux ($10^{-12} \text{ erg cm}^{-2} \text{ s}^{-1}$)	1–10 keV BB/PL luminosity ($10^{35} \text{ erg s}^{-1}$)
0724210201	0.79(3)	1.9(2)	$2.3^{+0.5}_{-0.7}$	$4.5^{+8.9}_{-3.5}$	5.0(1) / 3.3(2)	$1.7^{+0.2}_{-0.3} / 1.0^{+0.4}_{-0.3}$
0700980101	0.78(3)	2.1(2)	$1.7^{+0.8}_{-1.3}$	< 6.8	5.7(1) / 2.2(2)	2.0(3) / 0.5(3)
0724210501	0.79(4)	$2.1^{+0.3}_{-0.2}$	$2.3^{+0.5}_{-0.6}$	< 4.5	5.8(1) / 1.8(2)	$2.0^{+0.1}_{-0.2} / 0.3^{+0.3}_{-0.2}$
0690441801	$0.72^{+0.03}_{-0.04}$	1.6(3)	$2.6^{+0.5}_{-0.8}$	$4.5^{+8.8}_{-3.8}$	1.9(1) / $2.1^{+0.1}_{-0.2}$	0.8(2) / 0.8(3)
0743630201-301	0.71(6)	1.3(3)	$2.1^{+0.7}_{-1.4}$	$1.6^{+6.1}_{-1.5}$	1.2(1) / 1.7(2)	0.5(2) / 0.4(3)
0743630401-501	$0.67^{+0.10}_{-0.07}$	1.2(5)	$2.0^{+0.4}_{-0.7}$	$6.3^{+9.7}_{-4.9}$	0.7(1) / 2.0(4)	0.3(2) / < 0.5
NTZ						
Obs. ID	kT (keV)	β_{bulk}	$\Delta\phi$ (rad)	NTZ norm (10^{-1})	1–10 keV abs flux ($10^{-12} \text{ erg cm}^{-2} \text{ s}^{-1}$)	1–10 keV luminosity ($10^{35} \text{ erg s}^{-1}$)
0724210201	0.85(2)	$0.72^{+0.09}_{-0.40}$	$0.40^{+0.04}_{-0.24}$	$1.62^{+0.07}_{-0.12}$	8.3(1)	2.5(2)
0700980101	$0.85^{+0.02}_{-0.03}$	$0.70^{+0.04}_{-0.34}$	$0.40^{+0.03}_{-0.23}$	$1.58^{+0.14}_{-0.11}$	7.9(1)	2.3(2)
0724210501	0.84(2)	0.6(2)	$0.41^{+0.02}_{-0.25}$	1.5(1)	7.6(1)	2.3(3)
0690441801	$0.77^{+0.04}_{-0.06}$	$0.5^{+0.3}_{-0.2}$	$0.42^{+0.06}_{-0.25}$	$0.94^{+0.10}_{-0.07}$	4.0(1)	1.3(2)
0743630201-301	$0.76^{+0.07}_{-0.10}$	> 0.2	$0.43^{+0.64}_{-0.03}$	$0.61^{+0.09}_{-0.06}$	2.9(1)	0.9(3)
0743630401-501	$0.65^{+0.07}_{-0.24}$	$0.32^{+0.11}_{-0.09}$	$0.60^{+0.78}_{-0.17}$	$0.68^{+0.27}_{-0.07}$	2.7(1)	0.9(3)

2.2.4 Pulse phase-resolved spectral analysis

To search for spectral variability as a function of rotational phase and time, we first extracted all the spectra of the *Chandra* observations selecting three pulse phase intervals (see Figure 2.2): peak ($\phi=0.5-0.9$), minimum ($\phi=0.2-0.5$), and secondary peak ($\phi=0.9-1.2$). We adopted the same extraction regions and performed the same data analysis as for the phase-averaged spectroscopy.

For each of the three different phase intervals, we fitted the spectra of all *Chandra* observations jointly in the 0.3–8 keV energy band with an absorbed black body model and tying the hydrogen column density to be the same in all the observations (the pile-up model was included). Since the values of the column density are consistent with being the same at a 90 per cent confidence level ($1.90(4) \times 10^{23} \text{ cm}^{-2}$, $1.82(4) \times 10^{23} \text{ cm}^{-2}$, and $1.83_{-0.04}^{+0.05} \times 10^{23} \text{ cm}^{-2}$ for the peak, the secondary peak and the minimum, respectively), we fixed N_{H} to $1.9 \times 10^{23} \text{ cm}^{-2}$, i.e. to the best-fit value determined with the phase-averaged spectroscopy (see Table 2.3). We obtained a good fit in all cases, with $\chi_{\nu}^2 = 1.04$ for 1005 d.o.f. for the peak, $\chi_{\nu}^2 = 1.10$ for 635 d.o.f. for the secondary peak, and $\chi_{\nu}^2 = 0.99$ for 713 d.o.f. for the pulse minimum. The fit residuals were not optimal for energies $\gtrsim 6 - 7$ keV for the peak spectra, due to the larger pile-up fraction. We extracted the source counts excluding the central piled up photons (within a radial distance of 0.7 arcsec from the source position), and repeated the analysis for the peak spectra: the residuals are now well shaped, and the inferred values for the spectral parameters did not change significantly.

The temporal evolution of the black body temperature and radius for both the peak and the pulse minimum are shown in Figure 2.7. No particular trend is observed for the inferred temperatures, whereas the size of the emitting region is systematically lower for the pulse minimum. This is consistent with a viewing geometry that allows us to observe the hot spot responsible for the thermal emission almost entirely at the peak of the pulse profile, and only for a small fraction at the minimum of the pulsation.

The higher statistics of the *XMM-Newton*/EPIC-pn data allowed us to put more stringent constraints on the variations of the X-ray spectral parameters along the spin phase. We extracted the background-subtracted spectra in six different phase intervals for each observation, as shown in Figure 2.7. We fitted all spectra with a BB+PL model, adopting the same prescriptions used for the phase-averaged spectroscopy in the filtering of the spectral channels. We tied the hydrogen column density and the power-law photon indices to the best-fit values determined with the phase-averaged analysis (see Table 2.4). We obtained statistically acceptable results in all cases. The evolutions of the black body temperature and emitting radius as a function of the rotational phase for all the observations are shown in Figure 2.7. Variability of both the parameters along the rotational phase is more significant during the first observation (a fit with a constant yields $\chi_{\nu}^2 = 2.6$ for 5 d.o.f. in both cases) than in the following observations ($\chi_{\nu}^2 \leq 1.4$ for 5 d.o.f. in all cases).

To search for possible phase-dependent absorption features in the X-ray spectra of SGR 1745–2900 (similarly to the one detected in SGR 0418+5729; Tiengo et al. 2013), we produced images of energy versus phase for each of the eight EPIC-pn observations.

We investigated different energy and phase binnings. In Figure 2.8 we show the image for the observation with the highest number of counts (obs. ID 0724210201), produced by binning the source counts into 100 phase bins and 100-eV wide energy channels. The spin period modulation is clearly visible, as well as the large photoelectric absorption below 2 keV. For all observations we then divided these values first by the average number of counts in the same energy bin and then by the corresponding 0.3–10 keV count rate in the same phase interval. No prominent features can be seen in any of the images.

2.2.5 X-ray brightness radial profiles

For all the *Chandra* observations, we used the *Chandra* Ray Tracer (CHART⁷; Carter et al. 2003) to simulate the best available PSF for SGR 1745–2900, setting the exposure time of each simulation equal to the exposure time of the corresponding observation. For the input spectrum in CHART we employed the black body spectrum of Table 2.3, accounting for the pile-up. We then projected the PSF rays on to the detector plane via the Model of AXAF Response to X-rays software (MARX⁸, version 4.5.0; Wise et al. 2003). We extracted the counts of both the simulated PSFs and the ACIS event files through 50 concentric annular regions centred on the source position and extending from 1 to 30 pixels (1 ACIS-S pixel corresponds to 0.492 arcsec). We then generated the X-ray brightness radial profiles and normalized the nominal one (plus a constant background) to match the observed one at a radial distance of 4 pixels, i.e. at a distance at which pile-up effects are negligible. A plot of the observed and simulated surface brightness fluxes (in units of counts \times pixel⁻²) versus radial distance from the position of SGR 1745–2900 is shown in Figure 2.9 for the observation with the highest number of counts (obs. ID 15041).

Extended emission around SGR 1745–2900 is clearly detected in all the observations, and it is likely dominated by the intense Galactic Centre diffuse emission. A detailed analysis of the diffuse emission, including its spatial extension and spectral properties, is beyond the scope of this thesis.

2.3 Discussion

2.3.1 Outburst evolution and comparison with other magnetars

The past decade has seen a great success in detecting magnetar outbursts, mainly thanks to the prompt response and monitoring of the *Swift* mission, and to the dedicated follow-up programs of *Chandra*, *XMM-Newton*, and more recently, *NuSTAR*. The detailed study of about ten outbursts has shown many common characteristics (see Rea & Esposito 2011 for a review; see also Figure 2.10), although the precise triggering mechanism of these outbursts, as well as the energy reservoir responsible for sustaining the emission over many months, remains uncertain.

⁷See <http://cxc.cfa.harvard.edu/chart>

⁸See <http://space.mit.edu/CXC/MARX>.

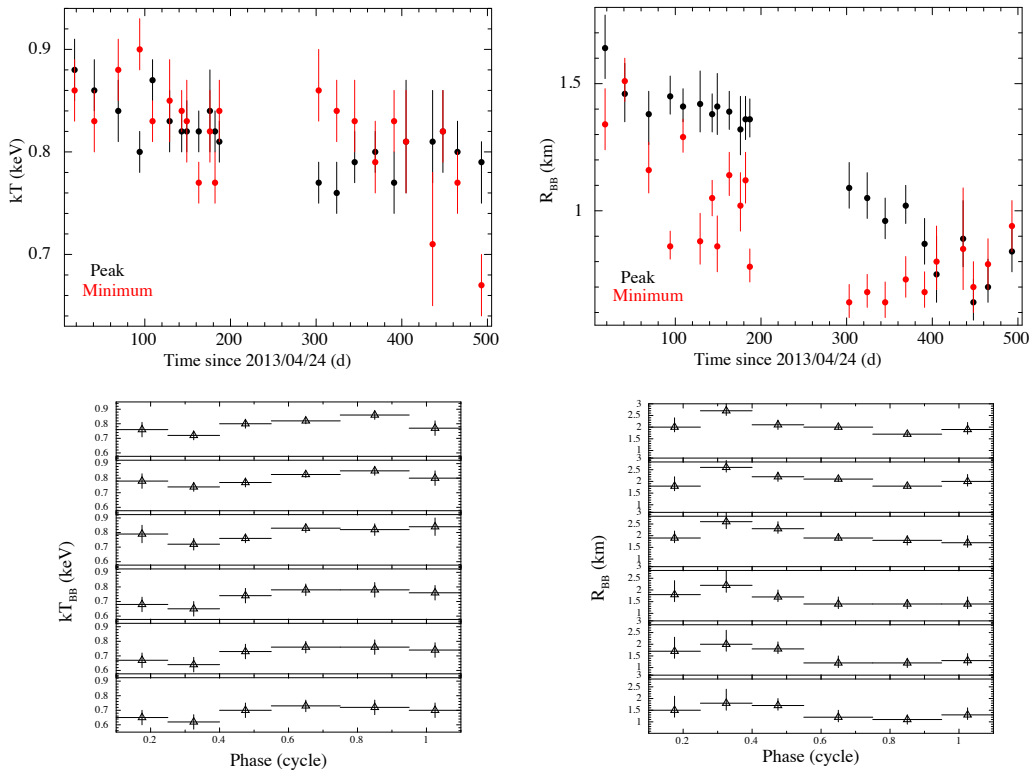


Figure 2.7: *Top panels:* evolution of the black body temperatures (left) and radii (right) for the peak (black points) and the minimum (red points) of the pulse profile for the *Chandra* observations. *Bottom panels:* evolution of the black body temperatures (left) and radii (right) as a function of the rotational phase for the *XMM-Newton* observations. Spectra of consecutive observations were coadded (obs. ID 0743630201-301 and 0743630401-501; see the two lower panels).

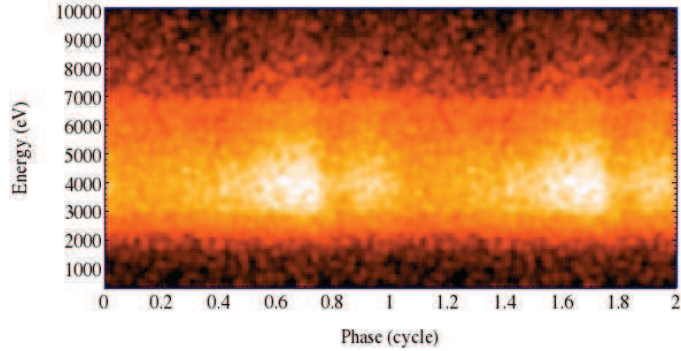


Figure 2.8: Energy versus phase image for the *XMM-Newton* observation with the highest number of counts (obs. ID 0724210201). The image was obtained by binning the EPIC-pn source counts into 100 phase bins and energy channels of 100 eV, to better visualize the shape of the pulse profile and its dependence on energy.

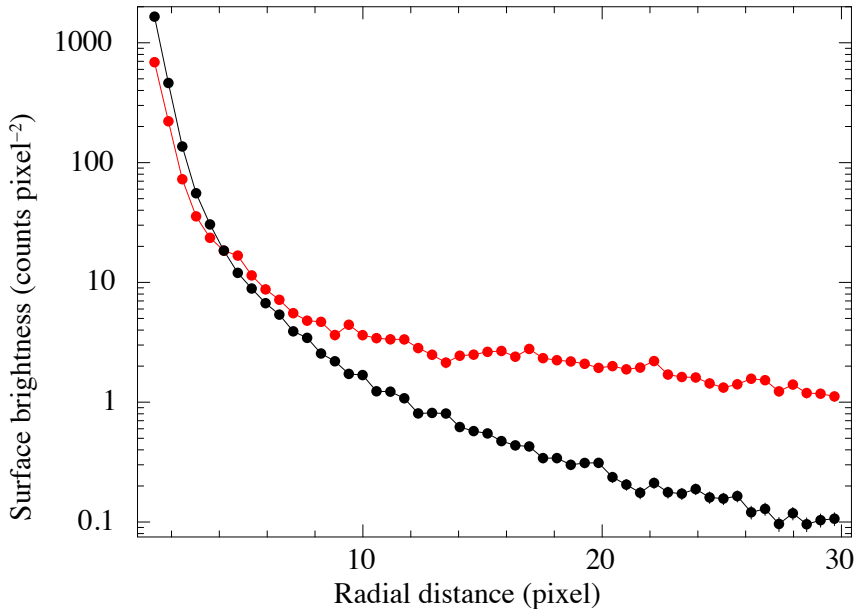


Figure 2.9: Radial profile of the surface brightness for both the ACIS-S image of SGR 1745–2900 (red dots) and the CHART/MARX PSF plus a constant background (black dots) for the observation with the highest number of counts (obs. ID 15041). The simulated surface brightness has been normalized to match the observed one at 4 pixels (one ACIS-S pixel corresponds to 0.492 arcsec). Extended emission around SGR 1745–2900 is clearly detected in all the observations.

All the outbursts that have been monitored with sufficient detail are compatible with a rapid (<days) increase in luminosity up to a maximum of a few 10^{35} erg s $^{-1}$ and a thermally dominated X-ray spectrum which softens during the decay. In the case of SGR 0501+4516 and 1E 1547–5408, a non-thermal component extending up to 100–200 keV appears at the beginning of the outburst, and becomes undetectable after weeks/months (Rea et al. 2009; Bernardini et al. 2011; Kuiper et al. 2012).

The initial behavior of the 2013 outburst decay of SGR 1745–2900 was compatible with those observed in other magnetars. The outburst peak, the thermal emission peaked at about 1 keV, the small radiating surface (about 2 km in radius), and the overall evolution in the first few months, were consistent with the behavior observed in other outbursts. However, after an additional year of X-ray monitoring, it became clear that the subsequent evolution of SGR 1745–2900 showed distinct characteristics. The source flux decay appears extremely slow: it is the first time that we observe a magnetar with a quiescent luminosity $< 10^{34}$ erg s $^{-1}$ remaining at a luminosity $> 10^{35}$ erg s $^{-1}$ for more than one year, and with a temperature decreasing by less than 10% from the initial ~ 1 keV. A further interesting feature of this source is that the non-thermal component (as detected by *XMM-Newton*) persisted on a very long temporal baseline during the outburst evolution. The flux due to the power-law component does not change significantly in time and, as a result, its fractional contribution to the total flux is larger at late times: ~ 520 d after the outburst onset, $\lesssim 50$ per cent of the 1–10 keV absorbed flux is due to the non-thermal component.

We first modelled the decay empirically to gauge the characteristic decay timescales. We adopted three different functions to model the black body temperature, radius and 1–10 keV absorbed flux temporal evolutions (see Figure 2.5): (i) a linear model; (ii) a power-law: $f(t) = f_{0,PL} \times t^{-\Gamma}$; (iii) an exponential: $f(t) = f_{0,exp} \times \exp[-(t - t_0)/\tau]$, where t_0 is the epoch of the first burst detected (which we fixed to 2013 April 24 in all cases) and τ is the e-folding time.

The temporal evolution of the magnetar temperature is well represented by a linear model ($\chi^2_{\nu} = 0.7$ for 23 d.o.f.), with initial temperature $kT_{BB,0} = 0.85(1)$ keV and slope $(-1.77 \pm 0.04) \times 10^{-4}$. The hot spot shrinking is best modeled by an exponential ($\chi^2_{\nu} = 0.8$ for 23 d.o.f.). Best-fit parameters are $\tau = 640 \pm 62$ d and initial radius $R_{BB,0} = 2.60 \pm 0.08$ km. The shape of the flux decline appears to change in time and in fact none of these models can accurately describe the overall decay of the magnetar flux. The flux decay during the first 100 days since the outburst onset is well modelled by a linear plus exponential model with $\tau = 37 \pm 2$ d ($\chi^2_{\nu} = 1.5$ for 4 d.o.f.). After ~ 100 days, the best fitting model turns out to be an exponential with $\tau = 253 \pm 5$ d ($\chi^2_{\nu} = 1.4$ for 15 d.o.f.).

2.3.2 Crustal cooling modelling

We applied the crustal cooling model (see e.g. Pons & Rea 2012) to the data collected during the 1.5-yr outburst of SGR 1745–2900. Although this model was successful in explaining several other magnetar outbursts (Rea et al. 2012, 2013b), in this case we could not reproduce the very slow cooling and high luminosity observed for this source.

We ran several models varying the total injected energy, the angular size, and the depth of the region where the energy is released, but we could not find any set of parameters that could satisfactorily fit the data.

In the framework of the starquake model, the maximum temperature reached in the region where the energy is released is limited by neutrino emission processes. This internal temperature determines the maximum surface temperature and hence the luminosity at which the outburst peaks. For injected energies $> 10^{43}$ erg, there is no significant increase in the peak luminosity because the crustal temperature saturates (at about $3 - 5 \times 10^9$ K) due to the efficient neutrino processes. After reaching the maximum luminosity (between 1 hr and 1 d depending on the depth and injection rate), the cooling curve tracks the thermal relaxation of the crust. Independent of the initial injected energy and surface temperature, the luminosity is expected to drop below 10^{35} erg s^{-1} in < 20 -30 days (see e.g. Figure 1 in Pons & Rea 2012), due to neutrino emission processes in the crust (mainly plasmon decay, and probably neutrino synchrotron for magnetar field strengths).

In Figure 2.11 (left-hand panel, lower curves) we show an example of the expected cooling curve of a magnetar with the same characteristics of SGR 1745–2900. We assume that an energy release of $\simeq 10^{45}$ erg heats up a layer of the outer crust up to 3×10^9 K. We also assume that the event affects the entire magnetar surface, to create the most favorable scenario (the luminosity simply scales with the area of the emitting region), and that the layer where the energy is injected extends from an external boundary at $\rho_{\text{OUT}} \sim 3 \times 10^9$ g cm^{-3} , to an inner boundary at $\rho_{\text{IN}} \sim 2$ and 4×10^{10} g cm^{-3} (we show these two cases in the two lower curves of Figure 2.11, left-hand panel). Even in this most favorable case, the high luminosities observed at late times are difficult to reconcile with any cooling model. In particular, injecting more energy or changing ρ_{OUT} will only affect the peak luminosity during the first days or weeks. On the other hand, injecting energy deeper into the crust (i.e. at higher ρ_{IN}), is expected to change the late time evolution only slightly. This can be seen by comparing the solid and dashed lines in the left-hand panel of Figure 2.11, which correspond to $\rho_{\text{IN}} = 2$ and 4×10^{10} g cm^{-3} , respectively.

For illustrative purposes, we also show the cooling curves obtained when plasmon and synchrotron neutrino processes are switched off (see the upper curves in the left-hand panel of Figure 2.11). These provide a much closer match to the data; however, there is no clear reason why these neutrino processes should not operate in these conditions. This example is only meant to highlight the relevance of understanding neutrino processes in the crust, especially under the presence of strong fields. Another possibility to fit the data is to tune the energy injection, which must be maintained during the first ~ 200 days, resulting in a higher luminosity at late times. If we assume that only a region 5 km in radius is affected (this is closer to the ~ 2 km emitting region observed), we need a continuous injection of at least $\sim 10^{44}$ erg s^{-1} (per day) for about 200 days, which results in a total energy of a few 10^{46} erg. While this energy budget may not be unrealistic, a physical mechanism that can operate for such a long timescale is not known. A possibility might be a continuous injection of energy to keep the surface at high temperatures for so long, although in this latter case we should possibly expect more SGR-like bursts during the first hundreds days.

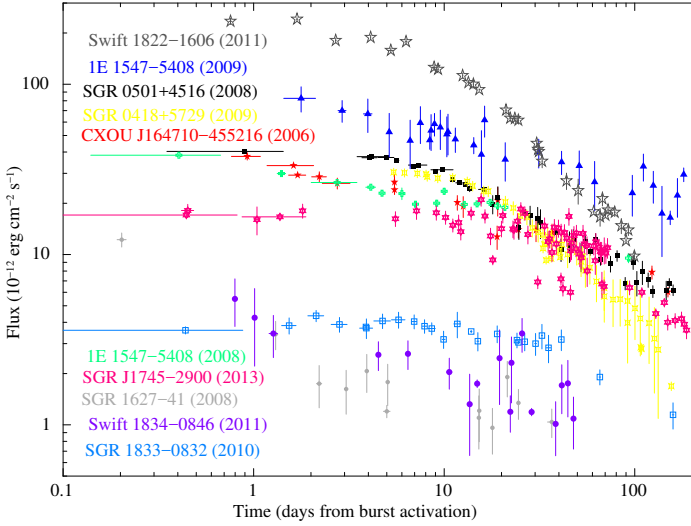


Figure 2.10: Flux decay of all magnetar outbursts monitored with imaging instruments. Fluxes are absorbed in the 1–10 keV energy range (adapted and updated from Rea & Esposito 2011).

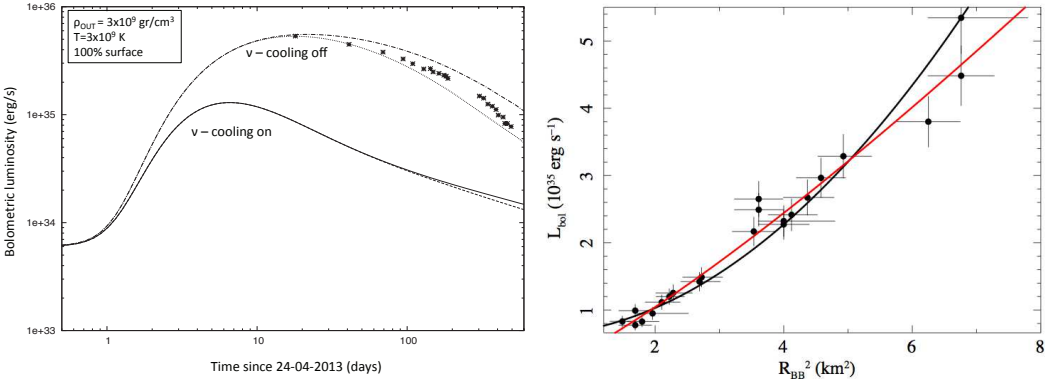


Figure 2.11: *Left-hand panel*: crustal cooling curves attempting at modelling the luminosity decrease of SGR 1745–2900. Luminosities are bolometric and calculated assuming a distance of 8.3 kpc. For the neutrino-cooling on and off set of curves, the lower and upper curves are relative to $\rho_{\text{IN}} = 2$ and $4 \times 10^{10} \text{ g cm}^{-3}$, respectively. *Right-hand panel*: bolometric luminosity as a function of the square of the black body radius at infinity. Solid lines represent the fits with a quadratic function (black) and a generic power-law ($\alpha = 1.23 \pm 0.08$; red).

2.3.3 Bombardment by magnetospheric currents in a bundle

In this section we discuss the possibility that the prolonged high luminosity of SGR 1745–2900 is in part due to external particle bombardment as a consequence of the existence of a twisted magnetic field bundle. A valid alternative model to the crustal cooling scenario invokes the presence of magnetospheric currents flowing along a gradually shrinking magnetic bundle, and heating the surface from outside. According to Beloborodov (2007, 2013), this bundle can untwist on different timescales: i) in the equatorial regions of the magnetosphere, where the magnetic field reaches a few stellar radii, currents are dissipated after weeks or months, while ii) at higher latitudes (close to the poles), a bundle may untwist more slowly, possibly in one to ten years. Here, particles can reach Lorentz factors of a few tens (Beloborodov 2007). In this scenario, a quasi steady-state outflow of electrons and positrons is maintained thanks to magnetic pair production close to the surface. The non-negligible electric voltage along the magnetic field lines and the radiative force due to Compton scattering regulate the streams of positrons and electrons along the field line.

The presence of a non-thermal component observed by *NuSTAR* (Mori et al. 2013; Kaspi et al. 2014), and confirmed also by our *XMM-Newton* observations on a much longer temporal baseline, is suggestive of a large density of magnetospheric particles which boost thermal photons emitted from the surface via resonant Compton scattering, providing the power-law component. In this context, the observed ~ 2 km size of the emitting black body is consistent with a relatively small j-bundle. In the scenario in which the outburst evolution is dominated by an untwisting bundle and the poloidal magnetic field has a dipole geometry, the luminosity is expected to decrease with the square of the black body area ($A_b = 4\pi R_{BB}^2$; Beloborodov 2007, 2009). A flatter dependence may arise from a more complex field geometry. In Figure 2.11 (right-hand panel) we show the fits of the bolometric luminosity as a function of R_{BB}^2 with two different models, a quadratic function $L_{\text{bol}} \propto A_b^2$ (black line; $\chi_\nu^2 = 1.3$ for 23 d.o.f.) and a power-law $L_{\text{bol}} \propto A_b^\alpha$ (red line; $\chi_\nu^2 = 0.8$ for 23 d.o.f.). For the latter model we find $\alpha = 1.23(8)$. Interestingly, a similar relation was observed also for the outburst decay of SGR 0418+5729 (Rea et al. 2013b) and CXOU J1647–4552 (An et al. 2013).

In the following we will assess, using first order approximations, whether the particle density needed to keep the footprint of the bundle at a temperature of ~ 1 keV for the first hundreds of days after the outburst onset is consistent with the particle density in the bundle responsible for the non-thermal power-law tail. The power of the infalling particles is $E_{\text{kin}}\dot{N}$, where E_{kin} is the kinetic energy of a single particle at the surface and \dot{N} is the total number of infalling particles per unit time. If this kinetic energy is transferred by the infalling particles to the footprint of the bundle, and produces thermal luminosity from the footprint surface, then:

$$L_X = A_b \sigma T^4 = E_{\text{kin}} \dot{N} = n \Gamma m_e c^3 A_b, \quad (2.1)$$

where A_b is the area of the footprint surface, T is the spot temperature, n is the density of the infalling particles (assumed to be electrons and/or positrons, created by means of

pair production), and Γ is the Lorentz factor. We calculated the density of the infalling particles by considering the kinetic energy they need to heat the base of the bundle spot. For a given temperature, one can estimate n as

$$n_{\text{bomb}} = \frac{\sigma T^4}{m_e \Gamma c^3} \sim 4.2 \times 10^{22} \frac{[kT/(1 \text{ keV})]^4}{\Gamma} \text{cm}^{-3}. \quad (2.2)$$

On the other hand, we can estimate the density of the particles responsible for the resonant Compton scattering which produces the X-ray tail as

$$n_{\text{rcs}} \simeq \frac{J_B \mathcal{M}}{ve} \simeq \frac{MB}{4\pi\beta er} \sim 1.7 \times 10^{16} \frac{MB_{14}}{\beta} \left(\frac{r}{R_*}\right)^{-1} \text{cm}^{-3}, \quad (2.3)$$

where $\vec{J}_B = (c/4\pi)\vec{\nabla} \times \vec{B}$ is the conduction current, B is the local magnetic field, and r is the length-scale over which B varies ($R_* \sim 10^6$ cm is the star radius). In the magnetosphere of a magnetar the real current is always very close to J_B and it is mostly conducted by e^\pm pairs (Beloborodov 2007). The abundance of pairs is accounted for by the multiplicity factor \mathcal{M} which is the ratio between the actual charge density (including pairs) and the minimum density needed to sustain J_B ; the latter corresponds to a charge-separated flow in which the current is carried only by electrons (and ions). If the same charge population is responsible for both resonant Compton scattering and surface heating, the densities given by eqs. (2.2) and (2.3) should be equal. This implies

$$B_{14} \left(\frac{r}{R_*}\right)^{-1} \mathcal{M}\Gamma = 2.5 \times 10^6 \left(\frac{kT}{1 \text{ keV}}\right)^4. \quad (2.4)$$

According to Beloborodov (2013), both the Lorentz factor and the pair multiplicity change along the magnetic field lines, with typical values of $\mathcal{M} \sim 100$ (i.e. efficient pair creation), $\Gamma \sim 10$ in the largest magnetic field loops, and $\mathcal{M} \sim 1$ (i.e. charge-separated plasma), $\Gamma \sim 1$ in the inner part of the magnetosphere. The previous equality cannot be satisfied for a typical temperature of $\sim 0.8 - 1$ keV, unless the magnetic field changes over an exceedingly small length-scale, a few meters at most. It appears, therefore, very unlikely that a single flow can explain both surface heating and resonant up-scattering.

2.4 Conclusions

The spectacular angular resolution of *Chandra* and the large effective area of *XMM-Newton*, together with an intense monitoring of the Galactic Centre region, has allowed us to collect an unprecedented dataset covering the outburst of SGR 1745–2900, with very little background contamination (which can be very severe in this region of the Milky Way).

The analysis of the evolution of the spin period allowed us to find three different timing solutions between 2013 April 29 and 2014 August 30, which show that the source period derivative has changed at least twice, from $6.6 \times 10^{-12} \text{ s s}^{-1}$ in 2013 April at the outburst

onset, to $3.3 \times 10^{-11} \text{ s s}^{-1}$ in 2014 August. While the first \dot{P} change could be related with the occurrence of an SGR-like burst (Kaspi et al. 2014), no burst has been detected from the source close in time to the second \dot{P} variation (although we cannot exclude it was missed by current instruments). This further change in the rotational evolution of the source might be related with the timing anomaly observed in the radio band around the end of 2013 (Lynch et al. 2015), unfortunately during our observing gap.

The 0.3–8 keV source spectrum is perfectly modelled by a single black body with temperature cooling from ~ 0.9 to 0.75 keV in about 1.5 years. A faint non-thermal component is observed with *XMM–Newton*. It dominates the flux at energies > 8 keV at all the stages of the outburst decay, with a power-law photon index ranging from ~ 1.7 to ~ 2.6 . It is most probably due to resonant Compton scattering onto non-relativistic electrons in the magnetosphere.

Modelling the outburst evolution with crustal cooling models has difficulty in explaining the high luminosity of this outburst and its extremely slow flux decay. If the outburst evolution is indeed due to crustal cooling, then magnetic energy injection needs to be continuous over at least the first ~ 200 days.

The presence of a small twisted bundle sustaining currents bombarding the surface region at the base of the bundle, and keeping the outburst luminosity so high, appears a viable scenario to explain this particular outburst. However, detailed numerical simulations are needed to confirm this possibility.

This source is rather unique, given its proximity to Sgr A*. In particular, it has a > 90 per cent probability of being in a bound orbit around Sgr A* according to our previous N-body simulations (Rea et al. 2013a), and the recent estimates inferred from its proper motion (Bower et al. 2015). We will continue monitoring the source with *Chandra* and *XMM–Newton* for the coming year.

Magnetar-like activity from the central compact object in the supernova remnant RCW103

Rea N., Borghese A., Esposito P., Coti Zelati F.,¹ Bachetti M., Israel G. L., De Luca A. (2016),
Magnetar-like activity from the central compact object in the SNR RCW 103,
Published in The Astrophysical Journal Letters, Volume 828, Issue 1, pp. 13–18

¹"The first four author equally contributed to this work". Author contribution: I discovered the spatial coincidence of the bursting source with the X-ray source at the centre of the supernova remnant. I reduced and analysed data of all *Swift* observations carried out after the onset of the last outburst. I reduced data of the joint *Chandra* plus *NuSTAR* observations carried out soon after the outburst onset and performed timing and spectral analysis (both averaged and time-resolved). I reduced data from archival *XMM-Newton* observations and performed spectral analysis. I modeled empirically the long-term X-ray light curve. I wrote parts of the sections relative to the data analysis (Section 3.2) and the results (Section 3.3.3 and 3.3.4). I contributed to the revision of the manuscript in a subsequent phase and in the preparation of the answers to the referee's requests.

The 6.67 hr periodicity and the variable X-ray flux of the central compact object (CCO) at the centre of the supernova remnant RCW 103, named 1E 161348–5055, have been always difficult to interpret within the standard scenarios of an isolated neutron star or a binary system. On 2016 June 22, the Burst Alert Telescope (BAT) onboard *Swift* detected a magnetar-like short X-ray burst from the direction of 1E 161348–5055, also coincident with a large long-term X-ray outburst. Here we report on *Chandra*, *NuSTAR* and *Swift* (BAT and XRT) observations of this peculiar source during its 2016 outburst peak. In particular, we study the properties of this magnetar-like burst, we discover a hard X-ray tail in the CCO spectrum during outburst, and we study its long-term outburst history (from 1999 to 2016 July). We find the emission properties of 1E 161348–5055 consistent with it being a magnetar. However, in this scenario, the 6.67 hr periodicity can only be interpreted as the rotation period of this strongly magnetized neutron star, which therefore represents the slowest pulsar ever detected, by orders of magnitude. We briefly discuss the viable slow-down scenarios, favoring a picture involving a period of fall-back accretion after the supernova explosion, similarly to what is invoked (although in a different regime) to explain the ‘anti-magnetar’ scenario for other CCOs.

3.1 Introduction

The central compact object 1E 161348–5055, laying within the supernova remnant (SNR) RCW 103, defied any interpretation for more than two decades because of its puzzling phenomenology. Originally identified as a prototypical radio-quiet isolated neutron star (Tuohy & Garmire 1980), more recent observations settled the case for a truly unique phenomenology. First, the source shows a dramatic long-term variability, with large outbursts (factor 100 in flux), possibly recurrent on a time scale of few years. Moreover, the source features a puzzling periodicity at 6.67 hours with an extremely variable profile along different luminosity levels (De Luca et al. 2006). Such a temporal behaviour, coupled to the young age and to the lack of an optical/infrared counterpart (De Luca et al. 2008) make 1E 161348–5055 unique among all compact objects. Several interpretations on the nature of this system have been proposed, from a young low-mass X-ray binary system, to an isolated, slowly spinning young magnetar with a substantial fossil-disk, or even a binary magnetar. Even more peculiar pictures have been proposed, but none of them is straightforward, and require highly non-standard assumptions about the formation and evolution of compact objects in supernova explosions to explain the overall observational properties (Garmire et al. 2000; De Luca et al. 2006, 2008; Li 2007; Pizzolato et al. 2008; Bhadkamkar & Ghosh 2009; Esposito et al. 2011; Liu et al. 2015; Popov et al. 2015).

A millisecond burst from a region overlapping the SNR RCW 103 triggered the *Swift* Burst Alert Telescope (BAT) on 2016 June 22 at 02:03 UT (D’Aì et al. 2016). These short X-ray bursts are the hallmark of the soft gamma repeater (SGR) and anomalous X-ray pulsar (AXP) classes, believed to be isolated NSs powered by the strength and instabilities of their 10^{14-15} G magnetic fields (aka magnetars; Duncan & Thompson 1992; Olausen & Kaspi 2014; Turolla, Zane & Watts 2015). In this chapter, we report on the analysis

of the magnetar-like burst detected by *Swift* BAT, on simultaneous *Chandra* and *Nuclear Spectroscopic Telescope Array (NuSTAR)* observations performed soon after the burst, and on the long-term *Swift* XRT monitoring (Section 3.2). We put our results in the context of all *Swift*, *Chandra*, and *XMM–Newton* observational campaigns of 1E 161348–5055 from 1999 until 2016 July in Section 3.3. We discuss our findings and derive constraints on the nature of this puzzling object in Section 3.4.

3.2 X-ray observations and data analysis

3.2.1 *Swift*

The *Swift* X-ray Telescope (XRT) has been monitoring 1E 161348–5055 almost monthly, starting from April 2006 (Esposito et al. 2011). We have analyzed all *Swift* XRT observations in photon counting mode from 2006 April 18 until 2016 July 20 (93 pre-burst and 20 post-burst observations, for an exposure of 236.2 ks). The last *Swift* XRT observation prior to the burst was performed on 2016 June 22 from 01:30–01:42 UT (finished ~ 20 min before the burst trigger), and showed the source already in an enhanced X-ray state (1–10 keV absorbed flux of $\sim 1.2 \times 10^{-10}$ erg cm $^{-2}$ s $^{-1}$), while the previous observation was on 2016 May 16 from 13:47 – 15:47 UT with the source still at a low flux rate (1–10 keV absorbed flux of $\sim 1.7 \times 10^{-12}$ erg cm $^{-2}$ s $^{-1}$; see Figures 3.1 and 3.4).

Data were processed and analyzed with the tasks included in the HEASOFT software package (v.6.19) and the calibration files in the 2016-05-02 CALDB release. The XRT source counts were extracted from a circular region centered on the most accurate position of the CCO (RA = 16^h17^m36^s.23, Dec = $-51^{\circ}02'24''.6$ (J2000.0); De Luca et al. 2008) with a radius of 10 pixels (1 pixel = 2.36 arcsec), and the background events from an annulus of radii 10–20 pixels. The observation ~ 20 min before the BAT trigger yielded a severe pile-up, and was analyzed excising the inner 3.5 pixels of the extraction region.

We analyzed the BAT data of the burst (trigger 700791, obs. ID 00700791000). The T_{90} duration of the event (the time during which 90 per cent of the burst counts were collected) was 9 ± 1 ms and its total duration was ~ 10 ms. These durations were computed by the Bayesian blocks algorithm BATTBLOCKS on mask-weighted light curves binned at 1 ms in the 15–150 keV (Scargle 1998), where essentially all the emission is contained. For the burst only, mask-tagged light curves, images and spectra were created. We extracted a 15–150-keV sky image and performed a blind source detection over the whole duration of the burst: a single, point-like source was detected at high significance (14.5σ) at the best-fit coordinates R.A. = 16^h17^m29^s.62, Decl. = $-51^{\circ}03'07''.9$ (J2000.0), with an uncertainty radius of 1.5 arcmin (1σ , including a systematic error of 0.25 arcmin; Tueller et al. 2010). This position is consistent with a single known X-ray source: 1E 161348–5055 (see Figure 3.1). No other X-ray source was detected within the burst error circle in the XRT data, with a 3σ upper limit on the count rate of <0.003 counts s $^{-1}$ (in the 0.5–10 keV energy band). Together with the exceptionally high X-ray flux of 1E 161348–5055 at the epoch of the burst, this strongly points to the CCO in RCW 103 as the origin of the burst.

3.2.2 *Chandra*

After the burst trigger, 1E 161348–5055 was observed with the Advanced CCD Imaging Spectrometer spectroscopic array (ACIS-S; Garmire et al. 2003) aboard the *Chandra X-Ray Observatory*, starting on 2016 June 25 at 09:20:07 until 22:00:38 UT, for an on-source exposure time of 44.2 ks (obs ID: 18878). The ACIS-S was configured in continuous clocking (CC) mode with FAINT telemetry format, yielding a readout time of 2.85 ms at the expense of one dimension of spatial information. The source was positioned on the back-illuminated S3 chip.

We analyzed the data following the standard analysis threads² with the *Chandra* Interactive Analysis of Observations software (CIAO, v. 4.8; CALDB v. 4.7.2). We accumulated the source photon counts within a box of dimension 3×3 arcsec² centered on the position of the CCO. The background was estimated by collecting photons within two rectangular regions oriented along the readout direction of the CCD, symmetrically placed with respect to the target and both lying within the remnant, whose spatial extension is ~ 9 arcmin in diameter (Frank, Burrows & Park 2015). The average source net count rate was 3.352 ± 0.009 counts s⁻¹, which guarantees no pile up issues in the data set.

We have also analyzed all archival *Chandra* observations pointing at <30 arcsec from our target (24 observations from 1999 September 26 until 2015 January 13; see Figure 3.4). Source photons from timed-exposure mode observations were extracted from a 2-arcsec circular region, and the background from an annulus with radii 4–10 arcsec. These observations were used for the timing and spectral long-term analysis (see below). When necessary, we corrected for pile up effects by using the model of Davis (2001).

3.2.3 *NuSTAR*

NuSTAR (Harrison et al. 2013) observed 1E 161348–5055 starting on 2016 June 25 at 06:46:47 UT until June 26 at 18:42:50 UT, for a total on-source exposure time of 70.7 ks (obs ID: 90201028002), simultaneously with the *Chandra* observation (Section 3.2.2). The data were processed using version 1.6.0 of the *NuSTAR* Data Analysis Software (NUSTARDAS; using version 59 of the clock file to account for clock drifts caused by temperature variation of the detectors). We used the tool NUIPIPELINE with default options for good time interval filtering to produce cleaned event files, and we removed time intervals corresponding to passages through the South Atlantic Anomaly. We ran the NUPRODUCTS script to extract light curves and spectra and generated instrumental response files separately for both focal plane modules (FPMA and FPMB). We collected the source counts within a circular region of radius 40 arcsec around the CCO position. The background subtracted source count rate in the 3–79 keV was 0.27 ± 0.03 counts s⁻¹. We checked that a 30 arcsec extraction region gives consistent results. Background was estimated from two 60 arcsec circular regions on the same chip, one inside and one outside the ghost rays-contaminated area. We verified that the two background estimations did not significantly affect spectral modeling (see Figure 3.3).

²See <http://cxc.harvard.edu/ciao/threads/pointlike>.

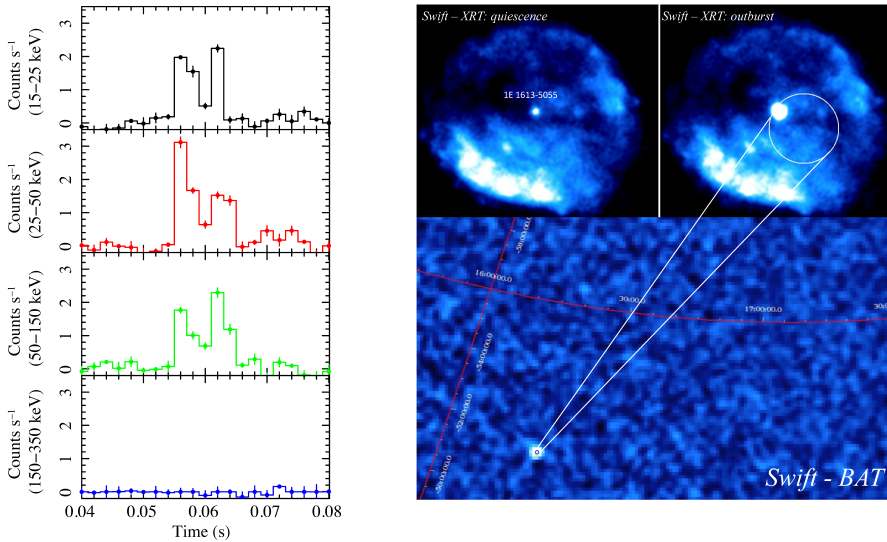


Figure 3.1: Left panel: *Swift* BAT burst light curves at different energies (bin size: 2 ms). Right panel: *Swift* BAT 15–150 keV image of the burst detected on 2016 June 22 (bottom). Two *Swift* XRT co-added 1–10 keV images of the SNR RCW103 during the CCO quiescence state (from 2011 April 18 to 2016 May 16; exposure time ~ 66 ks; top-left) and outburst (from 2016 June 22 to 2016 July 20; exposure time ~ 67 ks; top-right). The white circle is the positional accuracy of the detected SGR-like burst, which has a radius of 1.5 arcmin (see text for details).

3.3 Results

3.3.1 Burst properties

The light curve of the *Swift* BAT burst shows a double-peak profile (Figure 3.1). We fit the spectra of the two peaks with single-component models typically used for magnetar bursts: a power-law, a black body, and a bremsstrahlung component (e.g., Israel et al. 2008). Only the black body model provided an acceptable fit for both peaks. The first ~ 5 ms of the event can be fit by a black body with $kT = 9.2 \pm 0.9$ keV ($\chi^2_{\nu} = 1.03$ (36 dof), null hypothesis probability (nhp) = 0.42), while for the second peak the black body temperature is $kT = 6.0 \pm 0.6$ keV ($\chi^2_{\nu} = 1.22$ (36 dof), nhp = 0.16). The total burst flux is $(1.6 \pm 0.2) \times 10^{-6}$ erg cm $^{-2}$ s $^{-1}$ in the 15–150 keV range (corresponding to an average luminosity of 2×10^{39} erg s $^{-1}$). All errors are given at 1σ confidence level throughout the chapter, and we assume a 3.3 kpc distance (Caswell et al. 1975).

3.3.2 Timing analysis

For the timing analysis, photon arrival times were reported to the Solar System barycentre frame, using the DE200 ephemerides and the *Chandra* CCO position (see above). We per-

formed a blind search both for fast periodic and aperiodic signals using our new *Chandra* and *NuSTAR* data sets, using the XRONOS timing package as well as the Z_n^2 test (Buccheri et al. 1983). We did not find any periodic signal via Fourier transform, but in both observations we detected the known ~ 6.67 hr periodic modulation (see Figure 8.2). We inferred 3σ pulsed fraction upper limits (as explained in Israel & Stella 1996) of 5 per cent (0.01–10 Hz), 6 per cent (10–100 Hz) and in the 7–9 per cent range for the highest sampled frequencies (100–200 Hz) for the *Chandra* observation. A similar analysis carried out on the *NuSTAR* data resulted in 3σ upper limits of 12 per cent (0.01–3 Hz), and in the 26–34 per cent range at higher frequencies (3–1000 Hz).

In Figure 3.2 we show the determination of the ~ 6.67 hr period using the longest datasets in the X-ray archives, with the light curves of the two most extreme cases of a pure single peak (from *XMM-Newton* in 2005; De Luca et al. 2006), and a clear double peak (in 2016 June; this thesis). The 3–79 keV light curve of the *NuSTAR* data and the simultaneous 1–8 keV *Chandra* data were fit by two sinusoidal harmonics with fundamental periods 24095 ± 167 s (at TJD 17565.0) and 23983 ± 263 s (at TJD 17564.7), respectively. We also studied the profile as a function of the energy in the 1–25 keV band, and found that the profile may smooth to a single peak with increasing energy (see left-hand panel Figure 3.3). Pulsed fractions (defined as $\text{Max} - \text{Min} / \text{Max} + \text{Min}$ of the profile) are 40 ± 1 per cent in the 1–8 keV band, and 41 ± 5 per cent for the 10–20 keV interval.

Studying the timing properties of 1E 161348–5055 is complicated by the changing pulse profile. However, if we assume the ephemeris of Esposito et al. (2011; solution ‘A’; constant period: $24030.42(2)$ s; see the paper for a discussion of the assumptions and the validity of the solution), and extrapolate the phase of the minimum predicted for the fundamental harmonic, this is consistent within 2σ ($\Delta\phi = 0.03 \pm 0.02$ for the 1–8 keV *Chandra* profile, and $\Delta\phi = 0.08 \pm 0.04$ for the 10–15 keV *NuSTAR* profile) with that of the second minimum in the left-hand panel of Figure 3.3, around phase $\phi \sim 0.9$ (implying $|\dot{P}| < 7 \times 10^{-10}$ s s $^{-1}$).

3.3.3 Spectral analysis

We started the spectral analysis by simultaneously fitting the new *Chandra* and *NuSTAR* observations (see right-hand panel of Figure 3.3). We found that although the *Chandra* spectrum alone is well fit with two blackbodies, this is not the case when taking into account also the *NuSTAR* hard X-ray spectrum of 1E 161348–5055. A good fit is found for a model comprising two absorbed ($N_{\text{H}} = 2.05(5) \times 10^{22}$ cm $^{-2}$) blackbodies with temperatures $kT_1 = 0.52 \pm 0.01$ keV and $kT_2 = 0.93 \pm 0.05$ keV, with radii $R_1 = 2.7 \pm 0.7$ km and $R_2 = 0.4 \pm 0.2$ km, plus the addition of a power-law component with photon index $\Gamma = 1.20 \pm 0.25$ (adding a constant between the two instruments to account for inter-calibration uncertainties, which was always within 10 per cent). The total absorbed flux in the 0.5–30 keV energy range is $(3.7 \pm 0.1) \times 10^{-11}$ erg cm $^{-2}$ s $^{-1}$, and the joint fit gives $\chi_\nu^2 = 1.04$ (660 dof; nhp = 0.2). A model with a black body plus two power-laws results in a slightly worse fit with $\chi_\nu^2 = 1.20$ (660 dof; nhp = 2×10^{-4}), and bad residual shape.

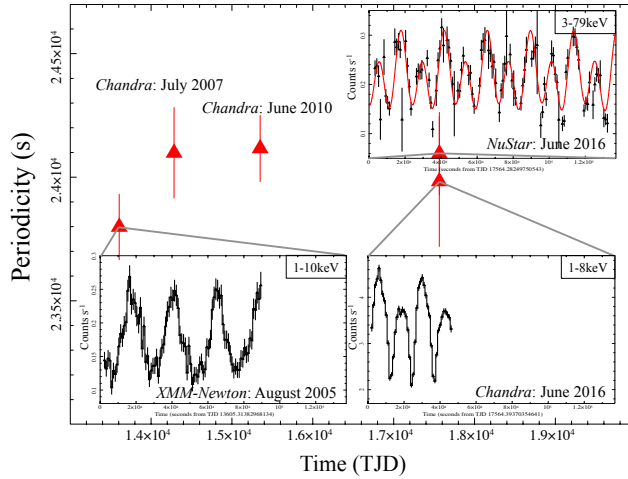


Figure 3.2: Period determination for the longest available archival X-ray observations, with the superimposed light curve binned at 1 ks bin^{-1} .

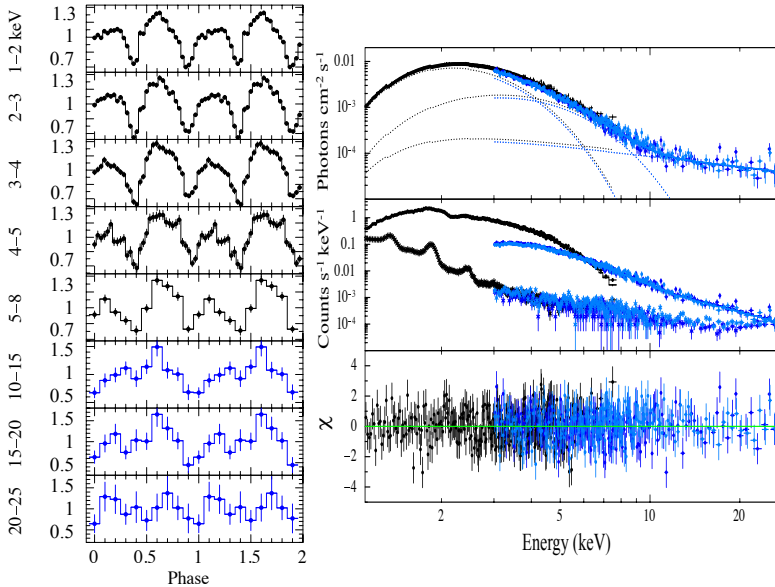


Figure 3.3: Left-hand panel: Energy-dependent folded light-curve for the simultaneous *Chandra* (black) and *NuSTAR* (blue) observations soon after the 2016 burst. Right-hand panel: Simultaneous spectral fit of the *Chandra* (black) and *NuSTAR* (light and dark blue) data with two absorbed blackbodies and a power-law component. The background spectrum is also plotted in the middle panel.

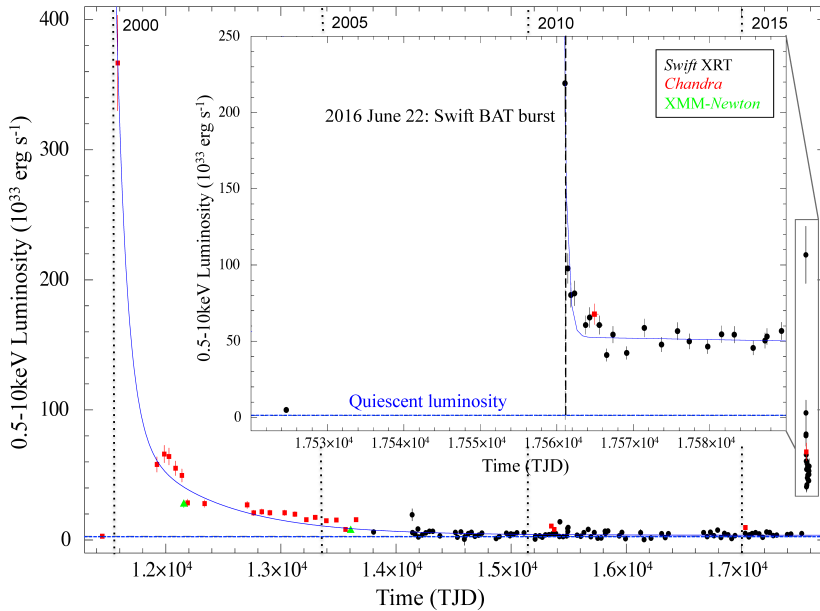


Figure 3.4: Long-term 0.5–10 keV luminosity history of 1E 161348–5055 as observed from 1999 September 26 until 2016 July 20 by *Chandra* (red squares), *XMM–Newton* (green triangles) and *Swift* (black circles). Dashed line represents the source quiescent luminosity. The inset is a zoom of the 2016 outburst.

3.3.4 Outburst history

To study the outburst history of 1E 161348–5055, we reanalyzed all the available *Chandra*, *XMM–Newton* and *Swift* data of the source acquired from 1999 until 2016 July (see Figure 3.4). All spectra were fit by fixing the absorption column density to the value derived using *Chandra* ($N_{\text{H}} = 2 \times 10^{22} \text{ cm}^{-2}$) plus two black body components (because the hard X-ray power-law is not required by the fit in the 1–8 keV range, and contributes less than 10 per cent to the flux in this band). We show the extrapolated 0.5–10 keV luminosity in Figure 3.4. This source underwent two outbursts in the past ~ 17 years. The first outburst can be empirically fit by a constant plus three exponential functions, resulting in a total (impulsive plus persistent) emitted energy in the 0.5–10 keV band of $E_{1st-out} \sim 9.9 \times 10^{42} \text{ erg}$. This outburst was characterized by heating of two different regions on the surface, with the two blackbodies in the X-ray spectra cooling and shrinking from the outburst peak until quiescence: $kT_1 \sim 0.6\text{--}0.4 \text{ keV}$ ($R_1 \sim 5 - 1 \text{ km}$), and $kT_2 \sim 1.4\text{--}0.7 \text{ keV}$ ($R_2 \sim 1.4 - 0.1 \text{ km}$). This new second outburst, that started < 1 month before the SGR-like burst, shows similar energetic and spectral decomposition so far ($E_{2nd-out} \sim 1.6 \times 10^{42} \text{ erg}$). Furthermore, our *NuSTAR* observation shows for the first time that during the outburst peak this source emits up to $\sim 30 \text{ keV}$ (with emission certainly modulated until $\sim 20 \text{ keV}$; Figure 3.3).

3.4 Discussion

We report on the analysis of a magnetar-like short burst from the CCO 1E 161348–5055 (D’Ai et al. 2016), and study its coincident X-ray outburst activity. This short ms-burst and its spectrum, the X-ray outburst energetics of this source, the spectral decomposition, and surface cooling (see Section 3.3) are all consistent with observations of magnetar SGR-like bursts and outbursts (see Rea & Esposito 2011, and reference therein, for an observational review). This is the second X-ray outburst detected from 1E 161348–5055, and it shows for the first time a coincident SGR-like burst and a non-thermal component up to ~ 30 keV. Two-peak SGR-bursts with similar luminosity and spectra have been observed in other magnetars (see e.g. Aptekar et al. 2001, Götz et al. 2004, Collazzi et al. 2015). Due to their ms-timescales and relatively soft spectra, these events cannot be interpreted as Type I X-ray bursts or short GRBs (see Galloway et al. 2008; Sakamoto et al. 2011). On the other hand, hard X-ray emission has been detected for at least half of the magnetar population (Olausen & Kaspi 2014). Sometimes this emission is steady, but other times transient and connected with the outburst peaks. Magnetar outbursts are expected to be produced by the instability of strong magnetic bundles which stress the crust (from outside or inside: Beloborodov 2009, Li, Levin & Beloborodov 2016, Perna & Pons 2011, Pons & Rea 2012). This process heats the surface in one or more regions, and at variable depth inside the NS crust, which in turn drives the outburst duration. The high electron density in these bundles might also cause resonant cyclotron scattering of the seed thermal photons, creating non-thermal high-energy components in the spectrum. Such components can be transient if the untwisting of these bundles during the outburst decay produces a decrease in the scattering optical depth. Furthermore, magnetospheric re-arrangements are expected during these episodes, and are believed to be the cause of the short SGR-like bursts (see Turolla, Zane & Watts 2015 for a review). Repeated outbursts on several-year timescales have been detected in at least four magnetars (Bernardini et al. 2011; Kuiper et al. 2012; Archibald et al. 2015), and their recurrence time is expected to be related to the source magnetic field strength and configuration, and to the NS age (see Perna & Pons 2011; Viganò et al. 2013).

In this scenario, the only puzzling property of 1E 161348–5055, which makes it unique among any SGR, AXP, CCO or other known NS, is the 6.67 hr long periodicity, which would represent the longest spin period ever detected in a pulsar. On the other hand, the extreme variability of the modulation in time and energy strongly disfavor this modulation being due to an orbital period (see detailed discussion in De Luca et al. 2008, Pizzolato et al. 2008), but remain fully consistent with the usual pulse profile variability observed in actively flaring magnetars (see e.g. Rea et al. 2009, 2013; Rodríguez Castillo et al. 2014).

Spin periods of isolated X-ray pulsars are observed to be limited to ~ 12 s, with the slowest pulsars indeed being the magnetars. This period distribution is explained as due to Hall-Ohmic magnetic field decay during the evolution of these neutron stars (see Pons, Viganò & Rea 2013). The slowest isolated pulsar that magnetic field decay might produce is $\sim 30 - 50$ s, according to self-consistent 2D simulations (e.g. Viganò et al. 2013),

if we consider the generous case of field threading the stellar core, zero dissipation from crustal impurities, and an initial field ranging from 10^{13} to 10^{15} G, while using typical spin period at birth in the range of 1–300 ms. Regardless of the model inputs, we can in no case reproduce hours-long spin periods.

Given the strong evidence for the magnetar nature of the X-ray emission of this source, we are now left with discussing all possible slow-down mechanisms other than the typical pulsar dipolar loss. Since its discovery, many authors have already discussed several scenarios (see De Luca et al. 2006; Li 2007; Pizzolato et al. 2008; Bhadkamakar & Gosh 2009; Lui et al. 2015; Popov, Kaurov, & Kamiker 2015). We will highlight and discuss the possibilities that remain open, along with their possible deficiencies.

The first possibility could be a long-lived fossil disk (Chatterjee, Hernquist & Narayan 2000), which forms via the circularization of fall-back material after the supernova explosion (see i.e. De Luca et al. 2006; Li 2007). This might result in substantially slowing the spin period. However, recent studies on the formation of fossil disks apparently disfavor their existence around NSs under reasonable assumption on the magnetic torque in the pre-SN phase (Perna et al. 2014). On the other hand, the magnetar flaring activity during its lifetime would most probably expel such thin disks very quickly.

Another possibility is that 1E 161348–5055 is a magnetar in a low mass X-ray binary with an M6 companion (De Luca et al. 2008), emitting as though it were isolated, but that had its spin period tidally locked to the orbital motion of the system (see e.g. Pizzolato et al. 2008). However also in this case, fine-tuning is needed to explain how a very low-mass companion remains gravitationally bound to the magnetar after the SN explosion.

The most viable interpretation, in line with what has been proposed for other CCO systems (the ‘anti-magnetars’: see e.g. Halpern & Gotthelf 2010; Torres-Forné et al. 2016), seems to be of a magnetar that had a strong SN fall-back accretion episode in the past (Chevalier 1989). In particular, if 1E 161348–5055 is born with a magnetic field and spin period such that when the fall-back accretion begins, the source is in the propeller regime (Illarionov & Sunyaev 1975; Li 2007; Esposito et al. 2011), then the accreting material will not reach the surface and bury the B-field, as for the ‘anti-magnetar’ CCOs, but in the first years or more of the magnetar lifetime matter will accrete onto the magnetosphere, hence with a substantially larger spin-down torque. When the fall-back accretion stops, the magnetar continues to evolve as any other isolated pulsar, but with a substantially longer spin period.

Chapter 4

The discovery and monitoring of magnetar SGR J1935+2154

Israel G. L., Esposito P., Rea N., Coti Zelati F.,¹ Tiengo A., Campana S., Mereghetti S., Rodriguez Castillo G. A., Götz D., Burgay M., Possenti A., Zane S., Turolla R., Perna R., Cannizzaro G., Pons J. (2016),

The discovery, monitoring and environment of SGR J1935–2154,

Published in Monthly Notices of the Royal Astronomical Society,

Volume 457, Issue 4, pp. 3448–3456

¹Author contribution: I discovered pulsations at the spin period which led to the identification of the source as a magnetar. I reduced *Swift*, *Chandra* and *XMM-Newton* data and performed spectral analysis (see also Chapter 7) as well as study of the diffuse emission.

We report on the discovery of a new member of the magnetar class, SGR J1935+2154, and on its timing and spectral properties measured thanks to an extensive observational campaign carried out between 2014 July and 2015 March with *Chandra* and *XMM-Newton* (11 pointings). We discovered the spin period of SGR J1935+2154 through the detection of coherent pulsations at a period of about 3.24 s. The magnetar is slowing-down at a rate of $\dot{P}=1.43(1)\times 10^{-11}$ s s⁻¹ and with a decreasing trend due to a negative \ddot{P} of $-3.5(7)\times 10^{-19}$ s s⁻². This implies a surface dipolar magnetic field of $\sim 2.2\times 10^{14}$ G, a characteristic age of ~ 3.6 kyr and a spin-down luminosity $L_{sd} \sim 1.7\times 10^{34}$ erg s⁻¹. The source spectrum is well modelled by a black body with temperature of about 500 eV plus a power-law component with photon index ~ 2 . The source showed moderate long-term variability, with a flux decay of ~ 25 per cent during the first 4 months since its discovery, and a re-brightening of the same amount during the ensuing 4 months. The X-ray data were also used to study the source environment. We discovered a diffuse emission extending on spatial scales from about 1 arcsec up to at least 1 arcmin around SGR J1935+2154 both in *Chandra* and *XMM-Newton* data. This component is constant in flux (at least within uncertainties) and its spectrum is well modelled by a power-law with photon index steeper than that of the pulsar. Though a scattering halo origin seems to be more probable we cannot exclude that part, or all, of the diffuse emission is due to a pulsar wind nebula.

4.1 Introduction

Energetic pulsars are known to produce particle outflows, often resulting in spectacular pulsar wind nebulae (PWNe) of which the Crab is the most famous example (Weisskopf et al. 2000). Magnetars are expected to produce particle outflows as well, either in quiescence or during outbursts accompanying bright bursts. Because of the strong magnetic fields associated with this class of neutron stars, the idea of a wind nebula around a magnetar is thus promising. There has not been yet a confirmed detection of such a nebula, but some cases of ‘magnetically powered’ X-ray nebulae around pulsars with relatively high magnetic fields have been suggested. A peculiar extended emission has been reported around the rotating radio transient RRAT J1819–1458 (Rea et al. 2009; Camero-Arranz et al. 2013), with a nominal X-ray efficiency $\eta_X \sim 0.2$, too high to be only rotationally powered. The authors suggested that the occurrence of the nebula might be connected with the high magnetic field ($B = 5\times 10^{13}$ G) of the pulsar. Similarly, Younes et al. (2012) reported the discovery of a possible wind nebula around Swift J1834–0846, with an X-ray efficiency $\eta_X \sim 0.7$ (but see Esposito et al. 2013 for a different interpretation in terms of a dust scattering halo).

SGR J1935+2154 is a new member of the magnetar family, and was discovered thanks to the detection of low-Galactic latitude short bursts by *Swift* on 2014 July 5 (Stamatikos et al. 2014). Follow-up observations carried out by *Chandra* on July 15 and 29 allowed us to precisely locate the source and detect its spin period ($P=3.25$ s; Israel et al. 2014) confirming that SGR J1935+2154 is indeed a magnetar. The position of SGR J1935+2154 is coincident with the centre of the Galactic supernova remnant (SNR) G57.2+0.8 of undeter-

mined age and at a possible, but uncertain, distance of 9 kpc (Sun et al. 2011; Pavlovic et al. 2013).

In this chapter we report on the results of an *XMM-Newton* and *Chandra* observational campaign covering the first 8 months of the SGR J1935+2154 outburst. Our observational campaign is ongoing with *XMM-Newton*, and its long-term behavior will be reported elsewhere. We also report upper limits on the radio emission derived from *Parkees* observations (Burgay et al. 2014). We first describe the data analysis, then summarize the results we obtained for the parameters, properties and environment of this new magnetar. Finally we discuss our findings in the context of the magnetar scenario.

4.2 X-ray observations

4.2.1 *Chandra*

Chandra observations of SGR J1935+2154 were carried out three times during 2014 July and August (see Table 4.1) in response to the detection of short SGR-like bursts from the source. The first dataset was acquired with the ACIS-S instrument in Faint imaging (Timed Exposure) and 1/8 subarray mode (time resolution: ~ 0.44 s), while the subsequent two pointings were obtained with the ACIS-S in Faint timing (Continuous Clocking) mode (time resolution 2.85 ms).

The data were reprocessed with the Chandra Interactive Analysis of Observations software (CIAO, version 4.6) using the calibration files available in the *Chandra* CALDB 4.6.3 database. The scientific products were extracted following standard procedures, but adopting extraction regions with different size in order to properly subtract the underlying diffuse component (see Section 4.3.2 and Figure 4.1). Correspondingly, for the first observation (Faint imaging) we used circular regions of radius 1.5 arcsec (3 arcsec) for the source (diffuse emission) associated to a background annular region with inner and outer radius 1.6 arcsec and 3 arcsec (10 arcsec, 15 arcsec), respectively. Furthermore we used rectangular boxes of 3×2 arcsec² (and 4×2 arcsec²) sides aligned to the CCD readout direction for the remaining two observations in CC mode. For the background we used two rectangular boxes of 1.5×1.5 arcsec² (and 2×2 arcsec²) at the sides of the source extraction region. For the spectra, the redistribution matrices and the ancillary response files were created using SPECEXTRACT. For the timing analysis, we applied the Solar system barycentre correction to the photon arrival times with AXBARY.

4.2.2 *XMM-Newton*

XMM-Newton observations of SGR J1935+2154 were carried out between 2015 September and March (see Table 4.1) to monitor the source decay and study the source properties. We used the data collected with the European Photon Imaging Camera (EPIC), which consists of two MOS (Turner et al. 2001) and one pn (Strüder et al. 2001) CCD detectors. The raw data were reprocessed using the *XMM-Newton* Science Analysis Software (SAS, version 14.0) and the calibration files in the CCF release of 2015 March. The pn operated in

Full Window (time resolution of about 73 ms) while the MOSs were set in Small Window (time resolution of 300 ms), therefore optimized for the timing analysis. The intervals of flaring background were located by intensity filters (see e.g. De Luca & Molendi 2004) and excluded from the analysis. Source photons were extracted from circles with radius of 40 arcsec. The pn background was extracted from an annular region with inner and outer radii of 45 and 90 arcsec, respectively (also in this case the choice was dictated by the diffuse emission component; see Section 4.3.2 and Figure 4.1). Photon arrival times were converted to the Solar system barycenter with the SAS task BARYCEN using the source coordinates as inferred from the *Chandra* pointings (see Section 4.3.1). The ancillary response files and the spectral redistribution matrices for the spectral analysis were generated with ARFGEN and RMFGEN, respectively. In order to maximize the signal to noise ratio we combined, when needed, the spectra from the available EPIC cameras and averaged the response files using EPICSPECCOMBINE. In particular, the latter command was routinely applied for the study of the dim diffuse emission.

4.2.3 *Swift*

The *Swift* X-Ray Telescope (XRT) uses a front-illuminated CCD detector sensitive to photons between 0.2 and 10 keV (Burrows et al. 2005). Two readout modes can be used: photon counting (PC) and windowed timing (WT). The PC mode provides images and a 2.5 s time resolution; in WT mode only one-dimensional imaging is preserved with a time resolution of 1.766 ms. Data were processed with XRTPIPELINE (version 12), and filtered and screened with standard criteria, correcting for effective area and dead columns. Events were extracted from a 20 pixel radius region around the source position. For spectroscopy we used the spectral redistribution matrices in CALDB (20130101, v014 for the PC), while the ancillary response files were generated with XRTMKARF.

4.3 Analysis and results

4.3.1 Position

We used the *Chandra* ACIS-S observation carried out on 2014 July 15, the only one in imaging mode, to precisely locate SGR J1935+2154. Only one bright source was detected in the S7 CCD operating at 1/8 of the nominal field of view. The refined position of the source, calculated with WAVDETECT, is RA = $19^{\text{h}}34^{\text{m}}55^{\text{s}}.5978\text{s}$, Dec = $+21^{\circ}53'47''.7864$ (J2000.0; statistical uncertainty of 0.02 arcsec) with an uncertainty radius of 0.7 arcsec at 90 per cent confidence level. This position is consistent with that of SGR J1935+2154 measured by *Swift*: RA = $19^{\text{h}}34^{\text{m}}55^{\text{s}}.68$, Dec = $+21^{\circ}53'48''.2$, J2000.0, radius of 2.3 arcsec at 90 per cent confidence level (Cummings et al. 2014). Correspondingly, we are confident that the source we detected in the *Chandra* image is indeed the source first detected by *Swift* BAT and later by XRT and responsible for the observed SGR-like bursts.

Table 4.1: Summary of the *Swift*, *Chandra* and *XMM–Newton* observations used in this work and carried out between 2014 July and 2015 March.

Mission / Obs. ID	Instrument	Date	Exposure (ks)
<i>Swift</i> / 603488000	XRT	Jul 5	3.4
<i>Swift</i> / 603488002	XRT	Jul 6	4.3
<i>Swift</i> / 603488004	XRT	Jul 7	9.3
<i>Swift</i> / 603488006	XRT	Jul 8	3.7
<i>Swift</i> / 603488008	XRT	Jul 13	5.3
<i>Swift</i> / 603488009	XRT	Jul 13	3.0
<i>Chandra</i> / 15874	ACIS-S	Jul 15	10.1
<i>Swift</i> / 603488010	XRT	Jul 16	7.1
<i>Chandra</i> / 15875	ACIS-S ^a	Jul 28	75.4
<i>Chandra</i> / 17314	ACIS-S ^a	Aug 31	29.2
<i>XMM</i> / 0722412501	EPIC	Sep 26	19.0
<i>XMM</i> / 0722412601	EPIC	Sep 28	20.0
<i>XMM</i> / 0722412701	EPIC	Oct 04	18.0
<i>XMM</i> / 0722412801	EPIC	Oct 16	9.7
<i>XMM</i> / 0722412901	EPIC	Oct 24	7.3
<i>XMM</i> / 0722413001	EPIC	Oct 27	12.6
<i>XMM</i> / 0748390801	EPIC	Nov 15	10.8
<i>XMM</i> / 0764820101	EPIC	Mar 25	28.4

^a Data collected in continuous clocking mode (CC).

4.3.2 Spatial analysis

Upon visual inspection of the X-ray images, it is apparent that SGR J1935+2154 is embedded in a patch of diffuse emission. To assess this in detail, we built for each pn observation a radial profile in the 0.4–10 keV band and fit a point spread function (approximated by a King model; Read et al. 2011) to it. In each instance, the inner part of the profile can be fit by a King model with usual core radius and slope values, whereas at radii $\approx 30 - 40$ arcsec the data start to exceed significantly the model prediction. Since we obtained consistent results from all the 2014 observations, we repeated the same analysis on the stacked images to improve the signal-to-noise ratio of the data. We also selected the photons in the 1–6 keV energy range, since the spectral analysis shows that the diffuse emission is more prominent in this band (see Section 4.3.4). The combined 2014 *XMM-Newton* profile is shown in black in Figure 4.2. The diffuse emission emerges at $\gtrsim 30$ arcsec from SGR J1935+2154 and extends to at least 70 arcsec. It is however not possible to determine where the feature ends, owing to both the low signal-to-noise at large distance from the point source and the gaps between the CCDs. The profile of the latest *XMM-Newton* dataset has been obtained separately from the remaining datasets in order to look for shape variabilities of the diffuse component on long timescales. The two pn profiles are in agreement within the uncertainties (according to a Kolmogorov–Smirnov test, there is a substantial probability, >50 per cent, that the two profiles have been extracted from the same distribution), though a possible shift of the diffuse component towards larger radii might be present in the 30 - 40 arcsec radius interval.

A similar analysis was carried out by using the longest *Chandra* dataset. Though the latter is in CC mode, the field is not particularly crowded and only faint point-like objects are detected in the field of view. Correspondingly, it is still possible to gather information over smaller scales than in the *XMM-Newton* data. The ACIS-S PSF was simulated using the Chandra Ray Tracer (CHART) and Model of AXAF Response to X-rays (MARX version 5.0.0-0) software packages². The result of this analysis is shown in blue in Figure 4.2. Diffuse emission is clearly present in the *Chandra* data and starts becoming detectable at a distance of >1 arcsec from the source. Due to poor statistics we have no meaningful information at radii larger than ~ 15 arcsec. Therefore, we are not able to assess if the diffuse structures detected by *XMM-Newton* and *Chandra* are unrelated or linked somehow.

²For more details on the tasks see <http://cxc.harvard.edu/chart/index.html> and <http://space.mit.edu/cxc/marx/index.html>

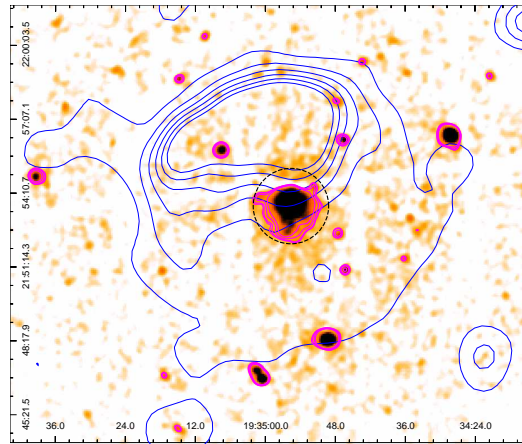


Figure 4.1: 98ks-long *XMM-Newton* PN image of the region around SGR J1935+2154; the 1.4 GHz radio map of SNR G57.2+0.8 is also shown (blue contours from the VLA Galactic Plane Survey; Stil et al. 2006). The *XMM-Newton* image was smoothed with a Gaussian function with a radius of 4 arcsec and magenta contours are displayed to emphasise the extended emission around SGR J1935+2154. The black dashed circle marks a distance of 90 arcsec from the SGR J1935+2154 position.

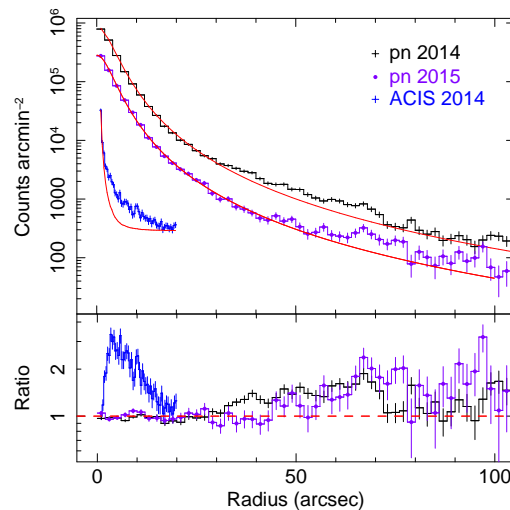


Figure 4.2: 2014 and 2015 *XMM-Newton* and *Chandra* surface brightness (black crosses, purple squares and blue crosses, respectively) as a function of the distance from SGR J1935+2154 compared with their Point Spread Functions (PSF; red lines). The ratios between the data and the PSF are plotted in the bottom panel.

4.3.3 Timing analysis

The 0.5-10 keV events were used to study the timing properties of the pulsar. The average count rate obtained from *Chandra* and *XMM-Newton* was 0.11 ± 0.02 counts s^{-1} and 0.21 ± 0.01 counts s^{-1} , respectively. Coherent pulsations at a period of about 3.24 s were first discovered in the 2014 July 29 *Chandra* observation carried out in CC mode (Israel et al. 2014). The pulse shape is nearly sinusoidal and does not show variations as a function of time. Also the pulsed fraction, defined as the semi-amplitude of the sinusoid divided by the source average count rate, is time independent (within uncertainties) and in the 17 – 21 per cent range (1σ uncertainty of about 1.5 per cent). Additionally, the pulse shape does not depend on the energy range, though a shift in phase of about 0.16 cycles is clearly detected between the soft (0.5-1.5 keV) and hard (3.0-12.0 keV) energy bands, with hard photons anticipating the soft ones (see right-hand panel of Figure 4.3).

A refined value of $P=3.244978(6)$ s (1σ confidence level; epoch 56866.0 MJD) was inferred based on a phase-coherent analysis. Because of the long time elapsed between the epoch of the first period determination and those of the other *Chandra* observations we were not able to further extend the timing solution based on the *Chandra* data. Therefore, we inferred a new phase-coherent solution by means of the seven *XMM-Newton* pointings carried out between the end of September and mid November 2014 (red filled circles in the left-hand panel of Figure 4.3). The new solution also included a first period derivative component: $P=3.2450656(2)$ s and $\dot{P}=1.37(3) \times 10^{-11}$ s s^{-1} (1σ confidence level; epoch 56926.0 MJD; $\chi^2=3.1$ for 4 degrees of freedom).

The latter timing solution was accurate enough to include the previous *Chandra* pointings (black filled circles in the left-hand panel of Figure 4.3). The final timing solution, encompassing the whole dataset, is reported in Table 4.2 and includes a second period derivative acting in the direction of decelerating the rate of period change \ddot{P} . The inclusion of the new \ddot{P} component yields an F -test probability of 8×10^{-4} and 10^{-7} of not being needed (when considering only the *XMM-Newton* datasets or the whole ten pointings in the fit, respectively). Moreover, the new timing solution implies a rms variability of only 55 ms, corresponding to a timing noise level of less than 2 per cent, well within the value range observed in isolated neutron stars. The second period derivative we found is unlikely the result of a change, as a function of time, of the pulse profiles, which are almost sinusoidal and show no evidence for variation (see the right-hand panel of Figure 4.3).

We notice that this analysis is valid under the assumption that the location and geometry of the emitting region remains constant throughout the observations, as suggested by studies of other transient magnetars (see Perna & Gotthelf 2008; Albano et al. 2010).

The accuracy of the timing solution reported in Table 4.2 is not good enough to coherently include the 2015 March *XMM-Newton* data. Correspondingly, we inferred the period for this latest pointing similarly to what reported above finding a best value of $P=3.24528(6)$ s (95 per cent confidence level; epoch 57106.0 MJD). This is less than 2σ away from the expected period extrapolated from the timing solution in Table 4.2. The pulse profile parameters changed significantly with respect to the previous datasets with a pulsed fraction of only 5 ± 1 per cent (1σ) and a more asymmetric shape.

Table 4.2: Timing results for SGR J1935+2154.

Epoch T_0 (MJD)	56926.0
Validity range (MJD)	56853.6 – 56976.4
$P(T_0)$ (s)	3.2450650(1)
$\dot{P}(T_0)$	$1.43(1) \times 10^{-11}$
$\ddot{P}(T_0)$ (s^{-1})	$-3.5(7) \times 10^{-19}$
$\nu(T_0)$ (Hz)	0.30816023(1)
$\dot{\nu}(T_0)$ (Hz s^{-1})	$-1.360(3) \times 10^{-12}$
$\ddot{\nu}(T_0)$ (Hz s^{-2})	$3.3(7) \times 10^{-20}$
rms residual (ms)	55
χ^2_ν (d.o.f.)	0.57 (6)
B_p (Gauss)	2.2×10^{14}
τ_c (yr)	3600
L_{sd} (erg s^{-1})	1.7×10^{34}

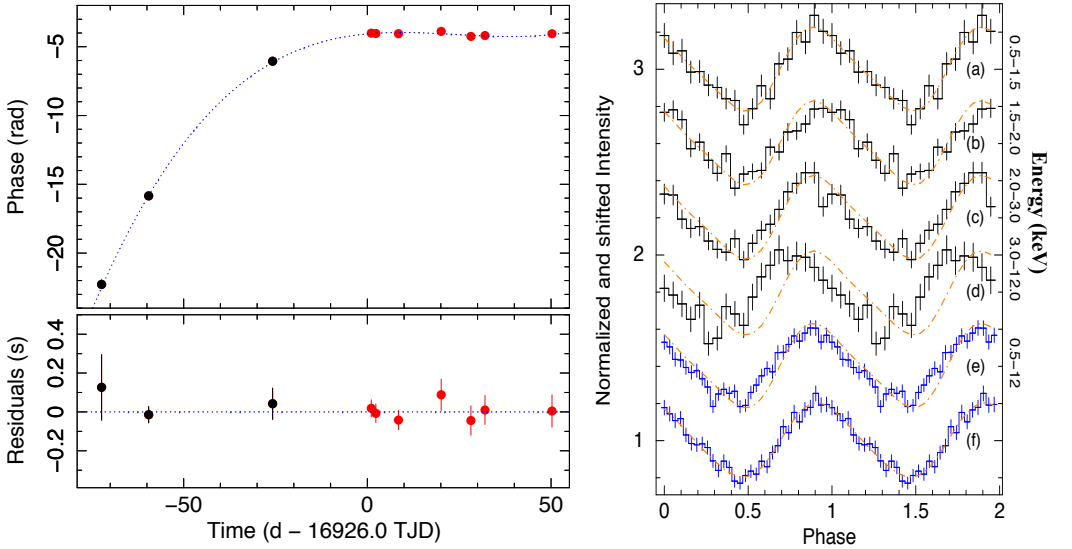


Figure 4.3: *Left-hand panel*: phase evolution of SGR J1935+2154 as a function of time fitted with a linear plus a quadratic plus a cubic components (top) and residuals with respect to our best phase-coherent solution, in units of seconds (bottom). Black and red points mark the *Chandra* and *XMM-Newton* observations, respectively. *Right-hand panel*: *Chandra* plus *XMM-Newton* background-subtracted pulse profiles (arbitrary shifted on the y-axis). From top to bottom they refer to: (a) 0.5-1.5 keV, (b) 1.5-2.0 keV, (c) 2.0-3.0 keV, (d) 3.0-12.0 keV and (e) 0.5-12.0 keV. The dashed orange curve marks the best fit (by assuming a model with two sinusoids) of profile (a): a systematic shift towards smaller phases (advance in time) as a function of energy is evident. Profile (f) has been obtained by aligning profiles from (a) to (d).

4.3.4 Spectral analysis

For the phase-averaged spectral analysis (performed with XSPEC 12.8.2 fitting package; Arnaud 1996) we started by considering all the datasets together. Then, we concentrated on the 2014 July 29 data, being the longest and highest statistics *Chandra* pointing (about 75 ks effective exposure for 8200 photons) and the *XMM-Newton* EPIC pn spectra (effective exposure time of about 105 ks and about 22000 events). A log of the spectral fits is given in Table 4.3. To account for the diffuse component (see Section 4.3.2) we used the regions we described in Section 4.2.1 and 4.2.2 to extract the background spectra of the point-like central source, which we later considered as the diffuse component spectra.

We started by fitting all the 10 spectra of the 2014 observations separately by leaving all the parameters free to vary. The absorption was constrained to be the same among observations. Photons having energies below about 0.8 keV and above 10 keV were ignored, owing to the very few counts from SGR J1935+2154 (energy channels were rebinned in a way of having at least 30 events). All the energy channels consistent with zero after the background subtraction were ignored. The abundances used were those of Wilms et al. (2000). The spectra were not well fitted by any single component model such as a power-law (PL) or black body (BB), which gave a reduced χ^2 in the 1.2 – 1.8 range depending on the adopted single component (282 and 407 degrees of freedom, hereafter d.o.f., for the *Chandra* and *XMM-Newton* spectra, respectively). The canonical two-component model often used to model magnetars spectra, i.e. an absorbed BB plus PL, resulted in a good fit with reduced χ^2 of 0.99 (280 d.o.f.) and 1.03 (405 d.o.f.) for the *Chandra* and *XMM-Newton* spectra, respectively. The inclusion of a further spectral component (the BB in the above procedure) was evaluated to have a formal *F*-test probability corresponding to 4.5σ and 7.0σ (for *Chandra* and *XMM-Newton*, respectively) of being significant.

A flux variation of the order of about 25 per cent was clearly detected between the *Chandra* and *XMM-Newton* 2014 pointings. On the other hand no significant flux variation was detected among the *XMM-Newton* observations. Correspondingly, we combined the seven *XMM-Newton* 2014 spectra together to increase the counting statistics (we used the SAS task EPICSPECCOMBINE). By using the latter spectrum we obtain an *F*-test probability of 7.8σ for the significance of the inclusion of the BB component. In Figure 8.7 we report the *XMM-Newton* combined source spectrum (in black) together with the *Chandra* spectrum of the longest pointing (in red; the two further *Chandra* spectra are not shown for clarity purposes). We note that, within about 1σ uncertainties, the *Chandra* and *XMM-Newton* spectral parameters are consistent with each other with the exception of the flux.

The latest *XMM-Newton* pointing, carried out in 2015 March, was not combined with the previous ones in order to look for spectral variability on long time scales. While the PL plus BB spectral decomposition holds also for this dataset, the flux significantly increased by about 25 per cent reaching a level similar to that of the longest *Chandra* pointing in 2014 July. It is evident from Table 4.3 that the only significantly changed parameter is the flux of the PL component.

Due to the poor statistics of the *Swift* XRT spectra we only inferred the 1–10 keV fluxes by assuming the PL plus BB model obtained by the combined *XMM-Newton* spectrum

and including a scale factor which was free to vary to track the flux variation through the outburst. Figure 4.5 shows all the 1–10 keV absorbed fluxes inferred from the *Swift*, *Chandra* and *XMM–Newton* spectra. It is evident that the source is still variable above a general decay trend.

The same background regions used to correct the EPIC pn source spectra were then assumed as a reliable estimate of the diffuse emission. For the background of the diffuse emission we considered two regions laying far away (at a distance >4 arcmin) from the pulsar and in two different CCDs obtaining similar results in both cases. We first fit all the seven spectra together. The use of one spectral component gave a relatively good fit with a reduced χ^2 of 1.22 and 1.33 (107 d.o.f.) for an absorbed PL and BB model, respectively. Then we left all the parameters free to vary, resulting in a reduced χ^2 of 1.15 and 1.18 (95 d.o.f.) for the PL and BB model, respectively. While no improvement was achieved for the BB model, the PL model appears to vary among *XMM–Newton* observations at about 2.0σ confidence level. Therefore, we conclude that there is no suggestion of variability for the diffuse emission. A combined (from the seven *XMM–Newton* pointings) spectrum for the diffuse emission was obtained, in a way similar to that already described for the source spectrum. The *XMM–Newton* combined spectrum of the diffuse emission and the results of the spectral fitting for the PL model are shown in Figure 4.4 and in Table 4.3. Two facts can be immediately evinced: a simple model is not a good approximation for the diffuse emission and the absorbing column is significantly different from the one we inferred for the magnetar. In particular, we note that the largest values of the residuals originated from few ‘random’ data points rather than by an up-and-down trend (often suggesting a wrong adopted continuum component; see blue points in Figure 8.7). Also for the diffuse emission we kept separated the 2015 *XMM–Newton* observation to look for spectral variations. Unfortunately, the low statistics prevented us to check if changes in the spectral parameters are present. The inferred 1–10 keV absorbed flux is $(1.67^{+0.03}_{-0.05}) \times 10^{-13}$ erg cm $^{-2}$ s $^{-1}$, in agreement with the 2014 value.

4.3.5 Pre-outburst observations

Swift XRT observed SGR J1935+2154 twice before its activation during the *Swift* Galactic plane survey (see Campana et al. 2014). The first observation took place on 2010 December 10 for 514 s (obs ID 00045278001). SGR J1935+2154 is far off-axis (~ 10 arcmin) and we derived a 3σ upper limit of 3.2×10^{-2} counts s $^{-1}$.

The second observation took place on 2011 August 28 for 617 s (obs ID 00045271001). SGR J1935+2154 is detected at a rate $(1.6 \pm 0.6) \times 10^{-2}$ counts s $^{-1}$. Assuming the same spectral model of the *XMM–Newton* observations (see Section 4.3.4 and Table 4.4), we derive a 1–10 keV luminosity of $(9 \pm 4) \times 10^{33}$ erg s $^{-1}$ (including errors in the count rate and assuming a distance of 9 kpc).

The field was also imaged during the *ROSAT* all-sky survey twice, but the high column density prevents any firm upper limit on the absorbed flux.

Table 4.3: *Chandra* and *XMM–Newton* spectral results. Errors are at a 1σ confidence level for a single parameter of interest.

Mission (Model)	N_{H}^a (10^{22} cm^{-2})	Γ	kT (keV)	R_{BB}^b (km)	Flux ^c (10^{-12} cgs)	Luminosity ^c (10^{34} cgs)	χ^2_{ν} (dof)
<i>SOURCE EMISSION</i>							
CXO (BB + PL)	2.0 ± 0.4	2.8 ± 0.8	0.45 ± 0.03	1.9 ± 0.2	1.24 ± 0.06	3.1 ± 0.5	0.97 (165)
XMM (BB + PL)	1.6 ± 0.2	1.8 ± 0.5	0.47 ± 0.02	1.6 ± 0.1	0.89 ± 0.05	1.7 ± 0.4	1.02 (74)
XMM ^d "	1.6 ± 0.2	2.1 ± 0.4	0.48 ± 0.02	1.6 ± 0.2	1.19 ± 0.06	2.4 ± 0.5	0.93 (109)
<i>DIFFUSE EMISSION</i>							
XMM (PL)	3.8 ± 0.4	3.8 ± 0.3	—	—	0.14 ± 0.02	0.6 ± 0.1	1.94 (23)

^a We used the abundances of Wilms, Allen & McCray (2000).

^b The black body radius is calculated at infinity and for an arbitrary distance of 9 kpc.

^c In the 1–10 keV energy band; fluxes are observed values, luminosities are de-absorbed quantities.

^d 2015 March *XMM–Newton* observation.

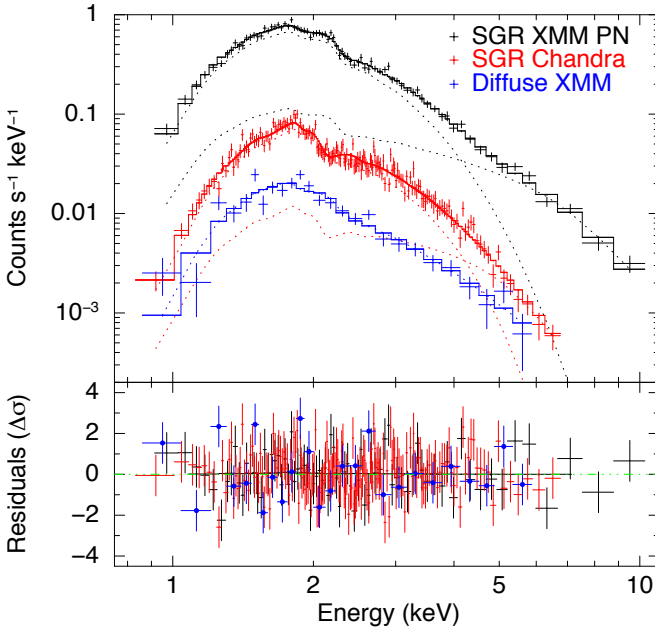


Figure 4.4: Spectra of SGR J1935+2154 and of the diffuse emission around the pulsar. From top to bottom: SGR J1935+2154 cumulative *XMM–Newton* PN spectrum, the SGR J1935+2154 *Chandra* ACIS spectrum of observation 15875 and the cumulative *XMM–Newton* PN spectrum of the diffuse emission (upper plot). Residuals (in σ units) are shown and refer to the absorbed BB+PL model for SGR J1935+2154 and to a PL model for the diffuse component.

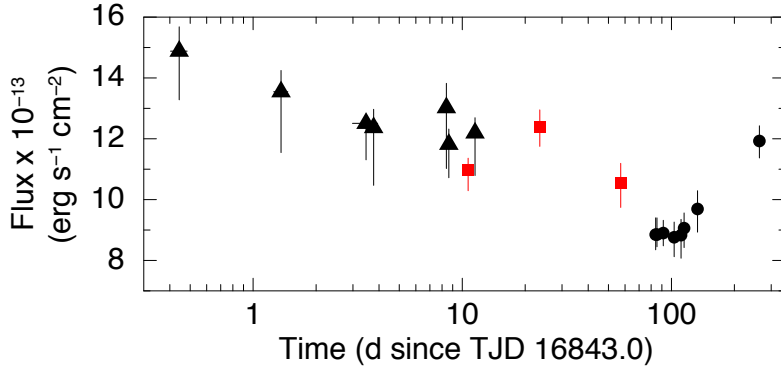


Figure 4.5: Temporal evolution for the absorbed 1–10 keV flux of SGR J1935+2154 obtained by using datasets from *Swift* (black triangles), *Chandra* (red squares) and *XMM–Newton* (black circles). The zero on the x-axis marks the epoch of the *Swift* BAT trigger.

4.4 Radio observations

The first radio follow-up observations of SGR J1935+2154 were carried out on 2014 July 9 and 14 with the Ooty Radio Telescope (ORT) and the Giant Meterwave Radio Telescope (GMRT), at 326.5 and 610.0 MHz, respectively (Surnis et al. 2014). No pulsed radio emission was detected down to a flux of 0.4 mJy and 0.2 mJy at 326.5 and 610.0 MHz (assuming a 10 per cent duty cycle), respectively.

The source was observed with the *Parkes* radio telescope at 10-cm and 20-cm in four epochs between August 1 and 3, shortly after the detection of X-ray pulsations (Israel et al. 2014), and again at 10-cm on September 28, almost simultaneously with one of our *XMM–Newton* observations. Observations at 10-cm were obtained using the ATNF Digital Filterbanks DFB3 (used in search mode with a sampling time of 1 ms) and DFB4 (in folding mode) at a central frequency of 3100 MHz, over 1024 MHz of bandwidth. 20-cm observations were acquired using the reconfigurable digital backend HIPSr (HI-Pulsar signal processor) with a central frequency of 1357 MHz, a 350 MHz bandwidth and a sampling time of 64 μs . Further details of the observations are summarized in Table 4.4.

Data were folded in 120-s long sub-integrations using the ephemeris in Table 4.2 and then searched over a range of periods, spanning ± 1.5 ms with respect to the X-ray value of any given observing epoch, and over dispersion measures (DM) up to 1000 pc cm^{-3} .

The data acquired in search mode were also blindly searched over DMs up to 1000 pc cm^{-3} both for periodic signals and single dedispersed pulses. The 20-cm data were searched in real time using HEIMDALL³, while the 10-cm data were analysed with the package SIGPROC⁴. No pulsed signal with a period similar to that detected in X-rays, nor single dispersed pulses were found down to a signal-to-noise ratio of 8. Table 4.4 lists the upper limits obtained at each epoch and frequency.

³See <http://sourceforge.net/projects/heimdall-astro/> for further details.

⁴See <http://sigproc.sourceforge.net/>

Table 4.4: Radio observations of SGR J1935+2154. The receiver used was either the 10-cm feed of the coaxial 10–50 cm (Granet et al. 2005) or the central beam of the 20-cm multibeam receiver (Staveley-Smith et al. 1996); S_{min} denotes the flux density upper limit for a pulsed signal with a 3.2 s period; S_{min}^{sp} denotes the flux density upper limit for a single pulse of 32 ms duration.

UT Start	Receiver	Exposure (h)	S_{min} (mJy)	S_{min}^{sp} (mJy)
2014 Aug 01 at 11:34	10-50cm	3.0	0.04	68
2014 Aug 02 at 11:22	10-50cm	3.0	0.04	68
2014 Aug 03 at 12:29	20cm-MB	1.5	0.05	61
2014 Aug 03 at 13:32	10-50cm	1.0	0.07	68
2014 Sep 28 at 08:34	10-50cm	2.0	0.05	68

4.5 Discussion

Thanks to an intensive *Chandra* and *XMM–Newton* observational campaign of SGR J1935+2154 covering the first 8 months since the first bursts detected by *Swift* BAT, we were able to infer the main timing and spectral properties of this newly identified member of the magnetar class. In particular, we discovered strong coherent pulsations at a period of about 3.24 s in a *Chandra* long pointing carried out in 2014 July. Subsequently, by using the *XMM–Newton* observations (spaced so as to keep the pulse phase coherence among pointings) we started building a timing solution by means of a phase-fitting technique. We were able to phase-connect all the 2014 *Chandra* and *XMM–Newton* datasets and we inferred both a first and second period derivative. These findings further confirm that SGR J1935+2154 is indeed a magnetar which is slowing-down at a rate of about half a millisecond per year. However, this trend is slowing-down due to a negative \ddot{P} (see Table 4.2). The accurate timing solution allowed us also to infer the dipolar magnetic field strength, an upper limit on the true pulsar age and the corresponding spin-down luminosity (under usual assumptions).

SGR J1935+2154 is a seemingly young object, ≤ 3 kyr, with a B_p value ($\sim 2.2 \times 10^{14}$ Gauss) well within the typical range of magnetars. The X-ray emission is pulsed. The pulse shape is energy independent (within uncertainties) and it is almost sinusoidal with a ~ 20 per cent pulsed fraction (measured as the semi-amplitude of the sinusoid divided by the average count rate) during 2014. It becomes less sinusoidal with a pulsed fraction of only 5 per cent during the latest *XMM–Newton* observation. We detected an energy-dependent phase shift (~ 0.16 cycles at maximum), with the hard photons anticipating the soft ones. This behavior is not very common among known magnetars, 1RXS J1708–4009 being a notable exception (though with a different trend in energy; see Israel et al. 2001; Rea et al. 2005). In 1RXS J1708–4009 the shift is likely associated to the presence of a (spin phase) variable hard X-ray component extending up to at least 100 keV (Kuiper et al. 2006; Götz et al. 2007). Similarly, the pulse profile phase shift of SGR J1935+2154 might

be due to the presence of at least two distinct components (peaks) with different weight at different energies. The non detection of emission from SGR J1935+2154 at energies above 10 keV does not allow us to firmly assess the cause of the shift.

The source spectrum can be well described by the canonical two-component model often applied to magnetars, i.e. an absorbed black body plus a power-law ($kT \sim 0.5$ keV and $\Gamma \sim 2$). The 1–10 keV absorbed flux of SGR J1935+2154 of 1.5×10^{-12} erg cm $^{-2}$ s $^{-1}$ is among the lowest observed so far from magnetars at the beginning of their outbursts. Although it is possible that we missed the outburst onset (which perhaps occurred before the first burst epoch), a backward search of burst activity in the BAT data at the position of SGR J1935+2154 gave negative results (Cummings & Campana 2014). Emission from SGR J1935+2154 is detected in an archival *Swift* XRT pointing in 2011 at a flux only a factor of few lower than that detected soon after the burst emission. At current stage we cannot exclude that the source has not reached the quiescent level or that it has a relatively bright quiescent luminosity. This latter possibility is partially supported by the unusual properties of SGR J1935+2154 which displays both intervals of flux weakening and brightening superimposed to a slow decay. We note that the latest *XMM-Newton* pointing occurred less than 20 days from the *Konus-Wind* detection of the first intermediate flare from this source (Golenetskii et al. 2015).

A significant diffuse emission, extending from >1 arcsec up to more than 1 arcmin around the magnetar, was clearly detected both by *Chandra* and *XMM-Newton*. Because of the use of different instruments/modes at different epochs we were not able to test if the diffuse component varied in time (as expected in the case of scattering by dust clouds on the line-of-sight) between the *Chandra* and *XMM-Newton* pointings. The component does not change significantly among the *XMM-Newton* pointings. The *Chandra* data allowed us to sample the spatial distribution of the component only up to about 20 arcsec (at larger radii we are hampered by the statistics), while the lower spatial resolution of the *XMM-Newton* pn allowed us to detect the diffuse emission only beyond about 20 arcsec. We do not detect any flux variation for the diffuse emission among the eight *XMM-Newton* pointings despite the pulsar enhancement of about 20 per cent between 2014 October and 2015 March, a result which would favour a magnetar wind nebula (MWN) interpretation. The PL model used to fit the pn spectra implies a relatively steep photon index of about 3.8 which is similar to what observed for the candidate MWN around Swift J1834–0846 (Younes et al. 2012), but at the same time is steeper than the PL photon index of SGR J1935+2154 suggesting that the dust scattering scenario might be more likely.

For Swift J1834–0846 two diffuse components have been identified: a symmetric component extending up to about 50 arcsec, interpreted as a dust scattering halo (Younes et al. 2012; Esposito et al. 2013), and an asymmetric component extending up to 150 arcsec proposed as a wind nebula (Younes et al. 2012). The spectrum of the former component has a PL photon index steeper than that of the magnetar (which however, at variance with SGR J1935+2154, is well fitted by a single PL alone likely due to a very high absorption which hampers the detection of any soft BB), while the latter has a flatter spec-

trum. To compare the properties of the diffuse emission around Swift J1834–0846 and SGR J1935+2154, we fitted the *Chandra* and *XMM–Newton* spectra of SGR J1935+2154 with a PL alone obtaining a photon index of 4.4 ± 0.1 and 4.3 ± 0.1 (we used only photons in the 1.5–8.0 keV band similarly to the case of Swift J1834–0846) implying that the diffuse component might have a spectrum flatter than that of the magnetar and favoring the wind nebula scenario. In the latter case the efficiency at which the rotational energy loss of a pulsar, \dot{E}_{rot} , is radiated by the PWN is given by $\eta_X = L_{X,\text{pwn}}/\dot{E}_{\text{rot}} = (0.6 \times 10^{34}/1.7 \times 10^{34}) \simeq 0.35$, not that different from what inferred from similar components around Swift J1834–0846 and RRAT J1819–1458 (Rea et al. 2009; Younes et al. 2012). Further *XMM–Newton* and/or *Chandra* observations taken at flux levels significantly different from those we recorded so far should help in settling the nature of the diffuse emission.

A search for radio pulsed emission from SGR J1935+2154 gave negative result down to a flux density of about 0.5 mJy (and 70 mJy for a single pulse). It has been suggested that whether or not a magnetar can also shine as a transient radio pulsar might depend on the ratio between its quiescent X-ray luminosity and spin-down luminosity, given that all magnetars with detected radio pulsed emission have this ratio smaller than ~ 0.3 (Rea et al. 2012), at variance with typical radio-quiet magnetars that have quiescent X-ray luminosity normally exceeding their rotational power. Based on the coherent timing solution we inferred a spin-down luminosity of about $2 \times 10^{34} \text{ erg s}^{-1}$. At the present stage it is also rather difficult to obtain a reliable value for the quiescent luminosity due to the uncertainties on the distance and the flux of the *Swift* pre-burst detection. If a distance of 9 kpc is assumed, the *Swift* faintest flux converts to a luminosity of about $5 \times 10^{33} \text{ erg s}^{-1}$, which results in $L_X/L_{sd} \sim 0.25$, close to the 0.3 limiting value. However, if the distance is larger and/or the quiescent flux is a factor of few larger than that estimated from *Swift*, the source would move toward higher values of $L_{X,\text{qui}}/L_{sd}$ in the ‘radio-quiet’ region of the fundamental plane (see left panel of Figure 2 in Rea et al. 2012). Correspondingly, the non detection of radio pulsations might be not that surprising.

The uncertainty in the quiescent level of this new magnetar makes any attempt to infer its evolutionary history rather uncertain. Given the short characteristic age (a few kyrs, which is most probably representative of the true age given that no substantial field decay is expected over such a time span), the present value of the magnetic field is likely not that different from that at the moment of birth. The above reviewed timing characteristics would then be consistent with a quiescent bolometric luminosity of the order of $\sim 5 \times 10^{33-34} \text{ erg s}^{-1}$ (see Figures 11 and 12 in Viganò et al. 2013), depending on the assumed magnetic field geometry and envelope composition.

Constraints on its outburst luminosity evolution can be put from general considerations (see Pons & Rea 2012; Viganò et al. 2013). If we assume that the flux derived by the pre-outburst *Swift* observations provides a correct estimate of the magnetar quiescence, and we rely on a distance of 9 kpc, then the source luminosity increases from a quiescent level of $L_{X,\text{qui}} \sim 7 \times 10^{33} \text{ erg s}^{-1}$ to a ‘detected’ outburst peak of $L_{X,\text{out}} \sim 4 \times 10^{34} \text{ erg s}^{-1}$. Such luminosity variation within the outburst (about a factor of 5) is rather small for a magnetar

with a medium-low quiescent level (see Figure 2 of Pons & Rea 2012). In particular, the outburst peak luminosity usually reaches about $L_{X,out} \sim 5 \times 10^{35} \text{ erg s}^{-1}$, due to the typical energies released in magnetars' crustal fractures (about 10^{44-45} erg ; Pons & Rea 2012; Perna & Pons 2011), coupled with estimates of the neutrino cooling efficiencies (Pons & Rea 2012). If there are no intrinsic physical differences between this outburst and other magnetar outbursts (see Rea & Esposito 2011), then we can foresee two possibilities to explain the relatively low maximum luminosity detected.

The first possibility is that we have missed the real outburst peak of SGR J1935+2154, which was then caught already during its outburst decay. In this case the quiescent luminosity claimed by the archival *Swift* observation might be correct, and the magnetar had a flux increase during the outburst, but we could catch it only thanks to an SGR-like burst detected when the magnetar had already cooled down substantially. Given the typical outburst cooling curves, we can roughly estimate that in this scenario we observed the source about 10-40 days after its real outburst onset.

The second possibility is that the source distance is farther than the assumed SNR distance of 9 kpc (note that the method used by Pavlovic et al. (2013) to infer this distance implies a relatively large degree of uncertainty, even a factor of two in both directions). To have an outburst peak luminosity in line with other magnetars, SGR J1935+2154 should have a distance of $\sim 20-30 \text{ kpc}$. At this distance the assumed *Swift* quiescent level would also be larger ($\sim 7 \times 10^{34} \text{ erg s}^{-1}$), hence a factor of ~ 5 in increase in luminosity in the outburst would then be in line with what observed (and predicted) in other cases (see again Figure 2 of Pons & Rea 2012). However, in the direction of SGR J1935+2154, the Galaxy extends until $\sim 14 \text{ kpc}$ (Hou et al. 2009), making such a large distance rather unlikely.

We then suggest that the very low peak flux of the outburst of SGR J1935+2154 has no different physics involved with respect to other magnetar outbursts, but we have simply missed the onset of the outburst. If the flux detected by *Swift* before the outburst was its quiescent level, we envisage that the outburst onset occurred about a month before the first X-ray burst detection. If future observations will set the source at a lower quiescent level, the outburst peak should have occurred even longer before we first detected its activity.

The variable spin-down rate of magnetar XTE J1810–197

Pintore F., Bernardini F., Mereghetti S., Esposito P., Turolla R., Rea N., Coti Zelati F.,¹
Israel G. L., Tiengo A., Zane S. (2016),
The variable spin-down rate of the transient magnetar XTE J1810–197,
Published in Monthly Notices of the Royal Astronomical Society,
Volume 458, Issue 2, pp. 2088–2093

We have analyzed *XMM–Newton* and *Chandra* observations of magnetar XTE J1810–197 spanning more than 11 years, from the initial phases of the outburst in 2003 to the current quiescent level. We investigated the evolution of the pulsar spin period and we found evidence for two distinct regimes: during the outburst decay, $\dot{\nu}$ was highly variable in the range $-(2 - 4.5) \times 10^{-13} \text{ Hz s}^{-1}$, while during quiescence the spin-down rate was more stable at an average value of $-1 \times 10^{-13} \text{ Hz s}^{-1}$. Only during ~ 3000 days (from MJD 54165 to MJD 56908) in the quiescent stage it was possible to find a phase-connected timing solution, with $\dot{\nu} = -4.9 \times 10^{-14} \text{ Hz s}^{-1}$, and a positive second frequency derivative, $\ddot{\nu} = 1.8 \times 10^{-22} \text{ Hz s}^{-2}$. These results are in agreement with the behavior expected if the outburst of XTE J1810–197 was due to a magnetospheric twist.

¹Author contribution: I reduced and analysed all *Chandra* and *XMM–Newton* data, and performed the spectral analysis to estimate spectral parameters and fluxes.

5.1 Introduction

XTE J1810–197 was discovered with the *RXTE* as a 5.45-s X-ray pulsar (Ibrahim et al. 2004) during a bright outburst in 2003, and associated to a previously known but unclassified *ROSAT* source. Further multiwavelength observations (Rea et al. 2004; Woods et al. 2005; Halpern et al. 2008), led to classify XTE J1810–197 as a magnetar candidate.

XTE J1810–197 likely spent at least 23 years in quiescence (at a flux of $\sim 7 \times 10^{-13}$ erg cm $^{-2}$ s $^{-1}$ in the 0.5–10 keV energy band) before entering in outburst, in the 2003, when the flux increased by a factor of ~ 100 (Gotthelf et al. 2004). For an estimated distance of 3.5 kpc (Camilo et al. 2006; Minter et al. 2008), the maximum observed luminosity was $\sim 10^{35}$ erg s $^{-1}$, but XTE J1810–197 might have reached an even higher luminosity, since the initial part of the outburst was missed. XTE J1810–197 was also the first magnetar from which pulsed radio emission was detected (Camilo et al. 2006, 2007). A large, unsteady spin-down of $\dot{P} \sim 10^{-11}$ s s $^{-1}$ was measured during the outburst decay through radio and X-ray observations, which suggested that the surface dipolar magnetic field is $\sim 2 \times 10^{14}$ G (Gotthelf et al. 2004; Ibrahim et al. 2004; Camilo et al. 2006).

The spectrum of XTE J1810–197 during the outburst has been modeled by several authors with two or three black body components of different temperature. The colder one has been interpreted as the (persistent) emission from the whole neutron star surface, while the hotter ones have been associated to cooling regions responsible for the outburst (Gotthelf et al. 2004; Bernardini et al. 2009, 2011; Alford & Halpern 2016). The appearance of hot spots could be due to the release of (magnetic) energy deep in the crust, or to Ohmic dissipation of back-flowing currents as they hit the star surface (Perna & Gotthelf 2008; Albano et al. 2010; Beloborodov 2009; Pons & Rea 2012). The X-ray pulse profile was energy-dependent and time-variable in amplitude, and it could be generally modelled by a single sinusoidal function (e.g. Ibrahim et al. 2004; Camilo et al. 2007; Bernardini et al. 2009, 2011; Alford & Halpern 2016).

Here we report on the pulse period evolution of XTE J1810–197 exploiting the full set of *XMM–Newton* and *Chandra* X-ray observations carried out in the years 2003–2014 during the outburst decay and in the following quiescent period.

5.2 Observations and data reduction

We made use of 24 *XMM–Newton* and 14 *Chandra* observations of XTE J1810–197 totaling an exposure time of ~ 830 ks (see the log of observations in Table 5.1).

The *XMM–Newton* data were reduced using SAS v. 14.0.0 and the most recent calibration files. We used the data obtained with the EPIC instrument, which consists of one pn camera and two MOS cameras. For each observation, we selected events with single and double pixel events ($\text{PATTERN} \leq 4$) for EPIC-pn and single, double, triple and quadruple pixel events ($\text{PATTERN} \leq 12$) for EPIC-MOS. We set ‘FLAG=0’ so to exclude bad pixels and events coming from the CCD edge. The source and background events were extracted from circular regions of radius 30 arcsec and 60 arcsec, respectively. Time intervals with

Table 5.1: Log of the *XMM–Newton* and *Chandra* observations. The quoted epoch refers to the mean time of the observation.

Obs. No.	Satellite	Obs. ID	Epoch MJD	Duration (ks)
1	<i>Chandra</i>	4454	52 878.9386632	4.3
2	<i>XMM–Newton</i>	0161360301	52 890.5595740	9.5
3	<i>XMM–Newton</i>	0161360401	52 890.7083079	2.1
4	<i>XMM–Newton</i>	0152833201	52 924.1677914	7.0
5	<i>Chandra</i>	5240	52 944.6289075	5.4
6	<i>XMM–Newton</i>	0161360501	53 075.4952632	17.2
7	<i>XMM–Newton</i>	0164560601	53 266.4995129	26.7
8	<i>XMM–Newton</i>	0301270501	53 447.9973027	40.0
9	<i>XMM–Newton</i>	0301270401	53 633.4453382	40.0
10	<i>XMM–Newton</i>	0301270301	53 806.7899360	41.8
11	<i>Chandra</i>	6660	53 988.8111877	31.8
12	<i>XMM–Newton</i>	0406800601	54 002.0627203	48.1
13	<i>XMM–Newton</i>	0406800701	54 165.7713547	60.2
14	<i>XMM–Newton</i>	0504650201	54 359.0627456	72.7
15	<i>Chandra</i>	7594	54 543.0034395	31.5
16	<i>XMM–Newton</i>	0552800301	54 895.5656089	4.3
17	<i>XMM–Newton</i>	0552800201	54 895.6543341	63.6
18	<i>XMM–Newton</i>	0605990201	55 079.6256771	19.4
19	<i>XMM–Newton</i>	0605990301	55 081.5548494	17.7
20	<i>XMM–Newton</i>	0605990401	55 097.7062563	12.0
21	<i>Chandra</i>	11102	55 136.6570779	26.5
22	<i>Chandra</i>	12105	55 242.6870526	15.1
23	<i>Chandra</i>	11103	55 244.7426533	14.6
24	<i>XMM–Newton</i>	0605990501	55 295.1863453	7.7
25	<i>Chandra</i>	12221	55 354.1368700	11.5
26	<i>XMM–Newton</i>	0605990601	55 444.6796630	9.1
27	<i>Chandra</i>	13149	55 494.1643981	16.8
28	<i>Chandra</i>	13217	55 600.9885520	16.2
29	<i>XMM–Newton</i>	0671060101	55 654.0878884	17.4
30	<i>XMM–Newton</i>	0671060201	55 813.3872852	13.7
31	<i>Chandra</i>	13746	55 976.3735837	22.5
32	<i>Chandra</i>	13747	56 071.3650797	22.1
33	<i>XMM–Newton</i>	0691070301	56 176.9826811	15.7
34	<i>XMM–Newton</i>	0691070401	56 354.1968379	15.7
35	<i>XMM–Newton</i>	0720780201	56 540.8584298	21.2
36	<i>Chandra</i>	15870	56 717.3097928	22.1
37	<i>XMM–Newton</i>	0720780301	56 720.9705351	22.7
38	<i>Chandra</i>	15871	56 907.9508362	21.7

high particle background were removed.

In three observations (7, 13 and 35) we found inconsistent values between the phases of the pulses derived (as described in the next Section) from the MOS and pn data. This is due to a known sporadic problem in the timing of EPIC-pn data, causing a shift of ± 1 second in the times attributed to the counts. We identified the times at which the problems occurred and corrected the data by adding (or subtracting) 1 second to the photon time of arrival from the instant when the problem occurred (see Martin-Carrillo et al. 2012).

The *Chandra* observations were reduced using the CIAO v.4.7 software and adopting the standard procedures. Source events were extracted from a region of 2 arcsec radius around the position of XTE J1810–197 and background counts from a similar region close to the source.

Photon arrival times of both satellites were converted to the Solar system barycenter using the milliarcsec radio position of XTE J1810–197 (RA = 272.462875 deg, Dec. = –19.731092 deg, (J2000); Helfand et al. 2007)) and the JPL planetary ephemerides DE 405.

5.3 Timing analysis

In order to study the evolution of the spin frequency from outburst to quiescence (i.e. covering the whole data set) we initially measured the spin frequency in each individual pointing by applying a phase-fitting technique in every observation. The phase of a pulse is defined as $\phi = \phi_0 + \int \nu dt$, where ν is the spin frequency. If the coherence of the signal is maintained between subsequent observations, the data can be fitted by the polynomial:

$$\phi(t) = \phi_0 + \nu_0(t - T_0) + \frac{1}{2}\dot{\nu}(t - T_0)^2 + \frac{1}{6}\ddot{\nu}(t - T_0)^3 + \dots \quad (5.1)$$

where T_0 is the reference epoch, ν_0 is the frequency at T_0 , $\dot{\nu}$ is the spin frequency derivative and $\ddot{\nu}$ is the second-order spin frequency derivative (see e.g. Dall’Osso et al. 2003).

Thanks to the large counting statistics of each single observation, it was possible to obtain accurate measurements of the frequencies by applying the phase-fitting technique to a number of short time intervals (durations from 300 s to 5 ks, depending on the counting statistics) within each observation and we were able to align the pulse-phases by use only the linear term of Eq. 5.1. The frequencies derived in this way and the absorbed 0.3–10 keV flux of XTE J1810–197 are plotted as a function of time in Figure 5.1.

To derive the fluxes plotted in Figure 5.1, we fitted the time-averaged spectrum of each observation with a model consisting of two to three blackbodies (see e.g. Bernardini et al. 2009; Alford & Halpern 2016 for more details). The interstellar absorption was kept fixed to the value of $5.7 \times 10^{21} \text{ cm}^{-2}$, derived from the spectrum of the first *XMM-Newton* observation. The temperatures that we found for the three blackbodies ($\sim 0.1, 0.3$ and 0.5 keV) are consistent with those reported in Bernardini et al. 2009 and Alford & Halpern 2016, to which we refer for more details. The maximum flux observed by *XMM-Newton* during the outburst was $(3.18 \pm 0.04) \times 10^{-11} \text{ erg cm}^{-2} \text{ s}^{-1}$ (absorbed and in

Table 5.2: Best-fitting timing solutions for 13 (solution 1) and 15 (solution 2) *XMM-Newton* and *Chandra* observations. T_0 indicates the reference epoch. Errors are at 1σ .

Parameter	Solution 1	Solution 2
Time range (MJD)	55079–55814	55079–56071
T_0 (MJD)	55444.0	55444.0
ν_0 (Hz)	0.18048121335(44)	0.18048121599(27)
$\dot{\nu}$ (Hz s $^{-1}$)	$-9.2059(16) \times 10^{-14}$	$-9.2085(16) \times 10^{-14}$
$\ddot{\nu}$ (Hz s $^{-2}$)	$5.7(3) \times 10^{-23}$	$3.80(13) \times 10^{-23}$
P (s)	5.540742892(14)	5.540742811(8)
\dot{P} (s s $^{-1}$)	$2.8262(5) \times 10^{-12}$	$2.8270(5) \times 10^{-12}$
\ddot{P} (s s $^{-2}$)	$-1.75(9) \times 10^{-21}$	$-1.16(4) \times 10^{-21}$
χ^2_ν (dof)	0.9 (9)	5.0 (11)

the 0.3–10 keV energy range). The flux decreased until about MJD 54500, after which it remained rather constant (see also Gotthelf & Halpern 2007; Bernardini et al. 2011; Alford & Halpern 2016). We found that the flux slowly decreased, finally reaching a constant value of $(7.5 \pm 0.2) \times 10^{-13}$ erg cm $^{-2}$ s $^{-1}$ (absorbed and in the 0.3–10 keV band), which we derived by fitting with a constant the fluxes of all the observations after MJD 54500 (see Fig. 5.1). This value is within the range of fluxes measured by *ROSAT*, *ASCA* and *Einstein* before the onset of the outburst ($(5 - 10) \times 10^{-13}$ erg cm $^{-2}$ s $^{-1}$; Gotthelf et al. 2004).

It is clear from Fig. 5.1 that the source timing properties tracked remarkably well the evolution of the flux. The average spin-down rate was larger during the first 3–4 years, during the outburst decay, and then it decreased while the source was in (or close to) quiescence. We can distinguish two time intervals, separated at MJD ~ 54000 , in which a linear fit can approximately describe the frequency evolution. The slopes of the two linear functions are $(-3.9 \pm 0.2) \times 10^{-13}$ Hz s $^{-1}$ ($\chi^2_\nu/dof = 6.7/9$) and $(-1.00 \pm 0.05) \times 10^{-13}$ Hz s $^{-1}$ ($\chi^2_\nu/dof = 1.8/24$) before and after MJD 54000, respectively. These values represent the long-term averaged spin-down rates, but the residuals of the linear fits indicate that the time evolution of the frequency derivative is more complex. To better investigate this behavior, we performed several linear fits to small groups of consecutive frequency measurements. We adopted a moving-window approach by using partially overlapping sets of points. In this way we obtained the $\dot{\nu}$ values plotted in Figure 5.1. They show a highly variable spin-down rate, especially during the outburst decay, when it ranged from -4.5×10^{-13} Hz s $^{-1}$ to -0.5×10^{-13} Hz s $^{-1}$.

Phase-coherent timing solutions for XTE J1810–197 have been reported for the initial part of the outburst (Ibrahim et al. 2004; Camilo et al. 2007). We tried to phase-connect all the *XMM-Newton* and *Chandra* observations, but this turned out to be rather difficult due to the large timing noise. However, we were able to find a phase-connected solution for the observations from 18 to 31 (i.e., those performed from MJD 55079 to MJD 55814),

as follows. For each observation, we folded the EPIC (pn plus MOS) or *Chandra* data at a frequency of 0.18048 Hz (corresponding to $P = 5.54078$ s, the average spin period after MJD 54100). For each observation the phase of the pulsation was then derived by fitting a constant plus a sinusoid to the folded pulse profile in the 0.3–10 keV energy range. We initially aligned, with only the linear term in Eq. 5.1, the *XMM–Newton* observations 18 and 19 that were the most closely spaced (~ 2 days). Then, we included one by one the other observations, as the uncertainty on the best-fitting parameters became increasingly smaller allowing us to connect more distant points. We included higher order derivatives only if the improvement in the fit was significant in the timing solution. After the inclusion of *Chandra* observations 21 and 22, the quadratic term became statistically significant, while the third order polynomial term was needed after the inclusion of observations 25 and 26. The best fitting parameters of the final solution are reported in Table 5.2 and the fit is shown in Figure 5.1. The fit with ν , $\dot{\nu}$ and $\ddot{\nu}$ gives a good description of the data ($\chi^2_{\nu}=0.9$ for 9 dof: solution 1 in Table 5.2 and Figure 5.1). The inclusion of the two observations at MJD 55976 and MJD 56071 (observations 31 and 32) yields best fitting parameters (solution 2 in Table 5.2 and Figure 5.1) consistent with those obtained by Camilo et al. (2016) for the same set of observations, but with a higher χ^2_{ν} with respect to solution 1.

Some timing irregularity occurred also when the source was in quiescence. In particular, around MJD ~ 55400 , the spin-down rate was much larger than the quiescent average value and larger than that seen during the outburst decay. Quite remarkably, also a spin-up episode was detected. This is better illustrated in Figure 5.1 which shows the frequency measurements around this time. Unfortunately, the sparse coverage and the large error bars of some points do not allow us to establish whether this was a sudden event, like an anti-glitch, or simply due to an increased timing noise episode. Assuming that the time irregularity is an anti-glitch, we fitted the data in the time range MJD 54300–57000 with the following simple model:

$$\begin{aligned} \nu(t) &= \nu_0 + \dot{\nu}_0 \cdot t & \text{for } t < t_g \\ \nu(t) &= \nu_0 + \dot{\nu}_0 \cdot t + \Delta\nu \cdot e^{-(t-t_g)/\tau} & \text{for } t > t_g \end{aligned}$$

where τ is the decay time and t_g is the time of the glitch, which we kept fixed in the fit. If the glitch occurred immediately after observation 25 ($t_g = 55354$), we obtained a good fit ($\chi^2_{\nu} = 1.14$ for 21 dof, shown by the solid line in Figure 5.1) with $\Delta\nu = (6.5 \pm 5.8) \times 10^{-5}$ Hz, $\tau = 51 \pm 21$ days, $\nu_0 = 0.18093(3)$ Hz and $\dot{\nu}_0 = -9.4(3) \times 10^{-14}$ Hz s $^{-1}$. If instead the glitch occurred at observation 26 ($t_g = 55444$), we obtain $\Delta\nu < 1 \times 10^{-4}$ Hz and $\tau < 200$ days (3σ upper limits).

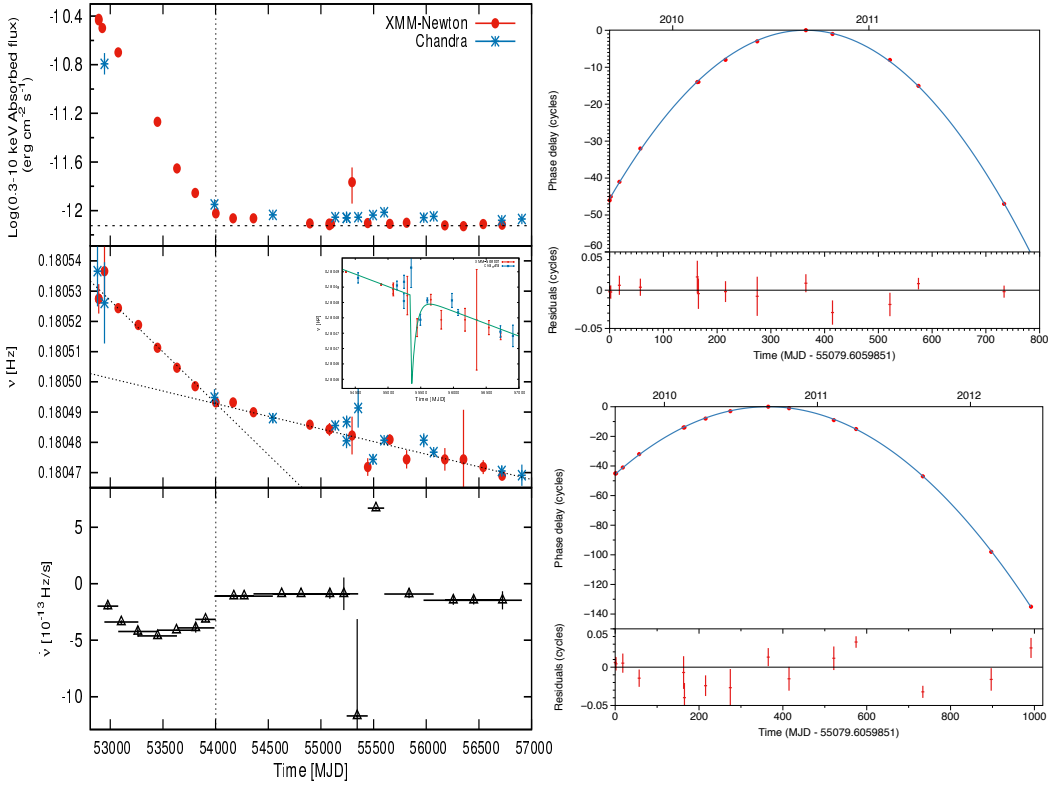


Figure 5.1: *Left-hand panel*: evolution of the logarithmic absorbed flux in the 0.3–10 keV energy range (top). The dashed line is the linear fit to the data after MJD 54500. The errors are at 90 per cent confidence level; spin frequency of XTE J1810–197 along the outburst as found in the single observations (centre). The dashed lines indicate the fits with two linear functions to the data before and after MJD 54000. The inset shows the frequencies measured around the time of the possible anti-glitch with the solid line representing the best-fit discussed in the text; frequency derivatives as measured by linear fits of small subset of observations (bottom). The horizontal error bars indicate the time interval spanned by the observations used in each fit. The vertical, dashed line indicates the epoch after which is possible to phase-connect the data. Errors in the central and bottom panels are at 1σ . *Right-hand panel*: phase-connection of ~ 800 (top) and ~ 1000 (bottom) days of *XMM-Newton* and *Chandra* data using a third order polynomial function. Top panels: the red points are the measured phases, one for each observation, and the solid line is the best fit model; bottom panels: residuals with respect to the best-fitting model.

5.4 Discussion

Variations in the spin-down rate are not uncommon in magnetars and have been observed both in transient and persistent sources. They are believed to originate from changes in the magnetosphere geometry and particles outflow which produce a varying torque on the neutron star. Since also the emission properties from magnetars depend on the evolution of their dynamic magnetospheres, some correlation between spin-period evolution and radiative properties is not surprising.

The most striking examples, among persistent magnetars, are given by SGR 1806–20 and 1E 1048.1–5937. The average spin-down rate of SGR 1806–20, as well as its spectral hardness, increased in the ~ 4 yr of enhanced bursting activity which led to the giant flare of 2004 December (Mereghetti et al. 2005). However, a further increase (by a factor of 2–3) of the long term spin-down rate occurred both in 2006 and 2008, while the flux and bursting rate showed no remarkable changes (Younes et al. 2015). In 1E 1048.1–5937 significant enhancements of the spin-down rate, which then subsided through repeated oscillations, have been observed to lag the occurrence of X-ray outbursts (Archibald et al. 2015). Other persistent magnetars, for which phase-coherent timing solutions extending over several years could be maintained, showed $\dot{\nu}$ variations and/or glitches, sometimes related to changes in the source flux and the emission of bursts (e.g., Dib & Kaspi 2014).

Transient magnetars offer the best opportunity to investigate the correlations between the variations in the spin-down rate and the radiative properties. However, the observations of transient magnetars carried out up to now have shown a variety of different behaviors. Furthermore, for many of them, no detailed information is available on the spin-down during the quiescent state, that instead we now have found in this work for XTE J1810–197. No firm conclusion on the evolution of the spin-down rate could be derived from the two outbursts of CXOU J1647–4552, for which a positive $\dot{\nu}$ was reported only during the decay of the first outburst, while the insufficient time coverage prevented such a measure for the second one (Rodríguez Castillo et al. 2014). A positive $\dot{\nu}$ was reported for both Swift J1822.3–1606 (which went in outburst in 2011 July and was subsequently monitored for about 500 days; Rodríguez Castillo et al. 2015), as well as for SGR J1935+2154 (outburst in 2014 July, time coverage ~ 260 days; Israel et al. 2016), and, tentatively, also for SGR 0501+4516 (for this source observations actually covered part of the quiescent state but phase connection along the entire dataset could not be ensured; Camero et al. 2014). On the other hand, an increase of the spin-down rate during the outburst decay was reported for SGR 1745–2900 (Kaspi et al. 2014; Coti Zelati et al. 2015).

Our analysis of *XMM-Newton* and *Chandra* data spanning 11 years has shown that in XTE J1810–197 the spin frequency evolution tracked remarkably well the luminosity state. During the outburst decay, the average spin-down rate was $(-3.9 \pm 0.2) \times 10^{-13} \text{ Hz s}^{-1}$, but large variations around this value were seen (see also Halpern & Gotthelf 2005; Camilo et al. 2007; Bernardini et al. 2009). During the long quiescent state after the end of the outburst, the average spin-down rate was a factor of ~ 4 smaller. Although some timing noise was still present, the variations in $\dot{\nu}$ were smaller in the quies-

cent state, except for a few months in summer 2010. The timing irregularities in that period might have been caused by the occurrence of an anti-glitch, similar to that seen in the persistent magnetar 1E 2259+586 (Archibald et al. 2013). We found that the pulse-shape in the 0.3–10 keV energy range was nearly sinusoidal and the pulse fraction decreased along the outburst decay, as already reported by e.g. Perna & Gotthelf (2008), Bernardini et al. (2009) and Albano et al. (2010). We note that the pulse-shape remained nearly sinusoidal also during quiescence (see also Bernardini et al. 2011; Alford & Halpern 2016).

The spectral properties of magnetars are commonly explained in terms of the twisted magnetosphere model (Thompson, Lyutikov & Kulkarni 2002), according to which part of the magnetic helicity is transferred from the internal to the external magnetic field, which acquires a non-vanishing toroidal component (a twist). The currents required to support the twisted external field resonantly up-scatter thermal photons emitted by the star surface, leading to the formation of the power-law tails observed up to hundreds of keV. Since twisted fields have a weaker dependence on the radial distance with respect to a dipole, the higher magnetic field at the light cylinder radius results in an enhanced spin-down rate. The increased activity of magnetars is often associated to the development (or an increase) of a twist, which leads to higher fluxes, local surface temperature increases, harder spectra and larger spin-down rates. However, this holds for globally twisted fields (meaning that the twist affects the entire external field). The transport of helicity from the interior is mediated by the star crust: the crust must yield, allowing a displacement of the field lines. Crustal displacements are small compared to the star radius, so the twist is most likely localized to a bundle of field lines anchored on the displaced platelet (Beloborodov 2009). Once implanted, the twist must necessarily decay to maintain its own supporting currents, unless energy is constantly supplied from the star interior. The sudden appearance of a localized twist and its subsequent decay can explain some of the observed properties of transient magnetars (Beloborodov 2009; Albano et al. 2010), including the fact that their spectra are often thermal, as in the case of XTE J1810–197, since resonant Compton scattering may be not very effective, although the mechanism responsible for the heating of the star surface is still unclear (either Ohmic dissipation by backflowing currents or deep crustal heating; Beloborodov 2009; Pons & Rea 2012). If strong enough, a localized twist can still influence the spin-down rate, which is expected to increase first and then decrease as the magnetosphere untwists, as we observed in XTE J1810–197.

5.5 Conclusions

XTE J1810–197 was the first transient magnetar to be discovered and it is probably one of the best studied. We were able to trace in detail its spectral properties over the long (~ 3 years) outburst decay and to monitor it during quiescence for several years afterwards. By investigating the evolution of its spin frequency with all the available *XMM-Newton* and *Chandra* data, we found evidence for two distinct regimes: during the outburst decay, $\dot{\nu}$ was highly variable in the range $-(2 - 4.5) \times 10^{-13} \text{ Hz s}^{-1}$, while during quiescence the spin-down rate was more stable and had an average value smaller by a factor ~ 4 .

This evolution of the spin-down rate is in agreement with the suggestion that the outburst of magnetars may be caused by a strong twist of a localized bundle of magnetic field lines (Beloborodov 2009). Evidences for an evolution of $\dot{\nu}$ in other transient magnetars are far less conclusive, possibly reflecting the fact that, if the twist is not very strong, or the twisted bundle too localized, the effects on the spin-down rate are smaller. A detailed calculation of the spin-down torque for a spatially-limited twisted field requires a full non-linear approach and has not been presented yet. Beloborodov (2009) discussed a simple estimate, valid for small twists ($\psi < 1$ rad):

$$\Delta\mu/\mu \sim (\psi^2/4\pi) \log(u_*/u_{LC}), \quad (5.2)$$

where $\Delta\mu$ is the “equivalent” increase in the dipole moment produced by the twist and u is the area of the j -bundle, evaluated at the star surface (u_*) and at the light cylinder (u_{LC}). Since $\Delta\dot{\nu}/\dot{\nu} \sim 2\Delta\mu/\mu$, the observed fractional variation of $\dot{\nu}$ of a factor of ~ 4 (see Figure 5.1) cannot be achieved with a small twist, $\psi < 1$ rad. This indicates that the (maximal) twist in XTE J1810–197 was most probably larger, $\psi \gtrsim 1$ rad, so that Equation (5.2) does not hold anymore. A quite large value of the twist in the outburst of XTE J1810–197 was also inferred by Beloborodov (2009), on the (qualitative) basis that only a strong twist can produce a change of the spin-down rate.

Discovery of a strongly phase-variable spectral feature in the isolated neutron star RX J0720.4–3125

Borghese A., Rea N., Coti Zelati F.,¹ Tiengo A., Turolla R. (2015),

**Discovery of a strongly phase-variable spectral feature
in the isolated neutron star RX J0720.4–3125,**

Published in The Astrophysical Journal Letters, Volume 807, Issue 1, pp. 20–24

We present the discovery of a strongly phase-variable absorption feature in the X-ray spectrum of the nearby, thermally-emitting, isolated neutron star RX J0720.4–3125. The absorption line was detected performing detailed phase-resolved spectroscopy in 20 *XMM-Newton* observations, covering the period 2000 May – 2012 September. The feature has an energy of ~ 750 eV, an equivalent width of ~ 30 eV, and it is significantly detected for only ~ 20 per cent of the pulsar rotation. The absorption feature appears to be stable over the timespan covered by the observations. Given its strong dependence on the pulsar rotational phase and its narrow width, a plausible interpretation is in terms of resonant proton cyclotron absorption/scattering in a confined magnetic structure very close to the neutron star surface. The inferred field in such a magnetic loop is $B_{\text{loop}} \sim 2 \times 10^{14}$ G, a factor of ~ 7 higher than the surface dipolar magnetic field.

¹Author contribution: I reduced and analysed a large portion of the data. In particular, I performed the spectral analysis (both averaged and phase resolved) for the longest observation as well as for a few other observations. I contributed in writing some parts of the manuscript and in its revision at a later stage.

6.1 Introduction

RX J0720.4–3125 was discovered by Haberl et al. (1997) as an isolated, pulsating neutron star with an 8.39 s spin period. The X-ray spectrum is best modelled by a black body ($kT \sim 85$ eV) plus a broad (~ 70 eV wide) absorption feature centered at ~ 270 eV (Haberl et al. 2004). A further, narrow (~ 5 eV wide) line was identified in *XMM–Newton* Reflection Grating Spectrometer (RGS) data at ~ 570 eV (Hohle et al. 2012a and references therein), possibly due to Oxygen circumstellar/interstellar absorption. Unlike other XDINSs, RX J0720.4–3125 exhibits long-term variations in its timing and spectral parameters. In the period 2001–2003 the total flux stayed almost constant, whereas the black body temperature increased from ~ 84 to over 94 eV, and also the pulse profile, the black body radius, and the equivalent width of the absorption feature changed. In the following years this trend appeared to reverse, with a decrease of the surface temperature. Two main explanations for this behaviour were proposed: either free precession, which predicts a cyclic pattern (Haberl et al. 2006), or a glitch that occurred around $\text{MJD} = 52866 \pm 73$ days (van Kerkwijk et al. 2007). According to the most recent analyses (Hohle et al. 2009, 2012b), the interpretation in terms of a single sudden event around the proposed glitch epoch seems favoured.

In this chapter we reanalyze all the archival *XMM–Newton* observations of RX J0720.4–3125, performing a detailed phase-resolved spectral analysis. In Section 7.4 we report on the data analysis, and present the discovery of a second, new, phase-dependent absorption feature in the X-ray spectrum, the possible origin of which is discussed in Section 6.3.

6.2 Data analysis and results

RX J0720.4–3125 was observed 20 times by the *XMM–Newton* satellite using the European Photon Imaging Cameras (EPIC). We used here only data obtained with the pn camera (Strüder et al. 2001) because less affected by pile-up (see Table 6.1). We processed the data using the Science Analysis Software (SAS, version 13.5.0), adopting the most recent calibration files available, and we removed any particle flare via good-time-intervals. All arrival times were referred to the Solar System barycenter (source coordinates $\text{RA} = 07^{\text{h}}20^{\text{m}}24^{\text{s}}.961$, $\text{Dec} = -31^{\circ}25'50''.21$, J2000.0; Kaplan et al. 2003), and a rotational phase was assigned to the source counts of all the observations using the timing solution of Hohle et al. (2012b). For the source distance we assumed $D = 286$ pc (Tetzlaff et al. 2011). All errors are reported at the 90 per cent confidence level.

Spectral analysis was performed using the XSPEC analysis package (version 12.8.2, Arnaud 1996), using a minimum of 100 counts per bin for each spectrum, the χ^2 statistics and a maximum oversampling of the spectral energy resolution of a factor of 3. The fits were restricted to energies between 0.3 and 1.2 keV to exclude the broad absorption line at ~ 270 eV so as to reduce the number of degrees of freedom (dof). We extracted the source spectra from a circular region of radius 30 arcsec centered on the source point spread function (PSF) and the background counts from a circle of the same size far from

Table 6.1: Summary of the *XMM-Newton*/EPIC-pn observations of RX J0720.4–3125^a.

Obs. ID	Obs. Date YYYY-MM-DD	Read-out mode / filter	Live time (ks)	Source net count rate (counts s ⁻¹)	Pile-up fraction ratios <i>r</i> =0''–30''
0124100101	2000 May 13	FF / thin	42.8	6.46(1)	0.963(3)
0132520301	2000 Nov 21	FF / medium	22.7	5.60(2)	0.964(4)
0156960201	2002 Nov 06	FF / thin	25.6	6.60(2)	0.969(3)
0156960401	2002 Nov 08	FF / thin	27.1	6.54(2)	0.966(3)
0158360201	2003 May 02	SW / thick	51.0	3.480(8)	1.011(3)
0161960201	2003 Oct 27	SW / thin	12.6	7.52(2)	1.013(5)
0164560501	2004 May 22	FF / thin	32.0	6.96(1)	0.971(3)
0300520201	2005 Apr 28	FF / thin	38.1	6.86(1)	0.968(3)
0300520301	2005 Sep 22	FF / thin	39.1	6.93(1)	0.969(3)
0311590101	2005 Nov 12	FF / thin	33.5	6.75(1)	0.970(3)
0400140301	2006 May 22	FF / thin	17.6	6.83(2)	0.970(4)
0400140401	2006 Nov 05	FF / thin	17.6	6.90(2)	0.966(4)
0502710201	2007 May 05	FF / thin	17.4	6.80(2)	0.968(4)
0502710301	2007 Nov 17	FF / thin	20.1	7.71(2)	0.971(4)
0554510101	2009 Mar 21	FF / thin	16.7	6.84(2)	0.967(4)
0601170301	2009 Sep 22	FF / thin	15.0	6.77(2)	0.968(4)
0650920101	2011 Apr 11	FF / thin	17.6	6.61(2)	0.973(4)
0670700201	2011 May 02	FF / thin	23.6	6.73(2)	0.965(3)
0670700301	2011 Oct 01	FF / thin	22.2	6.60(2)	0.972(3)
0690070201	2012 Sep 18	FF / thin	22.3	6.60(2)	0.970(3)

^a FF: full-frame (time resolution of 73 ms); SW: small window (time resolution of 6 ms). Live time refers to the duration of the observations after filtering for background flares (see text). Count rates refer to the spectra extracted within a circular region with `PATTERN = 0`. Errors on the count rates are quoted at the 1σ confidence level. Pile-up fraction ratios were calculated for single events alone and in the 0.1–1.2 keV energy range using the `SAS EPATPLOT` tool.

the source and on the same CCD. For Small Window and Full Frame observations the pile-up level, estimated by means of the SAS EPATPLOT tool, was < 1.5 per cent and 4 per cent, respectively (see Table 6.1). To mitigate the pile-up we restricted our spectral analysis to photons having FLAG = 0 and PATTERN = 0.

We started our analysis from the 2003 May 2 observation, this being the longest observation, and least affected by pile-up (the pn was operating in Small Window mode). The phase-averaged spectrum is well fitted by an absorbed² black body (reduced chi-square $\chi^2_\nu = 1.17$ for 130 dof) yielding the following parameters: column density $N_H = 1.9(3) \times 10^{20} \text{ cm}^{-2}$, black body temperature $kT_{\text{BB}} = 82.1 \pm 0.6 \text{ eV}$ and black body radius $R_{\text{BB}} = 6.3 \pm 0.6 \text{ km}$.

To study in detail the spectral variability with phase, we produced a phase-energy image by binning the EPIC-pn source counts into 100 rotational phase channels and 25-eV-wide energy channels, and then normalizing to the phase-averaged energy spectrum. The image (see Figure 6.1) shows a feature in the phase interval 0.1–0.3, which gives a strong hint for the presence of an absorption line at $\sim 750 \text{ eV}$ in the corresponding spectrum. Above $\sim 1 \text{ keV}$ the source counts become background dominated.

To better investigate the significance of the feature, we performed a phase-resolved spectral analysis for the 2003 May 2 observation dividing the rotational cycle in five equal phase bins. For the spectrum relative to phase 0.1–0.3 the addition of a Gaussian line in absorption to the black body continuum leads to a significant improvement in the shape of residuals, while a simple black body model gives an acceptable fit for all the other phase bins. Both the GABS and GAUSS models result in $\chi^2_\nu = 0.88$ for 89 dof, corresponding to an F -test probability of 3.5×10^{-7} . We multiplied this value by 5, considering the five phase-intervals as trials. In this way we obtained a significance of $\sim 5\sigma$. The values for line energy and width obtained from the two models are compatible within the errors. The best-fit TBABS*(BBDYRAD + GAUSS) model gave the following parameters: $kT_{\text{BB}} = 83.0 \pm 0.1 \text{ eV}$, $R_{\text{BB}} = 6.3 \pm 0.3 \text{ km}$, line energy $E_{\text{line}} = 745^{+17}_{-27} \text{ eV}$, width $\sigma = 42^{+51}_{-33} \text{ eV}$ and normalization of $-9.2^{+3.5}_{-9.2} \times 10^{-5}$ (the column density was frozen at the value obtained for the phase-averaged spectrum). The equivalent width of the feature is 28^{+9}_{-11} eV . Table 6.2 summarizes the results of the phase-resolved spectroscopy for the 2003 May 2 observation using the TBABS*(BBDYRAD + GAUSS) model. Figure 6.2 shows the phase-resolved spectrum relative to phase 0.1–0.3 (black) in comparison with that at phase 0.5–0.7 (red): the absorption feature clearly shows up in the residuals.

The same phase-averaged and phase-resolved analysis was then repeated for all the remaining *XMM-Newton* observations in search for the presence of the 745 eV absorption line. Since observations in Full Frame mode were affected by pile-up, their spectra were extracted from an annular region extending from 15 to 30 arcsec from the nominal source position, this time including also events with PATTERN ≤ 4 . The resulting values of the line equivalent width and the F -test probability as a function of time are shown in Figure 6.3 (left-hand panel), and clearly indicate that the presence of the feature is unconstrained in

²We took into account the effects of interstellar absorption along the line of sight through the TBABS model with the VERN cross sections (Verner et al. 1996) and the WILM abundances (Wilms et al. 2000).

most of the observations, possibly because of their lower statistics.

We then performed a simultaneous fit of the spectra in the 0.1–0.3 phase bin for all the observations in Full Frame mode with the Thin filter (18 spectra in total; see Table 6.1). We constrained N_{H} and the line energy to be the same (to minimize the free parameters), and the width of the feature was frozen at the value obtained for the 2003 May observation. The phase-dependent feature is detected at an energy of 785 ± 13 eV for the TBABS*(BBODYRAD+GAUSS) model ($\chi^2_{\nu} = 0.96$ for 556 dof); normalizations and equivalent widths are consistent within the errors in all the spectra. The TBABS*BBODYRAD model gives $\chi^2_{\nu} = 1.03$ for 575 dof. The F -test probability for the inclusion of the Gaussian absorption line is 4.2×10^{-6} , which corresponds to a significance level of $\sim 4.5\sigma$ (taking into account the number of trials).

To further test the presence of this feature in data taken before and after 2003 May 2, we combined all the spectra except that of 2003 May 2. We used the SAS EPICSPEC-COMBINE tool to merge the spectra and average the response matrices. For the combined spectrum in the phase range 0.1–0.3, the best-fit with a black body model yields $\chi^2_{\nu} = 2.04$ for 123 dof; including a Gaussian absorption line, χ^2_{ν} decreases to 1.48 for 121 dof. The parameters for the phase-dependent line are: $E_{\text{line}} = 795^{+15}_{-14}$ eV, normalization of $(-8.3 \pm 1.7) \times 10^{-5}$ and equivalent width of 27^{+6}_{-5} eV for the GAUSS model (the line width was fixed to the value obtained from the 2003 May 2 observation). The F -test probability is 1.3×10^{-9} and the significance is equal to 6σ (again considering 5 trials).

As a further check, we built a combined spectrum comprising all observations. This spectrum, created by merging all the spectra extracted from a 15 – 30 arcsec annular region with $\text{PATTERN} \leq 4$, has an exposure time of 406.8 ks and a much improved statistics. The 0.1–0.3 phase-resolved spectrum shows an absorption feature at energy 787^{+15}_{-14} eV with normalization of $-7.9^{+1.6}_{-1.7} \times 10^{-5}$ and equivalent width of 26^{+4}_{-5} eV for the GAUSS model; also in this case we froze the line width at the value estimated for the longest observation. The F -test probability for the inclusion of the absorption feature is now 4.7×10^{-9} and, taking into consideration the number of trials, the significance level is again $\sim 6\sigma$. As shown in panel d of Figure 6.2, the spectral feature is clearly detectable in the fit residuals of the merged observations, and the line significance increases with respect to the 2003 May observation alone.

In the spectra relative to the other phase intervals the line equivalent width is always < 13 eV, and the F -test probability is always $> 3 \times 10^{-3}$ (see Figure 6.3, right-hand panel). The response of the pn camera has slightly changed (see, e.g., Sartore et al. 2012) over the twelve years spanned by the observations, hence mixing spectra obtained with different settings over such a long period certainly introduce large systematic errors which are difficult to quantify. However, a spectral feature present only in a given phase interval cannot result from systematic effects, which are definitely independent on the rotational phase. While the line is mostly evident in the 2003 May 2 observation, which we used to derive the best estimate of the line parameters, the considerations presented above strongly suggest that the feature was present also in the other observations, with properties which appear relatively stable over the 12 yr period covered by *XMM-Newton* data.

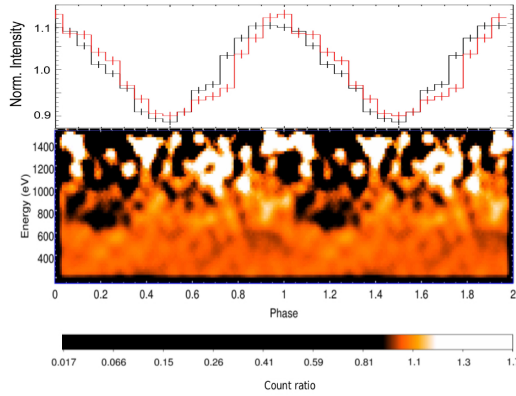


Figure 6.1: *Top panel*: pulse profile for the 2003 May 2 observation (red) and for all observations merged together (black). *Bottom panel*: normalized energy versus phase image obtained by binning the EPIC source counts into 0.01 phase bins and 25 eV energy channels for the observation performed on 2003 May 2.

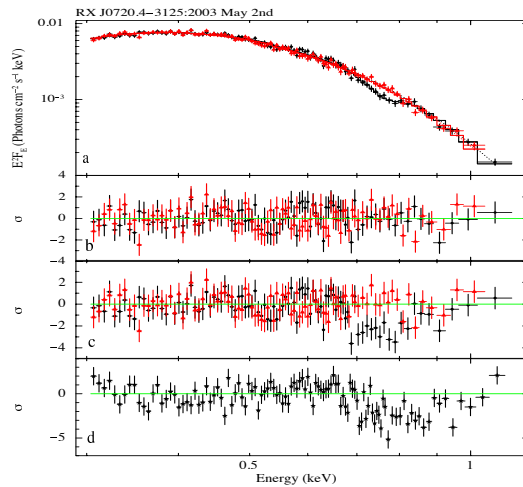


Figure 6.2: From top to bottom. Panel *a*: spectrum of the 0.1–0.3 phase interval (black circles) fitted with an absorbed black body plus a Gaussian profile (GAUSS model); the spectrum in the phase range 0.5–0.7 together with the best fitting model (TBABS*BBODYRAD) is also shown (red triangles). Both spectra are from the 2003 May 2 observation. Panel *b*: residuals with respect to these models. Panel *c*: residuals of the previous spectra after setting the line normalization to zero. Panel *d*: residuals of the spectrum relative to phase 0.1–0.3 after merging the phase-resolved spectra of all observations listed in Table 6.1.

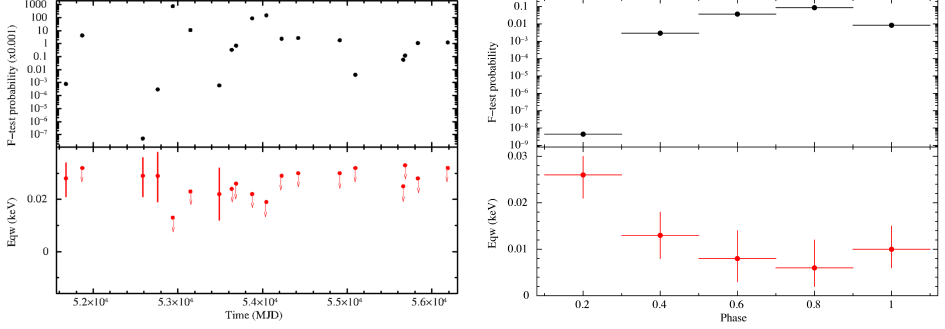


Figure 6.3: *Left-hand panel*: temporal evolution of the F -test probability and line equivalent width for the spectra in the 0.1–0.3 phase range for all *XMM-Newton* observations (the two observations performed during 2002 November were merged being only two days apart). *Right-hand panel*: F -test probability and equivalent width as a function of the spin phase for the spectrum of all merged observations.

Table 6.2: Pulse phase spectroscopy for the 2003 May 2 observation.

Parameter ^a	0.1–0.3	0.3–0.5	0.5–0.7	0.7–0.9	0.9–1.1
BB					
kT_{BB} (eV)	81.1(6)	81.9(6)	82.2(6)	82.6(6)	82.5(9)
R_{BB} (km)	$6.4^{+0.6}_{-0.5}$	$6.0^{+0.6}_{-0.5}$	$6.1^{+0.6}_{-0.5}$	$6.4^{+0.6}_{-0.5}$	$6.4^{+0.7}_{-0.6}$
Flux ^b	0.86(1)	0.82(1)	0.86(1)	0.95(1)	0.95(1)
Unabs. Flux ^b	1.07	1.01	1.06	1.17	1.17
NHP ^d	7.2×10^{-2}	5.9×10^{-1}	6.9×10^{-1}	4.2×10^{-2}	2.7×10^{-1}
χ^2_ν	1.22	0.96	0.92	1.26	1.09
dof	92	90	92	97	75
BB+GAUSS					
kT_{BB} (eV)	$83.0^{+1.5}_{-0.9}$	82.4(9)	$82.2^{+0.7}_{-0.6}$	82.7(8)	$82.4^{+1.0}_{-0.9}$
R_{BB} (km)	6.0(6)	$6.0^{+0.6}_{-0.5}$	$6.1^{+0.6}_{-0.5}$	$6.3^{+0.6}_{-0.5}$	6.4(6)
E_{line} ^c (eV)	745^{+17}_{-27}	745	745	745	745
σ ^c (eV)	$41.7^{+31.3}_{-33.8}$	41.7	41.7	41.7	41.7
Norm	$9.2^{+3.5}_{-9.2} \times 10^{-5}$	$\leq 2.7 \times 10^{-5}$	$\leq 1.7 \times 10^{-5}$	$\leq 2.9 \times 10^{-5}$	$\leq 2.4 \times 10^{-5}$
Eq. Width (eV)	28^{+9}_{-11}	6^{+9}_{-5}	≤ 8	≤ 11	≤ 13
F -test (10^{-3})	3.5×10^{-7}	232	1000	750	>1000
NHP ^d	7.9×10^{-1}	6.0×10^{-1}	6.6×10^{-1}	3.6×10^{-2}	2.5×10^{-1}
χ^2_ν	0.88	0.95	0.93	1.27	1.11
dof	89	89	91	96	74

^a The hydrogen column density was frozen at the value obtained for the phase averaged spectra: $N_H = 1.9 \times 10^{20} \text{ cm}^{-2}$.

^b Fluxes are calculated in the 0.3–1.2 keV energy range and in units of $10^{-11} \text{ erg cm}^{-2} \text{ s}^{-1}$.

^c Line energy and width were frozen at the value obtained for the phase interval 0.1 – 0.3: $E_{\text{line}} = 745 \text{ eV}$ and $\sigma = 42 \text{ eV}$.

^d NHP is the Null Hypothesis Probability.

6.3 Discussion

A careful re-analysis of all available *XMM-Newton* observations of the isolated neutron star RX J0720.4–3125 revealed the presence of a phase-dependent absorption feature at ~ 750 eV, which is mostly evident during the decline of the pulse profile (phases 0.1–0.3). The feature was first significantly detected (at $\sim 5\sigma$ confidence level) in the 2003 May 2 observation, which was the longest and was less affected by pile-up. Phase-dependent spectral analysis of the remaining datasets, which cover the period 2000 May–2012 September, indicates that the feature is likely present at all epochs and its properties are consistent with being constant over the timespan covered by available observations (~ 12 yrs). This suggests that the feature may be long-lasting and not associated to the timing anomalies (possibly due to a glitch) which occurred in 2003 (van Kerkwijk et al. 2007; Hohle et al. 2012b).

An absorption feature with somewhat similar properties has been discovered in the spectrum of the ‘low-field’ magnetar SGR 0418+5729 ($B_{\text{dip}} \sim 6 \times 10^{12}$ G; Tiengo et al. 2013). In both cases the feature is present only in a narrow phase interval ($\sim 1/5$ of the phase cycle), but in SGR 0418+5729 the line energy is higher ($\gtrsim 2$ keV) and strongly variable in phase (by a factor ~ 5 in one tenth of the phase cycle). No clear variation of the line energy with phase is seen in RX J0720.4–3125, although this might reflect the fact that the source counts become background dominated at energies just above that of the feature. Tiengo et al. (2013) interpreted the feature in SGR 0418+5729 as due to proton cyclotron resonant scattering in a baryon-loaded magnetic loop close to the star surface. The B -field variation along the loop explains the strong dependence of the line energy with phase, since photons emitted from the surface intersect the loop at different positions.

The similarities between the two features are suggestive that the same mechanism may be at work in RX J0720.4–3125. If the feature is a (broadened) proton cyclotron line, its energy is $E_{\text{line}} = 0.63(B_{\text{loop}}/10^{14} \text{ G})/(1+z)$ keV, where $1/(1+z) \sim 0.7$ is the gravitational redshift at the star surface. The implied magnetic field in the loop is $B_{\text{loop}} \sim 1.8 \times 10^{14}$ G, a factor of ~ 7 larger than the the equatorial value of the dipole magnetic field at the surface, $B_{\text{dip}} \sim 2.5 \times 10^{13}$ G. A preliminary calculation using the same geometrical model as in Tiengo et al. (2013) shows that the energy of the line and its appearance only for ~ 20 per cent of the star period can indeed be reproduced. It should be noted, however, that the exact geometry of the magnetic structure is likely different in the two sources. In the case of SGR 0418+5729, in fact, X-ray photons come from a quite small, hot spot with size ~ 1 km, while the emitting region of RX J0720.4–3125, albeit not uniform, is larger ($R_{\text{BB}} \sim 6$ km).

A further possibility is that the line results from atomic absorption in the neutron star (magnetized) atmosphere. The strong dependence of the feature on the star rotational phase may be due to local inhomogeneities in the star surface magnetic field (as in the cyclotron scenario above) and/or to a clumpy structure of the atmosphere itself. The possibility that primary photons come from a small hot spot appears, on the other hand, unlikely, given the relatively large radiation radius and the broad shape of the pulse profile. If

the feature arises from bound-bound (or bound-free) transitions, the atmosphere composition is most probably He or mid-Z elements (see, e.g., Pavlov & Bezchastnov 2005; Mori & Ho 2007). The ionization energy for H is, in fact, below ~ 0.7 keV for fields $\lesssim 10^{14}$ G (above this value the feature may be washed out by vacuum resonance mode conversion, e.g. Van Kerkwijk & Kaplan 2007 and references therein).

The presence of proton cyclotron lines produced by resonant scattering/absorption in confined, high- B structures close to the star surface, where the magnetic field is a factor $\gtrsim 10$ higher than the dipole, would be supportive of a picture in which the magnetic field of (highly magnetized) neutron stars is complex, with substantial deviations from a pure dipole on the small scales. In recent years, a better (although far from being conclusive) understanding of how stellar magnetic fields are generated and amplified indicates that strong, non-dipolar field components are ubiquitous, from massive stars (Braithwaite & Spruit 2005) to proto-neutron stars (Obergaugingler, Janka & Aloy 2014). It is now well established that internal toroidal field components, multipolar surface structures, as well as very localized B-field bundles must be present in many neutron stars, especially in highly-magnetized ones. The recent discovery of sources showing strong magnetic-powered flares and outbursts, but with low dipolar magnetic fields, $\lesssim 10^{13}$ G, further strengthens this idea (Rea et al. 2010, 2012, 2014; Turolla & Esposito 2013).

Finally, we stress that the absorption feature reported here for the first time is unlikely related to the broad absorption feature at 270 eV (Haberl et al. 2004, 2006). Even if the two may have the same physical origin, i.e. a proton cyclotron resonance, the latter implies a lower magnetic field, $\sim 5 \times 10^{13}$ G, comparable to the spin-down estimate, $B_{\text{dip}} \sim 2.4 \times 10^{13}$ G, indicating that in this hypothesis it is related to the large-scale field. Actually broad absorption features have been detected in all the XDINSs, with the exception of RX J1856.5–3754 (e.g. Turolla 2009), but the strong phase variability we observe for the 0.75 keV line of RX J0720.4–3125 sets it apart.

This is the first time that a complex magnetic field structure is observed in an XDINS, although this result is not unexpected, if, as suggested by many investigations, XDINSs are aged magnetars (Viganò et al. 2013; see also Turolla 2009).

Chapter 7

Systematic study of magnetar outbursts

Coti Zelati F. et al., *To be submitted*

So far, several magnetar outbursts have been the object of many observational campaigns in the soft X-ray band. Although detailed studies have been conducted for each of these events, an overall systematic analysis of their spectral properties, from the very first active phases throughout the decay, is still missing. Here we report the results of the spectral modelling for 18 magnetar outbursts through a reduction and reanalysis of data of more than 800 X-ray observations. We track the temporal evolution of the flux and luminosity for all these events, and investigate the anti-correlation between the maximum flux increase reached during these episodes and the source quiescent X-ray flux. We model empirically the decays of the bolometric luminosities, and estimate the characteristics decay time scales and the total energetics involved.

7.1 Introduction

In the last decades, several magnetar outbursts have been monitored in the X-rays, especially following the advent of the new generation of imaging instruments on board *Swift*, *Chandra* and *XMM–Newton*, leading to a number of unexpected breakthroughs which have changed our understanding of these objects. A systematic and homogeneous re-analysis is required to properly compare their properties, accurately model their cooling curves, and unveil possible correlations among different parameters such as the energetics, the strength of the magnetic field and the quiescent luminosity, to mention a few.

Here we present the results of the X-ray spectral modelling for 18 magnetar outbursts using all the available data acquired by the *Swift*, *Chandra* and *XMM–Newton* X-ray observatories, as well as data collected in a handful of observations by the instruments aboard *BeppoSAX*, *ROSAT* and *RXTE*. This sums up to more than 800 observations, for a total dead-time corrected on source exposure time of about 11.5 Ms. The work is structured as follows: in Section 7.2 we introduce the sample of magnetars considered in this study, and the monitoring campaigns that were activated following the detection of their outbursts; in Section 7.3 we describe the data reduction and extraction procedures; in Section 7.4 we report details on the spectral analysis; in Section 7.5 we exploit the results of our analysis to construct the light curves for each outburst; in Section 7.6 we investigate the relation existing between the quiescent level of magnetars and their maximum flux increase. The results of the detailed modelling of the outbursts evolution with the crustal cooling models developed by Pons & Rea (2012) will be presented in a forthcoming work.

7.2 The magnetar sample

In this section we summarize the properties of the 14 magnetars that so far have undergone at least one outburst, and which were the subjects of our study.

7.2.1 SGR 1627–41

SGR 1627–41 was discovered on 1998 June 15 (Kouveliotou et al. 1998), when three consecutive bursts were detected by the Burst and Transient Source Experiment (BATSE) aboard the *Compton Gamma Ray Observatory*. More than 100 prominent bursts were recorded from the same location within the subsequent 6 weeks, and the X-ray counterpart was identified two months later by the Narrow Field Instrument on board *BeppoSAX* (Woods et al. 1999). The burst detections signaled the onset of an outburst, which gradually recovered a quiescent level over the course of the ensuing decade.

Quite unexpectedly, on 2008 May 28 the Burst Alert Telescope (BAT; Barthelmy et al. 2005) aboard *Swift* triggered on tens of bursts from SGR 1627–41 (Palmer et al. 2008), the clear demonstration that the source was reactivating. A conspicuous enhancement of the persistent X-ray flux was measured (a factor of about 100 larger with respect to 3 months and a half before), and the magnetar nature of the source was incontrovertibly

settled with the detection of 2.59-s X-ray pulsations in *XMM–Newton* data sets (with $\dot{P} \sim 1.9 \times 10^{-11} \text{ s s}^{-1}$; Esposito et al. 2009a).

7.2.2 1E 2259+586

After more than two decades of rather persistent activity since its discovery at the centre of the supernova remnant (SNR) G109.1-1.0 (CTB 109) in 1979 December (Fahlman & Gregory 1981), the 6.98-s X-ray pulsar 1E 2259+586 attracted attention on 2002 June 18, when more than 80 bursts were detected within 3 h of observing time by the *Rossi X-ray Timing Explorer (RXTE)*, and the persistent flux rose by a factor of ~ 10 compared to the quiescent level (Kaspi et al. 2003). Eight *XMM–Newton* observations were carried out to study the subsequent evolution of the outburst.

Nearly ten years later, on 2012 April 21, the Gamma-ray Burst Monitor (GBM) on board the *Fermi* gamma-ray space telescope triggered on a single 40-ms long event (Foley et al. 2012), which was accompanied by an increase in the soft X-ray flux (as observed about a week later by the X-ray Telescope (XRT) on board *Swift*).

7.2.3 XTE J1810–197

Originally a soft and faint X-ray source serendipitously recorded by the *Roentgen Satellite (ROSAT)* during four observations between 1991 and 1993, the transient nature of XTE J1810–197 was disclosed in 2003, when the *RXTE* detected it at an X-ray flux a factor about 100 larger with respect to the pre-outburst level. X-ray pulsations were measured at a period of 5.54 s, making XTE J1810–197 the first magnetar showing a major outburst in all respects (Ibrahim et al. 2004). Radio pulsations at the spin period were detected about one year later, a property never observed before in any other magnetar which proved that pulsed radio emission could definitely be produced in magnetar-strength fields (Camilo et al. 2006). Although the initial phases of the outburst were missed, XTE J1810–197 has been studied in great detail over the last 12 years, especially with the *Chandra* and *XMM–Newton* observatories and up to the return to quiescence.

7.2.4 SGR 1806–20

Initially catalogued as a classical γ -ray burst (GRB 790107) based on observations by the *Konus* experiment (Mazets et al. 1981) and other all-sky monitors of the interplanetary network (Laros et al. 1986), SGR 1806–20 was recognized to be a member of a distinct class of astrophysical transients after the detection of more than 100 bursts of soft γ -rays between 1979 and 1986 (Laros et al. 1987). Two observations were carried out by the *Advanced Satellite for Cosmology and Astrophysics* soon after an intense bursting activity in 1993 October (as unveiled by BATSE), leading to the identification of a previously uncatalogued, persistent, point-like X-ray counterpart (Murakami et al. 1994, Sonobe et al. 1994). The spin period, ~ 7.5 s, was measured in 1996 November by means of 5 *RXTE*

observations that were performed following the n th reactivation of the source (Kouveliotou et al. 1998).

SGR 1806–20 experienced an exceptionally intense flare on 2004 December 27 (the most energetic gamma-ray transient event ever observed, reaching a peak luminosity of a few 10^{47} erg s⁻¹ for a distance of 8.7 kpc and under the assumption of isotropic emission; Hurley et al. 2005, Palmer et al. 2005) and then stabilized at an approximately steady level over the subsequent seven years (Younes, Kouveliotou & Kaspi 2015).

7.2.5 CXOU J164710.2–455216

CXOU J164710.2–455216 was discovered in 2005 during an X-ray survey of the young cluster of massive stars Westerlund 1, and tentatively identified as a magnetar candidate based on the value of its spin period, 10.61 s, the X-ray spectral properties, and the lack of infrared counterparts (Muno et al. 2006). The case was clinched the following year, when a rather intense burst lasting about 20 ms was fortuitously detected by the *Swift* BAT from the direction of the source, on 2006 September 21 (Krimm et al. 2006). This episode was indeed associated with an abrupt enhancement of the X-ray flux, which marked the onset of a magnetar-like outburst.

The source underwent another weaker outburst on 2011 September 19, when 4 more sporadic bursts were detected from the source position (Baumgartner et al. 2011; Rodríguez Castillo et al. 2014).

7.2.6 SGR 0501+4516

SGR 0501+4516 joined the magnetar family on 2008 August 22, after the *Swift* BAT detection of a series of short bursts of soft γ -rays (< 100 keV; Barthelmy et al. 2008), and the discovery of pulsations at a period of 5.76 s from the X-ray afterglow (Gögüş et al. 2008). The source continued to be active over the following 36 hours, showing a total of about 30 bursts. It was soon recognized that the bursting activity was related to the onset of an outburst, and several X-ray observations were promptly undertaken.

7.2.7 1E 1547–5408

Discovered by the *Einstein* satellite on 1980 March 2 during a search for X-ray counterparts of unidentified γ -ray sources (Lamb & Markert 1981), 1E 1547–5408 (aka SGR 1550–5418) was later suspected to be a magnetar candidate based on its X-ray spectral properties, the observed decrease of the 0.5–10 keV flux by a factor of ~ 7 between 1980 and 2006, and its putative association with the SNR G327.24–0.13 (Gelfand & Gaensler 2007). The ‘smoking gun’ in favor of this classification came with the measurement of 2.07-s pulsations from the radio counterpart (Camilo et al. 2007), later confirmed also in the X-rays (Halpern et al. 2008).

On 2008 October 3, the *Swift* BAT triggered on and localized a short burst from a position consistent with that of 1E 1547–5408 (Krimm et al. 2008). *Swift* executed a

prompt slew, and the XRT started observing the field only 99 s after the BAT trigger, catching the source at a flux a factor about 20 above that in quiescence.

No further bursts were reported until 2009 January 22, when the source resumed a new state of extreme bursting activity (Gronwall et al. 2009, Connaughton & Briggs 2009), culminating in a storm of more than 200 soft γ -ray bursts recorded by the *International Gamma-Ray Astrophysics Laboratory* (*INTEGRAL*) in a few hours (Mereghetti et al. 2009), and characterized by a considerable increase in the persistent X-ray flux. The source was repeatedly observed in the X-rays after the burst trigger (especially with *Swift*), leading to one of the most intensive samplings of a magnetar outburst ever performed.¹

7.2.8 SGR 0418+5729

SGR 0418+5729 was discovered after the detection of a couple of short hard X-ray bursts on 2009 June 5 with *Fermi* GBM and other instruments sensitive to the hard X-ray range (van der Horst et al. 2009, 2010). Coherent X-ray pulsations were observed at a period of 9.1 s 5 days later during an *RXTE* pointing (Göğüş et al. 2009). Since then, *Swift*, *Chandra* and *XMM-Newton* observed the field of the new source for a total of 39 pointings. It took more than three years of continuous monitoring to unambiguously establish the first derivative of the spin period, making this source the magnetar with the lowest inferred surface dipolar magnetic field known to date,² $\sim 1.2 \times 10^{13}$ G (Rea et al. 2013a).

7.2.9 SGR 1833–0832

SGR 1833–0832 was discovered on 2010 March 19, when the *Swift* BAT triggered on and localized a short (< 1 s) hard X-ray burst in a region close to the Galactic plane (Gelbord et al. 2010, Göğüş et al. 2010a) and the fast slew of the XRT promptly detected a previously unnoticed 7.57-s X-ray pulsator (Esposito et al. 2010; Göğüş et al. 2010). Starting right after its discovery, *Swift* and *XMM-Newton* pointed their instruments towards the source multiple times for the first ~ 160 d of the outburst decay.

7.2.10 Swift J1822.3–1606

On 2011 July 14, the detection of a magnetar-like burst by the *Swift* BAT and of an associated bright and persistent XRT counterpart heralded the existence of a new magnetar, Swift J1822.3–1606 (Cummings et al. 2011), with a spin period of 8.43 s (Göğüş et al. 2011a). Swift J1822.3–1606 was densely monitored in the X-rays until 2012 November

¹*Swift* and *XMM-Newton* observations performed from 2007 June to October caught the magnetar at a flux initially a factor of ~ 16 larger than the quiescent one, and which then faded (Halpern et al. 2008). This suggests that the source was likely recovering from another outburst occurred prior to 2007 June. We do not include the analysis of this outburst in this study owing to the unknown epoch of the episode onset and the sparse X-ray coverage.

²This value is computed using the spin-down formula for force-free magnetospheres by Spitkovsky (2006), and assuming an aligned rotator. It refers to the dipolar component of the surface magnetic field at the polar caps.

17, covering a time span of ~ 1.3 years. With an estimated surface dipolar magnetic field of $\sim 6.8 \times 10^{13}$ G (Rodríguez Castillo et al. 2016, and references therein), it also belongs to the sub-class of the so called ‘low- \dot{P} magnetars’.

7.2.11 Swift J1834.9–0846

The BAT aboard *Swift* was triggered by a short SGR-like burst on 2011 August 7 (D’Elia et al. 2011). This episode was not isolated: a second burst from the same direction on the sky was recorded by the *Fermi* GBM approximately 3.3 hr later (Guiriecx et al. 2011), and another similar event triggered the BAT again on August 29 (Hoversten et al. 2011). The magnetar nature of this newly discovered source was nailed down with the discovery of pulsations at 2.48 s from the X-ray counterpart (Göğüş et al. 2011b). *Swift*, *Chandra* and *XMM-Newton* observed this new SGR for a total of 25 times since the first burst detection.

Swift J1834.9–0846 represents a unique case among magnetars. It is indeed embedded in a patch of diffuse X-ray emission with a complex spatial structure consisting of a symmetric component within ~ 50 arcsec around the magnetar, and an asymmetric component stretched towards the south–west of the point source and extending up to ~ 150 arcsec. The former was interpreted as a halo created by the scattering of X-rays by intervening dust (dust-scattering halo; Kargaltsev et al. 2012; Esposito et al. 2013). The latter was attributed to a magnetar-powered wind nebula based on its highly absorbed power-law-like X-ray spectrum, the flux constancy and the absence of statistically significant variations in the spectral shape over a time span of 9 years, between 2005 and 2014 (Younes et al. 2016). If it be so, Swift J1834.9–0846 would provide the first observational evidence for the existence of wind nebulae around magnetically-powered pulsars.

7.2.12 1E 1048.1–5937

The discovery of 1E 1048.1–5937 dates back to 1979 July 13, when *Einstein* detected 6.44-s pulsed X-ray emission from a point-like source in the Carina Nebula (Seward, Charles & Smale 1986). With four long-term outbursts shown to date, this source holds the record as the most prolific outbursting magnetar hitherto known. The first three flux enhancements were observed in 2001, 2002 and 2007 by *RXTE*, which monitored this source about twice per month from 1999 February to 2011 December (see Dib & Kaspi 2014 and references therein). An additional flux increase was observed in 2011, and the subsequent evolution was the object of a prolonged monitoring campaign with *Swift*, to which two *Chandra* and one *XMM-Newton* observations have to be added. The outbursts are remarkably periodic, with a recurrence time of about 1800 d (Archibald et al. 2015).

7.2.13 SGR 1745–2900

At a projected separation of 0.1 pc from the supermassive black hole at the Centre of the Milky Way, Sagittarius A* (hereafter Sgr A*), SGR 1745–2900 is the closest neutron star to a black hole ever observed, and it spins with a period of about 3.76 s. According to

numerical simulations and to the recently detected proper motion, it is likely in a bound orbit around Sgr A* (Rea et al. 2013b; Bower et al. 2015; Coti Zelati et al. 2015).

SGR 1745–2900 is the object of an ongoing intensive monitoring campaign by *Chandra*, still more than three years after the detection of the first ~ 30 ms long soft gamma-ray burst from the source on 2013 April 25 (Kennea et al. 2013).

7.2.14 SGR 1935+2154

The most recent addition to the magnetar class is represented by SGR 1935+2154, whose existence was announced on 2014 July 5 once more through the detection of low-Galactic latitude short bursts by *Swift* BAT (Stamatikos et al. 2014). A deep follow-up observation carried out by *Chandra* enabled to determine its spin period (3.24 s; Israel et al. 2014), and the post-outburst behaviour was then observed with *Swift*, *Chandra* and *XMM–Newton*. On 2015 February 22 the BAT triggered on another burst from the source (D’Avanzo et al. 2015), which led to further monitoring through 14 observations with *Swift* and two with *XMM–Newton*. Another 50-ms long burst was detected in 2015 December by *INTEGRAL* in the soft gamma rays (Mereghetti et al. 2015), albeit no concurrent increase was observed in the X-ray emission over the long-term behaviour (Coti Zelati et al. 2015b). The source reactivated once more on 2016 May 16 (Barthelmy et al. 2016), and bursting activity was observed over the following ~ 5 days.

7.3 Data reduction and extraction

In this Section we describe the standard procedures employed to extract the scientific products (source and background spectra) and create or assign the response and auxiliary files starting from the raw *Swift*, *XMM–Newton* and *Chandra* data files publicly available. In addition to these data sets, we also looked at other few observations carried out with the Medium-Energy Concentrator Spectrometer (MECS; Boella et al. 1997) on board *BeppoSAX*, the *ROSAT* Position Sensitive Proportional Counter (PSPC; Pfeffermann et al. 1987), and the Proportional Counter Array (PCA; Jahoda et al. 1996) instrument of the *RXTE*. In particular, we focused on the data concerning the quiescent stages (pre-outburst observations), or the very early phases, of the outbursts. These data sets revealed to be crucial to estimate fluxes and luminosities for the magnetar XTE J1810–197 during quiescence or at the very early stages of the outburst decay (i.e., SGR 1627–41 during its 1998 event and SGR 0418+5729), and were reduced and analysed as described by Esposito et al. (2008, 2010) and Rea et al. (2009, 2012).

7.3.1 *Swift* data

The X-ray Telescope (XRT; Burrows et al. 2005) on board the *Swift* satellite uses a front-illuminated charge-coupled device (CCD) detector sensitive to photons with energies between 0.2 and 10 keV, with an effective area of about 110 cm^2 at 1.5 keV. Two readout

modes are now available: photon counting (PC) and windowed timing (WT). In the former the entire CCD is read every 2.5073 s, whereas in the latter 10 rows are compressed in one, and only the central 200 (out of 600) columns are read out. One-dimensional imaging is preserved, achieving a time resolution of 1.7675 ms and thus providing a larger dynamic range of measurable source intensities (see Hill et al. 2004 for a detailed description of the XRT readout modes).

We processed the data with standard screening criteria (Capalbi et al. 2005) and generated exposure maps with the task XRTPIPELINE (version 0.13.2) from the FTOOLS package (Blackburn 1995), using the best available source position (see Table 1 in Olausen & Kaspi 2014³) and the spacecraft attitude file. We selected events with grades 0–12 and 0 for the PC and WT data⁴, respectively, and extracted the source and background spectra using XSELECT (v. 2.4). We accumulated the source counts from a circular region centered on the source position and with a radius of 20 pixels (one XRT pixel corresponds to about 2.36 arcsec). A noteworthy exception is represented by the magnetar Swift J1834.9–0846, for which we opted for a circle of radius 6 pixels to minimize the contribution from the surrounding diffuse emission (see Section 7.2.11). To estimate the background in the PC-mode data, we extracted the events within an annulus centred on the source position with inner and outer radius of 40 and 80 pixels, respectively (12 and 19 pixels for Swift J1834.9–0846). For the observations targeting the 2009 outburst of 1E 1547–5408 we considered instead a circle as far as possible from the source, to reduce the contamination by the three expanding dust scattering X-ray rings (see Tiengo et al. 2010). For the WT-mode data we adopted a region far from the target and of the same size as that used for the source.

For all the observations we built exposure-corrected and background-subtracted light curves for the source event file using XRTLCCORR and LCMATH (the latter accounting also for different areas of the source and background extraction regions). We binned them with different time resolutions, and removed possible bursts/flares episodes by applying intensity filters to the event lists. This procedure aims at minimizing flux overestimates, and avoiding possible spectral distortions induced by the bursting emission, which is typically harder than that of the underlying continuum.

In case an observation in PC mode suffered from photon pile-up (typically this occurs when the source net count rate exceeds ~ 0.6 counts s^{-1}), we determined the extent of the piled-up region as follows. First, we modeled the wings of the radial profile of the source point-spread function (at a distance > 15 arcsec from the centre) with a King function (see Moretti et al. 2005). We then extrapolated the model back to the core of the PSF, and compared it to the data points. The region where the observed PSF lies underneath the

³See also the McGill Online Magnetar Catalog at <http://www.physics.mcgill.ca/~pulsar/magnetar/main.html>.

⁴Because of issues in the modelling of the response matrix files, spectra of heavily absorbed sources ($N_H \gtrsim 10^{22}$ cm⁻²) occasionally are known to exhibit a bump and/or turn-up at low energy (typically below 1 keV) in WT mode for events with grades ≥ 1 . See http://www.swift.ac.uk/analysis/xrt/digest_cal.php.

extrapolation of the King function was then excluded from our analysis.⁵

We created the observation-specific ancillary response files with XRTMKARF (v. 0.6.3), thereby correcting for the loss of counts due to hot columns and bad pixels, and accounting for different extraction regions, telescope vignetting and PSF corrections. We then assigned the appropriate redistribution matrix available in the HEASARC calibration data base,⁶ and excluded bad spectral channels (at energy < 0.3 keV). We co-added individual spectra and responses for contiguous observations with very few counts and that were carried out with the same observing mode, to improve the statistics quality and increase the signal-to-noise ratio.⁷ For extensively monitored outbursts we also constructed the long-term 0.3–10 keV count-rate light curves (using the online *Swift* XRT data products generator; see Evans et al. 2009 for details), to roughly gauge the decay timescales (see Figure 7.1).

7.3.2 XMM–Newton data

The *X-ray Multi-Mirror Mission (XMM–Newton)*; Jansen et al. 2001) carries three co-aligned X-ray telescopes, each with an European Photon Imaging Camera (EPIC) imaging spectrometer at the focus. Two of the EPIC spectrometers use Metal Oxide Semiconductor CCD arrays (MOS cameras; Turner et al. 2001) and one uses pn CCDs (pn camera; Strüder et al. 2001). They all cover the 0.1–15 keV energy range with an effective area of about 500 cm² for each MOS and 1400 cm² for the pn at 1.5 keV. In the present work we will consider only data acquired with the pn camera, which provides the spectra with the highest counting statistics owing to its larger effective area.

The pn camera can operate in different imaging configurations. In full frame mode (FF; 73.4-ms time resolution), all pixels of the 12 CCDs are read out simultaneously and the full field of view (FoV) is covered. In large window mode (LW; 47.7-ms time resolution), only half of the area in all CCDs is read out and in small window mode (SW; 5.7-ms time resolution) just one single CCD is used to collect data. The pn can also operate in timing mode, where data from a predefined area on one CCD chip are collapsed into a one-dimensional row to be read every 30 μ s.

We retrieved the raw observation data files from the *XMM–Newton* Science Archive,⁸ and processed them to produce calibrated, concatenated photon event lists using the EP-PROC tool of the *XMM–Newton* Science Analysis System (SAS⁹ v. 15.0; Gabriel et al. 2004) and the most up to date calibration files available (XMM-CCF-REL-332). For each observation we built a light curve of single pixel events (PATTERN = 0) for the entire FoV, and discarded episodes (if any) of strong soft-proton flares of solar origin using intensity filters. We then estimated the amount of residual contamination in each event file by com-

⁵See <http://www.swift.ac.uk/analysis/xrt/xrtpileup.php>

⁶See <http://www.swift.ac.uk/analysis/xrt/rmfarf.php>.

⁷Ancillary response files were weighted by the net number of counts of the source in each observation.

⁸nxa.esac.esa.int/

⁹See <http://www.cosmos.esa.int/web/xmm-newton/sas>

paring the area-corrected count rates in the in- and out-of-FoV regions of the detector,¹⁰ and verified that it was negligible or low in all cases (here ‘negligible’ and ‘low’ are defined following De Luca & Molendi 2004). We extracted the source photons from a circular region centred on the source position and with a typical radius of 20–30 arcsec, depending on the source brightness, the presence of closeby sources, and the distance from the edge of the CCD. The background was extracted from a circle located on the same CCD, and the position and size of the region were determined so as to guarantee similar low-energy noise subtraction and avoid detector areas possibly contaminated by out-of-time events from the source or too near to the CCD edges (we used the EBKGREG tool, which typically yielded larger radii for the cases where the source was particularly faint, e.g. SGR 1627–41 or SGR 0418+5729 close to the quiescent level). The case of Swift J1834.9–0846 stands apart owing to the surrounding extended emission (see Section 7.2.11), and the photon counts were collected within similar regions as those adopted by Younes et al. (2016).

We built background-subtracted and exposure-corrected light curves with different time binnings using the EPICLCCORR task, which also corrects the time series for any relevant instrumental effect such as bad pixels, chip gaps, PSF variation, vignetting, quantum efficiency and dead time, and accounts for the different sizes of the source and background extraction regions. We then removed possible source flaring episodes by applying ad hoc intensity filters on the light curves.

We estimated the potential impact of pile-up by comparing the observed event pattern distribution as a function of energy with the theoretical prediction in the 0.3–10 keV energy interval, by means of the EPATPLOT task. For piled-up sources, we selected the most suitable annular extraction region for the source counts via an iterative procedure, by excising larger and larger portions of the inner core of the source PSF until a match was achieved between the observed and expected distributions at the 1- σ confidence level for both single and double pixel events.

We employed the standard filtering procedure in the extraction of the scientific products, retaining only single and double pixel events optimally calibrated for spectral analysis ($PATTERN \leq 4$), and excluding border pixels and columns with higher offset for which the pattern type and the total energy are known with significantly lower precision ($FLAG = 0$). We calculated the area of source and background regions using the BACKSCALE tool, and generated the redistribution matrices and effective area files with RMFGEN and ARFGEN, respectively. We used the EPISPECCOMBINE task to co-add the spectra and average the response files of closeby observations carried out with the same instrumental setup (i.e. same observing mode and optical blocking filter in front of the pn CCD) and with a relatively scarce number of counts, to obtain a reasonable number of spectral bins for a meaningful spectral analysis.

¹⁰We used the script provided by the *XMM-Newton* EPIC Background working group available at <http://www.cosmos.esa.int/web/xmm-newton/epic-scripts/#flare>.

7.3.3 *Chandra* data

The *Chandra X-Ray Observatory* includes two focal plane instruments: the Advanced CCD Imaging Spectrometer (ACIS; Garmire et al. 2003) and the High Resolution Camera (HRC; Zombeck et al. 1995). The ACIS operates in the 0.2–10 keV energy range with an effective area of about 340 cm² at 1 keV. It consists of an imaging (ACIS-I) and a spectroscopic (ACIS-S) CCD arrays. The HRC covers the 0.1–10 keV interval with an effective area of about 225 cm² at 1 keV and comprises the HRC-I and the HRC-S detectors. The former optimized for wide-field imaging, the latter designed for spectroscopy.¹¹

The ACIS detectors enable two modes of data acquisition: the timed exposure (TE) mode, and the continuous clocking (CC) mode. In the former, each chip is exposed for a nominal time of 3.241 s (or a sub-multiple, if only a sub-array of a chip is being read-out). In the latter, data are transferred from the imaging array to the frame store array every 2.85 ms, at the expense of one dimension of spatial information.

We analysed the data following the standard analysis threads¹² with the *Chandra* Interactive Analysis of Observations software (CIAO, v. 4.8; Fruscione et al. 2006) and the calibration files stored in the *Chandra* CALDB (v. 4.7.1). Only non-dispersed (zeroth-order) spectra were extracted for observations where a grating array was used. We applied the CHANDRA_REPRO script to reprocess the data and generate new ‘level 2’ events files with the latest time-dependent gain, charge transfer inefficiency correction, and sub-pixel adjustments. For TE-mode data and on-axis targets, we collected the source photons from a circular region around the source position with a radius of 2 arcsec. An important outlier is SGR 1745–2900 amid the Galactic Centre, for which the counts were accumulated within a 1.5-arcsec radius circular region. A larger radius would have indeed included too many counts from Sgr A* (see Coti Zelati et al. 2015a for details). We note that the *Chandra* PSF exhibits significant variations in size and shape across the focal plane. Therefore, for the few cases where the target of interest was located far from the position of the aim point, we proceeded as follows. First, we accurately measured the coordinates of the source centroid by applying the CIAO source detection algorithm WAVDETECT (Freeman et al. 2002) to the count image. We adopted the default ‘Ricker’ wavelet (‘Mexican Hat’ wavelet) functions with scales ranging from 1 to 16 pixels with a $\sqrt{2}$ step size and the default value for the source pixel threshold (SIGTHRESH = 10⁻⁶). We then calculated the off-axis angle from the pointing direction, and used the CIAO tool PSFSIZE_SRCS to estimate the radius of the 90 per cent encircled counts fraction at 3 keV. In all cases the background was extracted from an annulus centred on the source location. For observations with the ACIS set in CC mode, source events were instead collected through a rectangular region of dimension 4 arcsec along the readout direction of the CCD and 5 arcsec in the orthogonal direction. Background events were extracted within two similar boxes oriented along the image strip, symmetrically placed with respect to the target and sufficiently far from the position of the source, to minimize the contribution from the PSF wings.

¹¹Observations performed with the HRC-I were not analysed since this camera provides only a limited energy resolution on the detected photons.

¹²See <http://cxc.harvard.edu/ciao/threads/pointlike>.

We filtered the data for flares from particle-induced background (e.g., Markevitch et al. 2003) by running the `DEFLARE` routine on the lightcurves, and estimated the impact of photon pile-up in the TE-mode observations using the `PILEUP_MAP` tool, which outputs an image of counts per ACIS frame. On the other hand, the fast readout of the ACIS in the CC-mode ensured in all cases that the corresponding spectra were not affected by pile-up. Because of the sharp *Chandra* PSF, discarding photons in the core of the PSF to correct for pile-up effects results in a significant loss of counts. Spectral distortions were then mitigated directly in the spectral modelling, as described in Section 7.4.

We created the source and background spectra, the associated redistribution matrices and ancillary response files using the `SPEXTRACT` script.¹³ Spectra and auxiliary and response files for contiguous observations with low counting statistics were combined using the `COMBINE_SPECTRA` script.

7.4 Spectral analysis

We generally grouped the background-subtracted spectra to have at least 20 counts in each spectral bin using `GRPPHA`, to allow for fitting using the χ^2 statistics. For the spectra with the largest number of counts (typically those extracted from *XMM-Newton* and *Chandra* observations, but in some cases also from *Swift* pointings at the earliest stages of the most powerful outbursts), we adopted a higher grouping minimum and the optimal binning prescription of Kaastra & Bleeker (2016). Conversely, in case the available number of counts was too low, we opted for a lower grouping minimum (e.g., down to at least one count per energy channel for the *Swift* XRT spectra of SGR 1627–41 and Swift J1834.9–0846), and used the Cash statistics (*C*-statistics; Cash 1979).

We performed the spectral analysis separately for the *Swift*, *Chandra* and *XMM-Newton* data, owing to known cross-calibration uncertainties (e.g. Tsujimoto et al. 2011) and their remarkably different effective areas and energy dependence, which translate into different counting statistics and hence best-fitting models in most cases (the larger the statistics available, the larger the number of spectral components required to properly fit the data).

For the spectral modelling we employed the `XSPEC`¹⁴ spectral fitting package (v. 12.9.0; Arnaud 1996), and applied the Levenberg–Marquardt minimization algorithm (Press et al. 1992). We restricted our analysis to the energy interval whereby the calibration of the spectral responses is best known, i.e. 0.3–10 keV for *Swift*/XRT and *XMM-Newton*/EPIC (with some exceptions for the XRT WT-mode data; see below), 0.3–8 keV for *Chandra*, 1.8–10 keV for *BeppoSAX*/MECS, 0.1–2.4 keV for *ROSAT*/PSPC, and 3–10 keV for *RXTE*/PCA. For the faintest outbursts (e.g. those of CXOU J164710.2–455216 and the 2008 event from 1E 1547–5408) and heavily absorbed sources (e.g. SGR 1833–0832 and Swift J1834.9–0846), we further limited our study to photons with energy above 1 or 2 keV, owing to the few available counts at lower energy. On the other hand, the spectra of SGR 0418+5729

¹³Ancillary response files are automatically corrected to account for continuous degradation in the ACIS CCD quantum efficiency.

¹⁴See <http://heasarc.gsfc.nasa.gov/xanadu/xspec/>

softened significantly as the source approached the quiescent phase. The few photons at energy $\gtrsim 3$ keV were overwhelmed by the background and hence discarded (see Figure 7.2 for a set of high-quality X-ray spectra of the outbursts that were monitored multiple times by *XMM-Newton* and/or *Chandra*). In some cases, spectra acquired by *Swift* and with the XRT configured in WT mode exhibited some residual bumps due to calibration uncertainties below ~ 1 keV, in spite of the grade 0 selection for the event files. Since these features would yield a misleading (systematically underestimated) value for the absorption column density, we decided to filter out the spectral channels at low energy.

If a mild pile-up fraction is detected in a *Chandra* observation (typically at the early stages of the outburst), the multiplicative pile-up model of Davis (2001) was included, as implemented in XSPEC. Following the prescriptions reported in ‘*The Chandra ABC Guide to Pile-up*’,¹⁵ the only parameters allowed to vary were the grade-migration parameter and the fraction of events within the central, piled up, portion of the source PSF. The photoelectric absorption by the interstellar medium along the line of sight was described through the Tuebingen-Boulder model (TBABS in XSPEC notation), and we adopted the photoionization cross-sections from Verner et al. (1996) and the chemical abundances from Wilms, Allen & McCray (2000)¹⁶. We tested a set of different single and double-component empirical models for the spectral fitting: a black body (BBODYRAD; BB), a power-law (PL), a black body plus a power-law (BB+PL) and the superposition of two blackbodies (2BB).

For each outburst we started by fitting together the spectra acquired by *Swift* XRT¹⁷ to the BB+PL and 2BB models (with the exception of XTE J1810–197, the 2008 outburst of SGR 1627–41, SGR 0418+5729, SGR 1833–0832, Swift J1834.9–0846, the 2011 outburst of CXOU J164710.2–455216 and SGR 1935+2154, for which a single absorbed black body model provided an acceptable fit across the entire data set) and all the parameters left free to vary from observation to observation. The absorption column density was left free to vary as well, but with the request to be the same at all stages of the outburst evolution. For extensively monitored sources (i.e., SGR 0501+4516, 1E 1547–5408 during the 2009 outburst, Swift J1822.3–1606, 1E 1048.1–5937, 1E 2259+586 during the 2012 outburst and SGR 1935+2154) the joint modelling was performed on groups of 20 spectra. In most cases, spectra of observations carried out at late stages of the outburst were adequately described by an absorbed black body alone and the addition of a second component was not statistically required. However, removal of the second component in the modelling of the corresponding spectra would typically lead to systematically lower values for the column density and the black body temperature, which are inconsistent with those inferred for the previous stages and do not properly track the decrease in the BB

¹⁵See http://cxc.harvard.edu/ciao/download/doc/pileup_abc.

¹⁶The use of abundances by Wilms et al. (2000) typically yields values for the column density about 30 per cent larger than those estimated assuming the abundances from Anders & Grevesse (1989), however with no substantial differences on the estimates of the fluxes.

¹⁷For SGR 1745–2900 we considered instead *Chandra* data alone, since only the exquisitely sharp PSF of the ACIS instrument enables to single out the magnetar counterpart in the crowded region of the Galactic Centre. See Coti Zelati et al. (2015) for details.

temperature (this is more evident especially in the case of the BB+PL spectral decomposition, where the spectral hardening induced by the PL is more relevant). For this reason we decided to retain the second component in the spectral fits, and freeze its pivotal parameter (the power-law photon index in the BB+PL model or the temperature of the second black body in the 2BB model) to the value inferred for the spectrum of the last pointing where the second component is significantly detected. Alternatively, this parameter was tied up between all these data sets. For both alternative strategies, the normalizations of the spectral components were left free to vary. We then derived stringent upper limits on the contribution of the additional spectral component, and verified that the fits to the single spectra yielded values for the column density and the other parameters consistent with those inferred from the joint modelling.

We point out that the C -statistics enables parameter estimation and identification of confidence levels, but does not provide a goodness-of-fit criterion. For the cases where the C -statistics was employed, we then evaluated the quality of the fit by means of Monte Carlo simulations. We used the `GOODNESS` command within `XSPEC` to simulate a total of 1000 spectra based on a Gaussian distribution of parameters centered on the best-fitting model parameters and with Gaussian width set by the 1σ errors on the parameters. In all cases the percentage of simulations having a C -statistics value lower than that obtained from the best fit of the actual data turned out to be $\lesssim 50$ per cent (the fiducial value below which the fit is considered to be acceptable).

The above-mentioned fitting procedure was subsequently repeated for the *XMM-Newton* and *Chandra* data sets. In the cases of XTE J1810–197 and the 2002 outburst of 1E 1547–5408, the higher statistics quality available from *XMM-Newton* observations allowed us to probe more refined models, such as the sum of three thermal components (3BB). Because the internal calibration accuracy of the pn CCD for on-axis sources is estimated to be better than 2 per cent at the 1σ confidence level (Smith 2015¹⁸), we added an extra 2 per cent systematic error term to each spectral channel in these cases, as also recommended by the online threads. We then assessed the number of required spectral components by means of the Fisher-test (e.g. Bevington 1969), setting a minimum threshold of 3σ (99.7 per cent) for the statistical significance of the improvement in the fit. Best-fitting models are reported in Table 7.1.

7.5 Cooling curves and empirical modelling

For each fitted spectrum we calculated the total absorbed flux, the luminosity for the additive components and the total one (all in the 0.3–10 keV energy range). Unabsorbed fluxes were calculated using the convolution model `CFLUX`, and converted to luminosities (as measured by an observer at infinity) assuming the best constrained value for the distance of the source (see e.g. Table 7 of Olausen & Kaspi 2014; and the online cata-

¹⁸See <http://xmm2.esac.esa.int/docs/documents/CAL-TN-0018>

logues¹⁹). Throughout this work all the uncertainties are quoted at the 1σ confidence level for a single parameter of interest ($\Delta\chi^2 = 1$; Lampton, Margon & Bowyer 1976), whereas the upper limits are reported at the 3σ confidence level. For each outburst we checked that the unabsorbed fluxes inferred for observations carried out with different instruments approximately at the same epoch were consistent with each other within the cross-correlation uncertainties, especially for the cases where different models were employed to fit the data sets.

We stress that the extrapolation of the power-law component to low energy is known to overestimate the source flux by a large factor, since the absorption model tends to increase the value for the column density in response to the steep rise of the power-law at low energy. Therefore, to estimate bolometric luminosities for the cases where a power-law spectral component was required, we fitted again all data with resonant Compton scattering models, obtaining in all cases equivalently acceptable results. In particular, we applied the NTZ model (Nobili et al. 2008a,b), which is based on three-dimensional Monte Carlo simulations. The topology of the magnetic field is assumed to be a globally twisted, force-free dipole in the model, and its parameters are the surface temperature (assumed to be the same over the whole surface), the bulk motion velocity of the charges in the magnetosphere, the twist angle and a normalization constant. We point out that this model has the same number of free parameters and hence the same statistical significance as the empirical two-component models mentioned above (2BB and BB+PL). We then determined the 0.01–100 keV fluxes after having defined dummy response matrices with the DUMMYRSP command in XSPEC. An uncertainty of 10 per cent was assigned to each flux.

All cooling curves are shown in a series of figures (see Figures 7.4–7.16), and include the evolution of the absorbed fluxes and of the 0.3–10 keV luminosities (for both the single spectral components, and the total one). We also show all temporal decays of the bolometric luminosities in Figure 7.18. We refer each curve to the epoch of the outburst onset, defined as the time of the first burst detection from the source (mostly with *Swift* BAT or *Fermi* GBM), or of the giant flare in the case of SGR 1806–20. For XTE J1810–197 and 1E 1048.1–5937, for which no bursts were detected (see Sections 7.2.3 and 7.2.12, respectively), we adopted the epoch of the observation where an increase in the X-ray flux was first measured as the reference epoch. The decays of the X-ray luminosities of the single spectral components and of the total bolometric luminosities were fitted to a constant (dubbed L_q and representing the quiescent level) plus one or more exponential functions (dubbed EXP, 2EXP, and 3EXP in the following) of the form:

$$L(t) = L_q + A \times \exp \left[- \frac{(t - t_s)}{\tau} \right],$$

$$L(t) = L_q + A \times \exp \left[- \frac{(t - t_s)}{\tau_1} \right] + B \times \exp \left[- \frac{(t - t_s)}{\tau_2} \right].$$

¹⁹See <http://www.neutronstarcooling.info> and <http://www.physics.mcgill.ca/~pulsar/magnetar/table2.html>.

L_q was fixed at the quiescent value or, in cases of non detections, constrained to be lower than the upper limit (see e.g. Table 7.4 for the quiescent values of the bolometric luminosities). The only exception is represented by the 2008 outburst of 1E 1547–5408. In this case we did not include the constant term because the source did not reach the historical quiescent level before undergoing a new outburst only ~ 3.5 months after the first episode. t_s represents the epoch of the outburst onset and was fixed to 0 in all cases. τ_i denotes the e -folding time.

We then estimated the total outburst impulsive energetics by integrating the model over the whole duration of the event, and extrapolating it to the quiescent value for the cases where the observational campaign was not extended enough to completely follow the return to the pre-outburst state. Best-fitting models and corresponding parameters are reported in Table 7.2. We note that the assumed 10 per cent error on each bolometric value likely represents only an underestimate (the largest uncertainty arising from the poorly constrained distance of the source in almost all cases). For some extensively monitored outbursts we verified that the choice of larger uncertainties on these values yielded lower values for the χ^2 , as expected, however with no significant alteration of the decay pattern and of our estimates for the characteristic time scales and the amount of energy released during the event.

Table 7.1: Spectral fitting results of magnetar outbursts. The year of the outburst onset is indicated in parentheses. NTZ refers to a resonant Compton scattering model based on three-dimensional Monte Carlo simulations (Nobili et al. 2008a,b), and was applied only in the cases where a power-law spectral component was needed when fitting the data to ‘empirical’ models. To account for interstellar absorption, we adopted the TBABS model, photoionization cross-sections from Verner et al. (1996) and chemical abundances from Wilms et al. (2000). The hydrogen column density was tied up among all the observations targeting a specific source and errors on this parameter are quoted at the 1σ confidence level.

Source	Observatory (# obs)	Best-fitting model	N_{H} (emp) (10^{22} cm^{-2})	N_{H} (NTZ)
SGR 1627–41 (1998)	<i>BeppoSAX</i> (4)	BB	6 ± 1	–
	<i>XMM-Newton</i> (2)	BB	6^{+2}_{-1}	–
	<i>Chandra</i> (4)	BB	10^{+2}_{-1}	–
SGR 1627–41 (2008)	<i>Swift</i> (21)	BB	9 ± 2	–
	<i>XMM-Newton</i> (1)	2BB	22 ± 5	–
	<i>Chandra</i> (4)	BB	10 ± 2	–
1E 2259+586 (2002)	<i>XMM-Newton</i> (8)	3BB	0.816 ± 0.007	–
1E 2259+586 (2012)	<i>Swift</i> (44)	2BB (1–20)	0.38 ± 0.01	–
		2BB (21–44)	0.38 (fixed)	–
XTEJ1810–197 (2003)	<i>Swift</i> (4)	BB	–	–
	<i>XMM-Newton</i> (22)	3BB (1–11)	1.22 ± 0.02	–
		2BB (11–22)		–
<i>Chandra</i> (12)	2BB	–		
SGR 1806–20 (2004)	<i>XMM-Newton</i> (10)	2BB	8.5 ± 0.1	–
CXOU J164710.2–455216 (2006)	<i>Swift</i> (18)	BB+PL	3.06 ± 0.08	$2.43^{+0.04}_{-0.03}$
	<i>XMM-Newton</i> (5) ^a	BB+PL	3.01 (fixed)	2.39 (fixed)
		<i>Chandra</i> (5)	BB+PL	3.01 ± 0.04
CXOU J164710.2–455216 (2011)	<i>Swift</i> (7)	BB	2.6 ± 0.3	–
	<i>XMM-Newton</i> (1)	2BB	2.5 ± 0.1	–
		<i>Chandra</i> (1)	BB	2.8 ± 0.1
SGR 0501+4516 (2008)	<i>Swift</i> (62) ^b	BB+PL (1–20)	1.319 (fixed)	$0.708^{+0.007}_{-0.006}$
		BB+PL (21–40)	1.319 (fixed)	0.71 ± 0.03
		BB+PL (41–62)	1.319 (fixed)	0.708 (fixed)
	<i>XMM-Newton</i> (6)	BB+PL	1.319 ± 0.009	0.705 ± 0.004
	<i>Chandra</i> (1)	BB+PL	1.33 ± 0.03	0.85 ± 0.01
1E 1547–5408 (2008)	<i>Swift</i> (15)	BB+PL	4.9 ± 0.1	$4.65^{+0.05}_{-0.07}$
	<i>Chandra</i> (5)	BB+PL	5.1 ± 0.2	4.83 ± 0.06
1E 1547–5408 (2009)	<i>Swift</i> (99)	BB+PL (1–20)	$4.91^{+0.03}_{-0.13}$	4.59 ± 0.09
		BB+PL (21–40)	4.91 (fixed)	4.59 (fixed)
		BB+PL (41–60)	4.91 (fixed)	4.59 (fixed)
		BB+PL (61–80)	4.91 (fixed)	4.59 (fixed)
		BB+PL (81–99)	4.91 (fixed)	4.59 (fixed)
	<i>XMM-Newton</i> (2) ^a	BB+PL	4.9 (fixed)	4.65 (fixed)
		<i>Chandra</i> (3)	BB+PL	5.0 ± 0.1
SGR 0418+5729 (2009)	<i>Swift</i> (24)	BB	$0.30^{+0.03}_{-0.02}$	–
	<i>XMM-Newton</i> (11)	2BB (1)	$0.57^{+0.04}_{-0.03}$	–
		BB (2–11)	0.29 ± 0.04	–
	<i>Chandra</i> (4)	BB	0.2 ± 0.1	–
SGR 1833–0832 (2010)	<i>Swift</i> (27)	BB	13.1 ± 0.9	–
	<i>XMM-Newton</i> (3)	BB	15.5 ± 0.4	–
		<i>Chandra</i> (1)	BB	13.7 ± 0.9

Table 7.1: Continued.

Source	Observatory (# obs)	Best-fitting model	N_{H} (emp) (10^{22} cm^{-2})	N_{H} (NTZ)
Swift J1822.3–1606 (2011)	<i>Swift</i> (60)	BB+PL (1–20)	0.68 (fixed)	0.289 (fixed)
		BB+PL (21–40)	0.68 (fixed)	0.289 (fixed)
		BB+PL (40–60)	0.68 (fixed)	0.289 (fixed)
	<i>XMM-Newton</i> (5)	BB+PL	0.68 ± 0.01	0.289 ± 0.004
Swift J1834.9–0846 (2011)	<i>Chandra</i> (5)	BB+PL	0.62 ± 0.02	0.283 ± 0.005
	<i>Swift</i> (19)	BB	19 (fixed)	–
	<i>XMM-Newton</i> (3)	BB	15 ± 1	–
	<i>Chandra</i> (4)	BB	19 ± 1	–
1E 1048.1–5937 (2011)	<i>Swift</i> (55)	BB (1–20)	0.61 ± 0.02	–
		BB (21–40)	0.61 (fixed)	–
		BB (41–55)	0.61 (fixed)	–
	<i>XMM-Newton</i> (1)	3BB	1.03 ± 0.03	–
SGR 1745–2900 (2013)	<i>Chandra</i> (2)	2BB	0.97 ± 0.03	–
	<i>Chandra</i> (35)	BB	18.7 ± 0.1	–
SGR 1935+2154 (2014)	<i>Swift</i> (32)	BB (1–20)	2.3 ± 0.2	–
		BB (21–32)	2.3 (fixed)	–
	<i>XMM-Newton</i> (9)	2BB	2.37 ± 0.07	–
	<i>Chandra</i> (3)	2BB	2.8 ± 0.1	–

^a The absorption column density was fixed to a value compatible with that inferred from the fits of the data sets from the other X-ray instruments, because a significant excess in the fit residuals was detected below about 1 keV independently on the choice of the background region and of the adopted spectral model (see e.g. Bernardini et al. 2009 for this issue). We obtained acceptable fits in all cases.

^b The absorption column density was fixed to the value obtained from the fit to the *XMM-Newton* spectra, because the XRT was operating in WT in all cases and bumps of instrumental origin were present at $\sim 0.8 - 1$ keV (see the text). We obtained acceptable fits in all cases.

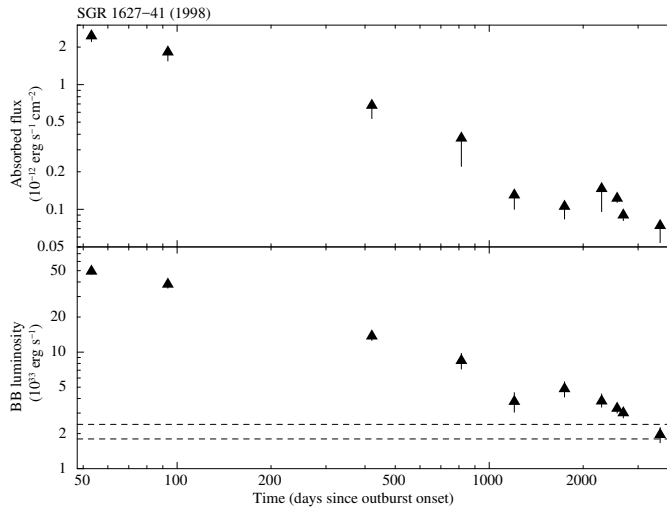


Figure 7.1: Temporal evolution of the fluxes and luminosities for the BB model applied to the X-ray data of SGR 1627–41. The dashed lines mark the 1- σ confidence level range for the quiescent luminosity (see Table 7.4). A distance of 11 kpc has been assumed.

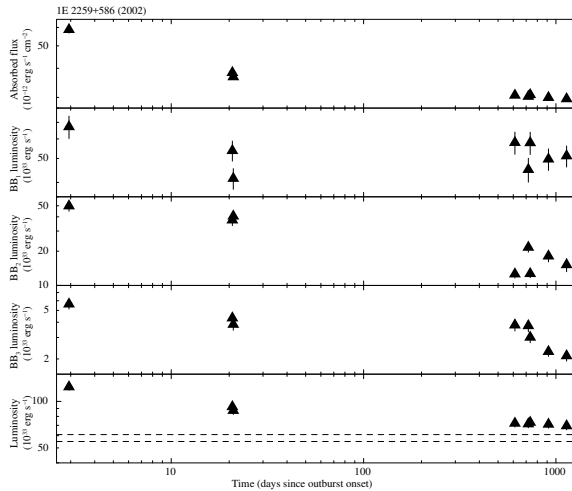


Figure 7.2: Temporal evolution of the fluxes and luminosities for the 3BB model applied to the *XMM-Newton* data of the 2002 outburst of 1E 2259+586. The dashed lines mark the 1- σ confidence level range for the quiescent luminosity (see Table 7.4). A distance of 3.2 kpc has been assumed.

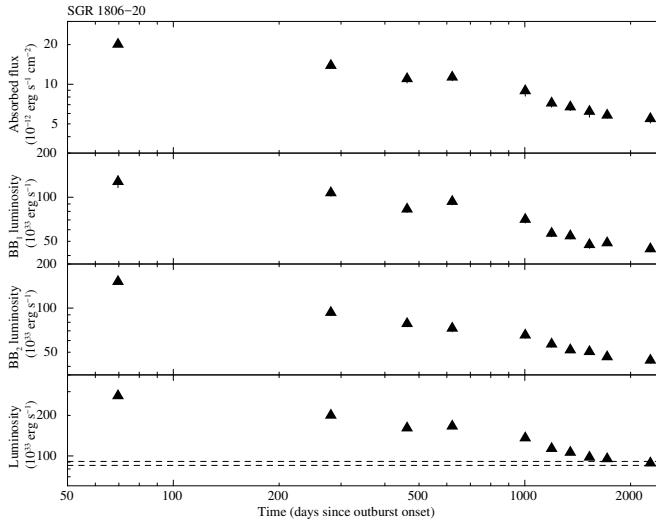


Figure 7.3: Temporal evolution of the fluxes and luminosities for the 2BB model applied to the *XMM-Newton* data of SGR 1806–20. The dashed lines mark the $1\text{-}\sigma$ confidence level range for the quiescent luminosity (see Table 7.4). A distance of 8.7 kpc has been assumed.

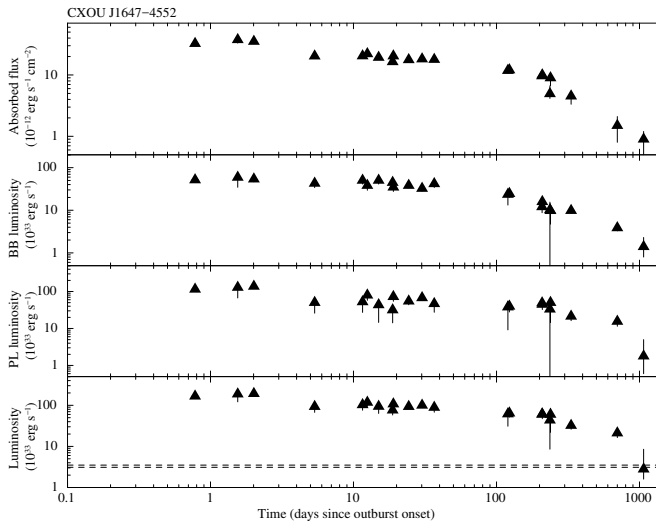


Figure 7.4: Temporal evolution of the fluxes and luminosities for the BB+PL model applied to the X-ray data of CXOU J164710.2–455216. The dashed lines mark the $1\text{-}\sigma$ confidence level range for the quiescent luminosity (see Table 7.4). A distance of 4 kpc has been assumed.

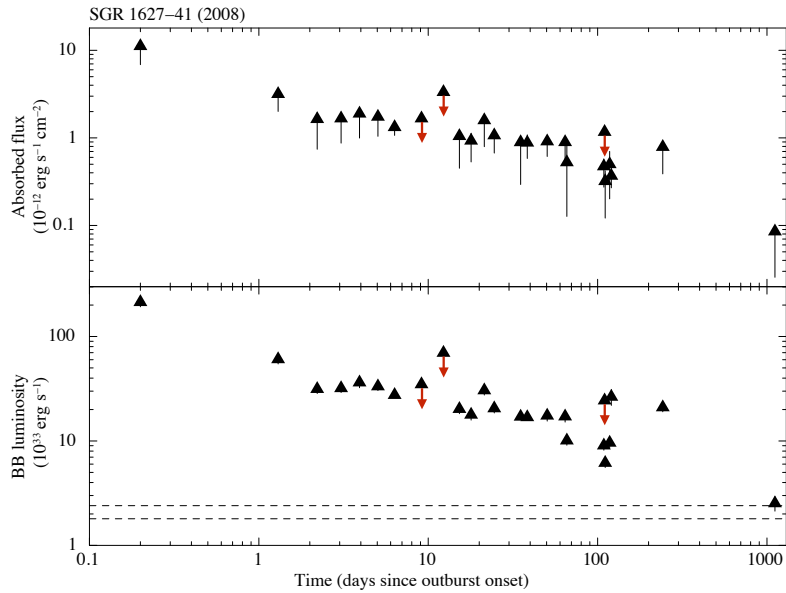


Figure 7.5: Temporal evolution of the fluxes and luminosities for the BB model applied to the X-ray data of SGR 1627–41. The dashed lines mark the $1\text{-}\sigma$ confidence level range for the quiescent luminosity (see Table 7.4). The red arrows indicate the $3\text{-}\sigma$ upper limits. A distance of 11 kpc has been assumed.

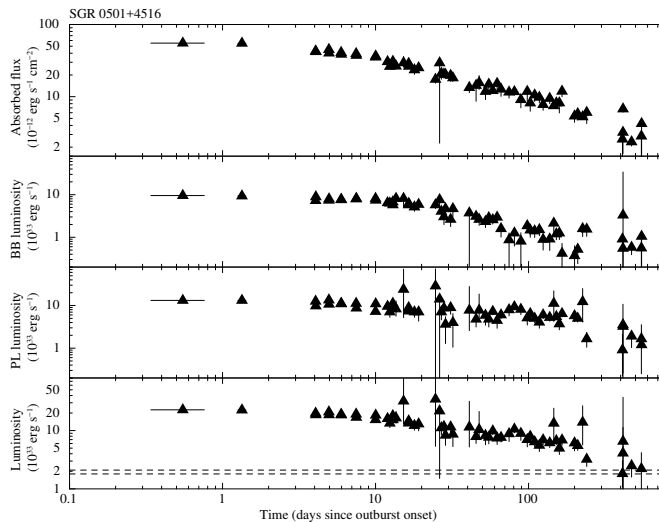


Figure 7.6: Temporal evolution of the fluxes and luminosities for the BB+PL model applied to the *Swift* XRT data of SGR 0501+4516. The dashed line marks the approximate value for the quiescent luminosity (see Table 7.4). A distance of 1.5 kpc has been assumed.

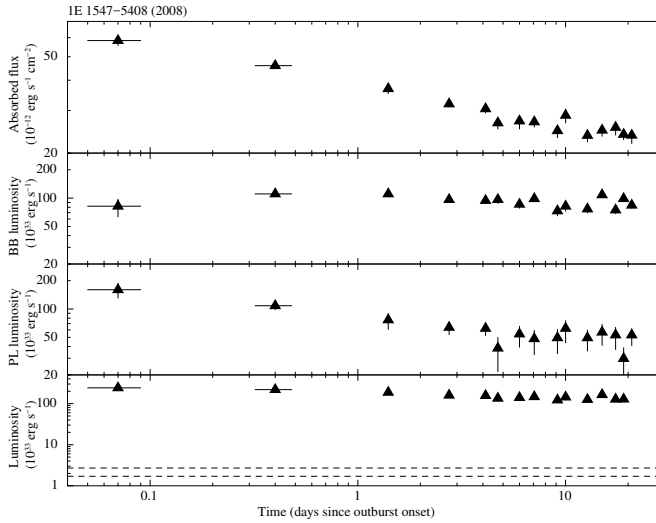


Figure 7.7: Temporal evolution of the fluxes and luminosities for the BB+PL model applied to the *Swift* XRT data of the 2008 outburst of 1E 1547–5408. The dashed lines mark the 1- σ confidence level range for the quiescent luminosity (see Table 7.4). A distance of 4.5 kpc has been assumed.

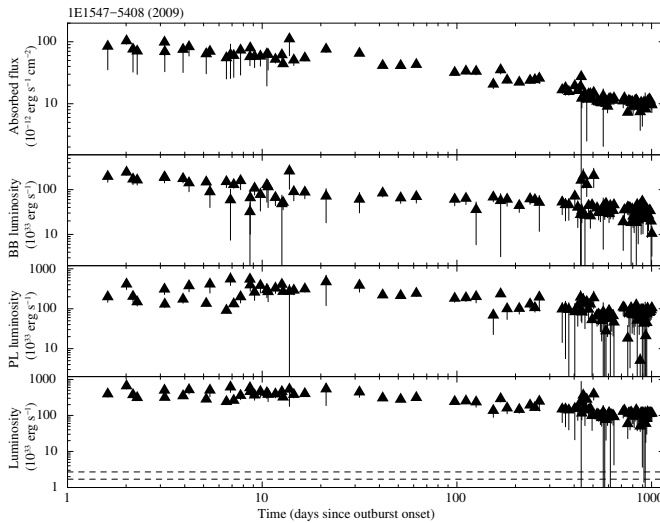


Figure 7.8: Temporal evolution of the fluxes and luminosities for the BB+PL model applied to the *Swift* XRT data of the 2009 outburst of 1E 1547–5408. The dashed lines mark the 1- σ confidence level range for the quiescent luminosity (see Table 7.4). A distance of 4.5 kpc has been assumed.

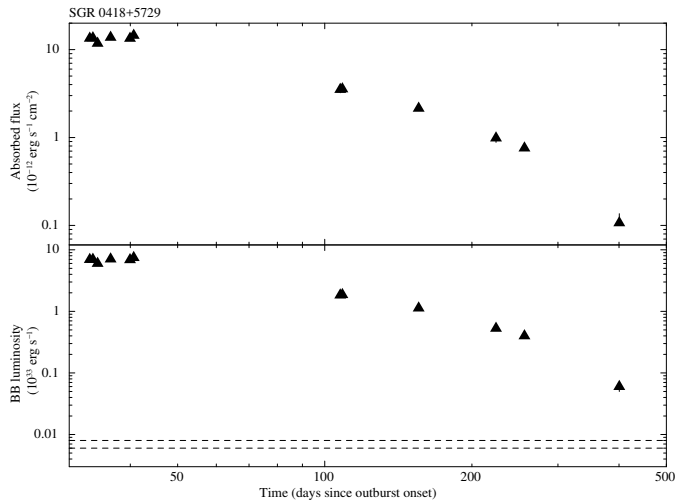


Figure 7.9: Temporal evolution of the fluxes and luminosities for the BB+PL model applied to the *Swift* XRT data of the outburst of SGR 0418+5729. The dashed lines mark the $1\text{-}\sigma$ confidence level range for the quiescent luminosity (see Table 7.4). A distance of 2 kpc has been assumed.

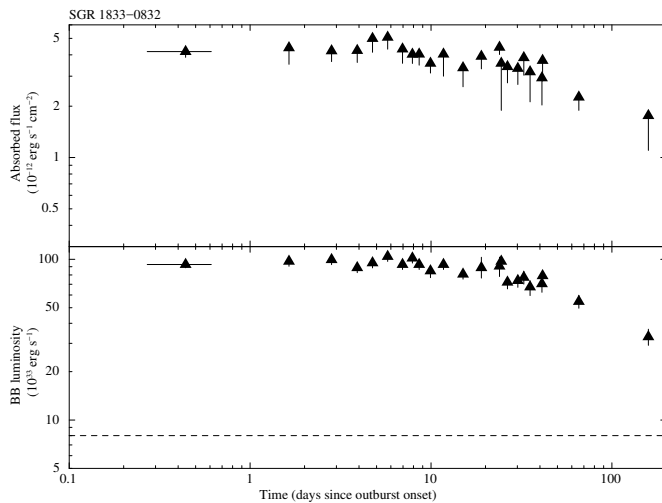


Figure 7.10: Temporal evolution of the fluxes and luminosities for the BB+PL model applied to the *Swift* XRT data of the outburst of SGR 1833–0832. The dashed line marks the upper limit (at the $3\text{-}\sigma$ confidence level) for the quiescent luminosity (see Table 7.4). A distance of 10 kpc has been assumed.

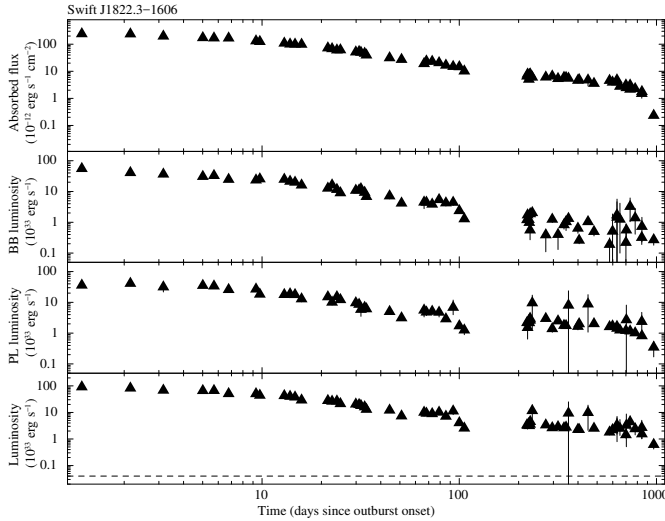


Figure 7.11: Temporal evolution of the fluxes and luminosities for the BB+PL model applied to the outburst of Swift J1822.3–1606. The dashed line marks the value for the quiescent luminosity (see Table 7.4). A distance of 1.6 kpc has been assumed.

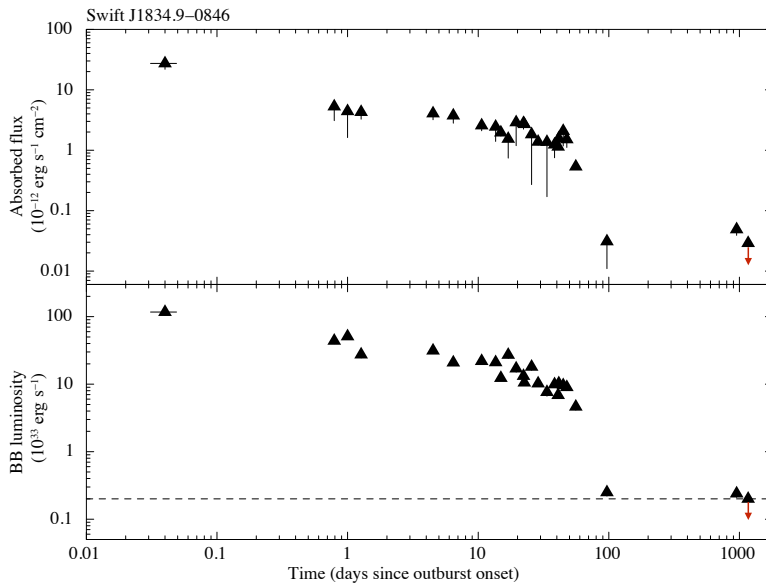


Figure 7.12: Temporal evolution of the fluxes and luminosities for the BB model applied to the X-ray data of the outburst of Swift J1834.9–0846. The dashed line marks the upper limit (at the 3- σ confidence level) for the quiescent luminosity (see Table 7.4). The red arrows indicate the 3- σ upper limits. A distance of 4.2 kpc has been assumed.

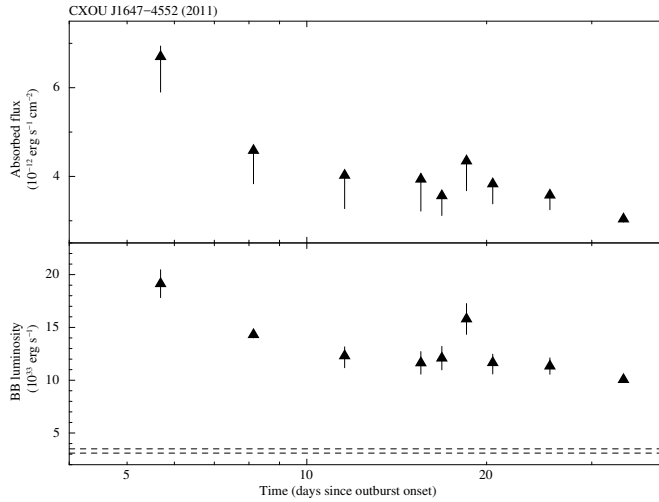


Figure 7.13: Temporal evolution of the fluxes and luminosities for the BB model applied to the X-ray data of the 2011 outburst of CXOU J164710.2–455216. The dashed lines mark the $1\text{-}\sigma$ confidence level range for the quiescent luminosity (see Table 7.4). A distance of 4 kpc has been assumed.

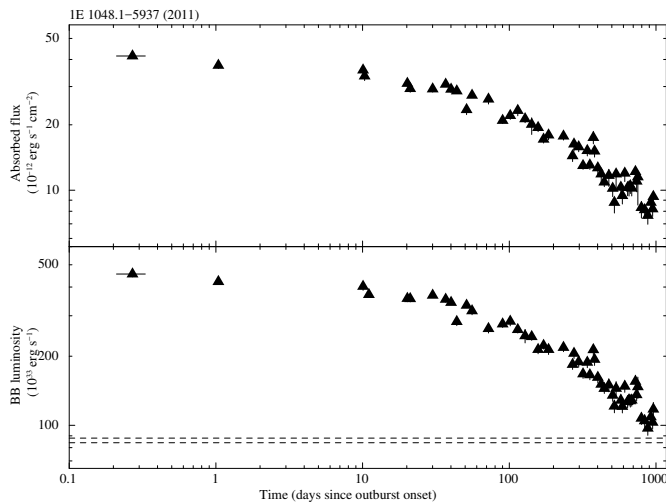


Figure 7.14: Temporal evolution of the fluxes and luminosities for the BB model applied to the *Swift* XRT data of the 2011 outburst of 1E 1048.1–5937. The dashed lines mark the $1\text{-}\sigma$ confidence level range for the quiescent luminosity (see Table 7.4). A distance of 9 kpc has been assumed.

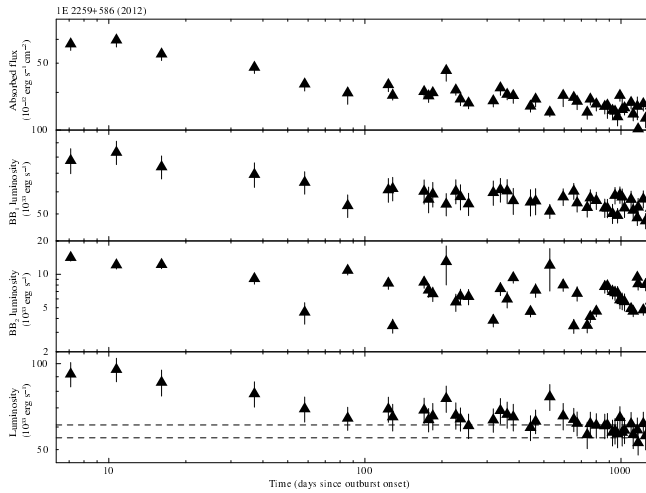


Figure 7.15: Temporal evolution of the fluxes and luminosities for the 2BB model applied to the *Swift* data of the 2012 outburst of 1E 2259+586. The dashed lines mark the 1- σ confidence level range for the quiescent luminosity (see Table 7.4). A distance of 3.2 kpc has been assumed.

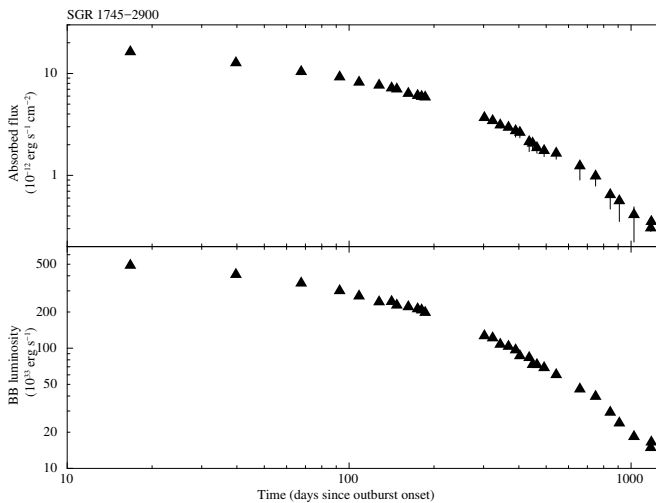


Figure 7.16: Temporal evolution of the fluxes and luminosities for the BB+PL model applied to the *Chandra* data of the outburst of SGR 1745–2900. The dashed lines mark the 1- σ confidence level range for the quiescent luminosity (see Table 7.4). A distance of 8.3 kpc has been assumed.

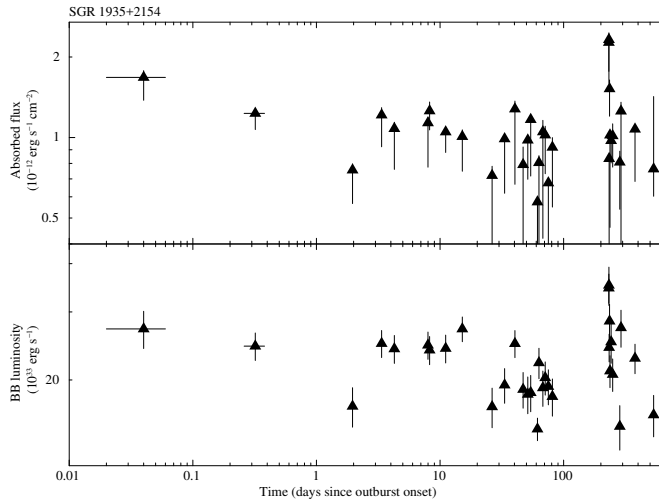


Figure 7.17: Temporal evolution of the fluxes and luminosities for the BB model applied to the *Swift* XRT data of the outburst of SGR 1935+2154. A distance of 9 kpc has been assumed (see Israel et al. 2016).

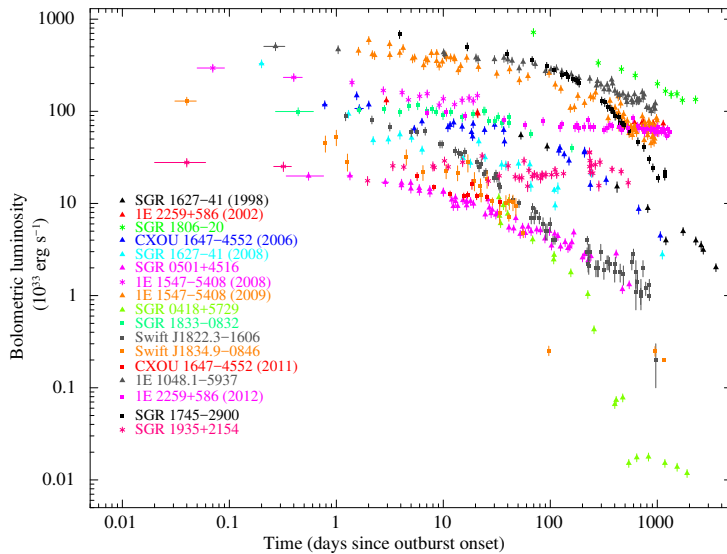


Figure 7.18: Temporal evolution of the bolometric (0.01–100 keV) luminosities for all outbursts re-analysed in the present work. The distances assumed are those quoted in Table 7 of Olausen & Kaspi (2014) (see also the McGill magnetar catalogue).

Table 7.2: Results of the empirical modelling of the outburst decays for the total bolometric luminosities. The cooling curves were fitted with one or multiple exponential functions plus a constant (see the text for details). Errors on the best-fitting parameters are quoted at the 1σ confidence level for a single parameter of interest.

Source	Component	Best-fitting decay model	τ (d)	τ_1 (d)	τ_2 (τ_3) (d)	E (erg)
SGR 1627–41 (1998)	bol	2EXP	–	234^{+37}_{-38}	1307^{+373}_{-245}	1.8×10^{42}
1E 2259+586 (2002)	bol	EXP	21 ± 13	–	–	1.4×10^{41}
CXOU J1647–4552 (2006)	bol	3EXP	–	238^{+13}_{-17}	53 ± 3 ($2.4^{+0.8}_{-0.6}$)	1.3×10^{42}
SGR 1627–41 (2008)	bol	3EXP	–	387^{+55}_{-54}	32^{+6}_{-5} ($0.56^{+0.07}_{-0.06}$)	1.0×10^{42}
SGR 0501+4516	bol	2EXP	–	13 ± 2	147^{+12}_{-11}	9.3×10^{40}
1E 1547–5408 (2008)	bol	EXP	$2.0^{+0.6}_{-0.5}$	–	–	1.3×10^{42}
1E 1547–5408 (2009)	bol	2EXP	–	1643^{+336}_{-228}	90^{+10}_{-9}	1.8×10^{43}
SGR 0418+5729	bol	EXP	75 ± 1	–	–	8.3×10^{40}
SGR 1833–0832	bol	EXP	128^{+26}_{-4}	–	–	1.1×10^{42}
Swift J1822.3–1606	bol	3EXP	–	460^{+35}_{-31}	28^{+4}_{-3} (7 ± 2)	3.0×10^{41}
Swift J1834.9–0846	bol	2EXP	–	17.7 ± 0.4	0.08 ± 0.01	1.5×10^{41}
CXOU J1647–4552 (2011)	bol	EXP	47 ± 16	–	–	5.5×10^{40}
1E 1048.1–5937	bol	2EXP	–	382^{+45}_{-31}	39^{+26}_{-16}	8.3×10^{42}
1E 2259+586 (2012)	bol	EXP	206^{+115}_{-74}	–	–	3.4×10^{41}
SGR 1745–2900	bol	2EXP	–	324^{+27}_{-17}	81^{+6}_{-20}	1.0×10^{43}

7.6 Quiescent flux vs. maximum flux increase

Figure 7.19 shows the maximum flux increase as a function of the quiescent (steady) X-ray flux for all magnetars that so far have displayed enhancements and/or variability in their X-ray emission. To have a more complete sample, we have also included SGR 1900+14 and 1E 1841–045. In fact, although extensive X-ray observations in the *Swift*, *XMM–Newton* and *Chandra* era did not detect major X-ray outbursts from these targets, re-brightenings or subtle variations around their persistent activity have been nevertheless reported throughout the last 15 years. SGR 1900+14 exhibited a giant flare in 1998, and re-brightened in the X-rays on two occasions, 2001 April and 2006 March. Its flux decline has been monitored by *Chandra* and *XMM–Newton* until 2008, and after both episodes the source reached the same minimum flux level, which we identify as the bona fide quiescent one (Göğüş et al. 2011; see also Figure 7.1 for the *Swift* XRT light curve). 1E 1841–045 also showed sporadic bursting activity between 2010 May and 2011 July (a total of 9 bursts were indeed recorded by *Swift* BAT and *Fermi* GBM), and some deviation from the source historical persistent X-ray flux has been noticed between 2008 and 2011 (Lin et al. 2011). The source has been subsequently monitored by *Swift* XRT about 120 times until the end of 2016 April (see again Figure 7.1 for an updated long-term X-ray light curve). Finally, a recent analysis by Scholz et al. (2014) has shown that the flux of the magnetar 1RXS J170849.0–400910 has remained constant within uncertainties between 2003 and 2013, in contradiction with previous claims (Götz et al. 2007). In particular, the maximum variability for the X-ray flux is constrained to be lower than 10 per cent over this decade. We also verified that the source remained approximately steady over the last 3 years (between 2013 April and 2016 May), by visually inspecting the long-term X-ray light curve generated using the 58 *Swift* XRT observations carried out during this period. In light of these characteristics, we decided not to include this source for our purposes.

For each magnetar, spectra relative to the first observation following the outburst onset were fitted again, but this time individually, to accurately measure fluxes and luminosities at the very early phases of the outburst. For the sources showing low-level variability (see above), we extracted and fitted the spectrum relative to the observation where the source is found at the highest flux ever. The inferred values are listed in Table 7.3. The quiescent 0.3–10 keV fluxes and luminosities for all magnetars monitored so far are reported in Table 7.4. Bolometric luminosities are also quoted. We also calculated the flux during pre-outburst observations (if available), and considered the lowest value historically to estimate the quiescent level. For the sources where only low-level variability has been reported, we focused on the observations with high counting statistics to derive the persistent flux.

In all cases, the spectra were fitted using thermal models (i.e., one or multiple black body components) or the NTZ model, to avoid possible overestimates in the values for the fluxes introduced when fitting a power-law model to the data. For *ROSAT* data, we extrapolated the 0.3–2.4 keV fluxes after having assigned new response matrices with DUMMYRSP. For the cases where the source is not detected, we applied the SRCFLUX task of CIAO (for the *Chandra* observations of Swift J1834.9–0846 and SGR 1745–2900)

and the EUPPER tool of SAS (for the *XMM-Newton* observation of SGR 1833–0832) to derive conservative $3\text{-}\sigma$ upper limits on the net count rates. We found values of 2×10^{-4} , 1.1×10^{-3} and 7×10^{-4} counts s^{-1} for Swift J1834.9–0846, SGR 1745–2900 and SGR 1833–0832, respectively. We then assumed a black body spectral model with $kT = 0.2 - 0.6$ keV (see e.g. Table 3 in Olausen & Kaspi 2014), and the same column density derived from the joint spectral fits of the outburst decay, to infer upper limits on the fluxes with the Portable, Interactive Multi-Mission Simulator (PIMMS, v. 4.8). For the case of SGR 1833–0832, we compared our estimate with that calculated using the ‘Flux Limits from Images from *XMM-Newton*’ server (FLIX²⁰), and obtained consistent results. We stress that this procedure gives only a coarse approximation for the upper limits, these being strongly dependent on the unknown black body temperature in quiescence.

A significant anti-correlation between the quiescent X-ray flux (luminosity) and the maximum flux (luminosity) increase can be clearly observed in Figures 7.19 and 7.20 (at a significance of 5σ for the case of Figure 7.19, according to the Spearman rank correlation test).

²⁰See <http://www.ledas.ac.uk/flix/flix.html>

Table 7.3: Maximum fluxes and luminosities (0.3–10 keV) for magnetars showing major outbursts or variations in their persistent emission. Errors are reported at the 1σ confidence level.

Source	Date	Observatory	Obs ID	Exposure (ks)	Abs/Unabs flux (erg cm ⁻² s ⁻¹)	L_p (erg s ⁻¹)
SGR 1627–41	1998 Aug 07	<i>BeppoSAX</i>	70566001	44.9	$(2.4 \pm 0.1) \times 10^{-12}$ $(3.6 \pm 0.2) \times 10^{-12}$	$(5.2 \pm 0.3) \times 10^{34}$
SGR 1900+14	2001 Apr 22	<i>Chandra</i>	2458	20.1	$(1.02 \pm 0.02) \times 10^{-11}$ $(1.86 \pm 0.05) \times 10^{-11}$	$(3.48 \pm 0.09) \times 10^{35}$
1E 2259+586	2002 Jun 21	<i>XMM-Newton</i>	0155350301	18.4	$(5.87 \pm 0.01) \times 10^{-11}$ $(1.006 \pm 0.009) \times 10^{-10}$	$(1.23 \pm 0.01) \times 10^{35}$
SGR 1806–20	2004 Oct 06	<i>XMM-Newton</i>	0164561101	12.9	$(2.68 \pm 0.02) \times 10^{-11}$ $(4.0 \pm 0.1) \times 10^{-11}$	$(3.62 \pm 0.09) \times 10^{35}$
SGR 1900+14	2006 Mar 29	<i>Chandra</i>	6709	40.0	$(6.10 \pm 0.09) \times 10^{-12}$ $(1.20 \pm 0.03) \times 10^{-11}$	$(2.24 \pm 0.06) \times 10^{35}$
CXOU J1647–4552	2006 Sep 21	<i>Swift</i>	00030806001	7.7	$(3.36 \pm 0.08) \times 10^{-11}$ $(6.1 \pm 0.5) \times 10^{-11}$	$(1.2 \pm 0.1) \times 10^{35}$
4U 0142+61	2007 Jan 13	<i>XMM-Newton</i>	0404860301	4.4	$(1.260 \pm 0.004) \times 10^{-10}$ $(2.329 \pm 0.006) \times 10^{-10}$	$(3.612 \pm 0.009) \times 10^{35}$
SGR 1627–41	2008 May 28	<i>Swift</i>	00312579001	2.0	$(1.2 \pm 0.2) \times 10^{-11}$ $(2.2 \pm 0.4) \times 10^{-11}$	$(3.2 \pm 0.6) \times 10^{35}$
SGR 0501+4516	2008 Aug 23	<i>XMM-Newton</i>	0560191501	33.8	$(4.03 \pm 0.01) \times 10^{-11}$ $(1.28 \pm 0.08) \times 10^{-10}$	$(3.4 \pm 0.2) \times 10^{34}$
1E 1547–5408	2008 Oct 03	<i>Swift</i>	00330353000	4.1	$(6.2 \pm 0.2) \times 10^{-11}$ $(9.4 \pm 0.7) \times 10^{-11}$	$(2.3 \pm 0.2) \times 10^{35}$
1E 1547–5408	2009 Jan 23	<i>Swift</i>	00340923000	1.7	$(8.2 \pm 0.5) \times 10^{-11}$ $2.0^{+1.4}_{-0.4} \times 10^{-10}$	$5^{+3}_{-1} \times 10^{35}$
SGR 0418+5729	2009 Jun 11	<i>RXTE</i>	94048–03–01–00	5.2	$(3.31 \pm 0.06) \times 10^{-11}$ $(3.41 \pm 0.06) \times 10^{-11}$	$(1.63 \pm 0.03) \times 10^{34}$
SGR 1833–0832 ^a	2010 Mar 20	<i>Swift</i>	00416485000	29.0	$(4.0 \pm 0.2) \times 10^{-12}$ $(8.5 \pm 0.7) \times 10^{-12}$	$(1.02 \pm 0.08) \times 10^{35}$
1E 1841–045	2011 Jul 02	<i>Swift</i>	00456505000	1.4	$(2.0 \pm 0.2) \times 10^{-11}$ $(2 \pm 1) \times 10^{-10}$	$(1.7 \pm 0.9) \times 10^{36}$
Swift J1822.3–1606	2011 Jul 16	<i>Swift</i>	00032033001	1.6	$(2.35 \pm 0.04) \times 10^{-10}$ $(2.61 \pm 0.05) \times 10^{-10}$	$(8.0 \pm 0.2) \times 10^{34}$
Swift J1834.9–0846	2011 Aug 07	<i>Swift</i>	00458907000	1.5	$(3.2 \pm 0.6) \times 10^{-11}$ $(4.8 \pm 0.8) \times 10^{-11}$	$(1.0 \pm 0.2) \times 10^{35}$
CXOU J1647–4552	2011 Sep 25	<i>Swift</i>	00030806020	3.1	$(6.5 \pm 0.5) \times 10^{-12}$ $(1.1 \pm 0.2) \times 10^{-11}$	$(2.1 \pm 0.4) \times 10^{34}$
1E 1048.1–5937	2011 Dec 31	<i>Swift</i>	00031220066	2.0	$(4.6 \pm 0.3) \times 10^{-11}$ $(5.9 \pm 0.4) \times 10^{-11}$	$(5.7 \pm 0.4) \times 10^{35}$
1E 2259+586	2012 Apr 28	<i>Swift</i>	00032035021	3.9	$(5.7 \pm 0.1) \times 10^{-11}$ $(7.5 \pm 0.2) \times 10^{-11}$	$(9.2 \pm 0.2) \times 10^{34}$
SGR 1745–2900	2013 Apr 29	<i>Chandra</i> ^b	14701	9.7	$\sim 1.8 \times 10^{-11}$ $\sim 8.3 \times 10^{-11}$	$\sim 6.8 \times 10^{35}$
SGR 1935+2154 ^c	2014 Jul 05	<i>Swift</i>	00603488000	3.4	$(1.7 \pm 0.2) \times 10^{-12}$ $(2.6 \pm 0.4) \times 10^{-12}$	$(2.5 \pm 0.4) \times 10^{34}$

^a A distance of 10 kpc has been assumed.

^b We consider here the first *Chandra* observation, carried out with the HRC. The flux was estimated assuming a black body model at 0.9 keV and column density $N_{\text{H}} = 1.87 \times 10^{23} \text{ cm}^{-2}$.

Table 7.4: Quiescent fluxes and luminosities for magnetars showing major outbursts or variations in their persistent emission. Bolometric luminosities are also listed. Errors are reported at the 1σ confidence level, upper limits at the 3σ confidence level.

Source	Date	Observatory	Obs ID	Exposure (ks)	Abs/Unabs flux (erg cm ⁻² s ⁻¹)	$L_{X,q}$ (erg s ⁻¹)	$L_{bol,q}$
SGR 1627-41	2008 Feb 12-13	<i>XMM-Newton</i>	0502140101	47.5	$(8 \pm 1) \times 10^{-14}$ $(1.5 \pm 0.3) \times 10^{-13}$	$(2.2 \pm 0.4) \times 10^{33}$	$\sim 2.3 \times 10^{33}$
SGR 1900+14	2005 Sep 22	<i>XMM-Newton</i>	0305580201	19.1	$(3.92 \pm 0.05) \times 10^{-12}$ $(6.7 \pm 0.2) \times 10^{-12}$	$(1.25 \pm 0.04) \times 10^{35}$	$\sim 1.4 \times 10^{35}$
1E 2259+586 ^a	2014 Nov 04 – 2015 Nov 17	<i>Swift</i>	00032035087-114	40.1	$(3.55 \pm 0.02) \times 10^{-11}$ $(4.74 \pm 0.03) \times 10^{-11}$	$(5.8 \pm 0.3) \times 10^{34}$	$\sim 6.1 \times 10^{34}$
XTE J1810-197	1993 Apr 03	<i>ROSAT/PSPC</i>	RP900399N00	5.3	$\sim 5.3 \times 10^{-13}$ $\sim 1.7 \times 10^{-11}$	$\sim 2.5 \times 10^{34}$	$\sim 3.2 \times 10^{34}$
SGR 1806-20	2011 Mar 23	<i>XMM-Newton</i>	0654230401	22.4	$(5.49 \pm 0.07) \times 10^{-12}$ $(9.0 \pm 0.3) \times 10^{-12}$	$(8.2 \pm 0.3) \times 10^{34}$	$\sim 1.4 \times 10^{35}$
XCXOU J1647-4552	2009 Aug 24	<i>XMM-Newton</i>	0604380101	38.2	$(8.0 \pm 0.2) \times 10^{-13}$ $(1.72 \pm 0.08) \times 10^{-12}$	$(3.3 \pm 0.2) \times 10^{33}$	$\sim 3.5 \times 10^{33}$
4U 0142+61	2004 Jul 24	<i>XMM-Newton</i>	0206670201	21.9	$(1.215 \pm 0.002) \times 10^{-10}$ $(2.309 \pm 0.003) \times 10^{-10}$	$(3.58 \pm 0.05) \times 10^{35}$	$\sim 3.8 \times 10^{35}$
SGR 0501+4516	2009 Dec 07 –2010 Feb 21	<i>Swift</i>	0032117465-68	25.1	$(2.5 \pm 0.1) \times 10^{-12}$ $(4.4 \pm 0.3) \times 10^{-12}$	$(1.2 \pm 0.8) \times 10^{33}$	$\sim 1.3 \times 10^{33}$
1E 1547-5408	2006 Jul 01	<i>Chandra</i>	7287	9.5	$(3.2 \pm 0.3) \times 10^{-13}$ $(9 \pm 2) \times 10^{-13}$	$(2.2 \pm 0.5) \times 10^{33}$	$\sim 2.3 \times 10^{33}$
SGR 0418+5729	2014 Aug 13-18	<i>XMM-Newton</i>	0741970201-401	108.1	$(1.01 \pm 0.06) \times 10^{-14}$ $(1.6 \pm 0.2) \times 10^{-14}$	$(7 \pm 1) \times 10^{30}$	$\sim 8 \times 10^{30}$
SGR 1833-0832 ^b	2006 Sep 16	<i>XMM-Newton</i>	0400910101	8.3	$\lesssim 6 \times 10^{-14}$ $\lesssim 7 \times 10^{-13}$	$\lesssim 8 \times 10^{33}$	$\lesssim 8 \times 10^{33}$
1E 1841-045	2000 Jul 29	<i>Chandra</i> ^c	730	10.5	$(2.33 \pm 0.03) \times 10^{-11}$ $(5.00 \pm 0.04) \times 10^{-11}$	$(4.32 \pm 0.03) \times 10^{35}$	$\sim 4.6 \times 10^{35}$
Swift J1822.3-1606	2014 Mar 08	<i>XMM-Newton</i>	0722520101	40.3	$(2.3 \pm 0.8) \times 10^{-13}$ $(6.5 \pm 1.0) \times 10^{-13}$	$(2.0 \pm 0.5) \times 10^{32}$	$\sim 2.3 \times 10^{32}$
Swift J1834.9-0846	2009 Jun 06	<i>Chandra</i>	10126	46.6	$\lesssim 1 \times 10^{-14}$ $\lesssim 1 \times 10^{-13}$	$\lesssim 2 \times 10^{32}$	$\lesssim 2 \times 10^{32}$
1E 1048.1-5937	2011 Aug 06	<i>XMM-Newton</i>	0654870101	21.9	$(5.56 \pm 0.04) \times 10^{-12}$ $(8.9 \pm 0.2) \times 10^{-12}$	$(8.6 \pm 0.2) \times 10^{34}$	$\sim 8.9 \times 10^{34}$
SGR 1745-2900	1999 Sep 21 – 2012 Oct 29	<i>Chandra</i>	129 obs ^d	4808.6	$\lesssim 2 \times 10^{-14}$ $\lesssim 1.5 \times 10^{-12}$	$\lesssim 1 \times 10^{34}$	$\lesssim 1 \times 10^{34}$
SGR 1935+2154 ^e	2014 Oct 04	<i>XMM-Newton</i>	0722412701	16.1	$(8.6 \pm 0.2) \times 10^{-13}$ $(1.7 \pm 0.2) \times 10^{-12}$	$(1.6 \pm 0.1) \times 10^{34}$	$\sim 1.9 \times 10^{34}$

^b The steady level of the source is slightly lower after the 2012 outburst (as measured with *Swift*) compared to that after the 2002 outburst (as measured with *XMM-Newton*), but they are however consistent with each other within the errors. We then consider the more precise value derived from the *XMM-Newton* data sets.

^b A distance of 10 kpc has been assumed.

^c The field around the source has been observed three times by *Chandra* (two with the ACIS set in TE mode and one in CC mode). We consider here the CC-mode observation to minimize pile-up issues.

^d See <http://www.sgra-star.com> for the 2012 *Chandra* X-ray Visionary Project for HETGS Observations of Sgr A* (see e.g. Table 1 in Neilsen et al. 2013 for the log of the observations).

^e A distance of 9 kpc has been assumed.

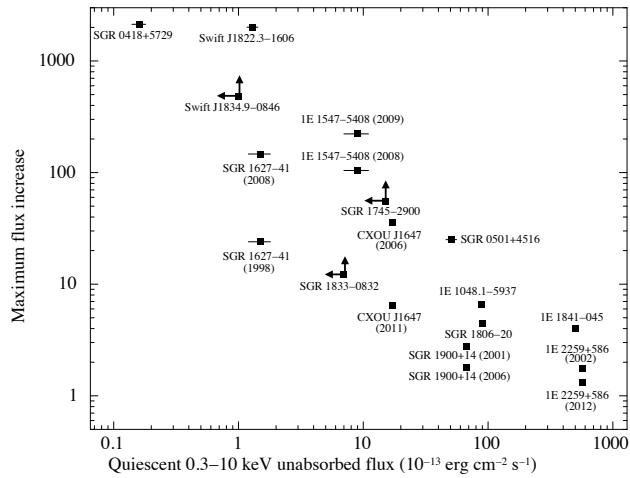


Figure 7.19: Quiescent X-ray unabsorbed flux versus maximum flux increase (all in the 0.3–10 keV band) for all magnetars showing outbursts or variations in their persistent emission. Uncertainties on the maximum flux increase were obtained by propagating the errors on both the maximum and quiescent fluxes. The year of outburst onset is indicated in parentheses for sources that underwent more than one outburst. Errors in the measurements include the uncertainties in the flux values, and upper and lower limits are indicated by arrows.

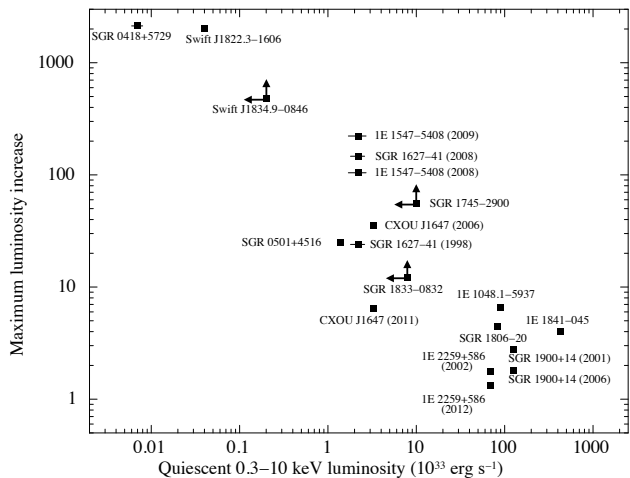


Figure 7.20: Quiescent X-ray luminosity versus maximum luminosity increase (all in the 0.3–10 keV band) for all magnetars showing outbursts or variations in their persistent emission. The year of outburst onset is indicated in parentheses for sources that underwent more than one outburst. Errors in the measurements include the uncertainties in the flux values, and upper and lower limits are indicated by arrows.

7.7 *Swift* XRT light curves

Here we report a series of figures showing the cooling curves for several magnetars outbursts as observed by the X-ray Telescope on board *Swift*. The 0.3–10 keV light curves were created by exploiting both PC- and WT-mode data, and using the online *Swift* XRT data products generator (http://www.swift.ac.uk/user_objects/). This tool corrects for instrumental artifacts such as pile up and bad columns on the CCD (see Evans et al. 2007, 2009 for more details). The source intensity is expressed in terms of the count rate, and thus it does not rely upon the particular choice of the model adopted to describe the spectral data.

7.8 High-statistics quality X-ray spectra and fitted models

Here we report a series of figures showing several high-quality spectra and the best-fitting empirical models (see Table 7.1) for the outbursts that were repeatedly monitored by the *XMM-Newton* or *Chandra* observatories. In each case we plot the $E \times F(E)$ unfolded spectra and the models, to highlight the contributions of the different spectral components to the total X-ray emission (i.e. multiple blackbodies or black body plus power-law; see the dashed lines in the figures) as a function of time. Post-fit residuals in units of standard deviations are also plotted at the bottom of each panel. In all cases, the data points have been re-binned for plotting purpose, to better visualize the trend in the spectral residuals. The colors are associated with the chronological order of the observations according to the following code: black, red, green, blue, light blue, magenta, yellow, orange, yellow+green, green+cyan, blue+cyan, blue+magenta, red+magenta, dark grey, light grey.

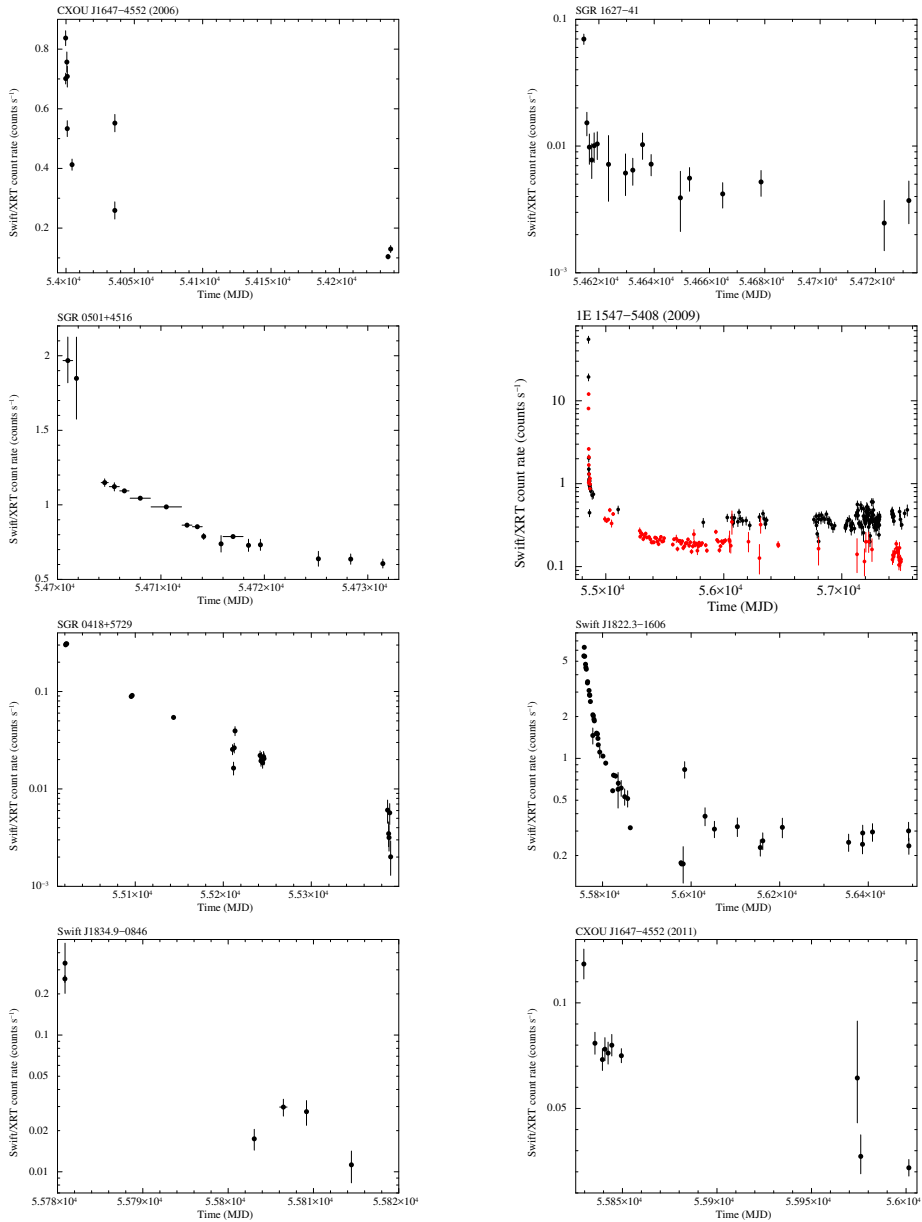


Figure 7.21: *Swift* XRT long-term 0.3–10 keV light curves of densely monitored magnetar outbursts, created using the online *Swift* XRT data products generator (Evans et al. 2009). In case both PC- and WT-mode data are available, black (red) dots refer to data acquired with the XRT set in WT (PC) mode.

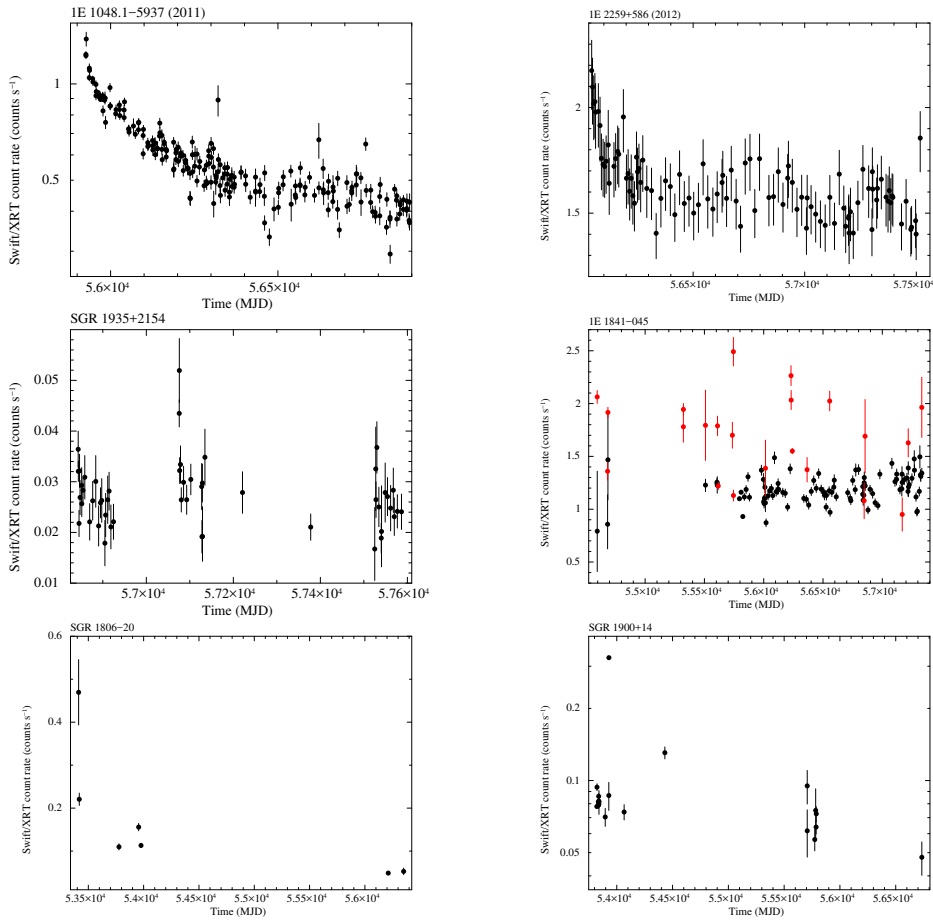


Figure 7.1: Continued.

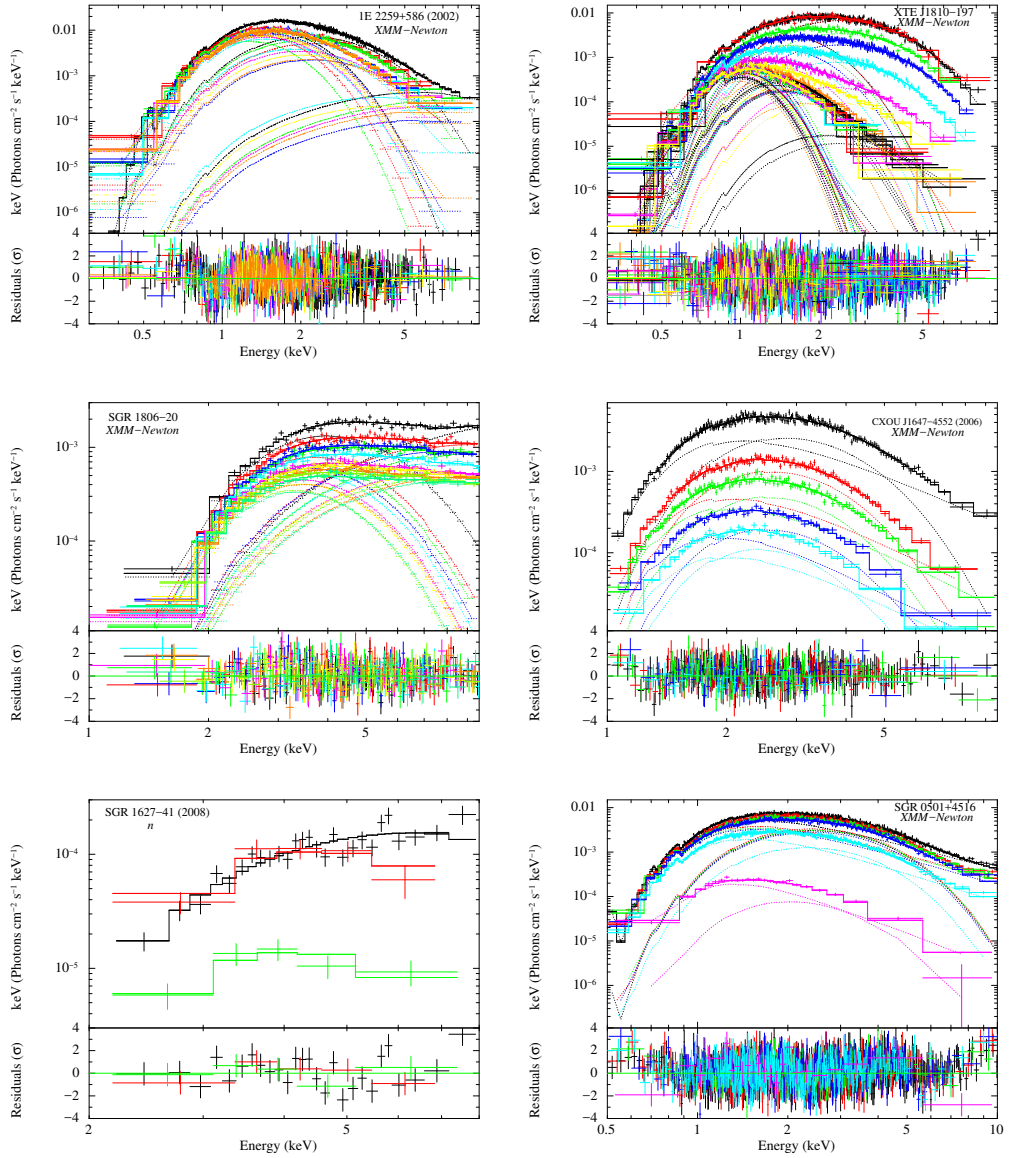


Figure 7.2: High quality spectra for magnetar outbursts that were repeatedly monitored with the *XMM-Newton* or *Chandra* observatories.

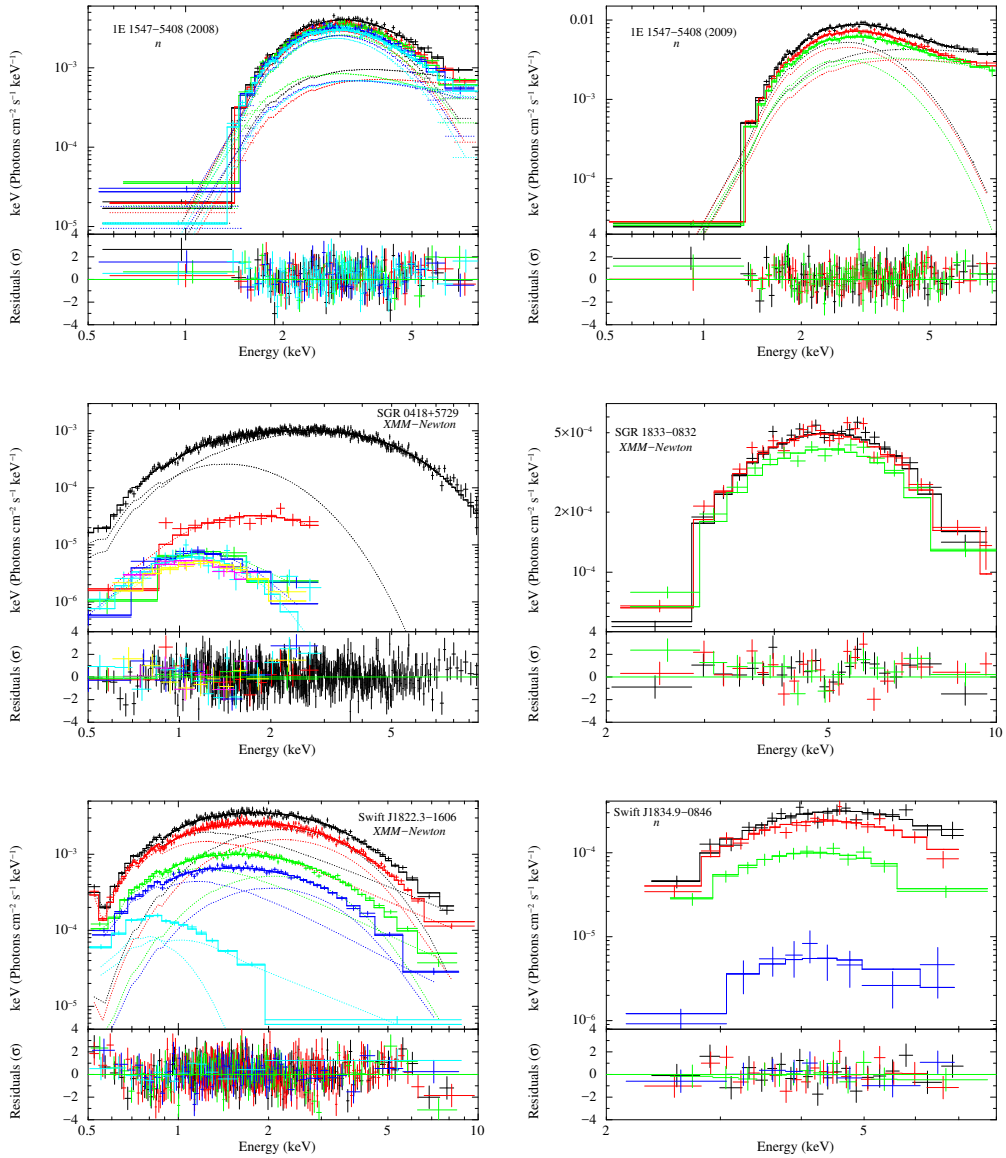


Figure 7.2: Continued.

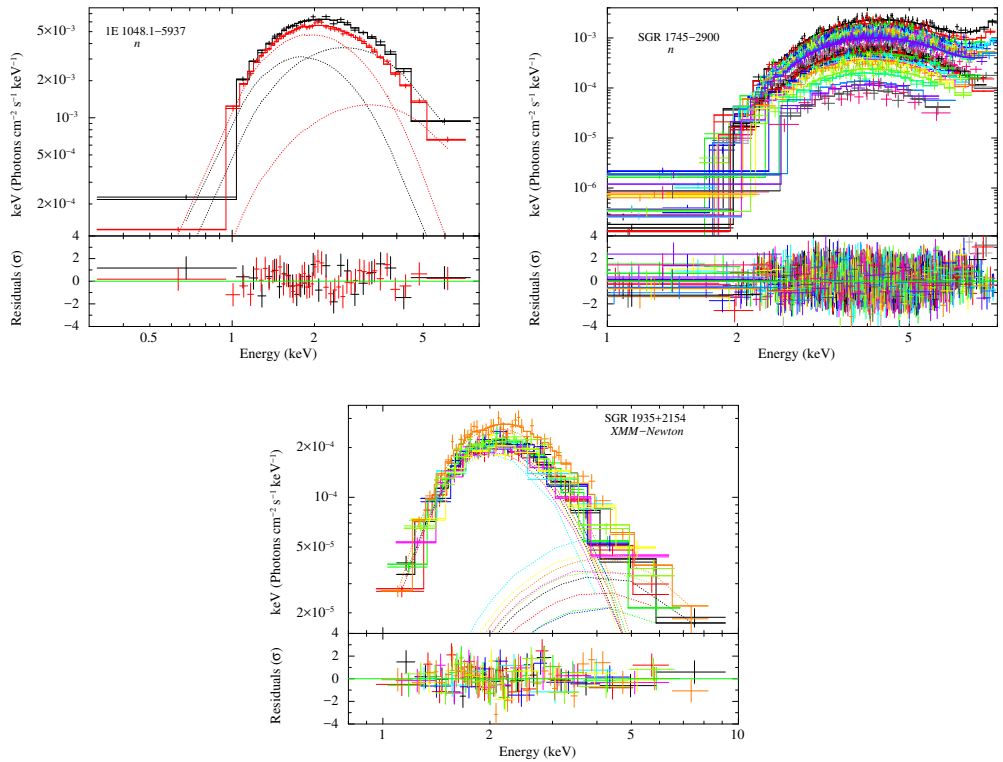


Figure 7.2: Continued.

Multiwavelength study of PSR J1023+0038 and its transitions

Coti Zelati F., Baglio M. C., Campana S., D’Avanzo P., Goldoni P., Masetti N., Muñoz-Darias T., Covino S., Fender R. P., Jiménez Bailón E., Otí-Floranes H., Palazzi E., Ramón-Fox F. G. (2014),
Engulfing a radio pulsar: the case of PSR J1023+0038,
Published in Monthly Notices of the Royal Astronomical Society,
Volume **444**, Issue 2, pp. 1783–1792

Campana S., Coti Zelati F., Papitto A., Rea N., Torres D. F.,
Baglio M. C., D’Avanzo P. (2016),
**A physical scenario for the high and low X-ray luminosity
states in the transitional pulsar PSR J1023+0038**,
Published in Astronomy & Astrophysics, Volume **594**, pp. 31–37

FIRST J102347.6+003841 was discovered by Bond et al. (2002) in the radio band and initially classified as a magnetic cataclysmic variable. Optical studies revealed signs for the presence of an accretion disk in 2001 (Szkody et al. 2003; Wang et al. 2009a), which led to identify this system as a neutron star LMXB (Thorstensen & Armstrong 2005; Homer et al. 2006). The discovery of an eclipsing 1.69-ms radio pulsar, PSR J1023+0038, in a 4.75-h binary system (Archibald et al. 2009), made it the first system showing the potential to alternate an X-ray state, powered by accretion and typical of LMXBs, to its radio pulsar phase, powered by rotation (see Section 1.3). PSR J1023+0038 is a particularly well-studied system owing to its proximity (1368_{-39}^{+42} pc, determined via a radio interferometric measurement of geometric parallax; Deller et al. 2012). Long-term radio observations of the system between 2007 June and 2013 June have provided accurate determination of the rotational and orbital parameters (Archibald et al. 2013), and an estimate of 9.7×10^7 G for the dipolar component of the neutron star magnetic field. The companion is a $\sim 0.24 M_{\odot}$ star, possibly underfilling its Roche lobe by 15 – 20 per cent (McConnell et al. 2014).

8.1 Phenomenology of the system in its current state

PSR J1023+0038 has been the object of extensive multi-wavelength monitoring campaigns since 2013 June, when radio pulsations were not detected at all orbital phases with the Lovell Telescope at Jodrell Bank (Stappers et al. 2014), and double-peaked $H\alpha$ emission lines – the signature of an accretion disk – were clearly observed in the optical spectrum (Halpern et al. 2013; see also Linares et al. 2014; Takata et al. 2014; Bogdanov et al. 2015; McConnell et al. 2015). During the period 2013 July – August, PSR J1023+0038 remained below the sensitivity threshold of the Burst Alert Telescope hard X-ray monitoring instrument on board *Swift*, resulting in a 15–50 keV upper limit for the luminosity of $\sim 10^{35}$ erg s $^{-1}$ (Stappers et al. 2014) and thus ruling out a major accretion outburst from this system.

Radio timing monitoring programs have failed in detecting pulsations at the neutron star spin period in the last 3 years (Patruno et al. 2014; Stappers et al. 2014; Archibald et al. 2015; Bogdanov et al. 2015; Jaodand et al. 2016). Imaging observations between 2013 November and 2014 April unveiled a rapidly variable emission with a flat spectrum, possibly related to partially absorbed synchrotron emission originating in material outflowing from the system (e.g., in the form of a weakly collimated jet; Deller et al. 2015). The gamma-ray flux of J1023 has quintupled compared to the long-term average value attained during the rotation-powered state, and enhanced 0.1–300 GeV flux has persisted until at least 2014 October (Stappers et al. 2014; Takata et al. 2014; Deller et al. 2015). A search for steady emission above 300 GeV with *VERITAS* resulted instead in an upper limit of 6.9×10^{-13} erg cm $^{-2}$ s $^{-1}$ at the 95 per cent confidence level (Aliu et al. 2016).

The X-ray monitoring campaign with the XRT aboard *Swift* (still ongoing) detected the system at a 0.5–10 keV luminosity of 2.5×10^{33} erg s $^{-1}$ on 2013 October 18 (Kong 2013; Patruno et al. 2014), a factor ~ 30 larger than the value attained in the rotation-powered radio pulsar state ($\sim 9 \times 10^{31}$ erg s $^{-1}$; Archibald et al. 2010; Bogdanov et al. 2011). Evidence for significant X-ray variability was detected in the *Swift* data sets on

time scales of a few tens of seconds (Patruno et al. 2014), but also of days/weeks (Takata et al. 2014; Deller et al. 2015; this thesis). However, a set of 9 observations carried out with the larger collecting area of the X-ray instruments on board *XMM-Newton* between 2013 November and 2015 December have all revealed a puzzling trimodal behavior of the system in the soft X-rays: J1023 spends about 70–80 per cent of the time in a stable ‘high’ mode (with 0.3–10 keV luminosity of $\sim 3 \times 10^{33}$ erg s⁻¹), which unpredictably alternates to a ‘low’ mode (for about 20 per cent of the time), where the 0.3–10 keV luminosity drops to $\sim 5 \times 10^{32}$ erg s⁻¹. Sporadic, brighter flaring episodes are also observed – although not in all the observations – reaching luminosities of the order of $\sim 10^{34}$ erg s⁻¹ (Jaodand et al. 2016). The switches between these modes occur on a timescale of tens of seconds. Coherent X-ray pulsations at the neutron star spin period (with a rms pulsed fraction of ~ 8 per cent) are detected only when the system is in the high mode (with an upper limit of 2.4 per cent for the rms pulsed fraction in the low mode, at the 95 per cent confidence level; Archibald et al. 2015). The phase-connected timing solution reported by Jaodand et al. (2016) shows that the average neutron star spin-down rate in the LMXB state is about 27 per cent larger than that observed during the rotation-powered radio pulsar state. This strongly suggests not only that the main pulsar spin-down mechanism (i.e., the pulsar wind) has been operating since the formation of an accretion disk in the system about 3 yr ago, but also that the outflow of material has increased the spin down and largely prevails over the spin-up torque imparted by the accreting material.

NuSTAR observations of PSR J1023+0038 (Li et al. 2014, Tendulkar et al. 2014) confirmed the increase of PSR J1023+0038 luminosity from $\sim 7.4 \times 10^{32}$ erg s⁻¹ between 2013 June 10 – 12 to $\sim 5.8 \times 10^{33}$ erg s⁻¹ and up to 1.2×10^{34} erg s⁻¹ between 2013 October 19 – 21 (in the 3 – 79 keV energy interval). The time series in the LMXB state (2013 October) show significant aperiodic variations, mostly in the form of sharp-edged, flat-bottomed dips with ingress and egress timescales between 30 and 60 s.

In the optical, the system was ~ 1 mag brighter on 2013 October 16 – 23 than in June and somewhat bluer (Halpern et al. 2013). An increase in the UV emission by ~ 3.5 mag was also noticed in the data of the UVOT aboard *Swift* (Patruno et al. 2014). Time-resolved optical photometry of the system in the LMXB state revealed a sinusoidal modulation due to the irradiated companion and disk, with rapid (i.e., down to ~ 20 s) flaring activity superimposed (Shahbaz et al. 2015; McConnell et al. 2015). Rectangular, flat-bottomed dips randomly distributed along the orbital phase are also observed (Shahbaz et al. 2015). These are characterized by a median duration of ~ 250 s and a median ingress/egress time of ~ 20 s, and are remarkably similar to the X-ray mode-switching behaviour. Modelling of optical photometric data suggests that the companion may be underfilling its Roche lobe, possibly implying that the wind from the companion may represent the main channel of mass transfer in the system (McConnell et al. 2015). Baglio et al. (2016) conducted the first optical polarimetric study of the system, and suggested that the measured linear polarisation in the optical emission and its possible modulation at the orbital period could be ascribable to Thomson scattering with free electrons in the disk.

This wealth of multiwavelength data sets have revealed unique properties, and a uni-

fied scenario able of taking into account all these phenomenological characteristics has represented a tough challenge in the last years. A few scenarios have been put forward trying to account for the wealth of data from the radio to the GeV energy range. These involve a propeller mechanism, an engulfed radio pulsar, direct accretion onto the neutron star, as well as a possible radio jet (Li et al. 2014; Patruno et al. 2014; Takata et al. 2014; Deller et al. 2015; Papitto & Torres 2015, to mention a few). However, a physical interpretation for the fast transitions mentioned above is not available at present.

8.2 Structure of the chapter

This chapter is devoted to the multiwavelength study and modeling of PSR J1023+0038 (J1023 in the following), and is structured in two parts. *The analysis and interpretation of our multiwavelength observations of the system, described in the first part, was performed and completed well before we became aware that deep XMM-Newton observations (later published by Archibald et al. 2015; Bogdanov et al. 2015) revealed the existence of three distinct X-ray modes in the LMXB state¹ (see Section 8.1) and the presence of spin-powered X-ray pulsations in the high mode.* These findings rule out the possibility that, at least in the high mode, J1023 is active as a pure rotation-powered radio pulsar. Indeed, in Coti Zelati et al. (2014, MNRAS, 444, 1783) we put forward a theoretical interpretation based on a completely enshrouded radio pulsar and proposed that the radio pulsar could be still active, but undetectable in the radio band due to a large amount of ionized material surrounding the compact object. Our initial interpretation was based on a rich amount of observational data: we report on a large number of *Swift* observations carried out in the X-ray and UV/optical bands between 2013 October and 2014 May in Section 8.3. We focus on new optical and infrared photometry of this system with data from the REM telescope, the Liverpool Telescope, the 2.1-m telescope at the San Pedro Mártir Observatory and the 1.52-m telescope at the Loiano observing station in Section 8.4. We report the results of new optical spectroscopy in Section 8.5. We derive a strictly contemporaneous spectral energy distribution (SED) in Section 8.6. We put forward our scenario in Section 8.7, and draw the conclusions of this first study in Section 8.8. In the second part of the Chapter we interpret the observed repeated transitions between the high and low X-ray modes in terms of fast swings between the propeller and radio pulsar regimes, and show how this picture can satisfactorily reproduce the X-ray spectral properties of the different modes (without contemplating whether this is a unique hypothesis). We base our analysis on *XMM-Newton* data, which provide the highest signal to noise data (Campana et al. 2016, A&A, 594, 31). In Section 8.9 we briefly describe the physical interpretation of the mode switching. In Section 8.10 we describe the extraction of *XMM-Newton* spectra and in Section 8.11 their fitting. A brief timing analysis is described in Section 8.12. In Section 8.13 we discuss our results and draw our conclusions. *The reader is referred*

¹Here and in the following, I adopt the term ‘mode’ to distinguish between the three modes of X-ray brightness observed during the LMXB state. This must not be confused with the term ‘state’, which refers to the rotation-powered pulsar and LMXB regimes of the system.

mainly to the second part of the Chapter for a more accurate description of the physical properties of the system, in particular for a better characterization of the X-ray variability, a proper estimate of the contribution of the different components to the system emission, the value of the different system parameters (also in relation to the different modes).

8.3 Swift observations

The *Swift* satellite (Gehrels et al. 2004) observed J1023 51 times between 2013 October 18 and 2014 May 12. The observations were carried out both in the soft X-ray (0.3–10 keV) and in the UV/optical bands with the XRT and the UVOT, respectively. We report the main characteristics of the observations in Table 8.1. The first 10 observations were already analysed by Takata et al. (2014).

8.3.1 X-ray data

X-ray data were collected by the XRT in photon counting mode (2.5-s time resolution). We processed them using the default parameter settings with XRTPIPELINE (v. 0.12.8) and determined the count rates through the ‘sosta’ command of XIMAGE (v. 4.5.1). We downloaded the spectral files using the *Swift* XRT data products generator (Evans et al. 2009). We assigned the latest version of the calibration files available in 2014 May to the spectral files and grouped the source spectra to have at least 20 counts per bin. Spectra were then analysed with the XSPEC (v. 12.8.1) spectral fitting package (Arnaud 1996) using the χ^2 statistics. In all the fits we took into account the effects of interstellar absorption through the TBABS model with cross-sections from Verner et al. (1996) and abundances from Wilms, Allen & McCray (2000). We fit the overall spectrum (i.e. the sum of the spectra of all the 51 pointings, corresponding to a total exposure of 92.8 ks) with a power-law model, and obtained an acceptable $\chi^2_\nu = 0.98$ for 788 d.o.f. In the following parameter errors and upper limits are computed with $\Delta\chi^2 = 2.706$, corresponding to 90 per cent confidence level for a single parameter of interest. We reveal the presence of a non-negligible absorption ($N_H = [5.2 \pm 0.07] \times 10^{20} \text{ cm}^{-2}$; a fit with an unabsorbed power-law yields an unacceptable $\chi^2_\nu = 1.12$ for 789 d.o.f.). The photon index is $\Gamma = 1.56 \pm 0.03$ and the mean unabsorbed 0.3–10 keV flux is $(1.15 \pm 0.02) \times 10^{-11} \text{ erg cm}^{-2} \text{ s}^{-1}$, corresponding to a luminosity of $(2.58 \pm 0.05) \times 10^{33} \text{ erg s}^{-1}$. We searched for possible iron line features by superimposing a Gaussian model centered at 6.4 and 6.9 keV. We found upper limits of 35 and 47 eV for the equivalent width, respectively. The addition of a soft component (either a black body or a neutron star hydrogen atmosphere model) is not statistically required.

To investigate spectral variability as a function of the X-ray flux, we separated the observations in two count rate ranges (below and above $0.25 \text{ counts s}^{-1}$; see Table 8.1) and we summed together the corresponding spectra. We then fitted the two spectra separately with an absorbed power-law ($\chi^2_\nu = 1.04$ for 679 d.o.f. for the low-counting rate spectrum and $\chi^2_\nu = 0.86$ for 739 d.o.f. for the high-counting rate spectrum). The values obtained for the column density ($N_{H,L} = 5.4^{+1.3}_{-1.2} \times 10^{20} \text{ cm}^{-2}$; $N_{H,H} = 5.1^{+1.0}_{-0.9} \times 10^{20} \text{ cm}^{-2}$) and

Table 8.1: *Swift* XRT and UVOT observational log. The observation marked with * was already analysed by Patruno et al. (2014) and Takata et al. (2014). Observations marked with ** were already analysed by Takata et al. (2014).

Obs. ID	Date	XRT exposure (ks)	UVOT filter (mode)	XRT count rate (counts s ⁻¹)
00080035003*	2013 Oct 18	10.0	<i>U</i> , <i>UVW1</i> (img)	0.28 ± 0.01
00033012001**	2013 Oct 31	1.9	<i>U</i> (img)	0.20 ± 0.01
00033012002**	2013 Nov 04	2.1	<i>U</i> (img)	0.28 ± 0.01
00033012003**	2013 Nov 06	1.0	<i>UVW1</i> (evt)	0.21 ± 0.02
00033012004**	2013 Nov 07	1.0	<i>UVW1</i> (evt)	0.19 ± 0.02
00033012005**	2013 Nov 08	1.3	<i>UVW1</i> (evt)	0.36 ± 0.02
00033012007**	2013 Nov 10	1.1	<i>UVW1</i> (evt)	0.21 ± 0.02
00033012008**	2013 Nov 11	1.2	<i>UVW1</i> (evt)	0.16 ± 0.01
00033012009**	2013 Nov 12	2.3	<i>UVW1</i> (evt)	0.23 ± 0.01
00033012010**	2013 Nov 13	1.1	<i>UVW1</i> (evt)	0.14 ± 0.01
00033012011	2013 Nov 14	1.1	<i>UVW1</i> (evt)	0.23 ± 0.02
00033012012	2013 Nov 15	1.1	<i>UVW1</i> (evt)	0.19 ± 0.01
00033012013	2013 Nov 16	2.0	<i>UVW1</i> (evt)	0.23 ± 0.01
00033012014	2013 Nov 17	1.0	<i>UVW1</i> (evt)	0.27 ± 0.02
00033012015	2013 Nov 18	1.0	<i>UVW1</i> (evt)	0.29 ± 0.02
00033012016	2013 Nov 19	1.0	<i>UVW1</i> (evt)	0.30 ± 0.02
00033012017	2013 Nov 20	1.8	<i>U</i> (img)	0.37 ± 0.01
00033012018	2013 Nov 23	1.9	<i>UVW1</i> , <i>UVW2</i> , <i>UVM2</i> (img)	0.29 ± 0.02
00033012019	2013 Nov 28	2.1	<i>U</i> (img)	0.30 ± 0.01
00033012020	2013 Nov 30	4.5	<i>UVM2</i> (evt)	0.29 ± 0.01
00033012021	2013 Dec 02	0.7	<i>UVW1</i> , <i>UVW2</i> , <i>UVM2</i> (img)	0.05 ± 0.01
00033012022	2013 Dec 11	3.0	<i>UVW1</i> (img)	0.30 ± 0.02
00033012023	2013 Dec 14	1.0	<i>UVW1</i> , <i>UVW2</i> , <i>UVM2</i> (img)	0.24 ± 0.01
00033012024	2013 Dec 12	2.7	<i>UVW1</i> (img)	0.20 ± 0.01
00033012025	2013 Dec 17	1.8	<i>UVW1</i> (img)	0.17 ± 0.01
00033012026	2013 Dec 21	2.6	<i>UVW1</i> (img)	0.20 ± 0.03
00033012027	2013 Dec 25	2.8	<i>UVW1</i> , <i>UVW2</i> , <i>UVM2</i> (img)	0.26 ± 0.01
00033012028	2014 Jan 02	0.5	<i>UVW1</i> , <i>UVW2</i> , <i>UVM2</i> (img)	0.28 ± 0.01
00033012029	2014 Jan 12	2.8	<i>UVW1</i> , <i>UVW2</i> , <i>UVM2</i> (img)	0.22 ± 0.01
00033012030	2014 Jan 16	2.0	<i>UVW2</i> (img)	0.24 ± 0.01
00033012032	2014 Jan 22	0.6	<i>UVW2</i> , <i>UVM2</i> (img)	0.16 ± 0.02
00033012033	2014 Jan 24	3.0	<i>UVW2</i> (img)	0.35 ± 0.01
00033012034	2014 Jan 27	3.1	<i>U</i> (img)	0.25 ± 0.01
00033012036	2014 Feb 09	3.3	<i>UVW2</i> (img)	0.20 ± 0.01
00033012037	2014 Feb 11	1.0	<i>UVW1</i> , <i>UVW2</i> , <i>UVM2</i> (img)	0.24 ± 0.02
00033012038	2014 Feb 13	2.3	<i>UVW2</i> (img)	0.22 ± 0.01
00033012039	2014 Feb 19	2.8	<i>UVW1</i> (img)	0.26 ± 0.01
00033012040	2014 Feb 21	0.4	<i>UVW1</i> , <i>UVW2</i> , <i>UVM2</i> (img)	0.21 ± 0.03
00033012041	2014 Feb 27	0.5	<i>UVW1</i> (img)	0.64 ± 0.05
00033012042	2014 Mar 03	1.0	<i>UVW1</i> , <i>UVW2</i> , <i>UVM2</i> (img)	0.61 ± 0.04
00033012043	2014 Mar 05	1.6	<i>UVW2</i> (img)	0.27 ± 0.01
00033012044	2014 Mar 11	2.4	<i>UVW1</i> (img)	0.54 ± 0.03
00033012046	2014 Mar 12	1.8	<i>U</i> (img)	0.21 ± 0.01
00033012047	2014 Mar 23	1.0	<i>UVW1</i> , <i>UVW2</i> , <i>UVM2</i> (img)	0.21 ± 0.02
00033012049	2014 Apr 13	0.08	<i>UVW2</i> (img)	0.20 ± 0.07
00033012050	2014 Apr 16	0.9	<i>UVW1</i> , <i>UVW2</i> , <i>UVM2</i> (img)	0.28 ± 0.02
00033012051	2014 Apr 22	1.0	<i>UVW1</i> , <i>UVW2</i> , <i>UVM2</i> (img)	0.18 ± 0.01
00033012052	2014 Apr 25	2.1	<i>UVW2</i> (img)	0.28 ± 0.01
00033012053	2014 Apr 27	3.0	<i>U</i> , <i>UVW1</i> , <i>UVW2</i> (img)	0.19 ± 0.01
00033012054	2014 May 02	0.8	<i>UVW1</i> , <i>UVW2</i> , <i>UVM2</i> (img)	0.33 ± 0.02
00033012055	2014 May 12	1.0	<i>UVW1</i> , <i>UVW2</i> , <i>UVM2</i> (img)	0.24 ± 0.01

the photon index ($\Gamma_L = 1.57 \pm 0.04$; $\Gamma_H = 1.57_{-0.03}^{+0.04}$) are consistent with being constant within the errors. Indeed, changes in the power-law normalization alone are enough to account for the observed spectral changes. We conclude that the spectral shape remains almost the same independently of flux variations.

On 2014 February 27, the net X-ray count rate increased to ~ 0.64 counts s^{-1} , a factor ~ 3 higher than that registered only 6 d before. The intensity decreased back on March 5, but the system was again at a high level on March 11. The following day the count rate returned back to roughly its average value (see Figure 8.1 for the X-ray light curve). These detections result in an upper limit of ~ 13 d for the duration of such flares. Spectral data of the 3 observations with the highest count rates (Obs. ID 00033012041,42,44) are well described by an absorbed power-law model ($\chi^2_\nu = 0.82$ for 385 d.o.f., for a total exposure time of 3.8 ks) with hydrogen column density and photon index consistent with the average values ($N_H < 5.8 \times 10^{20}$ cm^{-2} , $\Gamma = 1.5 \pm 0.1$). The unabsorbed 0.3–10 keV flux is $(2.5 \pm 0.2) \times 10^{-11}$ erg cm^{-2} s^{-1} , which translates in to a luminosity $L_X = (5.6_{-0.4}^{+0.5}) \times 10^{33}$ erg s^{-1} , a factor ~ 2.2 higher than the average value.

8.3.2 UV data, X-ray/UV correlations and power spectra

J1023 has been monitored with the UVOT in event mode using the *UVW1* filter (central wavelength 2600 Å) for 13 consecutive observations, from 2013 November 6 to 19 (Obs. ID 00033012003 – 00033012016). We processed these data with the COORDINATOR and UVOTSCREEN tasks and we extracted all the light curve data with XSELECT (v. 2.4), adopting as extraction region a circle centered on the source with a radius of 10 pixels (1 UVOT pixel = 0.502 arcsec).

To search for possible correlations between the X-ray and UV emissions on time-scales of days, we extracted the XRT events in the November 6 – 19 period using a circle centered on the source with a radius of 15 pixels (1 XRT pixel = 2.36 arcsec). The 0.3–10 keV and *UVW1* light curves of J1023 during this period are shown in the right-hand panel of Figure 8.1. We found a strong correlation between the X-ray and UV light curves, with a significance probability of 99.6 per cent according to Spearman’s test. We also investigated if such correlation exists on shorter time-scales by analysing each of the three observations with the longest exposures (Obs. ID 00033012009, 00033012013, 00033012020). We found that both the X-ray and the UV emissions are variable during each observation and that the correlation is always significant (see Table 8.2).

We searched for possible X-ray and/or UV periodicities by inspection of the *Swift* XRT and UVOT observations performed between 2013 November 6 and 19. We note that due to the *Swift* XRT sensitivity, the time resolution does not enable the detection of pulsations at the pulsar spin period. First, we applied barycentric corrections to each event file with the BARYCORR task, using the DE-200 Solar system ephemeris. We then summed all the event files and built the power spectra both in the 0.3–10 keV band and in the *UVW1* filter with POWSPEC. No prominent features can be observed, implying that the X-ray and UV emissions are not modulated at the 4.75-h orbital period (see also Tendulkar et al. 2014).

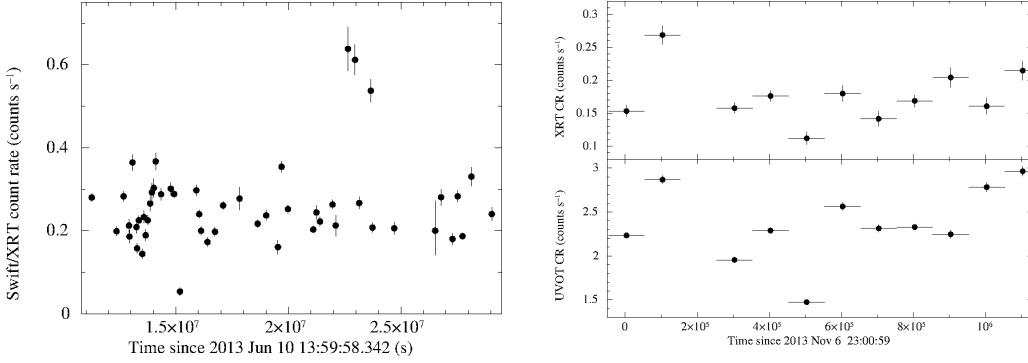


Figure 8.1: Light curves of J11023. *Left-hand panel*: in the 0.3–10 keV light curve (2013 October 18 – 2014 May 12). Bin time equals one single observation. *Right-hand panel*: in the 0.3–10 keV and *UVW1* filter (2013 November 6 – 19). Bin time equals 10^5 s.

Table 8.2: X-ray/UV variability and correlations in single *Swift* observations of J1023. A bin time of 50 s was adopted for each light curve. Reported χ^2_ν values are derived from fitting the light curves with a constant. P_s is the significance probability for the X-ray/UV correlation according to Spearman’s correlation test.

Obs. ID	Energy band	Average CR (counts s ⁻¹)	χ^2_ν (d.o.f)	P_s (%)
00033012009	X-ray	0.09 ± 0.01	4.30 (47)	95.8
	UV	2.18 ± 0.05	5.38 (47)	
00033012013	X-ray	0.12 ± 0.01	2.84 (39)	97.7
	UV	2.28 ± 0.06	2.63 (39)	
00033012020	X-ray	0.17 ± 0.01	2.85 (92)	99.8
	UV	1.22 ± 0.03	2.81 (92)	

8.4 Optical and infrared photometry

J1023 was monitored in the optical and NIR bands with the REM telescope (Zerbi et al. 2001; Covino et al. 2004) at the La Silla Observatory on 2013 November 17 and 30, and in the optical with the 2-m Liverpool Telescope (LT) on 2014 February 2.

8.4.1 REM observations

The system was observed simultaneously in the g , r , i and z optical SDSS filters (4000–9500 Å) using the ROSS2 instrument. Two sets of 18 and 36 images were acquired during the two nights, respectively (150-s integration time each). The images were flat-field and bias corrected using standard procedures, and all the magnitude values for the objects in the field were obtained using aperture photometry techniques (DAOPHOT; Stetson 2000). The flux calibration was performed using five SDSS² stars present in the field. About 85 per cent of the orbital period was covered in each optical filter.

The system was observed also in the NIR band using the REMIR infrared camera. A set of 12 images were acquired with the J , H , K filters (1–2.3 μm) during the first night; 24, 22 and 20 images were obtained in the J , H , K filters during the second night (75-s integration time each). Magnitudes were extracted using the same procedure employed in the optical analysis, and were then calibrated against eight field stars whose magnitudes are tabulated in the 2MASS catalogue³.

8.4.2 Liverpool telescope observations

J1023 was observed in the g (4770 Å) and i (7625 Å) optical SDSS filters also with the IO:O instrument of the LT. The seeing remained almost constant below 1 arcsec for the whole night. A set of 63 images (90-s integration time each) were obtained in the two filters, covering about the 80 per cent of the orbital period in each band. Image reduction and magnitude extractions were carried out following the same prescriptions as for the REM data. The flux calibration was performed using nine SDSS field stars.

8.4.3 Results

The optical counterpart star of J1023 is detected in the single observations by REM in the g , r and i filters, but not in the z band (a value of 16.2 ± 0.2 mag is obtained for the magnitude in this band when all images are summed together, for a total integration time of 2700 s). It is also detected by the LT in the g and i filters. The light curves present a sinusoidal modulation at the 4.75-h orbital period (see Figure 8.2). To study the modulation, we fitted the data with a simple sinusoidal function, although it provides only an approximation to the data. The results of the fit are reported in Table 8.3. The source shows a single minimum around phase 0 (i.e. at the inferior conjunction of the companion

²See <http://sdss3.org/dr10/>

³See <http://www.ipac.caltech.edu/2mass/>

Table 8.3: Results of the optical and NIR photometry of J1023. Magnitudes are not corrected for reddening, whose parameters are reported in the last column and are derived from Cox (2000). Errors are quoted at a 90 per cent confidence level.

Filter	Telescope/Instrument	Semi-amplitude (mag)	Mean magnitude (mag)	Maximum (phase)	A_λ
g	REM/ROSS2	0.43 ± 0.01	16.70 ± 0.01	0.440 ± 0.002	0.21 ± 0.05
	LT/IO:O	0.55 ± 0.01	16.447 ± 0.002	0.393 ± 0.001	
r	REM/ROSS2	0.34 ± 0.01	16.32 ± 0.01	0.427 ± 0.003	0.14 ± 0.04
i	REM/ROSS2	0.30 ± 0.01	16.16 ± 0.01	0.419 ± 0.001	0.11 ± 0.03
	LT/IO:O	0.38 ± 0.01	15.994 ± 0.002	0.386 ± 0.001	
J	REM/REMIR	0.26 ± 0.05	15.41 ± 0.03	0.41 ± 0.02	0.05 ± 0.01
H	REM/REMIR	–	14.94 ± 0.03	–	0.03 ± 0.01

star) and a maximum around phase 0.5 (superior conjunction), which is suggestive of a companion star strongly irradiated by the compact object and it is the typical variability expected (and observed) for an accreting millisecond pulsar (Homer et al. 2001; Campana et al. 2004; D’Avanzo et al. 2007; Deloye et al. 2008; Wang et al. 2009b, 2013; Baglio et al. 2013).

The NIR phase-resolved light curves are shown in Figure 8.3. The source is not detected in the single observations in the K band (a value of 15.2 ± 0.2 mag is obtained for the magnitude in this band when all images are summed together, for a total integration time of 1350 s). The fit of the H -band light curve with a constant gives $\chi^2_\nu \sim 4$ for 65 d.o.f., thus indicating that some variability is indeed observed for J1023 in this band. However, an F -test proves that a sinusoidal fit does not improve the significance of the fit. Therefore, we conclude that we are probably observing some kind of random variability around an average magnitude of 14.94 ± 0.03 mag (see Table 8.3). In the J band, the light curve is better described by a sinusoidal model than by a constant alone (the F -test gives a significance of 2.8×10^{-5}). All the fit parameters are reported in Table 8.3.

The $g-r$ color derived from the REM optical data and the $g-i$ color obtained from the LT data set (see Figure 8.4) are larger at phase 0 than at phase 0.5. This means a bluer spectrum at the superior conjunction, as expected for an irradiated companion star. If we suppose the companion to be a main sequence star, the unabsorbed overall average colors $g-r = 0.31 \pm 0.07$ mag and $r-i = 0.13 \pm 0.05$ mag derived from the REM data are marginally consistent with a G -type star (Cox 2000). We note however that the average $J-H$ color (0.45 ± 0.04 mag) is indicative of a much colder star (a K -type star). This inconsistency can be explained assuming the contribution of at least another component to the system emission, such as an accretion disk around the compact object and/or a shock front between matter outflowing from the companion and the relativistic pulsar wind. If this is verified, all the calculated magnitudes refer to a multi component emission and cannot give any estimate of the star surface temperature.

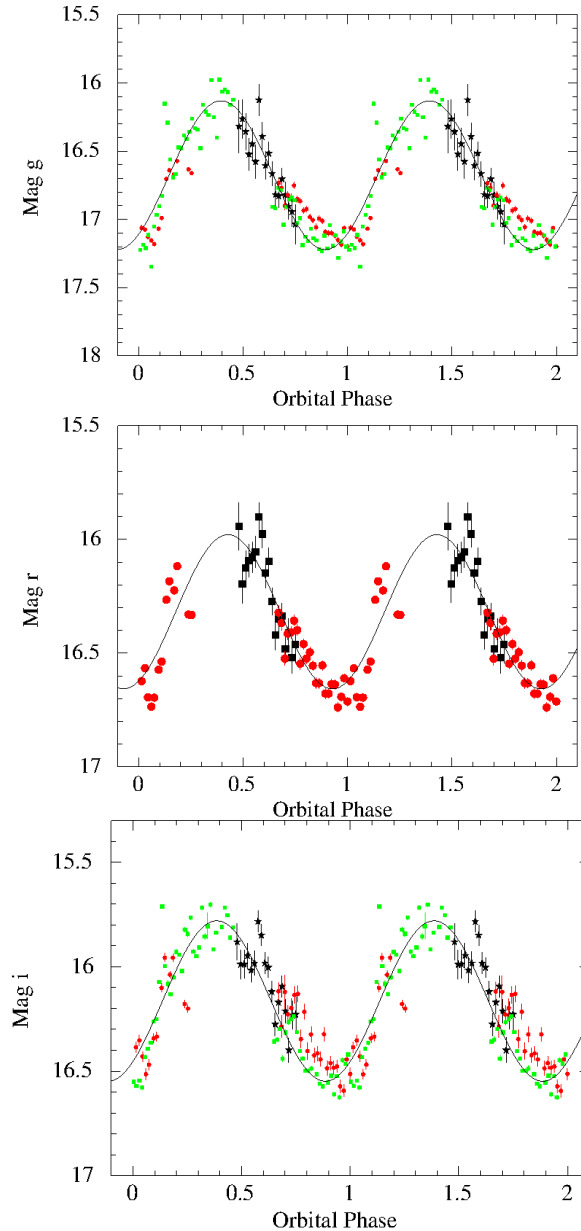


Figure 8.2: Optical light curves of J1023. Black stars and red dots refer to the REM 2013 November 17 and 30 data sets respectively; green squares refer to the LT data set. We calculated the orbital phases based on the ephemeris of Archibald et al. (2009). Phase 0 corresponds to the inferior conjunction of the companion. The g and i LT curves were rescaled to the mean REM 2013 Nov 30 magnitude, by adding 0.22 mag to the g LT light curve data and 0.17 mag to the i LT light curve data. Data were fitted with a constant plus sinusoid model, with the sinusoidal period fixed to the orbital period of the system (4.75 h). Two cycles of the system are drawn for clarity in each plot. Top panel: g light curve; middle panel: r light curve; bottom panel: i light curve.

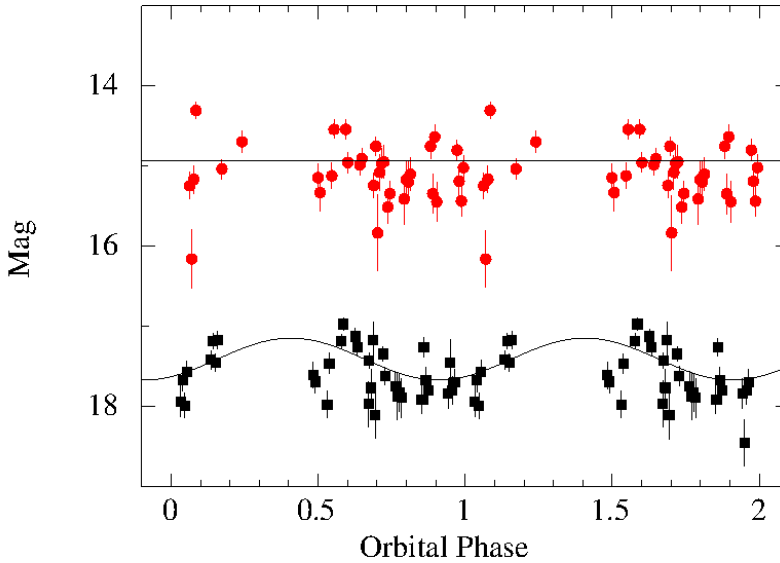


Figure 8.3: H (red dots) and J (black squares) light curves for J1023. The J -band light curve has been rescaled by 2 mag to eliminate any overlap of the two light curves. Two cycles are drawn for clarity.

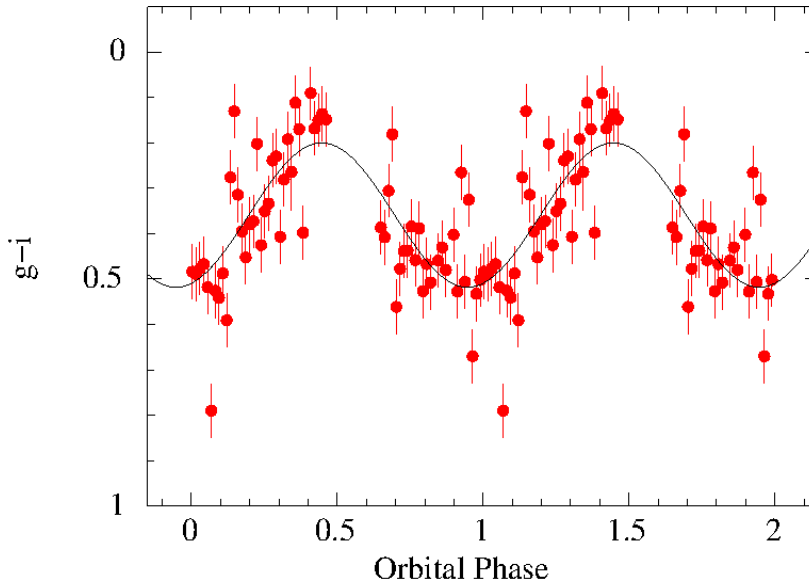


Figure 8.4: $g-i$ folded color light curve obtained from the LT data. Fitting the data with a constant plus sinusoid model yields an average color $g-i = 0.36 \pm 0.01$, a semi-amplitude of 0.16 ± 0.02 and an orbital phase for the maximum of 0.39 ± 0.001 ($\chi^2 = 178.9$ for 57 d.o.f.).

Table 8.4: Log of optical spectroscopy observations of J1023.

Date (mid exposure) YYYYMMDD	Exposure (s)	Telescope/Observatory	Orbital Phase
20131204.44641	1800	2.1m/SPM	0.982
20131204.46790	1800	2.1m/SPM	0.090
20131204.48981	1800	2.1m/SPM	0.201
20131204.51290	1200	2.1m/SPM	0.318
20131210.19627	1800	1.5m/Loiano	0.111

Table 8.5: Results of optical emission lines analysis.

Line	EW (Å)	FWHM (km s ⁻¹)	Peak separation (km s ⁻¹)
H α	-30.0 ± 0.2	1260 ± 110	720 ± 50
H _{eI} 5876	-17.3 ± 0.2	1300 ± 70	510 ± 200
H _{eI} 6678	-7.9 ± 0.2	1560 ± 970	760 ± 60
H _{eI} 7065	-4.9 ± 0.2	1350 ± 180	760 ± 170

8.5 Optical spectroscopy

J1023 optical spectra were obtained on 2013 December 4 with the 2.1-m telescope at the San Pedro Mártir Observatory (México) equipped with the Boller & Chivens spectrograph. We obtained four optical spectra with exposure times of 1200 or 1800 s, each one covering the 4000 – 7800 Å wavelength range, with a resolution of ~ 6.5 Å (350 km s⁻¹). An additional 1800-s spectrum was obtained on 2013 December 10 at the Loiano Astronomical Observatory (Italy) using the 1.5-m telescope equipped with the BFOSC spectrograph, covering the 4000 – 8500 Å wavelength range, with a resolution of about 10 Å (480 km s⁻¹). The log of the optical spectroscopy observations is shown in Table 8.4.

Data were reduced using standard procedures for bias subtraction and flat-field correction. Wavelength calibration was carried out using copper-argon lamps. Instrumental flexures during our observations were then accounted for using atmospheric emission lines in the sky spectra.

The flux-calibrated spectra show a blue continuum with broad emission lines superposed. We clearly detect H α , H β , H γ , H δ and HeI (λ 4472, 4713, 4921, 5016–5048, 5876, 6678, 7065), all showing a double-horned profile, likely related to the presence of an accretion disk (see Figure 8.5).

From the analysis of the co-added San Pedro Mártir spectra, we measure an equivalent width EW ~ -30 Å, a FWHM ~ 1300 km s⁻¹ and a peak separation of ~ 720 km s⁻¹ for the H α line. These values are consistent with the findings of Halpern et al. (2013), Takata et al. (2014) and Linares et al. (2014). We repeated the same analysis for the other main emission lines, excluding those with wavelength < 4800 Å (being too close to each other to enable a detailed quantitative analysis). The results are reported in Table 8.5. Fully consistent values are found from the analysis of the single spectrum obtained in Loiano.

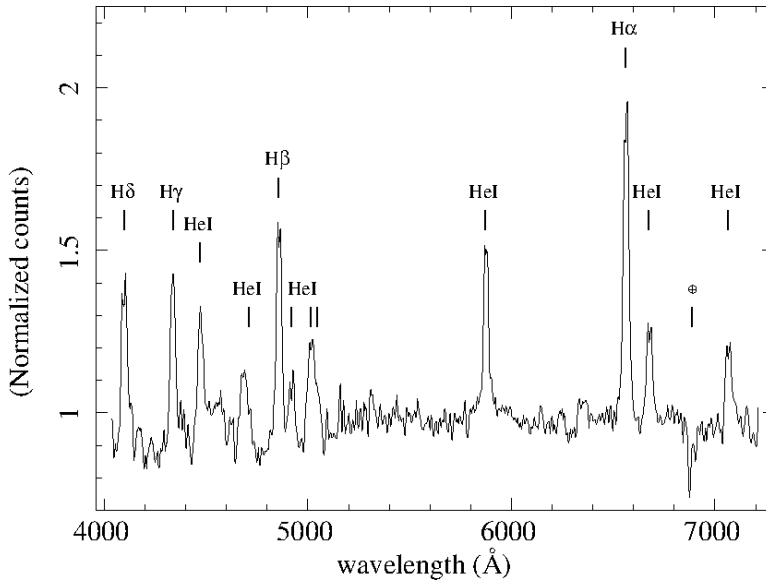


Figure 8.5: Optical spectrum of J1023 obtained on 2013 Dec 4 with the 2.1-m telescope at the San Pedro Mártir Observatory. The most prominent emission lines are marked. Double profiles are clearly visible.

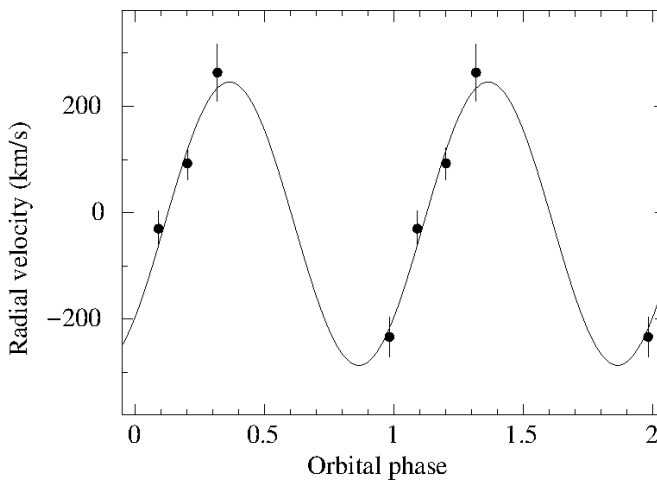


Figure 8.6: Radial velocity curve of J1023 computed using a G5 V spectral template. Two orbital phases are shown for clarity. The best sine-wave fit provides a systemic velocity $\gamma = -20.6 \pm 120.8 \text{ km s}^{-1}$ and a radial velocity $K_2 = 266.2 \pm 28.8 \text{ km s}^{-1}$.

Radial velocities were measured from the four San Pedro Mártir optical spectra through cross-correlation with a G5 V template star⁴. Prior to cross-correlating, the spectra were barycentric corrected and rebinned to a uniform velocity scale. Cross-correlation was performed in the range 5130 – 6300 Å, after masking the H_{eI} λ5876 emission line from the accretion disk. A fit with a constant plus sinusoid function provides a systemic velocity $\gamma = -20.6 \pm 120.8 \text{ km s}^{-1}$ and a radial velocity $K_2 = 266.2 \pm 28.8 \text{ km s}^{-1}$ (see Figure 8.6). Despite the large uncertainties (mainly due to the low statistics), these values are fully consistent with the results obtained by Thorstensen & Armstrong (2005) during the system quiescence.

8.6 Spectral energy distribution

J1023 was observed strictly simultaneously by *Swift* and REM for ~ 3 min on 2013 November 30, while it was at orbital phase 0.9 (near the neutron star superior conjunction). We extracted the corresponding source and background X-ray spectra adopting a circle centered on the source with a radius of 15 pixels in the former case and a circle positioned in a location free from known X-ray sources with a radius of 30 pixels in the latter case. We created the ancillary response file for the extracted spectrum with XRTMKARF, to correct the count rate for the presence of bad pixels, vignetting and hot columns. Finally, we assigned the latest version of the redistribution files. Fluxes in the optical and infrared bands were estimated through the aperture photometry technique. The unabsorbed SED from the NIR to the X-ray bands is shown in Figure 8.7.

We attempted to account for the NIR, optical, UV and X-ray SED with the simple model of an irradiated star plus the contribution of a shock front. For the star component we assumed an irradiated black body model (for the details of the modelling see Eqs. [8]-[9] of Chakrabarty 1998) which depends on the irradiating luminosity (L_{irr}), the source distance (D), the radius of the companion star (R_c), the albedo of the star (η_*) and the binary separation (a).

We fitted the data by using L_{irr} as a free parameter and fixing $D = 1368 \text{ pc}$ (Deller et al. 2012), $R_c = 0.43 R_\odot$ (Archibald et al. 2009) and $\eta_* = 0.1$. The binary separation $a = [G(M_X + M_c)(P_{orb})^2/(4\pi)^2]^{1/3}$ was obtained by fixing $M_X = 1.4 M_\odot$ and $M_c = 0.24 M_\odot$ (Deller et al. 2012). We modelled the shock front component with a simple power-law, by leaving its normalization and index free to vary. The best fit is obtained for $L_{irr} \sim 5 \times 10^{34} \text{ erg s}^{-1}$, consistent with the estimated dipole spin-down luminosity of the ms radio pulsar ($L_{sd} = [4.43 \pm 0.04] \times 10^{34} \text{ erg s}^{-1}$; Archibald et al. 2013). However, such model provides a rather poor fit to the data, particularly in the UV region ($\chi^2 = 46.6$ for 10 d.o.f.; see Figure 8.7, top panel).

To check for a more realistic solution, we tried to fit our data by adding to the model the contribution of an irradiated accretion disk by using L_{irr} and the internal disk radius (R_{in})

⁴In order to avoid problems in comparing spectra obtained with different instruments, we did not include the Loiano spectrum in the radial velocity analysis. Furthermore, we note that the orbital phase at which it was observed is already covered by the San Pedro Mártir spectra.

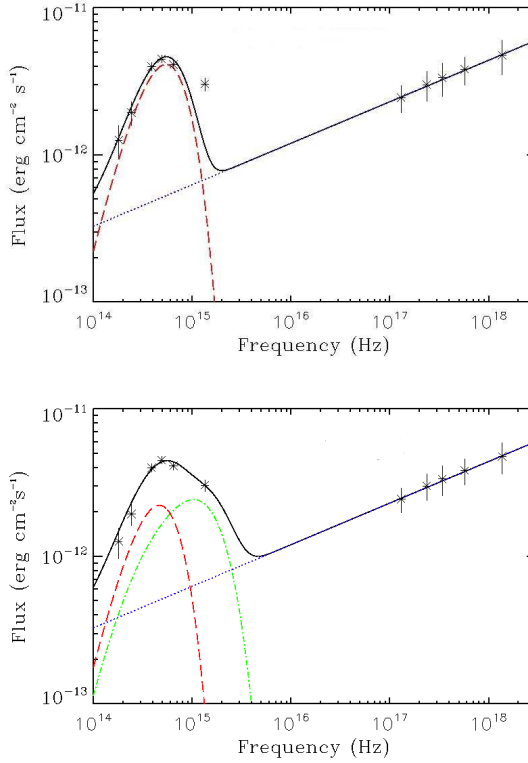


Figure 8.7: Spectral energy distribution from NIR to X-rays obtained using data collected at the same time (within ~ 3 m) corresponding to an orbital phase of 0.9. In the top panel we report the fit with a model made by the companion star (red dashed line) and the shock emission powered by the neutron star spin-down luminosity (blue dotted line). In the bottom panel, the same data are fitted with the addition of an accretion disk contribution (green dash-dotted line).

as free parameters (Eqs. [10]-[15] of Chakrabarty 1998). We fixed the X-ray albedo of the disk to 0.95 (Chakrabarty 1998) and the mass transfer rate to $10^{-11} M_{\odot} \text{ y}^{-1}$, as predicted by Verbunt (1993) for a short-period X-ray binary with a main-sequence companion star and where the mass transfer is kept going by loss of angular momentum from the system. For each possible radius R_{in} , we assumed an outer disk radius of $0.3a$ (where a is the binary separation). The fit improves ($\Delta\chi^2 = 41.8$ with respect to the star plus shock model; see Figure 8.7, bottom panel) and we obtain an acceptable solution for $L_{irr} \sim 1 \times 10^{34} \text{ erg s}^{-1}$ and an inner radius for the emitting region $R_{in} \sim 2 \times 10^9 \text{ cm}$. More sophisticated models are beyond the scope of this study.

8.7 Enshrouding of a radio pulsar

Millisecond radio pulsars in binary systems can interact with the companion star if the orbital separation is small enough. In recent years an increasing number of the so-called spider radio pulsars have been discovered (see Roberts 2011), following the first discoveries of the redback PSR J1740–5340 in the globular cluster NGC 6397 (with a non-degenerate companion, D’Amico et al. 2001) and the black widow PSR B1957+20 (with a brown dwarf companion, Reynolds et al. 2007). The interaction between the relativistic pulsar wind and matter outflowing from the companion can give rise to different geometries depending on the relative strengths of the two components. In the case of a strong relativistic wind (high pressure), matter outflowing from the companion is pushed in a narrow cometary tail around it, as in the case of PSR B1957+20. In the case of a weaker relativistic pulsar wind (or strong matter pressure) more extended patterns can be obtained, giving rise to extensive eclipses of the radio signal during the orbital period. A further case has been envisaged by Tavani (1991), where a large amount of matter is outflowing from the companion, completely engulfing the radio pulsar. In this regime the radio pulsar is still active, but its signal is completely undetectable in the radio band due to the high free-free absorption.

Arons & Tavani (1993) developed the theory of high-energy emission by the relativistic shock produced by the pulsar wind in the nebula surrounding the binary and by the shock constraining the mass outflow from the companion star. Particularly compelling to J1023 is the case of PSR B1259–63. This is a millisecond pulsar orbiting a high mass Be companion in a very eccentric orbit. Far from the companion, the X-ray emission is dominated by shock-powered high-energy emission produced by the interaction between the relativistic wind from the pulsar and matter outflowing from the companion. The spectrum is described by a hard power-law with $\Gamma \sim 1.5$, extending up to 200 keV (and more) as detected with COMPTON/OSSE (Grove et al. 1995). During its orbital evolution, the pulsar disappears close to periastron. During the passage an increase in luminosity and a softening of the power-law $\Gamma \sim 1.9 - 2$ are observed (Tavani & Arons 1997). A change to a propeller regime has been excluded (Campana et al. 1995).

Three characteristic radii define the fate of matter falling on to a magnetized, fast spinning neutron star: the magnetospheric radius, r_m (where the pressure of the inflowing matter balances the magnetic dipole pressure), the corotation radius, r_c (where matter in Keplerian orbit corotates with the neutron star), and the light cylinder radius, r_{lc} (where field lines attached to the neutron star rotate at the speed of light). The last two radii depend only on the neutron star spin and in the case of J1023 their values are $r_c = 24$ km (for a neutron star mass of $1.7 M_\odot$) and $r_{lc} = 80$ km. The magnetospheric radius depends on the neutron star magnetic field and on the mass inflow rate. It can be expressed as

$$r_m = 57 \dot{M}_{15}^{-2/7} M_{1.7}^{-1/7} R_6^{12/7} B_8^{4/7} \text{ km},$$

where \dot{M}_{15} is the mass accretion rate on to the magnetosphere in units of 10^{15} g s^{-1} , $M_{1.7}$ and R_6 are the neutron star mass and radius in units of $1.7 M_\odot$ and 10 km, respectively,

and B_8 is the magnetic field normalized to 10^8 G (Perna, Bozzo & Stella 2006). Due to the inclination of the magnetic moment with respect to the rotation axis, the magnetospheric radius can be larger up to a factor 1.5 (Perna et al. 2006).

The magnetic field of J1023 has been estimated to be $B = 9.7 \times 10^7$ G (Archibald et al. 2013). Depending on the mass inflow rate, matter can reach the neutron star surface ($r_m \lesssim r_c$, accretion powered), be halted or strongly reduced at the neutron star magnetosphere by the propeller mechanism ($r_c \lesssim r_m \lesssim r_{lc}$, still accretion powered) or be ejected by the pulsar pressure ($r_m \gtrsim r_{lc}$, spin-down powered). These regimes occur for lower and lower mass accretion rates. When a radio pulsar reactivates it is more difficult to quench it. This is simply due to the fact that the mass inflow pressure has overcome the radiation pulsar pressure throughout the binary separation (Campana et al. 1998; Burderi et al. 2001). This is why it is so difficult to quench a fast spinning millisecond radio pulsar when it reactivates. It is not easy to account for the minimal luminosity needed to quench J1023. Following Burderi et al. (2001), we can estimate a quenching luminosity of $\sim 5 \times 10^{35}$ erg s $^{-1}$. This is much larger than the observed X-ray luminosities and would suggest that the radio pulsar is still active, but unobservable.

We note that a propeller model has been proposed to explain the emission characteristics of XSS J12270–4859 (Papitto, Torres & Li 2014) and such model may apply to J1023 in its current state as well. In this model the power-law emission is interpreted as resulting from synchrotron emission at the interface between the disk and the magnetosphere. Based on energetic grounds, this model is slightly disfavoured by the data, despite the appealing feature of easily explaining the presence of a (truncated) accretion disk. The minimum luminosity expected in the propeller regime is obtained when the magnetospheric radius is close to the light cylinder radius. In the case of J1023, this luminosity is $\sim 8 \times 10^{33}$ erg s $^{-1}$, whereas the maximum luminosity expected in the propeller regime is $\sim 3 \times 10^{35}$ erg s $^{-1}$. The observed mean X-ray luminosity is $\sim 3 \times 10^{33}$ erg s $^{-1}$ and during the flare it rises to $\sim 6 \times 10^{33}$ erg s $^{-1}$. By contrast the full spin-down luminosity is $\sim 4 \times 10^{34}$ erg s $^{-1}$. Based on *NuSTAR* data, Tendulkar et al. (2014) estimated an average value for the X-ray luminosity which is close to the minimum luminosity expected in the propeller regime, whereas the peak luminosity should be in the propeller luminosity interval.

8.8 Conclusions – Part I

We presented the results of 51 *Swift* XRT and UVOT observations of the binary millisecond radio pulsar J1023 carried out in the 2013 October – 2014 May period and the results of optical and NIR photometry and optical spectroscopy of this system.

The X-ray spectrum of J1023 is best modelled by an absorbed power-law, with a column density of $(5.2 \pm 0.07) \times 10^{20}$ cm $^{-2}$ and a photon index ~ 1.6 . The contribution from any possible soft component is negligible and no iron line features can be detected. Spectral changes can be accounted for by changes of the power-law normalization alone. These observational features are consistent with shock-powered emission produced by the pulsar/outflow interaction (Tavani & Arons 1997) and with the enshrouding of J1023 by a

large amount of matter, material which is however not enough to quench the radio pulsar. The enshrouding is testified by the mild increase in the column density and by the softening of the power-law photon index compared to the previous quiescent period (Archibald et al. 2010; Bogdanov et al. 2011): the former rose from < 1 to $\sim 5 \times 10^{20} \text{ cm}^{-2}$, the latter changed from $\sim 1.2 - 1.3$ to ~ 1.6 (Tavani & Arons 1997). At the end of 2014 February, X-ray flares were detected, with a 0.3–10 keV luminosity of $\sim 5.6 \times 10^{33} \text{ erg s}^{-1}$ (a factor ~ 2.2 higher than the average X-ray luminosity). The peak luminosity of J1023 during flaring is large, encompassing a sizeable fraction of the spin-down luminosity and thus leaving open the possibility for emission in the propeller state (Papitto et al. 2014).

The shock-powered emission scenario can be well reconciled with both the reported switch off in the radio band and the increase in the gamma-ray emission. According to this, the radio pulsar signal is completely shielded by scattering and/or free–free absorption by a large amount of outflowing matter, whereas the increase in the gamma-ray emission can be naturally explained in terms of an enhancement of the shock emission (Archibald et al. 2013; Patruno et al. 2014; Stappers et al. 2014; Takata et al. 2014; Tendulkar et al. 2014).

A strong correlation exists between the X-ray and the UV count rates in the 2013 November 6 – 19 period both on time-scales of days and of a few tens of seconds, suggesting that the same emission mechanism is powering part of the X-ray and UV emission.

Optical and infrared photometric observations show that the companion star is irradiated by the spin-down emission of the radio pulsar, but also suggest that other emission mechanisms must be at work. In fact, double-peaked emission lines in the optical spectra indicate that an accretion disk exists around the system, as shown also from multi-wavelength observations performed since 2013 June (Patruno et al. 2014; Stappers et al. 2014; Takata et al. 2014; Tendulkar et al. 2014). The peak separation of the horns of the emission lines is $\sim 700 - 800 \text{ km s}^{-1}$. This value is consistent with that reported by Halpern et al. (2013), Takata et al. (2014) and Linares et al. (2014), suggesting that the disk thickness has not changed significantly between 2013 October and December.

The SED from the NIR to the X-ray band is well represented by a model consisting of an irradiated companion, an accretion disk and a shock emission. The SED reveals a minimal contribution of the disk to the X-ray emission and may indicate that accretion on to the neutron star is not occurring (see also Takata et al. 2014). In fact, this is what is expected not to completely quench the pulsar mechanism and the relativistic wind. The SED also shows that more than half of the UV emission (~ 60 per cent fractional contribution to the total flux) is emitted from the accretion disk, with the remaining part arising from the intra-binary shock (~ 40 per cent). The modelling of the SED allowed us to estimate the inner radius of the emitting region ($R_{in} \sim 250 r_{1c}$), consistent with the value reported by Takata et al. (2014) for the inner edge of the accretion disk, and the spin-down luminosity of the radio pulsar ($L_{irr} \sim 1 \times 10^{34} \text{ erg s}^{-1}$), possibly involving some shielding.

If this picture is correct, the disk should not extend down to the magnetosphere, but it should be halted further outside. The disk should then be partially supported or strongly evaporated by the NS spin-down luminosity, as it was suggested for some white dwarfs (Meyer & Meyer-Hofmeister 1994).

8.9 The physical picture for the X-ray mode transitions

The high X-ray mode of J1023 is characterised by X-ray pulsations (rms pulsed fraction ~ 8 per cent) and a high luminosity ($\sim 7 \times 10^{33}$ erg s $^{-1}$, 0.3–79 keV, resulting in a bolometric correction ~ 2 with respect to the 0.3–10 keV energy band, Tendulkar et al. 2014; Papitto & Torres 2015). The most direct interpretation to account for coherent pulsations is that some matter reaches the neutron star surface. Taking at face value, if the high mode luminosity is converted into an accretion rate (\dot{M}) as $L = G M \dot{M} / R$, with M and R the neutron star mass ($M = 1.4 M_{\odot}$) and radius ($R = 10$ km), and G the gravitational constant, one obtains $\dot{M} = 4 \times 10^{13}$ g s $^{-1}$. With this rate one can compute the Alfvén radius r_A at which the pressure of the neutron star magnetosphere is able to halt the inflowing matter in spherical symmetry ($r_A \sim \mu^4 / (2 G M \dot{M}^2)^{1/7}$, where μ is the magnetic dipole moment; $\mu = B R^3$ within the light cylinder). Here \dot{M} is the effective mass inflow rate at the magnetospheric boundary. It can be lower than the mass inflow rate from the companion star if matter is lost during the inflowing process or viscously transmitted through the disk at a lower rate. Assuming the mass accretion rate estimated from the X-ray luminosity one gets $r_A \sim 148$ km. The Alfvén radius in case of disk accretion differs by a small factor from the one derived in spherical symmetry, $r_m = k_m r_A$, with k_m ranging from 0.5 to 1 (Ghosh & Lamb 1978; Bozzo et al. 2009; Papitto & Torres 2015). With these boundaries the magnetospheric radius for disk accretion is $r_m \sim 74 - 148$ km.

The corotation radius for J1023 is $r_c = 24$ km and the light cylinder radius is $r_{lc} = 80$ km. According to standard accretion theory (e.g. Illarionov & Sunyaev 1975; Campana et al. 1998) if $r_m > r_{lc}$, as suggested above, matter cannot accrete onto the neutron star surface, rather the neutron star should get rid of the infalling matter and shine as a radio pulsar. This simple calculation shows that we need more pressure from the infalling matter to push the neutron star magnetosphere deeper inwards, in order to have accretion of some matter on the surface and generate X-ray pulsations. The easiest way is to have a larger amount of accreting matter (i.e. a larger \dot{M} with respect to that estimated from the X-ray luminosity). This matter, however, should not release its entire gravitational energy content even if stopped at the magnetospheric boundary (i.e. $G M \dot{M} / r_m$), simply because we do not detect it. This additional matter cannot evaporate along its accretion flow toward the neutron star nor can it be channelled into a large base jet, because we need matter pressure at the magnetospheric boundary. A possibility is to have an advection-dominated accretion flow where radiation is trapped into the disk and only a percentage of what is produced can be radiated (Narayan et al. 1996). With more matter pressure the innermost disk boundary can be pushed within the light cylinder radius and close to the corotation radius. If this happens, matter can still no longer accrete unimpeded onto the neutron star surface (propeller regime), being halted by the super-Keplerian rotation of the magnetosphere. In the propeller regime however, some matter can leak through the magnetosphere reaching the star surface (e.g., Romanova et al. 2004, 2005; Ustyugova et al. 2006). This can generate the observed coherent pulsations in X-rays. If this were the

case, in the X-ray band we should observe two contributions: radiation from the advective disk up to distance between the corotation and the light cylinder radius, and a pulsed X-ray component arising from matter leaking through the magnetosphere and accreting onto the surface. A non-thermal component associated to a hot corona above the disk, as usually observed in X-ray binaries, should complete the picture. More compelling to this case can be the action of the neutron star magnetosphere onto the infalling matter generating a non-thermal continuum as a result of the propeller action (Papitto & Torres 2015).

The low X-ray mode instead is characterised by the lack of X-ray pulsation, with an upper limit of < 2.4 per cent on the rms pulsed fraction, well below the value observed in the high mode. The 0.3–10 keV luminosity is a factor ~ 6 lower than that in the high mode, at a level of $\sim 5 \times 10^{32}$ erg s $^{-1}$ (Archibald et al. 2015; Bogdanov et al. 2015), resulting in a 0.3–79 keV luminosity of $\sim 10^{33}$ erg s $^{-1}$ (Tendulkar et al. 2014). In order to have pulsations some matter has to reach the neutron star surface (unless one accepts a rotationally powered pulsar to remain permanently active, which is subject to strong caveats, see Papitto & Torres 2015). According to numerical simulations, in the propeller regime some matter always finds its way to the star surface, possibly except when a ‘strong’ propeller sets in (Romanova et al. 2005). However, due to the low neutron star magnetic field and fast spin period of J1023, the light cylinder radius is of the same order of the corotation radius and a strong propeller is difficult to build up (D’Angelo & Spruit 2010). We are then led to require that the system must expel the incoming matter outside the light cylinder radius to avoid accretion. Pushing out the material from the light cylinder will reactivate the pulsar particle wind and prevent matter from falling onto the neutron star. A radio pulsar can eventually turn on, even if its reactivation requires more stringent constraints. If this were the case, its detectability would be problematic due to the enshrouding by a large wealth of material. A shock front between the relativistic particle wind and the incoming matter should develop, as observed in several ‘spider’ pulsars (Tavani 1991; Kulkarni et al. 1992). This front can convert $\sim 1 - 10$ per cent of the rotational power into X-rays with a typical synchrotron spectrum with $\Gamma \sim 2$ (Arons & Tavani 1993). Solutions with a disk surviving just outside the light cylinder exist (Ekşi & Alpar 2005). This outer disk should remain in place and accumulate matter during the low mode. Finally, the particle wind is quenched and disk advances back toward the corotation radius. Even if matter is prevented from falling directly onto the neutron star surface, the polar caps will still be hot because of the short timescale of the mode switching, and can in principle still generate pulsations at a lower level. The polar cap temperature when matter is not accreting is driven by the outer and inner crust heat content and it should be cooler (or hotter) than the temperature experimented during the accretion phase, depending on the temperature contrast among the innermost and outermost regions. The cooling time of the neutron star atmosphere is very short so that the switch between an accretion-driven emission to a crustal-driven emission is quite fast (Campana et al. 1998; Brown, Bildsten & Rutledge 1998; Colpi et al. 2001).

In the radio pulsar state the X-ray luminosity of J1023 is lower, $\sim 10^{32}$ erg s $^{-1}$ (0.3–10 keV; Archibald et al. 2010; Bogdanov et al. 2011; Li et al. 2014) and pulsations are

detected in the radio and X-ray bands. The rms pulsed fraction in X-rays is 11 ± 2 per cent (1σ confidence level; Archibald et al. 2011). The pulsar X-ray spectrum can be described by a neutron star atmosphere plus power-law model. This is not directly evident from *XMM-Newton* (Archibald et al. 2010) and *Chandra* (Bogdanov et al. 2011) spectra alone, but, when fitted together, this spectral model provides a much better description of the data (5.4σ based on an F -test). This model is typical of radio pulsars with a thermal component coming from the polar cap and a power-law of magnetospheric origin.

The flaring mode in this description stands apart. It can be hardly related to an increase of the mass inflow rate since pulsations are not detected. It could be due to flaring activity in the disk, possibly related to some magnetic reconnection (Zurita, Casares & Shahbaz 2003) or to some plasmoid ejections in a jet. We do not consider this mode any further.

8.9.1 The spectral model

Unique among LMXBs, J1023 is characterised by three different modes when its X-ray luminosity drops below $\sim 10^{34}$ erg s $^{-1}$, apart from the flaring mode. According to our picture, in the high mode the X-ray spectrum could be described by a composite model made by a power-law (non-thermal component), an advection dominated disk with free temperature and inner radius (this is achieved by using the DISKPBB model within XSPEC with $p = 0.5$), and a heated polar cap emission modelled with NSATMOS (Heinke et al. 2006) within NSATMOS with a free radius (smaller than the neutron star radius) and temperature. The low mode is more complex. According to our picture in the low mode there should coexist an enshrouded radio pulsar and an outer disk. To model the X-ray spectrum in this mode we should include a power-law non-thermal component (describing either the activity in the outermost parts of the disk or, more probably, the shock interaction of the radio pulsar wind with the incoming matter, in this last case we would predict $\Gamma \sim 2$, as due to synchrotron radiation), a disk component with an inner radius much larger than the light cylinder radius and a radio pulsar emission made by a thermal component and a magnetospheric one (NSATMOS+POW). We require that the disk temperature and inner disk radius are such that they lie on the same $T(r) \propto r^{-p}$ curve in the high and low modes, i.e. the high mode will have a higher temperature and a smaller inner disk radius, whereas the low mode will have a lower temperature and a larger inner disk radius lying on the same $T(r) \propto r^{-p}$ curve. The size of the polar cap is held fixed among the high and low modes, even if the temperature is allowed to vary. The magnetospheric pulsar component is free. Finally, in our picture the radio pulsar state is completely determined by the low mode spectrum with only the pulsar components (thermal and non-thermal) being present, but fixed in all their parameters to those of the low mode. All spectra will be corrected for absorption using the same absorbing column density. A picture of our physical scenario is shown in Figure 8.8.

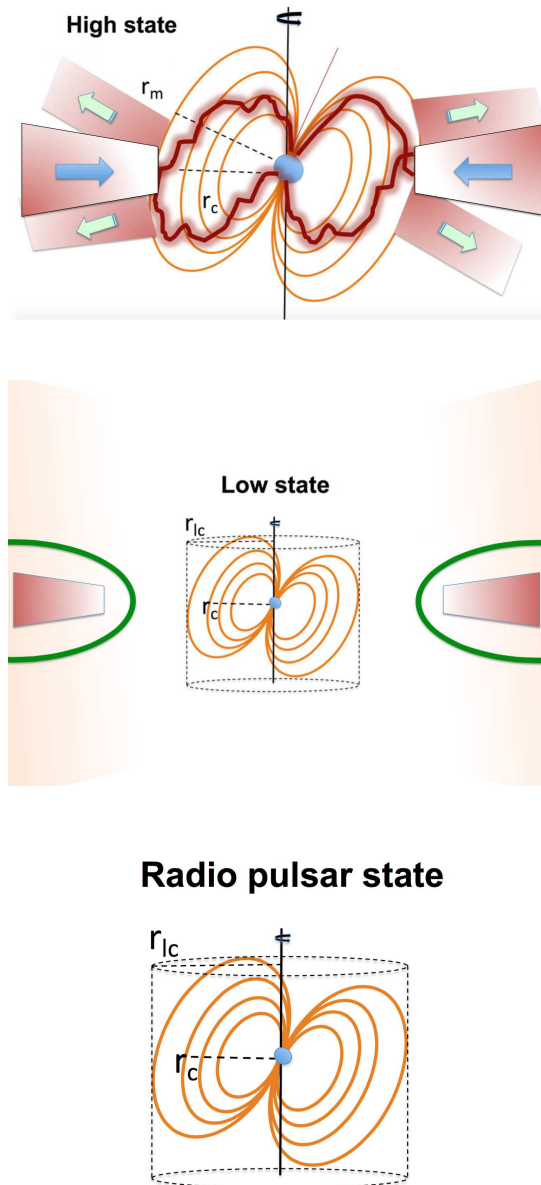


Figure 8.8: Cartoon view (not to scale) of the three modes of J1023. The high mode is depicted in the top panel, the low mode in the middle one and the pulsar state in the lowest panel. The corotation radius is 24 km and the light cylinder radius is 80 km. The magnetospheric radius changes with the J1023 state. See text for more details.

Table 8.6: Log of *XMM–Newton/Chandra* observations of J1023.

Obs. ID.	Obs. start (YYYY-MM-DD)	Instrument	Duration (ks)	High mode dur. - ks (counts)	Low mode dur. - ks (counts)
0720030101	2013-11-10	pn (FT)	128.4	85.2 (287431)	25.0 (21482)
		MOS (SW)	128.8	83.6 (169920)	24.6 (8466)
0742610101	2014-06-10	pn (FT)	116.7	63.8 (189226)	26.2 (12453)
		MOS (SW)	118.5	62.7 (138779)	25.9 (8379)
0748390101	2014-11-21	pn (FT)	32.4		
		MOS (SW)	34.3		
0748390501	2014-11-23	pn (FT)	32.9	61.0 (180708)	19.3 (9386)
		MOS (SW)	34.8	60.0 (128561)	19.1 (6026)
0748390601	2014-11-28	pn (FT)	16.9		
		MOS (SW)	20.6		
0748390701	2014-12-17	pn (FT)	32.5		
		MOS (SW)	34.4		
0560180801	2008-11-26	MOS (FW)	34.2	Quiescence (2136)	
11075 (<i>Chandra</i>)	2010-03-26	ACIS-S	86.2	Quiescence (3306)	

Exposure times for MOS refers to the MOS 2 detector (MOS 1 times are very similar), after cleaning for soft proton flares.

MOS counts for high and low mode spectra are the sum of MOS 1 and MOS 2 counts.

Exposure times and total counts for the last set of observations in the transitional mode were summed up.

8.10 Data analysis

We consider three sets of recent observations of J1023 with *XMM–Newton*. These are long observations carried out during 2013–2014. The first two sets (2013 November and 2014 June) were discussed by Archibald et al. (2015) and Bogdanov et al. (2015). The last set comprising 4 ToO observations (2014 November) is described in Jaodand et al. (2016), see Table 8.6 for a log of them.

Data reduction was performed with the *XMM–Newton* Science Analysis Software (SAS) version `xmmsas_20131209_1901-13.0.0` and the latest calibration files. We considered only EPIC data. Data were reprocessed with `EMPROC` and `EPPROC` locally, and grade filtered using `PATTERN 0–12 (0–4)` for MOS (pn) data, and `FLAG==0` and `#XMMEA_EM(P)` options. MOS data were all acquired with the thin filter and in small window mode; pn data with the thin filter and in timing (fast-timing) mode. Proton flares affected only the latest part of the 2014 June and one of the 2014 November observations, and were filtered out. The source events from the pn were extracted using a 7 pixel region centred on source. The MOS events were extracted from a 870 pixel circular region centred on source. Background events were extracted from similar regions close to the source and free of sources. RGS data were not considered in the following, containing less than 10 per cent of MOS counts. No narrow emission or absorption lines were detected. We included a zero-width iron line with energy free to vary within the 6.40–6.93 keV range, and

derived an upper limit on the equivalent width of < 23 , < 86 , and < 115 eV, for the high and low modes, and the radio pulsar state, respectively, at the 90 per cent confidence level.

For each observation, we combined the 0.3–10 keV background-subtracted and exposure-corrected light curves of the three CCD cameras (all binned at a time resolution of 10 s) using the EPICLCCORR tool in the SAS and the FTOOLS package. As already reported in previous studies the light curves are characterised by a low rate mode, a high rate mode, as well as random flares. The count rate ranges for the high and low modes are remarkably stable over all observations (see also Archibald et al. 2015; Bogdanov et al. 2015; Jaodand et al. 2016). For this reason, we decided to generate good time intervals by adopting the same thresholds for the count rate ranges as in Bogdanov et al. (2015) to disentangle the different modes. With these curves we identified low and high (and flaring) intervals for J1023, following closely Bogdanov et al. (2015) prescriptions: good time intervals (GTI) were generated for the low mode requiring the overall count rate to lie in the 0.0–2.1 counts s^{-1} interval and for the high mode in the 4.1–11 counts s^{-1} . Spectra were extracted using these GTIs for the two modes accordingly. Ancillary response files were generated for each spectrum using ARFGEN and redistribution matrices were generated for each observation using RMFGEN. MOS 1 and MOS 2 data and responses were combined for each observation. Data concerning the 2014 November campaign, consisting of 4 observations, were summed and response files weighted along the total counts number. MOS spectra were rebinned to have 100 counts per spectral bin, pn data to have 200 counts due to the higher background. MOS data were fitted in the 0.3–10 keV energy range, pn data in the 0.6–10 keV due to the larger calibration uncertainties in timing mode.

Quiescent data were taken from a 34 ks *XMM-Newton* observation (Archibald et al. 2010) and a 83 ks *Chandra* observation (Bogdanov et al. 2011). *XMM-Newton* data were analysed as above, without considering however pn data (operated in timing mode) due to the faintness of the source. No proton flare episode is present in the data. MOS 1 and MOS 2 data were collected with the thin filter and were summed up. *Chandra* data were acquired in standard Timed Exposure (TE) mode with the ACIS-S detector. Data were first reprocessed using the CHANDRA_REPRO tool and then analysed using CIAO 4.6 (CALDB 4.5.9). Photons were extracted from a 5-arcsec circular region and the background from an annular region free of sources. All the spectra were rebinned to have 50 counts per spectral bin. Data were retained within the 0.3–8 keV energy range.

8.11 Spectral fitting

We took the existing *XMM-Newton* data on J1023 (360 ks) and separate them into a (pure) high (210 ks) and low (70 ks) mode, and radio pulsar (34 ks *XMM-Newton* plus 83 ks *Chandra*) state. We fit the corresponding X-ray spectra with a composite model.

As described above, the high mode is modelled by a power-law, a radiatively-inefficient disk with free temperature and inner radius (this is achieved by using the DISKPBB model within XSPEC with $p = 0.5$), and a heated polar cap emission modelled with NSATMOS with a free radius (smaller than the neutron star radius) and temperature. A different

power-law, the same radiatively-inefficient disk with free temperature (and radius computed accordingly), together with a heated polar cap emission at the same emission radius plus a free power-law accounting for the magnetospheric emission was adopted for the low mode modelling. The quiescent radio pulsar emission has been fitted with exactly the same neutron star atmosphere component and exactly the same magnetospheric component as the low mode, with no additional parameters.

All spectra were corrected for absorption using the same absorbing column density⁵ (TBABS, Wilms et al. 2000, using VERN cross sections and WILM abundance pattern). The same normalisation constant was adopted for all the low mode and quiescent MOS spectra (fixed to one). The other MOS constants were all within 4 per cent of the fixed value. Constants for the pn were all 10 per cent lower and for *Chandra* ACIS-S 3 per cent higher. This indicates that the spectra taken in the high and low mode over more than one year are really stable. Given the huge number of counts heavily binned, we assigned a 2 per cent systematic uncertainty to each spectral channel (added in quadrature), as recommended by Smith (2015),⁶ The fit worked very well with $\chi^2_{\nu} = 1.032$ for 3885 degrees of freedom (see Table 8.7 and Figure 8.9), with a null hypothesis probability of 7.9 per cent. In case of no systematic error we obtain $\chi^2_{\nu} = 1.135$.

We find that the disk component is highly significant in the high mode, with an F -test probability of 10^{-9} (6.1σ). On the contrary, the disk component vanishes in the low mode. The absolute values of the radii are difficult to work out, given the known problems in associating the inner disk region to the model normalisation (Kubota et al. 1998), easily involving uncertainties by a factor of $\gtrsim 2$. Taken at face value and with a system inclination of 42° (Archibald et al. 2009, 2013), one gets for the high mode an inner disk radius $r_{\text{high}} = 21^{+9}_{-7}$ km, very close to the corotation radius of 24 km and fully consistent, given the uncertainties, to lie within the corotation radius and the light cylinder radius (i.e. in the propeller regime). The temperature of the disk in the low mode cannot be determined but only an upper limit can be set (consistent with our predictions). This in turn provides a lower limit to the inner disk radius of $\gtrsim 210$ km, well outside the light cylinder radius (~ 80 km).

⁵We tested that the column densities of the three states are consistent within the errors, the one relative to the radio pulsar state being the lowest.

⁶See <http://xmm2.esac.esa.int/docs/documents/CAL-TN-0018>

Table 8.7: X-ray spectral fits of J1023.

Parameter	High mode	Low mode	Radio pulsar state
N_H (10^{20} cm $^{-2}$)	$5.25^{+0.63}_{-0.60}$	tied all	tied all
power-law Γ_D	1.54 ± 0.02	2.00 ± 0.03	–
power-law N_D (10^{-4})	16.7 ± 0.5	2.9 ± 0.7	–
Disk T (eV)	138^{+21}_{-17}	< 43	–
Disk norm. N_d	103^{+109}_{-55}	$> 1.1 \times 10^4$	–
NS atmos. T (eV)	155^{+16}_{-14}	75^{+8}_{-7}	tied Low mode
NS atmos. Em. Radius (km)	$2.6^{+0.6}_{-0.5}$	tied all	tied all
NS power-law Γ_P	–	0.97 ± 0.07	tied Low mode
NS power-law N_P (10^{-5})	–	3.3 ± 0.3	tied Low mode

¹ Errors are quoted at the 90 per cent confidence level for one parameter of interest. The fit provides $\chi^2_\nu = 1.032$ for 3885 dof, after the addition of a systematic error of 2 per cent.

² The effective neutron star temperatures were not corrected for the gravitational redshift.

³ Radii were computed assuming a source distance of 1.37 kpc.

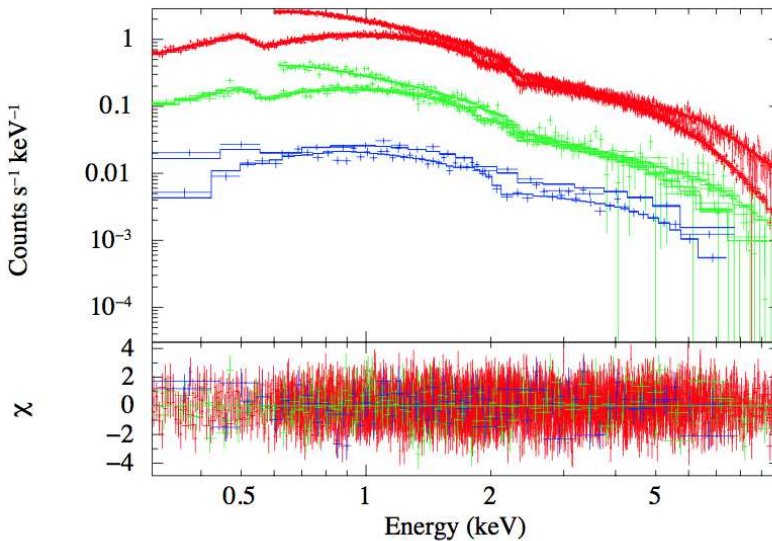


Figure 8.9: *XMM-Newton* and *Chandra* spectra of J1023. Upper spectra (in red) refer to the pn (0.6–10 keV) and MOS (0.3–10 keV) high mode spectra. Middle spectra (in green) refer to pn and MOS low mode spectra. The lowest spectra (in blue) refer to the radio pulsar state (among the two curves the highest refers to *XMM-Newton* data and the lowest to *Chandra* data). The fitting model is described in the text.

Table 8.8: 0.3–10 keV fluxes of the different components of J1023.

Parameter	Total/Components	High mode	Low mode	Radio pulsar state
Abs flux ($\text{erg cm}^{-2} \text{ s}^{-1}$)	Total	1.4×10^{-11}	2.0×10^{-12}	5.6×10^{-13}
	power-law	1.2×10^{-11} (89.8%)	1.4×10^{-12} (71.7%)	–
	Ineffic. disk	4.8×10^{-13} (3.4%)	$< 0.1 \times 10^{-13}$ (–)	–
	NS thermal	9.5×10^{-13} (6.8%)	0.4×10^{-13} (1.9%)	0.4×10^{-13} (6.5%)
	Magn. power-law	–	5.2×10^{-13} (26.4%)	5.2×10^{-13} (93.5%)
Unabs flux ($\text{erg cm}^{-2} \text{ s}^{-1}$)	Total	1.5×10^{-11}	2.2×10^{-12}	5.9×10^{-13}
Luminosity (erg s^{-1})	Total	3.4×10^{33}	5.0×10^{32}	1.3×10^{32}

Fluxes refer to the mean of the MOS detectors. The calibration constant is 0.92 for the pn and 1.02 for *Chandra*/ACIS-S. The fractional contribution of each component to the total absorbed flux is indicated in parentheses. The ratio between the high and low mode fluxes is 7.1, and the ratio between the low mode and radio pulsar fluxes is 3.5.

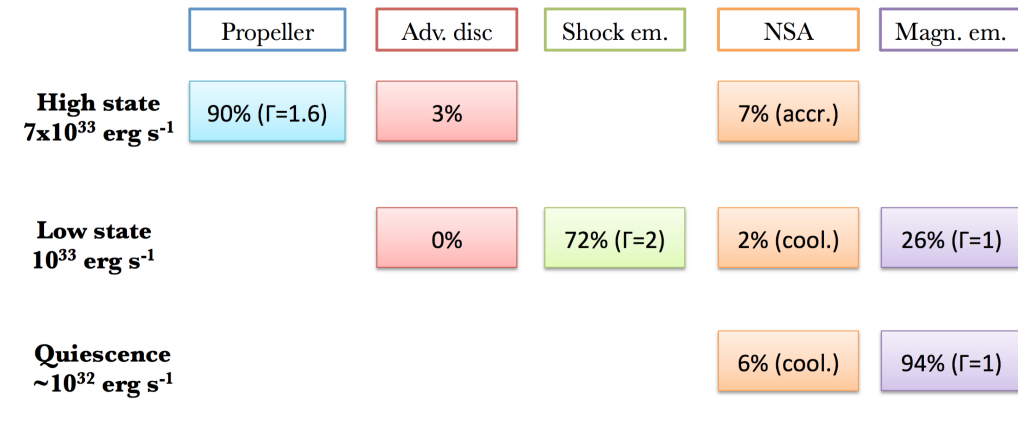


Figure 8.10: Schematic view of the proposed spectral decomposition of J1023 and of the fractional contribution of the different components to the X-ray emission of the different states. Note that the quiescent emission increases by a factor of ~ 5 if the power-law component extends up to 100 keV.

8.12 Timing analysis

Following Archibald et al. (2015), we adopted a definition of the pulsed flux in terms of root-mean-squared (rms) modulation. For a signal $f(\phi)$ (with ϕ the phase angle), the rms modulation is defined as:

$$F_{\text{rms}} = \int (f(\phi) - \bar{f})^2 d\phi$$

where \bar{f} is the mean of the signal. With this definition Archibald et al. (2015) estimated an rms pulsed fraction of 8.13 ± 0.14 per cent in the high mode (0.3–10 keV), an upper limit of < 2.8 per cent in the low mode at the 95 per cent confidence level (0.3–10 keV), and 11 ± 2 per cent in the radio pulsar state in the 0.3–2.5 eV energy range (with a non-detection in the 0.3–10 keV; Archibald et al. 2015).

Based on our picture, in the low mode we expect a heavily enshrouded pulsar. The pulsed signal of the pulsar can in principle be detected in the low mode. We rescale the observed pulsed fraction in the radio pulsar state to the higher total flux in the low mode, and predict to detect X-ray pulsations in the low mode at a level of ~ 2 per cent in the soft energy band (0.3–2.5 keV).

We searched the two longest uninterrupted *XMM-Newton* observations (IDs 0720030101 and 0742610101) for pulsations. We first isolated the low mode as described above. After barycentering the data, we corrected for the 4.75 hr orbital modulation and restricted the energy range of the pn data to 0.3–2.5 keV energy range. We then searched for pulsations at the known period, determined from the analysis of the corresponding high mode (and in full agreement with published results, Bogdanov et al. 2014; Archibald et al. 2015). We do not detect any pulsed signal and derive 90 per cent confidence level upper limits on the fractional rms pulsed emission of < 3.1 and < 3.6 per cent for the two observations, respectively. These were derived fitting the pulse profile with two harmonics (as the radio pulsar pulsed profile) and subtracting for the background. These limits, even if tight, still leave open the possibility that a radio pulsar-like signal is present in the low mode.

8.13 Conclusions – Part II

Transitional pulsars, and J1023 and XSS J12270–4859 in particular, show rapid ($\lesssim 10$ s) transitions from a high X-ray luminosity mode during which pulsations are observed (rms pulsed fraction ~ 8 per cent) to a low mode a factor of ~ 7 dimmer and showing no signs of pulsations (rms pulsed fraction < 2.4 per cent; De Martino et al. 2013; Bogdanov et al. 2014; Archibald et al. 2015; Papitto et al. 2015). Similar transitions were also observed in the optical band in J1023, possibly indicating a slightly longer transition time ~ 20 s (Shahbaz et al. 2015). These mode transitions are hardly explained by current modelling of these sources.

Transitional pulsars and IGR J18245–2452 in particular (Papitto et al. 2013) have shown the possibility to alternate episodes of accretion on the neutron star surface to radio pulsar activity on a timescale of less than a week. In this chapter we put forward a physical

scenario to account for rapid transitions among high and low modes on a much faster timescale. We postulate that transitions among the propeller regime and the radio pulsar regime are the main driver for the high and low X-ray luminosity modes. This implies that J1023 can push matter outside the light cylinder and this can get back close to the corotation radius on a 10 s timescale. The dynamical timescale or free fall timescale at the light cylinder radius are much shorter than 10 s (of the order of milliseconds), whereas the disk viscous timescale is instead longer (hundreds of seconds). This indicates that the disk replenishment should occur on a free-fall-like timescale. Even if we do not investigate the physical mechanism for alternating the high and low modes, we developed a spectral model to account for the observed spectra as well as the radio pulsar state. This model is clearly ad hoc and cannot be proven to be unique, but it provides a satisfactory description of the observed characteristics.

In the high X-ray mode J1023 is in the propeller regime. The X-ray spectrum consists of a non-thermal component, which accounts for the majority of the flux. This can come from a hot corona above the disk or, more likely, from the propelling magnetosphere shocking the inflowing matter. Indeed the average *Fermi*/LAT spectrum is described by a power-law with photon index 1.8 ± 0.2 , with a cutoff at an energy of ~ 2.3 GeV (Takata et al. 2014), consistent with our photon index. A propeller model to account for the main characteristics of the high mode has been developed by Papitto & Torres (2015). In their model the inflowing matter is propelled outwards by the rapidly rotating neutron star magnetosphere. Electrons can be accelerated to energies of a few GeV at the turbulent disk-magnetosphere boundary. Synchrotron and self-synchrotron Compton emission is able to account for the observed X-ray and GeV emission, respectively (Papitto & Torres 2015). This model applies tout-court to our description of the high mode. Additional ingredients to model the high mode X-ray spectrum are a radiatively inefficient accretion disk, able to push the inner boundary close to the corotation radius but not emitting too much luminosity and some matter leaking through the neutron star magnetosphere to account for the pulsed emission. The inner disk radius derived from spectral modelling is consistent to lie close to the corotation radius. The fraction of the flux emitted from the neutron star is 7 per cent. This flux arises from a small region on the surface and can give rise to pulsations. Its incidence on the total flux is consistent with the observed rms pulsed fraction of 8 per cent.

In the low mode of J1023 the pulsar wind suddenly turns on. The spectral model to fit the low mode X-ray spectrum is made of a power-law with $\Gamma \sim 2$. This can be interpreted as the shock emission coming from the interaction of the relativistic pulsar wind with the inflowing matter. The fraction of spin-down luminosity converted into 0.3–10 keV luminosity is ~ 2 per cent, which is in line with other radio pulsars converting their spin-down power into X-rays. The accretion disk in this model is pushed outside the light cylinder radius and our spectral model does not require the presence of a disk in this mode, allowing us to set a lower limit to the disk inner edge well outside the light cylinder. Since a radio pulsar is active in this state we added two further spectral components. These are motivated by X-ray observations of radio pulsars. One is thermal in origin arising

from the neutron star polar cap and the other is of magnetospheric origin. These two components were used to fit simultaneously an *XMM–Newton* and a *Chandra* spectra taken when J1023 was in quiescence with a radio pulsar detected in the radio band. The radius of the thermal component is kept the same for all the three states. This nested spectral model can satisfactorily reproduce the X-ray spectra of the three different states (see Table 8.7 and Figure 8.10). Even if active during the low mode a radio pulsar would be hardly detectable due to the large amount of ionised material in the surrounding, producing a large free-free absorption (Campana et al. 1998; Burderi et al 2001; Deller et al. 2015).

The flat-spectrum radio emission can be associated to an outflow from the system, arising from synchrotron emission. This can be in form of a jet (Deller et al. 2015) or it can be launched due to the propeller effect (Papitto & Torres 2015). Optical polarisation observations detected a positive signal in V and R and put a strong upper limit in I (Baglio et al. 2016). In addition, a weak modulation with the orbital period is revealed. These observations would argue against a structured jet outflow and have been interpreted as due to Thomson scattering of the companion star light with electrons in the disk corona or in a large scale outflow (Baglio et al. 2016).

The mechanism responsible for the transition from and to the high and low state is not fully clear. It heavily relies on inhomogeneities of the accretion flow to reduce the effective mass inflow rate and lead the magnetosphere to expand beyond the corotation radius. The transition from the low mode to the high mode can be understood in terms of build up of matter at the outer disk boundary, able to quench on a very short time scale the turned on radio pulsar. Further simultaneous observations from NIR to hard X-rays are clearly needed. This will allow us to study correlations and lags, and to prove the possible reprocessing of radiation due to the outermost regions of the accretion disk. In particular, correlations and lags will provide us with a unique tool to investigate the changes in the disk size in the two flux modes. According to our picture, the inner disk should be disrupted by the pulsar wind in the low mode and the effects on the outer disk need to be explored.

The magnetic cataclysmic variable RX J2015.6+3711

Coti Zelati F., Rea N., Campana S., de Martino D.,
Papitto A., Safi-Harb S., Torres D. F. (2016),

**Multiwavelength study of RX J2015.6+3711: a magnetic
cataclysmic variable with a 2-h spin period,**

Published in Monthly Notices of the Royal Astronomical Society,
Volume 456, Issue 2, pp. 1913–1923

The X-ray source RX J2015.6+3711 was discovered by *ROSAT* in 1996 and recently proposed to be a cataclysmic variable (CV). Here we report on an *XMM–Newton* observation of RX J2015.6+3711 performed in 2014, where we detected a coherent X-ray modulation at a period of 7196 ± 11 s and discovered other significant ($> 6\sigma$) small-amplitude periodicities which we interpret as the CV spin period and the sidebands of a possible ~ 12 hr periodicity, respectively. The 0.3–10 keV spectrum can be described by a power-law ($\Gamma = 1.15 \pm 0.04$) with a complex absorption pattern, a broad emission feature at 6.60 ± 0.01 keV, and an unabsorbed flux of $(3.16 \pm 0.05) \times 10^{-12}$ erg cm $^{-2}$ s $^{-1}$. We observed a significant spectral variability along the spin phase, which can be ascribed mainly to changes in the density of a partial absorber and the power-law normalization. Archival X-ray observations carried out by the *Chandra* satellite, and two simultaneous X-ray and UV/optical pointings with *Swift*, revealed a gradual fading of the source in the soft X-rays over the last 13 years, and a rather stable X-ray-to-optical flux ratio ($F_X/F_V \approx 1.4 - 1.7$). Based on all these properties, we identify this source with a magnetic CV, most probably of the intermediate polar type. The 2 hr spin period makes RX J2015.6+3711 the second slowest rotator of the class, after RX J0524+4244 (‘Paloma’; $P_{\text{spin}} \sim 2.3$ hr). Although we cannot unambiguously establish the true orbital period with these observations, RX J2015.6+3711 appears to be a key system in the evolution of magnetic CVs.

A.1 Introduction

Cataclysmic variables (CVs) are interacting binary systems in which a white dwarf (WD) accretes matter from a late-type low mass main sequence star through Roche lobe overflow. Typical orbital periods of these systems are of a few hours (see Warner 1995 for a review). About 20–25 per cent of the known CVs harbour WDs with magnetic field in the $10^5 - 10^8$ G range, and are called magnetic CVs (mCVs; Ferrario, de Martino & Gänsicke 2015). The mCVs are further classified as polars and intermediate polars (IPs) based on the strength of their magnetic field. The former systems are characterized by very high magnetic fields ($B \sim 10^7 - 10^8$ G) that are able to synchronise the WD spin with the orbital period to a very high degree ($P_{\text{spin}} \simeq P_{\text{orb}}$). The latter are believed to possess weaker fields ($B \lesssim 10^7$ G) because of the asynchronous rotation of the WD. They have in fact spin periods of a few hundreds of seconds and orbital periods of a few hours, with a spin-to-orbit period ratio $P_{\text{spin}}/P_{\text{orb}} \approx 0.05 - 0.15$ (Norton, Wynn & Somerscales 2004).

RX J2015.6+3711 was discovered by the High Resolution Imager on board *ROSAT* in 1996 August, during a survey of the gamma-ray source 3EG J2016+3657 in the EGRET catalog (Halpern et al. 2001). It has optical and near-infrared magnitudes of $R \sim 17.5$, $J = 15.54 \pm 0.08$, $H = 15.04 \pm 0.11$ and $K = 14.79 \pm 0.15$ (see Halpern et al. 2001 and the Two-Micron All-Sky Survey catalog¹). RX J2015.6+3711 lies in the error box of the variable *Fermi* source 3FGL J2015.6+3709 (Acero et al. 2015) and within a crowded region of high-energy emitting sources. The blazar B2013+370 is only ~ 1.6 arcmin away and it is also compatible with the position of the *Fermi* source (Bassani et al. 2014). Furthermore, the supernova remnant CTB 87 is located at an angular separation of about 5.2 arcmin from the source (Matheson, Safi-Harb & Kothes 2013).

The spatial coincidence of RX J2015.6+3711 with the GeV source has opened the new possibility (Bassani et al. 2014) that it may belong to the class of the recently discovered transitional millisecond pulsars (TMPs). TMPs are neutron star low-mass X-ray binary systems (LMXBs) that are observed to switch between accretion and rotation-powered emission on timescales ranging from a few weeks to a few years (see e.g. Papitto et al. 2013). The possibility of RX J2015.6+3711 being such a system is not remote if one considers the cases of the sources PSR J1023+0038 and XSS J12270–4859. These were initially classified as mCVs (Thorstensen & Armstrong 2005; Masetti et al. 2006) and subsequently recognized to be gamma-ray emitters with a 0.1–10 GeV luminosity of a few 10^{33} erg s^{-1} , comparable to that in the X-rays (Stappers et al. 2014; de Martino et al. 2010, 2013). Multiwavelength observations over the last years led observers to identify these sources as TMPs (see Bogdanov et al. 2015 and references therein; de Martino et al. 2015 and references therein).

However, while this work was in preparation, Halpern & Thorstensen (2015) suggested that the source might be a mCV of the polar type, on the basis of the characteristics of its optical spectrum and the discovery of an energy dependent 2-hr X-ray modulation in archival *Chandra* data, on which we report independently here in detail using also a long

¹See <http://www.ipac.caltech.edu/2mass/releases/second/>.

Table A.1: Journal of the X-ray observations used in this work.

Instrument	Obs. ID	Date	Exp ^a (ks)	Mode ^b
<i>Chandra</i> ACIS-S	1037	2001 Jul 08	17.8	TE FAINT (3.241 s)
<i>Swift</i> XRT	00035639003	2006 Nov 17	7.4	PC (2.507 s)
<i>Chandra</i> ACIS-I	11092	2010 Jan 16–17	69.3	TE VFAINT (3.241 s)
<i>Swift</i> XRT	00041471002	2010 Aug 06–10	7.3	PC (2.507 s)
<i>XMM–Newton</i> pn	0744640101	2014 Dec 14–16	108.2	FF (73.4 ms)
<i>XMM–Newton</i> MOS 1/2			122.3	FF (2.6 s)

^a Deadtime corrected on-source time.

^b TE: Timed Exposure, FAINT: Faint telemetry format, VFAINT: Very Faint telemetry format, FF: Full Frame, LW: Large Window, PC: Photon Counting; the temporal resolution is given in parentheses.

XMM–Newton observation.

Here we attempt to better assess the nature of RXJ2015.6+3711 through a detailed analysis of a recent *XMM–Newton* observation, and a reanalysis of archival *Chandra* and *Swift* observations. We describe the X-ray and UV/optical observations and present the results of our data analysis in Section A.2 and A.3. We discuss our results in Section A.4. Conclusions follow in Section A.5.

A.2 X-ray observations and data analysis

The field of RXJ2015.6+3711 was observed multiple times by the X-ray imaging instruments on board the *XMM–Newton*, *Chandra* and *Swift* satellites. A summary of the observations used in our study is reported in Table A.1.

A.2.1 *XMM–Newton*

A deep *XMM–Newton* observation (PI: Safi-Harb) was carried out using the European Photon Imaging Cameras (EPIC), starting on 2014 December 14 (see Table A.1) and with CTB 87 placed at the aim point. The pn (Strüder et al. 2001) and the two MOS (Turner et al. 2001) CCD cameras were configured in full-frame window mode. The medium optical blocking filter was positioned in front of the cameras.

We processed the raw data files using the EPPROC (for pn data) and EMPROC (for MOS data) tasks of the *XMM–Newton* Science Analysis System (SAS², version 14.0), with the most up to date calibration files available. The data were affected by strong soft-proton flares of solar origin. For the timing analysis we decided to dynamically subtract the scaled background in each bin of the source light curves binned at 10 s. For the spectral analysis we built the light curve of the entire field of view and discarded episodes of

²See <http://xmm.esac.esa.int/sas/>.

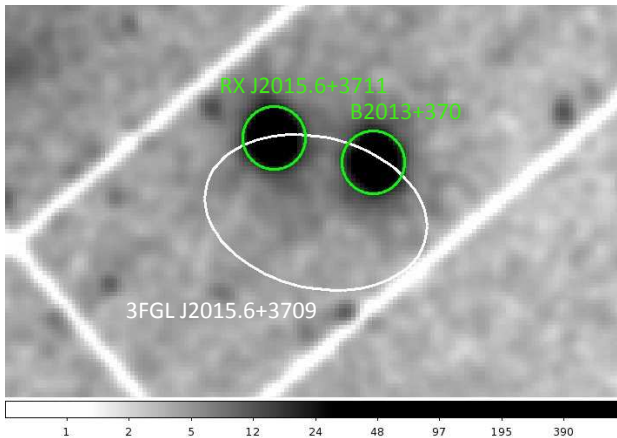


Figure A.1: *XMM-Newton* EPIC-pn 0.3–10 keV image of the field around RX J2015.6+3711. The field size is about 12×7.5 arcmin². North is up, east to the left. Both RX J2015.6+3711 and the blazar B2013+370 were located on CCD 5 and their positions are marked with green circles, each with a radius of 30 arcsec. The white ellipse is centered at RA = $20^{\text{h}}15^{\text{m}}33^{\text{s}}.6$, Dec = $+37^{\circ}10'12''.2$ (J2000.0) and represents the position (at the 95 per cent confidence level) of the source 3FGL J2015.6+3709 in the *Fermi* Large Area Telescope 4-year point source catalog (Acero et al. 2015; see also Kara et al. 2012). (See the online version of the article for the colour figure.)

flaring background using intensity filters. This reduced the effective exposure time to approximately 77.8, 107.3 and 106.8 ks for the pn, MOS 1 and MOS 2, respectively.

The field of RX J2015.6+3711 observed by the pn camera is shown in Figure A.1. The image was created by selecting events with PATTERN=0, (FLAG & 0x2fa002c)=0 for the 0.3–0.5 keV range, PATTERN ≤ 4 , (FLAG & 0x2fa002c)=0 for the 0.5–1.0 keV range and PATTERN ≤ 4 , (FLAG & 0x2fa0024)=0 for the 1.0–10 keV range, to remove any traces of hot pixels and bad columns, and was also smoothed with a Gaussian filter with a kernel radius of 3 pixels (one EPIC-pn pixel corresponds to about 4.1 arcsec).

We extracted the source photons from a circular region centered at the optical position of the source (RA = $20^{\text{h}}15^{\text{m}}36^{\text{s}}.98$, Dec = $+37^{\circ}11'23''.2$ (J2000.0); see Halpern et al. 2001) and with a radius of 30 arcsec, to avoid contamination from the closeby blazar. The background was extracted from a similar region, far from the source location and on the same CCD (see Bassani et al. 2014 for an overview of the nearby X-ray emitting sources). We converted the photon arrival times to Solar System barycenter reference frame using the SAS task BARYCEN and restricted our analysis to photons having energies between 0.3 and 10 keV. We verified that data were not affected by pile-up through the EPATPLOT script. The 0.3–10 keV average source net count rates are $(2.74 \pm 0.02) \times 10^{-1}$, $(8.98 \pm 0.09) \times 10^{-2}$ and $(8.83 \pm 0.09) \times 10^{-2}$ counts s⁻¹ for the pn, MOS 1 and MOS 2,

respectively.

We applied the standard filtering procedure in the extraction of the spectra, retaining only events optimally calibrated for spectral analysis ($\text{FLAG} = 0$) and with $\text{PATTERN} \leq 4(12)$ for the pn (MOS) data. We generated the corresponding redistribution matrices and ancillary response files with the `RMFGEN` and `ARFGEN` tools, respectively, and grouped the background-subtracted spectra to have at least 100 counts in each spectral bin.

Timing analysis

The 0.3–10 keV background-subtracted and exposure-corrected light curve of RX J2015.6+3711 is reported in Figure A.2. It was generated by combining the time series from the EPIC cameras during the periods when all three telescopes acquired data simultaneously, using the `EPICLCCORR` tool of `SAS` and other tasks in the `FTOOLS` package (Blackburn 1995). The light curve clearly shows a periodic modulation. We computed a Fourier transform of the pn light curve and found indeed a prominent peak at a frequency of $\sim 1.39 \times 10^{-4}$ Hz (at a significance level of about 27σ , estimated taking into account the presence of the underlying white noise component and the number of independent Fourier frequencies examined in the power spectrum; see the top panel of Figure A.3). A search for periodicities at millisecond periods was precluded owing to the temporal resolution of the pn camera in full frame readout mode, which implies a Nyquist limiting frequency of about 6.8 Hz. We show in the inset of Figure A.3 the Fourier power spectral density of RX J2015.6+3711, produced by calculating the power spectrum into 2405 s-long consecutive time intervals, averaging the 48 spectra so evaluated and rebinning geometrically the resulting spectrum with a factor 1.05. A closer inspection of the power spectrum around the frequency of the main peak revealed excess of power up to the second harmonic and also at frequencies of about 9.4×10^{-5} , 1.20×10^{-4} , 1.65×10^{-4} and 2.55×10^{-4} Hz (in all cases at a significance level larger than 6σ ; see the bottom panel of Figure A.3). The power spectra filtered in different energy intervals show no evidence for significant peaks above ~ 3 keV.

To refine our period estimate for the main peak in the power spectrum, we performed an epoch-folding search of the light curve by binning the profile into 16 phase bins and searching with a period resolution of 13 s. We then fitted the peak in the χ^2 versus trial period distribution as described by Leahy (1987) and derived a best period $P = 7196 \pm 11$ s (at the 90 per cent confidence level), consistent within the errors with that reported (independently) by Halpern & Thorstensen (2015).

The pn light curve folded on P is shown in the left-hand panel of Figure A.4. The profile is asymmetric and is characterized by a prominent peak in the phase interval $\sim 0.1 - 0.4$, followed by a minimum in the $0.6 - 0.9$ range. We also produced an energy versus phase image by binning the source counts into 100 phase bins and 100-eV wide energy channels and normalizing to the phase-averaged energy spectrum and pulse profile. A lack of counts is evident at energy $\lesssim 2$ keV and in the phase interval corresponding to the minimum of the profile (see again the left-hand panel of Figure A.4).

The profiles are approximately phase-aligned at different energies within statistical uncertainties, but their morphology changes as a function of energy (see the middle panel of

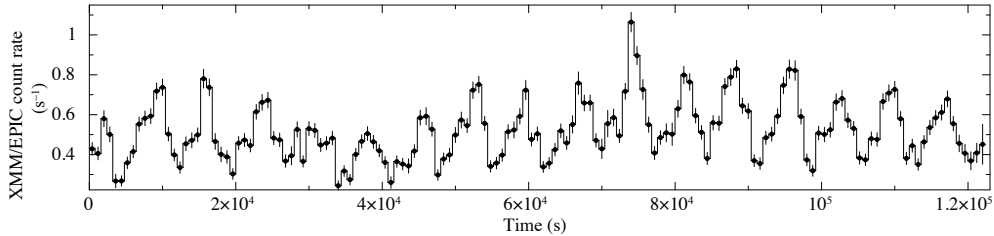


Figure A.2: 0.3–10 keV background-subtracted and exposure-corrected light curve of RX J2015.6+3711 obtained with the *XMM-Newton* EPIC cameras with a binning time of 800 s.

Figure A.4). In particular we observe a secondary hump in the phase interval 0.8–1.1 in the softest band (0.3–1 keV), a feature that is nearly absent in the 1–2 keV interval. To assess the significance of the observed pulse shape variations as a function of energy, we compared the 0.3–1 keV and 1–2 keV folded profiles using a two-sided Kolmogorov–Smirnov test (Peacock 1983; Fasano & Franceschini 1987). The result shows that the difference between these energy ranges is highly significant: the probability that the two profiles do not come from the same underlying distribution is in fact $\sim 4 \times 10^{-7}$, corresponding to a significance of $\sim 5.3\sigma$.

We also analyzed the temporal evolution of the pulse shape in the 0.3–10 keV energy band by dividing the entire duration of the pn observation into four consecutive time intervals, each of length $4P$, and folding the corresponding light curves on P . As shown in the right-hand panel of Figure A.4, the shape of the profile clearly changes as time elapses.

We evaluated the pulsed fractions by fitting a constant plus two sinusoidal functions to the 32-bin folded light curves and considering the semi-amplitude measured from the fundamental frequency component (the sinusoidal periods were fixed to those of the fundamental and second harmonic components). The inclusion of higher harmonic components in the fits was not statistically needed, as determined by means of an F -test. The 0.3–10 keV pulsed fractions are 29 ± 1 , 29 ± 2 and 30 ± 2 per cent for the pn, MOS 1 and MOS 2 data sets, respectively (uncertainties are reported at the 90 per cent confidence level). The amplitude of the modulation decreases as the energy increases: for pn data we calculated pulsed fractions of 62 ± 4 , 44 ± 2 , 22 ± 3 , 17 ± 3 and 9 ± 4 per cent in the 0.3–1, 1–2, 2–3, 3–5 and 5–10 keV energy ranges, respectively. The pulsed fraction is however consistent with the average value over the entire duration of the observation.

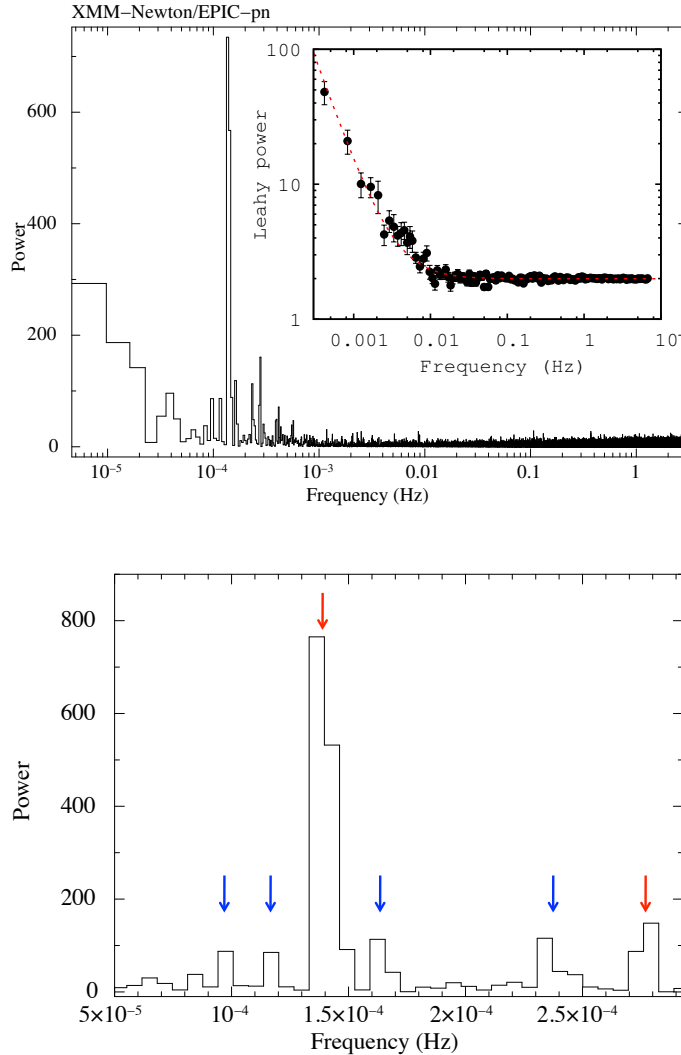


Figure A.3: Top panel: 0.3–10 keV power spectrum of RX J2015.6+3711 obtained from *XMM-Newton* EPIC-pn data. Inset: Fourier power spectral density of RX J2015.6+3711. The red dashed line represents the modeling of the white and red noise components, i.e. the sum of a constant and a power-law function: $P(\nu) = K + C\nu^{-\beta}$, with $K = 1.99(1) \text{ Hz}^{-1}$ and $\beta = 1.59(8)$. Bottom panel: 0.3–10 keV power spectrum of RX J2015.6+3711 restricted to the frequency range between 5×10^{-5} and 3×10^{-4} Hz. The main peak and that of the second harmonic are highlighted with red arrows, whereas the other significant power peaks are marked with blue arrows. All these peaks are detected at a significance level above 6σ (see the text). (See the online version of the article for the colour figure.)

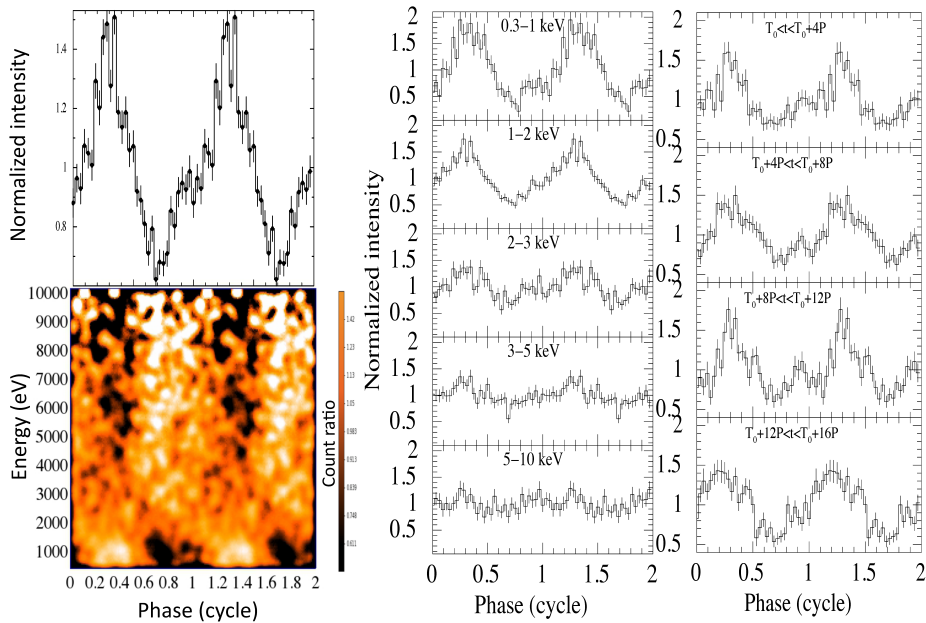


Figure A.4: Left-hand panel, top: 0.3–10 keV background-subtracted and exposure-corrected light curve of RX J2015.6+3711 (from *XMM-Newton*/EPIC-pn data) folded on the period $P=7196$ s and sampled in 32 phase bins. Epoch $T_0=57\,005.6889669$ MJD was used as reference. Left-hand panel, bottom: normalized energy versus phase image for the pn data of RX J2015.6+3711 (see the text for details). Middle panel: 32-bin pulse profiles in five different energy bands. Energy increases from top to bottom. Right-hand panel: 32-bin pulse profiles in four different time intervals (0.3–10 keV). Time increases from top to bottom. Two cycles are shown in all cases for better visualization. (See the online version of the article for the colour figure.)

Phase-averaged spectral analysis

We fitted the spectra of the three EPIC cameras together in the 0.3–10 keV energy range using the XSPEC³ spectral fitting package (v. 12.9.0; Arnaud 1996). We adopted a set of different single-component models: a black body (BBODYRAD in XSPEC notation), an optically-thin thermal bremsstrahlung, an accretion disk consisting of multiple black body components (DISKPBB) and a power-law (PEGPWRLW). To describe the absorption by the interstellar medium, we used the Tuebingen-Boulder model (TBABS), with photoionization cross-sections from Verner et al. (1996) and solar chemical abundances from Wilms, Allen & McCray (2000). We included an overall normalization factor to account for calibration uncertainties among the three different X-ray detectors⁴ and tied up all the parameters across the three data sets. In the following we will quote all the uncertainties at a 90 per cent confidence level for a single parameter of interest ($\Delta\chi^2 = 2.706$), unless otherwise specified.

A black body model is rejected by the data ($\chi^2_\nu = 5.2$ for 368 degrees of freedom; dof hereafter). The bremsstrahlung model yields $\chi^2_\nu = 1.54$ for 368 dof, with the temperature pegged to the highest allowed value of 200 keV. In the disk model, the temperature is allowed to have a radial dependence, $T(r) \propto r^{-p}$. Fixing p to 0.75 (i.e., reproducing the standard geometrically thin and optically thick accretion disk of Shakura & Sunyaev 1973) gives $\chi^2_\nu = 1.30$ for 368 dof. If we leave this parameter free to vary we obtain $\chi^2_\nu = 1.18$ for 367 dof, with $p = 0.68^{+0.01}_{-0.02}$. An F -test gives a chance probability of $\sim 1.1 \times 10^{-9}$, corresponding to a 6.3σ improvement. However, the inferred value for the temperature at the inner radius of the disk is $\gtrsim 5.9$ keV, which is quite implausible. We find instead $\chi^2_\nu = 1.19$ for 368 dof for the power-law model. However, structured residuals are clearly visible at energy $\lesssim 0.6$ keV and around 6.6 keV. The inclusion of a partial covering absorber (PCFABS), accounting for additional partial absorption, and a Gaussian feature (GAUSS) in emission, leads to an improvement in the shape of these residuals and to a more satisfactory modeling of the data (see Figure A.5). We obtain $\chi^2_\nu = 0.97$ for 363 dof. The best-fitting parameters are listed in Table A.2. The interstellar absorption column density, $N_{\text{H,ISM}} \sim 2 \times 10^{21} \text{ cm}^{-2}$, is about one order of magnitude lower than the total Galactic value in the direction of the source ($\sim 1.25 \times 10^{22} \text{ cm}^{-2}$; Willingale et al. 2013), implying a closeby location of this source within our Galaxy. The nearby source CTB 87, believed to be at a distance of about 6.1 kpc, has a much higher N_{H} value of $1.4 \times 10^{22} \text{ cm}^{-2}$ (Matheson et al. 2013), further supporting the closer distance of this source. The partial (≈ 83 per cent) column density is larger than the interstellar column density by a factor of ~ 3 (see Table A.2), suggesting that the majority of the contribution to the observed absorption is due to an absorber localized close to the source. The broad emission feature around 6.6 keV is suggestive of different contributions, in particular thermal and fluorescent iron lines. The 0.3–10 keV unabsorbed flux is $(3.16 \pm 0.05) \times 10^{-12} \text{ erg cm}^{-2} \text{ s}^{-1}$.

³See <http://heasarc.gsfc.nasa.gov/xanadu/xspec/>

⁴This factor was fixed to 1 for the pn spectrum, and left free to vary for both the MOS 1 and MOS 2 spectra.

Table A.2: Average spectral fit results for the *XMM-Newton* observation of RX J2015.6+3711. pn and MOSs spectra were fitted together to the TBABS*PCFABS*(PEGPWRLW+GAUSS) model in the 0.3–10 keV energy range. Uncertainties are quoted at the 90 per cent confidence level for a single parameter of interest.

Parameter	Value
$N_{\text{H,ISM}}^a$ (10^{21} cm $^{-2}$)	2 ± 1
$N_{\text{H,pcf}}$ (10^{21} cm $^{-2}$)	$6.1^{+1.0}_{-0.7}$
Covering fraction (per cent)	83^{+10}_{-16}
Γ	1.15 ± 0.04
Energy of line (keV)	6.61 ± 0.09
Width of line (keV)	$0.24^{+0.11}_{-0.08}$
Normalization of line (10^{-6} cm $^{-2}$ s $^{-1}$)	$5.2^{+1.9}_{-1.6}$
Equivalent width (keV)	0.18 ± 0.06
Absorbed flux b (10^{-12} erg cm $^{-2}$ s $^{-1}$)	$2.75^{+0.05}_{-0.03}$
Unabsorbed flux b (10^{-12} erg cm $^{-2}$ s $^{-1}$)	3.16 ± 0.05
χ^2_{ν} (dof)	0.97 (363)
Null hypothesis probability	6.5×10^{-1}

^a The abundances are those of Wilms et al. (2000). The photoelectric absorption cross-sections are from Verner et al. (1996).

^b In the 0.3–10 keV energy range.

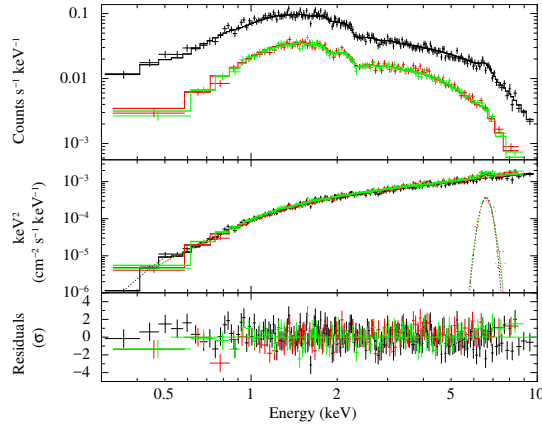


Figure A.5: 0.3–10 keV average spectrum of RXJ2015.6+3711 extracted from *XMM-Newton* EPIC data. The solid line represents the best-fitting model, i. e. the superposition of an absorbed power-law and a Gaussian feature in emission. $E^2 \times f(E)$ unfolded spectra (middle panel) and post-fit residuals in units of standard deviations (bottom panel) are also shown. Black, red and green colors refer to the pn, MOS 1 and MOS 2 data sets, respectively. (See the online version of the article for the colour figure.)

Phase-resolved spectral analysis

The normalized energy versus phase image relative to the 7196-s periodicity hints at a phase-variable emission, possibly due to a varying absorption along the line of sight (see the left-hand panel of Figure A.4). To better investigate the variability of the X-ray emission along the phase, we computed a hardness ratio between the hard (2–10 keV) and soft (0.3–2 keV) counts along the cycle (see Figure A.6). We then carried out a phase-resolved spectroscopy accordingly, selecting the following four phase intervals: 0.1–0.4 (corresponding to the softest state, around the maximum of the modulation), 0.4–0.6, 0.6–0.9 (related to the hardest state, close to the minimum of the modulation) and 0.9–1.1.

We used all EPIC (pn + MOSs) data and fitted the spectra together to the best-fitting average model. We fixed the interstellar absorption column density, the power-law photon index and the centroid and width of the Gaussian feature at the phase-averaged values, after having verified that the lower statistics in the phase-resolved spectra did not allow us to study possible differences for the values of the parameters of the Gaussian feature. We obtained an acceptable $\chi^2_{\nu} = 1.01$ for 199 dof. Tying up the partial column density across the spectra yielded a significantly worse fit ($\chi^2_{\nu} = 1.50$ for 202 dof). Therefore, as shown in Table A.3, the variability of the X-ray emission along the phase cycle can be successfully ascribed to changes in both the density and spatial extension of the localized absorbing material, and the power-law normalization. In particular, the partial column density is

Table A.3: Phase-resolved spectral fit results for the *XMM-Newton* observation of RXJ2015.6+3711. pn and MOSs spectra were fitted together to the TBABS*PCFABS*(PEGPURLW+GAUSS) model in the 0.3–10 keV energy range. The interstellar absorption column density and the power-law photon index were fixed at the phase-averaged values, resulting in $\chi^2_\nu = 1.01$ for 199 dof (see the text). Uncertainties and lower limits are quoted at a 90 per cent confidence level for a single parameter of interest.

Phase range	$N_{\text{H,pcf}}$ (10^{21} cm^{-2})	Cvf ^a (per cent)	Abs flux ^b ($10^{-12} \text{ erg cm}^{-2} \text{ s}^{-1}$)	Unabs flux ^b ($10^{-12} \text{ erg cm}^{-2} \text{ s}^{-1}$)
0.1 – 0.4 (max)	$2.8^{+0.8}_{-0.4}$	$\gtrsim 81$	$3.23^{+0.07}_{-0.06}$	3.62 ± 0.09
0.4 – 0.6	$3.2^{+1.3}_{-0.6}$	$\gtrsim 77$	$2.62^{+0.09}_{-0.08}$	$2.95^{+0.11}_{-0.10}$
0.6 – 0.9 (min)	12.0 ± 0.2	84 ± 3	$2.30^{+0.07}_{-0.06}$	2.77 ± 0.10
0.9 – 1.1	$8.2^{+0.2}_{-0.1}$	86^{+5}_{-4}	$2.78^{+0.08}_{-0.09}$	3.27 ± 0.12

^b Covering fraction of the partial absorber.

^b In the 0.3–10 keV energy range.

significantly larger at the minimum (about $1.2 \times 10^{22} \text{ cm}^{-2}$) than at the maximum ($\sim 2.8 \times 10^{21} \text{ cm}^{-2}$). Unabsorbed 0.3–10 keV fluxes are (2.77 ± 0.10) and $(3.62 \pm 0.09) \times 10^{-12} \text{ erg cm}^{-2} \text{ s}^{-1}$, respectively (see Table A.3). The phase-resolved spectra together with the best-fitting model are shown in the right-hand panel of Figure A.6 (only for pn data for plotting purpose).

To better characterize the phase-dependence of the parameters, we repeated the analysis (only for pn data) by dividing the phase cycle into 10 equal intervals, each of width 0.1 in phase, and fitting the corresponding spectra together to the same model as above. We obtained $\chi^2_\nu = 0.96$ for 404 dof. The evolution of the parameters and the fluxes along the cycle is shown in Figure A.7. An anti-correlation between the partial absorption column density and the X-ray intensity can be seen in the figure.

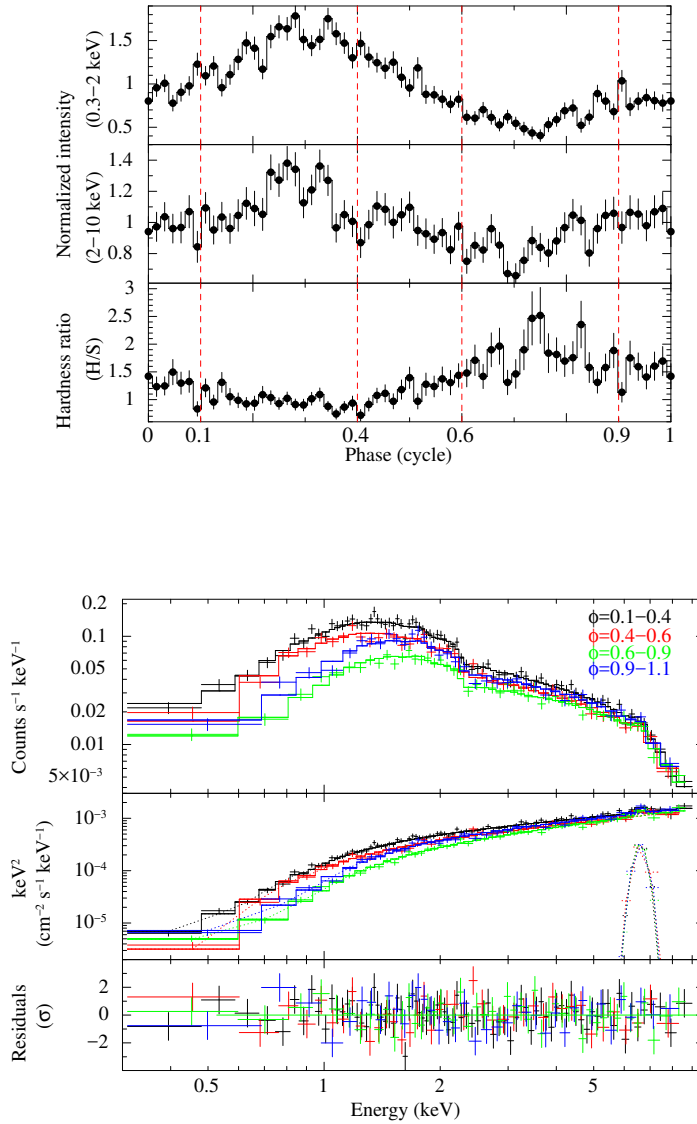


Figure A.6: Top panel: 64-bin pulse profile of RX J2015.6+3711 in two different energy intervals. The hardness ratio between the hard and soft bands is also plotted at the bottom. The red vertical dashed lines indicate the phase ranges used for the phase-resolved spectral analysis. Bottom panel: phase-resolved spectra of RX J2015.6+3711 extracted from *XMM-Newton* EPIC-pn data. The solid lines represent the best-fitting model to the data (a power-law plus a Gaussian feature in emission, both corrected for interstellar and local absorption). $E^2 \times f(E)$ unfolded spectra (middle panel) and post-fit residuals in units of standard deviations (bottom panel) are also shown. (See the online version of the article for the colour figure).

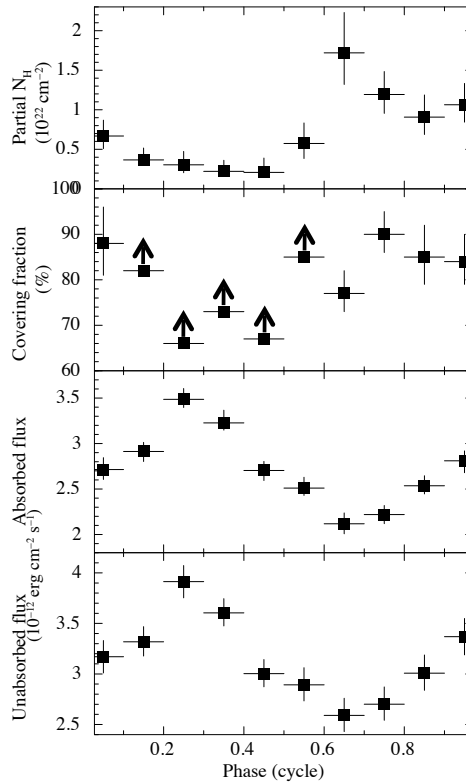


Figure A.7: Evolution of the column density and covering fraction of the partial absorber and of the 0.3–10 keV fluxes as a function of the phase for the *XMM-Newton* observation of RX J2015.6+3711. The 10 pn spectra (each corresponding to a 0.1-wide phase interval) were fitted together to the TBABS*PCFABS*(PEGPRLW+GAUSS) model in the 0.3–10 keV energy range (see the text for details). Uncertainties and lower limits (indicated by arrows) are reported at a 90 per cent confidence level for a single parameter of interest.

A.2.2 *Chandra*

The *Chandra* satellite observed RX J2015.6+3711 twice, on 2001 July 8 and 2010 January 16–17 (see Table A.1). The first observation (obs. ID 1037; PI: Garmire) was performed with the Advanced CCD Imaging Spectrometer spectroscopic CCD array (ACIS-S; Garmire et al. 2003) set in faint timed-exposure (TE) imaging mode. The total exposure was about 17.8 ks and the source was positioned on the back-illuminated S3 chip. The second observation (obs. ID 11092; PI: Safi-Harb) used instead the imaging CCD array (ACIS-I) operated in very faint TE mode and lasted about 69.3 ks. The source was positioned on the I3 chip.

We analyzed the data following the standard analysis threads⁵ with the *Chandra* Interactive Analysis of Observations software (CIAO, v. 4.7; Fruscione et al. 2006) and the calibration files in the *Chandra* CALDB (v. 4.6.9).

The source fell close to the edge of the CCD in the 2001 observation and was very far off-axis in that carried out in 2010 (for both these observations the aim point of the ACIS was indeed the supernova remnant CTB 87, which is located at an angular distance of ~ 5.2 arcmin from the nominal position of RX J2015.6+3711). Source photons were then collected from a circular region around the source position with a radius of 15 arcsec. Background was extracted from a nearby circle of the same size. We converted the photon arrival times to Solar System barycenter reference frame using the CIAO tool AXBARY and restricted our analysis to photons having energies between 0.3 and 8 keV. The average source net count rates in this band are $(8.5 \pm 0.2) \times 10^{-2}$ and $(1.23 \pm 0.01) \times 10^{-1}$ counts s^{-1} for the first and second observation, respectively.

We created the source and background spectra, the associated redistribution matrices and ancillary response files using the SPEXTRACT script.⁶ We grouped the background-subtracted spectra to have at least 30 and 100 counts in each spectral bin for the first and second observation, respectively.

Timing analysis

Recently, timing analysis of the longest *Chandra* observation (obs. ID 11092) unveiled the presence of the 2-hr periodicity observed in the *XMM-Newton* data (Halpern & Thorstensen 2015). The energy-dependent light curves folded on this period closely resemble the profiles derived from the *XMM-Newton* observation (see e.g. Figure 17 of Halpern & Thorstensen 2015), with a modulation amplitude that decreases as the energy increases. We confirmed this detection in the soft X-ray band (0.5–2 keV) and verified that, except for the harmonic, the other periodicities discovered in the *XMM-Newton* observation are not visible, likely due to the lower counting statistics in the *Chandra* data sets.

Our searches for periodicities in the data of the other observation (obs. ID 1037) were instead inconclusive. Only one power peak is visible and we note that it is coincident with

⁵See <http://cxc.harvard.edu/ciao/threads/pointlike>.

⁶Ancillary response files are automatically corrected to account for continuous degradation in the ACIS CCD quantum efficiency.

the frequency of known artificial signal due to the source dithering off the chip at regular time intervals.⁷

Spectral analysis

The values for the source net count rate translate into a pile-up fraction of about 10 and 15 per cent for the first and the second observation, respectively, as estimated with PIMMS (v 4.8).⁸ We then accounted for possible spectral distortions using the model of Davis (2001), as implemented in XSPEC, and following the recommendations in ‘*The Chandra ABC Guide to Pile-up*’.⁹ We fitted the two spectra together in the 0.3–8 keV energy range with an absorbed power-law model and all the parameters left free to vary. However, the column density was compatible between the two epochs at the 90 per cent confidence level and thus was tied up. We obtained $\chi^2_{\nu} = 1.21$ for 118 dof, with $N_{\text{H}} = (6 \pm 1) \times 10^{21} \text{ cm}^{-2}$. The spectrum was harder in 2001 ($\Gamma = 0.6 \pm 0.1$) than in 2010 ($\Gamma = 0.95 \pm 0.06$). The emission feature around 6.6 keV is not detected, likely due to the lower statistics compared to the *XMM-Newton* data sets. The addition of a Gaussian feature in emission with parameters fixed at the values derived from the *XMM-Newton* observation (see Table A.2) yields upper limits for the equivalent width of 52 and 119 eV in 2001 and 2010, respectively (at a 90 per cent confidence level). The 0.3–10 keV unabsorbed fluxes at the two epochs were $(9.0 \pm 0.6) \times 10^{-12}$ and $(4.05 \pm 0.09) \times 10^{-12} \text{ erg cm}^{-2} \text{ s}^{-1}$. The soft X-ray flux of RX J2015.6+3711 was thus larger in 2001 than in 2010 and 2014 (the epoch of the *XMM-Newton* observation) by a factor of ~ 2.2 and ~ 2.8 , respectively.

A.2.3 *Swift*

Our analysis of *Swift* data is mainly aimed at comparing the simultaneous soft X-ray and ultraviolet/optical fluxes of RX J2015.6+3711 at different epochs. Therefore, we focus here on the two longest observations of the source (obs IDs: 00035639003, 00041471002; see Table A.1). The X-ray Telescope (XRT; Burrows et al. 2005) was set in photon counting mode in both cases.

We processed the data with standard screening criteria and generated exposure maps with the task XRTPIPELINE (v. 0.13.1) from the FTOOLS package. We selected events with grades 0–12 and extracted the source and background event files using XSELECT (v. 2.4). We accumulated the source counts from a circular region centered at the peak of the source point-spread function and with a radius of 20 pixels (one XRT pixel corresponds to about 2.36 arcsec). To estimate the background, we extracted the events within a circle of the same size sufficiently far from the blazar and other point sources.

We created the observation-specific ancillary response files (using exposure maps) with XRTMKARF, thereby correcting for the loss of counts due to hot columns and bad pixels and accounting for different extraction regions, vignetting and PSF corrections. We

⁷See <http://cxc.harvard.edu/ciao/why/dither.html>.

⁸See <http://heasarc.gsfc.nasa.gov/cgi-bin/Tools/w3pimms/w3pimms.pl>.

⁹See [http://cxc.harvard.edu/ciao/download/doc/pile-up\\$_-\\$abc](http://cxc.harvard.edu/ciao/download/doc/pile-up$_-$abc).

then assigned the redistribution matrices v012 and v014 available in the HEASARC calibration database to the 2006 and 2010 data sets, respectively.¹⁰ We grouped the spectral channels to have at least 20 counts in each spectral bin and fitted in the 0.3 to 10 keV energy interval with an absorbed power-law model. The inferred 0.3–10 keV unabsorbed fluxes are ~ 6.9 and 4.1×10^{-12} erg cm⁻² s⁻¹ in 2006 and 2010, respectively. This is in line with a fading trend of the source in about 10 yr.

A.3 UV/optical observations and data analysis

RXJ2015.6+3711 was not positioned on the detectors of the *XMM-Newton* Optical/UV Monitor telescope (Mason et al. 2001) throughout the observation. We thus focused on the two observations by the Ultra-violet and Optical Telescope (UVOT; Roming et al. 2005) aboard *Swift*, which lasted about 7.0 and 7.2 ks, respectively, and were carried out in image mode. All the available filters were used in both cases (see Table A.4), providing a wavelength coverage within the 1700–6000 Å range. We performed the analysis for each filter and on the stacked images. First, we ran the UVOTDETECT task and found the UV and optical counterpart of RXJ2015.6+3711 at position RA = 20^h15^m36^s.959, Dec = +37°11′22″.70 (J2000.0), which is compatible with the location reported by Halpern et al. (2001) within the errors. We then used the UVOTSOURCE command, which calculates detection significances, count rates corrected for coincidence losses and dead time of the detector, flux densities and magnitudes through aperture photometry within a circular region, and applies specific corrections due to the detector characteristics. We adopted an extraction radius of 5 and 3 arcsec for the UV and optical filters, respectively, and applied the corresponding aperture corrections. The derived values for the absorbed magnitudes at the two different epochs are listed in Table A.4 (magnitudes are expressed in the Vega photometric system; see Poole et al. 2008 for more details and Breeveld et al. 2010, 2011 for the most updated zero-points and count rate-to-flux conversion factors). The source is brighter in all bandpasses in 2006 than in 2010, confirming the fading of the source also in the optical and UV.

To estimate the X-ray-to-optical flux ratio at the two different epochs of the *Swift* observations, we determined the unabsorbed 2–10 keV fluxes measured by the XRT and considered the values for the *V*-band magnitudes observed by the UVOT (central wavelength of 5468 Å and full-width at half-maximum of 769 Å). Adopting the value of the interstellar hydrogen column density derived from our model fit to the phase-averaged X-ray spectrum, and a conversion factor of $N_{\text{H}}/A_{\text{V}}$ of $(2.87 \pm 0.12) \times 10^{21}$ cm⁻² mag⁻¹ (according to the relation of Foight et al. 2015), we estimated an optical extinction $A_{\text{V}} = 0.60 \pm 0.12$ mag. We note that this value is lower than the integrated line-of-sight optical extinction at the position of the source, $A_{\text{V}} \sim 5.0$ mag, computed according to the recalibration (Schlafly & Finkbeiner 2011) of the extinction maps from Schlegel, Finkbeiner & Davis (1998). Using the Vega magnitude-to-flux conversion, we inferred dereddened *V*-band fluxes for the

¹⁰See <http://www.swift.ac.uk/analysis/xrt/rmfarf.php>.

Table A.4: *Swift* UVOT observations of RX J2015.6+3711 at two different epochs. Magnitudes are in the Vega photometric system and are not corrected for interstellar extinction. Uncertainties are quoted at a 1σ confidence level, whereas upper limits are given at a 3σ confidence level.

Filter	Date	Exposure (s)	Magnitude (mag)
UVW2	2006 Nov 17	2421	19.76 ± 0.14
	2010 Aug 6–10	944	19.96 ± 0.25
UVM2	2006 Nov 17	1567	19.83 ± 0.21
	2010 Aug 6–10	4940	21.22 ± 0.36
UVW1	2006 Nov 17	1210	18.51 ± 0.09
	2010 Aug 6–10	629	> 19.98
U	2006 Nov 17	598	17.65 ± 0.06
	2010 Aug 6–10	298	18.95 ± 0.14
B	2006 Nov 17	598	18.00 ± 0.05
	2010 Aug 6–10	236	19.28 ± 0.14
V	2006 Nov 17	598	17.19 ± 0.06
	2010 Aug 6–10	182	17.94 ± 0.13

source of $(4.6 \pm 0.8) \times 10^{-12}$ erg cm $^{-2}$ s $^{-1}$ in 2006 and $(2.3 \pm 0.4) \times 10^{-12}$ erg cm $^{-2}$ s $^{-1}$ in 2010. The X-ray-to-optical flux ratio is then $F_X/F_V = 1.4 \pm 0.2$ and 1.7 ± 0.2 , respectively (at the 1σ confidence level), thus compatible between the two epochs.

A.4 Discussion

Based on the wealth of observations we have collected for RX J2015.6+3711, from the optical to the X-rays, we can now explore the possibility that this source indeed belongs to the class of mCVs, as proposed by Halpern & Thorstensen (2015).

A.4.1 The X-ray periodicities and the accretion geometry

The X-ray properties of mCVs are strongly related to the accretion flow onto the WD. The accretion configuration is different for the two subclasses of mCV: in polars the high magnetic fields prevent the formation of an accretion disk and material flows in a column-like funnel; in IPs matter accretes either via a truncated disk (or ring; Warner 1995) or via a stream as in the polars (the diskless accretion model first proposed by Hameury, King & Lasota 1986). Whether the disk forms, or not, close to the WD surface, the infalling material is magnetically channeled towards the polar caps, resulting in emission strongly pulsed at the spin period of the accreting WD in disk accretors or at the beat period in disk-less accretors. Matter is de-accelerated as it accretes, and a strong standing shock

develops in the flow above the WD surface. X-rays are then radiated from the post-shock plasma.

Within the mCV scenario, the ~ 2 -hr modulation discovered in the X-ray (0.3–10 keV) emission of RXJ2015.6+3711 (see A.2.1) can be naturally interpreted as the trace of the accreting WD spin period. The spin modulation has a highly structured shape that resembles those observed in IPs rather than in polars, which show instead a typical on/off behaviour due to self occultation of the accreting pole and thus alternate bright and faint phases (see Warner 1995; Matt et al. 2000 for the prototypical polar; Ramsay et al. 2009, Traulsen et al. 2010 and Bernardini et al. 2014 for more recent studies). The modulation has a large amplitude (about 30 per cent) and the detection of the second harmonic suggests that accretion occurs onto two polar regions located at the opposite sides of the WD surface, and both visible. The main accreting pole produces the sinusoidal modulation, whereas the other pole is responsible for the secondary hump observed around the minimum of the spin pulse profile (see Figure A.4). The relative contribution of the two poles to the observed emission can be quantitatively estimated from the fundamental-to-second harmonic amplitude ratio, which is ~ 3 for this system.

The additional weaker periodicities detected in the power spectrum can be identified as the orbital sidebands of the spin pulse in an IP system. Theory predicts that, if accretion onto the WD occurs via a funnel rather than a disk, the asynchronous rotation of the WD should produce modulation not only at the spin frequency (ω), but also at the orbital (Ω) and beat ($\omega - \Omega$) frequencies. Higher harmonics of the beat frequency may be present for specific combinations of the system inclination and the offset angle between the magnetic and spin axes (see Wynn & King 1992). Setting the spin frequency as $\omega = 1.39 \times 10^{-4}$ Hz, the frequencies 9.4×10^{-5} , 1.20×10^{-4} , 1.65×10^{-4} and 2.6×10^{-4} Hz (at which excess of power is observed, see A.2.1) would correspond to the sideband frequencies $\omega - 2\Omega$, $\omega - \Omega$, $\omega + \Omega$ and $2\omega - \Omega$, respectively, for a putative binary orbital frequency $\Omega \sim 2.26 \times 10^{-5}$ Hz (i.e. an orbital period $P_{\text{orb}} \sim 12$ hr). We note that the X-ray power spectrum does not show any evident signal at this putative period, which is not surprising given the low amplitude of the sideband $\omega - \Omega$ and $\omega + \Omega$ signals (~ 6 and 8 per cent, respectively).

Although the prominent peak at the spin frequency in the X-ray power spectrum implies that accretion occurs predominantly through a Keplerian disk (the circulating material loses all knowledge of the orbital motion; see Wynn & King 1992), the detection of the orbital sidebands suggests that a non negligible fraction of matter leaps over the disk and is directly channeled onto the WD magnetic poles within an accretion column. This sort of hybrid accretion mode, dubbed ‘disk-overflow’, is supported by theoretical simulations (see e.g. Armitage & Livio 1998) and it has been observed in other confirmed IPs (see Bernardini et al. 2012, and references therein). The spin-to-beat amplitude ratio of 4.8 ± 0.4 (at the 90 per cent confidence level) implies that approximately 80 per cent of matter is accreted through the disk-fed mode.

The spin modulation amplitude decreases as the energy increases (the pulsed fraction is only about 9 per cent above 5 keV). This behaviour is typical for IPs. In these systems the softest X-rays are more prone to absorption from neutral material in the pre-shock

flow, whereas X-rays at higher energies are essentially unaffected by photo-electric absorption, resulting in a decrease of the modulation amplitude (Rosen, Mason & Cordova 1988). Furthermore, the overall pulse shape changes with time (see the right-hand panel of Figure A.4), in particular the intensity of the secondary peak increases. Such variations are also observed in a few similar systems (e.g. Bernardini et al. 2012; Hellier 2014), and are likely due to the different accretion modes occurring in these binaries.

A.4.2 The X-ray spectral properties

The average X-ray spectrum of RX J2015.6+3711 can be described by an absorbed hard power-law ($\Gamma = 1.15 \pm 0.04$) plus a broad (~ 0.25 keV) Gaussian emission feature at 6.61 ± 0.09 keV. The absorption is provided by the interstellar medium component (with column density $N_{\text{H,ISM}} \sim 2 \times 10^{21} \text{ cm}^{-2}$) plus a thicker ($N_{\text{H,pcf}} \sim 6 \times 10^{22} \text{ cm}^{-2}$) absorber partially covering the X-ray emitting regions. A partial covering absorption and the iron complex are defining properties of mCVs (e.g., Yuasa et al. 2010; Girish & Singh 2012; Ezuka & Ishida 1999). The large width for the line is suggestive of both thermal and fluorescent contributions (i.e. the 6.67 keV He-like and the 6.97 keV H-like lines, plus the 6.4 keV fluorescent line). In particular the fluorescent line is produced by reflection of X-rays from cold matter that could be the WD surface or the pre-shock flow.

We observe a conspicuous hardening at the minimum of the rotational phase cycle and we find that the phase-variable emission can be accounted for mainly by changes in the amount of local absorbing material and the power-law normalization. Moreover, the partial column density is anti-correlated with the X-ray flux along the cycle. The variability in the extension of the local absorber (covering fraction) is instead less significant and only lower limits can be inferred around the maximum of the modulation. Although localised absorption is also detected in the X-ray light curves of polars, this is generally pronounced during the bright phase where the typical dips are due to absorption when the accretion column points towards the observer.

The spectral changes along the modulation phase in RX J2015.6+3711 are typically observed in IPs and can be explained within the accretion curtain scenario presented by Rosen et al. (1988). According to their model, the modulation is mainly caused by spin-dependent photoelectric absorption from pre-shock material flowing from the disk towards the polar caps in arc-shaped structures extending above the WD. In this context, the spin-phase modulation of RX J2015.6+3711 in the soft X-rays likely reflects changes in the absorption along the curtains. At the minimum of the rotational phase the softest X-ray photons from the WD surface are highly absorbed, resulting in a spectral hardening and a decrease in the amount of emission. On the other hand, at the maximum of the modulation, the absorption is less efficient and the radiation intensity will be larger.

A.4.3 The long-term X-ray variability and multiwavelength emission

RX J2015.6+3711 appears to have gradually faded in the X-rays since 2001 (see A.2.2 and A.2.3), a behaviour that is not uncommon in mCVs of the IP type (Warner 1995).

The simultaneous X-ray and UV/optical observations of RXJ2015.6+3711 carried out with *Swift* enable a straight estimate of the flux in different energy bands (see Section A.3). The source appears to be brighter in 2006 November than in 2010 August in all bands. The ratio between the unabsorbed X-ray and optical flux is roughly the same at the two epochs: $F_X/F_V \sim 1.4 - 1.7$. If we interpret the X-ray luminosity as accretion luminosity, the rather stable ratio suggests that both the X-ray and optical luminosities are tracing changes in the mass accretion rate. Moreover, a relatively low value for the ratio is not surprising for the CVs, which have X-ray-to-optical flux ratios much lower with respect to LMXBs (see van Paradijs & Verbunt 1984; Patterson & Raymond 1985; Motch et al. 1996), with the mCVs showing higher ratios compared to non-magnetic systems (see Verbunt et al. 1997). Therefore, both the intrinsic emission of the disk and the X-ray reprocessed radiation provide an important contribution to the UV and optical emission in these systems.

A.4.4 The system parameters

The 2-hr spin pulsations pin down RXJ2015.6+3711 as the second slowest rotating WD in the class of IPs (after RXJ0524+4244, also known as "Paloma", with $P_{\text{spin}} \sim 2.3$ hr; see Schwarz et al. 2007). If the additional peaks detected in the X-ray power spectrum are indeed the orbital sidebands, then the estimated orbital period of the system of about 12 hr would imply a degree of asynchronism $P_{\text{spin}}/P_{\text{orb}} \sim 0.16$, which is larger than that observed for most of the long-orbital period IPs (Norton et al. 2004; Bernardini et al. 2012; see also the catalogue available at the Intermediate Polar Home Page¹¹). Taken at face value, the long spin period would be peculiar when compared to other slow rotators which are all short orbital period systems, including the IP Paloma.

For a system with orbital period of about 12 hr, the likely companion would be a G- or early K-type star (Smith & Dhillon 1998). Adopting an absolute magnitude in the *K*-band in the range 3.50–4.51 mag (Bilir et al. 2008), using the value for the *K*-band magnitude of RXJ2015.6+3711 (14.79 ± 0.15 mag), and assuming that the donor star in this binary system totally contributes at these wavelengths, the estimated distance would be in the range 1–2 kpc, with no intervening absorption. Our estimate does not change significantly if the effects of interstellar absorption are considered, since adopting the optical reddening derived in Section A.3 and the extinction coefficients at different wavelengths of Fitzpatrick (1999), the absorption in this band is only $A_K \sim 0.07$ mag.

A.5 Conclusions

A deep *XMM-Newton* observation of RXJ2015.6+3711, together with archival *Chandra* and *Swift* observations, allowed us to unambiguously identify this source with a magnetic cataclysmic variable.

¹¹See <http://asd.gsfc.nasa.gov/Koji.Mukai/iphome/catalog/members.html>

Although we did not detect directly the orbital period of the system, several properties point toward the intermediate polar identification, and the 2 hr modulation as the white dwarf spin period. In particular, no coherent signal is observed at shorter periods (ruling out the presence of a lower spin period¹²), and the presence of additional weaker periodicities close to the most significant one at 2 hr could be reconciled with orbital sidebands for a putative orbital period of about 12 hr. In this case the system would be an intermediate polar with an anomalous spin-to-orbit period ratio for its long orbital period. Alternatively, the orbital period could be one of the sideband periods itself, and in this case RX J2015.6+3711 would resemble systems like Paloma (Schwarz et al. 2007) or IGR J1955+0044 (Bernardini et al. 2013), which are characterized by a high spin-to-orbit period ratio ($P_{\text{spin}}/P_{\text{orb}} \sim 0.9$) and are believed to be intermediate polars (or pre-polars) on their way to reach synchronism.

Both the shape and the spectral characteristics of the 2 hr modulation are typical of the intermediate polars. The amplitudes of the different modulations indicate that accretion takes place onto the two polar caps mostly through a truncated disk (about 80 per cent), with a non negligible contribution from an accretion stream, again a peculiarity shared by several intermediate polars.

Further optical observations are planned to shed light on the exact orbital period of this intriguing system, which in any case appears to play a key role in understanding of the evolution of magnetic cataclysmic variables.

¹²Note that to date no IP has been observed with a detected orbital period, but no evidence for the spin period.

Appendix **B**

Swift J174540.7–290015: a new accreting binary in the Galactic Centre

Ponti G., Jin C., De Marco B., Rea N., Rau A., Haberl F., Coti Zelati E.,¹
Bozzo E., Ferrigno C., Bower G. C., Demorest P. (2016),
Swift J174540.7–290015: a new accreting binary in the Galactic Centre,
Published in Monthly Notices of the Royal Astronomical Society,
Volume 461, Issue 3, pp. 2688–2701

¹Author contribution: I reduced and analysed data of the *XMM–Newton* observation (including timing and spectral analysis) immediately after it was performed, in order to nail down the nature of the source. I reduced data of all *Swift* observations and performed spectral analysis. I searched for possible nIR counterparts in *VLT* data. I reduced and analysed data of a *Chandra* observation of the field, especially in search for periodicities in the time series.

We report on the identification of the new Galactic Centre transient *Swift* J174540.7–290015 as a likely low mass X-ray binary located at only 16 arcsec from Sgr A*. This transient was detected on 2016 February 6 during the *Swift* monitoring of the Galactic Centre, and it showed long-term spectral variations compatible with a hard to soft state transition. We observed the field with *XMM-Newton* on February 26 for 35 ks, detecting the source in a soft state characterised by a low level of variability and a soft X-ray thermal spectrum with a high energy tail (detected by *INTEGRAL* up to ~ 50 keV), typical of either accreting neutron stars or black holes. We observed: i) a high column density of neutral absorbing material, suggesting that *Swift* J174540.7–290015 is located near or beyond the Galactic Centre and; ii) a sub-Solar Iron abundance, and we argue that Iron is depleted into dust grains. The lack of detection of Fe K absorption lines, eclipses or dipping suggests that the accretion disk is observed at a low inclination angle. Radio observations did not detect any radio counterpart to *Swift* J174540.7–290015. No evidence for X-ray or radio periodicity is found. The location of the transient was observed also in the near-IR pre- and post-outburst. Within the *Chandra* error region we find multiple objects that display no significant variations.

B.1 Introduction

Sgr A* (Genzel et al. 2010), the supermassive black hole (BH) at the Galactic Centre (GC), generates a deep gravitational potential that is expected to bind tens of thousands of stellar remnants, such as neutron stars (NS) or BHs that have settled dynamically into the central parsec of the Milky Way (Morris 1993; Lee 1995; Miralda-Escudé & Gould 2000; Munro et al. 2005). Deep radio surveys were so far unsuccessful in detecting either ordinary or millisecond pulsars, leading to the ‘missing pulsar problem’ (Wharton et al. 2012; Dexter & O’Leary 2014). Surprisingly, a few years ago the magnetar SGR 1745–2900 was discovered via its outburst activity (Mori et al. 2013; Rea et al. 2013; Eatough et al. 2013; Kaspi et al. 2014; Coti Zelati et al. 2015), representing the first radio and X-ray pulsar discovered in the Galactic Centre region (at less than a few parsecs from Sgr A*). Many millisecond radio pulsars are expected in the field, but currently none has been detected. Because of the three body interaction between this concentration of degenerate stars and multiple stellar systems, a large population of X-ray binaries is also expected. The monitoring of X-ray transients allows us to study this population (Pfahl & Loeb 2004; Munro et al. 2005; Hopman 2009; Faucher-Giguere & Loeb 2011).

The majority of accreting X-ray binaries spend most of their time in a quiescent state (below the detection limit), sporadically interrupted by outbursts during which the X-ray luminosity rises by many orders of magnitudes (Fender & Belloni 2012). Pioneering works on monitoring of GC X-ray sources have been performed with *Chandra* and *Swift* (Munro et al. 2005; Wijnands et al. 2006; Campana et al. 2009; Degenaar et al. 2012, 2015).

Swift J174540.7–290015 was discovered by the *Swift* satellite on 2016 February 6 (Reynolds et al. 2016) during the first X-ray observation after the GC exited the Solar constraint window. The *Swift* X-ray telescope (XRT) data showed a bright (absorbed flux

of $\sim 2 \times 10^{-10}$ erg cm $^{-2}$ s $^{-1}$ in the 2 – 10 keV range) transient located at less than 16 arcsec from Sgr A* (Reynolds et al. 2016). Swift J174540.7–290015 was detected also in the 20–80 keV energy range (Esposito et al. 2016), while observations with the Karl G. Jansky Very Large Array (VLA) and Giant Metrewave Radio Telescope (GMRT) did not detect the radio counterpart or any pulsation (Bower et al. 2016; Maan et al. 2016). Within a week from this discovery, *Chandra* observed the field and refined the transient position to RA = 17^h45^m40^s.66±0.34, Dec = –29°00′15″.61±0.33 (J2000.0), where no previous X-ray sources were ever detected (Baganoff et al. 2016). Therefore, Swift J174540.7–290015 is a new transient source.

In this appendix we report the identification of the source as a low-inclination X-ray binary hosting a neutron star or a black hole, most probably with a low mass companion. We discuss the temporal and spectral characteristics of the transient using the long-term daily X-ray monitoring of the field performed by the *Swift* satellite, the high energy long term monitoring provided by the *INTEGRAL* satellite, a 35 ks *XMM–Newton* observation obtained in Director’s Discretionary Time (to study the dust scattering halo) performed about 20 days after the onset of the outburst as well as VLA observations. Finally, we report on the search for the near-IR counterpart using VLT/*NaCo* and GROND data.

B.2 X-ray observations and data reduction

B.2.1 *XMM–Newton*

XMM–Newton (Jansen et al. 2001) observed Swift J174540.7–290015 on February 26 for 35 ks. We processed this data set starting from the observation data files. The data have been treated using the latest version (15.0.0) of the *XMM–Newton* Science Analysis System (SAS) with the most recent (2016 March 13) calibration files. We used all EPIC cameras (Strüder et al. 2001; Turner et al. 2001) equipped with the medium filter. The arrival times of the events were corrected to the Solar system barycentre, applying the BARYCEN task of SAS. We screened the periods of enhanced particle-induced activity by inspecting the EPIC-pn 10–15 keV light curves extracted from a circular region with a radius of 5 arcmin close to the border of the field of view, and binned with 5 s resolution. We then filtered out all the periods where the count rate exceeded 0.85 counts s $^{-1}$.

The main focus of the observation was the study of the full extension of the dust scattering halo around the source, hence the EPIC-pn camera was set in Full Frame mode (frame time of 73.4 ms). On the other hand, both EPIC-MOS 1 and MOS 2 were configured in timing mode, with a frame time of 1.75 ms. A bad column is falling in the centre of the extraction region in the EPIC-MOS 1 camera, inducing lower statistics. Therefore these data have been used only for consistency checks. To reduce pile up in the data of the EPIC pn camera, source photons were extracted from an annular region. The outer radius of the annulus was limited to 40 arcsec, to avoid contribution from the low mass X-ray binary AX J1745.6–2901 (Ponti et al. 2015) and the inner radius has been fixed to 15 arcsec. By comparing this spectrum from the wings of the Point Spread Function

with the pile-up free EPIC-MOS 2 spectrum, we verified that it is not affected by pile up. We note that the magnetar SGR 1745–2900 is located inside the source extraction region. However, the magnetar is currently observed at a 2–10 keV absorbed flux of $\sim 3.8 \times 10^{-13}$ erg cm $^{-2}$ s $^{-1}$, about three orders of magnitude lower than the instantaneous 2–10 keV flux of *Swift* J174540.7–290015 ($\sim 2.9 \times 10^{-10}$ erg cm $^{-2}$ s $^{-1}$). Therefore, SGR 1745–2900 gives a negligible contribution to the light curves and spectra of *Swift* J174540.7–290015.

A strong contribution from the emission of the supernova remnant Sgr A East (Maeda et al. 2002; Ponti et al. 2015) is expected within the EPIC-pn extraction region of *Swift* J174540.7–290015, therefore we extracted the background plus diffuse emission from a long archival observation (obs ID 0505670101) during which AX J1745.6–2901 had flux and spectral properties similar to the ones during this observation (being in the soft state and at similar flux), the magnetar SGR 1745–2900 was in quiescence and Sgr A* did not show any flare (Ponti et al. 2015). In the EPIC-MOS 2 camera, the source photons were extracted between rawx 285 and 330. The larger extraction region, imposed by the timing mode, implies a larger contribution from AX J1745.6–2901 and diffuse emission, compared to the EPIC-pn spectrum. We converted the source extraction region (from rawx coordinates into sky coordinates through the SAS task ECOORDCONV) and we extracted the background plus diffuse emission from the EPIC-MOS 2 camera, during the above-mentioned observation (obs ID 0505670101), when *Swift* J174540.7–290015 was in quiescence.

The combination of high column density of absorbing material ($N_H = 18.7 \times 10^{22}$ cm $^{-2}$) and the intense diffuse emission towards the Galactic Centre, prevent us from obtaining a good characterisation of the source emission below ~ 2 keV (e.g., the low energy absorption edges). For this reason in this work we do not consider the data from the Reflection Grating Spectrometer instruments.

Spectral fitting was performed using XSPEC version 12.8.2. The spectra were grouped so that each bin contains at least 30 counts.

B.2.2 *Swift*

The *Swift* X-ray Telescope (XRT) has been monitoring the central ~ 15 arcmin of the Galaxy daily since 2012 (Degenaar et al. 2015). We downloaded from the HEASARC data archive the *Swift* photon counting (PC) mode datasets for the 31 observations carried out between 2016 February 5 and 2016 March 10. These comprise 31 observations. To characterise the contribution from the background plus complex diffuse emission within the extraction region of *Swift* J174540.7–290015 (which contains a contribution from SGR 1745–2900 and AX J1745.6–2901), we used the *Swift* data before the outburst of *Swift* J174540.7–290015. Since there was no *Swift* observation of this region between 2015 November 3 and 2016 February 5, we retrieved 15 *Swift* observations between 2015 October 15 and 2015 November 2 in PC mode when the source was quiescent. These 15 observations are used to measure the background plus diffuse emission underneath *Swift* J174540.7–290015.

Because of the high absorption column density towards the source, we considered only data in the 2–10 keV band. Images and spectra were produced using the XSELECT (v2.4c) package. Swift J174540.7–290015 is very bright, and significant pile up affects all the PC mode observations. We followed the standard XRT pile-up thread to determine the pile-up level.² We extracted the products from an annulus with inner radius of 15 arcsec, to ensure that spectra, fluxes and light curves are not affected by pile up. A 40-arcsec outer radius is used to include most source flux and less contamination from AX J1745.6–2901. We manually adjusted the astrometry of all datasets by visually inspecting the images of all the observations and correcting the relative position between Swift J174540.7–290015 and AX J1745.6–2901. This allows us to correct the astrometry shifts, which would otherwise affect the PSF correction and the correct determination of the source flux. We ensured that the uncertainties in the PSF correction are not the cause of the observed source variability. We also note that the background flux underneath Swift J174540.7–290015 is only 3 per cent of the source flux in the 2–10 keV band, so it does not significantly contaminate the light curve of Swift J174540.7–290015.

In addition to the PC mode data, there exist also 12 windowed timing (WT) mode observations of Swift J174540.7–290015. The WT mode provides higher time resolution and more counts compared to the PC mode, but the 1-dimensional image in the WT mode makes it difficult to determine the background underneath the source region from previous observations. However, since the background flux is only 3 per cent of the source flux, we use the WT mode observations as an independent check of the PC mode results.

Swift J174540.7–290015 is not piled up in the WT mode, so we defined a circular source region of radius 20 arcsec, centered on the pixel which is the perpendicular projection of the source position on the 1-dimensional WT mode image (again we consider only data in the 2–10 keV band). The choice of a 20-arcsec radius was a compromise between including more source flux and less contamination from AX J1745.6–2901. For eleven WT mode observations, there were also PC mode observations on the same day, for which we could compare the spectra between the two modes. For nine observations, both the spectral shape and normalization were consistent between the two modes, except that WT mode provided more counts and thus higher S/N. The remaining two WT mode spectra (Obs ID: 00035063134, 00035063136) have the same spectral shape as in the PC mode but with different normalisation. We found that this is caused by the bad pixels within the source extraction region in these two WT mode observations, which affected the source flux and PSF correction, but did not affect the spectral shape. We excluded these two observations from further analysis. Since the source spectra from WT mode observations were consistent with the PC mode, and the background underneath Swift J174540.7–290015 was much weaker than the source itself, we decided to apply the same background flux and spectra for the WT mode data as for the PC mode, and this should not affect our results.

The exposure maps and ancillary files for the spectra were computed with the XRTEX-POMAP and XRTMKARF tools provided in the HEASOFT (6.18) software.

²See <http://www.swift.ac.uk/analysis/xrt/pileup.php>.

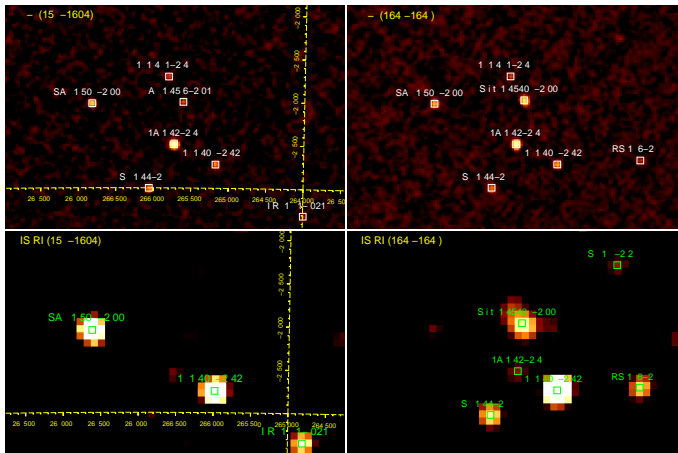


Figure B.1: Mosaiked JEM-X (3–10 keV) and IBIS/ISGRI (20–40 keV) images around the position of *Swift* J174540.7–290015 obtained from the revolutions 1597–1604 performed before the source outburst (top and bottom left) and the revolutions 1643–1648 performed during the first part of the source outburst (top and bottom right). *Swift* J174540.7–290015 is only detected from revolution 1643 onward in IBIS/ISGRI, while AX J1745.6–2901 is detected in the earlier revolutions at a position consistent with *Swift* in JEM-X, albeit at a much lower luminosity (see text for details).

B.2.3 *INTEGRAL*

The outburst of the source was observed by *INTEGRAL* starting from 2016 February 11, i.e. during satellite revolution 1643. At the time of writing, only consolidated *INTEGRAL* data up to revolution 1652 were made available and thus we were able to observe the evolution of the source hard X-ray emission until 2016 March 6. As the source is located right into the Galactic Centre, which is a complex and crowded region, we also made use of the last data collected toward this region before the outburst of *Swift* J174540.7–290015. These included data during revolutions 1597, 1603, and 1604, covering the period from 2015 October 11 to 19.

INTEGRAL observations are divided into ‘science windows’ (SCWs), i.e., pointings with typical durations of ~ 2 –3 ks. We considered only SCWs where the source was within a maximum off-axis angle of 12 deg from the satellite aim point, in order to reduce the uncertainties on the energy calibrations. All data were analyzed by using version 10.2 of the Off-line Scientific Analysis software (OSA) distributed by the ISDC (Courvoisier et al. 2003). We first extracted the mosaics acquired by the ISGRI detector of the Imager on Board the *INTEGRAL* Satellite (IBIS/ISGRI; Ubertini et al. 2003; Lebrun et al. 2003) in the 20–100 keV energy band and the mosaics of the Joint European X-Ray Monitor (JEM-X; Lund et al. 2003) in the 3–10 keV energy band by summing up all data in revolutions from 1597 to 1604. No source was detected at a position consistent with *Swift* J174540.7–290015 in the 20–100 keV energy band and we estimated a 3σ

upper limit of 3 mCrab in the corresponding energy range (corresponding³ to roughly 5.4×10^{-11} erg cm⁻² s⁻¹). From the JEM-X mosaic, we noticed that AX J1745.6–2901 was detected at a position consistent with that of Swift J174540.7–290015. The limited spatial resolution of the JEM-X instrument does not allow us to disentangle the emission of AX J1745.6–2901 from that of Swift J174540.7–290015. Therefore, we decided to extract a JEM-X spectrum of AX J1745.6–2901 from an observation taken before the outburst of Swift J174540.7–290015. We then used this file as a background for the spectrum of Swift J174540.7–290015, which we obtained from later observations (we checked in the *Swift* data that AX J1745.6–2901 did not go through major flux and/or state changes during the considered period). The JEM-X spectrum of AX J1745.6–2901 could be well fit ($\chi^2_{\nu}/\text{dof}=0.5/5$) with a power-law model of photon index $\Gamma = 2.2 \pm 0.5$. The absorbed flux in the 3–10 keV energy band was $\sim 3.5 \times 10^{-10}$ erg cm⁻² s⁻¹.⁴

For all *INTEGRAL* revolutions from 1643 to 1652, we built the IBIS/ISGRI and JEM-X mosaics, and extracted the source spectra in 13 energy bins for ISGRI and 8 energy bins for JEM-X (we used data from both the JEM-X1 and JEM-X2 units). The JEM-X spectrum obtained during revolution 1643 revealed a 3–20 keV flux of $\sim 1 \times 10^{-9}$ erg cm⁻² s⁻¹, therefore AX J1745.6–2901 contaminated the emission from Swift J174540.7–290015 by no more than 30 per cent (see also Figure B.1). As AX J1745.6–2901 was not detected in the previous IBIS/ISGRI mosaic, the recorded 20–100 keV flux of 7.4×10^{-10} erg cm⁻² s⁻¹ is to be completely attributed to Swift J174540.7–290015. This object remained bright in all *INTEGRAL* data we used, and was detected at high significance in the IBIS/ISGRI and JEM-X mosaics of all revolutions.

B.2.4 Karl G. Jansky Very Large Array

VLA observations of Swift J174540.7–290015 were carried out on two epochs, 2016 February 25 and 2016 March 25. As we will discuss later (see Section B.5.1), Swift J174540.7–290015 was in the soft state during at least the first of these VLA observations. In each epoch, data were obtained in two frequency bands, *C* and *Ku*, with central frequencies of 6.0 and 15.0 GHz, respectively. The VLA correlator was simultaneously configured for imaging and a phased array beam centered on Swift J174540.7–290015.

Imaging data were obtained over frequency ranges of 3.976 – 8.072 GHz and 12.952 – 17.048 GHz, respectively. The correlator was configured to produce cross-correlations that were split into 64 frequency windows each with 128 channels in dual circular polarization. These imaging data were reduced using the CASA VLA pipeline. The radio galaxy 3C 286 was used to set the flux calibration and the compact source J1744–3116 was used as a phase calibration source for Swift J174540.7–290015. Additional steps of self-calibration with Sgr A* as the reference were performed using only visibilities with

³The conversion between the upper limit on the source count-rate and flux has been done by using the observations of the Crab in revolution 1597, as described in Bozzo et al. (2016).

⁴Note that both the JEM-X and ISGRI spectra used in the present work were extracted from the instrument mosaics with the MOSAIC_SPEC tool rather than running the OSA software down to the SPE level, in order to avoid contamination issues (see discussion in Bozzo et al. 2016).

baselines longer than $50 k\lambda$ and $20 k\lambda$ in *Ku* and *C* bands, respectively. Images of the field around Swift J174540.7–290015 using only these long baseline visibilities were produced. These long baselines filtered out much of the substantial emission associated with the Northern arm of Sgr A West. No radio source was identified at the location of *Swift* in either epoch at either frequency.

We also recorded high time resolution data from a phased array beam at the position of Swift J174540.7–290015. In both frequency bands, these data were taken with 4.096 GHz total bandwidth divided into 1024 frequency channels at $250 \mu\text{s}$ time resolution. We searched for dispersed, periodic signals over dispersion measures ranging from 0 to $10\,000 \text{ pc cm}^{-3}$ and pulse frequency drift (source acceleration) up to $5 \times 10^{-5} \text{ Hz s}^{-1}$. At both frequencies, pulses from the bright, nearby 3.76-s magnetar SGR 1745–2900 were detected with high signal-to-noise ratio, but no other significant periodicities were found. Assuming 10 per cent pulse duty cycle, the $10\text{-}\sigma$ flux density limits for the periodicity searches were $30 \mu\text{Jy}$ at *C*-band and $45 \mu\text{Jy}$ at *Ku*-band.

We assume a distance to the source equal to 8 kpc (Genzel et al. 2010; Gillessen et al. 2013). Error bars are quoted at the 90 per cent confidence level for a single parameter of interest. We also assume that the accretion disk is observed face on. This is in agreement with the indication (see Section B.4) that the system is observed at low inclination ($i < 60^\circ$; Frank et al. 1987; Diaz-Trigo et al. 2006; Ponti et al. 2016). Would the inclination be $i = 60^\circ$, the inner disk radii and luminosities would be 1.4 and 2 times larger, respectively.

B.3 Short term variability

B.3.1 The *XMM–Newton* light curve

Figure B.2 shows the PSF corrected EPIC-pn light curve in the 2–10 keV band with 200 s bins. No variability is observed and the data are well fit with a constant that is shown by the red dashed line ($\chi^2 = 161.7$ for 170 degrees of freedom; dof). No bursts or dipping events are observed during the *XMM–Newton* observation (White & Mason 1985; Frank et al. 1987; Diaz-Trigo et al. 2006). To refine our capability to detect bursts and dips we investigated a variety of energy bands and time bins. No bursts are detected in light curves with time bins as short as sub-second. We also investigated soft energy bands, where the effect of dipping is stronger (Diaz-Trigo et al. 2006; Ponti et al. 2016), and their hardness ratio, but no dipping events were found.

B.3.2 Timing analysis: broad band noise

We extracted MOS and pn light curves in the energy bands 2–10 keV, 2–6 keV, and 6–10 keV, with a time resolution of 3.5 ms and 200 ms, respectively. The power spectral density function (PSD) was computed in each energy band and for each instrument separately. The Poisson noise level was estimated from the mean power at frequencies $> 50 \text{ Hz}$, where counting noise variability dominates. The relatively long frame time of the EPIC pn instrument in Full Frame observing mode prevents us from sampling these frequencies.

Therefore, the Poisson noise level cannot be accurately estimated, thus we did not consider the EPIC-pn PSD further.

Figure B.3 shows the PSD of the MOS data in the 2–10 keV band. For comparison we also plot the PSD of the BH X-ray binary GX 339-4 in a high-luminosity hard state (De Marco et al. 2015). *Swift* J174540.7–290015 displays significantly less power than observed in a typical hard state of a BH X-ray binary. Indeed, the 2–10 keV fractional root-mean-square (rms) variability amplitude (e.g. Nandra et al. 1997; Vaughan et al. 2003; Ponti et al. 2004) in the 0.1–64 Hz frequency interval is estimated to be 0.07 ± 0.02 . This value is consistent with what is typically observed in either a BH or NS X-ray binary in a soft/soft-intermediate state (Muñoz-Darias et al. 2011, 2014).

B.3.3 Timing analysis: search for periodic signals

We searched for periodic signals using the *XMM-Newton* pn and MOSs data, as well as *Swift* WT-mode data (being sensible to signals between the Nyquist frequency, and the frequency resolution of each dataset; van der Klis 1988). We used a modified version of the XRONOS analysis software to search for periodicities following the prescriptions described in Vaughan et al. (1994), and we did not find any periodic or quasi-periodic signal in any of the X-ray observations (we had accounted for the number of bins searched, and the different dof of the noise power distribution in the non-detection level). We have searched all dataset performing Fast Fourier Transforms over the total length of the observations, but also over small intervals of 0.5, 1, 3, and 5 ks in order to search for signals that might have been possibly smeared by Doppler shifts due to hour-long orbital periods. Unfortunately, the dataset with by far the largest number of counts, the EPIC-pn, make our searches insensitive to fast spinning pulsars (i.e. with spin periods of $\lesssim 146$ ms, i.e. twice the Nyquist limit).

We computed the 3σ upper limits on the sinusoid semi-amplitude pulsed fraction (PF) according to Vaughan et al. (1994) and Israel & Stella (1996). The deepest limits at frequencies < 6 Hz were derived from the EPIC-pn data, having the larger number of collected photons. Note that given the nature of this source, if a very short orbital period causes Doppler smearing of the putative signal (i.e. if the signal is not strong enough to be detected in our small ~ 1 ks chunks that might be free of Doppler smearing), these PF limits are not constraining. To have a handle on the PF limits on faster periodicities (anyway smaller than 300 Hz), we used the MOSs data (taken in timing mode: 1.75 ms timing resolution) as well as the *Swift* WT data (1.7 ms timing resolution), although having to cope with a much reduced number of counts, and again using the full length of the observation and searching in small consecutive time intervals. We show the resulting 3σ upper limit on the PF for any periodic signal (if not Doppler smeared in the presence of a short orbital period) for both pn and MOS 2 data in Figure B.4.

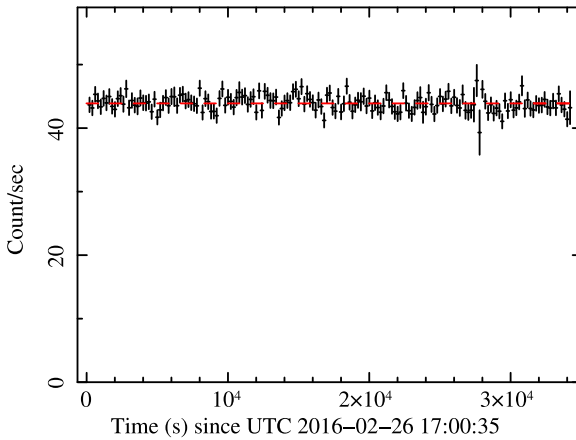


Figure B.2: PSF corrected EPIC-pn light curve of Swift J174540.7–290015 in the 2–10 keV band. The light curve is extracted from an annular region with inner and outer radii of 15 arcsec and 40 arcsec, respectively, and binned at 200 s. No bursts (not even in 1 s binned light light curves) or dips are observed. The red dashed line shows the best-fitting with a constant (which results in 43.9 counts s⁻¹ and $\chi^2 = 161.7$ for 170 dof).

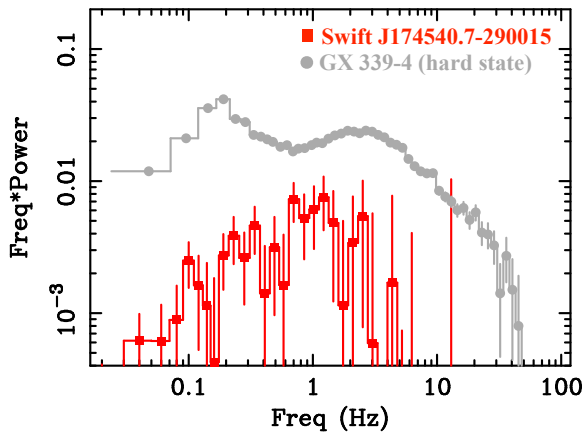


Figure B.3: Power spectral density (in units of $[rms/mean]^2$) of Swift J174540.7–290015 (red squares), computed from MOS 2 data in the 2–10 keV energy band. The 2–10 keV PSD of GX 339–4 in a high-luminosity hard state (De Marco et al. 2015) is reported for comparison (gray dots).

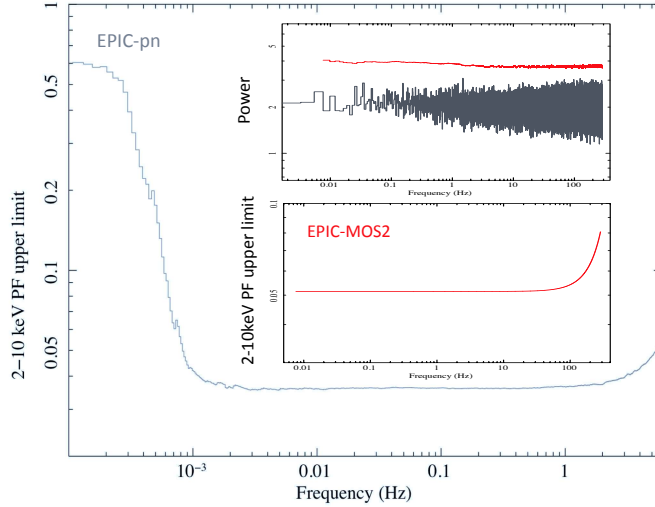


Figure B.4: *Main panel*: pulsed fraction 3σ upper limits as derived for the 2–10 keV EPIC-pn. The fractional PF is in units of 100 per cent. *Upper inset*: MOS 2 power density spectra. *Lower inset*: fractional pulsed fraction 3σ upper limits as derived for the 2–10 keV MOS 2.

B.4 Spectral analysis of the deep XMM–Newton observation

B.4.1 Characterisation of the mean spectrum

We fit the EPIC-pn spectrum by always including an absorption component from neutral matter plus the contribution from the dust scattering halo. The neutral absorption is fitted with the model TBNEW (see Wilms et al. 2000, 2011) with cross sections of Verner et al. (1996) and abundances of Wilms et al. (2000). The dust scattering halo is fitted with the model DUST (Predehl & Schmitt 1995). We assume that the dust scattering optical depth at 1 keV is related to the X-ray absorbing column density by the relation: $\tau = 0.324 \times (N_H/10^{22} \text{ cm}^{-2})$, as in Nowak et al. 2012. However, we note that a more proper modelling of the dust scattering effect on the observed spectrum requires better knowledge about the location and properties of the dust along the line of sight (Smith, Valencic & Corrales 2016), as well as a better constrained location of Swift J174540.7–290015, which would then require detailed analysis of the extended emission from the dust scattering halo. This is already beyond the scope of this thesis.

We first fit the spectrum with a series of single component models. We start with an absorbed power-law model (DUST*TBNEW*POWERLAW in XSPEC). Large residuals remain at high energy ($\chi^2 = 1530.9$ for 1189 dof; see Table B.1). Moreover, the best-fitting power-law photon index is unrealistically high ($\Gamma = 5.76 \pm 0.04$), clearly indicating the thermal nature of this emission. Therefore, we fit the spectrum with either an absorbed

Table B.1: Best-fitting parameters of the EPIC-pn and MOS 2 spectra with a single component models. Column densities (N_H) are in units of 10^{22} cm^{-2} , temperatures (kT_{BB} and kT_{DBB}) are in units of keV, the power-law normalisation (A_{PL}) is in units of photons $\text{keV}^{-1} \text{ cm}^{-2} \text{ s}^{-1}$ at 1 keV, the disk black body normalisation (A_{DBB}) is in units of $(R_{in}/\text{km})^2/(D/10 \text{ kpc})^2$, where R_{in} is the apparent inner disk radius (in km units), D is the distance of the source (in units of 10 kpc) and the black body normalisation (A_{BB}) is in units of $L_{39}/(D/10 \text{ kpc})^2$, where L_{39} is the source luminosity in units of $10^{39} \text{ erg s}^{-1}$.

Single component model	
DUST*TBNEW*POWERLAW	
N_H	25.6 ± 0.2
Γ	5.76 ± 0.04
A_{PL}	128 ± 8
χ^2/dof	$1530.9 / 1189$
DUST*TBNEW*BBODY	
N_H	13.7 ± 0.2
kT_{BB}	0.693 ± 0.003
A_{BB}	0.0152 ± 0.0003
χ^2/dof	$2897.9 / 1189$
DUST*TBNEW*DISKBB	
N_H	15.9 ± 0.1
kT_{DBB}	0.832 ± 0.006
A_{DBB}	278 ± 14
χ^2/dof	$2479.3 / 1189$

black body (DUST*TBNEW*BBODY) or an absorbed multi-temperature disk black body component (DUST*TBNEW*DISKBB). None of these two models provides an acceptable fit, all resulting in significant residuals at high energies (see Table B.1).

The large residuals at high energy clearly indicate the presence of a second emission component. Therefore, we added the contribution provided by a thermal Comptonisation component (reproduced by the NTHCOMP model; Zdziarski et al. 1996; Zycki et al. 1999). We fix the electron temperature to a high value of 50 keV (consistent results are obtained by fixing the electron temperature to e.g. 20 or 100 keV). The fit with an absorbed black body plus thermal Comptonisation model provides a satisfactory description of the data (see Table B.2). The best-fitting black body parameters are $kT_{BB} = 0.54 \pm 0.01 \text{ keV}$ and $R_{BB} = 35 \pm 11 \text{ km}$. The fit with an absorbed multi-temperature disk black body plus Comptonisation emission provides a temperature of $kT = 0.66 \pm 0.02 \text{ keV}$ and a very reasonable inner disk radius of $r_{in} \sim 27 \pm 10 \text{ km}$ (or $\sim 6.5 r_S$, with $r_S = 2GM/c^2$, where G is the gravitational constant, M is the mass of the compact object, assumed to be $M = 1.4 M_\odot$ and c is the speed of light), however the fit is slightly worse (see Table B.2). Nevertheless, in both these cases, we observe a rather large spectral index

Table B.2: Best-fitting parameters of the EPIC-pn and MOS 2 spectra with two component models. The absorption was described through the model DUST*TBNEW. The black body normalisation (A_{BB}) is in units of $(R/\text{km})^2/(D/10 \text{ kpc})^2$, where R is the source radius in units of km. For the definition of the units of all the other parameters, see Table B.1. †These are the parameters associated to the second minimum in the χ^2 distribution.

	BBODY+NTHCOMP	DISKBB+NTHCOMP	BBODY+DISKBB	DISKBB+BBODY†
Model	(1)	(2)	(3)	(4)
N_H	17.0 ± 0.3	18.7 ± 0.3	16.9 ± 0.3	18.5 ± 0.3
kT_{BB}	0.54 ± 0.01		0.56 ± 0.01	1.58 ± 0.01
A_{BB}	1900 ± 200		1882 ± 190	$1.6^{+0.7}_{-0.5}$
kT_{DBB}		0.66 ± 0.02	1.86 ± 0.14	0.68 ± 0.01
A_{DBB}		1170^{+180}_{-150}	$0.9^{+0.5}_{-0.3}$	1060 ± 130
Γ	3.8 ± 0.3	3.4 ± 0.4		
A_Γ	$6.7^{+2.6}_{-1.9} \times 10^{-2}$	$4^{+6}_{-3} \times 10^4$		
χ^2/dof	1255.2 / 1187	1272.8 / 1187	1246.2 / 1187	1262.7 / 1187

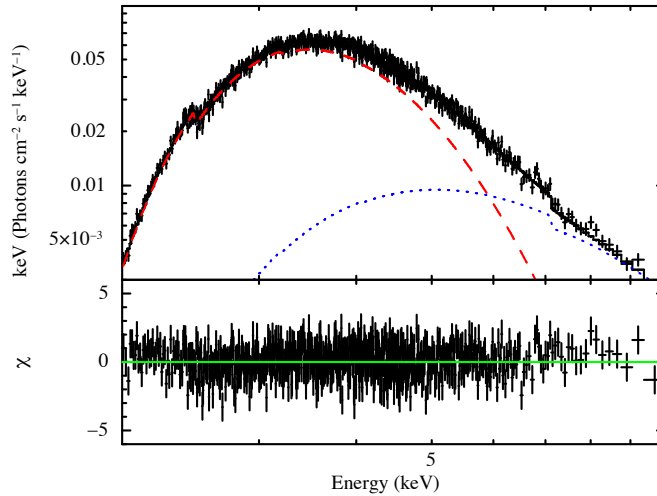


Figure B.5: *Top panel*: EPIC-pn mean spectrum fitted with a black body plus thermal Comptonization component, all absorbed by neutral material. The red dashed and blue dotted lines show the contribution from the black body and thermal Comptonization components, respectively (see Table B.2). *Bottom panel*: residuals compared to the best-fitting model.

for the Comptonisation component, with values $\Gamma \sim 3.5 - 3.8$. Therefore, we substituted the Comptonisation component with a second thermal component. On a statistical ground we obtained an improved solution with the sum of an absorbed black body (with $kT_{BB} = 0.56 \pm 0.01$ keV) plus a multi-temperature disk black body emission ($kT_{DBB} = 1.86 \pm 0.14$ keV). However, we note that the best-fitting inner radius of the disk black body component is $r_{in} = 0.8 \pm 0.5$ km, therefore inside the NS (see Table B.2). For this reason we deem this solution as unlikely. We note a second minimum in the χ^2 distribution ($\chi^2 = 1262.7$ for 1187 dof), leading to a solution with $kT_{BB} = 1.58 \pm 0.01$ keV plus a multi-temperature disk black body emission ($kT_{DBB} = 0.68 \pm 0.01$ keV). The best-fitting inner radius of the disk black body component now results to be $r_{in} = 26 \pm 9$ km (corresponding to $\sim 6 r_S$), while the black body component is produced from a region with radius of about 1 km (Table B.2).

In conclusion, the shape of the *XMM-Newton* spectrum is dominated by a thermal component (either black body or disk black body, with temperature of $kT_{BB} \sim 0.55$ keV, $kT_{DBB} \sim 0.67$ keV) plus an additional component at higher energy that could be reproduced either by a steep Comptonization component (perhaps associated with the corona seen in accreting systems) or a black body emission (possibly generated by the hotter parts on the surface of a NS). Any of these possibilities appear viable, based uniquely on the *XMM-Newton* data. In Section B.5.1 and Section B.5.2, we will investigate further the source radiative process and we will break this model degeneracy by studying the *Swift* and *INTEGRAL* long term spectral evolution.

B.4.2 Ionised absorption

High inclination accreting BHs and NSs are known to display ionised absorption features, whenever they are observed in the soft state (Nielsen et al. 2009; Ponti et al. 2012, 2016). No narrow Fe K absorption or emission line is evident in the spectra of Swift J174540.7–290015. Fitting the spectrum with additional narrow Gaussian absorption lines, we compute upper limits on the line equivalent width (EW) as stringent as $EW < 10$ eV to the presence of Fe XXV and Fe XXVI lines, therefore excluding the presence of either a disk wind or an ionised atmosphere (Diaz-Trigo et al. 2006; Ponti et al. 2012, 2014, 2015, 2016; Miller et al. 2015). Similar upper limits are valid for narrow emission lines between 6.4 and 7 keV. We also note that the addition of a broad Fe K emission line is not required.

B.4.3 X-ray properties of the interstellar medium

The observation of the bright state of Swift J174540.7–290015 allows us to investigate the properties of the interstellar medium (ISM) along a line of sight placed at less than ~ 16 arcsec from Sgr A* (Baganoff et al. 2016). To perform the investigation of the X-ray properties of the ISM, we reproduced the source emission with the absorbed disk black body plus black body model (model 4 in Section B.4.1 and Table B.2). The absorption is fitted with the TBNEW model and the effect of the dust scattering halo was taken into

account (see Table B.2). We observed that using the PHABS absorption model, we measure a column density of absorbing material ($N_H = 18.3 \pm 0.3 \times 10^{22} \text{ cm}^{-2}$) consistent with the values observed using TBNEW or TBABS. On the other hand, a significantly lower value is observed if either the WABS model ($N_H = 12.6 \pm 0.2 \times 10^{22} \text{ cm}^{-2}$) or the Anders & Grevesse (1989) Solar abundances ($N_H = 12.1 \pm 0.2 \times 10^{22} \text{ cm}^{-2}$) are used.

Starting again from the best-fitting baseline model we explored the possibility to constrain the abundances of various elements by leaving the abundance of any metal producing edges in the 2–10 keV band free to vary (see Figure B.5). We observe that the abundances of Si, Cl, Cr, Ca, and Co are unconstrained, therefore we left their abundances fixed at the Solar value. On the other hand, Iron ($A_{Fe} = 0.5 \pm 0.4 A_{Z,\odot}$) and Argon ($A_{Ar} < 0.9 A_{Z,\odot}$) are under abundant, compared to Solar, while Sulphur ($A_S = 1.25^{+0.19}_{-0.14} A_{Z,\odot}$) appears to be slightly overabundant. We note that a larger column density of absorbing material ($N_H = 20.1 \pm 1.2 \times 10^{22} \text{ cm}^{-2}$) is required, once the Iron abundance is left free to vary.

B.5 Long term spectral variations

B.5.1 The *Swift* monitoring

We first fitted all *Swift* spectra with an absorbed power-law model (DUST*TBNEW*POWERLAW). Due to the lower statistics of the single ~ 1 ks spectra, we assumed a column density of $N_H = 25.6 \times 10^{22} \text{ cm}^{-2}$ (see Table B.1) as found when fitting the *XMM-Newton* EPIC spectra. This model cannot satisfactorily reproduce all spectra, especially when Swift J174540.7–290015 enters softer states. Nevertheless, by applying this simple model we can probe the evolution of the spectral shape by tracking the variations of the power-law photon index. Figure B.6 shows the best-fitting power-law photon index in the 2–10 keV band. We observe a gradual steepening of the spectral shape with time. In particular, very steep spectral shapes (with $\Gamma > 5$) are observed in the later observing period. Such large spectral indices might indicate a thermal nature of the emission mechanism. Therefore, we fitted all spectra with an absorbed multi-temperature disk black body model (DUST*TBNEW*DISKBB). Figure B.6 shows the best-fitting inner disk temperature as a function of the inner disk radius. A Kendall's rank correlation test provides a correlation coefficient of $\rho = -0.95$ and null hypothesis probability of 7×10^{-25} . Despite its significance, we think that this anti-correlation is induced by fitting the data with the wrong spectral model. Indeed, we note that: i) the spectra accumulated before MDJ 57442 (blue filled and violet open squares in Figure B.6) are better fit by a power-law component; ii) the best-fitting inner disk radii of these spectra are significantly lower than 10 km, implying that the accretion disk extends either inside the NS surface or inside the event horizon of a stellar mass BH during these observations. On the other hand, all spectra after MJD 57442 (red filled and orange open points in Figure B.6) are well fitted by this absorbed thermal emission model. However, these relatively low S/N spectra cannot rule out the presence of an additional component in the hard X-ray as observed by *XMM-Newton*. In Figure B.6 the orange open and red filled points cluster around a small parameter space, indicating

that these spectra also have similar shape. Moreover, this model cannot reproduce the spectra when there is clearly a hard component, as represented by the blue and purple squares in Figure B.6. Fitting these spectra requires a very high temperature ($kT \sim 1 - 8$ keV) of the thermal component and variations of the normalisation that imply unlikely variations of the thermal emitting area (see Figure B.6).

Finally we adopt model 2 of Table B.2 that is composed by the sum of a thermal multi-temperature disk black body component plus a power law: DUST*TBNEW* (DISKBB+POWERLAW). This model can well reproduce all the spectra. From top to bottom, Figure B.7 shows the source flux in the 2–5, 5–8 and 2–8 keV bands as well as the hardness ratio plotted against the observation date. During the first few days of the observations, Swift J174540.7–290015 showed a clear and significant flux increase, by a factor of 3–4. Very significant variability, stronger in the hard band, and a hard X-ray spectrum are observed up to MJD 57442 (see Figure B.7). Afterwards, the spectrum softens, with an hardness ratio < -0.5 , and no strong variability is observed anymore (see Figure B.7).

To enhance the signal-to-noise ratio, we combined⁵ the spectra obtained before and after MJD 57442. The combined spectra of these two periods are shown in Figure B.8 with blue and red symbols, respectively. To capture the bulk of the spectral variations and to avoid model degeneracies (as demonstrated by the higher statistic *XMM-Newton* spectrum), we consider here only a single emission component model. The spectral degeneracy will be broken by the addition of the *INTEGRAL* data, above 10 keV. The hard state spectrum is better fit ($\chi^2 = 613$ for 538 dof) by a simple absorbed power-law model with spectral index $\Gamma = 2.56 \pm 0.07$ ($N_H = 17.2 \pm 0.5 \times 10^{22}$ cm⁻²). A fit with either a single black body or multi-temperature disk black body component provides a significantly worse fit ($\Delta\chi^2 = 141$ and 56, respectively). The combined soft state spectrum is fit by a simple absorbed multi-temperature disk black body component with best-fitting temperature $kT_{in} = 0.80 \pm 0.02$ keV ($N_H = 16.8 \pm 0.7 \times 10^{22}$ cm⁻², $\chi^2 = 374$ for 329 dof) and inner disk radius $r_{in} = 15 \pm 2$ km. This value is fully compatible with what is expected by an accreting neutron star or black hole. Note that the best-fitting temperature is slightly lower than the mean value in Figure B.6, because the column density of neutral material (N_H) is allowed to vary when fitting the combined spectra. For the soft state combined spectrum, a fit with an absorbed power-law provides a slightly better fit ($\chi^2 = 353$ for 329 dof), however the suspiciously large best-fitting spectral index ($\Gamma = 5.8 \pm 0.w$, $N_H = 26 \pm 1 \times 10^{22}$ cm⁻²) disfavors this interpretation and leaves the disk black body model as the more physical interpretation. The marked spectral and variability difference before and after MJD 57442 is reminiscent of spectral transitions in accreting X-ray binaries (Fender et al. 2004; Remillard & McClintock 2006), and it suggests that Swift J174540.7–290015 might have undergone a state transition during the *Swift* monitoring campaign.

⁵We use the ADDSPEC tool in the FTOOLS 6.18 package to derive the combined source and background spectra, and grouped them with GRPPHA. Some observations with short exposure and very few counts are excluded from the spectral combination.

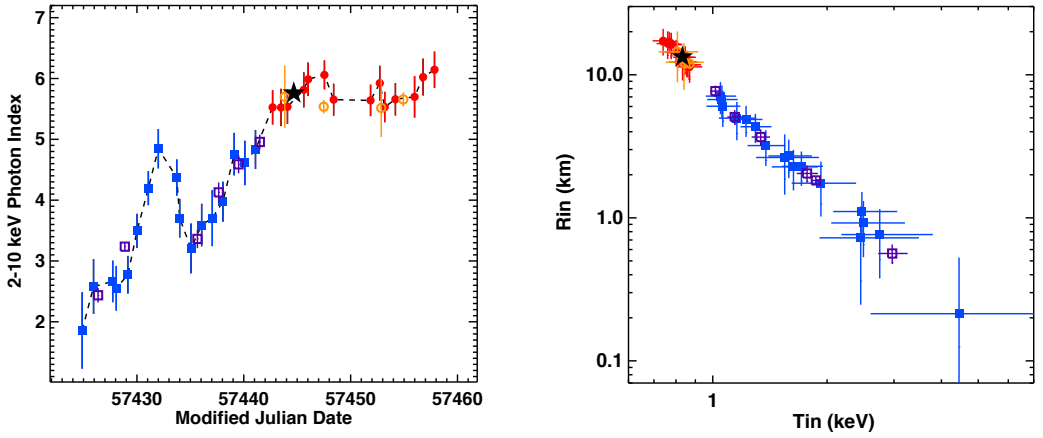


Figure B.6: *Left-hand panel*: spectral slope evolution of Swift J174540.7–290015. The square symbols indicate the hard state observations (filled blue - PC mode, empty purple - WT mode), while the circular symbols indicate the soft state observations (filled red - PC mode, empty orange - WT mode). The black star indicates the *XMM-Newton* observation. The photon indices are derived by fitting an absorbed power-law to the 2–10 keV spectrum of every observation, separately, assuming $N_H = 25.6 \times 10^{22} \text{ cm}^{-2}$ from fitting the *XMM-Newton* spectra. *Right-hand panel*: Inner disk temperature and flux derived from the best-fitting disk black body model to the spectrum of each *Swift* observation (with N_H fixed at $15.9 \times 10^{22} \text{ cm}^{-2}$). Color symbols have the same meaning as in the left-hand panel.

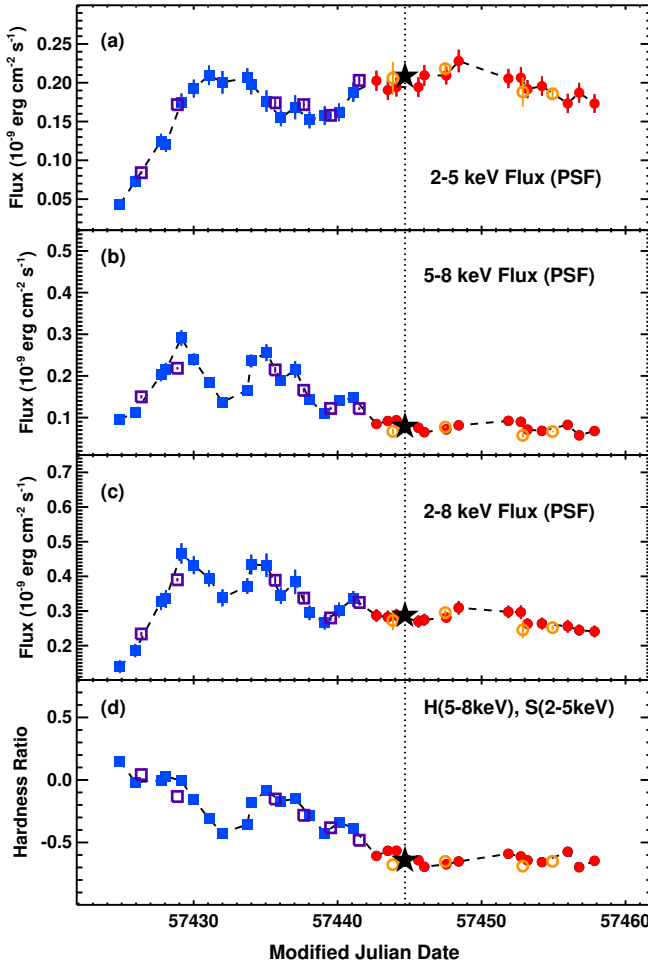


Figure B.7: Panels (a), (b) and (c) are the PSF corrected *Swift* XRT fluxes of Swift J174540.7–290015 in the 2–5 keV, 5–8 keV and 2–8 keV band, respectively. The blue filled square symbols correspond to the PC-mode observations when the source spectrum is dominated by a hard X-ray power-law component. The purple empty squares refer to the WT-mode observations. The red filled circular symbols correspond to the observations when the source spectrum is dominated by a soft X-ray thermal component (see Figure B.6). The orange empty circles refer to the WT-mode observations. Panel (d) shows the hardness ratio between the hard band (5–8 keV) and soft band (2–5 keV). In all panels, the black star and the dashed line indicate the *XMM-Newton* observation on 2016 February 26.

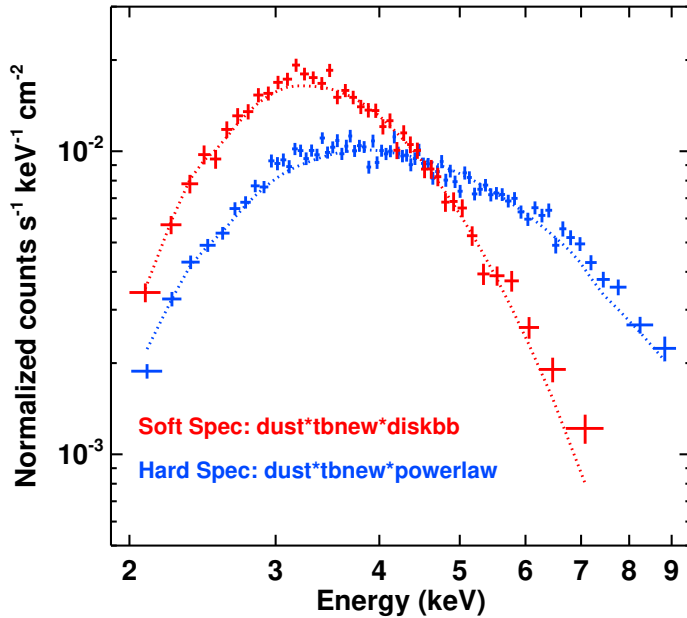


Figure B.8: Combined, background subtracted, *Swift* XRT spectra of the soft state (red) and hard state (blue). The combined soft state spectrum is well fitted by an absorbed disk black body ($N_H = 16.8 \times 10^{22} \text{ cm}^{-2}$, $kT_{in} = 0.80 \text{ keV}$), while the hard state is adequately described by an absorbed power-law component ($N_H = 17.2 \times 10^{22} \text{ cm}^{-2}$, $\Gamma = 2.56$).

B.5.2 The *INTEGRAL* monitoring

To break the degeneracies in the *XMM-Newton* and *Swift* data induced by the limited energy band considered, we investigated the source behavior in the *INTEGRAL* energy band. Figure B.9 shows the JEM-X and IBIS/ISGRI light curves of Swift J174540.7–290015 since the start of the outburst. The source is detected in all energy bands. In particular, a significant drop of hard X-ray emission ($E > 10 \text{ keV}$) is observed after day 20, in correspondence with the state transition inferred from the *Swift* data (Figure B.9).

We accumulated all *INTEGRAL* data that are quasi-simultaneous to *Swift* observations and we created a combined ‘hard state’ and ‘soft state’ spectrum (summing all ISGRI and JEM-X spectra from revolution 1643–1648 and 1649–1652, corresponding to MJD 57429–57441 and 57443–57453, respectively). We then performed a broad-band fit by considering these *INTEGRAL* and *Swift* spectra. As already clear from the analysis of the *XMM-Newton* and *Swift* data, a single component emission model is not an adequate description of the emission of Swift J174540.7–290015 (see Sections B.4.1 and B.5.1). Therefore, we began by applying the best-fitting double component models fitting the *XMM-Newton* spectrum (see Table B.2) to the cumulative *Swift* and *INTEGRAL* soft state

spectra. In all models that we explored, we included a normalisation factor (see Table B.3) to account for intercalibration uncertainties between the different instruments.

We first considered the absorbed double thermal component (CONS*ABS*(DISKBB+BBODY), see model 4 in Table B.2). This model (see Section B.4.1 and Table B.2) is composed by two thermal components peaking below 2 keV, and predicts very little emission above ~ 20 keV. On the other hand, even in the soft state, Swift J174540.7–290015 emits significant radiation above 20 keV. To account for the hard X-ray emission, this model increases the best-fitting temperature of the disk black body component and lowers the inner disk radius to unrealistic values. Indeed, the best-fitting temperature is $kT_{DBB} = 10_{-1.6}^{+2.6}$ keV and the inner disk radius is $r_{in} \sim 25$ m, the latter being too small for either a NS or a BH. For this reason we rule out this model.

We then tested the absorbed black body plus Comptonisation component (CONS*ABS*(BBODY+NTHCOMP), model 1 in Table B.2) as well as the absorbed disk black body plus Comptonisation component (CONS*ABS*(DISKBB+NTHCOMP), model 2 in Table B.2). Incidentally, we note that even adding the *INTEGRAL* data, the energy of the cutoff in the electron distribution is unconstrained ($E > 15$ keV). Therefore we fix this value to 50 keV, as in the previous fits (see Section B.4.1 and Table B.2). Both these thermal plus Comptonisation models provide a good description of the data ($\chi^2 = 357.0$ for 331 dof, $\chi^2 = 355.9$ for 331 dof, respectively). We note that the best-fitting parameters of the absorber, black body and disk black body components are consistent with those obtained by fitting the higher statistics *XMM-Newton* spectrum alone (see Table B.2). However, the addition of the *INTEGRAL* data allows us to obtain more reliable constraints on the parameters of the Comptonisation component. In particular, the photon index of the Comptonisation component ($\Gamma = 2.1$) is now consistent with the values typically observed in accreting compact objects. Moreover, the detection of X-ray emission up to ~ 50 keV allowed us to rule out that the soft state emission is only composed by a combination of purely thermal components.

We then fitted the combined hard state spectrum (see Figure B.10). The broad band spectra can be fit by an absorbed Comptonisation component plus either a black body or a disk black body (see models 1H and 2H in Table B.3). None of these two models provides a completely acceptable fit ($\chi^2 = 659.2$ for 552 dof and $\chi^2 = 648.9$ for 552 dof, respectively). We attribute this to the strong spectral and flux evolution (e.g., variation in photon index) observed during the hard state (see Section B.5.1), which cannot be properly taken into account by the fit of these combined spectra. It is clear, however, that the hardness ratio changed by a factor of ~ 3.4 between the hard ($F_{H,10-100 \text{ keV}} = 6.5 \times 10^{-10} \text{ erg cm}^{-2} \text{ s}^{-1}$, $F_{H,2-10 \text{ keV}} = 3.8 \times 10^{-10} \text{ erg cm}^{-2} \text{ s}^{-1}$) and soft ($F_{S,10-100 \text{ keV}} = 1.4 \times 10^{-10} \text{ erg cm}^{-2} \text{ s}^{-1}$, $F_{S,2-10 \text{ keV}} = 2.8 \times 10^{-10} \text{ erg cm}^{-2} \text{ s}^{-1}$) states (see Figure B.10). This reinforces the interpretation that the source underwent a state change during the monitored period.

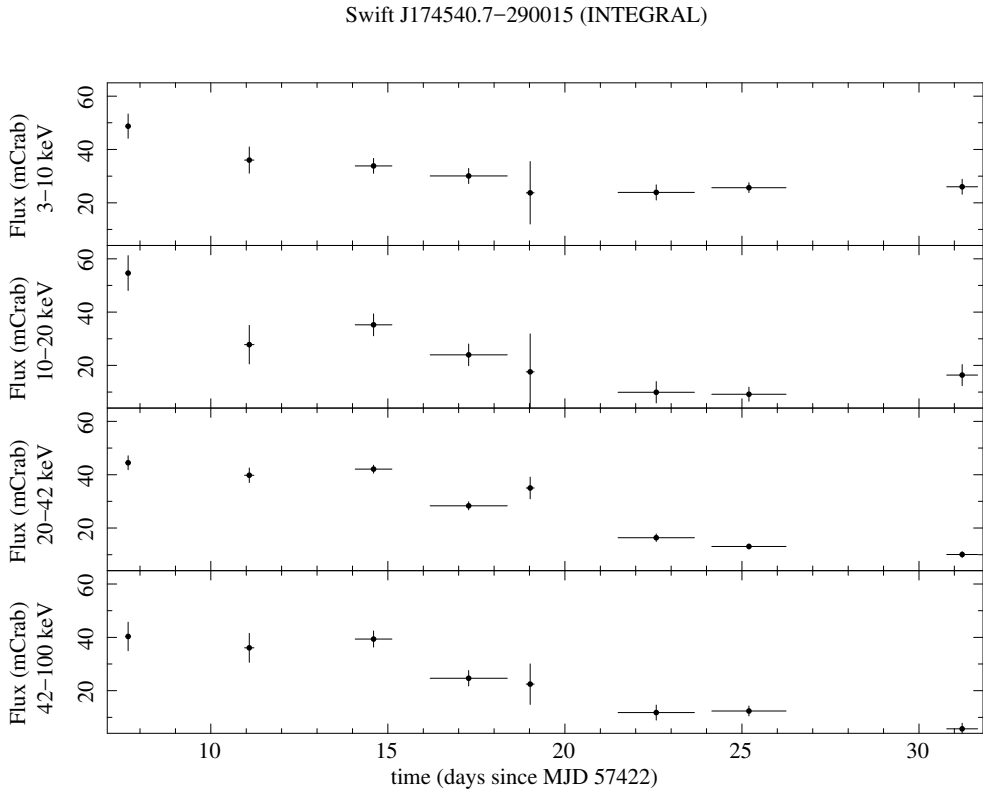


Figure B.9: JEM-X and IBIS/ISGRI light curves of Swift J174540.7–290015 in different energy bands. Each point is integrated for both instruments over an entire *INTEGRAL* revolution (from 1643 to 1652). The state transition inferred from the *Swift* data occurred around day 20. The *INTEGRAL* data show a simultaneous significant drop of hard X-ray emission ($E > 10$ keV), further confirming this interpretation.

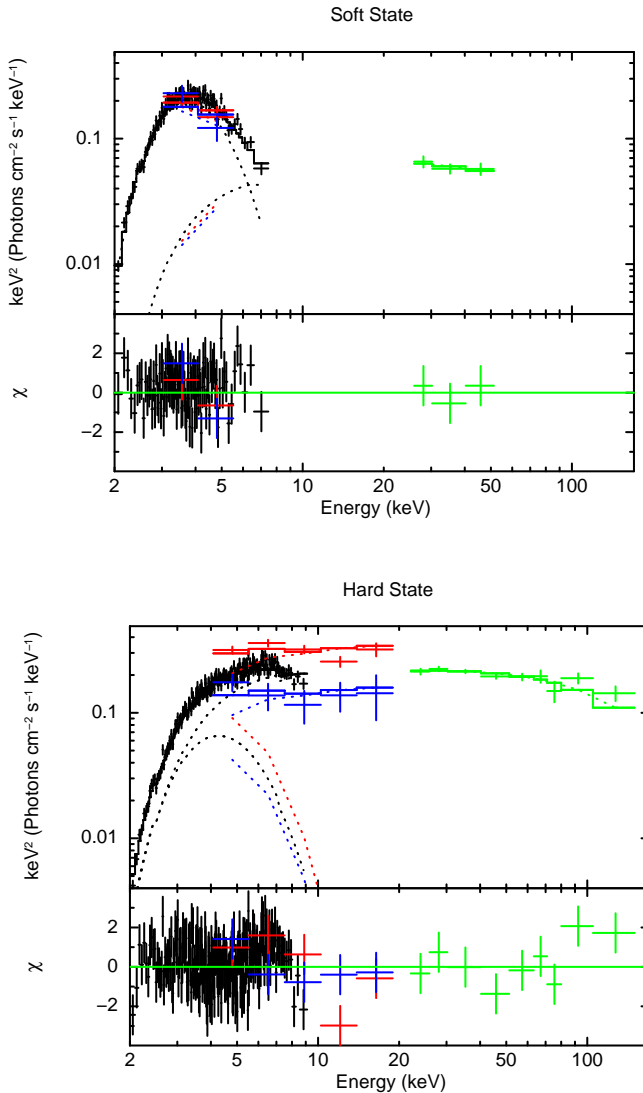


Figure B.10: Broad-band spectra of Swift J174540.7–290015 extracted during the soft and hard states (as defined in Section B.5.2). For the soft state (*top panel*), data from revolutions 1649–1652 have been used (in black, red, blue and green are the *Swift* XRT, JEM-X1, JEM-X2 and IBIS/ISGRI, respectively). For the hard state (*bottom panel*) we used data from the *INTEGRAL* revolutions 1643–1648 (same color scheme as before). The hard state spectrum is dominated by an absorbed Comptonisation component inducing significantly larger high energy flux. The soft state spectrum is dominated by an absorbed thermal component below ~ 10 keV and a Comptonisation tail at higher energies. See text for details.

Table B.3: Best-fitting parameters of the combined, nearly simultaneous *INTEGRAL* and *Swift* soft state and hard state spectra of Swift J174540.7–290015. The same models applied to the higher statistics *XMM–Newton* spectrum have been fitted to the combined broad band soft state (1S, 2S and 4S) spectrum, as well as to the hard state (1H, 2H) one. The absorption was described through the model *DUST*TBNEW*. For the definition of the units of all the other parameters, see Tables B.1 and B.2.

Model	Composite Soft State			Composite Hard State	
	DISKBB+BBODY	BBODY+NTHCOMP	DISKBB+NTHCOMP	DISKBB+NTHCOMP	BBODY+NTHCOMP
	(4S)	(1S)	(2S)	(2H)	(1H)
N_H	15.9 ± 0.9	17.1 ± 1.1	18.8 ± 1.0	14 ± 1	13 ± 1
kT_{BB}	0.62 ± 0.02	0.57 ± 0.03			0.8 ± 0.1
A_{BB}	1100 ± 350	1800 ± 800			68^{+63}_{-23}
kT_{DBB}	$10^{+2.6}_{-1.6}$		0.67 ± 0.04	1.2 ± 0.2	
A_{DBB}	$1^{+1.2}_{-0.5} \times 10^{-3}$		1100^{+700}_{-400}	14^{+21}_{-8}	
Γ		2.1 ± 0.4	2.1 ± 0.4	1.92 ± 0.05	1.94 ± 0.06
A_Γ		$1.4^{+1.0}_{-0.5} \times 10^{-2}$	$(2.9 \pm 1.7) \times 10^{-2}$	$(9 \pm 5) \times 10^{-3}$	$(2.4 \pm 1) \times 10^{-3}$
C_{JEMX1}	< 1.16	0.96 ± 0.2	1.0 ± 0.2	1.5 ± 0.2	1.5 ± 0.1
C_{JEMX2}	< 1.04	$1.3^{+1.5}_{-0.7}$	$1.4^{+1.6}_{-0.7}$	$1.0^{+0.2}_{-0.1}$	0.9 ± 0.1
C_{JSGRI}	< 1.06	0.89 ± 0.18	0.9 ± 0.2	0.9 ± 0.1	0.7 ± 0.1
χ^2/dof	369.5 / 331	357.0 / 331	355.9 / 331	648.9 / 552	659.2 / 552

B.6 Possible near infra-red counterpart

The location of Swift J174540.7–290015 was observed with the Gamma-Ray burst Optical Near-infrared Detector (GROND; Greiner et al. 2008) mounted at the MPG/ESO 2.2m telescope in La Silla, on 2016 February 19.35 UT. Observations were obtained simultaneously in the *J* and *H* photometric bands for 640 s integration time each⁶. The data were reduced with the standard tools and methods as described in Krühler et al. (2008). The photometry was performed using circular apertures with radii corresponding to the image full width at half maximum (1.1 arcsec in *J* and 1.4 arcsec in *H*), and calibrated against 2MASS stars in the same field.

A single bright source, reported also by Masetti et al. (2016) from archival *VVV* imaging, is observed at the *Chandra* X-ray position. The apparent aperture magnitudes (in the Vega system) are $J = 16.0 \pm 0.1$ and $H = 12.8 \pm 0.1$. The location of the new transient was also contained in a series of 15 GROND observations obtained on 2015 April 26.35 – 26.42 UT during the monitoring of another Galactic Centre transient. No variability was found for the bright near-IR source in the *J* or *H* band during this set of observations and the median magnitudes of $J = 16.1 \pm 0.1$ (seeing 1.1 arcsec) and $H = 12.57 \pm 0.10$ (1.6 arcsec) are consistent within errors with the post-outburst measurements.

The near-IR source density at the position of the transient is very high and GROND photometry corresponds to the co-addition of the flux of all sources within the aperture.

⁶GROND observes simultaneously in *g'*, *r'*, *i'*, *z'*, *J*, *H*, *K*. Due to the extreme Galactic foreground reddening affecting the optical bands and saturation affecting the *K*-band, only the *J* and *H* band data are discussed here.

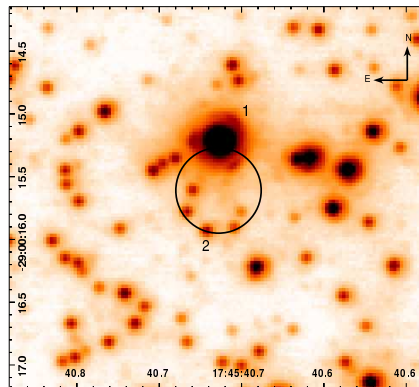


Figure B.11: VLT-*NaCo* archival *K*-band image of the field around Swift J174540.7–290015. The *Chandra* error circle (Baganoff et al. 2016) is shown by the black circle, with radius 0.34 arcsec. The bright candidate counterpart (1) as well as a fainter one (2) are indicated. See text for details. North is up, East is to the left.

Therefore, we can only conclude that the brightest source within the *Chandra* error circle, dominating the total emission, remained constant between the pre- and post-outburst observations and none of the fainter objects brightened to a level where it would increase the overall emission within the aperture by more than 0.1 mag.

The GC is routinely observed with adaptive optics using the Nasmyth Adaptive Optics System Near-Infrared Imager and Spectrograph (*NaCo*) at the Very Large Telescope (see Gillessen et al. 2009 for a description of the program and data reduction). Figure B.11 shows a stacked *NaCo* *K*-band image from archival (pre-outburst) observations. Besides the bright source dominating the GROND photometry, multiple fainter objects are resolved either inside or in close proximity to the *Chandra* error region (black circle). For the brightest source (see Figure B.11) we measure magnitudes of $H = 12.98 \pm 0.06$ and $K = 10.81 \pm 0.03$ while, for comparison, the faintest star (#2 in Figure B.11) has $H_{star2} = 17.24 \pm 0.06$ and $K_{star2} = 15.23 \pm 0.03$. The MPE-IR group obtained new *NaCo* data on 2016 March 16. No significant variation in brightness is observed for any of the sources within the *Chandra* error circle (Gillessen private communication).

The probability of having such a bright star within the *Chandra* error circle of ~ 0.4 arcsec² can be computed from the number of stars with $m_{K_s} > 11$ mag within an annulus centered on Sgr A^{*} and with inner and outer radii of $16 - 5$ arcsec and $16 + 5$ arcsec, respectively. This annulus includes the position of the putative near-IR counterpart. The observed surface density within the annulus is 0.032 stars arcsec⁻², implying a chance coincidence probability of ~ 1 per cent of finding a source with $m_{K_s} > 11$ mag within the *Chandra* error circle, i.e. that the bright source is not associated with the X-ray transient.

Using the average reddening towards the Galactic Centre of $A_K = 2.4 \pm 0.1$ mag (Fritz et al. 2011), the absolute *K*-band magnitude is $M_K = -6.1$. The star spectroscopically

shows the CO band heads in the K -band, which excludes stars hotter than spectral class F (Wallace & Hinkle 1997). The absolute magnitude would suggest it to be a late type giant or super giant star.

B.7 Discussion

We report the identification of a new X-ray binary, Swift J174540.7–290015, and results from the early phases of the evolution of its X-ray emission. Swift J174540.7–290015 reached an absorbed flux at the peak of 6×10^{-10} erg cm $^{-2}$ s $^{-1}$ in the 2–10 keV band. During the *XMM–Newton* observation, the source shows an absorbed and unabsorbed 2–10 keV flux of 2.9×10^{-10} and 1.45×10^{-9} erg cm $^{-2}$ s $^{-1}$, respectively (the latter corresponding to 5.3×10^{-9} erg cm $^{-2}$ s $^{-1}$ in the 0.1–10 keV band). During the *XMM–Newton* observation, Swift J174540.7–290015 showed a luminosity of 3.8×10^{37} erg s $^{-1}$ in the 0.1–10 keV band. Therefore, if Swift J174540.7–290015 is a NS with $M_{NS} = 1.4M_{\odot}$, the luminosity is ~ 20 per cent of the Eddington limit during the *XMM–Newton* observation (< 20 per cent if Swift J174540.7–290015 is a BH). Given these luminosities, Swift J174540.7–290015 does not belong to the class of faint X-ray transients (Wijnands et al. 2006).

We point out that Swift J174540.7–290015 is located at less than 16 arcsec from Sgr A* (the supermassive BH at the GC), less than 17 arcsec from SGR 1745–2900 (Rea et al. 2013; Mori et al. 2013; Coti Zelati et al. 2015) and less than 1.7 arcmin from the NS low mass X-ray binary AX J1745.6–2901 (Ponti et al. 2015, 2016), therefore it lies in the field of view of all *XMM–Newton* observations pointed towards one of these sources (Ponti et al. 2015a,b,c; 2016). No evidence for previous outbursts of Swift J174540.7–290015 is present in the *XMM–Newton*, *Chandra* and *Swift* archive (Degenaar et al. 2012; Ponti et al. 2015a,b). We compute the upper limit on the X-ray emission of Swift J174540.7–290015 during quiescence by stacking all *Chandra* ACIS-I observations between 1999 and 2011, for a total exposure of ~ 1.8 Ms. We observe 54 counts within 0.34 arcsec from the position of Swift J174540.7–290015, in the 0.5–10 keV band. This translates into an upper limit of 3.5×10^{-5} counts s $^{-1}$ at the 95 per cent confidence level (Gehrels 1986). Under the assumption that the quiescent spectrum of Swift J174540.7–290015 is described either by an absorbed ($N_H = 18.7 \times 10^{22}$ cm $^{-2}$) power-law (with spectral index $\Gamma = 2$) or a black body ($kT_{BB} = 0.3$ keV), this can be translated into a luminosity of $< 5 \times 10^{31}$ and $< 1.7 \times 10^{33}$ erg s $^{-1}$, respectively (in the 0.5–10 keV energy range). This upper limit is consistent with both a NS or BH origin of Swift J174540.7–290015 (Narayan et al. 1997; Garcia et al. 2001; Rea et al. 2011; Armas Padilla et al. 2014).

Radio observations did not detect either a steady or periodic counterpart to Swift J174540.7–290015. Steady emission is expected under two scenarios. First, the fundamental plane of BH activity can be used to predict the radio luminosity under the assumption that the system is in the low hard state (Plotkin et al. 2012). For a $10 M_{BH}$ black hole at the X-ray luminosity measured by *XMM–Newton*, we predict a radio flux density of 6 mJy. The scatter in the fundamental plane is approximately an order of magnitude, so that

values as high as 100 mJy are possible. The imaging non-detection with an rms of 6 mJy, thus, can neither rule out nor confirm the presence of a jet in this system. We note that by the time the first VLA observation has been taken, Swift J174540.7–290015 already transitioned to the soft state. Second, bright radio emission can be produced through interaction of a jet with the dense interstellar medium of the Galactic Centre. The low-mass X-ray binary CXOGC J174540.0–290031, located only 0.1 pc in projection from Sgr A*, reached a peak flux density of 100 mJy that was resolved into two lobes on either sides of the X-ray counterpart (Bower et al. 2005). The proximity of Swift J174540.7–290015 to Sgr A West suggests that it could produce similar interactions but we find no evidence for these.

The emission of Swift J174540.7–290015 during the *XMM–Newton* observation is dominated by a thermal component that can be well fitted either by multi-temperature disk black body, or black body emission. In addition, emission at higher energies (up to 20–50 keV) is clearly detected by *INTEGRAL*. The high energy emission is a clear sign for a Comptonisation component, ruling out a double thermal component consistent with the fits limited to energies below 10 keV. The disk black body plus Comptonisation scenario is perfectly compatible either with a NS or BH primary. In this framework, the Comptonisation component might be associated with the coronal emission typically observed in accreting sources and the multi-temperature disk black body could be produced by a standard accretion disk extending down to $\sim 6.5 r_S$ for a NS ($M_{NS} = 1.4 M_\odot$) or $\sim 2 r_S$ for a BH with $M_{BH} = 5 M_\odot$. In the second scenario (model 1 and 1S in Tables B.2 and B.3, respectively), the presence of the black body emission suggests that the primary is a NS. Also in this scenario, the Comptonisation might be due to coronal emission, but the soft radiation would be dominated by the boundary layer emission. However, the best-fitting black body radius appears to be too large ($R_{BB} = 35 \pm 11$ km) to be associated with a conceivable NS. Nevertheless, we cannot exclude that the large observed area, attributed to the black body emission, might be induced by the contribution from a disk emission component not considered in our modelling. Alternatively, the black body component might be in part produced by hot spots on the surface of the NS. Would this indeed be the case, then a pulsation should be present. However, this pulsation might be undetected either because of the weakness of the black body emission or because Swift J174540.7–290015 is a fast spinning millisecond pulsar (e.g., faster than our timing resolution, or a weak signal possibly also smeared by a Doppler orbital shift).

From the spectral behavior of Swift J174540.7–290015 we can rule out a high mass X-ray binary (HMXB) identification of the source. The spectra of HMXBs are characterised by a dominant hard power-law in the 0.2–10.0 keV band with typical photon indices of 1.0–1.5 for supergiant systems and around 0.9 for Be/X-ray binaries (e.g. Haberl et al. 2008; Bozzo et al. 2012; Bodaghee et al. 2012; Walter et al. 2015). HMXBs also do not show spectral state transitions as observed from Swift J174540.7–290015.

Swift J174540.7–290015 was initially identified as a possible magnetar due to its fast outburst rise. However, many observational characteristics of this new transient are at variance with what is usually observed in magnetar outbursts (see Rea & Esposito 2011

and Turolla, Zane & Watts 2015 for a review on outbursts and on magnetars in general, respectively). The strong variability of the outburst flux decay (see Figure B.7) is unseen in the outburst decay of magnetars, which are usually observed to decay smoothly toward quiescence. This is also in line with the interpretation of these outbursts as being due to a large energy injection in the magnetar crust triggered by the instability of the internal or external magnetic field (possibly by a strongly twisted magnetic bundle), with a consequent crustal heating and subsequent cooling (Beloborodov 2009; Pons & Rea 2012). Furthermore, if the source is placed at 8 kpc, the peak luminosity of the outburst is too high with respect to what is observed for magnetars, $L_X < 10^{36}$ erg s⁻¹, which is a limit believed to be regulated by the strong dependence on temperature of the crustal neutrino emissivity (Pons & Rea 2012). The deep upper limits on the PF of this new transient (see Figure B.4) are rather unlikely (although a few exceptions exist) compared with the usual strength (~ 20 – 80 per cent) observed for the periodic signals (in the 2–10 s range) of magnetars. Therefore, we believe that the magnetar interpretation for this new transient is extremely unlikely.

Observations of the X-ray reflection nebulae (irradiated molecular clouds within a few hundred parsecs from Sgr A^{*}) suggest either a solar or supersolar Iron abundance of the GC interstellar medium (Revnitsev et al. 2004; Terrier et al. 2010; Ponti et al. 2010, 2013, 2014b; Zhang et al. 2015). The observed low Iron abundance ($A_{Fe} = 0.5 \pm 0.4 A_{Z,\odot}$) of the neutral absorbing material towards Swift J174540.7–290015 is thus rather surprising also compared to the accepted Iron gradient in the Galactic disk (Friel et al. 2002; Pedicelli et al. 2009). We note that the measured value is consistent with the Iron abundance towards 4U 1820–303, an X-ray binary located at a distance of ~ 7.6 kpc, at less than 1 kpc from the GC (towards $l = 2.79^\circ$ and $b = -7.91^\circ$; Kuulkers et al. 2003; Pinto et al. 2010). The observed under abundance is also in line with the values measured towards a small sample of bright Galactic X-ray binaries (Juett et al. 2006). We attribute this to depletion of Iron into dust grains in the ISM. Indeed, depletion of elements in dust grains can reduce the effective cross section for absorption. In grains, the optical depth can be higher than one, therefore absorption will occur primarily on the surface. Moreover, Iron atoms located deeper into the grain will be shielded and they will not contribute to the absorption, effectively reducing the strength of the element absorption edge (e.g. Juett et al. 2006). The similarity of the observed Iron abundance with the abundances measured along many other line of sights, is consistent with the idea that a significant fraction of the absorption is produced in the ISM along the Galactic arms and therefore it does not carry information about the metal abundances characteristic of the GC region. Future detailed modelling of the dust scattering halo of AX J1745.6–2901 and Swift J174540.7–290015 will better constrain this.

Given the long-term X-ray variability and spectral decomposition, we identify Swift J174540.7–290015 as an accreting X-ray binary hosting a neutron star or a black hole, most likely with a low mass companion star. The discovery and identification of this new GC transient as well as the continuous X-ray monitoring of the central parsec is improving the determination of the population of stellar remnants orbiting Sgr A^{*}.

Bibliography

- [1] F. Acero et al. “Fermi Large Area Telescope Third Source Catalog”. In: *ApJS* 218, 23 (June 2015), p. 23. DOI: 10.1088/0067-0049/218/2/23. arXiv: 1501.02003 [astro-ph.HE].
- [2] A. Albano et al. “A Unified Timing and Spectral Model for the Anomalous X-ray Pulsars XTE J1810-197 and CXOU J164710.2-455216”. In: *ApJ* 722 (Oct. 2010), pp. 788–802. DOI: 10.1088/0004-637X/722/1/788. arXiv: 1007.5466 [astro-ph.HE].
- [3] C. Alcock, E. Farhi and A. Olinto. “Model for the 5 March 1979 gamma-ray transient”. In: *Physical Review Letters* 57 (Oct. 1986), pp. 2088–2091. DOI: 10.1103/PhysRevLett.57.2088.
- [4] J. Aleksić et al. “Observations of the magnetars 4U 0142+61 and 1E 2259+586 with the MAGIC telescopes”. In: *A&A* 549, A23 (Jan. 2013), A23. DOI: 10.1051/0004-6361/201220275. arXiv: 1211.1173 [astro-ph.HE].
- [5] J. A. J. Alford and J. P. Halpern. “Evolution of the X-Ray Properties of the Transient Magnetar XTE J1810-197”. In: *ApJ* 818, 122 (Feb. 2016), p. 122. DOI: 10.3847/0004-637X/818/2/122. arXiv: 1601.00757 [astro-ph.HE].
- [6] M. A. Alpar. “On Young Neutron Stars as Propellers and Accretors with Conventional Magnetic Fields”. In: *ApJ* 554 (June 2001), pp. 1245–1254. DOI: 10.1086/321393. eprint: astro-ph/0005211.
- [7] M. A. Alpar et al. “A new class of radio pulsars”. In: *Nature* 300 (Dec. 1982), pp. 728–730. DOI: 10.1038/300728a0.
- [8] H. An et al. “Deep NuSTAR and Swift Monitoring Observations of the Magnetar 1E 1841045”. In: *ApJ* 807, 93 (July 2015), p. 93. DOI: 10.1088/0004-637X/807/1/93. arXiv: 1505.03570 [astro-ph.HE].
- [9] H. An et al. “NuSTAR Observations of Magnetar 1E 1841-045”. In: *ApJ* 779, 163 (Dec. 2013), p. 163. DOI: 10.1088/0004-637X/779/2/163. arXiv: 1310.6221 [astro-ph.HE].

- [10] H. An et al. “NuSTAR Observations of X-Ray Bursts from the Magnetar 1E 1048.1-5937”. In: *ApJ* 790, 60 (July 2014), p. 60. DOI: 10.1088/0004-637X/790/1/60. arXiv: 1406.3377 [astro-ph.HE].
- [11] H. An et al. “Spectral and Timing Properties of the Magnetar CXOU J164710.2-455216”. In: *ApJ* 763, 82 (Feb. 2013), p. 82. DOI: 10.1088/0004-637X/763/2/82. arXiv: 1212.0184 [astro-ph.HE].
- [12] E. Anders and N. Grevesse. “Abundances of the elements - Meteoritic and solar”. In: 53 (Jan. 1989), pp. 197–214. DOI: 10.1016/0016-7037(89)90286-X.
- [13] J. Antoniadis et al. “A Massive Pulsar in a Compact Relativistic Binary”. In: *Science* 340 (Apr. 2013), p. 448. DOI: 10.1126/science.1233232. arXiv: 1304.6875 [astro-ph.HE].
- [14] R. L. Aptekar et al. “Konus Catalog of Soft Gamma Repeater Activity: 1978 to 2000”. In: *ApJS* 137 (Dec. 2001), pp. 227–277. DOI: 10.1086/322530. eprint: astro-ph/0004402.
- [15] A. M. Archibald et al. “A Radio Pulsar/X-ray Binary Link”. In: *Science* 324 (June 2009), p. 1411. DOI: 10.1126/science.1172740. arXiv: 0905.3397 [astro-ph.HE].
- [16] A. M. Archibald et al. “Accretion-powered Pulsations in an Apparently Quiescent Neutron Star Binary”. In: *ApJ* 807, 62 (July 2015), p. 62. DOI: 10.1088/0004-637X/807/1/62. arXiv: 1412.1306 [astro-ph.HE].
- [17] A. M. Archibald et al. “Long-Term Radio Timing Observations of the Transition Millisecond Pulsar PSR~J1023+0038”. In: *ArXiv e-prints* (Nov. 2013). arXiv: 1311.5161 [astro-ph.HE].
- [18] A. M. Archibald et al. “X-ray Variability and Evidence for Pulsations from the Unique Radio Pulsar/X-ray Binary Transition Object FIRST J102347.6+003841”. In: *ApJ* 722 (Oct. 2010), pp. 88–95. DOI: 10.1088/0004-637X/722/1/88. arXiv: 1008.1068 [astro-ph.HE].
- [19] R. F. Archibald et al. “An anti-glitch in a magnetar”. In: *Nature* 497 (May 2013), pp. 591–593. DOI: 10.1038/nature12159. arXiv: 1305.6894 [astro-ph.HE].
- [20] R. F. Archibald et al. “Repeated, Delayed Torque Variations Following X-Ray Flux Enhancements in the Magnetar 1E 1048.1-5937”. In: *ApJ* 800, 33 (Feb. 2015), p. 33. DOI: 10.1088/0004-637X/800/1/33. arXiv: 1412.2780 [astro-ph.HE].
- [21] M. Armas Padilla et al. “Swift J1357.2-0933: the faintest black hole?” In: *MNRAS* 444 (Oct. 2014), pp. 902–905. DOI: 10.1093/mnras/stu1487. arXiv: 1404.2134 [astro-ph.HE].
- [22] P. J. Armitage and M. Livio. “Hydrodynamics of the Stream-Disk Impact in Interacting Binaries”. In: *ApJ* 493 (Jan. 1998), pp. 898–908. DOI: 10.1086/305149. eprint: astro-ph/9709035.

- [23] K. A. Arnaud. “XSPEC: The First Ten Years”. In: *Astronomical Data Analysis Software and Systems V*. Ed. by G. H. Jacoby and J. Barnes. Vol. 101. Astronomical Society of the Pacific Conference Series. 1996, p. 17.
- [24] J. Arons and M. Tavani. “High-energy emission from the eclipsing millisecond pulsar PSR 1957+20”. In: *ApJ* 403 (Jan. 1993), pp. 249–255. DOI: 10.1086/172198.
- [25] W. Baade and F. Zwicky. “Remarks on Super-Novae and Cosmic Rays”. In: *Physical Review* 46 (July 1934), pp. 76–77. DOI: 10.1103/PhysRev.46.76.2.
- [26] D. C. Backer et al. “A millisecond pulsar”. In: *Nature* 300 (Dec. 1982), pp. 615–618. DOI: 10.1038/300615a0.
- [27] F. K. Baganoff et al. “Chandra Position of Galactic Center X-ray Transient Swift J174540.7-290015”. In: *The Astronomer’s Telegram* 8746 (Feb. 2016).
- [28] F. K. Baganoff et al. “Chandra X-Ray Spectroscopic Imaging of Sagittarius A* and the Central Parsec of the Galaxy”. In: *ApJ* 591 (July 2003), pp. 891–915. DOI: 10.1086/375145. eprint: astro-ph/0102151.
- [29] M. C. Baglio et al. “Different twins in the millisecond pulsar recycling scenario: Optical polarimetry of PSR J1023+0038 and XSS J12270-4859”. In: *A&A* 591, A101 (June 2016), A101. DOI: 10.1051/0004-6361/201628383. arXiv: 1605.00653 [astro-ph.SR].
- [30] M. C. Baglio et al. “The long-term evolution of the X-ray pulsar XTE J1814-338: A receding jet contribution to the quiescent optical emission?” In: *A&A* 559, A42 (Nov. 2013), A42. DOI: 10.1051/0004-6361/201322442. arXiv: 1309.5831 [astro-ph.SR].
- [31] M. G. Baring and A. K. Harding. “Resonant Compton upscattering in anomalous X-ray pulsars”. In: *AP&SS* 308 (Apr. 2007), pp. 109–118. DOI: 10.1007/s10509-007-9326-x. eprint: astro-ph/0610382.
- [32] S. D. Barthelmy, J. R. Cummings and J. A. Kennea. “Trigger 557640: Swift detection of burst from Sgr J1745-29.” In: *GRB Coordinates Network* 14805 (2013).
- [33] S. D. Barthelmy et al. “Trigger 565443: Swift detection of a burst from Sgr J1745-29.” In: *GRB Coordinates Network* 15069 (2013).
- [34] C. G. Bassa et al. “A state change in the low-mass X-ray binary XSS J12270-4859”. In: *MNRAS* 441 (June 2014), pp. 1825–1830. DOI: 10.1093/mnras/stu708. arXiv: 1402.0765 [astro-ph.HE].
- [35] L. Bassani et al. “The counterpart/s of IGR J20159+3713/SWIFT J2015.9+3715: dissecting a complex region with emission from keV to TeV”. In: *A&A* 561, A108 (Jan. 2014), A108. DOI: 10.1051/0004-6361/201322292. arXiv: 1310.7837 [astro-ph.HE].

- [36] A. M. Beloborodov. “Electron-Positron Flows around Magnetars”. In: *ApJ* 777, 114 (Nov. 2013), p. 114. DOI: 10.1088/0004-637X/777/2/114. arXiv: 1209.4063 [astro-ph.HE].
- [37] A. M. Beloborodov. “Untwisting Magnetospheres of Neutron Stars”. In: *ApJ* 703 (Sept. 2009), pp. 1044–1060. DOI: 10.1088/0004-637X/703/1/1044. arXiv: 0812.4873.
- [38] A. M. Beloborodov and Y. Levin. “Thermoplastic Waves in Magnetars”. In: *ApJL* 794, L24 (Oct. 2014), p. L24. DOI: 10.1088/2041-8205/794/2/L24. arXiv: 1406.4850 [astro-ph.HE].
- [39] A. M. Beloborodov and X. Li. “Magnetar Heating”. In: *ApJ* 833, 261 (Dec. 2016), p. 261. DOI: 10.3847/1538-4357/833/2/261. arXiv: 1605.09077 [astro-ph.HE].
- [40] A. M. Beloborodov and C. Thompson. “Corona of Magnetars”. In: *ApJ* 657 (Mar. 2007), pp. 967–993. DOI: 10.1086/508917. eprint: astro-ph/0602417.
- [41] F. Bernardini et al. “Characterization of new hard X-ray cataclysmic variables”. In: *A&A* 542, A22 (June 2012), A22. DOI: 10.1051/0004-6361/201219233. arXiv: 1204.3758 [astro-ph.HE].
- [42] F. Bernardini et al. “Emission geometry, radiation pattern and magnetic topology of the magnetar XTE J1810-197 in its quiescent state”. In: *MNRAS* 418 (Nov. 2011), pp. 638–647. DOI: 10.1111/j.1365-2966.2011.19513.x. arXiv: 1107.5302 [astro-ph.HE].
- [43] F. Bernardini et al. “From outburst to quiescence: the decay of the transient AXP XTE J1810-197”. In: *A&A* 498 (Apr. 2009), pp. 195–207. DOI: 10.1051/0004-6361/200810779. arXiv: 0901.2241 [astro-ph.HE].
- [44] F. Bernardini et al. “Multi-instrument X-ray monitoring of the January 2009 outburst from the recurrent magnetar candidate 1E 1547.0-5408”. In: *A&A* 529, A19 (May 2011), A19. DOI: 10.1051/0004-6361/201016197. arXiv: 1102.5419 [astro-ph.HE].
- [45] F. Bernardini et al. “On the nature of the hard X-ray sources SWIFT J1907.3-2050, IGR J12123-5802 and IGR J19552+0044”. In: *MNRAS* 435 (Nov. 2013), pp. 2822–2834. DOI: 10.1093/mnras/stt1434. arXiv: 1308.1230 [astro-ph.HE].
- [46] F. Bernardini et al. “Swift J0525.6+2416 and IGR J04571+4527: two new hard X-ray-selected magnetic cataclysmic variables identified with XMM-Newton”. In: *MNRAS* 453 (Nov. 2015), pp. 3100–3106. DOI: 10.1093/mnras/stv1673. arXiv: 1507.06442 [astro-ph.HE].
- [47] F. Bernardini et al. “Swift J2218.4+1925: a new hard-X-ray-selected polar observed with XMM-Newton”. In: *MNRAS* 445 (Dec. 2014), pp. 1403–1411. DOI: 10.1093/mnras/stu1819. arXiv: 1409.2257 [astro-ph.HE].

- [48] D. L. Bertsch et al. “Pulsed high-energy gamma-radiation from Geminga (1E0630 + 178)”. In: *Nature* 357 (May 1992), p. 306. DOI: 10.1038/357306a0.
- [49] H. Bhadkamkar and P. Ghosh. “Young pre-low-mass X-ray binaries in the propeller phase. Nature of the 6.7-h periodic X-ray source 1E 161348-5055 in RCW 103”. In: *A&A* 506 (Nov. 2009), pp. 1297–1307. DOI: 10.1051/0004-6361/200912552. arXiv: 0909.0159 [astro-ph.SR].
- [50] S. Bilir et al. “Luminosity-colour relations for thin-disc main-sequence stars”. In: *MNRAS* 390 (Nov. 2008), pp. 1569–1576. DOI: 10.1111/j.1365-2966.2008.13839.x. arXiv: 0808.1848.
- [51] G. S. Bisnovatyi-Kogan and B. V. Komberg. “Possible evolution of a binary-system radio pulsar as an old object with a weak magnetic field”. In: *Soviet Astronomy Letters* 2 (Aug. 1976), pp. 130–132.
- [52] J. K. Blackburn. “FTOOLS: A FITS Data Processing and Analysis Software Package”. In: *Astronomical Data Analysis Software and Systems IV*. Ed. by R. A. Shaw, H. E. Payne and J. J. E. Hayes. Vol. 77. Astronomical Society of the Pacific Conference Series. 1995, p. 367.
- [53] A. Bodaghee et al. “Supergiant X-ray binaries observed by Suzaku”. In: *American Institute of Physics Conference Series*. Ed. by R. Petre, K. Mitsuda and L. Angelini. Vol. 1427. American Institute of Physics Conference Series. Mar. 2012, pp. 52–55. DOI: 10.1063/1.3696150. arXiv: 1111.5310 [astro-ph.HE].
- [54] S. Bogdanov et al. “A Chandra X-Ray Observation of the Binary Millisecond Pulsar PSR J1023+0038”. In: *ApJ* 742, 97 (Dec. 2011), p. 97. DOI: 10.1088/0004-637X/742/2/97. arXiv: 1108.5753 [astro-ph.HE].
- [55] S. Bogdanov et al. “Coordinated X-Ray, Ultraviolet, Optical, and Radio Observations of the PSR J1023+0038 System in a Low-mass X-Ray Binary State”. In: *ApJ* 806, 148 (June 2015), p. 148. DOI: 10.1088/0004-637X/806/2/148. arXiv: 1412.5145 [astro-ph.HE].
- [56] S. Bogdanov et al. “X-Ray Observations of XSS J12270-4859 in a New Low State: A Transformation to a Disk-free Rotation-powered Pulsar Binary”. In: *ApJ* 789, 40 (July 2014), p. 40. DOI: 10.1088/0004-637X/789/1/40. arXiv: 1402.6324 [astro-ph.HE].
- [57] H. E. Bond et al. “FIRST J102347.6+003841: The First Radio-selected Cataclysmic Variable”. In: 114 (Dec. 2002), pp. 1359–1363. DOI: 10.1086/344381. eprint: astro-ph/0208383.
- [58] G. C. Bower et al. “A Radio Transient 0.1 Parsecs from Sagittarius A*”. In: *ApJ* 633 (Nov. 2005), pp. 218–227. DOI: 10.1086/444587. eprint: astro-ph/0507221.
- [59] G. C. Bower et al. “A Search for a Radio Counterpart to Swift J174540.7-290015”. In: *The Astronomer’s Telegram* 8793 (Mar. 2016).

- [60] G. C. Bower et al. “The Proper Motion of the Galactic Center Pulsar Relative to Sagittarius A*”. In: *ApJ* 798, 120 (Jan. 2015), p. 120. DOI: 10.1088/0004-637X/798/2/120. arXiv: 1411.0399 [astro-ph.HE].
- [61] E. Bozzo et al. “Can disk-magnetosphere interaction models and beat frequency models for quasi-periodic oscillation in accreting X-ray pulsars be reconciled?” In: *A&A* 493 (Jan. 2009), pp. 809–818. DOI: 10.1051/0004-6361:200810658. arXiv: 0811.0049.
- [62] E. Bozzo et al. “IGR J17451-3022: A dipping and eclipsing low mass X-ray binary”. In: *A&A* 589, A42 (May 2016), A42. DOI: 10.1051/0004-6361/201527501. arXiv: 1603.03353 [astro-ph.HE].
- [63] E. Bozzo et al. “XMM-Newton observations of four high mass X-ray binaries and IGR J17348-2045”. In: *A&A* 544, A118 (Aug. 2012), A118. DOI: 10.1051/0004-6361/201218900. arXiv: 1207.3719 [astro-ph.HE].
- [64] J. Braithwaite. “A differential rotation driven dynamo in a stably stratified star”. In: *A&A* 449 (Apr. 2006), pp. 451–460. DOI: 10.1051/0004-6361:20054241. eprint: astro-ph/0509693.
- [65] A. A. Breeveld et al. “An Updated Ultraviolet Calibration for the Swift/UVOT”. In: *American Institute of Physics Conference Series*. Ed. by J. E. McEnery, J. L. Racusin and N. Gehrels. Vol. 1358. American Institute of Physics Conference Series. Aug. 2011, pp. 373–376. DOI: 10.1063/1.3621807. arXiv: 1102.4717 [astro-ph.IM].
- [66] A. A. Breeveld et al. “Further calibration of the Swift ultraviolet/optical telescope”. In: *MNRAS* 406 (Aug. 2010), pp. 1687–1700. DOI: 10.1111/j.1365-2966.2010.16832.x. arXiv: 1004.2448 [astro-ph.IM].
- [67] E. F. Brown, L. Bildsten and R. E. Rutledge. “Crustal Heating and Quiescent Emission from Transiently Accreting Neutron Stars”. In: *ApJL* 504 (Sept. 1998), pp. L95–L98. DOI: 10.1086/311578. eprint: astro-ph/9807179.
- [68] R. Buccheri et al. “Search for pulsed gamma-ray emission from radio pulsars in the COS-B data”. In: *A&A* 128 (Nov. 1983), pp. 245–251.
- [69] L. Burderi et al. “Where May Ultrafast Rotating Neutron Stars Be Hidden?” In: *ApJL* 560 (Oct. 2001), pp. L71–L74. DOI: 10.1086/324220. eprint: astro-ph/0109088.
- [70] M. Burgay et al. “Parkes upper limits on the pulsed radio emission of SGR 1935+2154”. In: *The Astronomer’s Telegram* 6371 (Aug. 2014).
- [71] D. N. Burrows et al. “The Swift X-Ray Telescope”. In: 120 (Oct. 2005), pp. 165–195. DOI: 10.1007/s11214-005-5097-2. eprint: astro-ph/0508071.
- [72] A. Camero et al. “Quiescent state and outburst evolution of SGR 0501+4516”. In: *MNRAS* 438 (Mar. 2014), pp. 3291–3298. DOI: 10.1093/mnras/stt2432. arXiv: 1312.4305 [astro-ph.HE].

- [73] A. Camero-Arranz et al. “The extended X-ray emission around RRAT J1819-1458”. In: *MNRAS* 429 (Mar. 2013), pp. 2493–2499. DOI: 10.1093/mnras/sts531. arXiv: 1211.7340 [astro-ph.HE].
- [74] F. Camilo et al. “1E 1547.0-5408: A Radio-emitting Magnetar with a Rotation Period of 2 Seconds”. In: *ApJL* 666 (Sept. 2007), pp. L93–L96. DOI: 10.1086/521826. arXiv: 0708.0002.
- [75] F. Camilo et al. “Radio Disappearance of the Magnetar XTE J1810-197 and Continued X-ray Timing”. In: *ApJ* 820, 110 (Apr. 2016), p. 110. DOI: 10.3847/0004-637X/820/2/110. arXiv: 1603.02170 [astro-ph.SR].
- [76] F. Camilo et al. “Transient pulsed radio emission from a magnetar”. In: *Nature* 442 (Aug. 2006), pp. 892–895. DOI: 10.1038/nature04986. eprint: astro-ph/0605429.
- [77] S. Campana. “Linking Burst-Only X-Ray Binary Sources to Faint X-Ray Transients”. In: *ApJ* 699 (July 2009), pp. 1144–1152. DOI: 10.1088/0004-637X/699/2/1144. arXiv: 0905.0607 [astro-ph.HE].
- [78] S. Campana et al. “Indirect Evidence of an Active Radio Pulsar in the Quiescent State of the Transient Millisecond Pulsar SAX J1808.4-3658”. In: *ApJL* 614 (Oct. 2004), pp. L49–L52. DOI: 10.1086/425495. eprint: astro-ph/0408584.
- [79] S. Campana et al. “Pre-discovery observations of SGR 1935+2154 in Swift archival data.” In: *GRB Coordinates Network* 16535 (2014).
- [80] S. Campana et al. “Radio pulsar and accretion regimes of rapidly rotating magnetic neutron stars in early-type eccentric binaries.” In: *A&A* 297 (May 1995), p. 385. eprint: astro-ph/9411064.
- [81] S. Campana et al. “The neutron stars of Soft X-ray Transients”. In: *A&ARv.* 8 (1998), pp. 279–316. DOI: 10.1007/s001590050012. eprint: astro-ph/9805079.
- [82] C. R. Canizares et al. “The Chandra High-Energy Transmission Grating: Design, Fabrication, Ground Calibration, and 5 Years in Flight”. In: 117 (Oct. 2005), pp. 1144–1171. DOI: 10.1086/432898. eprint: astro-ph/0507035.
- [83] P. A. Caraveo. “Gamma-Ray Pulsar Revolution”. In: *Annu. Rev. Astro. Astrophys.* 52 (Aug. 2014), pp. 211–250. DOI: 10.1146/annurev-astro-081913-035948. arXiv: 1312.2913 [astro-ph.HE].
- [84] C. Carter et al. “ChaRT: The Chandra Ray Tracer”. In: *Astronomical Data Analysis Software and Systems XII*. Ed. by H. E. Payne, R. I. Jedrzejewski and R. N. Hook. Vol. 295. Astronomical Society of the Pacific Conference Series. 2003, p. 477.
- [85] L. M. Carter, J. R. Dickel and D. J. Bomans. “Expansion of the Supernova Remnant RCW 103”. In: 109 (Sept. 1997), pp. 990–997. DOI: 10.1086/133971.

- [86] J. L. Caswell et al. “Neutral hydrogen absorption measurements yielding kinematic distances for 42 continuum sources in the galactic plane”. In: *A&A* 45 (Dec. 1975), pp. 239–258.
- [87] J. Chadwick. “Possible Existence of a Neutron”. In: *Nature* 129 (Feb. 1932), p. 312. DOI: 10.1038/129312a0.
- [88] D. Chakrabarty. “High-Speed Optical Photometry of the Ultracompact X-Ray Binary 4U 1626-67”. In: *ApJ* 492 (Jan. 1998), pp. 342–351. DOI: 10.1086/305035. eprint: astro-ph/9706049.
- [89] P. Chatterjee, L. Hernquist and R. Narayan. “An Accretion Model for Anomalous X-Ray Pulsars”. In: *ApJ* 534 (May 2000), pp. 373–379. DOI: 10.1086/308748. eprint: astro-ph/9912137.
- [90] K. S. Cheng, C. Ho and M. Ruderman. “Energetic radiation from rapidly spinning pulsars. I - Outer magnetosphere gaps. II - VELA and Crab”. In: *ApJ* 300 (Jan. 1986), pp. 500–539. DOI: 10.1086/163829.
- [91] R. A. Chevalier. “Supernova Remnants in Molecular Clouds”. In: *ApJ* 511 (Feb. 1999), pp. 798–811. DOI: 10.1086/306710. eprint: astro-ph/9805315.
- [92] T. L. Cline et al. “Precise source location of the anomalous 1979 March 5 gamma-ray transient”. In: *ApJL* 255 (Apr. 1982), pp. L45–L48. DOI: 10.1086/183766.
- [93] A. C. Collazzi et al. “The Five Year Fermi/GBM Magnetar Burst Catalog”. In: *ApJS* 218, 11 (May 2015), p. 11. DOI: 10.1088/0067-0049/218/1/11. arXiv: 1503.04152 [astro-ph.HE].
- [94] M. Colpi et al. “Charting the Temperature of the Hot Neutron Star in a Soft X-Ray Transient”. In: *ApJL* 548 (Feb. 2001), pp. L175–L178. DOI: 10.1086/319107. eprint: astro-ph/0010572.
- [95] I. Contopoulos, C. Kalapotharakos and D. Kazanas. “A New Standard Pulsar Magnetosphere”. In: *ApJ* 781, 46 (Jan. 2014), p. 46. DOI: 10.1088/0004-637X/781/1/46. arXiv: 1310.4931 [astro-ph.HE].
- [96] F. Coti Zelati et al. “Engulfing a radio pulsar: the case of PSR J1023+0038”. In: *MNRAS* 444 (Oct. 2014), pp. 1783–1792. DOI: 10.1093/mnras/stu1552. arXiv: 1409.0427 [astro-ph.HE].
- [97] F. Coti Zelati et al. “The X-ray outburst of the Galactic Centre magnetar SGR J1745-2900 during the first 1.5 year”. In: *MNRAS* 449 (May 2015), pp. 2685–2699. DOI: 10.1093/mnras/stv480. arXiv: 1503.01307 [astro-ph.HE].
- [98] T. J.-L. Courvoisier et al. “The INTEGRAL Science Data Centre (ISDC)”. In: *A&A* 411 (Nov. 2003), pp. L53–L57. DOI: 10.1051/0004-6361:20031172. eprint: astro-ph/0308047.
- [99] S. Covino et al. “REM: a fully robotic telescope for GRB observations”. In: *Ground-based Instrumentation for Astronomy*. Ed. by A. F. M. Moorwood and M. Iye. Vol. 5492. Sept. 2004, pp. 1613–1622. DOI: 10.1117/12.551532.

- [100] A. N. Cox. *Allen's astrophysical quantities*. 2000.
- [101] J. R. Cummings and S. Campana. "SGR 1935+2154 Swift-BAT archival data search". In: *The Astronomer's Telegram* 6299 (July 2014).
- [102] A. D'Ai et al. "BAT trigger 700791 (the possible GRB 160622A) is 2E 1613.5-5053, the central source in SNR RCW103". In: *The Astronomer's Telegram* 9180 (June 2016).
- [103] S. Dall'Osso et al. "The Glitches of the Anomalous X-Ray Pulsar 1RXS J170849.0-400910". In: *ApJ* 599 (Dec. 2003), pp. 485–497. DOI: 10.1086/379213.
- [104] N. D'Amico et al. "An Eclipsing Millisecond Pulsar with a Possible Main-Sequence Companion in NGC 6397". In: *ApJL* 561 (Nov. 2001), pp. L89–L92. DOI: 10.1086/324562. eprint: astro-ph/0108250.
- [105] C. R. D'Angelo and H. C. Spruit. "Episodic accretion on to strongly magnetic stars". In: *MNRAS* 406 (Aug. 2010), pp. 1208–1219. DOI: 10.1111/j.1365-2966.2010.16749.x. arXiv: 1001.1742 [astro-ph.SR].
- [106] J. K. Daugherty and A. K. Harding. "Gamma ray pulsars: Extended polar CAP cascades from nearly aligned rotators." In: *A&AS* 120 (Nov. 1996), pp. 107–110.
- [107] P. D'Avanzo et al. "The optical counterpart of IGR J00291+5934 in quiescence". In: *A&A* 472 (Sept. 2007), pp. 881–885. DOI: 10.1051/0004-6361:20077395. arXiv: 0707.3037.
- [108] K. Davidson and J. P. Ostriker. "Neutron-Star Accretion in a Stellar Wind: Model for a Pulsed X-Ray Source". In: *ApJ* 179 (Jan. 1973), pp. 585–598. DOI: 10.1086/151897.
- [109] B. Davies et al. "The Progenitor Mass of the Magnetar SGR1900+14". In: *ApJ* 707 (Dec. 2009), pp. 844–851. DOI: 10.1088/0004-637X/707/1/844. arXiv: 0910.4859 [astro-ph.SR].
- [110] J. E. Davis. "Event Pileup in Charge-coupled Devices". In: *ApJ* 562 (Nov. 2001), pp. 575–582. DOI: 10.1086/323488.
- [111] A. De Luca and S. Molendi. "The 2-8 keV cosmic X-ray background spectrum as observed with XMM-Newton". In: *A&A* 419 (June 2004), pp. 837–848. DOI: 10.1051/0004-6361:20034421. eprint: astro-ph/0311538.
- [112] A. De Luca et al. "A Long-Period, Violently Variable X-ray Source in a Young Supernova Remnant". In: *Science* 313 (Aug. 2006), pp. 814–817. DOI: 10.1126/science.1129185. eprint: astro-ph/0607173.
- [113] A. De Luca et al. "Deep Infrared Observations of the Puzzling Central X-Ray Source in RCW 103". In: *ApJ* 682, 1185-1194 (Aug. 2008), pp. 1185–1194. DOI: 10.1086/588600. arXiv: 0803.2885.
- [114] B. De Marco et al. "The evolution of the disc variability along the hard state of the black hole transient GX 339-4". In: *MNRAS* 454 (Dec. 2015), pp. 2360–2371. DOI: 10.1093/mnras/stv1990. arXiv: 1509.00043 [astro-ph.HE].

- [115] D. de Martino et al. “Multiwavelength observations of the transitional millisecond pulsar binary XSS J12270-4859”. In: *MNRAS* 454 (Dec. 2015), pp. 2190–2198. DOI: 10.1093/mnras/stv2109.
- [116] D. de Martino et al. “The intriguing nature of the high-energy gamma ray source XSS J12270-4859”. In: *A&A* 515, A25 (June 2010), A25. DOI: 10.1051/0004-6361/200913802. arXiv: 1002.3740 [astro-ph.HE].
- [117] D. de Martino et al. “X-ray follow-ups of XSS J12270-4859: a low-mass X-ray binary with gamma-ray Fermi-LAT association”. In: *A&A* 550, A89 (Feb. 2013), A89. DOI: 10.1051/0004-6361/201220393. arXiv: 1212.1615 [astro-ph.HE].
- [118] N. Degenaar et al. “A four-year XMM-Newton/Chandra monitoring campaign of the Galactic centre: analysing the X-ray transients”. In: *A&A* 545, A49 (Sept. 2012), A49. DOI: 10.1051/0004-6361/201219470. arXiv: 1204.6043 [astro-ph.HE].
- [119] N. Degenaar et al. “The Swift X-ray monitoring campaign of the center of the Milky Way”. In: *Journal of High Energy Astrophysics* 7 (Sept. 2015), pp. 137–147. DOI: 10.1016/j.jheap.2015.03.005. arXiv: 1503.07524 [astro-ph.HE].
- [120] A. T. Deller et al. “A Parallax Distance and Mass Estimate for the Transitional Millisecond Pulsar System J1023+0038”. In: *ApJL* 756, L25 (Sept. 2012), p. L25. DOI: 10.1088/2041-8205/756/2/L25. arXiv: 1207.5670 [astro-ph.SR].
- [121] A. T. Deller et al. “Radio Imaging Observations of PSR J1023+0038 in an LMXB State”. In: *ApJ* 809, 13 (Aug. 2015), p. 13. DOI: 10.1088/0004-637X/809/1/13. arXiv: 1412.5155 [astro-ph.SR].
- [122] C. J. Deloye et al. “Optical observations of SAX J1808.4-3658 during quiescence”. In: *MNRAS* 391 (Dec. 2008), pp. 1619–1628. DOI: 10.1111/j.1365-2966.2008.14021.x. arXiv: 0810.0489.
- [123] J. Dexter and R. M. O’Leary. “The Peculiar Pulsar Population of the Central Parsec”. In: *ApJL* 783, L7 (Mar. 2014), p. L7. DOI: 10.1088/2041-8205/783/1/L7. arXiv: 1310.7022 [astro-ph.GA].
- [124] V. S. Dhillon et al. “High-speed, multicolour optical photometry of the anomalous X-ray pulsar 4U 0142+61 with ULTRACAM”. In: *MNRAS* 363 (Oct. 2005), pp. 609–614. DOI: 10.1111/j.1365-2966.2005.09465.x. eprint: astro-ph/0508039.
- [125] V. S. Dhillon et al. “Optical pulsations from the anomalous X-ray pulsar 1E1048.1-5937”. In: *MNRAS* 394 (Mar. 2009), pp. L112–L116. DOI: 10.1111/j.1745-3933.2009.00623.x. arXiv: 0901.1559 [astro-ph.HE].
- [126] V. S. Dhillon et al. “The first observation of optical pulsations from a soft gamma repeater: SGR 0501+4516”. In: *MNRAS* 416 (Sept. 2011), pp. L16–L20. DOI: 10.1111/j.1745-3933.2011.01088.x. arXiv: 1106.1355 [astro-ph.SR].

- [127] M. Díaz Trigo et al. “Spectral changes during dipping in low-mass X-ray binaries due to highly-ionized absorbers”. In: *A&A* 445 (Jan. 2006), pp. 179–195. DOI: 10.1051/0004-6361:20053586. eprint: astro-ph/0509342.
- [128] R. Dib and V. M. Kaspi. “16 yr of RXTE Monitoring of Five Anomalous X-Ray Pulsars”. In: *ApJ* 784, 37 (Mar. 2014), p. 37. DOI: 10.1088/0004-637X/784/1/37. arXiv: 1401.3085 [astro-ph.HE].
- [129] R. C. Duncan and C. Thompson. “Formation of very strongly magnetized neutron stars - Implications for gamma-ray bursts”. In: *ApJL* 392 (June 1992), pp. L9–L13. DOI: 10.1086/186413.
- [130] R. Eatough et al. “On-going radio observations of PSR J1745-2900 at Effelsberg, Nancay, and Jodrell Bank: flux density estimates, polarisation properties, spin-down measurement, and the highest dispersion measure measured.” In: *The Astronomer’s Telegram* 5058 (May 2013).
- [131] R. P. Eatough et al. “A strong magnetic field around the supermassive black hole at the centre of the Galaxy”. In: *Nature* 501 (Sept. 2013), pp. 391–394. DOI: 10.1038/nature12499. arXiv: 1308.3147 [astro-ph.GA].
- [132] K. Y. Ekşi and M. A. Alpar. “Disks Surviving the Radiation Pressure of Radio Pulsars”. In: *ApJ* 620 (Feb. 2005), pp. 390–397. DOI: 10.1086/425959. eprint: astro-ph/0409408.
- [133] R. F. Elsner and F. K. Lamb. “Accretion by magnetic neutron stars. I - Magnetospheric structure and stability”. In: *ApJ* 215 (Aug. 1977), pp. 897–913. DOI: 10.1086/155427.
- [134] P. Esposito et al. “Early X-ray and optical observations of the soft gamma-ray repeater SGR0418+5729”. In: *MNRAS* 405 (July 2010), pp. 1787–1795. DOI: 10.1111/j.1365-2966.2010.16551.x. arXiv: 1002.3506 [astro-ph.HE].
- [135] P. Esposito et al. “Swift monitoring of the central X-ray source in RCW 103”. In: *MNRAS* 418 (Nov. 2011), pp. 170–175. DOI: 10.1111/j.1365-2966.2011.19473.x. arXiv: 1107.3770 [astro-ph.HE].
- [136] P. Esposito et al. “X-ray and radio observations of the magnetar Swift J1834.9-0846 and its dust-scattering halo”. In: *MNRAS* 429 (Mar. 2013), pp. 3123–3132. DOI: 10.1093/mnras/sts569. arXiv: 1212.1079 [astro-ph.HE].
- [137] V. Esposito et al. “INTEGRAL observations of Swift J174540.7-290015”. In: *The Astronomer’s Telegram* 8684 (Feb. 2016).
- [138] P. A. Evans et al. “Methods and results of an automatic analysis of a complete sample of Swift-XRT observations of GRBs”. In: *MNRAS* 397 (Aug. 2009), pp. 1177–1201. DOI: 10.1111/j.1365-2966.2009.14913.x. arXiv: 0812.3662.
- [139] H. Ezuka and M. Ishida. “Iron Line Diagnostics of the Postshock Hot Plasma in Magnetic Cataclysmic Variables Observed with ASCA”. In: *ApJS* 120 (Feb. 1999), pp. 277–298. DOI: 10.1086/313181.

- [140] G. G. Fahlman and P. C. Gregory. “An X-ray pulsar in SNR G109.1-1.0”. In: *Nature* 293 (Sept. 1981), pp. 202–204. DOI: 10.1038/293202a0.
- [141] G. Fasano and A. Franceschini. “A multidimensional version of the Kolmogorov-Smirnov test”. In: *MNRAS* 225 (Mar. 1987), pp. 155–170. DOI: 10.1093/mnras/225.1.155.
- [142] C.-A. Faucher-Giguère and A. Loeb. “Pulsar-black hole binaries in the Galactic Centre”. In: *MNRAS* 415 (Aug. 2011), pp. 3951–3961. DOI: 10.1111/j.1365-2966.2011.19019.x. arXiv: 1012.0573 [astro-ph.HE].
- [143] R. Fender and T. Belloni. “Stellar-Mass Black Holes and Ultraluminous X-ray Sources”. In: *Science* 337 (Aug. 2012), p. 540. DOI: 10.1126/science.1221790. arXiv: 1208.1138 [astro-ph.HE].
- [144] R. P. Fender, T. M. Belloni and E. Gallo. “Towards a unified model for black hole X-ray binary jets”. In: *MNRAS* 355 (Dec. 2004), pp. 1105–1118. DOI: 10.1111/j.1365-2966.2004.08384.x. eprint: astro-ph/0409360.
- [145] M. Feroci et al. “A Giant Outburst from SGR 1900+14 Observed with the BeppoSAX Gamma-Ray Burst Monitor”. In: *ApJL* 515 (Apr. 1999), pp. L9–L12. DOI: 10.1086/311964. eprint: astro-ph/9902096.
- [146] L. Ferrario, D. de Martino and B. T. Gänsicke. “Magnetic White Dwarfs”. In: 191 (Oct. 2015), pp. 111–169. DOI: 10.1007/s11214-015-0152-0. arXiv: 1504.08072 [astro-ph.SR].
- [147] R. A. Fesen et al. “The Expansion Asymmetry and Age of the Cassiopeia A Supernova Remnant”. In: *ApJ* 645 (July 2006), pp. 283–292. DOI: 10.1086/504254. eprint: astro-ph/0603371.
- [148] A. Finzi and R. A. Wolf. “Possible Conversion of Rotational Energy of the Neutron Star in the Crab Nebula Into Energy of Relativistic Electrons”. In: *ApJL* 155 (Feb. 1969), p. L107. DOI: 10.1086/180312.
- [149] E. L. Fitzpatrick. “Correcting for the Effects of Interstellar Extinction”. In: 111 (Jan. 1999), pp. 63–75. DOI: 10.1086/316293. eprint: astro-ph/9809387.
- [150] E. Flowers and M. A. Ruderman. “Evolution of pulsar magnetic fields”. In: *ApJ* 215 (July 1977), pp. 302–310. DOI: 10.1086/155359.
- [151] D. R. Foight et al. “Probing X-Ray Absorption and Optical Extinction in the Interstellar Medium Using Chandra Observations of Supernova Remnants”. In: *ApJ* 826, 66 (July 2016), p. 66. DOI: 10.3847/0004-637X/826/1/66. arXiv: 1504.07274 [astro-ph.HE].
- [152] J. Frank, A. King and D. J. Raine. *Accretion Power in Astrophysics: Third Edition*. Jan. 2002, p. 398.
- [153] J. Frank, A. R. King and J.-P. Lasota. “The light curves of low-mass X-ray binaries”. In: *A&A* 178 (May 1987), pp. 137–142.

- [154] K. A. Frank, D. N. Burrows and S. Park. “Chandra Observations of SNR RCW 103”. In: *ApJ* 810, 113 (Sept. 2015), p. 113. DOI: 10 . 1088 / 0004 - 637X / 810/2/113. arXiv: 1508 . 01513 [astro-ph.HE].
- [155] E. D. Friel et al. “Metallicities of Old Open Clusters”. In: 124 (Nov. 2002), pp. 2693–2720. DOI: 10 . 1086/344161.
- [156] A. S. Fruchter, D. R. Stinebring and J. H. Taylor. “A millisecond pulsar in an eclipsing binary”. In: *Nature* 333 (May 1988), pp. 237–239. DOI: 10 . 1038 / 333237a0.
- [157] A. Fruscione et al. “CIAO: Chandra’s data analysis system”. In: *Society of Photo-Optical Instrumentation Engineers (SPIE) Conference Series*. Vol. 6270. June 2006, p. 62701V. DOI: 10 . 1117/12 . 671760.
- [158] B. M. Gaensler and P. O. Slane. “The Evolution and Structure of Pulsar Wind Nebulae”. In: *Annu. Rev. Astro. Astrophys.* 44 (Sept. 2006), pp. 17–47. DOI: 10 . 1146 / annurev . astro . 44 . 051905 . 092528. eprint: astro-ph / 0601081.
- [159] D. K. Galloway et al. “Thermonuclear (Type I) X-Ray Bursts Observed by the Rossi X-Ray Timing Explorer”. In: *ApJS* 179, 360-422 (Dec. 2008), pp. 360–422. DOI: 10 . 1086/592044. eprint: astro-ph/0608259.
- [160] M. R. Garcia et al. “New Evidence for Black Hole Event Horizons from Chandra”. In: *ApJL* 553 (May 2001), pp. L47–L50. DOI: 10 . 1086/320494. eprint: astro-ph/0012452.
- [161] G. P. Garmire et al. “1E 161348-5055”. In: 7350 (Jan. 2000).
- [162] G. P. Garmire et al. “Advanced CCD imaging spectrometer (ACIS) instrument on the Chandra X-ray Observatory”. In: *X-Ray and Gamma-Ray Telescopes and Instruments for Astronomy*. Ed. by J. E. Truemper and H. D. Tananbaum. Vol. 4851. Mar. 2003, pp. 28–44. DOI: 10 . 1117/12 . 461599.
- [163] F. P. Gavriil, V. M. Kaspi and P. M. Woods. “Magnetar-like X-ray bursts from an anomalous X-ray pulsar”. In: *Nature* 419 (Sept. 2002), pp. 142–144. DOI: 10 . 1038/nature01011. eprint: astro-ph/0209202.
- [164] N. Gehrels. “Confidence limits for small numbers of events in astrophysical data”. In: *ApJ* 303 (Apr. 1986), pp. 336–346. DOI: 10 . 1086/164079.
- [165] N. Gehrels et al. “The Swift Gamma-Ray Burst Mission”. In: *ApJ* 611 (Aug. 2004), pp. 1005–1020. DOI: 10 . 1086/422091.
- [166] R. Genzel, F. Eisenhauer and S. Gillessen. “The Galactic Center massive black hole and nuclear star cluster”. In: *Reviews of Modern Physics* 82 (Oct. 2010), pp. 3121–3195. DOI: 10 . 1103 / RevModPhys . 82 . 3121. arXiv: 1006 . 0064.

- [167] R. Genzel et al. “A study of the gas-star formation relation over cosmic time”. In: *MNRAS* 407 (Oct. 2010), pp. 2091–2108. DOI: 10.1111/j.1365-2966.2010.16969.x. arXiv: 1003.5180.
- [168] U. Geppert, D. Page and T. Zannias. “Submergence and re-diffusion of the neutron star magnetic field after the supernova”. In: *A&A* 345 (May 1999), pp. 847–854.
- [169] P. Ghosh and F. K. Lamb. “Accretion by rotating magnetic neutron stars. II - Radial and vertical structure of the transition zone in disk accretion”. In: *ApJ* 232 (Aug. 1979), pp. 259–276. DOI: 10.1086/157285.
- [170] P. Ghosh and F. K. Lamb. “Disk accretion by magnetic neutron stars”. In: *ApJL* 223 (July 1978), pp. L83–L87. DOI: 10.1086/182734.
- [171] P. Ghosh, C. J. Pethick and F. K. Lamb. “Accretion by rotating magnetic neutron stars. I - Flow of matter inside the magnetosphere and its implications for spin-up and spin-down of the star”. In: *ApJ* 217 (Oct. 1977), pp. 578–596. DOI: 10.1086/155606.
- [172] R. Giacconi. “Nobel Lecture: The dawn of x-ray astronomy”. In: *Reviews of Modern Physics* 75 (Aug. 2003), pp. 995–1010. DOI: 10.1103/RevModPhys.75.995.
- [173] R. Giacconi et al. “Discovery of Periodic X-Ray Pulsations in Centaurus X-3 from UHURU”. In: *ApJL* 167 (July 1971), p. L67. DOI: 10.1086/180762.
- [174] R. Giacconi et al. “Evidence for x Rays From Sources Outside the Solar System”. In: *Physical Review Letters* 9 (Dec. 1962), pp. 439–443. DOI: 10.1103/PhysRevLett.9.439.
- [175] S. Gillessen et al. “The distance to the Galactic Center”. In: *Advancing the Physics of Cosmic Distances*. Ed. by R. de Grijs. Vol. 289. IAU Symposium. Feb. 2013, pp. 29–35. DOI: 10.1017/S1743921312021060.
- [176] V. Girish and K. P. Singh. “X-ray observations of INTEGRAL discovered cataclysmic variable IGR J17195-4100”. In: *MNRAS* 427 (Nov. 2012), pp. 458–467. DOI: 10.1111/j.1365-2966.2012.21916.x. arXiv: 1208.3425 [astro-ph.HE].
- [177] T. Gold. “Rotating Neutron Stars and the Nature of Pulsars”. In: *Nature* 221 (Jan. 1969), pp. 25–27. DOI: 10.1038/221025a0.
- [178] T. Gold. “Rotating Neutron Stars as the Origin of the Pulsating Radio Sources”. In: *Nature* 218 (May 1968), pp. 731–732. DOI: 10.1038/218731a0.
- [179] P. Goldreich and W. H. Julian. “Pulsar Electrodynamics”. In: *ApJ* 157 (Aug. 1969), p. 869. DOI: 10.1086/150119.
- [180] S. Golenetskii et al. “IPN Triangulation of a bright burst from SGR 1935+2154.” In: *GRB Coordinates Network* 17699 (2015).

- [181] E. V. Gotthelf and J. P. Halpern. “The anatomy of a magnetar: XMM monitoring of the transient anomalous X-ray pulsar XTE J1810 197”. In: *AP&SS* 308 (Apr. 2007), pp. 79–87. DOI: 10.1007/s10509-007-9327-9. eprint: astro-ph/0608473.
- [182] E. V. Gotthelf, J. P. Halpern and J. Alford. “The Spin-down of PSR J0821-4300 and PSR J1210-5226: Confirmation of Central Compact Objects as Anti-magnetars”. In: *ApJ* 765, 58 (Mar. 2013), p. 58. DOI: 10.1088/0004-637X/765/1/58. arXiv: 1301.2717 [astro-ph.HE].
- [183] E. V. Gotthelf, J. P. Halpern and F. D. Seward. “Discovery of a 105 ms X-Ray Pulsar in Kesteven 79: On the Nature of Compact Central Objects in Supernova Remnants”. In: *ApJ* 627 (July 2005), pp. 390–396. DOI: 10.1086/430300. eprint: astro-ph/0503424.
- [184] E. V. Gotthelf, R. Petre and U. Hwang. “The Nature of the Radio-quiet Compact X-Ray Source in Supernova Remnant RCW 103”. In: *ApJL* 487 (Oct. 1997), pp. L175–L179. DOI: 10.1086/310900. eprint: astro-ph/9707035.
- [185] E. V. Gotthelf et al. “Imaging X-Ray, Optical, and Infrared Observations of the Transient Anomalous X-Ray Pulsar XTE J1810-197”. In: *ApJ* 605 (Apr. 2004), pp. 368–377. DOI: 10.1086/382232. eprint: astro-ph/0309745.
- [186] D. Götz et al. “Long term hard X-ray variability of the anomalous X-ray pulsar 1RXS J170849.0-400910 discovered with INTEGRAL”. In: *A&A* 475 (Nov. 2007), pp. 317–321. DOI: 10.1051/0004-6361:20078291. arXiv: 0709.3712.
- [187] D. Götz et al. “Spectral evolution of weak bursts from SGR 1806-20 observed with INTEGRAL”. In: *A&A* 417 (Apr. 2004), pp. L45–L48. DOI: 10.1051/0004-6361:20040080. eprint: astro-ph/0403018.
- [188] C. Granet et al. “The designing, manufacturing, and testing of a dual-band feed system for the parkes radio telescope”. In: *IEEE Antennas and Propagation Magazine* 47 (June 2005), pp. 13–19. DOI: 10.1109/MAP.2005.1532537.
- [189] J. Greiner et al. “GROND a 7-Channel Imager”. In: 120 (Apr. 2008), pp. 405–424. DOI: 10.1086/587032. arXiv: 0801.4801.
- [190] I. A. Grenier and A. K. Harding. “Gamma-ray pulsars: A gold mine”. In: *Comptes Rendus Physique* 16 (Aug. 2015), pp. 641–660. DOI: 10.1016/j.crhy.2015.08.013. arXiv: 1509.08823 [astro-ph.HE].
- [191] J. E. Grove et al. “Evidence for Shock Acceleration in the Binary Pulsar System PSR B1259-63”. In: *ApJL* 447 (July 1995), p. L113. DOI: 10.1086/309568.
- [192] C. Guidorzi et al. “Comparative study of the two large flares from SGR1900+14 with the BeppoSAX Gamma-Ray Burst Monitor”. In: *A&A* 416 (Mar. 2004), pp. 297–310. DOI: 10.1051/0004-6361:20034511. eprint: astro-ph/0312062.

- [193] F. Haberl, P. Eger and W. Pietsch. “XMM-Newton observations of the Small Magellanic Cloud: Be/X-ray binary pulsars active between October 2006 and June 2007”. In: *A&A* 489 (Oct. 2008), pp. 327–348. DOI: 10.1051/0004-6361:200810100. arXiv: 0806.4132.
- [194] F. Haberl et al. “A phase-dependent absorption line in the spectrum of the X-ray pulsar RX J0720.4-3125”. In: *A&A* 419 (June 2004), pp. 1077–1085. DOI: 10.1051/0004-6361:20034129. eprint: astro-ph/0312413.
- [195] F. Haberl et al. “Evidence for precession of the isolated neutron star <ASTROBJ>RX J0720.4-3125</ASTROBJ>”. In: *A&A* 451 (May 2006), pp. L17–L21. DOI: 10.1051/0004-6361:20065093. eprint: astro-ph/0603724.
- [196] F. Haberl et al. “RXJ0720.4-3125: strong evidence for an isolated pulsating neutron star.” In: *A&A* 326 (Oct. 1997), pp. 662–668.
- [197] J. P. Halpern and E. V. Gotthelf. “Spin-Down Measurement of PSR J1852+0040 in Kesteven 79: Central Compact Objects as Anti-Magnetars”. In: *ApJ* 709 (Jan. 2010), pp. 436–446. DOI: 10.1088/0004-637X/709/1/436. arXiv: 0911.0093 [astro-ph.HE].
- [198] J. P. Halpern and E. V. Gotthelf. “The Fading of Transient Anomalous X-Ray Pulsar XTE J1810-197”. In: *ApJ* 618 (Jan. 2005), pp. 874–882. DOI: 10.1086/426130. eprint: astro-ph/0409604.
- [199] J. P. Halpern and S. S. Holt. “Discovery of soft X-ray pulsations from the gamma-ray source Geminga”. In: *Nature* 357 (May 1992), pp. 222–224. DOI: 10.1038/357222a0.
- [200] J. P. Halpern and J. R. Thorstensen. “Optical Studies of 13 Hard X-Ray Selected Cataclysmic Binaries from the Swift-BAT Survey”. In: 150, 170 (Dec. 2015), p. 170. DOI: 10.1088/0004-6256/150/6/170. arXiv: 1510.00703 [astro-ph.HE].
- [201] J. P. Halpern et al. “3EG J2016+3657: Confirming an EGRET Blazar behind the Galactic Plane”. In: *ApJ* 551 (Apr. 2001), pp. 1016–1023. DOI: 10.1086/320238. eprint: astro-ph/0012508.
- [202] J. P. Halpern et al. “Discovery of Radio Emission from the Transient Anomalous X-Ray Pulsar XTE J1810-197”. In: *ApJL* 632 (Oct. 2005), pp. L29–L32. DOI: 10.1086/497537. eprint: astro-ph/0508534.
- [203] J. P. Halpern et al. “Optical Observations of the Binary MSP J1023+0038 in a New Accreting State”. In: *The Astronomer’s Telegram* 5514 (Oct. 2013).
- [204] J. P. Halpern et al. “Outburst of the 2 s Anomalous X-Ray Pulsar 1E 1547.0-5408”. In: *ApJ* 676, 1178-1183 (Apr. 2008), pp. 1178–1183. DOI: 10.1086/527293. arXiv: 0711.3780.

- [205] J. P. Halpern et al. “X-Ray Timing of PSR J1852+0040 in Kesteven 79: Evidence of Neutron Stars Weakly Magnetized at Birth”. In: *ApJ* 665 (Aug. 2007), pp. 1304–1310. DOI: 10.1086/519557. arXiv: 0705.0978.
- [206] J.-M. Hameury, A. R. King and J.-P. Lasota. “Accretion flows in the non-synchronous magnetic cataclysmic variables”. In: *MNRAS* 218 (Feb. 1986), pp. 695–710. DOI: 10.1093/mnras/218.4.695.
- [207] A. K. Harding and D. Lai. “Physics of strongly magnetized neutron stars”. In: *Reports on Progress in Physics* 69 (Sept. 2006), pp. 2631–2708. DOI: 10.1088/0034-4885/69/9/R03. eprint: astro-ph/0606674.
- [208] F. A. Harrison et al. “The Nuclear Spectroscopic Telescope Array (NuSTAR) High-energy X-Ray Mission”. In: *ApJ* 770, 103 (June 2013), p. 103. DOI: 10.1088/0004-637X/770/2/103. arXiv: 1301.7307 [astro-ph.IM].
- [209] V. Heard and R. S. Warwick. “XMM-Newton observations of the Galactic Centre Region - II. The soft-thermal emission”. In: *MNRAS* 434 (Sept. 2013), pp. 1339–1354. DOI: 10.1093/mnras/stt1102. arXiv: 1306.4186 [astro-ph.HE].
- [210] A. Heger et al. “How Massive Single Stars End Their Life”. In: *ApJ* 591 (July 2003), pp. 288–300. DOI: 10.1086/375341. eprint: astro-ph/0212469.
- [211] C. O. Heinke et al. “A Hydrogen Atmosphere Spectral Model Applied to the Neutron Star X7 in the Globular Cluster 47 Tucanae”. In: *ApJ* 644 (June 2006), pp. 1090–1103. DOI: 10.1086/503701. eprint: astro-ph/0506563.
- [212] D. J. Helfand et al. “VLBA Measurement of the Transverse Velocity of the Magnetar XTE J1810-197”. In: *ApJ* 662 (June 2007), pp. 1198–1203. DOI: 10.1086/518028. eprint: astro-ph/0703336.
- [213] C. Hellier. “The Magnetospheric Boundary in Cataclysmic Variables”. In: *European Physical Journal Web of Conferences*. Vol. 64. European Physical Journal Web of Conferences. Jan. 2014, p. 07001. DOI: 10.1051/epjconf/20136407001. arXiv: 1312.4779 [astro-ph.SR].
- [214] J. W. T. Hessels et al. “A Radio Pulsar Spinning at 716 Hz”. In: *Science* 311 (Mar. 2006), pp. 1901–1904. DOI: 10.1126/science.1123430. eprint: astro-ph/0601337.
- [215] A. Hewish et al. “Observation of a Rapidly Pulsating Radio Source”. In: *Nature* 217 (Feb. 1968), pp. 709–713. DOI: 10.1038/217709a0.
- [216] J. S. Heyl and L. Hernquist. “A quantum electrodynamics model for non-thermal emission from soft gamma repeaters and anomalous X-ray pulsars”. In: *MNRAS* 362 (Sept. 2005), pp. 777–783. DOI: 10.1111/j.1365-2966.2005.09338.x. eprint: astro-ph/0502349.

- [217] A. B. Hill et al. “The bright unidentified γ -ray source 1FGL J1227.9-4852: can it be associated with a low-mass X-ray binary?” In: *MNRAS* 415 (July 2011), pp. 235–243. DOI: 10.1111/j.1365-2966.2011.18692.x. arXiv: 1103.2637 [astro-ph.HE].
- [218] W. C. G. Ho and C. O. Heinke. “A neutron star with a carbon atmosphere in the Cassiopeia A supernova remnant”. In: *Nature* 462 (Nov. 2009), pp. 71–73. DOI: 10.1038/nature08525. arXiv: 0911.0672 [astro-ph.HE].
- [219] M. M. Hohle et al. “Narrow absorption features in the co-added XMM-Newton RGS spectra of isolated neutron stars”. In: *MNRAS* 419 (Jan. 2012), pp. 1525–1536. DOI: 10.1111/j.1365-2966.2011.19809.x. arXiv: 1109.2506 [astro-ph.SR].
- [220] M. M. Hohle et al. “Spectral and temporal variations of the isolated neutron star RX J0720.4-3125: new XMM-Newton observations”. In: *A&A* 498 (May 2009), pp. 811–820. DOI: 10.1051/0004-6361/200810812. arXiv: 0810.5319.
- [221] M. M. Hohle et al. “The continued spectral and temporal evolution of RX J0720.4-3125”. In: *MNRAS* 423 (June 2012), pp. 1194–1199. DOI: 10.1111/j.1365-2966.2012.20946.x. arXiv: 1203.3708 [astro-ph.HE].
- [222] L. Homer et al. “The optical counterpart to SAX J1808.4-3658: observations in quiescence”. In: *MNRAS* 325 (Aug. 2001), pp. 1471–1476. DOI: 10.1046/j.1365-8711.2001.04567.x. eprint: astro-ph/0102075.
- [223] L. Homer et al. “XMM-Newton and Optical Follow-up Observations of SDSS J093249.57+472523.0 and SDSS J102347.67+003841.2”. In: 131 (Jan. 2006), pp. 562–570. DOI: 10.1086/498346. eprint: astro-ph/0509802.
- [224] C. Hopman. “Binary Dynamics Near a Massive Black Hole”. In: *ApJ* 700 (Aug. 2009), pp. 1933–1951. DOI: 10.1088/0004-637x/700/2/1933. arXiv: 0906.0374 [astro-ph.CO].
- [225] L. G. Hou, J. L. Han and W. B. Shi. “The spiral structure of our Milky Way Galaxy”. In: *A&A* 499 (May 2009), pp. 473–482. DOI: 10.1051/0004-6361/200809692. arXiv: 0903.0721.
- [226] K. Hurley et al. “A giant periodic flare from the soft γ -ray repeater SGR1900+14”. In: *Nature* 397 (Jan. 1999), pp. 41–43. DOI: 10.1038/16199. eprint: astro-ph/9811443.
- [227] K. Hurley et al. “An exceptionally bright flare from SGR 1806-20 and the origins of short-duration γ -ray bursts”. In: *Nature* 434 (Apr. 2005), pp. 1098–1103. DOI: 10.1038/nature03519. eprint: astro-ph/0502329.
- [228] M. N. Iacolina et al. “Search for pulsations at high radio frequencies from accreting millisecond X-ray pulsars in quiescence”. In: *A&A* 519, A13 (Sept. 2010), A13. DOI: 10.1051/0004-6361/201014025. arXiv: 1006.4260 [astro-ph.HE].

- [229] A. I. Ibrahim et al. “Discovery of a Transient Magnetar: XTE J1810-197”. In: *ApJL* 609 (July 2004), pp. L21–L24. DOI: 10.1086/422636. eprint: astro-ph/0310665.
- [230] A. F. Illarionov and R. A. Sunyaev. “Why the Number of Galactic X-ray Stars Is so Small?” In: *A&A* 39 (Feb. 1975), p. 185.
- [231] U. S. Inan et al. “Ionization of the lower ionosphere by γ -rays from a Magnetar: Detection of a low energy (3-10 keV) component”. In: 26 (1999), pp. 3357–3360. DOI: 10.1029/1999GL010690.
- [232] G. Israel et al. “The Pulse-Phase-dependent Spectrum of the Anomalous X-Ray Pulsar 1RXS J170849-400910”. In: *ApJL* 560 (Oct. 2001), pp. L65–L69. DOI: 10.1086/324169. eprint: astro-ph/0108506.
- [233] G. L. Israel and L. Stella. “A New Technique for the Detection of Periodic Signals in “Colored” Power Spectra”. In: *ApJ* 468 (Sept. 1996), p. 369. DOI: 10.1086/177697. eprint: astro-ph/9603038.
- [234] G. L. Israel et al. “A Swift Gaze into the 2006 March 29 Burst Forest of SGR 1900+14”. In: *ApJ* 685, 1114-1128 (Oct. 2008), pp. 1114–1128. DOI: 10.1086/590486. arXiv: 0805.3919.
- [235] G. L. Israel et al. “Chandra discovery of 3.2s X-ray pulsations from SGR 1935+2154”. In: *The Astronomer’s Telegram* 6370 (Aug. 2014).
- [236] G. L. Israel et al. “The discovery, monitoring and environment of SGR J1935+2154”. In: *MNRAS* 457 (Apr. 2016), pp. 3448–3456. DOI: 10.1093/mnras/stw008. arXiv: 1601.00347 [astro-ph.HE].
- [237] F. Jansen et al. “XMM-Newton observatory. I. The spacecraft and operations”. In: *A&A* 365 (Jan. 2001), pp. L1–L6. DOI: 10.1051/0004-6361:20000036.
- [238] A. M. Juett et al. “High-Resolution X-Ray Spectroscopy of the Interstellar Medium. II. Neon and Iron Absorption Edges”. In: *ApJ* 648 (Sept. 2006), pp. 1066–1078. DOI: 10.1086/506189. eprint: astro-ph/0605674.
- [239] D. L. Kaplan et al. “The Nearby Neutron Star RX J0720.4-3125 from Radio to X-Rays”. In: *ApJ* 590 (June 2003), pp. 1008–1019. DOI: 10.1086/375052. eprint: astro-ph/0303126.
- [240] E. Kara et al. “Gamma-Ray Emission from Two Blazars Behind the Galactic Plane: B2013+370 and B2023+336”. In: *ApJ* 746, 159 (Feb. 2012), p. 159. DOI: 10.1088/0004-637X/746/2/159. arXiv: 1112.3312 [astro-ph.HE].
- [241] V. M. Kaspi and M. Kramer. “Radio Pulsars: The Neutron Star Population Fundamental Physics”. In: *ArXiv e-prints* (Feb. 2016). arXiv: 1602.07738 [astro-ph.HE].
- [242] V. M. Kaspi et al. “A Major Soft Gamma Repeater-like Outburst and Rotation Glitch in the No-longer-so-anomalous X-Ray Pulsar 1E 2259+586”. In: *ApJL* 588 (May 2003), pp. L93–L96. DOI: 10.1086/375683. eprint: astro-ph/0304205.

- [243] V. M. Kaspi et al. “Timing and Flux Evolution of the Galactic Center Magnetar SGR J1745-2900”. In: *ApJ* 786, 84 (May 2014), p. 84. DOI: 10.1088/0004-637X/786/2/84. arXiv: 1403.5344 [astro-ph.HE].
- [244] J. I. Katz, H. A. Toole and S. H. Unruh. “Yet another model of soft gamma repeaters”. In: *ApJ* 437 (Dec. 1994), pp. 727–732. DOI: 10.1086/175034. eprint: astro-ph/9404039.
- [245] J. A. Kennea et al. “Swift detection of a third burst from SGR J1745-29”. In: *The Astronomer’s Telegram* 5254 (Aug. 2013).
- [246] J. A. Kennea et al. “Swift Discovery of a New Soft Gamma Repeater, SGR J1745-29, near Sagittarius A*”. In: *ApJL* 770, L24 (June 2013), p. L24. DOI: 10.1088/2041-8205/770/2/L24. arXiv: 1305.2128 [astro-ph.HE].
- [247] J. A. Kennea et al. “Swift/BAT detection of a burst from SGR J1745-29”. In: *The Astronomer’s Telegram* 5124 (June 2013).
- [248] D. A. Kniffen et al. “Gamma radiation from the Crab Nebula above 35 MeV”. In: *Nature* 251 (Oct. 1974), pp. 397–399. DOI: 10.1038/251397a0.
- [249] V. I. Kondratiev et al. “New Limits on Radio Emission from X-ray Dim Isolated Neutron Stars”. In: *ApJ* 702 (Sept. 2009), pp. 692–706. DOI: 10.1088/0004-637X/702/1/692. arXiv: 0907.0054 [astro-ph.GA].
- [250] A. K. H. Kong. “Enhanced X-ray emission of the binary millisecond pulsar J1023+0038”. In: *The Astronomer’s Telegram* 5515 (Oct. 2013).
- [251] C. Kouveliotou et al. “An X-ray pulsar with a superstrong magnetic field in the soft γ -ray repeater SGR1806 - 20”. In: *Nature* 393 (May 1998), pp. 235–237. DOI: 10.1038/30410.
- [252] C. Kouveliotou et al. “Multiwavelength Observations of the Soft Gamma Repeater SGR 1900+14 during Its 2001 April Activation”. In: *ApJL* 558 (Sept. 2001), pp. L47–L50. DOI: 10.1086/323496. eprint: astro-ph/0107170.
- [253] T. Krühler et al. “The 2175 Å Dust Feature in a Gamma-Ray Burst Afterglow at Redshift 2.45”. In: *ApJ* 685, 376-383 (Sept. 2008), pp. 376–383. DOI: 10.1086/590240. arXiv: 0805.2824.
- [254] A. Kubota et al. “Evidence for a Black Hole in the X-Ray Transient GRS 1009-45”. In: 50 (Dec. 1998), pp. 667–673. DOI: 10.1093/pasj/50.6.667.
- [255] L. Kuiper et al. “Discovery of Luminous Pulsed Hard X-Ray Emission from Anomalous X-Ray Pulsars 1RXS J1708-4009, 4U 0142+61, and 1E 2259+586 by INTEGRAL and RXTE”. In: *ApJ* 645 (July 2006), pp. 556–575. DOI: 10.1086/504317. eprint: astro-ph/0603467.

- [256] L. Kuiper et al. “Temporal and Spectral Evolution in X- and γ -Rays of Magnetar 1E 1547.0-5408 since its 2008 October Outburst: The Discovery of a Transient Hard Pulsed Component after its 2009 January Outburst”. In: *ApJ* 748, 133 (Apr. 2012), p. 133. DOI: 10.1088/0004-637X/748/2/133. arXiv: 1201.5530 [astro-ph.HE].
- [257] S. R. Kulkarni et al. “X-ray detection of the eclipsing millisecond pulsar PSR1957+20”. In: *Nature* 359 (Sept. 1992), pp. 300–302. DOI: 10.1038/359300a0.
- [258] E. Kuulkers et al. “Photospheric radius expansion X-ray bursts as standard candles”. In: *A&A* 399 (Feb. 2003), pp. 663–680. DOI: 10.1051/0004-6361:20021781. eprint: astro-ph/0212028.
- [259] D. Lai. “Theory of Disk Accretion onto Magnetic Stars”. In: *European Physical Journal Web of Conferences*. Vol. 64. European Physical Journal Web of Conferences. Jan. 2014, p. 01001. DOI: 10.1051/epjconf/20136401001. arXiv: 1402.1903 [astro-ph.SR].
- [260] M. I. Large, A. E. Vaughan and B. Y. Mills. “A Pulsar Supernova Association?”. In: *Nature* 220 (Oct. 1968), pp. 340–341. DOI: 10.1038/220340a0.
- [261] J. G. Laros et al. “A new type of repetitive behavior in a high-energy transient”. In: *ApJL* 320 (Sept. 1987), pp. L111–L115. DOI: 10.1086/184985.
- [262] J. G. Laros et al. “The soft gamma-ray burst GB790107”. In: *Nature* 322 (July 1986), p. 152. DOI: 10.1038/322152a0.
- [263] J.-P. Lasota. “The disc instability model of dwarf novae and low-mass X-ray binary transients”. In: 45 (June 2001), pp. 449–508. DOI: 10.1016/S1387-6473(01)00112-9. eprint: astro-ph/0102072.
- [264] J. M. Lattimer. “The Nuclear Equation of State and Neutron Star Masses”. In: *Annual Review of Nuclear and Particle Science* 62 (Nov. 2012), pp. 485–515. DOI: 10.1146/annurev-nucl-102711-095018. arXiv: 1305.3510 [nucl-th].
- [265] D. A. Leahy. “Searches for pulsed emission - Improved determination of period and amplitude from epoch folding for sinusoidal signals”. In: *A&A* 180 (June 1987), pp. 275–277.
- [266] F. Lebrun et al. “ISGRI: The INTEGRAL Soft Gamma-Ray Imager”. In: *A&A* 411 (Nov. 2003), pp. L141–L148. DOI: 10.1051/0004-6361:20031367. eprint: astro-ph/0310362.
- [267] H. M. Lee. “Evolution of galactic nuclei with 10- M_{\odot} black holes”. In: *MNRAS* 272 (Feb. 1995), pp. 605–617. DOI: 10.1093/mnras/272.3.605. eprint: astro-ph/9409073.
- [268] L. Levin et al. “A Radio-loud Magnetar in X-ray Quiescence”. In: *ApJL* 721 (Sept. 2010), pp. L33–L37. DOI: 10.1088/2041-8205/721/1/L33. arXiv: 1007.1052 [astro-ph.HE].

- [269] K. L. Li et al. “NuSTAR Observations and Broadband Spectral Energy Distribution Modeling of the Millisecond Pulsar Binary PSR J1023+0038”. In: *ApJ* 797, 111 (Dec. 2014), p. 111. DOI: 10.1088/0004-637X/797/2/111. arXiv: 1410.4563 [astro-ph.HE].
- [270] X. Li and A. M. Beloborodov. “Plastic Damping of Alfvén Waves in Magnetar Flares and Delayed Afterglow Emission”. In: *ApJ* 815, 25 (Dec. 2015), p. 25. DOI: 10.1088/0004-637X/815/1/25. arXiv: 1505.03465 [astro-ph.HE].
- [271] X. Li, Y. Levin and A. M. Beloborodov. “Magnetar Outbursts from Avalanches of Hall Waves and Crustal Failures”. In: *ApJ* 833, 189 (Dec. 2016), p. 189. DOI: 10.3847/1538-4357/833/2/189. arXiv: 1606.04895 [astro-ph.HE].
- [272] X.-D. Li. “The Nature of the Compact X-Ray Source in Supernova Remnant RCW 103”. In: *ApJL* 666 (Sept. 2007), pp. L81–L84. DOI: 10.1086/521791. arXiv: 0708.0060.
- [273] P. S. Lii et al. “Propeller-driven outflows from an MRI disc”. In: *MNRAS* 441 (June 2014), pp. 86–100. DOI: 10.1093/mnras/stu495. arXiv: 1304.2703 [astro-ph.SR].
- [274] M. Linares. “X-Ray States of Redback Millisecond Pulsars”. In: *ApJ* 795, 72 (Nov. 2014), p. 72. DOI: 10.1088/0004-637X/795/1/72. arXiv: 1406.2384 [astro-ph.HE].
- [275] M. Linares et al. “PSR J1023+0038: phase-resolved optical spectroscopy and continued X-ray activity”. In: *The Astronomer’s Telegram* 5868 (Feb. 2014).
- [276] X. W. Liu et al. “The Extremely Long-period X-Ray Source in a Young Supernova Remnant: A Thorne-Żytkow Object Descendant?” In: *ApJ* 799, 233 (Feb. 2015), p. 233. DOI: 10.1088/0004-637X/799/2/233. arXiv: 1207.4687 [astro-ph.HE].
- [277] M. A. Livingstone et al. “The Spin-down of Swift J1822.3-1606: A New Galactic Magnetar”. In: *ApJL* 743, L38 (Dec. 2011), p. L38. DOI: 10.1088/2041-8205/743/2/L38. arXiv: 1109.5715 [astro-ph.HE].
- [278] M. Livio and R. E. Taam. “Possible models for the high-energy transient GB790107”. In: *Nature* 327 (June 1987), pp. 398–400. DOI: 10.1038/327398a0.
- [279] M. S. Longair. *High Energy Astrophysics*. Feb. 2011.
- [280] N. Lund et al. “JEM-X: The X-ray monitor aboard INTEGRAL”. In: *A&A* 411 (Nov. 2003), pp. L231–L238. DOI: 10.1051/0004-6361:20031358.
- [281] R. S. Lynch et al. “Green Bank Telescope and Swift X-Ray Telescope Observations of the Galactic Center Radio Magnetar SGR J1745-2900”. In: *ApJ* 806, 266 (June 2015), p. 266. DOI: 10.1088/0004-637X/806/2/266. arXiv: 1412.0610 [astro-ph.HE].

- [282] M. Lyutikov. “Magnetar giant flares and afterglows as relativistic magnetized explosions”. In: *MNRAS* 367 (Apr. 2006), pp. 1594–1602. DOI: 10.1111/j.1365-2966.2006.10069.x. eprint: astro-ph/0511711.
- [283] Y. Maan et al. “Search for pulsed radio emission from SWIFT J174540.7-290015”. In: *The Astronomer’s Telegram* 8729 (Feb. 2016).
- [284] Y. Maeda et al. “A Chandra Study of Sagittarius A East: A Supernova Remnant Regulating the Activity of Our Galactic Center?”. In: *ApJ* 570 (May 2002), pp. 671–687. DOI: 10.1086/339773. eprint: astro-ph/0102183.
- [285] V. M. Malofeev, D. A. Teplykh and O. I. Malov. “Detection of radio emission from the AXP 4U 0142+61”. In: *Astronomy Reports* 54 (Nov. 2010), pp. 995–999. DOI: 10.1134/S1063772910110053.
- [286] A. Martin-Carrillo et al. “The relative and absolute timing accuracy of the EPIC-pn camera on XMM-Newton, from X-ray pulsations of the Crab and other pulsars”. In: *A&A* 545, A126 (Sept. 2012), A126. DOI: 10.1051/0004-6361/201116576. arXiv: 1204.0978 [astro-ph.IM].
- [287] N. Masetti et al. “Unveiling the nature of INTEGRAL objects through optical spectroscopy. V. Identification and properties of 21 southern hard X-ray sources”. In: *A&A* 459 (Nov. 2006), pp. 21–30. DOI: 10.1051/0004-6361:20066055. eprint: astro-ph/0608394.
- [288] N. Masetti et al. “VVV near-infrared observations of the Swift J174540.7-290015 field”. In: *The Astronomer’s Telegram* 8737 (Feb. 2016).
- [289] K. O. Mason et al. “The XMM-Newton optical/UV monitor telescope”. In: *A&A* 365 (Jan. 2001), pp. L36–L44. DOI: 10.1051/0004-6361:20000044. eprint: astro-ph/0011216.
- [290] H. Matheson, S. Safi-Harb and R. Kothes. “X-Ray Observations of the Supernova Remnant CTB 87 (G74.9+1.2): An Evolved Pulsar Wind Nebula”. In: *ApJ* 774, 33 (Sept. 2013), p. 33. DOI: 10.1088/0004-637X/774/1/33. arXiv: 1307.1084 [astro-ph.HE].
- [291] G. Matt et al. “BeppoSAX observations of AM Herculis in intermediate and high states”. In: *A&A* 358 (June 2000), pp. 177–186. eprint: astro-ph/0004014.
- [292] E. P. Mazets et al. “Catalog of cosmic gamma-ray bursts from the KONUS experiment data”. In: *AP&SS* 80 (Nov. 1981), pp. 85–117. DOI: 10.1007/BF00649141.
- [293] E. P. Mazets et al. “Observations of a flaring X-ray pulsar in Dorado”. In: *Nature* 282 (Dec. 1979), pp. 587–589. DOI: 10.1038/282587a0.
- [294] O. McConnell et al. “Roche lobe underfilling of the secondary star in PSR J102347.6+0038”. In: *MNRAS* 451 (Aug. 2015), pp. 3468–3472. DOI: 10.1093/mnras/stv1197. arXiv: 1507.07710 [astro-ph.HE].

- [295] S. Mereghetti. “The strongest cosmic magnets: soft gamma-ray repeaters and anomalous X-ray pulsars”. In: *A&ARv* 15 (July 2008), pp. 225–287. DOI: 10.1007/s00159-008-0011-z. arXiv: 0804.0250.
- [296] S. Mereghetti, G. L. Israel and L. Stella. “New limits on the orbital parameters of 1E 1048.1-5937 and 1E 2259+586 from RXTE observations”. In: *MNRAS* 296 (May 1998), pp. 689–692. DOI: 10.1046/j.1365-8711.1998.01396.x. eprint: astro-ph/9710337.
- [297] S. Mereghetti, J. A. Pons and A. Melatos. “Magnetars: Properties, Origin and Evolution”. In: 191 (Oct. 2015), pp. 315–338. DOI: 10.1007/s11214-015-0146-y. arXiv: 1503.06313 [astro-ph.HE].
- [298] S. Mereghetti and L. Stella. “The very low mass X-ray binary pulsars: A new class of sources?” In: *ApJL* 442 (Mar. 1995), pp. L17–L20. DOI: 10.1086/187805.
- [299] S. Mereghetti, A. Tiengo and G. L. Israel. “The X-Ray Source at the Center of the Cassiopeia A Supernova Remnant”. In: *ApJ* 569 (Apr. 2002), pp. 275–279. DOI: 10.1086/339277. eprint: astro-ph/0111357.
- [300] S. Mereghetti et al. “INTEGRAL detection of a SGR-like burst likely from Sgr J1745-29.” In: *GRB Coordinates Network* 15236 (2013).
- [301] S. Mereghetti et al. “The Anomalous X-ray Pulsars”. In: *Neutron Stars, Pulsars, and Supernova Remnants*. Ed. by W. Becker, H. Lesch and J. Trümper. 2002, p. 29. eprint: astro-ph/0205122.
- [302] S. Mereghetti et al. “The First Giant Flare from SGR 1806-20: Observations Using the Anticoincidence Shield of the Spectrometer on INTEGRAL”. In: *ApJL* 624 (May 2005), pp. L105–L108. DOI: 10.1086/430669. eprint: astro-ph/0502577.
- [303] F. Meyer and E. Meyer-Hofmeister. “Accretion disk evaporation by a coronal siphon flow”. In: *A&A* 288 (Aug. 1994), pp. 175–182.
- [304] J. M. Miller et al. “Powerful, Rotating Disk Winds from Stellar-mass Black Holes”. In: *ApJ* 814, 87 (Dec. 2015), p. 87. DOI: 10.1088/0004-637X/814/2/87. arXiv: 1510.01177 [astro-ph.HE].
- [305] A. H. Minter et al. “Neutral Hydrogen Absorption toward XTE J1810-197: The Distance to a Radio-emitting Magnetar”. In: *ApJ* 676, 1189-1199 (Apr. 2008), pp. 1189–1199. DOI: 10.1086/529005. arXiv: 0705.4403.
- [306] J. Miralda-Escudé and A. Gould. “A Cluster of Black Holes at the Galactic Center”. In: *ApJ* 545 (Dec. 2000), pp. 847–853. DOI: 10.1086/317837. eprint: astro-ph/0003269.
- [307] K. Mori and W. C. G. Ho. “Modelling mid-Z element atmospheres for strongly magnetized neutron stars”. In: *MNRAS* 377 (May 2007), pp. 905–919. DOI: 10.1111/j.1365-2966.2007.11663.x. eprint: astro-ph/0611145.

- [308] K. Mori et al. “NuSTAR Discovery of a 3.76 s Transient Magnetar Near Sagittarius A*”. In: *ApJL* 770, L23 (June 2013), p. L23. DOI: 10.1088/2041-8205/770/2/L23. arXiv: 1305.1945 [astro-ph.HE].
- [309] M. Morris. “Massive star formation near the Galactic center and the fate of the stellar remnants”. In: *ApJ* 408 (May 1993), pp. 496–506. DOI: 10.1086/172607.
- [310] C. Motch et al. “New cataclysmic variables from the ROSAT All-Sky Survey.” In: *A&A* 307 (Mar. 1996), pp. 459–469.
- [311] T. Muñoz-Darias, S. Motta and T. M. Belloni. “Fast variability as a tracer of accretion regimes in black hole transients”. In: *MNRAS* 410 (Jan. 2011), pp. 679–684. DOI: 10.1111/j.1365-2966.2010.17476.x. arXiv: 1008.0558 [astro-ph.HE].
- [312] T. Muñoz-Darias et al. “Black hole-like hysteresis and accretion states in neutron star low-mass X-ray binaries”. In: *MNRAS* 443 (Oct. 2014), pp. 3270–3283. DOI: 10.1093/mnras/stu1334. arXiv: 1407.1318 [astro-ph.HE].
- [313] M. P. Muno et al. “An Overabundance of Transient X-Ray Binaries within 1 Parsec of the Galactic Center”. In: *ApJL* 622 (Apr. 2005), pp. L113–L116. DOI: 10.1086/429721. eprint: astro-ph/0412492.
- [314] T. Murakami et al. “X-ray identification of the soft γ -ray repeater 1806 - 20”. In: *Nature* 368 (Mar. 1994), pp. 127–129. DOI: 10.1038/368127a0.
- [315] K. Nandra et al. “ASCA Observations of Seyfert 1 Galaxies. I. Data Analysis, Imaging, and Timing”. In: *ApJ* 476 (Feb. 1997), pp. 70–82.
- [316] R. Narayan. “Advection-dominated Models of Luminous Accreting Black Holes”. In: *ApJ* 462 (May 1996), p. 136. DOI: 10.1086/177136. eprint: astro-ph/9510028.
- [317] R. Narayan, M. R. Garcia and J. E. McClintock. “Advection-dominated Accretion and Black Hole Event Horizons”. In: *ApJL* 478 (Apr. 1997), pp. L79–L82. DOI: 10.1086/310554. eprint: astro-ph/9701139.
- [318] J. Neilsen and J. C. Lee. “Accretion disk winds as the jet suppression mechanism in the microquasar GRS 1915+105”. In: *Nature* 458 (Mar. 2009), pp. 481–484. DOI: 10.1038/nature07680.
- [319] L. Nobili, R. Turolla and S. Zane. “X-ray spectra from magnetar candidates - I. Monte Carlo simulations in the non-relativistic regime”. In: *MNRAS* 386 (May 2008), pp. 1527–1542. DOI: 10.1111/j.1365-2966.2008.13125.x. arXiv: 0802.2647.
- [320] L. Nobili, R. Turolla and S. Zane. “X-ray spectra from magnetar candidates - II. Resonant cross-sections for electron-photon scattering in the relativistic regime”. In: *MNRAS* 389 (Sept. 2008), pp. 989–1000. DOI: 10.1111/j.1365-2966.2008.13627.x. arXiv: 0806.3714.

- [321] A. J. Norton, G. A. Wynn and R. V. Somerscales. “The Spin Periods and Magnetic Moments of White Dwarfs in Magnetic Cataclysmic Variables”. In: *ApJ* 614 (Oct. 2004), pp. 349–357. DOI: 10.1086/423333. eprint: astro-ph/0406363.
- [322] M. A. Nowak et al. “Chandra/HETGS Observations of the Brightest Flare Seen from Sgr A*”. In: *ApJ* 759, 95 (Nov. 2012), p. 95. DOI: 10.1088/0004-637X/759/2/95. arXiv: 1209.6354 [astro-ph.HE].
- [323] M. Obergaulinger, H.-T. Janka and M. A. Aloy. “Magnetic field amplification and magnetically supported explosions of collapsing, non-rotating stellar cores”. In: *MNRAS* 445 (Dec. 2014), pp. 3169–3199. DOI: 10.1093/mnras/stu1969. arXiv: 1405.7466 [astro-ph.SR].
- [324] S. A. Olausen and V. M. Kaspi. “The McGill Magnetar Catalog”. In: *ApJS* 212, 6 (May 2014), p. 6. DOI: 10.1088/0067-0049/212/1/6. arXiv: 1309.4167 [astro-ph.HE].
- [325] J. P. Ostriker and J. E. Gunn. “On the Nature of Pulsars. I. Theory”. In: *ApJ* 157 (Sept. 1969), p. 1395. DOI: 10.1086/150160.
- [326] R. Ouyed, D. Leahy and N. Koning. ““Anti-glitches” in the Quark-Nova model for AXPs I”. In: *AP&SS* 352 (Aug. 2014), pp. 715–718. DOI: 10.1007/s10509-014-1941-8. arXiv: 1307.1386 [astro-ph.HE].
- [327] R. Ouyed, D. Leahy and B. Niebergal. “Quark-nova remnants. I. The leftover debris with applications to SGRs, AXPs, and XDINs”. In: *A&A* 473 (Oct. 2007), pp. 357–368. DOI: 10.1051/0004-6361:20077412. eprint: astro-ph/0608536.
- [328] R. Ouyed, D. Leahy and B. Niebergal. “Quark-nova remnants. II. The degenerate torus case with applications to AXPs”. In: *A&A* 475 (Nov. 2007), pp. 63–70. DOI: 10.1051/0004-6361:20077426.
- [329] F. Pacini. “Energy Emission from a Neutron Star”. In: *Nature* 216 (Nov. 1967), pp. 567–568. DOI: 10.1038/216567a0.
- [330] F. Pacini. “Rotating Neutron Stars, Pulsars and Supernova Remnants”. In: *Nature* 219 (July 1968), pp. 145–146. DOI: 10.1038/219145a0.
- [331] B. Paczynski. “GB 790305 as a very strongly magnetized neutron star”. In: 42 (1992), pp. 145–153.
- [332] D. M. Palmer et al. “A giant γ -ray flare from the magnetar SGR 1806 - 20”. In: *Nature* 434 (Apr. 2005), pp. 1107–1109. DOI: 10.1038/nature03525. eprint: astro-ph/0503030.
- [333] A. Papitto and D. F. Torres. “A Propeller Model for the Sub-luminous State of the Transitional Millisecond Pulsar PSR J1023+0038”. In: *ApJ* 807, 33 (July 2015), p. 33. DOI: 10.1088/0004-637X/807/1/33. arXiv: 1504.05029 [astro-ph.HE].

- [334] A. Papitto, D. F. Torres and J. Li. “A propeller scenario for the gamma-ray emission of low-mass X-ray binaries: the case of XSS J12270-4859”. In: *MNRAS* 438 (Mar. 2014), pp. 2105–2116. DOI: 10.1093/mnras/stt2336. arXiv: 1312.0456 [astro-ph.HE].
- [335] A. Papitto et al. “Swings between rotation and accretion power in a binary millisecond pulsar”. In: *Nature* 501 (Sept. 2013), pp. 517–520. DOI: 10.1038/nature12470. arXiv: 1305.3884 [astro-ph.HE].
- [336] A. Papitto et al. “X-ray coherent pulsations during a sub-luminous accretion disc state of the transitional millisecond pulsar XSS J12270-4859”. In: *MNRAS* 449 (Apr. 2015), pp. L26–L30. DOI: 10.1093/mnrasl/slv013. arXiv: 1412.4252 [astro-ph.HE].
- [337] K. Parfrey, A. M. Beloborodov and L. Hui. “Dynamics of Strongly Twisted Relativistic Magnetospheres”. In: *ApJ* 774, 92 (Sept. 2013), p. 92. DOI: 10.1088/0004-637X/774/2/92. arXiv: 1306.4335 [astro-ph.HE].
- [338] K. Parfrey, A. M. Beloborodov and L. Hui. “Twisting, Reconnecting Magnetospheres and Magnetar Spindown”. In: *ApJL* 754, L12 (July 2012), p. L12. DOI: 10.1088/2041-8205/754/1/L12. arXiv: 1201.3635 [astro-ph.HE].
- [339] K. Parfrey, A. Spitkovsky and A. M. Beloborodov. “Torque Enhancement, Spin Equilibrium, and Jet Power from Disk-Induced Opening of Pulsar Magnetic Fields”. In: *ApJ* 822, 33 (May 2016), p. 33. DOI: 10.3847/0004-637X/822/1/33. arXiv: 1507.08627 [astro-ph.HE].
- [340] A. Patruno and A. L. Watts. “Accreting Millisecond X-Ray Pulsars”. In: *ArXiv e-prints* (June 2012). arXiv: 1206.2727 [astro-ph.HE].
- [341] A. Patruno et al. “A New Accretion Disk around the Missing Link Binary System PSR J1023+0038”. In: *ApJL* 781, L3 (Jan. 2014), p. L3. DOI: 10.1088/2041-8205/781/1/L3. arXiv: 1310.7549 [astro-ph.HE].
- [342] J. Patterson and J. C. Raymond. “X-ray emission from cataclysmic variables with accretion disks. I - Hard X-rays. II - EUV/soft X-ray radiation”. In: *ApJ* 292 (May 1985), pp. 535–558. DOI: 10.1086/163187.
- [343] G. G. Pavlov and V. G. Bezchastnov. “Once-ionized Helium in Superstrong Magnetic Fields”. In: *ApJL* 635 (Dec. 2005), pp. L61–L64. DOI: 10.1086/499270. eprint: astro-ph/0505464.
- [344] G. G. Pavlov and G. J. M. Luna. “A Dedicated Chandra ACIS Observation of the Central Compact Object in the Cassiopeia A Supernova Remnant”. In: *ApJ* 703 (Sept. 2009), pp. 910–921. DOI: 10.1088/0004-637X/703/1/910. arXiv: 0905.3190 [astro-ph.HE].
- [345] G. G. Pavlov et al. “The Compact Central Object in Cassiopeia A: A Neutron Star with Hot Polar Caps or a Black Hole?”. In: *ApJL* 531 (Mar. 2000), pp. L53–L56. DOI: 10.1086/312521. eprint: astro-ph/9912024.

- [346] M. Z. Pavlović et al. “The Radio Surface-brightness-to-Diameter Relation for Galactic Supernova Remnants: Sample Selection and Robust Analysis with Various Fitting Offsets”. In: *ApJS* 204, 4 (Jan. 2013), p. 4. DOI: 10.1088/0067-0049/204/1/4. arXiv: 1210.4602 [astro-ph.GA].
- [347] J. A. Peacock. “Two-dimensional goodness-of-fit testing in astronomy”. In: *MNRAS* 202 (Feb. 1983), pp. 615–627. DOI: 10.1093/mnras/202.3.615.
- [348] S. Pedicelli et al. “On the metallicity gradient of the Galactic disk”. In: *A&A* 504 (Sept. 2009), pp. 81–86. DOI: 10.1051/0004-6361/200912504. arXiv: 0906.3140 [astro-ph.SR].
- [349] R. Perna, E. Bozzo and L. Stella. “On the Spin-up/Spin-down Transitions in Accreting X-Ray Binaries”. In: *ApJ* 639 (Mar. 2006), pp. 363–376. DOI: 10.1086/499227. eprint: astro-ph/0511285.
- [350] R. Perna and E. V. Gotthelf. “Constraints on the Emission and Viewing Geometry of the Transient Anomalous X-Ray Pulsar XTE J1810-197”. In: *ApJ* 681, 522-529 (July 2008), pp. 522–529. DOI: 10.1086/588211. arXiv: 0803.2042.
- [351] R. Perna and J. A. Pons. “A Unified Model of the Magnetar and Radio Pulsar Bursting Phenomenology”. In: *ApJL* 727, L51 (Feb. 2011), p. L51. DOI: 10.1088/2041-8205/727/2/L51. arXiv: 1101.1098 [astro-ph.HE].
- [352] R. Perna et al. “The Fate of fallback Matter around Newly Born Compact Objects”. In: *ApJ* 781, 119 (Feb. 2014), p. 119. DOI: 10.1088/0004-637X/781/2/119. arXiv: 1312.4981 [astro-ph.HE].
- [353] E. Pfahl and A. Loeb. “Probing the Spacetime around Sagittarius A* with Radio Pulsars”. In: *ApJ* 615 (Nov. 2004), pp. 253–258. DOI: 10.1086/423975. eprint: astro-ph/0309744.
- [354] G. Pietrzyński et al. “An eclipsing-binary distance to the Large Magellanic Cloud accurate to two per cent”. In: *Nature* 495 (Mar. 2013), pp. 76–79. DOI: 10.1038/nature11878. arXiv: 1303.2063 [astro-ph.GA].
- [355] C. Pinto et al. “High-resolution X-ray spectroscopy of the interstellar medium. XMM-Newton observation of the LMXB GS 1826-238”. In: *A&A* 521, A79 (Oct. 2010), A79. DOI: 10.1051/0004-6361/201014836. arXiv: 1007.2796 [astro-ph.HE].
- [356] F. Pintore et al. “The variable spin-down rate of the transient magnetar XTE J1810-197”. In: *MNRAS* 458 (May 2016), pp. 2088–2093. DOI: 10.1093/mnras/stw351. arXiv: 1602.03359 [astro-ph.HE].
- [357] A. M. Pires et al. “XMM-Newton reveals a candidate period for the spin of the ”Magnificent Seven” neutron star RX J1605.3+3249”. In: *A&A* 563, A50 (Mar. 2014), A50. DOI: 10.1051/0004-6361/201423380. arXiv: 1401.7147 [astro-ph.HE].

- [358] F. Pizzolato et al. “1E 161348-5055 in the Supernova Remnant RCW 103: A Magnetar in a Young Low-Mass Binary System?” In: *ApJ* 681, 530-542 (July 2008), pp. 530–542. DOI: 10.1086/588084. arXiv: 0803.1373.
- [359] R. M. Plotkin et al. “Using the Fundamental Plane of black hole activity to distinguish X-ray processes from weakly accreting black holes”. In: *MNRAS* 419 (Jan. 2012), pp. 267–286. DOI: 10.1111/j.1365-2966.2011.19689.x. arXiv: 1105.3211 [astro-ph.HE].
- [360] J. A. Pons and N. Rea. “Modeling Magnetar Outbursts: Flux Enhancements and the Connection with Short Bursts and Glitches”. In: *ApJL* 750, L6 (May 2012), p. L6. DOI: 10.1088/2041-8205/750/1/L6. arXiv: 1203.4506 [astro-ph.HE].
- [361] J. A. Pons, D. Viganò and N. Rea. “A highly resistive layer within the crust of X-ray pulsars limits their spin periods”. In: *Nature Physics* 9 (July 2013), pp. 431–434. DOI: 10.1038/nphys2640. arXiv: 1304.6546 [astro-ph.SR].
- [362] G. Ponti, T. Muñoz-Darias and R. P. Fender. “A connection between accretion state and Fe K absorption in an accreting neutron star: black hole-like soft-state winds?” In: *MNRAS* 444 (Oct. 2014), pp. 1829–1834. DOI: 10.1093/mnras/stu1742. arXiv: 1407.4468 [astro-ph.HE].
- [363] G. Ponti et al. “Discovery of a Superluminal Fe K Echo at the Galactic Center: The Glorious Past of Sgr A* Preserved by Molecular Clouds”. In: *ApJ* 714 (May 2010), pp. 732–747. DOI: 10.1088/0004-637X/714/1/732. arXiv: 1003.2001 [astro-ph.HE].
- [364] G. Ponti et al. “Fifteen years of XMM-Newton and Chandra monitoring of Sgr A[?]: evidence for a recent increase in the bright flaring rate”. In: *MNRAS* 454 (Dec. 2015), pp. 1525–1544. DOI: 10.1093/mnras/stv1537. arXiv: 1507.02690 [astro-ph.HE].
- [365] G. Ponti et al. “Mapping the inner regions of MCG-6-30-15 with XMM-Newton”. In: *A&A* 417 (Apr. 2004), pp. 451–459. DOI: 10.1051/0004-6361:20031758. eprint: astro-ph/0312250.
- [366] G. Ponti et al. “On the Fe K absorption - accretion state connection in the Galactic Centre neutron star X-ray binary AX J1745.6-2901”. In: *MNRAS* 446 (Jan. 2015), pp. 1536–1550. DOI: 10.1093/mnras/stu1853. arXiv: 1409.3224 [astro-ph.HE].
- [367] G. Ponti et al. “On the past activity of Sgr A*”. In: *The Galactic Center: Feeding and Feedback in a Normal Galactic Nucleus*. Ed. by L. O. Sjouwerman, C. C. Lang and J. Ott. Vol. 303. IAU Symposium. May 2014, pp. 333–343. DOI: 10.1017/S174392131400088X.
- [368] G. Ponti et al. “The XMM-Newton view of the central degrees of the Milky Way”. In: *MNRAS* 453 (Oct. 2015), pp. 172–213. DOI: 10.1093/mnras/stv1331. arXiv: 1508.04445 [astro-ph.HE].

- [369] G. Ponti et al. “Traces of Past Activity in the Galactic Centre”. In: *Cosmic Rays in Star-Forming Environments*. Ed. by D. F. Torres and O. Reimer. Vol. 34. Astrophysics and Space Science Proceedings. 2013, p. 331. DOI: 10.1007/978-3-642-35410-6_26. arXiv: 1210.3034.
- [370] G. Ponti et al. “Ubiquitous equatorial accretion disc winds in black hole soft states”. In: *MNRAS* 422 (May 2012), pp. 11–15. DOI: 10.1111/j.1745-3933.2012.01224.x. arXiv: 1201.4172 [astro-ph.HE].
- [371] T. S. Poole et al. “Photometric calibration of the Swift ultraviolet/optical telescope”. In: *MNRAS* 383 (Jan. 2008), pp. 627–645. DOI: 10.1111/j.1365-2966.2007.12563.x. arXiv: 0708.2259.
- [372] S. B. Popov, A. A. Kaurov and A. D. Kaminker. “Central Compact Objects in Kes 79 and RCW 103 as ‘Hidden’ Magnetars with Crustal Activity”. In: 32, e018 (May 2015), e018. DOI: 10.1017/pasa.2015.18. arXiv: 1504.03279 [astro-ph.HE].
- [373] P. Predehl and J. H. M. M. Schmitt. “X-raying the interstellar medium: ROSAT observations of dust scattering halos.” In: *A&A* 293 (Jan. 1995).
- [374] J. E. Pringle and M. J. Rees. “Accretion Disc Models for Compact X-Ray Sources”. In: *A&A* 21 (Oct. 1972), p. 1.
- [375] V. Radhakrishnan and G. Srinivasan. “On the origin of the recently discovered ultra-rapid pulsar”. In: *Current Science* 51 (Dec. 1982), pp. 1096–1099.
- [376] G. Ramsay et al. “2XMMiJ225036.9+573154 - a new eclipsing AMHer binary discovered using XMM-Newton”. In: *MNRAS* 395 (May 2009), pp. 416–421. DOI: 10.1111/j.1365-2966.2009.14528.x. arXiv: 0901.3095 [astro-ph.GA].
- [377] M. L. Rawls et al. “Refined Neutron Star Mass Determinations for Six Eclipsing X-Ray Pulsar Binaries”. In: *ApJ* 730, 25 (Mar. 2011), p. 25. DOI: 10.1088/0004-637X/730/1/25. arXiv: 1101.2465 [astro-ph.SR].
- [378] N. Rea and P. Esposito. “Magnetar outbursts: an observational review”. In: *Astrophysics and Space Science Proceedings* 21 (2011), p. 247. DOI: 10.1007/978-3-642-17251-9_21. arXiv: 1101.4472.
- [379] N. Rea et al. “3XMM J185246.6+003317: Another Low Magnetic Field Magnetar”. In: *ApJL* 781, L17 (Jan. 2014), p. L17. DOI: 10.1088/2041-8205/781/1/L17. arXiv: 1311.3091.
- [380] N. Rea et al. “A Low-Magnetic-Field Soft Gamma Repeater”. In: *Science* 330 (Nov. 2010), p. 944. DOI: 10.1126/science.1196088. arXiv: 1010.2781 [astro-ph.HE].
- [381] N. Rea et al. “A New Low Magnetic Field Magnetar: The 2011 Outburst of Swift J1822.3-1606”. In: *ApJ* 754, 27 (July 2012), p. 27. DOI: 10.1088/0004-637X/754/1/27. arXiv: 1203.6449.

- [382] N. Rea et al. “A Strongly Magnetized Pulsar within the Grasp of the Milky Way’s Supermassive Black Hole”. In: *ApJL* 775, L34 (Oct. 2013), p. L34. DOI: 10.1088/2041-8205/775/2/L34. arXiv: 1307.6331.
- [383] N. Rea et al. “Correlated Infrared and X-ray variability of the transient Anomalous X-ray Pulsar XTE J1810-197”. In: *A&A* 425 (Oct. 2004), pp. L5–L8. DOI: 10.1051/0004-6361:200400052. eprint: astro-ph/0408087.
- [384] N. Rea et al. “Discovery of Extended X-Ray Emission Around the Highly Magnetic RRAT J1819-1458”. In: *ApJL* 703 (Sept. 2009), pp. L41–L45. DOI: 10.1088/0004-637X/703/1/L41. arXiv: 0906.1394 [astro-ph.HE].
- [385] N. Rea et al. “Post-glitch variability in the anomalous X-ray pulsar 1RXSJ170849.0-400910”. In: *MNRAS* 361 (Aug. 2005), pp. 710–718. DOI: 10.1111/j.1365-2966.2005.09201.x. eprint: astro-ph/0505400.
- [386] N. Rea et al. “Resonant Cyclotron Scattering in Magnetars’ Emission”. In: *ApJ* 686, 1245-1260 (Oct. 2008), pp. 1245–1260. DOI: 10.1086/591264. arXiv: 0802.1923.
- [387] N. Rea et al. “The first outburst of the new magnetar candidate SGR0501+4516”. In: *MNRAS* 396 (July 2009), pp. 2419–2432. DOI: 10.1111/j.1365-2966.2009.14920.x. arXiv: 0904.2413 [astro-ph.HE].
- [388] N. Rea et al. “The Fundamental Plane for Radio Magnetars”. In: *ApJL* 748, L12 (Mar. 2012), p. L12. DOI: 10.1088/2041-8205/748/1/L12. arXiv: 1202.3069 [astro-ph.GA].
- [389] N. Rea et al. “The Outburst Decay of the Low Magnetic Field Magnetar SGR 0418+5729”. In: *ApJ* 770, 65 (June 2013), p. 65. DOI: 10.1088/0004-637X/770/1/65. arXiv: 1303.5579 [astro-ph.GA].
- [390] N. Rea et al. “The X-ray Quiescence of Swift J195509.6+261406 (GRB 070610): An Optical Bursting X-ray Binary?” In: *ApJL* 729, L21 (Mar. 2011), p. L21. DOI: 10.1088/2041-8205/729/2/L21. arXiv: 1101.3483 [astro-ph.GA].
- [391] A. M. Read et al. “A new comprehensive 2D model of the point spread functions of the XMM-Newton EPIC telescopes: spurious source suppression and improved positional accuracy”. In: *A&A* 534, A34 (Oct. 2011), A34. DOI: 10.1051/0004-6361/201117525. arXiv: 1108.4835 [astro-ph.IM].
- [392] R. A. Remillard and J. E. McClintock. “X-Ray Properties of Black-Hole Binaries”. In: *Annu. Rev. Astro. Astrophys.* 44 (Sept. 2006), pp. 49–92. DOI: 10.1146/annurev.astro.44.051905.092532. eprint: astro-ph/0606352.
- [393] M. G. Revnivtsev et al. “Hard X-ray view of the past activity of Sgr A* in a natural Compton mirror”. In: *A&A* 425 (Oct. 2004), pp. L49–L52. DOI: 10.1051/0004-6361:200400064. eprint: astro-ph/0408190.
- [394] M. Reynolds et al. “New Galactic Center X-ray Transient Detected by Swift: SWIFT J174540.7-290015”. In: *The Astronomer’s Telegram* 8649 (Feb. 2016).

- [395] M. T. Reynolds et al. “The light curve of the companion to PSR B1957+20”. In: *MNRAS* 379 (Aug. 2007), pp. 1117–1122. DOI: 10.1111/j.1365-2966.2007.11991.x. arXiv: 0705.2514.
- [396] D. W. Richards and J. M. Comella. “The Period of Pulsar NP 0532”. In: *Nature* 222 (May 1969), pp. 551–552. DOI: 10.1038/222551a0.
- [397] M. S. E. Roberts. “New Black Widows and Redbacks in the Galactic Field”. In: *American Institute of Physics Conference Series*. Ed. by M. Burgay et al. Vol. 1357. American Institute of Physics Conference Series. Aug. 2011, pp. 127–130. DOI: 10.1063/1.3615095. arXiv: 1103.0819 [astro-ph.HE].
- [398] M. S. E. Roberts. “Surrounded by spiders! New black widows and redbacks in the Galactic field”. In: *Neutron Stars and Pulsars: Challenges and Opportunities after 80 years*. Ed. by J. van Leeuwen. Vol. 291. IAU Symposium. Mar. 2013, pp. 127–132. DOI: 10.1017/S174392131202337X. arXiv: 1210.6903 [astro-ph.HE].
- [399] G. A. Rodríguez Castillo et al. “Pulse phase-coherent timing and spectroscopy of CXOU J164710.2-45521 outbursts”. In: *MNRAS* 441 (June 2014), pp. 1305–1316. DOI: 10.1093/mnras/stu603. arXiv: 1403.7165 [astro-ph.HE].
- [400] G. A. Rodríguez Castillo et al. “The outburst decay of the low magnetic field magnetar SWIFT J1822.3-1606: phase-resolved analysis and evidence for a variable cyclotron feature”. In: *MNRAS* 456 (Mar. 2016), pp. 4145–4155. DOI: 10.1093/mnras/stv2490. arXiv: 1510.09157 [astro-ph.HE].
- [401] R. W. Romani. “Gamma-Ray Pulsars: Radiation Processes in the Outer Magnetosphere”. In: *ApJ* 470 (Oct. 1996), p. 469. DOI: 10.1086/177878.
- [402] M. M. Romanova et al. “MHD Simulations of Magnetospheric Accretion, Ejection and Plasma-field Interaction”. In: *European Physical Journal Web of Conferences*. Vol. 64. European Physical Journal Web of Conferences. Jan. 2014, p. 05001. DOI: 10.1051/epjconf/20136405001. arXiv: 1311.4597 [astro-ph.SR].
- [403] M. M. Romanova et al. “Propeller-driven Outflows and Disk Oscillations”. In: *ApJL* 635 (Dec. 2005), pp. L165–L168. DOI: 10.1086/499560. eprint: astro-ph/0511600.
- [404] M. M. Romanova et al. “The Propeller Regime of Disk Accretion to a Rapidly Rotating Magnetized Star”. In: *ApJL* 616 (Dec. 2004), pp. L151–L154. DOI: 10.1086/426586. eprint: astro-ph/0502266.
- [405] P. W. A. Roming et al. “The Swift Ultra-Violet/Optical Telescope”. In: 120 (Oct. 2005), pp. 95–142. DOI: 10.1007/s11214-005-5095-4. eprint: astro-ph/0507413.
- [406] S. R. Rosen, K. O. Mason and F. A. Cordova. “EXOSAT X-ray observations of the eclipsing magnetic cataclysmic variable EX Hya”. In: *MNRAS* 231 (Mar. 1988), pp. 549–573. DOI: 10.1093/mnras/231.3.549.

- [407] J. Roy, B. Bhattacharyya and P. S. Ray. “GMRT discovery of a 1.69 ms radio pulsar associated with XSS J12270-4859”. In: *The Astronomer’s Telegram* 5890 (Feb. 2014).
- [408] M. Ruderman, J. Shaham and M. Tavani. “Accretion turnoff and rapid evaporation of very light secondaries in low-mass X-ray binaries”. In: *ApJ* 336 (Jan. 1989), pp. 507–518. DOI: 10.1086/167029.
- [409] M. A. Ruderman and P. G. Sutherland. “Theory of pulsars - Polar caps, sparks, and coherent microwave radiation”. In: *ApJ* 196 (Feb. 1975), pp. 51–72. DOI: 10.1086/153393.
- [410] T. Sakamoto et al. “The Second Swift Burst Alert Telescope Gamma-Ray Burst Catalog”. In: *ApJS* 195, 2 (July 2011), p. 2. DOI: 10.1088/0067-0049/195/1/2. arXiv: 1104.4689 [astro-ph.HE].
- [411] M. Sakano et al. “XMM-Newton observations of Sagittarius A East”. In: *MNRAS* 350 (May 2004), pp. 129–139. DOI: 10.1111/j.1365-2966.2004.07571.x. eprint: astro-ph/0312541.
- [412] N. Sartore et al. “Spectral monitoring of RX J1856.5-3754 with XMM-Newton. Analysis of EPIC-pn data”. In: *A&A* 541, A66 (May 2012), A66. DOI: 10.1051/0004-6361/201118489. arXiv: 1202.2121 [astro-ph.HE].
- [413] J. D. Scargle. “Studies in Astronomical Time Series Analysis. V. Bayesian Blocks, a New Method to Analyze Structure in Photon Counting Data”. In: *ApJ* 504 (Sept. 1998), pp. 405–418. DOI: 10.1086/306064. eprint: astro-ph/9711233.
- [414] E. F. Schlafly and D. P. Finkbeiner. “Measuring Reddening with Sloan Digital Sky Survey Stellar Spectra and Recalibrating SFD”. In: *ApJ* 737, 103 (Aug. 2011), p. 103. DOI: 10.1088/0004-637X/737/2/103. arXiv: 1012.4804 [astro-ph.GA].
- [415] D. J. Schlegel, D. P. Finkbeiner and M. Davis. “Maps of Dust Infrared Emission for Use in Estimation of Reddening and Cosmic Microwave Background Radiation Foregrounds”. In: *ApJ* 500 (June 1998), pp. 525–553. DOI: 10.1086/305772. eprint: astro-ph/9710327.
- [416] P. Scholz et al. “Post-outburst X-Ray Flux and Timing Evolution of Swift J1822.3-1606”. In: *ApJ* 761, 66 (Dec. 2012), p. 66. DOI: 10.1088/0004-637X/761/1/66. arXiv: 1204.1034 [astro-ph.HE].
- [417] E. Schreier et al. “Evidence for the Binary Nature of Centaurus X-3 from UHURU X-Ray Observations.” In: *ApJL* 172 (Mar. 1972), p. L79. DOI: 10.1086/180896.
- [418] R. Schwarz et al. “Paloma (RX J0524+42): the missing link in magnetic CV evolution?” In: *A&A* 473 (Oct. 2007), pp. 511–521. DOI: 10.1051/0004-6361:20077684.

- [419] N. Shabaltas and D. Lai. “The Hidden Magnetic Field of the Young Neutron Star in Kesteven 79”. In: *ApJ* 748, 148 (Apr. 2012), p. 148. DOI: 10.1088/0004-637X/748/2/148. arXiv: 1110.3129 [astro-ph.HE].
- [420] T. Shahbaz et al. “The binary millisecond pulsar PSR J1023+0038 during its accretion state - I. Optical variability”. In: *MNRAS* 453 (Nov. 2015), pp. 3461–3473. DOI: 10.1093/mnras/stv1686. arXiv: 1507.07473 [astro-ph.HE].
- [421] N. I. Shakura and R. A. Sunyaev. “Black holes in binary systems. Observational appearance.” In: *A&A* 24 (1973), pp. 337–355.
- [422] R. M. Shannon and S. Johnston. “Radio properties of the magnetar near Sagittarius A* from observations with the Australia Telescope Compact Array”. In: *MNRAS* 435 (Aug. 2013), pp. L29–L32. DOI: 10.1093/mnrasl/slt088. arXiv: 1305.3036 [astro-ph.HE].
- [423] I. S. Shklovsky. “On the Nature of the Source of X-Ray Emission of SCO XR-1.” In: *ApJL* 148 (Apr. 1967), p. L1. DOI: 10.1086/180001.
- [424] P. Shull Jr. “The kinematics and structure of N49”. In: *ApJ* 275 (Dec. 1983), pp. 611–627. DOI: 10.1086/161559.
- [425] L. L. Smarr and R. Blandford. “The binary pulsar - Physical processes, possible companions, and evolutionary histories”. In: *ApJ* 207 (July 1976), pp. 574–588. DOI: 10.1086/154524.
- [426] D. A. Smith and V. S. Dhillon. “The secondary stars in cataclysmic variables and low-mass X-ray binaries”. In: *MNRAS* 301 (Dec. 1998), pp. 767–781. DOI: 10.1046/j.1365-8711.1998.02065.x. eprint: astro-ph/9808217.
- [427] R. K. Smith, L. A. Valencic and L. Corrales. “The Impact of Accurate Extinction Measurements for X-Ray Spectral Models”. In: *ApJ* 818, 143 (Feb. 2016), p. 143. DOI: 10.3847/0004-637X/818/2/143. arXiv: 1602.07766 [astro-ph.HE].
- [428] T. Sonobe et al. “Characteristics of the persistent emission of SGR 1806-20”. In: *ApJL* 436 (Nov. 1994), pp. L23–L25. DOI: 10.1086/187624.
- [429] A. Spitkovsky. “Time-dependent Force-free Pulsar Magnetospheres: Axisymmetric and Oblique Rotators”. In: *ApJL* 648 (Sept. 2006), pp. L51–L54. DOI: 10.1086/507518. eprint: astro-ph/0603147.
- [430] G. Srinivasan. “Recycled pulsars”. In: 54 (Mar. 2010), pp. 93–100. DOI: 10.1016/j.newar.2010.09.026.
- [431] D. H. Staelin and E. C. Reifenstein III. “Pulsating Radio Sources near the Crab Nebula”. In: *Science* 162 (Dec. 1968), pp. 1481–1483. DOI: 10.1126/science.162.3861.1481.
- [432] M. Stamatikos et al. “GRB 140705A: Swift detection of a short burst.” In: *GRB Coordinates Network* 16520 (2014).

- [433] B. W. Stappers et al. “A State Change in the Missing Link Binary Pulsar System PSR J1023+0038”. In: *ApJ* 790, 39 (July 2014), p. 39. DOI: 10.1088/0004-637X/790/1/39. arXiv: 1311.7506 [astro-ph.HE].
- [434] L. Staveley-Smith et al. “The Parkes 21 CM multibeam receiver”. In: 13 (Nov. 1996), pp. 243–248.
- [435] F. R. Stephenson and D. A. Green. “Historical supernovae and their remnants”. In: *Historical supernovae and their remnants, by F. Richard Stephenson and David A. Green. International series in astronomy and astrophysics, vol. 5. Oxford: Clarendon Press, 2002, ISBN 0198507666 5 (2002).*
- [436] P. B. Stetson. “Homogeneous Photometry for Star Clusters and Resolved Galaxies. II. Photometric Standard Stars”. In: 112 (July 2000), pp. 925–931. DOI: 10.1086/316595. eprint: astro-ph/0004144.
- [437] J. M. Stil et al. “The VLA Galactic Plane Survey”. In: 132 (Sept. 2006), pp. 1158–1176. DOI: 10.1086/505940. eprint: astro-ph/0605422.
- [438] T. E. Strohmayer et al. “Millisecond X-Ray Variability from an Accreting Neutron Star System”. In: *ApJL* 469 (Sept. 1996), p. L9. DOI: 10.1086/310261.
- [439] L. Strüder et al. “The European Photon Imaging Camera on XMM-Newton: The pn-CCD camera”. In: *A&A* 365 (Jan. 2001), pp. L18–L26. DOI: 10.1051/0004-6361:20000066.
- [440] X. H. Sun et al. “A Sino-German $\lambda 6$ cm polarization survey of the Galactic plane. VII. Small supernova remnants”. In: *A&A* 536, A83 (Dec. 2011), A83. DOI: 10.1051/0004-6361/201117693. arXiv: 1110.1106.
- [441] M. P. Surnis et al. “Upper limits on the pulsed radio emission of SGR 1935+2154 from the Ooty Radio Telescope and the Giant Meterwave Radio Telescope”. In: *The Astronomer’s Telegram* 6376 (Aug. 2014).
- [442] P. Szkody et al. “Cataclysmic Variables from the Sloan Digital Sky Survey. II. The Second Year”. In: 126 (Sept. 2003), pp. 1499–1514. DOI: 10.1086/377346. eprint: astro-ph/0306269.
- [443] J. Takata et al. “Multi-wavelength Emissions from the Millisecond Pulsar Binary PSR J1023+0038 during an Accretion Active State”. In: *ApJ* 785, 131 (Apr. 2014), p. 131. DOI: 10.1088/0004-637X/785/2/131. arXiv: 1312.0605 [astro-ph.HE].
- [444] P. H. T. Tam et al. “Evidence for Gamma-ray Emission from the Low-mass X-ray Binary System First J102347.6+003841”. In: *ApJL* 724 (Dec. 2010), pp. L207–L211. DOI: 10.1088/2041-8205/724/2/L207. arXiv: 1010.4311 [astro-ph.HE].
- [445] M. Tavani. “‘Hidden’ millisecond pulsars”. In: *ApJL* 379 (Oct. 1991), pp. L69–L73. DOI: 10.1086/186156.

- [446] M. Tavani and J. Arons. “Theory of High-Energy Emission from the Pulsar/Be Star System PSR 1259-63. I. Radiation Mechanisms and Interaction Geometry”. In: *ApJ* 477 (Mar. 1997), pp. 439–464. eprint: astro-ph/9609086.
- [447] S. P. Tendulkar et al. “NuSTAR Observations of the State Transition of Millisecond Pulsar Binary PSR J1023+0038”. In: *ApJ* 791, 77 (Aug. 2014), p. 77. DOI: 10.1088/0004-637X/791/2/77. arXiv: 1406.7009 [astro-ph.HE].
- [448] J. Terrell et al. “Periodicity of the gamma-ray transient event of 5 March 1979”. In: *Nature* 285 (June 1980), pp. 383–385. DOI: 10.1038/285383a0.
- [449] R. Terrier et al. “Fading Hard X-ray Emission from the Galactic Center Molecular Cloud Sgr B2”. In: *ApJ* 719 (Aug. 2010), pp. 143–150. DOI: 10.1088/0004-637X/719/1/143. arXiv: 1005.4807 [astro-ph.HE].
- [450] N. Tetzlaff et al. “The origin of RX J1856.5-3754 and RX J0720.4-3125 - updated using new parallax measurements”. In: *MNRAS* 417 (Oct. 2011), pp. 617–626. DOI: 10.1111/j.1365-2966.2011.19302.x. arXiv: 1107.1673.
- [451] C. Thompson and A. M. Beloborodov. “High-Energy Emission from Magnetars”. In: *ApJ* 634 (Nov. 2005), pp. 565–569. DOI: 10.1086/432245. eprint: astro-ph/0408538.
- [452] C. Thompson and R. C. Duncan. “Neutron star dynamos and the origins of pulsar magnetism”. In: *ApJ* 408 (May 1993), pp. 194–217. DOI: 10.1086/172580.
- [453] C. Thompson and R. C. Duncan. “The Giant Flare of 1998 August 27 from SGR 1900+14. II. Radiative Mechanism and Physical Constraints on the Source”. In: *ApJ* 561 (Nov. 2001), pp. 980–1005. DOI: 10.1086/323256. eprint: astro-ph/0110675.
- [454] C. Thompson and R. C. Duncan. “The soft gamma repeaters as very strongly magnetized neutron stars - I. Radiative mechanism for outbursts”. In: *MNRAS* 275 (July 1995), pp. 255–300. DOI: 10.1093/mnras/275.2.255.
- [455] C. Thompson, M. Lyutikov and S. R. Kulkarni. “Electrodynamics of Magnetars: Implications for the Persistent X-Ray Emission and Spin-down of the Soft Gamma Repeaters and Anomalous X-Ray Pulsars”. In: *ApJ* 574 (July 2002), pp. 332–355. DOI: 10.1086/340586. eprint: astro-ph/0110677.
- [456] D. J. Thompson et al. “SAS-2 high-energy gamma-ray observations of the VELA pulsar”. In: *ApJL* 200 (Sept. 1975), pp. L79–L82. DOI: 10.1086/181902.
- [457] J. R. Thorstensen and E. Armstrong. “Is FIRST J102347.6+003841 Really a Cataclysmic Binary?” In: 130 (Aug. 2005), pp. 759–766. DOI: 10.1086/431326. eprint: astro-ph/0504523.
- [458] A. Tiengo, P. Esposito and S. Mereghetti. “XMM-Newton Observations of CXOU J010043.1-721134: The First Deep Look at the Soft X-Ray Emission of a Magnetar”. In: *ApJL* 680, L133 (June 2008), p. L133. DOI: 10.1086/590078. arXiv: 0805.2294.

- [459] A. Tiengo et al. “A variable absorption feature in the X-ray spectrum of a magnetar”. In: *Nature* 500 (Aug. 2013), pp. 312–314. DOI: 10.1038/nature12386. arXiv: 1308.4987 [astro-ph.HE].
- [460] A. Torres-Forné et al. “Are pulsars born with a hidden magnetic field?” In: *MNRAS* 456 (Mar. 2016), pp. 3813–3826. DOI: 10.1093/mnras/stv2926. arXiv: 1511.03823 [astro-ph.SR].
- [461] I. Traulsen et al. “X-ray spectroscopy and photometry of the long-period polar AI Trianguli with XMM-Newton”. In: *A&A* 516, A76 (June 2010), A76. DOI: 10.1051/0004-6361/200913201. arXiv: 1004.1629 [astro-ph.SR].
- [462] J. Tueller et al. “The 22 Month Swift-BAT All-Sky Hard X-ray Survey”. In: *ApJS* 186 (Feb. 2010), pp. 378–405. DOI: 10.1088/0067-0049/186/2/378. arXiv: 0903.3037 [astro-ph.HE].
- [463] I. Tuohy and G. Garmire. “Discovery of a compact X-ray source at the center of the supernova remnant RCW 103”. In: *ApJL* 239 (Aug. 1980), pp. L107–L110. DOI: 10.1086/183303.
- [464] M. J. L. Turner et al. “The European Photon Imaging Camera on XMM-Newton: The MOS cameras : The MOS cameras”. In: *A&A* 365 (Jan. 2001), pp. L27–L35. DOI: 10.1051/0004-6361:20000087. eprint: astro-ph/0011498.
- [465] R. Turolla. “Isolated Neutron Stars: The Challenge of Simplicity”. In: *Astrophysics and Space Science Library*. Ed. by W. Becker. Vol. 357. Astrophysics and Space Science Library. 2009, p. 141. DOI: 10.1007/978-3-540-76965-1_7.
- [466] R. Turolla and P. Esposito. “Low-Magnetic-Field Magnetars”. In: *International Journal of Modern Physics D* 22, 1330024 (Nov. 2013), p. 1330024. DOI: 10.1142/S0218271813300243. arXiv: 1303.6052 [astro-ph.HE].
- [467] R. Turolla, S. Zane and A. L. Watts. “Magnetars: the physics behind observations. A review”. In: *Reports on Progress in Physics* 78.11, 116901 (Nov. 2015), p. 116901. DOI: 10.1088/0034-4885/78/11/116901. arXiv: 1507.02924 [astro-ph.HE].
- [468] R. Turolla et al. “Is SGR 0418+5729 Indeed a Waning Magnetar?” In: *ApJ* 740, 105 (Oct. 2011), p. 105. DOI: 10.1088/0004-637X/740/2/105. arXiv: 1107.5488 [astro-ph.HE].
- [469] P. Ubertini et al. “IBIS: The Imager on-board INTEGRAL”. In: *A&A* 411 (Nov. 2003), pp. L131–L139. DOI: 10.1051/0004-6361:20031224.
- [470] G. V. Ustyugova et al. ““Propeller” Regime of Disk Accretion to Rapidly Rotating Stars”. In: *ApJ* 646 (July 2006), pp. 304–318. DOI: 10.1086/503379. eprint: astro-ph/0603249.
- [471] A. J. van der Horst et al. “Discovery of a New Soft Gamma Repeater: SGR J0418 + 5729”. In: *ApJL* 711 (Mar. 2010), pp. L1–L6. DOI: 10.1088/2041-8205/711/1/L1. arXiv: 0911.5544 [astro-ph.HE].

- [472] M. van der Klis. “Fourier Techniques in X-ray Timing”. In: *Timing Neutron Stars*, eds. H. Ogelman and E.P.J. van den Heuvel. *NATO ASI Series C*, Vol. 262, p. 27-70. Dordrecht: Kluwer, 1988. Vol. 262. 1988, pp. 27–70.
- [473] M. H. van Kerkwijk and D. L. Kaplan. “Isolated neutron stars: magnetic fields, distances, and spectra”. In: *AP&SS* 308 (Apr. 2007), pp. 191–201. DOI: 10.1007/s10509-007-9343-9. eprint: astro-ph/0607320.
- [474] M. H. van Kerkwijk et al. “Spectral and Rotational Changes in the Isolated Neutron Star RX J0720.4-3125”. In: *ApJL* 659 (Apr. 2007), pp. L149–L152. DOI: 10.1086/518030. eprint: astro-ph/0703326.
- [475] J. van Paradijs, R. E. Taam and E. P. J. van den Heuvel. “On the nature of the ‘anomalous’ 6-s X-ray pulsars”. In: *A&A* 299 (July 1995), p. L41.
- [476] J. van Paradijs and F. Verbunt. “A comparison of soft x-ray transients and dwarf novae”. In: *American Institute of Physics Conference Series*. Ed. by S. E. Woosley. Vol. 115. American Institute of Physics Conference Series. May 1984, pp. 49–62. DOI: 10.1063/1.34556.
- [477] B. A. Vaughan et al. “Searches for millisecond pulsations in low-mass X-ray binaries, 2”. In: *ApJ* 435 (Nov. 1994), pp. 362–371. DOI: 10.1086/174818.
- [478] S. Vaughan et al. “On characterizing the variability properties of X-ray light curves from active galaxies”. In: *MNRAS* 345 (Nov. 2003), pp. 1271–1284. DOI: 10.1046/j.1365-2966.2003.07042.x. eprint: astro-ph/0307420.
- [479] F. Verbunt. “Origin and evolution of X-ray binaries and binary radio pulsars”. In: *Annu. Rev. Astro. Astrophys.* 31 (1993), pp. 93–127. DOI: 10.1146/annurev.aa.31.090193.000521.
- [480] F. Verbunt et al. “Cataclysmic variables in the ROSAT PSPC All Sky Survey.” In: *A&A* 327 (Nov. 1997), pp. 602–613.
- [481] D. A. Verner et al. “Atomic Data for Astrophysics. II. New Analytic FITS for Photoionization Cross Sections of Atoms and Ions”. In: *ApJ* 465 (July 1996), p. 487. DOI: 10.1086/177435. eprint: astro-ph/9601009.
- [482] D. Viganò and J. A. Pons. “Central compact objects and the hidden magnetic field scenario”. In: *MNRAS* 425 (Oct. 2012), pp. 2487–2492. DOI: 10.1111/j.1365-2966.2012.21679.x. arXiv: 1206.2014 [astro-ph.SR].
- [483] D. Viganò et al. “An assessment of the pulsar outer gap model - I. Assumptions, uncertainties, and implications on the gap size and the accelerating field”. In: *MNRAS* 447 (Mar. 2015), pp. 2631–2648. DOI: 10.1093/mnras/stu2564. arXiv: 1412.1289 [astro-ph.HE].
- [484] D. Viganò et al. “An assessment of the pulsar outer gap model - II. Implications for the predicted γ -ray spectra”. In: *MNRAS* 447 (Mar. 2015), pp. 2649–2657. DOI: 10.1093/mnras/stu2565. arXiv: 1412.1290 [astro-ph.HE].

- [485] D. Viganò et al. “Compact formulae, dynamics and radiation of charged particles under synchro-curvature losses”. In: *MNRAS* 447 (Feb. 2015), pp. 1164–1172. DOI: 10.1093/mnras/stu2456. arXiv: 1411.5836 [astro-ph.HE].
- [486] D. Viganò et al. “Spectral features in isolated neutron stars induced by inhomogeneous surface temperatures”. In: *MNRAS* 443 (Sept. 2014), pp. 31–40. DOI: 10.1093/mnras/stu1109. arXiv: 1406.0874 [astro-ph.HE].
- [487] D. Viganò et al. “Unifying the observational diversity of isolated neutron stars via magneto-thermal evolution models”. In: *MNRAS* 434 (Sept. 2013), pp. 123–141. DOI: 10.1093/mnras/stt1008. arXiv: 1306.2156 [astro-ph.SR].
- [488] J. K. Vogel et al. “NuSTAR Observations of the Magnetar 1E 2259+586”. In: *ApJ* 789, 75 (July 2014), p. 75. DOI: 10.1088/0004-637X/789/1/75. arXiv: 1408.0768 [astro-ph.HE].
- [489] L. Wallace and K. Hinkle. “Medium-Resolution Spectra of Normal Stars in the K Band”. In: *ApJS* 111 (Aug. 1997), pp. 445–458. DOI: 10.1086/313020.
- [490] R. Walter et al. “High-mass X-ray binaries in the Milky Way. A closer look with INTEGRAL”. In: *A&ARv*. 23, 2 (Aug. 2015), p. 2. DOI: 10.1007/s00159-015-0082-6. arXiv: 1505.03651 [astro-ph.HE].
- [491] Z. Wang et al. “An Accurate Determination of the Optical Periodic Modulation in the X-Ray Binary SAX J1808.4-3658”. In: *ApJ* 694 (Apr. 2009), pp. 1115–1120. DOI: 10.1088/0004-637X/694/2/1115. arXiv: 0812.2815.
- [492] Z. Wang et al. “Multiband Studies of the Optical Periodic Modulation in the X-Ray Binary SAX J1808.4-3658 during Its Quiescence and 2008 Outburst”. In: *ApJ* 765, 151 (Mar. 2013), p. 151. DOI: 10.1088/0004-637X/765/2/151. arXiv: 1108.4745 [astro-ph.HE].
- [493] Z. Wang et al. “SDSS J102347.6+003841: A Millisecond Radio Pulsar Binary That Had a Hot Disk During 2000-2001”. In: *ApJ* 703 (Oct. 2009), pp. 2017–2023. DOI: 10.1088/0004-637X/703/2/2017. arXiv: 0905.3899 [astro-ph.HE].
- [494] B. Warner. “Cataclysmic variable stars.” In: *Cambridge Astrophysics Series* 28 (1995).
- [495] M. C. Weisskopf et al. “Chandra X-ray Observatory (CXO): overview”. In: *X-Ray Optics, Instruments, and Missions III*. Ed. by J. E. Truemper and B. Aschenbach. Vol. 4012. July 2000, pp. 2–16. eprint: astro-ph/0004127.
- [496] R. S. Wharton et al. “Multiwavelength Constraints on Pulsar Populations in the Galactic Center”. In: *ApJ* 753, 108 (July 2012), p. 108. DOI: 10.1088/0004-637X/753/2/108. arXiv: 1111.4216 [astro-ph.HE].
- [497] N. E. White and K. O. Mason. “The structure of low-mass X-ray binaries”. In: 40 (Feb. 1985), pp. 167–194. DOI: 10.1007/BF00212883.

- [498] R. Wijnands and M. van der Klis. “A millisecond pulsar in an X-ray binary system”. In: *Nature* 394 (July 1998), pp. 344–346. DOI: 10.1038/28557.
- [499] R. Wijnands et al. “The XMM-Newton/Chandra monitoring campaign of the Galactic center region. Description of the program and preliminary results”. In: *A&A* 449 (Apr. 2006), pp. 1117–1127. DOI: 10.1051/0004-6361:20054129. eprint: astro-ph/0508648.
- [500] R. Willingale et al. “Calibration of X-ray absorption in our Galaxy”. In: *MNRAS* 431 (May 2013), pp. 394–404. DOI: 10.1093/mnras/stt175. arXiv: 1303.0843 [astro-ph.HE].
- [501] J. Wilms, A. Allen and R. McCray. “On the Absorption of X-Rays in the Interstellar Medium”. In: *ApJ* 542 (Oct. 2000), pp. 914–924. DOI: 10.1086/317016. eprint: astro-ph/0008425.
- [502] J. Wilms et al. “Don’t Use Wabs - Improved Absorption Models for the ISM”. In: *AAS/High Energy Astrophysics Division #11*. Vol. 42. Bulletin of the American Astronomical Society. Mar. 2010, p. 674.
- [503] P. M. Woods et al. “X-Ray Bursts from the Transient Magnetar Candidate XTE J1810-197”. In: *ApJ* 629 (Aug. 2005), pp. 985–997. DOI: 10.1086/431476. eprint: astro-ph/0505039.
- [504] S. E. Woosley and R. K. Wallace. “The thermonuclear model for gamma-ray bursts”. In: *ApJ* 258 (July 1982), pp. 716–732. DOI: 10.1086/160120.
- [505] G. A. Wynn and A. R. King. “Theoretical X-ray power spectra of intermediate polars”. In: *MNRAS* 255 (Mar. 1992), pp. 83–91. DOI: 10.1093/mnras/255.1.83.
- [506] G. Younes, C. Kouveliotou and V. M. Kaspi. “XMM-Newton Observations of SGR 1806-20 Over Seven Years Following the 2004 Giant Flare”. In: *ApJ* 809, 165 (Aug. 2015), p. 165. DOI: 10.1088/0004-637X/809/2/165. arXiv: 1507.05985 [astro-ph.HE].
- [507] G. Younes et al. “XMM-Newton View of Swift J1834.9-0846 and Its Magnetar Wind Nebula”. In: *ApJ* 757, 39 (Sept. 2012), p. 39. DOI: 10.1088/0004-637X/757/1/39. arXiv: 1206.3330 [astro-ph.HE].
- [508] T. Yuasa et al. “White dwarf masses in intermediate polars observed with the Suzaku satellite”. In: *A&A* 520, A25 (Sept. 2010), A25. DOI: 10.1051/0004-6361/201014542. arXiv: 1006.5323 [astro-ph.HE].
- [509] C. Zanni and J. Ferreira. “MHD simulations of accretion onto a dipolar magnetosphere. II. Magnetospheric ejections and stellar spin-down”. In: *A&A* 550, A99 (Feb. 2013), A99. DOI: 10.1051/0004-6361/201220168. arXiv: 1211.4844 [astro-ph.SR].

- [510] V. E. Zavlin et al. “Discovery of 424 Millisecond Pulsations from the Radio-quiet Neutron Star in the Supernova Remnant PKS 1209-51/52”. In: *ApJL* 540 (Sept. 2000), pp. L25–L28. DOI: 10.1086/312866. eprint: astro-ph/0005548.
- [511] A. A. Zdziarski, W. N. Johnson and P. Magdziarz. “Broad-band γ -ray and X-ray spectra of NGC 4151 and their implications for physical processes and geometry.” In: *MNRAS* 283 (Nov. 1996), pp. 193–206. DOI: 10.1093/mnras/283.1.193. eprint: astro-ph/9607015.
- [512] R. M. Zerbi et al. “The REM telescope: detecting the near infra-red counterparts of Gamma-Ray Bursts and the prompt behavior of their optical continuum”. In: *Astronomische Nachrichten* 322 (Dec. 2001), pp. 275–285. DOI: 10.1002/1521-3994(200112)322:5/6<275::AID-ASNA275>3.0.CO;2-N.
- [513] S. Zhang et al. “Hard X-Ray Morphological and Spectral Studies of the Galactic Center Molecular Cloud Sgr B2: Constraining Past Sgr A* Flaring Activity”. In: *ApJ* 815, 132 (Dec. 2015), p. 132. DOI: 10.1088/0004-637X/815/2/132. arXiv: 1507.08740 [astro-ph.HE].
- [514] P. Zhou et al. “Discovery of the Transient Magnetar 3XMM J185246.6+003317 near Supernova Remnant Kesteven 79 with XMM-Newton”. In: *ApJL* 781, L16 (Jan. 2014), p. L16. DOI: 10.1088/2041-8205/781/1/L16. arXiv: 1310.7705 [astro-ph.HE].
- [515] C. Zurita, J. Casares and T. Shahbaz. “Evidence for Optical Flares in Quiescent Soft X-Ray Transients”. In: *ApJ* 582 (Jan. 2003), pp. 369–381. DOI: 10.1086/344534.
- [516] P. T. Życki, C. Done and D. A. Smith. “The 1989 May outburst of the soft X-ray transient GS 2023+338 (V404 Cyg)”. In: *MNRAS* 309 (Nov. 1999), pp. 561–575. DOI: 10.1046/j.1365-8711.1999.02885.x. eprint: astro-ph/9904304.

List of publications

Publications directly related to this thesis.

Papers published in international refereed journals.

1. Rea N., Borghese A., Esposito P., Coti Zelati F., Bachetti M., Israel G. L., De Luca A. (2016), **Magnetar-like activity from the central compact object in the SNR RCW 103**, *The Astrophysical Journal Letters*, 828, 13
2. Campana S., Coti Zelati F., Papitto A., Rea N., Torres D. F., Baglio M. C., D'Avanzo P. (2016), **A physical scenario for the high and low X-ray luminosity states in the transitional pulsar PSR J1023+0038**, *Astronomy & Astrophysics*, 594, 31
3. Ponti G., Jin C., De Marco B., Rea N., Rau A., Haberl F., Coti Zelati F., Bozzo E., Ferrigno C., Bower G. C., Demorest P. (2016), **Swift J174540.7–290015: a new accreting binary in the Galactic Centre**, *Monthly Notices of the Royal Astronomical Society*, MNRAS, 461, 2688
4. Baglio M. C., D'Avanzo P., Campana S., Coti Zelati F., Covino S., Russell D. M. (2016), **Different twins in the millisecond pulsar recycling scenario: optical polarimetry of PSR J1023+0038 and XSS J12270–4859**, *Astronomy & Astrophysics*, 591, 101
5. Pintore F., Bernardini F., Mereghetti S., Esposito P., Turolla R., Rea N., Coti Zelati F., Israel G. L., Tiengo A., Zane S. (2016), **The variable spin-down rate of the transient magnetar XTE J1810–197**, *Monthly Notices of the Royal Astronomical Society*, 458, 2088
6. Israel G. L., Esposito P., Rea N., Coti Zelati F., Tiengo A., Campana S., Mereghetti S., Rodriguez Castillo G. A., Götz D., Burgay M., Possenti A., Zane S., Turolla R., Perna R., Cannizzaro G., Pons J. (2016), **The discovery, monitoring and environment of SGR J1935–2154**, *Monthly Notices of the Royal Astronomical Society*, MNRAS, 457, 3448

7. Coti Zelati F., Rea N., Campana S., de Martino D., Papitto A., Safi-Harb S., Torres D. F. (2016), **Multiwavelength study of RX J2015.6+3711: a magnetic cataclysmic variable with a 2-h spin period**, *Monthly Notices of the Royal Astronomical Society*, 456, 1913
8. Borghese A., Rea N., Coti Zelati F., Tiengo A., Turolla R. (2015), **Discovery of a strongly phase-variable spectral feature in the isolated neutron star RX J0720.4–3125**, *The Astrophysical Journal Letters*, 807L, 20
9. Pennucci T. T., Possenti A., Esposito P., Rea N., Haggard D., Baganoff F. K., Burgay M., Coti Zelati F., Israel G. L., Minter A. (2015), **Simultaneous multi-band radio and X-ray observations of the Galactic Center magnetar SGR J1745–2900**, *The Astrophysical Journal*, 808, 81
10. Coti Zelati F., Rea N., Papitto A., Viganò D., Pons J. A., Turolla R., Esposito P., Haggard D., Baganoff F. K., Ponti G., Israel G. L., Campana S., Torres D. F., Tiengo A., Mereghetti S., Perna R., Zane S., Mignani R. P., Possenti A., Stella L. (2015), **The X-ray outburst of the Galactic Centre magnetar SGR J1745–2900 during the first 1.5 year**, *Monthly Notices of the Royal Astronomical Society*, 449, 2685
11. Coti Zelati F., Baglio M. C., Campana S., D’Avanzo P., Goldoni P., Masetti N., Muñoz-Darias T., Covino S., Fender R. P., Jiménez Bailón E., Oti-Floranes H., Palazzi E., Ramón-Fox F. G. (2014), **Engulfing a radio pulsar: the case of PSR J1023+0038**, *Monthly Notices of the Royal Astronomical Society*, 444, 1783

Papers submitted or in preparation.

12. Coti Zelati F. et al., **Systematic study of magnetar X-ray outbursts**, to be submitted to *Monthly Notices of the Royal Astronomical Society*
13. Coti Zelati F. et al., **Chandra monitoring of the Galactic Centre magnetar SGR J1745–2900 during the initial 3.5 years of outburst decay**, to be submitted to *Monthly Notices of the Royal Astronomical Society*
14. Rea N., Coti Zelati F., Esposito P., D’Avanzo P., de Martino D., Israel G. L., Torres D. F., Campana S., Belloni T. M., Papitto A., Masetti N., Carrasco L., Possenti A., Wieringa M., De Oña Wilhelmi E., Li J., Bozzo E., Ferrigno C., Linares M., Tauris T. M., Hernanz M., Ribas I., Monelli M., Borghese A., Baglio M. C., Casares J. **Multi-band study of a new asynchronous magnetic cataclysmic variable and a flaring X-ray source**, submitted to *Monthly Notices of the Royal Astronomical Society* [arXiv:1611.04194]
15. Borghese A., Rea N., Coti Zelati F., Tiengo A., Turolla R., Zane S. (2016), **Detections and limits on narrow phase-dependent features in X-ray Dim Isolated Neutron Stars**, submitted to *Monthly Notices of the Royal Astronomical Society*

Proceedings of international conferences.

16. Zhang S. N. et al. (2016), **eXTP: Enhanced X-ray Timing and Polarization mission**, Proceedings of the *Society of Photo-Optical Instrumentation Engineers (SPIE)*, 9905
17. Coti Zelati F., Rea N., Papitto A., Viganò D., Pons J. A., Turolla R., Esposito P., Haggard D., Baganoff F. K., Ponti G., Israel G. L., Campana S., Torres D. F., Tiengo A., Mereghetti S., Perna R., Zane S., Mignani R. P., Possenti A., Stella L. (2015), **The X-ray outburst of the Galactic Centre magnetar SGR J1745–2900 as monitored by Chandra and XMM-Newton**, proceedings of the conference: ‘*Swift: 10 Years of Discovery*’

Astronomer’s Telegrams.

18. Burgay M., Possenti A., Kerr M., Esposito P., Rea N., Coti Zelati F., Israel G. L., Johnston S. (2016), **Pulsed Radio Emission from PSR J1119–6127 re-activated**, *The Astronomer’s Telegram*, 9366, 1
19. Burgay M., Possenti A., Kerr M., Esposito P., Rea N., Coti Zelati F., Israel G. L., Johnston S. (2016), **Pulsed Radio Emission from PSR J1119–6127 disappeared**, *The Astronomer’s Telegram*, 9286, 1
20. Bower G. C., Demorest P., Baganoff F., Corrales L., Deller A., Dexter J., Haggard D., Markoff S., Rea N., Coti Zelati F. (2016), **A Search for a Radio Counterpart to Swift J174540.7–290015**, *The Astronomer’s Telegram*, 8793, 1
21. Baganoff G. C., Corrales L. R., Neilsen J., Nowak M. A., Rea N., Coti Zelati F., Haggard D., Markoff S., Ponti G., Bower G. C., Garmire G. P. (2016), **Chandra position of Galactic Center X-ray Transient Swift J174540.7–290015**, *The Astronomer’s Telegram*, 8746, 1
22. Coti Zelati F., Campana S., Israel G. L., Rea N., Mereghetti S., Esposito P., Tiengo A. (2016), **Swift/XRT follow-up observation of SGR J1935+2154**, *The Astronomer’s Telegram*, 8449, 1
23. Coti Zelati F., Papitto A., Rea N., Bozzo E., Ferrigno C. (2015), **Swift follow-up observation of ASASSN-15tx**, *The Astronomer’s Telegram*, 8422, 1
24. Campana S., D’Avanzo P., Baglio M. C., Coti Zelati F., Kennea J. (2015), **Very rapid turn on of SAX J1808.4–3658**, *The Astronomer’s Telegram*, 7379, 1
25. D’Avanzo P., Campana S., Coti Zelati F., Palmer D. (2015), **Swift/XRT early time observations of SGR 1935+2154**, *The Astronomer’s Telegram*, 7138, 1

26. Burgay M., Israel G. L., Rea N., Possenti A., Coti Zelati F., Esposito P., Mereghetti S., Tiengo A. (2014), **Parke** upper limits on the pulsed radio emission of SGR 1935+2154, *The Astronomer's Telegram*, 6371, 1
27. Israel G. L., Rea N., Coti Zelati F., Esposito P., Burgay M., Mereghetti S., Possenti A., Tiengo A. (2014), **Chandra** discovery of 3.2s X-ray pulsations from SGR 1935+2154, *The Astronomer's Telegram*, 6370, 1
28. Haggard D., Baganoff F. K., Rea N., Coti Zelati F., Ponti G., Heinke C., Campana S., Israel G. L. Yusef-Zadeh F., Roberts D. (2014), **2014 Chandra X-ray Monitoring of Sgr A*/G2 and SGR J1745–29**, *The Astronomer's Telegram*, 6242, 1

GRB Coordinates Network circulars and reports.

29. Campana S., de Ugarte Postigo A., Thoene C. C., Gorosabel J., Rea N., Coti Zelati F. (2014), **Pre-discovery of SGR 1935+2154 in Swift archival observations**, *GRB Coordinates Network*, 16535, 1

Posters at international conferences.

30. Coti Zelati F., Rea N., Esposito P., D'Avanzo P., de Martino D., Borghese A. (2016), **Multi-band study of a new asynchronous magnetic cataclysmic variable**, poster for the *EXTraS Workshop* (Pavia)
31. Haggard D., Rea N., Coti Zelati F., Heinke C. O., Koch E., Bahramian A., Mori K., Degenaar N., Ponti G., Baganoff F. K. (2014), **New and Recurring Galactic Center X-ray Transients from Chandra, Swift, and XMM**, poster for the *14th Meeting of the American Astronomical Society High Energy Astrophysics Division* (Chicago)

Acknowledgements

Ringrazio Sergio e Nanda per la loro supervisione nel corso del mio dottorato. Devo a loro molto sia da un punto di vista professionale, per aver sempre risposto con chiarezza ai miei dubbi, sia da un punto di vista ‘umano’, per aver creato un’atmosfera stimolante e ricca di allegria. Ringrazio il professor Treves, per avermi concesso la libertà assoluta di scegliere dove poter svolgere i miei progetti di ricerca in questi anni, e Jason Hessels e Niccolò Bucciantini, per aver contribuito a migliorare la presentazione dei risultati contenuti in questa tesi.

Ringrazio tutti i miei amici che mi hanno aiutato a distrarmi dal lavoro in questi anni. Elencare tutte le esperienze condivise sarebbe impossibile, ma indubbiamente il mio livello di serenità e concentrazione al lavoro sarebbe stato decisamente più scarso senza le interminabili escursioni scialpinistiche e le più tranquille passeggiate sui monti sorgenti, le epiche avventure in barca a vela in compagnia del coraggioso equipaggio dell’Asentropé, le infinite serate in compagnia al bar di sempre e non solo, i viaggi estivi tra cui la ‘conquista’ del Gran Sasso, il giro dei Balcani e le Azzorre e, non da ultimo, le esperienze di volontariato con Legambiente e Libera, durante le quali ho anche avuto la possibilità di sfoggiare le mie (in)dubbe conoscenze astronomiche davanti al ‘grande’ pubblico internazionale. E si potrebbe proseguire all’infinito... Ringrazio chi si è ritagliato un po’ del proprio tempo per venire a farmi visita ad Amsterdam in più di un’occasione. Ringrazio Giada per le piacevolissime chiacchierate a ruota libera, i continui confronti sulle tematiche filosofico-scientifiche e il suo costante entusiasmo per i miei studi.

Ringrazio i miei ‘colleghi’ astrofisici dell’osservatorio astronomico di Merate, in particolare per aver sempre riposto la più totale fiducia nei miei confronti nello svolgere alcuni delicati compiti in foresteria, tra cui salare l’acqua per la pasta e smistare le porzioni. Grazie ai colleghi e amici dell’area Swift: Deborah, Cristina, Paolo, Andrea, Maria Grazia e Roga. Restano indelebili nella mia mente le lunghissime giornate trascorse in compagnia di Deb e Cri ai congressi e alle scuole di dottorato, dove si sono dimostrate estremamente efficaci nel ‘mettermi in luce’ di fronte ai grandi luminari della scienza (soprattutto nel corso delle cene e degli eventi sociali, approfittando della mia innegabile passione per i vini e gli amari e della mia decisamente rivedibile propensione al canto).

Thanks to all the wonderful people I had the luck to meet in Amsterdam. My first ac-

knowledge goes to Alice, in particular for her support during those periods where my workload was getting unmanageable and for her punctuality in answering to my doubts. I guess that attending schools and conferences with me was not exactly on the top of her wishes, yet there were also many pleasant things that we did together in these years! I thank Daniele, without whom probably I would be still locked out of my flat since a freezing winter night and these acknowledgements would never have begun. Thanks Rachel, Macla and Ylva for kindly hosting me during these years. I hope I managed to repay their kindness, at least minimally, with some tasty Italian dinners. I owe Macla a huge improvement in my dancing skills and I thank Ylva for teaching me several housekeeping tips that made every single corner of her flat shine. I thank my office mates, Dario, Yuri, Tullio, Gullo, Amruta, Nina, Mathieu, Manos, for having made the working environment particularly lively. I thank Gullo for our daily 'NBA group meetings', excellent to distract from the work. I thank Amruta for her masterful lectures on pulsars and for preparing delicious Indian food that I had the opportunity to taste in many occasions. Thanks Nina for all your time, the Russian food and the beautiful walks in the park. I thank Alicia, Chris, Chiara, Georgi, Kaustubh, Liliana, Oscar, Stefano, Theo and Tom (rigorously in alphabetical order) because their happiness and humour always made me optimistic. I thank Dario for having coined a new nickname that still echoes unmistakably in the corridors of the building (I could recognize Tom's voice among a trillion of different voices). I thank Paolo for teaching me many things since he arrived in Amsterdam half a year ago. I could also appreciate his undoubted artistic talent. I thank Susan, Milena and Vivian for their availability at any time and their persistent kindness. Thanks to all APIs for all the time spent together, including the sport events (football, volleyball, beach volleyball, curling), the unique dinners with polenta, champignon and Chianti, sushi (also homemade, thanks Felicia!), lobsters, hamburgers and more exotic cuisines. Thanks for all the parties (special thanks to the API's party house!) and the many beers at the Windmill and at the Oerknal...

I thank all the people I met in Barcelona during my repeated visits: Daniele, Alessandro, Jonatan, Nuria, Laura, Carles, Padu, Jian and I am forgetting someone else for sure. We enjoyed many interesting activities together, such as intense beach volleyball matches, dinners, concerts, the open-air cinema and above all the two-day long trip on the Pyrenees. I perfectly remember that extremely windy night spent in our small tent in the middle of nowhere under a stunning starry sky. I also attended an amazing expedition on the top of Gran Paradiso in the summer holidays with some of them, and my absolute lack of training in the flatness of the Netherlands in the previous months certainly made the trip even for epic for me. I thank in particular Daniele for the numerous conversations, for listening to my worries and doubts and for giving me always useful suggestions.

Desidero infine ringraziare la mia famiglia, a cui dedico la tesi. Mamma, papà, Michele: non mi avete mai fatto mancare il vostro sostegno morale e affettivo, specialmente nei momenti più difficili. Grazie di cuore.

*Francesco (Ciccio)
Calolziocorte, gennaio 2017*